Technische Universität München

TUM School of Natural Sciences

Elucidating the Degradation Mechanisms of Nickel-Rich Layered Oxide Cathodes for Lithium-Ion Batteries

Stefan Oswald

Vollständiger Abdruck der von der TUM School of Natural Sciences der Technischen Universität München zur Erlangung des akademischen Grades eines

Doktors der Naturwissenschaften (Dr. rer. nat.)

genehmigten Dissertation.

Vorsitz: Prof. Dr. Marc Georg Willinger

Prüfende der Dissertation: 1. Prof. Dr. Hubert A. Gasteiger

2. Prof. Dr. Matteo Bianchini (Universität Bayreuth)

3. Prof. Dr. Clare P. Grey (University of Cambridge)

Abstract

The available capacity of layered transition metal oxides, used as cathode active materials (CAMs) in lithium-ion batteries (LIBs), deteriorates during operation, thereby limiting the lifetime of a battery cell. To develop a more comprehensive and quantitative understanding of the mechanisms responsible for the associated capacity loss, including particle cracking and oxygen release, in this thesis, the degradation phenomena of nickel-rich CAMs are investigated combining surface area determination by krypton-gas physisorption (Kr-BET), electrochemical impedance spectroscopy (EIS) using a micro-reference electrode (µ-RE), and on-line electrochemical mass spectrometry (OEMS). To assess the impact of particle cracking, a novel impedance-based technique is developed and validated, which is then applied to quantify the extent of the cracking of CAM particles upon mechanical compression, upon extended charge/ discharge cycling, as well as at high state of charge. Single-crystalline particles, being one possible candidate to alleviate particle cracking, are benchmarked against their conventional polycrystalline analog – not only to evaluate the effect of the particle morphology on fundamental properties such as the extent of gas evolution, the dissolution of transition metals, and the (chemo)mechanical and thermal stability but also to elucidate their consequences on the performance in full-cells. Regarding their structural stability, the onset of the release of lattice oxygen at high degrees of delithiation is determined, exposing significant differences in the stability limit and thus in the available capacity of layered-transition-metal-oxide CAMs dependent on their composition.

Kurzfassung

Die verfügbare Kapazität von Übergangsmetallschichtoxiden, die als Kathodenaktivmaterialien (CAMs) in Lithiumionenbatterien (LIBs) eingesetzt werden, nimmt während des Betriebs ab, was die Lebensdauer einer Batteriezelle limitiert. Um ein umfassenderes und quantitatives Verständnis der Mechanismen zu entwickeln, die für den damit einhergehenden Kapazitätsverlust verantwortlich sind, werden die Degradationsphänomene von nickelreichen Kathodenaktivmaterialien, unter anderem das Brechen von Partikeln und die Sauerstoffentwicklung, in dieser Arbeit mittels Oberflächenbestimmung durch Kryptongasphysisorption (Kr-BET), elektrochemischer Impedanzspektroskopie (EIS) mithilfe einer Mikroreferenzelektrode (µ-RE) sowie elektrochemischer Massenspektrometrie (OEMS) untersucht. Um die Auswirkung des Brechens von Partikeln einzuschätzen wird eine neuartige impedanzbasierte Technik entwickelt und validiert, die dann angewendet wird, um das Ausmaß des Brechens von Kathodenaktivmaterialpartikeln durch mechanisches Verpressen, über zahlreiche Lade- und Entladezyklen oder bei hohen Ladezuständen zu quantifizieren. Einkristalline Partikel, die ein möglicher Materialansatz zur Abschwächung des Brechens von Partikeln sind, werden mit ihrem konventionellen polykristallinen Analogon verglichen – nicht nur um den Einfluss der Partikelmorphologie auf fundamentale Eigenschaften wie das Ausmaß der Gasentwicklung, die Übergangsmetallauflösung und die chemo-(mechanische) und thermische Stabilität zu bewerten, sondern auch um ihre Auswirkungen auf das Verhalten in Vollzellen aufzuklären. Im Bezug auf ihre strukturelle Stabilität wird das Einsetzen der Sauerstoffentwicklung bei hohen Delithiierungszuständen bestimmt, was signifikante Unterschiede des Stabilitätslimits und folglich der verfügbaren Kapazität von Übergangsmetallschichtoxid-basierten Kathodenaktivmaterialien aufdeckt.

List of Acronyms

Abbreviation	Description
BET	Brunauer-Emmett-Teller
BEV	battery electric vehicle
CAM	cathode active material
CC	constant-current or current collector
CCCV	constant-current/constant-voltage
CE	Coulombic efficiency
CEI	cathode-electrolyte interphase
CMC	carboxymethyl cellulose
CPE	constant-phase element
CV	constant voltage
DCIR	direct-current internal resistance
DMC	dimethyl carbonate
EC	ethylene carbonate
EV	electric vehicle
EIS	electrochemical impedance spectroscopy
FEC	fluoroethylene carbonate
FIB	focused ion beam
GEIS	galvano electrochemical impedance spectroscopy
GITT	galvanostatic intermittent titration technique
GWRE	gold-wire reference electrode
HF	high-frequency or hydrofluoric acid
LCO	lithium cobalt oxide
LEDC	lithium ethylene dicarbonate
LF	low-frequency
LFO	lithium difluorophosphate
LFP	lithium iron phosphate
LIB	lithium-ion battery

LMR-NCM	lithium- and manganese-rich NCM
LNO	lithium nickel oxide
LNMO	lithium nickel manganese oxide
LTO	lithium titanate
μ-RE	micro-reference electrode
MS	mass spectrometry
NCA	lithium nickel cobalt aluminum oxide
NCM	lithium nickel cobalt manganese oxide
NMP	N-methyl-2-pyrrolidone
OCP	open-circuit potential
OCV	open-circuit voltage
OEMS	on-line electrochemical mass spectrometry
PC	polycrystalline or propylene carbonate
PEIS	potentio electrochemical impedance spectroscopy
PVDF	polyvinylidene difluoride
SBR	styrene butadiene rubber
SC	single-crystalline
SEI	solid-electrolyte interphase
SEM	scanning electron microscopy
SHE	standard hydrogen electrode
SOC	state of charge
TBATFSI	tetramethylammonium bis(trifluoromethanesulfonyl)imide
TEM	transmission electron microscopy
TM	transition metal
TGA	thermogravimetric analysis
V2G	vehicle-to-grid
VC	vinylene carbonate
VGCF	vapor-grown carbon fibers
XRD	X-ray diffraction

What is a scientist after all?
It is a curious man looking through a keyhole,
the keyhole of nature, trying to know what's going on.

Jacques Yves Cousteau (1910 - 1997)

Contents

Contents

1 Introduction

1.1 The Transition into a Low-Carbon Economy

Over the past 800,000 years, the carbon dioxide (CO_2) concentration in the atmosphere of the earth had never exceeded 300 ppm before the appearance of humankind. This mark was first crossed in 1912, and the CO_2 level has increased to a value of 421 ppm as of June 2022 [1, 2].

Since the beginning of the industrial period in the late 18th century, more and more fossil fuels are being consumed producing CO_2 upon combustion, which accumulates in the atmosphere. Within in the same period, the global anthropogenic CO_2 emissions of $10\,\mathrm{Mt_{CO_2}}$/year in 1750 have followed an exponential rise, reaching a 3,500-fold value of $35\,\mathrm{Gt_{CO_2}}$/year in 2021 [1, 3, 4]. Over the past decades, the observed concentrations of gases such as CO_2, methane (CH_4), and nitrous oxide (N_2O) amongst others have hit a new all-time high every year [1]. These so-called greenhouse gases are mostly transparent to the light emitted from the sun, but can absorb, emit, and thus reflect light of the infrared part of the electromagnetic spectrum; hence, the natural greenhouse effect, i.e, the reflection of the thermal radiation from the surface of the earth with a wavelength of 7 to 14 µm, grows with the amount of greenhouse gases in the atmosphere [2, 5].

It is now widely accepted that the anthropogenic emission of these gases has been resulting in and will continue to cause a rise of the average temperature of the earth as well as changes of the climate in general. For the future, not only extreme weathers such as heat waves, storms, floods, and droughts are predicted, but also glacier and sea ice reduction, rising sea levels, and ocean acidification will change the ecosystem [6]. The extent of these phenomena will be dramatic, both for the ecosystem as well as for humanity – if the emission of greenhouse gases remains at such a high level.

Within the Paris Agreement, a legally binding international treaty of 2015, 196 parties committed to decrease greenhouse gas emissions and reach net-zero carbon emissions by the middle of the 21st century, aiming to limit the temperature rise to $2.0\,°C$ as

compared to pre-industrial levels. To achieve this target, the global CO_2 emissions have to be reduced by -4 %/year, while limiting the temperature rise to the preferred value of 1.5 °C requires a reduction in emissions by -8 %/year [7]. So far, based on the average temperature of the 20th century, the global average surface temperature has risen by 1.0 °C [1].

The main contributor to these emissions is the consumption of fossil fuels in industrial processes, in private households, for transportation, and for the generation of electricity. Currently, these processes are mostly based on the combustion of natural oil, gas, and coal. For the transition to a sustainable low-carbon energy economy, these sectors are required to replace fossil fuels with electricity that is generated from renewable sources. The majority of this renewable energy is expected to come from wind, solar, and hydropower, which are not only limited geographically but often alternate periodically, i.e., with time of day or time of year [8]. Therefore, the energy surplus available in times of high power needs to be stored and later consumed during times of low power. The required storage technology is expected to be based on electrochemical processes, due to the relatively high energy density that can be stored and released by the conversion of chemicals.

The electrochemical storage of electrical energy could be based on the production of hydrogen (H_2) in electrolysers during times of a surplus of the electricity production; its later consumption in fuel cells to generate electricity when it is needed [9, 10], however, might not be feasible in the future since the produced H_2 is expected to be essential for chemical processes, e.g., for the production of ammonia, methanol, and steel [11]. Therefore, the short-term storage on the order of hours or days might require rechargeable batteries [12]. In the case of lithium-ion batteries (LIBs), the round-trip energy efficiency, i.e., the ratio of the energy provided by during the discharge of a battery and the one required to charge it, is typically between 75 to 90 % on the system level, making them a highly relevant technology for energy storage in the future [13].

Even though the production capacity of high-energy LIBs has multiplied tenfold over five years from 64 GWh in 2016 to 631 GWh in 2020 [14–16], and even though their prices have dropped by an order of magnitude over the past 20 years from between 1000 and 2000 US$/kWh to between 100 and 200 US$/kWh [15], both mainly driven by the rising numbers in electric vehicle (EV) production [14], batteries with the sole purpose of storing the electricity surplus and releasing it back into the grid when needed are not viable from a cost perspective. Furthermore, since the amount of raw materials for batteries is limited, an efficient use of the available battery capacity is

essential. Therefore, vehicle-to-grid (V2G) operation has been proposed, using the available battery capacity in current and future battery electric vehicles (BEVs) to buffer the fluctuating electricity production and consumption [17]. The application of this concept requires BEVs with the ability to charge bidirectionally to return electric power into the grid during times of high demand. Since the majority of cars is parked at any given time, V2G is receiving rising attention, as it would allow to use the battery capacity of parked cars.

In Germany, more than 50 % of the total electrical energy of 583 TWh produced in 2021 stems from renewable sources, mainly based on solar and wind power, which fluctuate strongly with time of day and with the weather conditions [18–20]. Assuming an average battery pack size of 45 kWh for a typical BEV [21], the current fleet of more than 600.000 BEV passenger cars could store more than 27 GWh, which correspond to 1.7 % of the average daily electricity production of 1.6 TWh [22]. In theory, to hold the entire daily electricity production, the capacity of 36 million average BEVs would be required, which would be fulfilled by the complete electrification of the 49 million passenger cars currently registered in Germany. However, since only the production surplus needs to be stored, a significantly smaller number of BEVs would be already sufficient to buffer the fluctuating electricity production, highlighting the capability and importance of V2G operation in the future.

For this purpose, the state-of-the-art battery technology does not only have to be improved to satisfy the expectation of the customer regarding the driving range of a BEV but also to sustain more load cycles than actually required for solely driving the car. For vehicles which are allocated daily for V2G operation, the battery of a BEV does not only have to operate for the lifetime of the vehicle of more than 15 years but also withstand more than 5,000 charge/discharge cycles. Essentially, the transformation into a sustainable low-carbon energy economy crucially depends on the large-scale availability of durable batteries.

As the cathode active material (CAM) is the largest component of a LIB, both in weight and cost, the focus and purpose of this work is the understanding of the degradation mechanisms of the CAMs, aiming to develop strategies for the future design of improved CAMs. First, the degradation of CAMs induced by particle cracking is elucidated by a newly developed impedance-based method, while its consequences are alleviated by the modification of the particle morphology. Furthermore, the upper potential limit for the stable operation of a CAM, essential to ensure its structural stability at a high degree of delithiation, is determined dependent on its composition.

1.2 Lithium-Ion Battery Technology

The breakthrough of the commercial LIB, introduced by Sony in 1991, was driven by the digital revolution of the 21st century and the rise of portable devices such as mobile phones, cameras, and laptops, where energy and power density are crucial for the usability of the device [14, 23]. Since then, LIBs have become indispensable in diverse technologies such as portable electronics, power tools, medical devices, and electric mobility [14, 23], mainly due to their relatively high energy density of currently 260 Wh/kg or 700 Wh/l; furthermore, they are expected to be a key technology to enable the energy transition.

The Working Principle

State-of-the-art LIBs comprise two insertion electrodes, based either on transition metal (TM) oxides (LiMO$_2$, M being the transition metal) or phosphates (LiMPO$_4$) for the positive electrode and on graphite (C$_6$) (and possibly silicon (Si) or silicon oxide (SiO$_x$)) on the negative electrode, as it is depicted in Figure 1.1. The two electrodes are separated mechanically by a polymeric separator to prevent the physical contact of both electrodes and thus an electrical short circuit. This porous separator is soaked with a lithium-ion-conducting electrolyte, containing alkyl-carbonate-based solvents, a dissociated lithium salt, and possibly electrolyte additives. To ensure a sufficient ionic connection of the active material particles, a porous electrode is manufactured consisting of μm-sized particles, while its pores are also filled by the electrolyte. The proper mechanical stability regarding cohesion of the particles as well as the adhesion of the electrode to the current collector is obtained by using a polymeric binder, whereas conductive additives such as carbon particles or fibers enhance the electronic conductivity within the electrode. The metallic current collector foils, made of aluminum for the positive and of copper for the negative electrode, conduct the electrons from/to the reaction site to/from the external circuit.

In a secondary (i.e., a rechargeable) battery, electrical energy is stored as chemical energy by redox reactions and converted back reversibly. The charging is a non-spontaneous process, which requires external energy to drive the reaction (with the Gibbs free energy being $\Delta G > 0$), while discharging runs spontaneously and provides external energy ($\Delta G < 0$), since the intercalation of lithium ions (Li$^+$) in the positive electrode is thermodynamically favored. To charge the cell, an external source provides
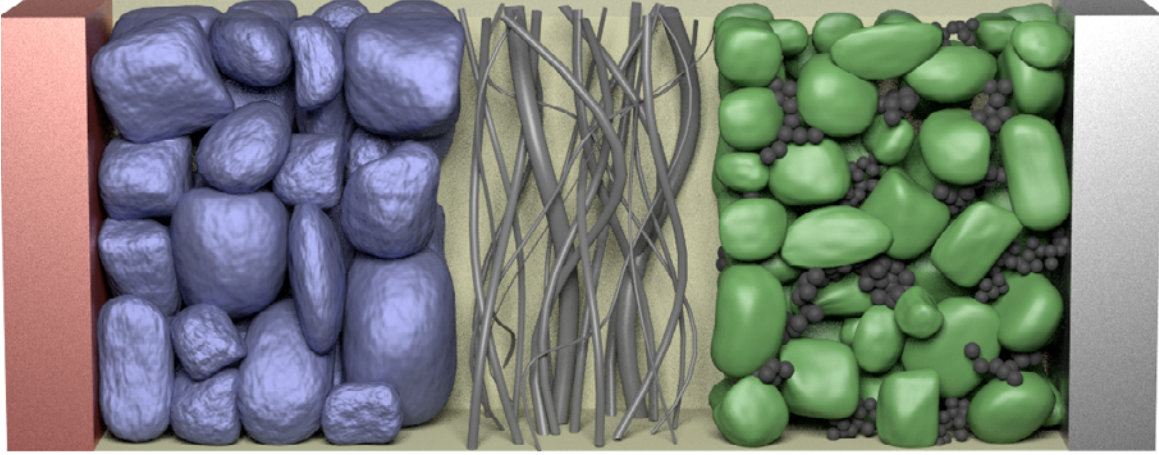
Figure 1.1 Schematic of a lithium-ion battery, consisting of the copper current collector (from left to right), the negative electrode, the separator, the positive electrode including the conductive additive, and the aluminum current collector, while all void space is occupied by electrolyte. Reprinted from Ender [24] under a Creative Commons BY-SA 3.0 DE license.

work and drives electrons from the positive electrode to the negative electrode, which is accompanied by the deintercalation of lithium ions at the positive electrode and a simultaneous intercalation at the negative one, as it is presented for $LiMO_2$ and C_6 in Equations 1.1 and 1.2 (from left to right), respectively.

$$LiMO_2 \rightleftharpoons Li_{1-x}MO_2 + Li^+ + x\,e^- \tag{1.1}$$

$$C_6 + x\,Li^+ + x\,e^- \rightleftharpoons Li_xC_6 \tag{1.2}$$
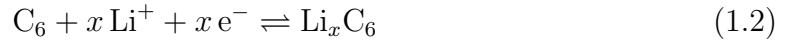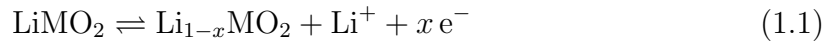
The two half-cell reactions can be combined to the full-cell reaction in Equation 1.3

$$LiMO_2 + C_6 \underset{\text{discharge}}{\overset{\text{charge}}{\rightleftharpoons}} Li_{1-x}MO_2 + Li_xC_6 \tag{1.3}$$
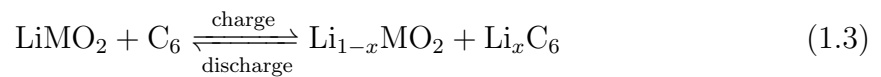
The external electronic current and the consequent lithium (de)intercalation during charge induce a concentration gradient of the conducting ions in the electrolyte, which is compensated by an ionic current between the electrodes. For the discharge, the reactions are reversed (i.e., Equations 1.1, 1.2, and 1.3 occur from right to left), what provides electrical energy and drives the external load. Originating from primary batteries, which only allowed for the discharge reaction, the positive electrode, where the reduction reaction takes place during discharge, is colloquially called cathode, while the negative one is called anode, as the oxidation reaction occurs here during discharge. Even though the host material is reduced/oxidized upon (de)lithiation, ideally, it does not undergo structural or morphological changes, what enables the highly reversible

charge/discharge reactions. The Coulombic efficiency (CE), which is a measure for the reversibility of the reactions and defined in Equation 1.4 by the ratio of the discharge capacity $Q_{\text{discharge}}$ and the charge capacity Q_{charge}, is typically close to 100% during the operation of LIBs (except for the first few so-called formation cycles).

$$\text{CE} = \frac{Q_{\text{discharge}}}{Q_{\text{charge}}} \tag{1.4}$$

Since the electrochemical potential of an electrode rests upon the chemical potential of the active species, e.g., on the environment of the lithium ions in the host structure as well as its degree of (de)lithiation, each active material shows a distinct potential profile, i.e., a curve which relates the potential of the electrode to the degree of (de)lithiation. It has to be noted that potentials which are referenced to the reduction potential of lithium (Li^+/Li) will be marked here using the notation of V_{Li}, whereby $0\,V_{\text{Li}}$ corresponds to -3.04 V against the standard hydrogen electrode (SHE).

The potential difference between the two electrodes results in the cell voltage $E_{\text{cell}} = E_{\text{cathode}} - E_{\text{anode}}$. In the absence of current, this voltage is called open-circuit voltage (OCV), what results from the difference of the open-circuit potential (OCP) of each electrode; during operation, however, overpotentials which arise from various (ohmic, kinetic, and mass-transport-related) resistances and which are required to drive the reaction add to the half-cell potential during delithiation, while they reduce the potential upon lithiation. The electrochemical potential (profile) directly affects the specific energy w (i.e., the gravimetric energy density) of an electrode (in units of Wh/kg), being the ratio of the energy W, either required for the charge or delivered upon discharge, and the (active) material mass m within the electrode

$$w = \frac{W}{m} = \int_0^q E(q')\,\mathrm{d}q' = q \cdot \bar{E} \tag{1.5}$$

which is defined by the integral of the potential $E(q')$ over the exchanged specific capacity (or charge) q (in units of mAh/g)

$$q = \frac{Q}{m} = \frac{z \cdot F}{M} \tag{1.6}$$

and can be simplified by the product of q and the mean potential $\bar{E}$, with Q being the total exchanged capacity, F the Faraday constant of $96,485$ As/mol, z the valency of the active species ($z = 1$ for lithium ions), and M the molar mass of the active

material. The energy required to charge an electrode (or cell) is generally larger than the energy gained during discharge, both due to the mentioned overpotentials required to drive the reaction as well as a CE which is typically just below $100\,\%$. The rate of the complete (dis)charge of an electrode (or battery cell) is commonly expressed by its C-rate (in units of $1/h$), which is defined by the ratio of the applied current I and the total available capacity. If a cell is charged within two hours, the applied current corresponds to a C-rate of $0.5\,1/h$ (or $C/2$).

$$C\text{-rate} = \frac{I}{Q} \tag{1.7}$$

Electrolyte Components and the Solid-Electrolyte Interphase

In contrast to aqueous battery systems such as lead-acid batteries, the higher operating voltage of LIBs requires the use of aprotic, organic **solvents** which are stable towards unwanted electrolyte oxidation up to $4.5\,\mathrm{V_{Li}}$. The commonly used alkyl carbonates include cyclic carbonates such as ethylene carbonate (EC) since they enable the sufficient dissolution of the salt to conducting ions by forming a solvation shell due to their high polarity and the high dielectric constant; in contrast, the added linear carbonates such as ethyl methyl carbonate (EMC) optimize the physical properties of the electrolyte, including its viscosity and its freezing point, to ensure good a ionic conductivity [25].

As conducting **salt**, lithium hexafluorophosphate ($LiPF_6$) is typically used in commercial LIBs, what is owed to its high solubility in non-aqueous, polar solvents and its high conductivity, e.g., of $12\,\mathrm{mS/cm}$ at $25\,^\circ\mathrm{C}$ for LP57 (i.e., 1 M $LiPF_6$ in EC:EMC 3:7 w/w) [26]. In the presence of trace amounts of water, $LiPF_6$ hydrolyzes and forms hydrofluoric acid (HF), additionally producing either lithium fluoride (LiF) and phosphoryl fluoride (POF_3) or lithium difluorophosphate ($LiPO_2F_2$, LFO) [27]. HF does not only passivate and thus protect the aluminum cathode current collector against corrosion upon reaction with its inherent oxide layer forming a passivating layer of aluminum fluoride (AlF_3) [28] but also induces unwanted reactions with the electrode materials, such as the corrosion of the CAM. Furthermore, the disproportionation of the $LiPF_6$ salt

$$LiPF_6 \rightleftharpoons LiF + PF_5 \tag{1.8}$$

is shifted to the right side at elevated temperatures, forming insoluble LiF and reactive phosphorus pentafluoride (PF_5) gas, what induces unwanted side reactions, limiting

the operation temperature of LIBs using $LiPF_6$ as conductive salt to $60\,°C$ [29, 30].

The stability towards the electrochemical oxidation of the mentioned electrolyte components is reported to be limited to $\sim 4.5\,V_{Li}$, at least at $25\,°C$, while electrochemical electrolyte oxidation may already occur at lower potentials for elevated temperatures [31, 32]. In contrast, as the low operating potential of most anode active materials exceeds the stability window of the electrolyte components, they get reduced electrochemically; fortunately, the reduction products, e.g., of EC, which decomposes below $0.8\,V_{Li}$, form a stable protective surface film [33]. This so-called **solid-electrolyte interphase** (SEI), first described by Peled in 1979 [34], is formed during the first formation cycle and consumes cyclable lithium, resulting in the first-cycle irreversible capacity loss, which scales with the specific surface area of the anode [35, 36]. The composition of the SEI depends strongly on the used electrolyte components (i.e., the solvents, the salt, and possible additives) as well as the applied formation and cycling conditions; nevertheless, the main components include LiF, lithium carbonate (Li_2CO_3), lithium ethylene dicarbonate (LEDC), lithium alkoxides (Li-OR), and polyolefins [37]. By conducting lithium ions but being insulating for electrons, the SEI offers the properties of a solid-state electrolyte, protecting the electrolyte from a continuous reduction. However, the SEI can be damaged through unwanted processes, e.g., by the volume change of the active material rupturing the SEI and exposing fresh surfaces, by reducing and incorporating TMs dissolved from the cathode active material, or by its decomposition at elevated temperatures, all consuming cyclable lithium when the SEI is restored.

The properties and the stability of the SEI can be improved by modifying its composition through the use of electrolyte **additives**, which are admixed with the standard electrolyte in quantities of up to $5\,\%$. Typical electrolyte additives are carbonates such as vinylene carbonate (VC) and (di)fluoroethylene carbonate (FEC (or DiFEC)) or LFO, all improving the long-term cycling stability [38–43]. Since the additives are reduced already at $\sim 1\,V_{Li}$, the reduction of the solvents, e.g., of EC, is suppressed and the composition of the SEI is modified to improve its stability.

Anode Active Materials

Titanium disulfide (TiS_2), which was introduced as CAM by Wittingham in 1976 to be the first material to (de)intercalate lithium ions reversibly, could only be synthesized in the delithiated state [44, 45]. Therefore, **lithium metal** was used as an anode con-

taining the required lithium inventory. Due to the repeated stripping and plating of lithium metal during operation, which does typically not occur in a perfectly homogeneous manner, cavities and dendrites form on the lithium-metal surface, whereby the latter may grow through the separator to the cathode. Upon contact of the lithium-metal dendrite and the cathode, an internal electrical short circuit would release (part of) the stored energy instantaneously in the form of heat, compromising the safety due to a fire hazard, what eliminated the use of lithium metal as anode in commercial LIBs. Due to the high specific capacity of pure lithium metal, however, it remains an anode material of interest, what stimulates many efforts to stabilize lithium metal for commercial applications, e.g., through advanced electrolyte formulations [46–48]. Current activities include the investigation of so-called anode-free LIBs, where, instead of an anode, a sole copper current collector is used, on which the lithium inventory of the cathode is plated, what would enhance the energy density of LIBs significantly [49–51].

To enable the safe production and operation of LIBs and thus their successful commercialization, the lithium-metal anode was replaced by carbonaceous anode active materials when the lithium-containing layered oxides and phosphates were found. For (natural or synthetic) **graphite** (C_6), the lithium ions intercalate between the graphene layers from the edge plane (see Figure 1.2), showing a staging behavior with various plateaus at a low potential of 0.05 to $0.25\,V_{Li}$ and a theoretical capacity of $372\,mAh/g$ when fully lithiated to the LiC_6 phase (see Equation 1.2) [36]. The use of graphite comes with low cost, a high electronic conductivity, and a high reversibility. The uniaxial volume expansion of $\sim$10 % perpendicular to the graphene layers, however, results in the cracking of the SEI and a subsequent reduction of electrolyte and consumption of lithium inventory by side reactions, what slightly decreases the CE of each cycle. Additionally, due to the graphite potential being close to the one of lithium metal, the risk of unwanted lithium plating becomes relevant, in particular, at high rates, low temperatures, high areal mass loadings, or low electrolyte concentrations [52, 53]. For graphite anodes, propylene carbonate (PC) cannot be used as electrolyte solvent molecule since it intercalates with the lithium ions into the active material, what results in the irreversible exfoliation/delamination of the graphene layers.

Silicon (Si) particles are often added to graphite anodes to increase the energy density of the cell. As the storage of lithium in the silicon active material is not based on intercalation but on the formation of an alloy, silicon provides a theoretical specific capacity of $3{,}579\,mAh/g$ for the full electrochemical lithiation to the $Li_{15}Si_4$ phase, being tenfold as compared to the one of graphite. Silicon has a higher operating potential of 0.3
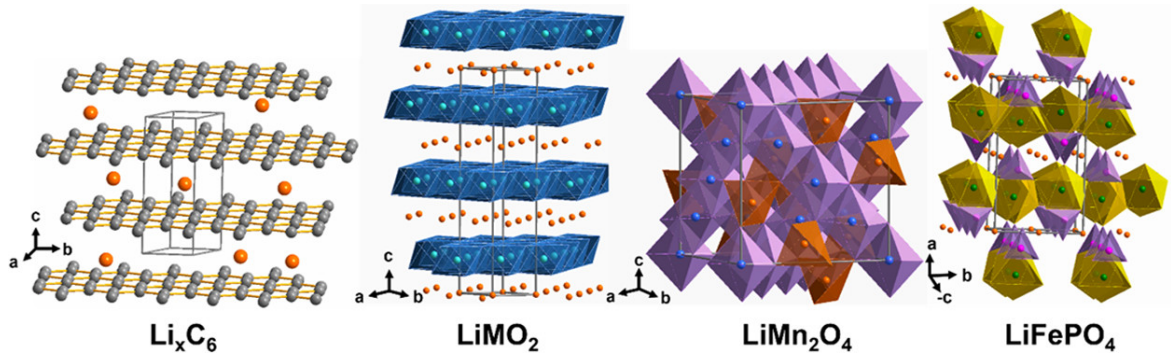
Figure 1.2 Crystal structure of graphite (Li_xC_6), layered lithium transition metal oxides ($LiMO_2$), spinel-type lithium manganese oxide ($LiMn_2O_4$), and lithium iron phosphate ($LiFePO_4$) (from left to right). Reprinted from Manthiram [61] under an open-access ACS AuthorChoice usage agreement.

to $0.5\,V_{Li}$, what does not compromise the energy density of the cell dramatically but impedes lithium plating and enables higher charging rates [54]. However, the volume expansion of $+280\,\%$ upon full lithiation induces mechanical stress, particle fracture, and even particle pulverization, resulting in the electronic isolation of silicon particles, both for nanometer- and micrometer-sized silicon particles [55, 56]. However, a new approach considers the partial lithiation of micrometer-sized particles, lithiating only an amorphized outer shell of the particles, while the core remains crystalline; this is achieved by limiting the cutoff potential to $170\,mV$, what ensures the mechanical stability of the particle [57, 58]. The repeated expansion and contraction upon delithiation, however, exposes fresh surfaces, what promotes electrolyte reduction and lithium inventory loss due to a continuous (re)formation of the SEI. This mechanism can be suppressed by the use of suitable electrolyte formulations which contain electrolyte additives such as fluoroethylene carbonate (FEC) or lithium nitrate ($LiNiO_3$); by this approach, however, the significant loss of lithium inventory is only postponed until the additive is consumed [38]. Therefore, current activities include the investigation of silicon encapsulated in a carbon shell, which separates silicon and electrolyte and thus allows for an improved CE and capacity retention [59, 60].

Lithium titanate ($Li_4Ti_5O_{12}$, LTO) is a spinel-type anode active material with a specific capacity of $175\,mAh/g$ (for the full lithiation to the $Li_7Ti_5O_{12}$ phase), which is exchanged during its potential plateau at $1.55\,V_{Li}$. Therefore, LTO provides a relatively low specific energy, however, its (de)lithiation is highly reversible since it operates within the stability window of the electrolyte components, suppressing electrolyte reduction and lithium inventory loss due to the absence of SEI formation. Furthermore, the high operation potential impedes lithium plating while the typically used nanoparticles enable the rate capability of the material, what enhances safety

and enables the utilization of LTO in high-power and/or low-temperature applications. Additionally, this so-called zero-strain anode material exhibits a small volume change of only +0.2 % upon full lithiation, impeding particle cracking [62]. Due to its prolonged cycled life, LTO is employed in medical devices and stationary energy storage applications. However, LTO reacts with the organic electrolyte, e.g., by reducing protic species in the electrolyte and evolving gas, e.g. H_2 [63, 64].

Cathode Active Materials

State-of-the-art LIBs are assembled in the discharged state, i.e., that the CAM provides the inventory of the active lithium, hence, determining the capacity of a full-cell. Therefore, both a high reversible capacity as well as a high operating potential are desired for CAMs to maximize the cells energy density. All commercially available active materials are based on 3d TMs such as manganese (Mn), iron (Fe), cobalt (Co), and nickel (Ni). In addition to the widely used layered lithium transition metal oxides (discussed below in Chapter 1.3), two cobalt-free alternatives are presented in the following.

Spinel-type lithium nickel manganese oxide ($LiNi_{0.5}Mn_{1.5}O_4$, LNMO) is derived from spinel-type manganese oxide ($LiMn_2O_4$, LMO). LMO was introduced by Thackeray et al. in 1983 and provided an operating voltage of $4.0\,V_{Li}$ and a theoretical capacity of $148\,mAh/g$, which was, however, limited practically to $120\,mAh/g$ [62, 65]. By replacing manganese partially with nickel, LNMO was synthesized by Gao et al. in 1996 [66] and is relatively cheap due to the high abundance of manganese. The high rate capability of LNMO is owed to the three-dimensional lithium-ion diffusion pathways of the spinel-type lattice (see Figure 1.2). Even though LNMO provides a theoretical capacity of only $147\,mAh/g$ (for the full delithiation to the $Ni_{0.5}Mn_{1.5}O_4$ phase), its high energy density is owed to its high operating potential of $\sim4.75\,V_{Li}$ (see orange data in Figure 1.3). On the downside, the high potential of the so-called high-voltage spinel gives rise to electrochemical electrolyte oxidation, in particular, at elevated temperature [31, 32, 39], what results in the formation of protic species and in TM dissolution, ultimately inducing a drastic capacity fade in full-cells [67–69].

Lithium transition metal phosphates have a phospho-olivine polyanion host structure. Their most common representative is **lithium iron phosphate** ($LiFePO_4$, LFP), introduced by Padhi et al. in 1997 [70, 71], providing a theoretical capacity of $170\,mAh/g$ (for the full delithiation to the $FePO_4$ phase), which is mainly delivered during its po-

tential plateau at $\sim$3.45 V_{Li} (see yellow data in Figure 1.3). LFP has a relatively stable host structure (see Figure 1.2), what allows to fully delithiate the material without degrading the structure, and is known for its low cost, thermal stability, and longevity; however, it exhibits a relatively poor electronic and ionic conductivity, the latter being due to the one-dimensional lithium-ion diffusion pathways. LFP is (de)lithiated by a two-phase reaction consisting of a fully lithiated and a fully delithiated phase; between the two phases, it exhibits a relative change of its unit cell volume of -6.8 % upon full delithiation [70], what results in stress and strain and eventually in particle cracking, as observed by scanning electron microscopy (SEM) and transmission electron microscopy (TEM) [72–74]. Nevertheless, LFP does provide a high-power capability when its particle size is reduced appropriately to typically 100 to 500 nm and when a carbonaceous surface coating is applied. Due to its low cost and high power, LFP serves in stationary energy storage applications, in power tools, or in heavy-duty or mass-produced EVs, but is not suitable where high energy density is required owed to its relatively low operating potential. Current activities also include the investigation of lithium manganese phosphate ($LiMnPO_4$, LMP) and lithium manganese iron phosphate ($LiMn_yFe_{1-y}PO_4$, LMFP) due to their higher operating voltage between 3.4 and 4.2 V_{Li} [75–77]. Similar to LNMO, LFP can be fully delithiated without CAM degradation due to the absence of detrimental changes of its crystal structure.

1.3 Advances in Layered Lithium Transition Metal Oxides

Development of Compositions

While LFP represented around 34 % of the total CAM production of 350,000 tons in 2018, layered lithium transition metal oxides ($LiMO_2$, M typically being a TM such as cobalt, nickel, manganese, and/or aluminum) were the most commonly used CAMs [14]. Synthesized in lithiated state by Mizushima and Goodenough in 1980 [78], **lithium cobalt oxide** ($LiCoO_2$) was the first commercially used member of the class of layered lithium transition metal oxides. Since it had been paired with a carbonaceous anode by Yoshino in 1985 and commercialized by Sony in 1991, it was the most widely used active material for more than 20 years [62].

In LCO (or layered oxides, in general), having an α-$NaFeO_2$ structure, the alternating layers of lithium ions (Li^+) and cobalt ions (Co^{3+}) (or TM ions, respectively), which re-
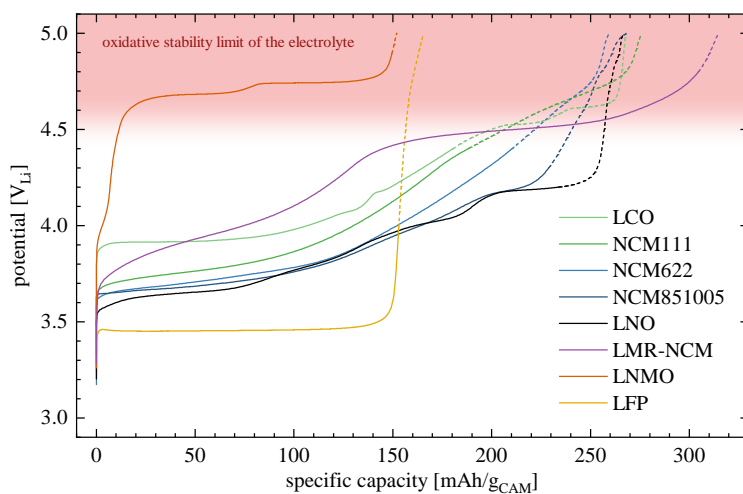
Figure 1.3 Representative cathode potential curves (i.e., the relationship of potential and specific capacity) of the first charge of CAMs: LCO (light green), NCM111 (green), NCM622 (blue), NCM851005 (dark blue), LNO (black), LMR-NCM (purple), LNMO (orange), and LFP (yellow). The data were collected in T-cells with LP57 electrolyte against a lithium-metal counter electrode and reference electrode, while the CAM was charged to $5.0\,\mathrm{V_{Li}}$ at $C/15$ based on the theoretical capacity of the CAM. The solid line marks the region of the capacity window used for practical cell operation, while the dotted line completes the curve for the full delithiation of the CAM. The potential region above the oxidative stability limit of $4.5\,\mathrm{V_{Li}}$ of the carbonate-based electrolyte is marked in light red.

side in octahedral sites, are separated by layers of oxygen ions (see Figure 1.2). Within these layers, lithium ions can move in-plane, i.e., within the two-dimensional pathways of the layered structure, via tetrahedral voids sharing faces with the octahedral sites. During operation, lithium ions are (de)intercalated reversibly from/into the solid host structure while the charge is compensated by the oxidation of the TM ions. Even though it provides a relatively large theoretical capacity of $274\,\mathrm{mAh/g}$, the practical capacity of pure LCO is typically limited to values between 150 and $170\,\mathrm{mAh/g}$ due to its structural instability at high degrees of delithiation [62]. Coating and doping efforts, however, have pushed the practical capacity up to $210\,\mathrm{mAh/g}$ [79]. Its capacity is delivered during a sloped potential profile with an average potential of $4.0\,\mathrm{V_{Li}}$ (see light green data in Figure 1.3), boosting its energy density, as the operating potential is significantly higher than the one of LFP. Due to the sloped potential profile (in contrast to the flat curves of LFP or LNMO), the amount of extracted lithium can be conveniently controlled by the applied upper cutoff potential.

Even though LCO accounted for only $11\,\%$ of the CAM market in 2018, it dominates the market for portable electronics, what is mainly owed to its relatively simple synthesis, high volumetric capacity, and longevity [62, 79]. On the downside, due to the high cobalt content, LCO is vulnerable to the relatively high cobalt price (of $\sim 50\,\mathrm{US\$/kg}$)

13

and price volatility as well as the fragile supply chain and the social concerns with regard to the mining conditions [80], altogether limiting the use of LCO to low-volume markets.

Since the CAM contributes $\sim$50 % to the cost of the cell, and since the CAM cost is governed by the raw material price [21, 81], it is desired to replace cobalt by cheaper metal ions such as nickel (24 US\$/kg), manganese (2 US\$/kg), and aluminum (2 US\$/kg) for the high-volume EV market [21, 80], what opened the field of the isostructural compounds of **lithium nickel cobalt manganese oxide** (NCM, $LiNi_xCo_yMn_zO_2$, $x + y + z = 1$) and lithium nickel cobalt aluminum oxide (NCA, $LiNi_xCo_yAl_zO_2$). As the NCM materials are labeled NCMxyz according to their composition (i.e., their TM ratio), $LiNi_{1/3}Co_{1/3}Mn_{1/3}O_2$, which emerged in the early 2000s [82, 83], is referred to as NCM111. The potential curve of NCM111 is shifted to lower potentials, providing a reversible capacity of 160 mAh/g when charged to 4.4 V_{Li} (see green data in Figure 1.3) at an average potential of 3.9 V_{Li}. To further reduce the required amount of cobalt and increase the available capacity at a given potential, the nickel content of NCMs has been increased continuously: typical representatives for nickel-rich NCMs such as NCM622 and NCM851005 operate at even lower potential but deliver a higher reversible capacity of up to 190 and 200 mAh/g, respectively (see blue and dark blue data in Figure 1.3, respectively). Recent work on NCMs with an ultra-high nickel content has even crossed the mark of 90 mol% of nickel among the transition metals [84–87]. Continuing this journey, current efforts (have restarted to) investigate the feasibility of the nickel-based end member **lithium nickel oxide** (LNO, $LiNiO_2$) [86, 88–92]: LNO was already discovered in the early 1990s by Dahn et al. and Ohzuku et al. [93–95], however, despite intensive research efforts, LNO has not been commercialized, owing to the complexity and cost of its synthesis as well as its high reactivity with moisture and electrolyte components.

Even though LCO, LNO, and the various NCMs are isostructural compounds, their physical and electrochemical properties differ depending on their **TM ratio** [21]. The structural and thermal stability is improved by the manganese content, while cobalt and nickel in the structure lower the decomposition temperature in the delithiated state [83, 84, 96]. The presence of cobalt reduces unwanted cation mixing, i.e., the amount of unwanted TMs in the lithium layer [83, 89, 97]. Consequently, a high nickel content diminishes the lithium diffusivity, possibly governed by the increased presence of nickel in the lithium layer, while cobalt enhances the kinetics [83]. Having more nickel as the redox-active species in the structure does not only provide more

capacity at lower potentials [96, 98] but also increases the reactivity with moisture during ambient storage or with the electrolyte during cell operation [89, 99, 100]. Since manganese is already present in the Mn^{4+} state, it cannot participate in the charge compensation and is therefore electrochemically inactive [101, 102], while, with increasing manganese content, nickel and cobalt have a lower oxidation state when fully lithiated, while it increases more rapidly upon delithiation.

Due to the relatively high price of nickel [80], research efforts also aim at CAMs comprising mainly the cheaper and more abundant TMs iron or manganese. As LFP and LNMO exhibit a relatively poor energy density as compared to NCMs, the interest in (cobalt-free) **lithium- and manganese-rich lithium nickel cobalt manganese oxides** (LMR-NCMs), which were introduced by Lu et al. in 2001 [103, 104], as next-generation CAMs is growing. In contrast to the stoichiometric NCMs, TM ions are replaced by additional lithium ions, which occupy the TM layer, either described by the one-phase representation of $Li[Li_\delta M_{1-\delta}]O_2$ or the two-phase notation of $x\, Li_2MnO_3 \bullet (1\text{-}x)\, LiMO_2$ [105, 106]. The additional lithium pushes the theoretical capacity to more than $300\,\mathrm{mAh/g}$ depending on the LMR-NCM composition, e.g., to $378\,\mathrm{mAh/g}$ for $Li[Li_{0.2}Ni_{0.2}Mn_{0.6}]O_2$ with $x = 0.5$, or $\delta = 0.2$, respectively. In practice, they provide a reversible capacity of up to $250\,\mathrm{mAh/g}$ at an average discharge potential of $\sim 3.5\,\mathrm{V_{Li}}$ [107]. To access their full capacity, LMR-NCMs are activated in the first cycle to $4.8\,\mathrm{V_{Li}}$ (see purple data in Figure 1.3), whereby the charge is not only compensated by the oxidation of the TM ions but also by the oxidation of the oxygen. This so-called anion redox during the voltage plateau at $\sim 4.5\,\mathrm{V_{Li}}$ is accompanied by the release of lattice oxygen in the near-surface region of the LMR-NCM particles, what induces a surface reconstruction as well as a chemical oxidation of the electrolyte components [104, 107–109]. In addition, as LMR-NCMs are operated at an upper cutoff potential of $4.7\,\mathrm{V_{Li}}$, their cell performance suffers from the additional electrochemical oxidation of the electrolyte at this high potential. Further challenges include the hysteresis of the potential curve over a charge/discharge cycle, which decreases the energy efficiency, as well as the potential fading upon extended cycling, which decreases the energy density of the cell [107, 110].

Degradation Phenomena

The available capacity of a LIB and thus its energy decrease within the lifetime of a cell. A variety of degradation phenomena can deteriorate the performance of the battery – not only by cyclic aging during operation (i.e., over the course of hundreds or thousands of charge/discharge cycles) but also by calendar aging occurring over time (e.g., upon long-term storage in the charged state and/or at elevated temperature) [111]. This capacity loss does not only originate from the loss of lithium inventory (e.g., due to continuous (re)formation of the SEI) but can also be induced by the degradation of the CAM, either due to the loss of active material or through impedance build-up [112]. In this chapter, the typical degradation phenomena occurring for stoichiometric layered oxides (i.e., LCO, LNO, and NCM compounds) are discussed.

Even before cell assembly, a CAM can deteriorate if it is stored inappropriately. Upon **ambient storage**, the CAM reacts with moisture and carbon dioxide (CO_2), not only forming unwanted surface contaminants such as hydroxides and carbonates but also intercalating protons [99, 100, 113]. Consequently, the proper processing of the deteriorated CAM can be hindered during slurry preparation by the gelation of the ink, often induced by the reaction of the hydroxides with the polymeric binder [96]. The decomposition of the contaminants and their reaction with the electrolyte during cell operation lead to extensive gas generation [100, 114, 115] while the insertion of protons alters the capacity retention of the CAM [116–118]. This effect is most pronounced for nickel-rich compounds due to the high reactivity of nickel [96, 99, 100].

Within the cell, LCO, LNO, and the NCM compounds (in contrast to LNMO and LMR-NCMs) are typically operated within the stability window of the carbonate-based electrolyte below $\sim$4.5 V_{Li} [31]; at elevated temperatures, however, the reaction kinetics of the **electrochemical electrolyte oxidation** are increased and its onset potential may be shifted to lower values [32], what results in the continuous decomposition of the electrolyte components and in gas evolution within the cell. The oxidation products include gaseous species such as carbon monoxide (CO) and CO_2 as well as protic species (e.g., HF), which can decompose the conducting salt and/or damage the CAM [30–32].

Even though the above discussed CAMs provide a theoretical capacity between 274 and 278 mAh/g, which can be almost fully accessed even below the stability limit of the electrolyte (e.g., 240 and 257 mAh/g for NCM851005 and LNO, respectively (see Figure 1.3)), their degree of delithiation must be limited in practical applications
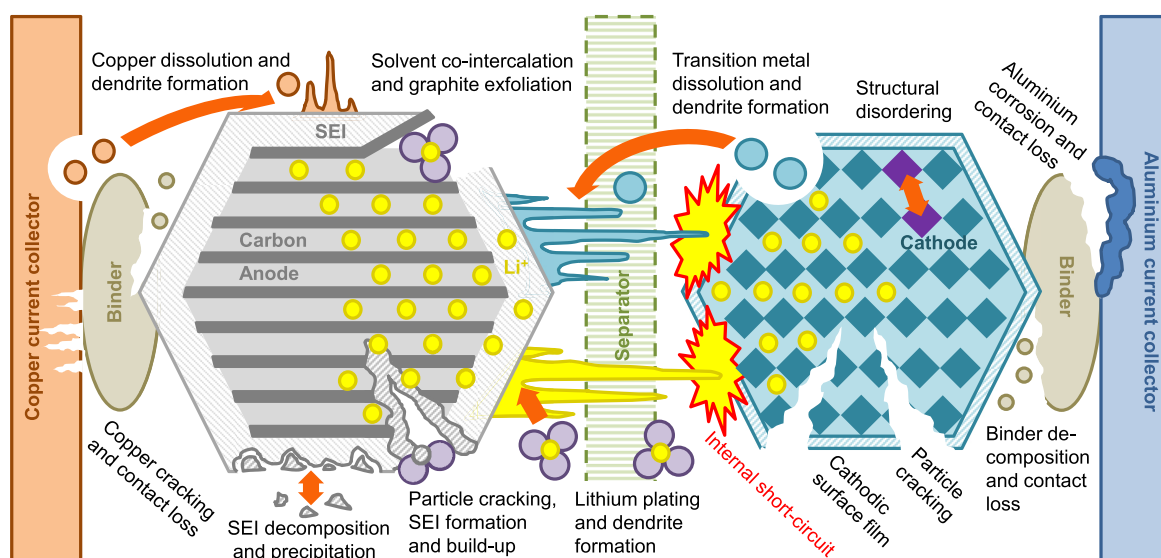
Figure 1.4 Schematic overview over degradation mechanisms occurring in a lithium-ion battery. Reprinted from Birkl et al. [112] under a Creative Commons BY 4.0 license.

to 150 to 220 mAh/g, depending on the composition. Otherwise, at high state of charge (SOC, here corresponding to the degree of delithiation x in $Li_{1-x}MO_2$), the delithiated layered structure becomes unstable and the oxygen ions become oxidized, what results in the release of oxygen from the lattice in the near-surface region of the CAM particles [31, 119]. The majority of this reactive (singlet) oxygen decomposes the electrolyte chemically, what results in the evolution of CO and CO_2 [31, 119–121]. This **oxygen release** is accompanied by the formation of an oxygen-deficient surface layer in the NCM, which is ionically and electronically less conductive as compared to the layered phase, increasing the impedance of the CAM [119, 122]. Furthermore, the rock-salt-type phase, reported to develop for the nickel-rich NCMs, cannot store any lithium ions, what results in the loss of active material [122]. For LCO, the release of oxygen and the formation of a spinel-type surface layer is reported to initiate at 50 %SOC [79, 123], while the onset of the oxygen release is reported to occur at 80 %SOC both for LNO [90, 124] as well as for the NCMs [119, 125]. Therefore, a direct comparison of various NCM composition charged to the same upper cutoff potential, as it is often done, e.g., for their capacity retention, is not meaningful since the degree of delithiation at a given cathode potential differs significantly (see Figure 1.3), while a meaningful comparison would need to be performed for similar degrees of delithiation.

The release of lattice oxygen promotes the formation of HF, which is associated with the **dissolution of transition metals** from the CAM due to acid etching on the CAM surface. This TM dissolution is most pronounced at high potential, or high SOC, re-

spectively [126–129], while only $\sim$0.1 wt% of TMs are dissolved for typical operation conditions (being on the order of one NCM monolayer), even after extended cycling at elevated temperature. Therefore, the extent of TM dissolution is insignificant with regard to loss of CAM [130, 131]; however, the dissolved TM ions diffuse/migrate to the anode where they get reduced at low potential and incorporated into the SEI [127]. In particular, manganese, being present in the SEI in the Mn^{+2} state, has been identified to be detrimental to the full-cell performance, as it either i) increases the electronic conductivity of the SEI what suppresses its passivating effect, or ii) promotes the conversion of the SEI components catalytically [132]. Essentially, manganese ions deposited on the anode promote the continuous growth of the SEI, what decomposes the electrolyte, generates gas, consumes lithium ions, and decreases the available capacity in a full-cell [127, 132]. The capacity loss scales with the amount of manganese ions in the anode, as each manganese ion traps around 10 to 100 lithium ions [130, 133, 134]. The use of SEI-stabilizing additives such as VC can mitigate the detrimental effect of the manganese ions [132]. Due to the reduced amounts of manganese, nickel-rich NCMs are expected to be less prone to the negative effects of TM dissolution.

In contrast to the near-surface region of the particles, the host structure of the bulk remains intact even upon full delithiation. However, the lattice parameters of the layered lithium transition metal oxides change when the lithium is removed, what is typically monitored by in situ X-ray diffraction (XRD). Both LCO as well as LNO exhibit sharp phase transitions upon (de)lithiation, which show as abrupt changes in the unit cell volume and correlate with the phase transitions observed from the plateaus of the potential profiles. While the relative **volume change** is only -1.5 % for LCO [135, 136], it abruptly increases to -9.0 % above 75 %SOC for LNO [88, 90, 95]. For NCMs, however, a continuous decrease of the unit cell volume is observed for an increasing degree of delithiation, resulting in volume changes, e.g., from -1.5 to -7.2 % when the NCMs are charged to 4.5 V_{Li}, while the nickel-rich NCMs exhibit more pronounced changes [98]. If the volume change of the NCM, however, is presented as a function of the degree of delithiation, or SOC, respectively, the extent of volume change is similar independent of the NCM composition [98, 137]. In addition to the volume change of the NCM unit cell, the volume change even occurs anisotropically, i.e., the two lattice parameters a and c expand/contract independently from each other; their ratio c/a provides a measure of this anisotropy [98, 138, 139].

This anisotropic volume change of the NCMs upon (de)lithiation forms cracks between the primary crystallites of the polycrystalline secondary agglomerates, which have been

assessed visually by tomography or by cross-sectional scanning electron microscopy or transmission electron microscopy prepared by a focused ion beam (FIB-SEM/-TEM) of charged and/or aged NCM electrodes [138, 140–142]. Even though these cracks seem to close reversibly upon lithiation, irreversible **particle cracking** occurs upon repeated charge/discharge cycling, which is often associated with a diminished capacity retention [137]. Particle cracking of NCM particles does not only result in an increased surface area, which gives rise to unwanted side reactions such as oxygen release, (electro)chemical oxidation of the electrolyte, and/or TM dissolution but also impedes the electronic contact within the NCM particles [143]. In contrast to all-solid-state batteries, where no penetration of the electrolyte into pores occurs, what diminishes the cycling performance drastically [144], the rate capability of LIBs using liquid electrolyte benefits from the improved apparent ionic diffusion due to the cracking of NCM particles [145].

Furthermore, **cation mixing** or lithium-nickel disorder, i.e., the mixing of lithium ions and TM ions within the NCM structure, diminishes the available specific capacity as well as the solid-state diffusion of lithium, when the nickel ions occupy the lithium sites [146]. This effect may occur upon synthesis and/or upon repeated charge/discharge cycling [147, 148] and is most pronounced for nickel-rich NCMs, while cobalt in the structure decreases and manganese increases the extent of cation mixing [83, 149–151].

Similar to the release of oxygen at high degrees of delithiation for typical operation temperatures [119, 152], the partially delithiated/charged layered oxides release lattice oxygen when they are heated. The onset temperature of this **thermal instability** appears between 170 and 320 °C and decreases with increasing degree of delithiation (both when compared for the same SOC or for the same cutoff potential) as well as with the nickel content [83, 84, 96, 153, 154]. This thermal decomposition is accompanied by an exothermic release of heat, what might trigger a thermal runaway and thus compromise the safety of a cell or even of the entire battery pack [155, 156]. Upon the release of oxygen, the layered oxides typically convert to a spinel-type structure, while the nickel-rich NCMs form a rock-salt-type phase [157].

To counter the aforementioned degradation phenomena, which mostly affect the CAM-electrolyte interface, approaches include the use of EC-free electrolytes in combination with SEI-forming additives, the doping of the bulk structure (e.g., to improve the conductivity of the CAM) as well as of the surface only (using dopants such as Mn, Al, Fe, Cr, Co, Mg, W, Zr, Ti, and B, from a few ppm up to 5 mol%) and/or the

application of surface coatings (using compounds such as Al_2O_3, B_2O_3, TiO_2, ZrO_2, and AlF_3) amongst others [154, 158, 159]. Since the surface doping or coating can only be applied to the accessible outer surface in the pristine state, which increases due to particle cracking upon cycling, untreated inner surface area is exposed upon cycling, what is expected to diminish the beneficial effect of a surface treatment. Therefore, significant efforts have been made to optimize the particle morphology to mitigate the detrimental consequences of particle cracking.

Particle Morphology and Microstructure

The increase of energy density and the reduction of the cobalt content – achieved over the last decade by a compositional adjustment through the increase of the nickel content of the NCM – has (almost) reached its limit since recent publications have already crossed the mark of 90 mol% [85–87, 160]. Due to the pronounced surface reactivity of nickel, however, the focus has shifted to the optimization of the morphology and the minimization the exposed nickel-rich surface to ensure cycle life, energy density, sustainability, and safety [161].

The **synthesis** of the conventional NCMs is mostly based on the co-precipitation of the TM hydroxide or TM carbonate precursor particles, which are precipitated from TM sulfates. By controlling the pH and by the addition of chelating agents, the kinetics of the particle growth can be controlled and spherical precursor particles are obtained, which then also govern the morphology and the particle size of the CAM particles. The CAM is finally synthesized by the calcination of the precursors with a lithium source such as lithium carbonate (Li_2CO_3) (or lithium hydroxide (LiOH) for nickel-rich compositions) under dry air (or pure oxygen) at temperatures between 650 and 1000 °C, depending on the NCM composition. The nickel-rich compositions require post-treatments after their synthesis, such as washing to remove residual lithium salts or surface coating to improve their cycling performance, as well as inert storage (in the absence of water) to prevent the formation of surface contaminants [96, 100, 113, 116, 161].

At first sight, the conventional NCMs consist of spherical particles with a diameter of typically 5 to 20 μm, minimizing the surface-area-to-volume ratio due to their sphericity. However, on closer inspection, their primary structure consists of hundreds to thousands of randomly oriented, densely packed crystallites with 50 to 500 nm in
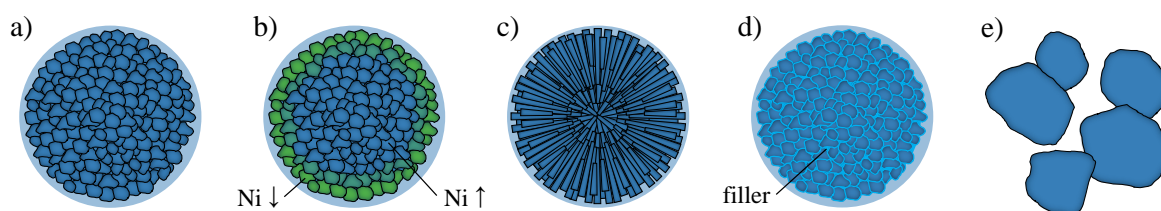
Figure 1.5 Schematic representation of the morphology and microstructure of **a)** a conventional polycrystalline particle, **b)** a polycrystalline particle synthesized with a radial gradient of the nickel concentration (lower nickel content in green), **c)** a polycrystalline particle consisting of elongated, radially oriented primary crystallites, **d)** a polycrystalline particle including a grain boundary reinforcement (light blue), and **e)** single-crystalline particles.

size, which are agglomerated to spherical secondary particles of 5 to 20 µm (see Figure 1.5a). As a consequence, this so-called **polycrystalline** (PC) particle morphology forms cracks upon repeated (de)lithiation. To mitigate the unwanted exposure of (fresh) nickel-rich surface of the PC particles, morphological and microstructural design considerations have generated the following approaches:

○ Surface modifications of the CAM particles have proven beneficial regarding their cycling performance. By adding compounds on the surface of the CAM, **surface coatings** may serve as physical barrier between CAM and electrolyte, scavenge HF from the electrolyte, or improve the mechanical stability of the particles, all protecting the reactive surface of nickel-rich CAMs [159, 162–164].

○ As a doping of the bulk changes the overall composition, while unwanted side reactions depend mainly on the surface composition, a modification by doping of the surface only is desired. A **surface doping** can be obtained by an additional calcination step after a surface coating is applied, also stabilizing the lattice structure of the CAM on the external surface [159, 165].

○ From the idea of a surface doping, the concept of **core-shell particles** or particles with a TM **concentration gradient** is derived. A heterogeneity of the TM distribution can be obtained during co-precipitation of the precursor by (continuously) changing the ratio of the TM sulfates in the feed. As a consequence, a nickel-depleted shell is obtained (typically low-nickel NCMs or LNMO), which protects the nickel-rich core (see Figure 1.5b) [166–170].

○ The anisotropic volume change of the randomly oriented primary crystallites, which results in the formation of cracks upon delithiation, can be countered by a modification of the size, shape, and orientation of the primary crystallites. Induced by the use of dopants, **elongated and radially aligned crystallites**

are obtained, which are expected to reduce the stress and strain within the particles upon delithiation (see Figure 1.5c) [169, 171, 172].

○ To alleviate particle cracking, a **filler substance**, such as Li_xCoO_2, Li_3PO_4, and $Li_xW_yO_z$, within the pores and between the primary crystallites can serve as glue, improving the adhesion between crystallites and, therefore, mechanically reinforcing the internal interfaces (see Figure 1.5d) [173–175].

○ Despite all the aforementioned efforts, it might not be possible to fully suppress the cracking of PC particles. As a last resort, monolithic and monodisperse primary particles with a size of 0.5 to 5 µm and without secondary structure, so-called **single-crystalline** (SC) particles, have been developed, which are expected to maintain the morphological integrity and eliminate particle cracking upon repeated (de)lithiation (see Figure 1.5e) [176–180].

Since the synthesis of nickel-rich NCMs is already more complex than the one of LCO or NCM111, additional processes or treatments to obtain a customized particle morphology and microstructure might be challenging (or expensive, at least) when considering the incorporation into a large-scale CAM production. In the case of SCs, the synthesis routes are more complex and thus more expensive, as they often require a higher calcination temperature of up to 1000 °C, the addition of a molten salt as flux agent, multi-step calcination, a washing step to remove excess lithium salts or flux agents, and a deagglomeration step (e.g., by grinding or ball-milling) [161]. Alternative approaches include the synthesis by hydrothermal methods [181, 182] or are based on the mechanical grinding of nano-sized transition metal oxide precursors, not requiring the co-precipitation of a precursor [183].

SC CAMs do not only allow to reach higher electrode densities due to the absence of inner pore volume [184, 185], but are expected to provide an enhanced (chemo)mechanical stability and to maintain their surface area upon repeated (de)lithiation. Therefore, the CAM surface area which is available in the cell can be defined by the synthesis conditions. Unwanted side reactions and parasitic currents decrease with a decreasing specific surface area and, therefore, with an increasing particle diameter, what may improve the cycle life of a full-cell. Similarly, a beneficial effect is expected with regard to the capacity fading caused by active material loss (e.g., by the formation of inactive rock-salt phase in the surface-near region of the particles due to the release of lattice oxygen), as the extent of the latter decreases with decreasing specific surface area. In contrast, however, an increasing particle size and, therefore, decreasing specific sur-

face area results in longer diffusion paths for the lithium ions within the particle as well as in an increasing mass-normalized charge-transfer resistance, both decreasing the kinetics of the CAM. Therefore, the sweet spot of the particle size of SC CAMs depends on the respective application, i.e., whether it is targeting high power, high energy, or long lifetime.

1.4 Objective of This Work

Within this context, the overall goal of this PhD thesis is the thorough investigation and comprehensive understanding of degradation phenomena associated with layered lithium transition metal oxides used as CAMs for LIBs. This work focuses on crucial processes including particle cracking, the release of lattice oxygen in the near-surface region at high SOC or upon heating, and the dissolution of transition metals. Furthermore, the impact of the CAM particle morphology as well as of the CAM composition on these degradation phenomena is evaluated.

In the first part (see Chapter 3), three studies introduce the development, validation, and application of a novel method which enables to track the surface area of an electrode and thus the particle cracking of an active material, using in situ electrochemical impedance spectroscopy. Thereby, the cracking of CAM particles is quantified upon mechanical compression, upon extended cycling for three upper cutoff potentials, or upon the release of lattice oxygen at high SOC. To allow for a broad accessibility of the method, the originally introduced configuration is modified to enable its use with a standard coin (half-)cell setup and a conventional battery cycler.

In the second part (see Chapter 4), three studies demonstrate the implications of the polycrystalline and the single-crystalline CAM particle morphology on the surface area changes upon mechanical compression, during the (de)lithiation within the first charge/discharge cycle, as well as at high SOC. Due to the observed absence of particle cracking for the single-crystalline CAM, the beneficial effect of the particle morphology is elucidated regarding the extent of gas evolution, the rate capability, and the thermal stability as well as the transition metal dissolution, the impedance build-up, and the capacity retention in full-cells.

In the final part (see Chapter 5), the structural stability is investigated for five CAMs with different composition as a function of upper cutoff potential or SOC. The stability limit is assessed both in cycling experiments as well as in gas evolution measurements,

elucidating the correlation of the release of lattice oxygen from the surface-near regions and the loss of discharge capacity due to the loss of CAM and/or impedance build-up.

Therefore, it is the main focus of this work to understand and subsequently mitigate the degradation phenomena of layered lithium transition metal oxides

- by providing methodology to quantify the extent as well as the consequences of particle cracking,

- by understanding the effect of the particle morphology on fundamental properties as well as on the long-term cycling performance, and

- by identifying their structural stability limit at high degrees of delithiation

to improve the available capacity and thus energy of LIBs as well as their lifetime.

2 Experimental Methods

2.1 Surface Area Determination by Gas Physisorption

The specific surface area of battery materials governs their electrochemical properties and side reactions during battery operation, such as the (de)intercalation kinetics, the irreversible capacity loss of anode materials during SEI formation, the irreversible capacity of CAMs within the first cycle, or the gas evolution. The morphology (i.e., the surface area as well as the pore size distribution) of porous solids and fine powders is typically investigated by gas physisorption experiments [186] and analyzed by the BET theory (abbreviated from the original publication of Brunauer, Emmett, and Teller in 1938 [187]), which is an extension of the Langmuir model.

When inert gas molecules get in contact with solids, they do not react chemically but can adsorb to its surface, while the amount of the adsorbed gas (adsorbate) depends on the type of the gas (adsorptive), its pressure, the temperature, the surface area of the sample (adsorbent) as well as its morphology. Due to the weak interaction of inert gases with solids, the experiments are performed at lower temperatures, typically cooled to $77\,\mathrm{K}$ and kept constant (i.e., in isothermal conditions) using liquid nitrogen. The pressure (or the concentration) of the adsorbing gas is increased stepwise (by repeatedly adding a known calibrated volume of gas), monitoring the equilibrium pressure and the adsorbed fraction of the gas added to the known volume of the sample tube, which are expected to follow Equation 2.1.

$$\frac{p/p_0}{n \cdot (1 - p/p_0)} = \frac{1}{n_{\mathrm{m}} \cdot C} + \frac{C - 1}{n_{\mathrm{m}} \cdot C} \cdot (p/p_0) \tag{2.1}$$

The BET equation describes the relationship of the specific amount of adsorbed gas n and the relative pressure p/p_0, where n_{m} is the specific monolayer capacity, p the equilibrium pressure, p_0 the saturation vapor pressure, and C a parameter related to the heat of adsorption. When plotting $\frac{p/p_0}{n(1-p/p_0)}$ as a function of p/p_0, the recorded

data is predicted to be linear in the region of $0.05 < p/p_0 < 0.30$ while the surface is being covered up to a complete monolayer. By fitting the linear region, n_m is extracted from Equation 2.1 and the specific surface area determined by the BET method a is obtained by

$$a = \frac{n_\mathrm{m} \cdot N_\mathrm{A} \cdot \sigma_\mathrm{m}}{m} \tag{2.2}$$

where N_A is the Avogadro constant, m the sample mass, and σ_m the molecular cross-sectional area of the adsorbate, latter being distinct for each kind of gas.

Before the measurement, the remaining void volume within the tube (already filled with the dried adsorbent) is determined, typically using helium gas. During the measurement, the pressure in the evacuated sample tube is increased step wise by adding a known amount of adsorbtive. Part of the added gas is adsorbed on the sample, while the rest remains gaseous and fills the void volume, both phases being in equilibrium. The difference between the amount of gas inserted into the sample tube and the gas remaining in the void volume equates to the amount of adsorbate on the sample, by which the surface area of the sample can be determined. Therefore, the precision of the measurement crucially depends on the ratio of the adsorbed amount and the one remaining in the void volume. As the gas is dosed accurately by a piston with a calibrated volume, the remaining error results mainly from the determination of the amount in the gas phase, using a pressure gauge. To increase the accuracy, the void volume is typically reduced, e.g., using a suitable size of the sample tube or by filler rods. Nevertheless, the accuracy is deteriorated when the amount of adsorbed gas is small as compared to adsorbate gas in the gas phase, in particular, for low absolute surface areas of the sample.

In practice, mainly nitrogen ($\sigma_\mathrm{m} = 0.162\,\mathrm{nm}^2$) is used as adsorbate, requiring a minimum absolute surface area of more than $\sim 1\,\mathrm{m}^2$ (at least, in the case of this work, but depending on the used device). Since the vapor pressure of krypton ($\sigma_\mathrm{m} = 0.205\,\mathrm{nm}^2$) at $77\,\mathrm{K}$ is much lower than the one of nitrogen ($p_{0,\mathrm{Kr}} \approx 200\,\mathrm{Pa}$ vs. $p_{0,\mathrm{N_2}} \approx 100\,\mathrm{kPa}$), the operating pressure, defined by the vapor pressure, is lower for krypton than for nitrogen and, since the adsorbed gas amount required to form a monolayer on the sample is similar for both gases, the amount of adsorbed krypton gas is relatively high as compared to the krypton gas remaining in the void volume [186, 188]. Therefore, mainly krypton gas is used in this work for BET measurements (abbreviated as Kr-BET) due to its higher sensitivity, enabling the surface area determination of electrodes from lab cells ($\varnothing\,11\,\mathrm{mm}$, $\sim 0.01\,\mathrm{m}^2$).

When electrodes are harvested from cycled cells to determine their surface area, in addition to the used glass fiber separators, a polymer-based separator is placed into the cell facing the investigated electrode; by this approach, no glass fibers remain on the electrodes (and, also, no electrode material remains on the separator) during cell disassembly, which could otherwise affect the results of the surface area determination. After harvesting the electrodes from the cells, the electrodes were washed in volatile carbonate-based solvents to remove all soluble species, such as non-volatile solvents (e.g., EC) and the conducting salt. Since the electrolyte comprises the same solvents, no affect of the washing on the surface area of the electrode is expected. After the sample preparation and the determination of its mass, the sample is typically degassed at elevated temperatures under dynamic vacuum. Within the frame of this work, the NCM powders or electrodes were dried at $120\,^{\circ}$C for at least 6 h. For electrodes investigated in the charged state, in particular, the handling under inert atmosphere between cell disassembly and surface area determination is crucial due to the relatively high reactivity of charged CAMs with ambient gases.

In this work, Kr-BET is determined for 13 points between $0.01 \leq p/p_0 \leq 0.30$, using an autosorb iQ (Quantachrome Instruments, USA). The determination of the specific surface area is used to evaluate the effect of mechanical compression (see Chapters 3.1 and 4.3), electrochemical (de)lithiation (see Chapters 4.1 and 4.3), the release of lattice oxygen at high SOC (see Chapter 3.2), and extended cycling (see Chapters 3.1 and 4.3) on the specific surface area of pristine CAM powders; furthermore, it allows to determine the surface-area-normalized capacitance, i.e., the correlation between the surface area and the capacitance of the material-specific electrochemical double layer.

2.2 Pseudo Full-Cells

In contrast to half-cells, comprising a lithium-metal counter electrode, or full-cells, employing pristine (silicon/)graphite or LTO, pseudo full-cells combine the advantages of both in order to investigate the electrochemical properties of the working electrode only. For the investigation of CAMs, ideally, the counter electrodes in pseudo full-cells should be capacitively oversized, partially lithiated, and should operate in a potential window in which the electrolyte components are stable against electrochemical reduction and oxidation. Thereby, measurements with pseudo full-cells provide a sufficient lithium inventory and suppress the cross-diffusion of side products formed electrochemically on the counter electrode [189, 190]. Even though the preparation of pseudo

full-cells is more tedious due to the pre-(de)lithiation of the counter electrode, the superposition of degradation phenomena such as loss of lithium inventory or cross-talk can be excluded, what allows for the investigation of the effects of the experimental condition and procedure on the working electrode only, as it was introduced for the investigation of the cycling performance as well as of the consumption of electrolyte components of silicon-based anodes [38, 42, 56, 191–193]. In this work, two different pseudo-full cell setups were employed depending on the experimental requirements:

Pre-lithiated, capacitively oversized LFP ($3.5\,\mathrm{mAh/cm^2}$ at 90 %SOC) serves as counter electrode in OEMS experiments of CAMs (see Chapter 2.3) since the typical electrolyte components are stable at the LFP potential of $3.45\,\mathrm{V_{Li}}$, thereby eliminating the formation of gaseous products from the counter electrode. Consequently, the gas evolution stemming exclusively from the CAM working electrode can be monitored both during the first charge (see Chapters 3.2 and 5) and over the course of up to five cycles (see Chapters 4.1 and 4.3).

Pre-lithiated, capacitively oversized LTO ($3.5\,\mathrm{mAh/cm^2}$ at 10, 30, or 90 %SOC) is employed as counter electrode for the impedance-based capacitance measurements in blocking conditions (see Chapter 2.4) since its lithium inventory allows for the full lithiation of the working electrode even if cyclable lithium is lost in side reactions (see Chapters 3.1, 3.2, 3.3, and 4.1). Additionally, due to its lower potential of $1.55\,\mathrm{V_{Li}}$ (corresponding to $-1.5\,\mathrm{V_{SHE}}$), LTO removes protic species such as HF upon reduction to molecular hydrogen from the electrolyte, which would otherwise result in the chemical delithiation of the lithiated GWRE, as it was observed by the loss of the reference potential after a few hours of cell operation when LFP is used instead (data not shown). Furthermore, this setup allows for the individual investigation of the stability limit of CAMs in extended cycling experiments of more than 200 cycles (see Chapter 5).

2.3 On-Line Electrochemical Mass Spectrometry

Operando mass spectrometry has proven valuable for the understanding of fundamental chemical, electrochemical, and thermal side reactions in electrochemical systems [195], such as the structural instability of CAMs [90, 107, 109, 119, 123, 152, 196] as well as the reductive or oxidative decomposition of the electrolyte components [32, 38, 39, 114, 132, 197–203].

Through on-line electrochemical mass spectrometry (OEMS), the evolution and con-
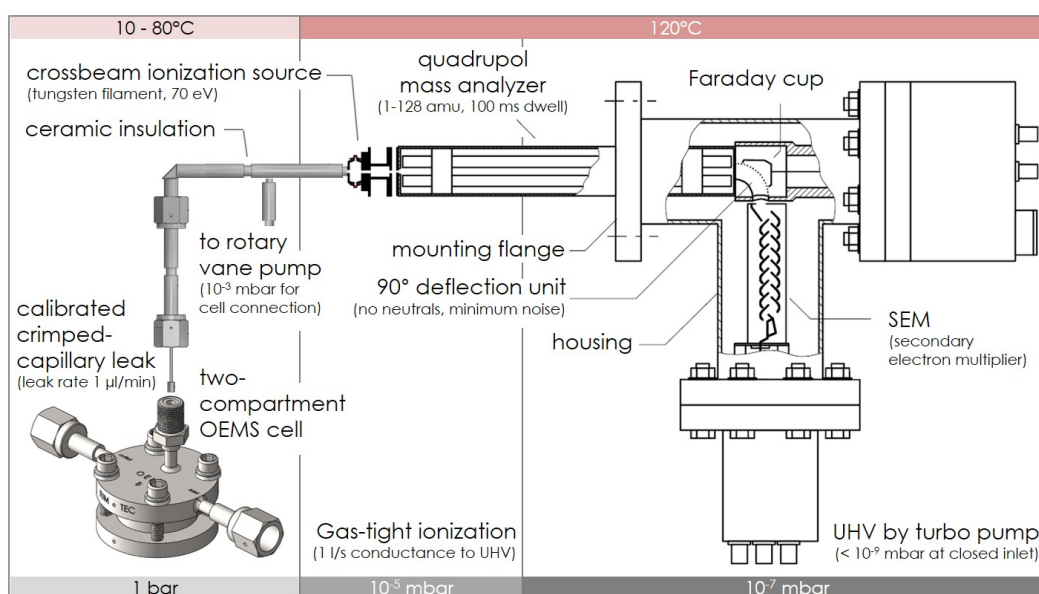
Figure 2.1 Schematic of the OEMS system. Gases evolved during cell cycling accumulate in the custom-made OEMS cell, which are continuously sampled via a capillary leak and analyzed by mass spectrometry. Reprinted from Metzger [194].

sumption of gaseous species is not only monitored simultaneously with the operation of the battery cell but also evaluated in a quantitative manner. The system deployed in this work was first presented by Tsiouvaras et al. [204] and later described in detail by Metzger [194]. The custom-made battery cell hardware containing the electrochemical cell is a closed system with a head space volume of ~ 11 ml, which is placed in a temperature-controlled chamber. The gas composition is probed continuously through a crimped capillary with a leak rate of $\sim 1\,\mu mol/min$, which is then analyzed by a mass spectrometer, as depicted in Figure 2.1. By this approach, the pressure within the cell decreases with time, limiting the experiment time to ~ 40 h. The amounts of evolved gas are sampled for each mass-over-charge ratio m/z of 1 to 128 amu with a time resolution of 10 s. After the experiment is completed, a calibration procedure with a calibration gas containing 2000 ppm of the relevant gases (e.g., H_2, O_2, C_2H_4, CO, and CO_2) in argon allows to convert the detected ion-current signal into ppm, or into $\mu mol/g$ by considering the head space volume of the cell and the electrode mass. To compensate for a change of the background signal, each experiment initiates with an OCV phase of 4 h, which is used to extrapolate the signals for the duration of the experiment.

In this work, the one-compartment cell design is used to avoid the large overpotentials introduced in CC mode by the resistive solid lithium-ion conductor of the two-

compartment cell [194]. To exclude any interference of the counter electrode with the measurement of the gas evolution of the working electrode, either i) LFP serves as non-gassing counter electrode (see Chapter 2.2), or ii) a half-cell setup with a lithium-metal counter electrode is used with an EC-only electrolyte, which solely forms ethylene gas upon reduction [33]. The use of an EC-only electrolyte does not only allow to exclusively track the oxygen evolution from the CAM working electrode but also improves the signal-to-noise ratio, resulting from the much lower vapor pressure and thus lower background signal of EC as compared to the one of the linear carbonates [201]. These two configurations are used to probe the oxygen release from CAMs with regards to its onset (see Chapters 3.2 and 5) as well as its extent (see Chapters 4.1 and 4.3).

2.4 Electrochemical Impedance Spectroscopy

Impedance spectroscopy is a powerful and non-destructive tool providing valuable information about electrical or electrochemical systems, characterizing, e.g., interfacial processes, dynamics of charge carriers, and geometric effects. The processes occurring in these systems have distinct time constants, which can be distinguished and characterized individually through impedance spectroscopy by probing various applied frequencies. In potentio (or galvano) electrochemical impedance spectroscopy (EIS), a small sinusoidal potential (or current) perturbation $U(t)$ (or $I(t)$) of a chosen frequency f (or angular frequency $\omega = 2\pi f$) is applied to the system while the current (or potential) response $I(t)$ (or $U(t)$) is recorded (PEIS (or GEIS)). This approach is performed for various frequencies of a whole frequency range, while the data of perturbation and response are fitted for each frequency by two sine functions:

$$U(t) = U_0 \cdot \sin(\omega t + \varphi_U) \tag{2.3}$$

$$I(t) = I_0 \cdot \sin(\omega t + \varphi_I) \tag{2.4}$$

Since electrochemical systems do not only consist of resistive but also of capacitive and inductive elements, which introduce a delay of Δt of the potential or current response, respectively, a phase shift $\Delta\varphi = \Delta t \cdot \omega$ between the perturbation and the response may occur:

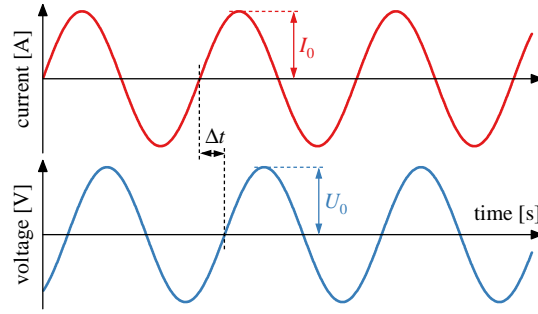$$\Delta\varphi = \varphi_U - \varphi_I \tag{2.5}$$

Figure 2.2 Exemplary potential and current data recorded during an impedance measurement, showing the sinusoidal waves of current (red) and potential (blue) and their respective amplitudes of I_0 and U_0 as well as the phase shift $\Delta\varphi = \Delta t \cdot \omega$. Data extracted from Figure 4 in reference [205].

After extracting the phase shift and the amplitude of current and potential from the data, all being dependent on the applied frequency, the absolute value of the impedance (in units of Ω) as well as the complex impedance are calculated using the definition of the impedance, in coherence with Ohm's law:

$$|\boldsymbol{Z}| = \frac{|U_0|}{|I_0|} \tag{2.6}$$

$$\boldsymbol{Z} = |\boldsymbol{Z}| \cdot \mathrm{e}^{\mathrm{i} \cdot \Delta\varphi} = |\boldsymbol{Z}| \cdot \cos(\Delta\varphi) + \mathrm{i} \cdot |\boldsymbol{Z}| \cdot \sin(\Delta\varphi) = \mathrm{Re}(\boldsymbol{Z}) + \mathrm{i} \cdot \mathrm{Im}(\boldsymbol{Z}) \tag{2.7}$$

For electrochemical systems, the data is typically represented in a so-called Nyquist plot, depicting the negative imaginary impedance $-\mathrm{Im}(\boldsymbol{Z})$ on the y-axis against the positive real impedance $\mathrm{Re}(\boldsymbol{Z})$ on the x-axis (see black data in Figure 2.3b for a battery full-cell) for the entire frequency range, creating an impedance spectrum.

Since an impedance spectrum of a battery cell comprises the convoluted impedance of both anode and cathode, which are added linearly to become the full-cell impedance, and since the features of the two electrodes often have similar characteristic frequencies, it remains a challenge to deconvolute their respective contributions. It has been demonstrated that the disassembly of two nominally identical cells and the subsequent assembly of the two anodes and the two cathodes in respective symmetric cells can provide the impedance contribution of one electrode (after the recorded data is divided by two), what is not only a tedious but also a destructive technique [107, 206–212]. In contrast, the use of a micro-reference electrode (µ-RE) allows to monitor the impedance contribution of each electrode in situ during operation, e.g., through a gold-wire reference electrode (GWRE): for this purpose, the lithiated tip of an insulated gold wire is placed between two separators (see Figure 2.3a), accurately defining its position between the electrodes, which also has a stable potential of $0.31\,\mathrm{V_{Li}}$, as it
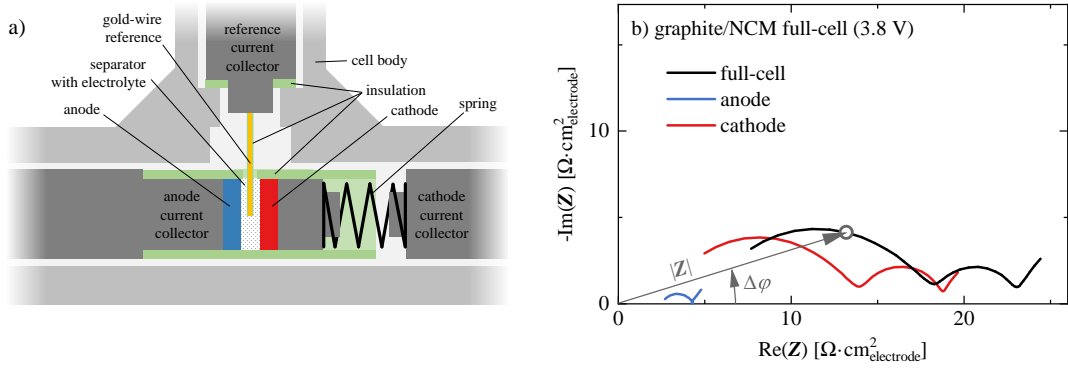
Figure 2.3 a) Cell setup for the use of a gold-wire reference electrode in a T-cell. Adapted from Solchenbach et al. [208]. **b)** Exemplary impedance spectra of a full-cell (black) with graphite anode (blue) and single-crystalline NCM851005 cathode (red) at $3.8\,\text{V}_{\text{Li}}$, or $\sim$50 %SOC, respectively, after 42 charge/discharge cycles in LP57 to $4.4\,\text{V}$ at $45\,^{\circ}\text{C}$, which were normalized to the geometric surface area of $0.94\,\text{cm}^2_{\text{electrode}}$ of the electrode. Data extracted from Figure 7 in Chapter 4.3 and depicted from $30\,\text{kHz}$ to $100\,\text{mHz}$. The gray arrows indicate the absolute value of the impedance $|\boldsymbol{Z}|$ as well as the phase angle $\Delta\varphi$ at a selected point (gray circle).

was demonstrated previously by Solchenbach et al. [208].

Typical impedance spectra of the positive and negative electrode, determined using a µ-RE, are depicted in Figure 2.3b: the full-cell impedance (black) deconvolutes to the anode (blue) and cathode (red) impedance, exhibiting various semicircles. To quantify the contribution of the different electrochemical processes, a spectrum is fitted by a suitable electrical equivalent circuit which comprises resistors, capacitors, and/or inductors, or serial and/or parallel combinations thereof. An ohmic resistance contributes only a real (frequency-independent) part to the impedance $\boldsymbol{Z}_{\text{R}} = R$, while a capacitor and an inductor contribute purely to the imaginary impedance part by $\boldsymbol{Z}_{\text{C}} = \frac{1}{\text{i}\omega C}$ and $\boldsymbol{Z}_{\text{L}} = \text{i}\omega L$, respectively, both in a frequency-dependent manner. For a resistor and a capacitor connected in parallel, the impedance spectrum follows the equation $\boldsymbol{Z}_{\text{R}\|\text{C}}(\omega) = \frac{R}{1+\text{i}\omega RC}$, resulting in a semicircle in the Nyquist representation with a diameter of R and an apex angular frequency of

$$\omega_{\text{max}} = \frac{1}{RC} \tag{2.8}$$

The capacitive behavior in real electrochemical systems, however, is not characterized by a physical capacitor but by a constant-phase element (CPE), which is described by $\boldsymbol{Z}_{\text{CPE}} = \frac{1}{(\text{i}\omega)^{\alpha}Q}$ and does not give a vertical line but a straight line which is tilted by the phase angle α, resulting from the surface roughness or the inhomogeneous distribution of different resistive and capacitive elements on the surface of the electrode [213–215].
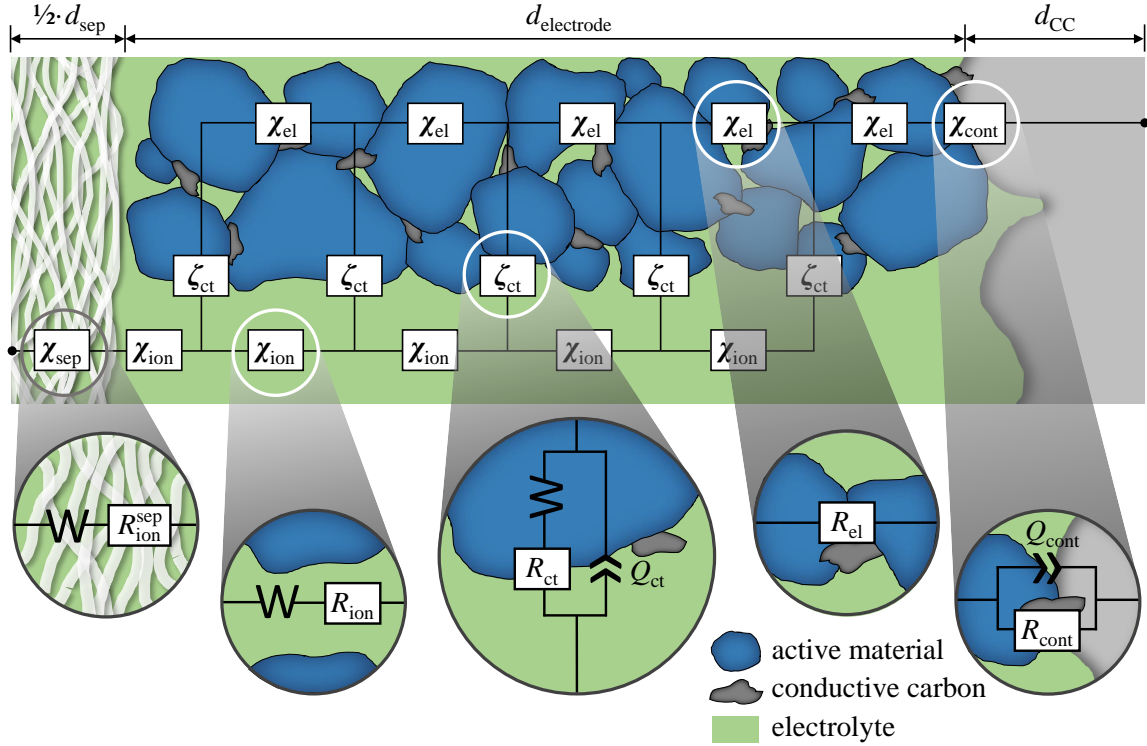
Figure 2.4 Schematic representation of the equivalent circuit of a porous battery electrode including a transmission line model, comprising active material (blue) and conductive carbon (black), filled by electrolyte (green), and enclosed by the separator (white) and the current collector (gray). Adapted from Hauck et al. [216].

To fit an entire impedance spectrum at once, an equivalent circuit comprising the required elements to represent the relevant physical processes is used: for one-dimensional porous electrodes, the equivalent circuit is based on a transmission line model [206, 207, 217–219], representing the ionic rail in the electrolyte as well as the electronic rail within the electrode, which are connected by a charge-transfer process; it is completed by the contact resistance of the electrode as well as the ionic resistance in the porous separator, as depicted in Figure 2.4, from right to left:

○ To enter the electrode from the current collector, the electrons pass the contact impedance χ_{cont}, comprising the contact resistance R_{cont}, which is connected in parallel with the double-layer capacitance of the current collector Q_{cont}.

○ Their travel through the electrode is hindered due to the electronic impedance χ_{el}, consisting of the ohmic resistance R_{el} between as well as within the particles of the electrode components.

○ The electrons either continue to move through the solid electrode via a series of χ_{el} elements or they participate in a charge-transfer reaction ζ_{ct}, which is

33

described by an R-Q element, consisting of the charge-transfer resistance R_{ct} and the double-layer capacitance Q_{ct} in the form of a CPE. In this reaction, the charge of the electrons is transferred from the solid to form ions in the liquid (or vice versa). To take into account the diffusion of lithium ions in the solid from/to the charge-transfer reaction, a so-called Warburg term $\boldsymbol{Z}_{\mathrm{W}} = \sigma\omega^{-1/2} - \mathrm{i}\sigma\omega^{-1/2}$ is added in series (depicted by the symbol W), accounting for the diffusion in the solid phase.

○ The lithium ions created/consumed in the charge-transfer reaction travel towards/from the counter electrode through the electrolyte, which is described by the ohmic resistance of the electrolyte R_{ion} as well as a respective Warburg element, accounting for the diffusion in the liquid phase.

○ The impedance of lithium ions moving through the porous separator $\boldsymbol{\chi}_{\mathrm{sep}}$ consists of the ionic resistance of the electrolyte $R_{\mathrm{ion}}^{\mathrm{sep}}$ and a respective Warburg term.

Further developments of the transmission line model complete the existing model by parameters such as the contribution of the non-active counter ion in the porous electrode and separator, of interphases formed on active materials (such as SEI/CEI), and the deposition of porous or inactive lithium on lithium-metal anodes [220–223]. Additionally, the electronic conductivity within an active material particle becomes relevant when particle cracking impedes the electronic conduction within a secondary agglomerate, as it is observed in Chapter 4.3; its proper physical description would require a transmission line model within each active material particle, which is limited by the electronic rail. However, the model depicted in Figure 2.4 has proven to represent typical battery electrodes sufficiently.

For a charged NCM electrode (at $4.3\,\mathrm{V_{Li}}$), the presented transmission line model results in the impedance spectra observed in the Nyquist plot in Figure 2.5 (red solid line): the shift in the real direction, corresponding to the so-called high-frequency resistance R_{HF}, mainly stems from the ohmic resistance of the ions in the porous separator $R_{\mathrm{ion}}^{\mathrm{sep}}$, but also contains, e.g., the resistance of the current collector or any external resistance of the setup, which can both be neglected in the context of lab-size battery cells. The left semicircle is attributed to the contact impedance $\boldsymbol{\chi}_{\mathrm{cont}}$, which is followed by a second semicircle for the electrode impedance: the latter contains the contribution of the charge-transfer resistance R_{ct}, the ionic pore resistance R_{ion}, as well as the electronic resistance R_{el} through the solid part of the electrode. At medium SOC (at $3.9\,\mathrm{V_{Li}}$, red dashed line), the first semicircle remains constant, while the second one
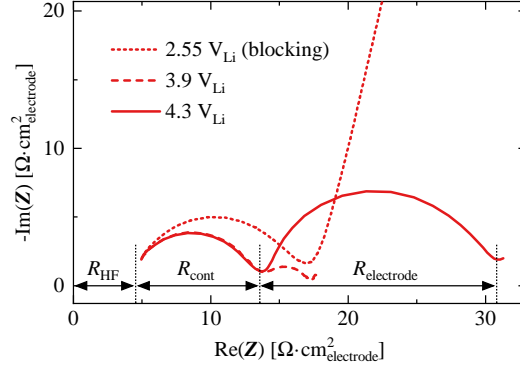
Figure 2.5 Exemplary impedance spectra of polycrystalline NCM851005 at three different potentials of 2.55 (red dotted line), 3.9 (red dashed line), and 4.3 V_{Li} (red solid line), corresponding to three SOCs of 0, 50, and 80 %SOC, respectively, which were normalized to the geometric surface area of 0.94 $cm^2_{electrode}$ of the electrode. NCM as working electrode compressed at 100 MPa in a pseudo full-cell with 60 µl LP57, two glass fiber separators, and a µ-RE, using pre-lithiated, capacitively oversized LTO as the counter electrode. Impedance spectra of the NCM working electrodes were recorded at 25 °C in CV mode for 2.55 V_{Li} and in OCV for 3.9 and 4.3 V_{Li} (15 mV amplitude, from 100 kHz to 100 mHz). The origin of each semicircle is labeled by the black arrows. The semicircle of the contact resistance R_{cont} of 3.9 and 4.3 V_{Li} lie on top of each other.

decreases in size due to a decrease in R_{ct} [122, 219, 224]. In the fully discharged state (at 2.55 V_{Li}, red dotted line), R_{cont} increases due to a change of the conductivity [225] of the CAM, as it is discussed in Chapter 4.1, while the semicircle of the electrode impedance converts into a capacitive branch in the form of a CPE, due to a semi-infinite R_{ct} in fully lithiated state [122, 219, 224], as discussed in Chapter 3.1.

The state of a semi-infinite charge-transfer resistance R_{ct} is also referred to as block-ing conditions, which is obtained when the (de)intercalation of lithium ions is not possible, either i) when an electrolyte based on non-intercalating ions is used (such as TBATFSI [224]), or ii) at a potential at which (de)intercalation is thermodynam-ically unfavorable (i.e., no charge is exchanged even though a potential change is applied [219]). The latter can be obtained for battery active materials upon full (de)lithiation, as previously shown for LNMO [219] or here for NCMs [224]. In this state, since R_{ct} is semi-infinite and thus blocking, the current through the charge-transfer impedance χ_{ct} passes only through Q_{ct}, appearing as a capacitive branch in the form of a CPE at low frequencies. An electrode in blocking conditions does not only allow for the extraction of the ionic pore resistance of the electrode and thus of the tortuosity of the electrode [206, 207, 218, 219] but also for the straight-forward extraction of Q_{ct} [224]; the extraction of the capacitance is more challenging in non-blocking conditions, i.e., for finite R_{ct}, since the charge-transfer impedance ζ_{ct} is in this case convoluted with R_{ion} [226].

The capacitance in electrochemical systems (such as Q_{ct} and Q_{cont}) originates from the electrochemical double layer, which is formed at the interface of a solid and the electrolyte by free charge carriers, i.e., by electrons in the solid and ions in the liquid phase. Ions with and without ionization shell are adsorbed at the electrode surface, forming the inner and outer Helmholtz layer, respectively; charge carriers which are attracted diffusely to the electrode create the Gouy-Chapman layer. This double layer can be (dis)charged similarly to a physical capacitor when it experiences an externally applied potential difference. Since the absolute capacitance of a capacitor is proportional to its surface area, the analysis of the capacitance allows to quantify the electrochemically active surface area (changes), as this has been observed for roughened metal electrodes [227, 228].

While the surface-area-normalized capacitance of carbon materials, e.g., used in supercapacitors, ranges on the order of 2 to $10\,\mu F/cm^2$ [229–231], the one of metals and their respective oxides exhibits capacitance values of 15 to $60\,\mu F/cm^2$ [232–236]. Interestingly, the surface-area-normalized capacitance of $\sim 28\,\mu F_{NCM}/cm^2_{NCM}$ is essentially identical for the two NCM compositions NCM622 and NCM851005 and does not change upon formation of the oxygen-depleted surface layer at high SOC, as observed in Chapter 3.2. As a consequence, the NCM capacitance determined by EIS (in units of $\mu F_{NCM}/cm^2_{NCM}$) can be translated directly into a physical surface area (in units of m^2/g_{NCM}). Therefore, the analysis of the capacitance is not only able to track relative changes of the electrode or NCM surface area but can also quantitatively determine the specific surface area of NCM materials in absolute values (after the subtraction of the contribution of the other components in the electrode). Nevertheless, the capacitance of an electrode is strongly dependent on the used materials, the applied potential, and the electrolyte composition, i.e., the type of salt and its concentration as well as the solvent type (see Chapter 3.1).

Therefore, in this work, EIS is used to monitor NCM particle cracking quantitatively through the evolution of the capacitance of an electrode (see Chapters 3.1, 3.2, 3.3, and 4.1), while the limitations of the method are illustrated in Chapter 4.2. Furthermore, it provides insight into the origin of the morphology-dependent differences of the resistance of a cell upon extended charge/discharge cycling in full-cells (see Chapter 4.3).

2.5 Thermogravimetric Analysis

Thermogravimetric analysis (TGA), being a method for the thermal analysis of materials, tracks the mass of a sample by a high-precision balance as a function of both time and temperature. During the TGA measurement, the sample temperature is changed according to a defined protocol, including heating and cooling steps or isothermal holds; additionally, the gas atmosphere can be adjusted according to the experimental requirements [237, 238].

The investigation by TGA elucidates physical phenomena, such as vaporization, adsorption, and desorption (e.g. (de)hydration), or chemical phenomena such as the thermal decomposition of the sample or solid-gas reactions, such as oxidation and reduction, depending on the used atmosphere (e.g., nitrogen or argon for inert conditions, air or pure oxygen for the oxidation, or hydrogen or carbon monoxide for the reduction). However, sample changes without mass change such as phase transitions of the crystal structure cannot be observed through TGA only; by using differential thermal analysis (DTA) or differential scanning calorimetry (DSC), however, physical and chemical changes can be deconvoluted. Additionally, by coupling TGA with mass spectrometry or infrared spectroscopy, the analysis of the evolved gases gives further insights into the composition of the sample and its reaction processes [237, 238].

The sample is placed in an open pan before it is heated inside of a closed furnace, which can be flushed by a chosen gas type and flow rate. For air-sensitive samples, such as charged battery electrodes, the exposure to the ambient atmosphere is prevented by enclosing the sample in a crimped gas-tight crucible (e.g., made of aluminum), which is punctured shortly before the experiment is initiated. The measurement is typically corrected by a reference run with an empty pan. For battery materials, the operating temperatures are found to range from 25 to 1200 °C and the applied heating rates vary on the order of 1 to 10 K/min.

The TGA method has proven useful for the characterization of CAMs, e.g., in the identification and quantification of surface contaminants [100, 239, 240] or in the investigation of the thermal stability of the CAM indicated by the decomposition temperature of delithiated or protonated NCMs [96, 113, 116, 241]. In this work, TGA is used to elucidate the thermal stability of charged NCM622 electrodes in dependence of the CAM particle morphology and surface area (see Chapter 4.1).

2.6 Further Characterization Techniques

In addition to the methods described in this chapter, images of active material powders and electrodes were taken in top view by scanning electron microscopy (SEM) (see Chapters 3.2, 4.1, and 4.3); cross-sectional images are taken of electrodes which were polished by a focused argon ion beam (FIB) (see Chapter 3.1). The images were collected by a tabletop microscope (JCM-6000, JEOL, Japan) in secondary electron mode, applying an acceleration voltage of 15 kV.

The used electrochemical methods include cyclic voltammetry to investigate the effect of the applied potential on the specific capacitance (see Chapter 3.1) as well as on the gas evolution (see Chapter 5) of electrodes consisting of conductive carbon and binder only. Furthermore, galvanostatic charge/discharge cycling is applied to half-cells, consisting of an electrode paired with a lithium-metal counter electrode, to full-cells, consisting of a graphite anode and a cathode, as well as to pseudo full-cells, as described in Chapter 2.2. In these cells, typical battery electrodes are cycled both in CC or CCCV mode, i.e., a constant-current (CC) mode with or without constant-voltage (CV) hold, respectively, either using conventional battery cyclers (Series 4000, Maccor, USA) or potentiostats with impedance capability (VMP3, BioLogic, France), to investigate their rate capability and/or their cycle life, or to deliberately age electrode materials for subsequent characterization. To exclude any contribution by the periphery, the cells are connected by separate cables for voltage and current. Depending on the requirements, the cells include a lithium-metal reference electrode to track the potentials of each electrode, or a micro-reference electrode (µ-RE, being a gold-wire reference electrode [208] in this work) to monitor the impedance of each electrode individually. Furthermore, some cycling protocols include direct-current internal resistance (DCIR) measurements (see Chapter 4.3 and Chapter 5), consisting of a (charge or discharge) direct-current pulse with a current I and a duration t_0 (of typically 1 or 10 s), while the cell is in OCV before and after the pulse. For a pulse starting at $t = 0$, the internal resistance R of the cell is calculated by Equation 2.9 [242].

$$R = \frac{\frac{U(2t_0) - U(0)}{2} - U(t_0)}{I} \tag{2.9}$$

3 Monitoring Particle Cracking by In Situ Impedance Spectroscopy

The integrity of the active material particles is essential to the lifetime of battery materials. The (chemo)mechanical cracking of particles, typically resulting from mechanical compression during manufacturing [243, 244] and/or their volume change upon repeated (de)lithiation [98, 138], alters the pristine morphology and is reported to be detrimental for the capacity retention of the battery cell. This performance loss due to cracking may originate from the loss of active material and/or from impedance build-up, both for anode (e.g., for silicon [55, 56]) and cathode (e.g., for LFP [72–74] or NCM [122, 245]) materials. Additionally, the increase in CAM surface area may give rise to unwanted side reactions on the freshly exposed electrode-electrolyte interfaces, such as (electro)chemical electrolyte oxidation [31, 121, 201], oxygen release at high state of charge [109, 119, 120], and/or transition metal dissolution [126, 127, 134]. So far, the integrity of CAM particles has been monitored qualitatively in ex situ experiments using microscopy (e.g., FIB-SEM/-TEM) [140, 160, 246] or tomography [142]. Since the mentioned methods are not only non-quantitative but also expensive regarding time, resources, and labor, and since each experiment contributes only a single data point to the whole data set, a new facile methodology is required to track and quantify the changes of the particle morphology in situ during cell operation.

This chapter describes the stepwise development process of a novel impedance-based method, which tracks the capacitance of an electrode as an indicator for its surface area and thus for particle cracking of active material particles. It is composed of three successive parts: i) the theoretical fundamentals enabling the capacitance determination of battery electrodes by EIS are derived and discussed and the relation between electrochemical capacitance and physical surface area is validated; ii) the effect of NCM composition and NCM particle morphology on the morphological and structural stability at high state of charge is illuminated; and iii) a simplification of the initially devised setup is deduced, enabling the utilization of the method in simple half-cells.

3.1 Theory and Validation

The article "Novel Method for Monitoring the Electrochemical Capacitance by In Situ Impedance Spectroscopy as Indicator for Particle Cracking of Nickel-Rich NCMs: Part I. Theory and Validation" was submitted to the peer-reviewed *Journal of the Electrochemical Society* in April 2020 and published online in June 2020 [224]. It is available as an open-access article and distributed under the terms of the Creative Commons Attribution Non-Commercial No Derivatives 4.0 License. This paper was awarded with the *Norman Hackerman Young Author Award 2020* of the Electrochemical Society. A permanent link to this article can be found under https://doi.org/ 10.1149/1945-7111/ab9187. The main findings of this paper were presented by Stefan Oswald as Poster #A004 at the Electrochemistry 2018 Meeting of the *Gesellschaft deutscher Chemiker* in Ulm, Germany, in September 2018, as well as in an oral presentation at the 70th Annual Meeting of the *International Society of Electrochemistry* in Durban, South Africa, in August 2019.

The objective of this work is the development, validation, and application of a technique which is capable of quantifying the cracking of CAM particles during electrode manufacturing and/or cell operation, which had not been reported in the literature before. Through the mathematical analysis of the impedance response of a CPE, it is first shown that the unique properties of the frequency point at $\sim 180\,\mathrm{mHz}$ of an electrode in blocking conditions allow for the extraction of the capacitance without a fit of the entire impedance spectrum. The proportional relation between the capacitance extracted by EIS at $180\,\mathrm{mHz}$ and the physical surface area obtained by Kr-BET is verified for mechanically compressed electrodes, exhibiting significant NCM particle cracking by visual investigation through FIB-SEM. By using a lithiated gold wire as μ-RE [208], the capacitance of PC NCM622 electrodes in the fully discharged state was monitored individually over 200 charge/discharge cycles to three different upper cutoff potentials between 3.9 and $4.5\,\mathrm{V_{Li}}$, inducing a repeated volume change $\Delta V/V$ between -1.0 and $-4.0\,\%$ for NCM622, respectively. The pronounced surface area increase at high potential of more than $+250\,\%$ is attributed to the increased volume change at higher SOCs and the subsequent irreversible cracking of the secondary agglomerates, which is verified in post mortem FIB-SEM images. Consequently, an accelerated capacity fading and impedance build-up is observed over 200 cycles for the higher upper cutoff potentials which stems (at least partially) from the fragmentation of the NCM secondary agglomerates. Finally, the impact of the volume change of the active mate-

rial is further highlighted by cycling experiments on LTO (exhibiting a volume change of +0.2 %) and LFP (-6.8 %) upon (de)lithiation: the capacitance of the "zero-strain" material LTO remains essentially unaffected over the course of 200 cycles while the one of LFP increases by more than +60 %.

To support the main article, additional information is provided for the benefit of the reader. The Supporting Information includes all relevant details about the validation of blocking conditions for LFP and LTO, the potential-dependent capacitance of carbon-only C65 and VGCF electrodes as well as the one of the NCM electrodes, and the discharge capacity as a function of cycle number of LFP, LTO, and NCM, including the dependence on the upper cutoff potential for the latter.

The determination of material-specific parameters such as the charge-transfer resistance and the diffusion kinetics of lithium in the solid phase in the form of the apparent diffusion coefficient requires knowledge of the surface area of the material and/or its particle size distribution [247–250]; this knowledge is also essential for the interpretation of results such as the thickness of the oxygen-depleted surface layer computed from the amount of released lattice oxygen [107, 109, 119] or the amount of dissolved transition metals [129, 130]. For these evaluations, typically, the values of the pristine CAM powder are considered. Due to the here observed significant increase of the capacitance and thus the surface area of both NCM and LFP, however, future studies should take into account the changes in the particle morphology when results are normalized to the surface area of the CAM. The technique has been applied by Sim et al. to elucidate the impact of calendering on the cycling performance of nickel-rich CAMs [251] as well as by Riewald et al. to correlate the synthesis conditions of LNO with its available surface area and its irreversible capacity [92].

Author contributions

S.O., D.P., and M.W. developed the concept of the impedance-based capacitance measurements. S.O. performed the simulations and calculations, conducted the electrochemical, impedance, and BET measurements, and analyzed the data. S.O. wrote and H.A.G. edited the manuscript. All authors discussed the results and commented on the manuscript.

Novel Method for Monitoring the Electrochemical Capacitance by In Situ Impedance Spectroscopy as Indicator for Particle Cracking of Nickel-Rich NCMs: Part I. Theory and Validation

Stefan Oswald,*,z Daniel Pritzl, Morten Wetjen, and Hubert A. Gasteiger**

Chair of Technical Electrochemistry, Department of Chemistry and Catalysis Research Center, Technical University of Munich, D-85748 Garching, Germany

Nickel-rich NCM (LiMO$_2$, with M = Ni, Co, and Mn) cathode active materials for lithium-ion batteries are being increasingly commercialized due to their high specific capacity. However, their capacity retention upon cycling is impaired by crack formation of NCM secondary agglomerates induced by the volume change upon repeated (de)lithiation that depends on the nickel content and the cutoff potential. Particle cracking leads to loss of electrical contact and enhanced side reactions caused by an increased surface area. Here, we introduce a novel method based on electrochemical impedance spectroscopy (EIS) in blocking conditions to quantify the increase in the active material's surface area upon cycling, utilizing the correlation between the surface area of the electrode and the electrochemical double-layer capacitance that is validated experimentally by comparing the capacitance and BET surface area increase of NCM electrodes upon mechanical compression. To quantify the cracking of the particles upon 200 charge/discharge cycles, we perform in situ EIS measurements utilizing a micro-reference electrode and monitor the cathode's impedance response. In addition, the crack formation of cycled NCM particles is validated visually by post mortem FIB-SEM. The effect of volume change on cracking is illuminated through the analysis of LFP and LTO as model materials.

Layered lithium nickel cobalt manganese oxide based materials (NCMs, Li$_{1+\delta}$Ni$_x$Co$_y$Mn$_z$O$_2$, $x+y+z+\delta = 1$) are commercially used cathode active materials (CAMs) in current lithium-ion batteries for electric vehicle applications,[1–3] owing to their technological maturity as well as their relatively high discharge capacity and discharge potential, resulting in superior energy and power density. To push the delivered specific capacity at the same upper cutoff potential closer to the theoretical limit of ∼275 mAh/g$_{NCM}$, the nickel content of these materials is increased to values of $x > 0.8$. The increased nickel content, however, implies a lower thermal stability, compromised safety, a lower onset potential for oxygen release, and a shorter cycle life.[3–5]

One proposed failure mechanism of nickel-rich NCMs is the structural degradation of the NCM particles and the electrode due to volumetric changes of the rhombohedral unit cell upon repeated (de)lithiation of the NCM crystallites.[6] De Biasi et al. showed by in situ X-ray diffraction that the volume change of the NCM unit cell increases with the nickel content.[7] In addition, the unit cell volume changes anisotropically due to the unequal variation of the *a*- and the *c*-axis lattice parameter, leading to changes in the *c/a* ratio upon (de)lithiation that are accompanied by severe stress and strain in the particle, and, therefore, to an even stronger evolution of cracks in the secondary agglomerates.[6–8] Many studies have visually shown the formation of cracks upon extended charge/discharge cycling in nickel-rich NCMs[6,9–13] and NCAs,[9,14–17] accompanied by an increase in specific surface area (i.e. in BET surface area) and by the penetration of electrolyte into the secondary particle, exposing the primary NCM particles to the electrolyte.[14] It is expected that the formation of cracks in the polycrystalline material enhances the degradation of NCM cycle life by various mechanisms: (i) the release of lattice oxygen at the freshly exposed electrode/electrolyte interface can result in the formation of a rock-salt layer that hinders lithium diffusion,[8,9,14,18,19] (ii) the reaction of the simultaneously released singlet oxygen with the electrolyte constituents produces

HF[20,21] that enhances active material loss due to transition metal dissolution,[22–24] and (iii) the eventual separation of fragments from the initial secondary NCM agglomerate, promoting loss of electrical contact of the active material.[6,16,25–27] Either one or a combination of these mechanisms will ultimately lead to increasing overpotentials and/or a loss of available capacity, limiting the discharge capacity of the cells.

Crack formation, either due to volume change upon electrochemical (de)lithiation[6,7] or due to mechanical compression upon calendering,[28,29] may have serious consequences with regard to cycle life—in particular, for CAMs having tailored surfaces to protect the sensitive (nickel-rich) core.[2,29,30] These include any type of gas-treated or coated CAM particles as well as particles with a nickel-deficient shell[31–33] or a nickel concentration gradient,[34,35] in which case the exposure of unprotected surfaces by cracking would be detrimental. This effect can be mitigated by tailor-made coatings or deliberate handling of CAMs, which is reported to help maintain the structure of the secondary agglomerates and to improve the cycling stability.[13,15,36,37] However, single crystalline CAMs are perhaps the most promising concept for suppressing the formation of cracks.[38,39]

In most previous studies investigating particle cracking, the electrodes had to be harvested from the cycled cells and prepared and analyzed by Kr-BET, FIB-SEM or even TEM, which are cumbersome and not generally available methods that furthermore require a large number of repeat analyses to be statistically significant. This study aims to develop a novel diagnostic tool to quantify particle cracking upon cycling using in situ electrochemical impedance spectroscopy (EIS) with a micro-reference electrode (based on a lithiated gold wire[40]). By taking into account suitable theoretical considerations, the electrochemical capacitance can be used as a measure for the electrode's electrochemically active surface area (i.e. the electrode surface area in contact with the electrolyte), which will be monitored upon the formation of cracks in cathode active material particles. In this study, we validate this method by comparing the evolution of capacitance determined by in situ EIS with a micro-reference electrode with physical surface area measurements by krypton gas physisorption, while the cracking of the particles is verified by FIB-SEM.

*Electrochemical Society Student Member.
**Electrochemical Society Fellow.
zE-mail: Stefan.Oswald@tum.de

Theoretical Considerations

Constant-phase element.—Electrochemical impedance spectroscopy (EIS) provides information about physical processes in electrochemical systems, which can be investigated due to their separation by different time constants. By applying an alternating potential or current in an EIS experiment to an ideal electrode/electrolyte interface in the absence of charge transfer, one would expect a purely capacitive behavior due to the capacitance of the electrochemical double layer. This theoretical capacitor appears as a vertical line in a Nyquist plot, what is expressed in complex notation as:

$$\mathbf{Z}_C = \frac{1}{\mathrm{i}\omega C} \qquad [1]$$

Assuming that the areal capacitance (i.e. the electrochemical capacitance per surface area) is distinct, constant, and uniformly distributed for each electrode material, the absolute capacitance C is a direct measure of the surface area of an electrode (see Eq. 2), a property which can, e.g. be used to assign observed features to physical properties, such as contact resistances.[41]

$$C \propto A \qquad [2]$$

Real systems like battery electrodes do not show a purely capacitive behavior, but rather have to be described by a constant-phase element (CPE).[42,43] This is commonly explained by surface roughness or a distribution of differently sized capacitive and resistive elements along the surface of the electrode.[44–46] This type of circuit element can be mathematically described through a transformation of the physical capacitor by introducing the CPE parameter Q with units $\mathrm{F/s}^{1-\alpha}$ and the phase angle α, which is independent of frequency and does not only appear as a clockwise tilt of the vertical line, but also shifts the frequency points on the line. In complex notation, this is expressed as:

$$\mathbf{Z}_{\mathrm{CPE}} = \frac{1}{(\mathrm{i}\omega)^{\alpha}Q} \qquad [3]$$

For $\alpha = 1$, one obtains the purely imaginary impedance of the physical capacitor (i.e. Eq. 3 simplifies to Eq. 1), whereas $0 < \alpha < 1$ adds a real resistive part. For $\alpha < 1$, Q does not represent a simple capacitance,[45] but should, nevertheless, scale with the electrochemically active surface area. When using Q as a measure for the surface area of the electrode, one either obtains the Q parameter from a fit of the capacitive branch of the Nyquist plot contributed by a CPE or utilizes a reasonable approximation.

Figure 1a shows the calculated impedance response of a physical capacitor with capacitance $C = 1 \cdot 10^{-3}$ F using Eq. 1 as well as of four CPEs defined by Eq. 3 with $Q = 1 \cdot 10^{-3}$ F/s$^{1-\alpha}$ and phase angle $\alpha \in \{0.95, 0.90, 0.85, 0.80\}$. For the CPEs, it appears that the imaginary part of the impedance Im($\mathbf{Z}$) at 180 mHz (blue open circles in Fig. 1a) is largely independent of the phase angle α. Through the analysis of the imaginary part of the CPE impedance as shown in Eq. 4, it becomes obvious that the dependence of the first factor $\frac{1}{\omega^{\alpha}Q}$ in the last term of Eq. 4 on the phase angle α is minor for frequencies close to $\omega = 2\pi f = 1$, i.e. for $f \approx 159$ mHz. Furthermore, for α values close to 1, the dependence of the sine term in the second factor of Eq. 4 is also very small.

$$\mathrm{Im}(\mathbf{Z}_{\mathrm{CPE}}) = \mathrm{Im}\left(\frac{1}{(\mathrm{i}\omega)^{\alpha}Q}\right) = \mathrm{Im}\left(\frac{1}{\omega^{\alpha}Q}\exp\left(\mathrm{i}\left(-\frac{\pi}{2}\alpha\right)\right)\right)$$

$$= \frac{1}{\omega^{\alpha}Q}\mathrm{Im}\left(\cos\left(-\frac{\pi}{2}\alpha\right) + \mathrm{i}\sin\left(-\frac{\pi}{2}\alpha\right)\right)$$

$$= \frac{1}{\omega^{\alpha}Q}\sin\left(-\frac{\pi}{2}\alpha\right) \qquad [4]$$

For this reason, one expects that the ratio of the imaginary part of the impedance of a CPE taken at phase angles close to $\alpha = 1$ and at
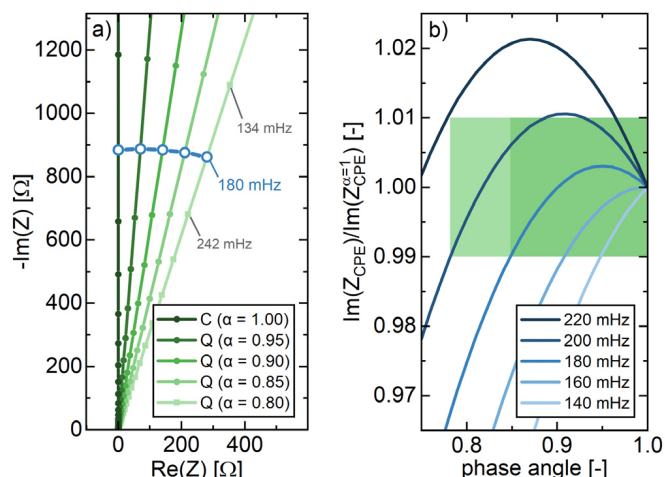

Figure 1. Simulation of constant-phase elements (CPEs) as defined in Eq. 3. (a) Nyquist plot of the impedance spectra of a pure physical capacitor ($C = 1 \cdot 10^{-3}$ F and $\alpha = 1.00$) as well as of four constant-phase elements ($Q = 1 \cdot 10^{-3}$ F/s$^{1-\alpha}$) with different phase angles ($\alpha \in \{0.95, 0.90, 0.85, 0.80\}$). (b) Calculation of the imaginary impedance of a CPE normalized to the imaginary part of the impedance of a capacitor, i.e. Im($\mathbf{Z}_{\mathrm{CPE}}$)/Im($\mathbf{Z}_{\mathrm{CPE}}^{\alpha=1}$), vs. the phase angle α for different frequencies as predicted by Eq. 5. For the frequency of $f = 180$ mHz, the imaginary impedance changes less than ± 1 % between phase angles of $\alpha = 1.00$ and $\alpha = 0.85$ (dark green area); for a frequency of $f = 200$ mHz, this applies for phase angles as small as $\alpha = 0.79$ (light green area). For $f = 160$ mHz, which also corresponds to $\omega = 2\pi f \approx 1$ s^{-1}, a purely sinusoidal behavior is observed.

frequencies close to $f = 159$ mHz normalized by the imaginary part of the impedance of an ideal capacitor, i.e. Im($\mathbf{Z}_{\mathrm{CPE}}$)/Im($\mathbf{Z}_{\mathrm{CPE}}^{\alpha=1}$), described by Eq. 5 will be close to 1.

$$\mathrm{Im}(\mathbf{Z}_{\mathrm{CPE}})/\mathrm{Im}(\mathbf{Z}_{\mathrm{CPE}}^{\alpha=1}) = -\omega^{1-\alpha} \cdot \sin\left(-\frac{\pi}{2}\alpha\right) \qquad [5]$$

This ratio of Im($\mathbf{Z}_{\mathrm{CPE}}$)/Im($\mathbf{Z}_{\mathrm{CPE}}^{\alpha=1}$) vs. phase angle α is depicted in Fig. 1b, showing that the influence of the phase angle α on the normalized imaginary impedance is less than 1 % for $f = 180$ mHz and $\alpha > 0.85$ or for $f = 200$ mHz and $\alpha > 0.79$. For the experiments shown in this study, the impedance spectra are recorded with eight frequency points per decade, which includes the point at 180 mHz, which is why we will be focusing on this frequency point in our further discussion. From Fig. 1b it becomes obvious that the imaginary part of the impedance at a frequency of $f = 180$ mHz is, at least to a good approximation, inversely proportional to Q (see last term in Eq. 4), even if the phase angle might change during the experiment. To avoid having to fit the CPE of each impedance spectrum and having to find Q and α, we take advantage of the following approximation:

$$Q \approx \frac{1}{\omega_0 \cdot (-\mathrm{Im}(\mathbf{Z}_{\omega_0}))} \qquad [6]$$

which is within an error of ± 1 % for $\omega_0 \approx 1$ s^{-1} corresponding to a frequency of $f_0 = 180$ mHz and for $\alpha > 0.85$. Note that in this case the units of Q represent those of a capacitor (i.e. F rather than F/s$^{1-\alpha}$). In the present study, we utilize this property to extract the relative change of the electrode's surface area by monitoring the change of the 180 mHz point and further compare this simplification to the exact result obtained from a fit of Q to legitimate its application experimentally. In summary, the CPE parameter Q is treated as a measure for the electrochemical capacitance, which is a good approximation at a frequency of 180 mHz and for phase angles of $\alpha > 0.85$.

Determination of surface area from impedance spectra.—In this study, we aim to use the capacitance of the electrochemical double layer of the entire composite electrode (i.e. consisting of

active material, conductive carbon, and binder) to track the cracking of active material particles due to mechanical compression or due to volume changes upon (de)lithiation. When exposed to mechanical stress, a material may develop cracks and open pores that can be penetrated by the electrolyte, thereby creating additional electrochemically active surface area. Assuming an ion radius of a lithium cation of 0.09 nm having a single-layer solvent shell of ethylene carbonate with 0.41 nm additional radius,[47] one would expect that pores larger than 1 nm in the active material can be filled by electrolyte and, therefore, be detected by probing the electrode capacitance for a given electrolyte. Any solid/electrolyte interface element of the electrode which is connected electronically through the solid part and ionically by the electrolyte thus forms an electrochemical double layer, providing a physical capacitance that can be charged or discharged similar to a physical capacitor through the displacement of ions and electrons when a potential difference is applied. In principal, this charge-transfer capacitance could be extracted from the respective *R-Q* semicircle in a Nyquist plot at any state of charge (SOC). In practice, however, the frequency range in which this charge-transfer resistance appears is similar to the ionic pore resistance, and thus these two contributions to the impedance can often not be discriminated, as discussed already by Landesfeind et al.[48] in the case of a transmission line model. However, the capacitance can be extracted separately when an electrode is in the state of quasi-infinite charge-transfer resistance, often referred to as *blocking conditions*.[49,50] For lithium-ion battery electrodes, this state is achieved either when the active material is i) fully lithiated or ii) fully delithiated or when iii) a non-intercalating electrolyte is used, whereby in all three of these cases no charge is transferred, even when a finite potential perturbation is applied.[48,51] Under these conditions, real electrode interfaces, often discussed through the Randles circuit,[42,43,52,53] then only show a purely capacitive behavior which, for low frequencies, can be described by a single constant-phase element (CPE). At these relatively low frequencies, this straight line in a Nyquist plot, in principal the onset of a huge semicircle, dominates the much smaller pore resistance and all other circuit elements, what allows the extraction of the charge-transfer capacitance from impedance spectra. Assuming a proportional relationship between capacitance and electrochemical surface area, and following the theoretical considerations discussed above, the change in surface area and, therefore, the cracking of the active material in the electrode can be monitored by electrochemical impedance spectroscopy utilizing Eq. 6.

Experimental

Electrode preparation.—NCM electrodes were prepared by mixing uncoated NCM622 ($Li_{1.01}Ni_{0.6}Co_{0.2}Mn_{0.2}O_2$, 0.3 m^2_{BET}/g,

BASF SE, Germany), vapor-grown carbon fibers (VGCF-H, 12.4 m^2_{BET}/g, Showa Denko, Japan), and polyvinylidene fluoride (PVDF, Kynar HSV 900, Arkema, France) at a mass ratio of 90:8:2 with N-methyl-2-pyrrolidone (NMP, anhydrous, Sigma Aldrich, Germany) in a planetary mixer (Thinky Corp., USA) for 17 min, using a three-step sequential mixing procedure. This slurry was coated onto the rough side of an aluminum foil (18 μm, MTI, USA) with a box-type coating bar (Erichsen, Hemer, Germany) using an automated coater (RK PrintCoat Instruments, United Kingdom), and dried in a convection oven at 50 °C for 5 h. The NCM622 electrodes had a loading of 9.7 mg_{AM}/cm^2 ($\equiv$1.8 mAh/cm^2 based on 184 mAh/g_{NCM622}). The same procedure was applied for lithium titanate (LTO, $Li_4Ti_5O_{12}$, 3.0 m^2_{BET}/g, Südchemie, Germany) and lithium iron phosphate (LFP, $LiFePO_4$, LFP 400, 20.7 m^2_{BET}/g, BASF SE, Germany); however, the slurry compositions and the conductive carbon type (C65, carbon black SuperC65, 64 m^2_{BET}/g, TIMCAL, Switzerland) were adapted in accordance with Table I. Furthermore, slurries without active material, one containing only VGCF and PVDF at a mass ratio of 8:2 and one containing only C65 and PVDF at a mass ratio of 1:1 were mixed with NMP, and coatings were prepared as described above.

Electrodes with a diameter of 10.95 mm were punched out from the above prepared electrode coatings as well as from commercially available LTO electrode sheets (LTO on aluminum, 3.5 mAh/cm^2, Custom Cells, Germany). For the electrochemical cycling tests, the electrodes were used uncompressed, except for the LFP electrodes which were compressed at 200 MPa for 30 s using a KBr press (Mauthe, PE-011). For the experiments on mechanical cracking, NCM622 electrodes were compressed at 50, 100, and 200 MPa for 30 s using the KBr press. All electrodes were dried in a Büchi oven at 120 °C under dynamic vacuum for at least 6 h and then transferred to an argon-filled glove box (<1 ppm O$_2$ and H$_2$O, MBraun, Germany) without exposure to air.

Cell assembly.—The experiments on mechanical cracking were conducted in symmetric cells with NCM622 electrodes (uncompressed as well as compressed at 50, 100, and 200 MPa) and with pure VGCF electrodes, which were assembled in spring-compressed T-cells (Swagelok, USA), using two glass fiber separators (glass microfiber filter, 691, VWR, Germany) and 60 μl of non-intercalating electrolyte[51] (10 mM TBATFSI in EC:EMC 3:7 w/w).

In preparation for the cycling experiments with NCM and LFP, capacitively oversized LTO electrodes (3.5 mAh/cm^2) are used as the counter electrode, which were pre-lithiated in spring-compressed T-cells using two glass fiber separators and 60 μl LP57 (1 M LiPF$_6$ in EC:EMC 3:7 w/w, <20 ppm H$_2$O, BASF, Germany) against metallic lithium (450 μm thick and 11 mm in diameter, Rockwood

Table I. Overview of the properties of the electrodes prepared and investigated in this study. The composition is stated as a mass ratio of active material (AM), conductive carbon (CC), and binder (B); also provided are the areal mass loadings of the electrode and the AM, together with the thickness of the final electrode (numbers in parenthesis refer to electrodes compressed at 200 MPa), and the Kr-BET areas are also specified. Further, the specific current values are listed which are taken to define a C-rate of 1 h^{-1} as well as the upper/lower cutoff potentials and the potential at which potential-controlled EIS data (PEIS) are acquired (all referenced vs. Li$^+$/Li, based on an LTO counter electrode potential of 1.55 V vs. Li$^+$/Li), latter corresponding to 0 %SOC.

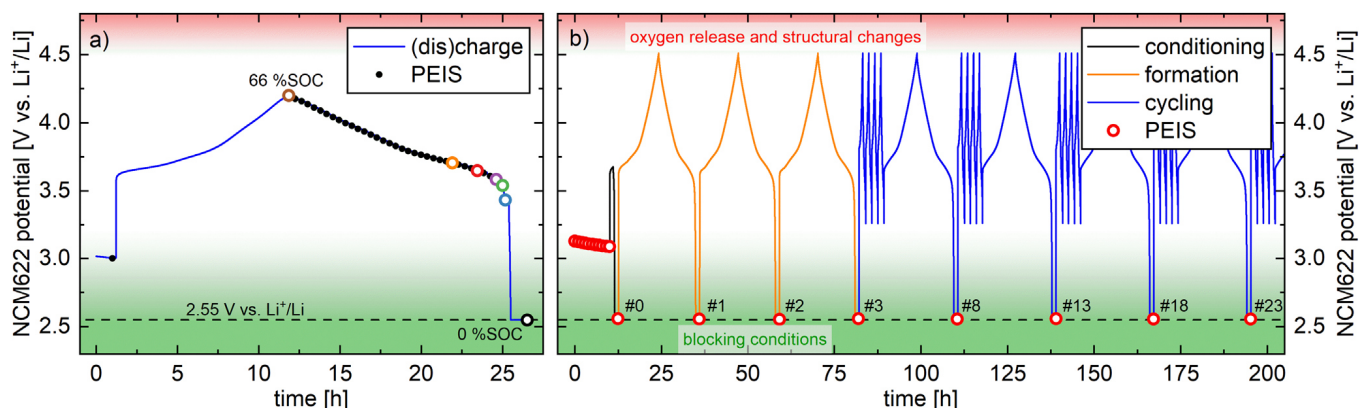|		Electrode material						
	Units	NCM622 (3.9 V)	NCM622 (4.2 V)	NCM622 (4.5 V)	LTO	LFP	VGCF only	C65 only
Composition AM:CC:B	wt%	90:8:2	90:8:2	90:8:2	90:5:5	93:4:3	0:80:20	0:10:10
Conductive carbon	—	VGCF	VGCF	VGCF	C65	C65	VGCF	C65
Areal electrode loading	mg$_{electrode}$/cm^2	10.8	10.8	10.8	10.3	13.9	1.1	0.9
Areal AM loading	mg$_{AM}$/cm^2	9.7	9.7	9.7	9.3	12.9	—	—
Electrode thickness	μm	~55 (~37)	~55 (~37)	~55 (~37)	~60	~116 (~75)	~40	~28
Active material BET	m^2/g$_{AM}$	0.3	0.3	0.3	3	20.7	—	—
Specific current @1C	mA/g$_{AM}$	184	184	184	170	150	—	—
Upper cutoff potential	V vs. Li$^+$/Li	3.90	4.20	4.50	2.05	3.80	—	—
Lower cutoff potential	V vs. Li$^+$/Li	2.55	2.55	2.55	1.05	2.95	—	—
Potential for PEIS	V vs. Li$^+$/Li	2.55	2.55	2.55	2.55	2.55	—	—

Figure 2. Cycling procedure shown exemplarily for an NCM622 working electrode in a pseudo full-cell with a pre-lithiated, capacitively oversized LTO as the counter electrode and a gold-wire reference electrode, whereby all potentials are shown vs. Li^+/Li (analogous procedures were used for LTO and LFP working electrodes). (a) Realization of blocking conditions by discharging the NCM622 working electrode to 2.55 V vs. Li^+/Li, holding it there for 1 h, and then conducting a PEIS at this potential (the colored open circles mark the potentials at which the EIS spectra shown in Fig. 4 were recorded). (b) Long-term cycling procedure, with an initial OCV phase of 10 h, a conditioning step (black line), three formation cycles (yellow lines), and cycling (blue lines). This is shown exemplarily for an NCM622 working electrode with an upper cutoff of 4.5 V vs. Li^+/Li, with the intermittent acquisition of EIS spectra (red circles), under blocking conditions at the points marked with #0, #1, etc.

Lithium, USA) to ~30 %SOC at a specific current of 15 mA/g_{AM} for 3 h, after having performed one full formation cycle at 15 mA/g_{AM}. For experiments with LTO as working electrode, pre-lithiated, capacitively oversized LTO counter electrodes were prepared using an equivalent procedure with a final charge to ~90 %SOC (corresponding to a lithium reservoir of ~3.15 mAh/cm^2) by charging for 9 h. After pre-lithiation, the LTO electrodes were harvested from the cells and used as the counter electrode in the pseudo full-cells for the electrochemical cycling tests (note that pseudo full-cell here refers to a cell with a specific working electrode and a pre-lithiated, capacitively oversized LTO electrode). The pre-lithiated, capacitively oversized LTO provides a stable half-cell potential of 1.55 V vs. Li^+/Li over a wide SOC window, a sufficiently large capacity to take up the lithium from the investigated NCM and LFP working electrodes or to provide the lithium for LTO working electrodes, and an excess of lithium compensating any lost lithium due to side reactions during cycling in order to fully (de)lithiate the working electrodes for the EIS measurements (i.e. for bringing the working electrodes into blocking conditions).

For the electrochemical cycling tests, spring-compressed T-cells with pre-lithiated, capacitively oversized LTO as the counter electrode and NCM, LFP, or LTO as working electrodes were assembled using two glass fiber separators and 60 μl LP57. Between the two separators, a micro-reference electrode (μ-RE) was installed, namely the gold-wire reference electrode (GWRE) based on the setup described by Solchenbach et al.,[40] whereby the GWRE was lithiated in situ at 150 nA over 1 h from the LTO counter electrode before cycling (note that the GWRE lithiation charge of ~0.15 μAh is negligible compared to the capacity of the counter electrode). This establishes a constant GWRE potential of 0.31 V vs. Li^+/Li,[40] which remained stable for more than 1200 h. For details about the cell setup and the preparation of the gold wire, please refer to the original publication.

To identify the specific capacitance contributed by only VGCF and PVDF or by only C65 and PVDF, the identical pseudo full-cell setup with pre-lithiated, capacitively oversized LTO (~30 %SOC) as counter electrode, two glass fiber separators, μ-RE (i.e. a GWRE) and 60 μl LP57 electrolyte was used with the respective VGCF or C65 electrodes as working electrode.

Impedance spectroscopy.—All electrochemical impedance spectra were included directly into the cycling procedure of a multi-channel potentiostat VMP3 (BioLogic, France) and recorded in a climate chamber (Binder, Germany) at 25 °C in potentiostatic mode (PEIS), with an amplitude of 15 mV for 8 points per decade

from 100 kHz to 100 mHz. This results in an acquisition time of ~10 min per PEIS. Each EIS spectrum consists of a full-cell spectrum (between working and counter electrode) and, by using a GWRE, also of the half-cell spectrum (i.e. between the working and the micro-reference electrode), including a frequency point at 180 mHz. In the case of symmetric cell measurements, impedance spectra were recorded 10 h after cell assembly.

Cell testing.—All electrochemical cycling tests were performed in a climate chamber (Binder, Germany) at 25 °C, using a multi-channel potentiostat (Biologic VMP3). Before cell cycling, the GWRE was lithiated using the LTO counter electrode (see above). To acquire EIS spectra under blocking conditions, represented by a semi-infinite charge-transfer resistance, the working electrode is cycled to a state of charge of 0 %SOC at a potential of 2.55 V vs. Li^+/Li for all active materials as indicated in the last line of Table I, i.e. to either full lithiation for LFP and NCM or to full delithiation for LTO working electrodes, where the working electrode was then held for 1 h prior to taking EIS spectra. This is illustrated in Fig. 2a for an NCM622 working electrode. After an initial OCV phase of 10 h, PEIS was measured at OCV (marked by the first black circle in Fig. 2a), followed by a C/10 charge ($\equiv$18.4 mA/g_{NCM} for NCM622) in constant current (CC) mode to the upper cutoff potential (4.2 V vs. Li^+/Li in this case). At this point, where the nominal state of charge if referenced to the theoretical capacity of NCM622 ($\equiv$276.5 mAh/g_{NCM}) is 66 %SOC, another PEIS was measured (see open red circle in Fig. 2a). Subsequently, the C/10 discharge in CC mode was continued in 10 min segments with a PEIS taken at the end of each segment, which was repeated until the lower cutoff potential (2.55 V vs. Li^+/Li for NCM622) was reached, which was defined as 0 %SOC. There, a constant voltage (CV) hold of 1 h was performed, followed by a final PEIS. The procedure was executed in a similar manner for LFP and LTO, using the cutoff potentials listed in Table I. However, since LTO is delithiated in its pristine state and cell cycling of LTO starts by lithiation, the charge to the upper and the discharge to the lower cutoff potential are switched for LTO in the above given description of the cycling procedure.

To investigate the specific capacitance of the pristine materials at different potentials, the same electrode setup as described above was assembled using NCM electrodes as working electrodes as well as setups using working electrodes comprising only VGCF and PVDF or comprising only C65 and PVDF. After an initial PEIS at OCV (at ~3.0 V vs. Li^+/Li for NCM622 and at ~2.8 V vs. Li^+/Li for VGCF working electrodes) and a first OCV phase of 1 h followed by

another PEIS measurement, the potential was held for 1 h at 2.85, 2.75, 2.65, and 2.55 V vs. Li^+/Li for NCM and at 3.05, 2.95, 2.85, 2.75, 2.65, and 2.55 V vs. Li^+/Li for VGCF and C65 electrodes, including a PEIS at the respective potentials.

The long-term cycling procedure shown exemplarily for an NCM622 working electrode in Fig. 2b was initiated by an OCV phase of 10 h, during which a PEIS was taken every 1 h (red open circles in Fig. 2b). During *conditioning* (black line in Fig. 2b), the electrodes were charged at C/10 ($\equiv$18.4 mA/g_{NCM} for NCM622) in CC mode for 1 h, then discharged to the lower cutoff potential of 2.55 V vs. Li^+/Li at C/10 in CC mode, where a CV hold of 1 h was performed, followed by a PEIS. Since nickel-rich CAMs are commonly slightly overlithiated (by up to 1 %) in the synthesis process, the conditioning step was included in the procedure to ensure comparable impedance spectra for each cycle, namely by assuring that similar SOCs are obtained by the potential hold of 1 h at 2.55 V vs. Li^+/Li, especially when using different NCM active materials. For the *formation* (yellow lines in Fig. 2b), three charge/discharge cycles are executed, with a charge to the upper cutoff potential at C/10 with a CV hold until the current dropped to below 0.1 mA ($\sim$C/20, CCCV mode), and with a discharge to the lower cutoff potential at C/10 with a final CV hold of 1 h before a PEIS was recorded (marked by the #1, #2, and #3 points in Fig. 2b). The formation was followed by *cycling* (blue lines) four times at 1C ($\equiv$184 mA/g_{NCM} for NCM622) in CCCV mode in charge, until the current dropped to 0.1 mA ($\sim$C/20), and at 1C in CC mode for the discharge. The fifth cycle was performed at C/10, identical to the formation cycles, followed by a 1 h CV hold at the lower cutoff potential and a PEIS. This set of five cycles was repeated for more than 200 charge/discharge cycles. The impedance spectra taken in blocking conditions are numbered by the number of full cycles that the electrodes had performed up to that point (e.g. #8 after the first set of the five blue cycles shown in Fig. 2b). Since LTO is delithiated in its pristine state, the charge to the upper and the discharge to the lower cutoff potential are switched for LTO in the description of the cycling procedure.

For the visual investigation by FIB-SEM, additional NCM622 cells were stopped after 0.5, 1.0, and 203.5 cycles to 4.2 V vs. Li^+/Li, including a potential hold at the respective target potential, namely 4.2 V vs. Li^+/Li for non-integer cycle numbers or 2.55 V vs. Li^+/Li for integer ones.

Cell disassembly.—After cycling, the electrodes were harvested from the cells for the krypton gas physisorption measurements to determine their specific surface area and for FIB-SEM analysis. Any residue of the conductive salt was removed from the electrodes in a three-step sequential washing procedure: first, they were washed for 5 min in 5 ml EC:EMC 3:7 w/w, followed by a soaking step of 24 h in 1 ml DMC, and, finally, a washing step of 5 min in 5 ml DMC.

Scanning electron microscopy.—The morphology of fresh, mechanically compressed electrodes as well as of the ones harvested and washed after charge/discharge cycling for 0.5, 1.0, and 203.5 cycles was investigated by FIB-SEM at BASF SE (Ludwigshafen, Germany), where the electrodes were cut by focused argon-ion beam (FIB) milling and their cross-sections were investigated by scanning electron micro-scopy (SEM) in backscattering mode at 10 kV.

Surface area analysis.—The surface area of the harvested and washed electrodes as well as of the compressed NCM622 electrodes was determined by krypton gas physisorption at 77 K, as previously presented by Friedrich et al.,[26] measuring isothermally at 13 points between $0.01 \leqslant p/p_0 \leqslant 0.30$, using an autosorb iQ (Quantachrome Instruments, USA). Comparative N_2-BET measurements for the pristine materials (VGCF, C65, and NCM622) are within ±10 % of the specific surface areas obtained by krypton physisorption. The advantage of the measurement with krypton is a superior sensitivity of this method, since only ca. 1/100 of the total surface area is

required for the physisorption measurements, so that Kr-BET areas can be obtained for 11 mm diameter electrodes, what would not be possible using N_2-BET. Prior to Kr-BET measurements, both powder samples as well as samples of pristine or harvested and washed electrodes were dried at 120 °C under vacuum for 6 h.

Results and Discussion

Mechanical compression of NCM622.—In the following, the effects of mechanical compression on NCM622 particle cracking and on the electrochemically accessible surface area or the surface area accessible by krypton gas physisorption are investigated and dis-cussed. Figure 3a shows the cross-sectional view of an uncompressed pristine NCM622 electrode recorded by FIB-SEM. The spherical shape of the secondary agglomerates (with $\sim$5–10 μm diameter) that are comprised of numerous primary crystallites ($\sim$0.1–0.5 μm) is intact for all shown particles, which is representative of the entire electrode. Void volumes in the core of the NCM particles result from the synthesis and are observed for all cross sections through the particle centers. In contrast, Fig. 3b illustrates the compression-induced breakage of the NCM secondary particles. The applied compression of 200 MPa does not only decrease the electrode porosity from 55 % to 27 % (reflected by a decrease in electrode thickness, see Table I), but is sufficient to break the mechanically fragile secondary agglomerates into many fragments or even into single primary particles. Similar behavior has been observed for calendered battery electrodes by electron microscopy[28] as well as by X-ray tomography.[54] Due to this breakage, additional NCM surface area is exposed for compressed electrodes as compared to the uncompressed material, which is accessible for krypton gas in Kr-BET measurements as well as for the electrolyte in battery cells.

Figure 3c depicts the impedance spectra of the symmetric cells assembled with VGCF electrodes as well as with NCM electrodes that were uncompressed or compressed at 50 MPa, 100 MPa, or 200 MPa, using non-intercalating 10 mM TBATFSI electrolyte. (Note that the difference in the specific high-frequency resistance (in $\Omega \cdot g_{electrode}$) of NCM electrodes (10.8 mg/ cm^2) and VGCF electrodes (1.1 mg/ cm^2) results from the normalization to the mass of the electrodes; the absolute high-frequency resistance of $\sim$130 Ω is similar for all cells and electrodes and is typical for the 10 mM TBATFSI electrolyte with a low conductivity of $\sim$300 μS/cm). For low frequencies, all materials show purely capacitive behavior, even the NCM622 electrodes, as their charge-transfer reaction is impeded by the electrolyte with non-intercalating ions.[51] It is observed that the absolute value of the imaginary impedance at the lowest frequency of 100 mHz decreases with increasing compression of the NCM electrodes. The same can be observed for the absolute value of the imaginary impedance of the 180 mHz point (open circles in Fig. 3c), which decreases from 16.6 $\Omega \cdot g_{electrode}$ for the uncompressed NCM622 electrodes to 14.5 $\Omega \cdot g_{electrode}$ for a compression of 50 MPa, further to 11.9 $\Omega \cdot g_{electrode}$ for 100 MPa, and even to 10.4 $\Omega \cdot g_{electrode}$ for 200 MPa. Since a decrease of the absolute value of the imaginary low-frequency impedance of a CPE element corresponds to an increase of its capacitance parameter Q (see Eq. 3), a compression of the NCM622 particles results in an increase in their capacitance. We assign this increase in capacitance to an increase in electrochemically active surface area of the NCM622 particles in the entire electrode, which would actually be expected based on the observed NCM622 particle breakage upon compression (see Fig. 3b). By fitting the capacitive branch between 100 mHz and 1 Hz with an R-Q element, the CPE parameter Q and the phase angle α can be determined, whereby the values of latter are noted in Fig. 3c. The decrease of α with increasing compression from 0.87 to 0.84 (visible by a clockwise tilt of the capacitive branch) is most likely related to the reduced relative contribution of the CPE with a very high value of $\alpha = 0.97$ that is characteristic of the VGCF carbon fibers to the total CPE as the NCM622 surface area increases. However, since the obtained values of α are close to or larger than
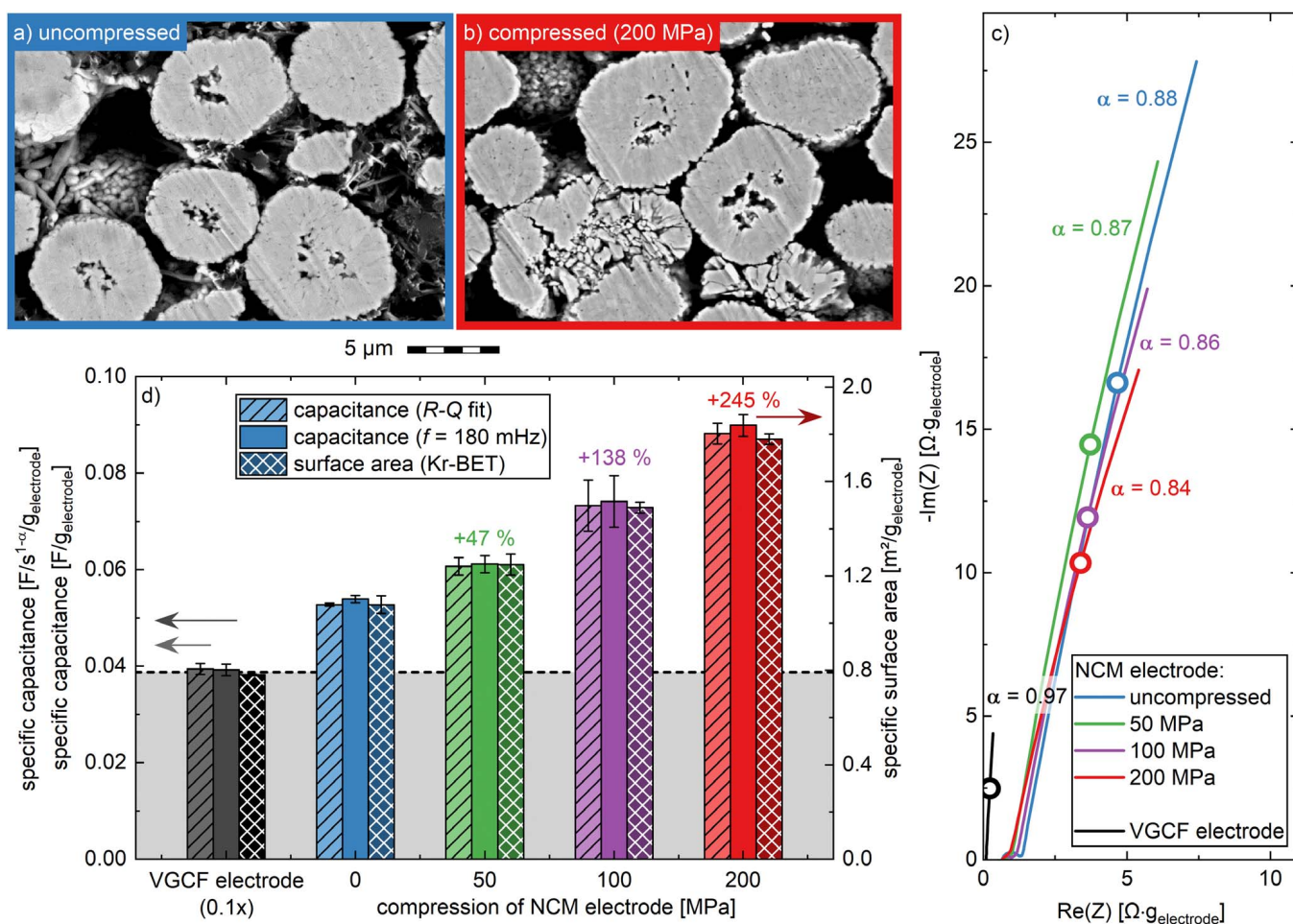
Figure 3. Effect of mechanical compression on pristine NCM622 electrodes: cross-sectional view by FIB-SEM in backscattering mode at 10 kV: (a) uncompressed electrode and (b) electrode compressed at 200 MPa. (c) Nyquist plots of symmetric cells at 25 °C with VGCF electrodes and with pristine NCM622 electrodes that were uncompressed or compressed at 50, 100, or 200 MPa, all assembled with 60 µl of 10 mM TBATFSI. The values for the phase angle α obtained from the fit of the capacitive branch by an R-Q element between 100 mHz and 1 Hz are listed in the figure, and the frequency points at 180 mHz are indicated by larger empty circles. (d) The left y-axis shows the specific capacitance extracted from the impedance spectra of the symmetric cells depicted in (c), either via a fit with an R-Q element between 100 mHz and 1 Hz (hatched bars) or via the imaginary impedance at 180 mHz according to Eq. 6 (solid bars). The right axis shows the specific surface area determined by krypton gas physisorption of VGCF electrodes and of pristine NCM622 electrodes that were uncompressed or compressed at 50, 100, or 200 MPa (cross-hatched bars). Note that the specific capacitance and the specific surface area for the VGCF electrode were divided by 10, accounting for the fact that 1 g of an NCM electrode contains 0.08 g VGCF and 0.02 g PVDF, which corresponds to that in 0.1 g of a VGCF electrode. The thus estimated capacitance and specific surface increase of the NM622 particles in the NCM622 electrodes (in %) is marked above each set of bars. The values shown here are calculated from the mean of two identical cell pairs for PEIS or of two electrodes for BET, and the error bars correspond to the minimum/maximum value of two measurements.

0.85, the assumptions used for Eq. 6 still apply, so that the approximate capacitance of the electrode can be obtained from the imaginary part of the impedance at 180 mHz.

In Fig. 3d, we compare the compression-induced increase of the specific capacitance $Q/m_{electrode}$ (left axis) of the NCM622 electrodes, extracted from the fit of the capacitive branch (hatched bars) or from the imaginary part of the impedance at 180 mHz via Eq. 6 (solid bars), with that of the increase of the specific surface area obtained by krypton gas physisorption (cross-hatched bars, plotted against the right axis). The specific capacitance of the pristine NCM622 electrode of 0.053 F/s$^{1-\alpha}$/g$_{electrode}$ increases by 15 % when it is compressed at 50 MPa, by 39 % at 100 MPa, and by even 67 % at 200 MPa (hatched bars in Fig. 3d). When the capacitance is not extracted from an R-Q fit, but simply through the imaginary value of the impedance at the 180 mHz point using Eq. 6 (see solid bars in Fig. 3d, plotted against the left axis), the obtained results (now in units of F/g$_{electrode}$) are essentially identical to the numerical Q-values extracted from the R-Q element fit, which experimentally proves the validity of the theoretical assumptions of this simplified

method. To determine the relative change of the capacitance of only the NCM622 particles upon compression, the capacitance contribution from the conductive carbon and binder must be subtracted. This contribution is measured through the same setup, using VGCF electrodes, yielding 0.394 F/s$^{1-\alpha}$/g$_{electrode}$ or 0.392 F/g$_{electrode}$ using Eq. 6. Since 1 g of the NCM622 electrode comprises 0.08 g of VGCF and 0.02 g of PVDF (see Table I), the capacitance contribution of the VGCF/binder composite in 1 g NCM622 electrode corresponds to 1/10 of that of the mass normalized capacitance of the VGCF electrode, i.e. 0.0394 F/s$^{1-\alpha}$/g$_{electrode}$, which is marked by the black hatched bar in Fig. 3d (or 0.0392 F/g$_{electrode}$ using Eq. 6, marked by the black solid bar). Assuming that the capacitance contribution of VGCF and PVDF in the NCM622 electrode is the same as that in the VGCF electrode, the capacitance contributed by the NCM622 particles in the NMC622 electrodes is the total capacitance of the NCM622 electrode minus 1/10 of the capacitance of the VGCF electrode, indicated by the capacitance extending beyond the black dashed horizontal line in Fig. 3d. Thus, if the capacitance increase of the NCM622 electrodes with compression is

referenced to the estimated NCM622 contribution, it increases by 47 %, 138 %, and 245 %, when compressing the NCM622 electrodes at 50, 100, and 200 MPa, respectively.

To prove that this increase in capacitance upon mechanical compression is proportional to the increase in the specific surface area of the electrodes and of the NCM622 particles in the electrodes, the specific surface area of the NCM622 electrodes was quantified by krypton BET. The Kr-BET surface area increases from 1.08 $m^2/g_{electrode}$ of the uncompressed NMC622 electrode by 16 %, 38 %, and 65 % for a compression of 50, 100, and 200 MPa, respectively (cross-hatched bars in Fig. 3d). This increase in the total specific surface area is within the error bars in perfect agreement with the observed increase in the total capacitance obtained by the impedance measurements (namely 15 %, 39 %, and 67 % for a compression of 50, 100, and 200 MPa, respectively). This not only proves that the increase in capacitance is indeed related to an increase in specific surface area (something one would anyways expect), but also the validity of the approximation that the Q parameter of the CPE response of the electrode (in units of $F/s^{1-\alpha}/g_{electrode}$) can be equated with the capacitance of the electrode (in units $F/g_{electrode}$), at least as long as the α-value is sufficiently large. Furthermore, it indicates that the estimation of the capacitance through the 180 mHz point is sufficiently accurate and is a valid approximation for the experiments conducted in this study.

Using the Kr-BET analysis, we can now examine whether the above estimate of the capacitance contribution by the NCM622 particles is valid. For this, we measured the Kr-BET area of the VGCF electrode (7.8 $m^2/g_{electrode}$), which is ∼20 % smaller than the predicted value of 9.9 $m^2/g_{electrode}$ based on the 12.4 $m^2/g_{electrode}$ for the pristine VGCF fibers and the 80 wt% VGCF content in the VGCF electrodes. (Note that the same was observed when comparing BET areas of several carbon blacks with that of electrodes made of carbon black and Nafion® binder, which was ascribed by partial pore blocking by the binder.[55]) By multiplying the VGCF electrode Kr-BET area by 0.1 (as explained above), the estimated Kr-BET area contribution from the VGCF/PVDF components to the NCM622 electrode would be 0.78 $m^2/g_{electrode}$ (black cross-hatched bar in Fig. 3d). Thus, the specific surface area measured for the NCM622 electrodes which extends above this value (black dashed line in Fig. 3d) would have to be equal to the specific surface area contributed by the pristine NCM622 particles. For the uncompressed NCM622 electrodes, the difference in specific surface area between the estimated contribution by the VGCF/PVDF components (0.78 $m^2/g_{electrode}$) and the one measured for the NCM622 electrode (1.08 $m^2/g_{electrode}$) equates to 0.30 $m^2/g_{electrode}$, which is identical with the BET surface area of the pristine NCM622 particles. This clearly proves our above assumption that the specific surface area and the capacitance contributions from the VGCF/binder components of the NCM622 electrode can be simply subtracted by using the mass-fraction corrected specific capacitances and specific surface areas of pure VCGF electrodes, thereby yielding the desired values for the specific surface area and the specific capacitance contributed solely by the NCM622 particles in the NCM622 electrodes.

Realization of blocking conditions for NCMs.—When cycling battery cells using a conventional electrolyte containing intercalating ions (a non-blocking electrolyte so to speak), blocking conditions that represent a state of quasi-infinite charge-transfer resistance can be achieved by either fully lithiating or fully delithiating the active material during the charge/discharge procedure. Since NCM materials become unstable and degrade significantly at high SOC,[5,56] NCMs cannot be fully delithiated reversibly, so blocking conditions can only be achieved towards 0 %SOC when the NCM is fully lithiated. To achieve full lithiation of the working electrode at selected points during a typical charge/discharge cycling procedure, a capacitively oversized, pre-lithiated counter electrode with a stable potential is required. For this, we here use LTO; a metallic lithium counter electrode would in principle also satisfy these requirements, but its long-term cycling stability is inferior to that of pre-lithiated LTO.
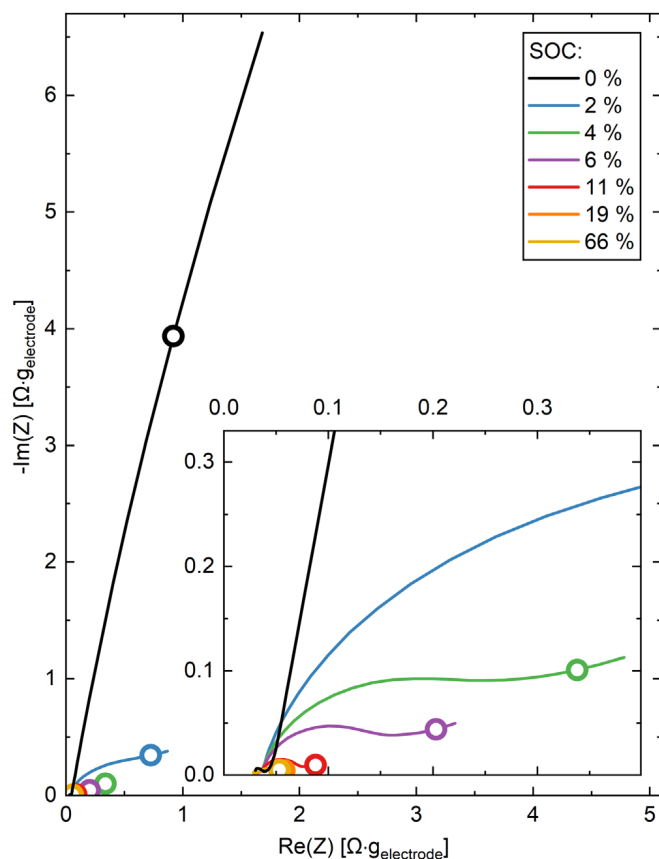
Figure 4. Realization of blocking conditions in conventional electrolyte, shown exemplarily for NCM622. For this, pseudo full-cells were assembled in Swagelok T-cells with 60 μl LP57, two glass fiber separators, and a μ-RE (i.e. a GWRE) using NCM622 as the working electrode and pre-lithiated, capacitively oversized LTO as the counter electrode. Following the procedure introduced in the experimental part and depicted in Fig. 2a, the impedance spectra of an NCM622 working electrode were recorded at 25 °C at different SOCs between 4.20 V and 2.55 V vs. Li⁺/Li, applying an amplitude of 15 mV from 100 kHz to 100 mHz. Nyquist plots of selected impedance spectra show an increasing charge-transfer semicircle with decreasing SOC, developing into blocking conditions for 0 %SOC. The frequency points at 180 mHz are indicated by large open circles.

Figure 4 depicts selected impedance spectra of an NCM622 electrode as a function of its SOC, extracted from the procedure depicted in Fig. 2a and using a GWRE to exclusively monitor the impedance spectra of the working electrode.[40] At 4.2 V vs. Li⁺/Li, corresponding to 66 %SOC when referenced to the theoretical NCM622 capacity of 276.5 mAh/g_{NCM}, the impedance spectrum in the Nyquist plot shows (apart from the HFR offset by the electrolyte resistance in the separator) only one relatively small semicircle of ∼0.015 $\Omega \cdot g_{electrode}$ with an apex frequency of 116 Hz (see yellow line in Fig. 4) that is assigned to the NCM622 charge-transfer resistance convoluted with the ionic pore resistance.[48] Upon decreasing the SOC to 19 %SOC (orange line), the size of the semicircle remains approximately constant and only grows significantly with each lithiation step at lower SOCs, as can be seen for the data at 11 %SOC (red line). After the final potential hold at 2.55 V vs. Li⁺/Li for 1 h, the semicircle is converted to a purely straight line of a CPE with $\alpha = 0.85$. At this low potential, the NCM622 active material is fully lithiated, which inhibits the charge-transfer reaction and thus increases the charge-transfer resistance to a very large, quasi-infinite value. In this state, the NCM622 active material shows only capacitive behavior, as observed for the impedance response of the NCM622 electrodes in non-intercalating electrolyte (see Fig. 3c); as the capacitive impedance response at low frequencies exceeds that of the ionic pore resistance by orders of magnitude, it can be used as

a direct measure of the electrode's surface area. By implementing a potential hold at 2.55 V vs. Li$^+$/Li into a charge/discharge cycling procedure with NCM cathodes, we are therefore able to monitor its capacitance from the impedance spectra in blocking conditions. As we have shown that the thus quantitively determined capacitance is proportional to the specific surface area of the NCM active material (see Fig. 3d), this approach allows to monitor the specific surface area change of NCM cathode active materials due to particle breakage over the course of charge/discharge cycling. As blocking conditions for NCMs can only be achieved at 0 %SOC, i.e. in the fully lithiated state in which the NCM unit cell volume is the largest, there is the possibility that cracks that may have formed at high SOCs (i.e. at low NCM unit cell volume) may have closed reversibly, so that the area between these cracks would not be wetted by electrolyte and not contribute to the measured capacitance. Therefore, only irreversible crack formation in the active material particles can be observed with this method utilizing blocking conditions.

Furthermore, blocking conditions could also be realized for electrodes comprising LTO or LFP, for both materials at a potential of 2.55 V vs. Li$^+$/Li (see Fig. S1 which is available online at stacks.iop.org/JES/167/100511/mmedia), following a procedure similar to the one used for the NCM622 electrodes. While layered oxides degrade at high SOCs and, therefore, cannot be fully delithiated to bring them into blocking conditions at 100 %SOC, other active materials, such as LFP, are stable at both ends of the SOC window, so that for these blocking conditions can be achieved at full lithiation as well as at full delithiation (shown, e.g. for LiNi$_{0.5}$Mn$_{1.5}$O$_4$[48]). For a better comparability with the pristine state, the impedance spectra were recorded in the fully lithiated state for LFP and in fully delithiated state for LTO, corresponding to 0 %SOC at 2.55 V vs. Li$^+$/Li for both materials.

Specific capacitance of pristine electrode constitutents.—As discussed above, to quantify the relative capacitance increase of the examined active material from the capacitance increase of the electrode, the specific capacitance of each electrode component needs to be identified. In the analysis based on symmetric cells presented in Fig. 3d, this was accomplished by subtracting the specific capacitance of the VGCF electrode from that of the NCM622 electrode. However, since the specific capacitance of a given electrode material will likely depend on both the potential and the type of electrolyte,[57] any comparative measurements and the measurements for the background correction due to the conductive carbon and the binder components must be conducted at the same potential and in the same electrolyte. For the following long-term cycling experiments with NCM622 electrodes in LP57 electrolyte, where we will conduct impedance analysis of the NCM622 working electrode in blocking conditions at 2.55 V vs. Li$^+$/Li, we have therefore evaluated the specific capacitance of the NCM622 and of the PVDF electrodes as a function of potential in the LP57 electrolyte (1 M LiPF$_6$ in EC:EMC 3:7 w/w), using pre-lithiated LTO as counter electrode and a μ-RE (i.e. a GWRE).

The specific capacitance of the pristine uncompressed NCM electrodes in the LP57 electrolyte at 2.55 V vs. Li$^+$/Li is 0.12 F/g$_{electrode}$ (based on two independent experiments; see Fig. S2), which is ∼9 % higher than the value of 0.11 F/g$_{electrode}$ obtained at OCV (corresponding to ∼3.0 V vs. Li$^+$/Li). Interestingly enough, while the latter potential should closely correspond to the NCM622 potential in the symmetric cell experiments conducted with non-intercalating electrolyte (10 mM TBATFSI in EC:EMC 3:7 w/w.), the specific capacitance we had obtained in this case is ∼2-fold lower (0.054 ± 0.01 F/g$_{electrode}$, see blue solid bar in Fig. 3d). The potential dependence of the specific capacitance of the VGCF electrode in the LP57 electrolyte is similarly weak as that of the NCM622 electrode (see Fig. S2), yielding 0.43 ± 0.01 F/g$_{electrode}$ at 2.55 V vs. Li$^+$/Li and ∼0.39 F/g$_{electrode}$ at OCV (corresponding to ∼2.8 V vs. Li$^+$/Li); in this case, the difference to the specific capacitance obtained in symmetric cells with non-intercalating

electrolyte is rather minor (0.39 F/g$_{electrode}$, see black solid bar in Fig. 3d). Due to these unpredictable but significant dependencies of the specific capacitances on potential and electrolyte type, it becomes clear that comparative measurements always must be done under identical conditions.

As commercial electrodes typically use C65 as conductive carbons (or other carbon blacks with similar BET surface area), we also examined the specific capacitance of C65 electrodes (50 wt% C65 and 50 wt% PVDF, see Table I). As one would expect due to the much higher BET area of C65 compared to VGCF fibers (64 vs. 12.4 m^2/g), the specific capacitance of C65 electrodes at 2.55 V vs. Li$^+$/Li amounting to 1.7 F/g$_{electrode}$ (see Fig. S2) is much higher than that of the VGCF electrodes (0.43 F/g$_{electrode}$).

Charge/discharge cycling of NCM622 electrodes.—To monitor the electromechanical NCM622 particle breakage upon cycling, the electrode must contain fully intact secondary agglomerates, i.e. NCM622 particles must not have been fractured by electrode compression before cell cycling. Based on our analysis of the effects of mechanical compression of the electrodes (see Fig. 3), this necessitates that uncompressed NCM622 electrodes are used. To ensure electronic connection throughout the entire electrode even without compression, vapor-grown carbon fibers with a length of 15 μm were used as conductive additives, rather than the commonly used C65 carbon black. As it will be shown later, the initial performance of these electrodes (for detailed composition, see Table I) is what one would expect for this NCM622 active material using C65 carbon black as conductive electrode constituent.

Prior to charge/discharge cycling, it was verified that the impedance spectra of the NCM622 working electrode are stable over time during the initial OCV phase of 10 h in order to exclude any time-dependent effect on the impedance (data not shown). Figure 5a shows three selected impedance spectra of the same NCM622 electrode after the conditioning cycle (referred to as #0), after 3 formation cycles (referred to as #3), and after 203 cycles with an upper cutoff potential of 4.2 V vs. Li$^+$/Li (see Fig. 2b for a sketch of the cycling procedure). First, it is observed that blocking conditions are achieved in all instances through the full lithiation of the NCM622 particles after the 1 h long potential hold at 2.55 V vs. Li$^+$/Li. It should be noted that the semicircle at high frequencies is due to a contact resistance, as was shown previously for uncompressed LFP[51,58] and uncompressed LiNi$_{0.5}$Mn$_{1.5}$O$_4$[41] electrodes. While the phase angle of the NCM622 electrodes during the initial OCV phase is approximately $\alpha = 0.90$ (data not shown), it decreases to $\alpha = 0.89$ after conditioning (see spectrum #0 in Fig. 5a), to $\alpha = 0.88$ after formation (see spectrum #3) and to $\alpha = 0.87$ after cycle 203 (see spectrum #203). Even for the highest upper cutoff potential of 4.5 V vs. Li$^+$/Li, the phase angle does not decrease below $\alpha = 0.85$ over a total of 303 test cycles (the full number of cycles are shown in Fig. S3), wherefore the theoretical considerations in the theory section still apply (see Fig. 1), so that the expected error for approximating the capacitance with the Q-value of the CPE extracted at a frequency of 180 mHz should still be below ±1 %. As illustrated by the impedance data for cells cycled to 4.2 V vs. Li$^+$/Li, the fact that the value of Q (or the capacitance) increases with increasing cycle number can be seen by the decreasing imaginary impedance at 180 mHz that is marked by the open by circles in Fig. 5a: it decreases from 6.90 Ω·g$_{electrode}$ after the conditioning cycle (cycle #0) to 4.94 Ω·g$_{electrode}$ after the 3 formation cycles, all the way to 3.36 Ω·g$_{electrode}$ after 203 cycles to an upper cutoff of 4.2 V vs. Li$^+$/Li. Based on Eq. 6, this corresponds to an increase of electrode capacitance of 40 % between cycle 0 and cycle 3, and of 109 % between cycle 0 and cycle 203.

Figure 5b shows this increase in capacitance of NCM622 electrodes, depicted as specific capacitance in units of F/g$_{electrode}$, vs. cycle number for NCM622 pseudo full-cells cycled to different upper cutoff potentials of 3.9, 4.2, and 4.5 V vs. Li$^+$/Li. For comparison, the specific capacitance of the pristine NCM622 electrode of 0.12 ± 0.00 F/g$_{electrode}$ (see Fig. S2) is marked by the two gray
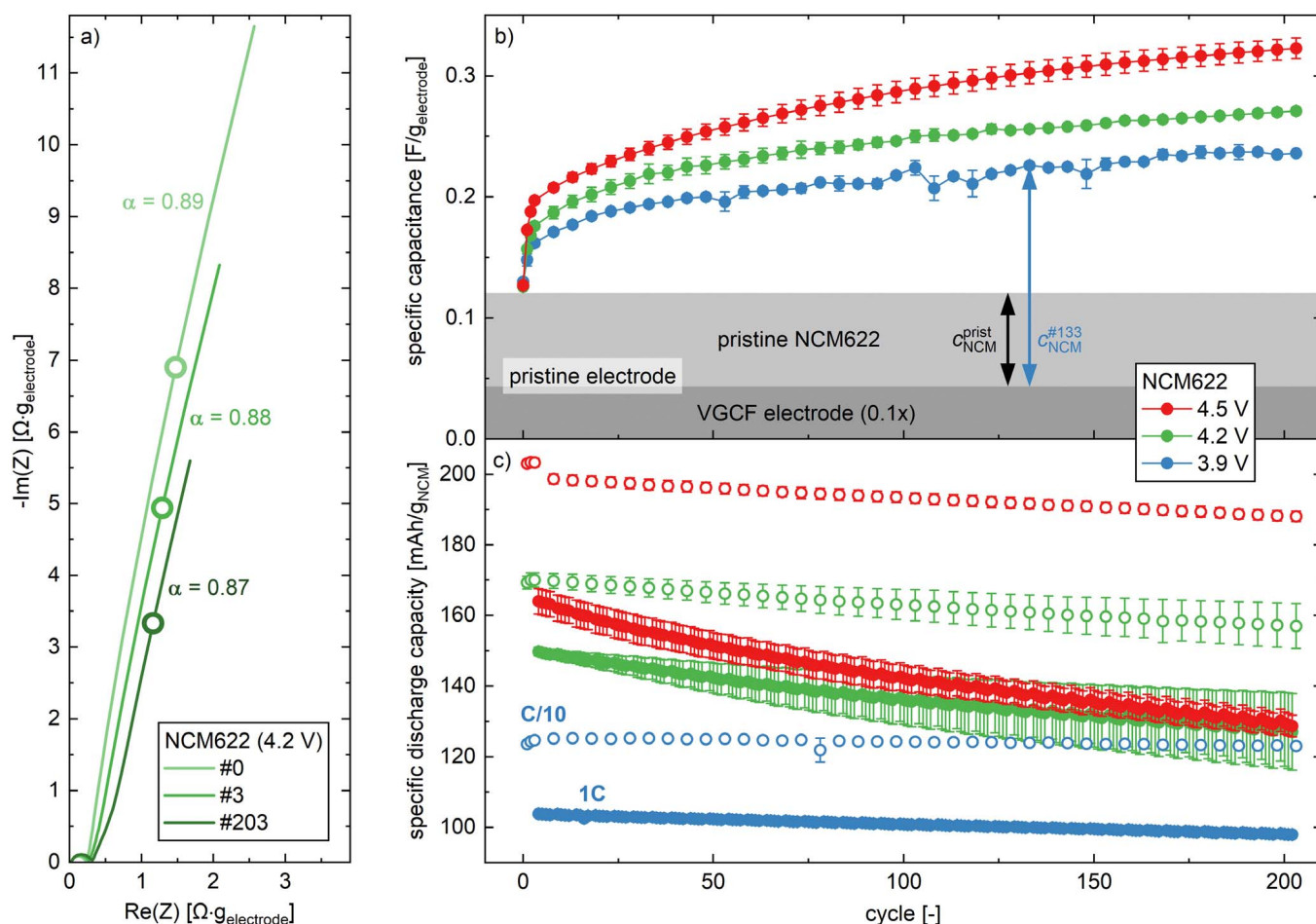
Figure 5. Electrochemical cycling of NCM622 in pseudo full-cells with 60 µl LP57, two glass fiber separators, and a µ-RE (i.e. a GWRE) using an uncompressed NCM622 working electrode and pre-lithiated, capacitively oversized LTO as the counter electrode. Following the procedure depicted in Fig. 2b, NCM622 was cycled at 25 °C to different upper cutoff potentials of 3.9 V (blue lines/symbols), 4.2 V (green lines/symbols), or 4.5 V (red lines/symbols) vs. Li$^+$/Li. Impedance spectra of the NCM622 working electrodes were recorded in blocking conditions after a potential hold at 2.55 V vs. Li$^+$/Li, applying an amplitude of 15 mV from 100 kHz to 100 mHz. The specific capacitance and the specific discharge capacity values shown here are calculated from the mean of two nominally identical cells, with the error bars corresponding to the minimum/maximum value of two cells. (a) Selected impedance spectra in blocking conditions of the NCM622 working electrode after the conditioning cycle (referred to as #0), after three formation cycles (referred to as #3), and after 203 cycles (referred to as #203) to an upper cutoff potential of 4.2 V vs. Li$^+$/Li (see also Fig. 2b). (b) Specific capacitance of the NCM622 working electrode extracted from the imaginary impedance at a frequency of 180 mHz in blocking conditions (see Eq. 6). The sum of the gray areas indicates the specific capacitance of the pristine uncompressed NCM622 working electrode, and the dark gray area shows the specific capacitance of a VGCF electrode multiplied by 0.1 (see text). (c) Specific discharge capacity normalized to the active material mass vs. cycle number following the procedure shown in Fig. 2b. The open circles show the discharge capacity at C/10 (after a CCCV charge at C/10), and the solid circles at 1C (after a CCCV charge at 1C).

colored areas. By subtracting 1/10 of the specific capacitance of a VGCF electrode which equates to 0.043 ± 0.01 F/g$_{electrode}$ (analogous to what was done when constructing Fig. 3d), indicated by the dark gray colored area in Fig. 5b, the capacitance contributed solely by the NCM622 active material is obtained (i.e. the light gray area). Furthermore, since it is assumed to be proportional to the surface area of the NCM622 active material, the relative increase of the surface area of the NCM622 particles with cycling should be proportional to the ratio of the thus estimated NCM622 capacitance at any given cycle number (marked by the blue arrow in Fig. 5b for cycle #133) and the NCM622 capacitance prior to cycling (marked by the black arrow).

After conditioning (cycle #0), the specific capacitance of the NCM electrodes is increased by ∼6 % compared to the pristine electrodes (marked by the light gray area). Since the unit cell volume change for this very small SOC change of 7.5 % (referenced to 276.5 mAh/g$_{NCM}$) is rather negligible ($\Delta V/V \approx -0.3$ %),[7] cracking of the NCM622 particles is not expected. Nevertheless, this small volume change seems to already be sufficient to increase the specific capacitance of the electrode, which we interpret to be caused by the formation of a small extent of irreversible cracks in the NCM

particles. This cracking at very small volume changes may be related to the fact that these NCM622 particles are not monocrystalline, but consist of thousands of primary particles, which may decrease the stability of the material upon even very small unit cell volume changes. For all three upper cutoff potentials, the major portion of the increase in specific capacitance (i.e. of surface area increase, presumably via crack formation) occurs during the first few cycles. For example, after the first three formation cycles an upper cutoff potential of 4.2V (green symbols), the NCM622 electrode capacitance increases by 47 % compared to the pristine electrode, and ultimately increases by 125 % after 203 cycles. The fact that the largest capacitance increase per cycle occurs over the first few cycles suggests that the crack formation due to the unit cell volume changes upon repeated (de)lithiation is most pronounced during the first cycles, until a major part of the mechanical stress is dissipated at the mechanically weakest interfaces and, therefore, a reduced rate of capacitance increase (i.e. a reduced crack formation rate) is observed for later cycles. After roughly 30 cycles, a continuous increase of the capacitance is observed for the three different cutoff potentials. This may not only be related to mechanical crack formation, but may also be caused by the chemical decomposition of Li$_2$CO$_3$, LiOH, and

Li$_2$O residuals remaining after the synthesis of the NCM622 active material, which might be decomposed chemically by protic species released upon cycling,[59] creating pores between the primary crystallites that also contribute to the continuous capacitance and surface area increase. In general, Fig. 5b shows that the capacitance increase is larger for higher cutoff potentials, as one might expect due to the associated larger unit cell volume changes (see below discussion). Based on these observations, we hypothesize that the unit cell volume changes upon (de)lithiation induce particle cracking and a concomitant increase in surface area, which is reflected by the increasing capacitance upon cycling.

Figure 5c shows the discharge capacities vs. cycle number for these NCM622 electrodes, from which one can examine how particle breakage might impact its cycling stability. As these tests were conducted with pre-lithiated, capacitively oversized LTO counter electrodes with a large lithium reservoir, capacity fading due to the loss of active lithium can be excluded. The open circles show the discharge capacity of the C/10 cycles ($\equiv$18.4 mA/g$_{NCM}$) conducted prior to each PEIS measurement in blocking conditions (every 5th cycle, see Fig. 2b), while the solid circles show the four 1C cycles conducted in between the PEIS measurements. The initial performance of these NCM622 electrodes with VGCF conductive carbon is reasonably close to what is reported for conventional NCM622 electrodes (i.e. with C65 conductive binder): at the upper cutoff potential of 4.5 V vs. Li$^+$/Li, the here obtained initial capacity of ~204 mAh/g$_{NCM}$ at C/10 and of ~165 mAh/g$_{NCM}$ at 1C (see red symbols in Fig. 5c) is comparable to the initial specific capacities of ~195 mAh/g$_{NCM}$ at C/10 and the ~175 mAh/g$_{NCM}$ at 1C reported by Jung et al.[60] (the latter cells were cycled against graphite, whereby 4.4 V vs. graphite correspond to roughly 4.5 V vs. Li$^+$/Li).

At C/10 and at the lowest cutoff potential of 3.9 V vs. Li$^+$/Li, the capacity remains at 124 mAh/g$_{NCM}$ for more than 200 cycles (blue open symbols in Fig. 5c). As the upper cutoff potential is increased to 4.2 or 4.5 V, a constant fading of the discharge capacity is observed over the 203 cycles, starting from the very first cycle: at 4.2 V from initially 169 to 157 mAh/g$_{NCM}$ after 203 cycles (−7 %), and at 4.5 V from initially 204 to 188 mAh/g$_{NCM}$ after 203 cycles (−8 %). Since the counter electrode provides an excess of cyclable lithium, and since overpotentials are relatively small at such a slow C-rate, the here observed capacity fading at C/10 must be related to an enhanced extent of particle breakage for these higher cutoff potentials, which we believe leads to a loss of the electronic connection to some fragments of the NCM622 active material. This furthermore suggests that the relatively small unit cell volume change of −1.0 % for an upper cutoff potential of 3.9 V and the associated particle cracking that is indicated by the capacitance increase (see Fig. 5b) is not sufficient to totally disconnect the NCM622 active material particles, otherwise some capacity fading would be observed.

At the higher rate of 1C, the capacity fading for a cutoff potential of 3.9 V vs. Li$^+$/Li is rather minor, from 104 mAh/g$_{NCM}$ at the beginning of test to 98 mAh/g$_{NCM}$ after 203 cycles (−6 %). Since in this case capacity fading is only noted at the higher rate of 1C, we assign this effect to an increased overpotential due to a poor electronic connectivity between the fragments of the cracked secondary NCM622 agglomerates, yet without a complete electronic isolation. Much higher capacity fading is observed for 4.2 V upper cutoff potential, namely from 150 to 127 mAh/g$_{NCM}$ (−15 %) over the same number of cycles, which we again ascribe to a poor electronic connectivity within the NCM622 secondary agglomerate due to more extensive cracking. At the highest upper cutoff potential of 4.5 V, the capacity fading at 1C is even more pronounced (from 164 to 129 mAh/g$_{NCM}$, corresponding to −21 %) and is approximately 3-fold higher than that at C/10 (−8 %). At such a high cutoff potential, however, the capacity fading will likely also have contributions from a rock-salt like surface layer that is formed upon lattice oxygen release, which is reported to occur at around 80 %SOC,[5] i.e. close to upper cutoff potentials of 4.5 V vs. Li$^+$/Li for NCM622.[60] The thus formed poorly conductive surface layer around the active material particles was suggested to increase the
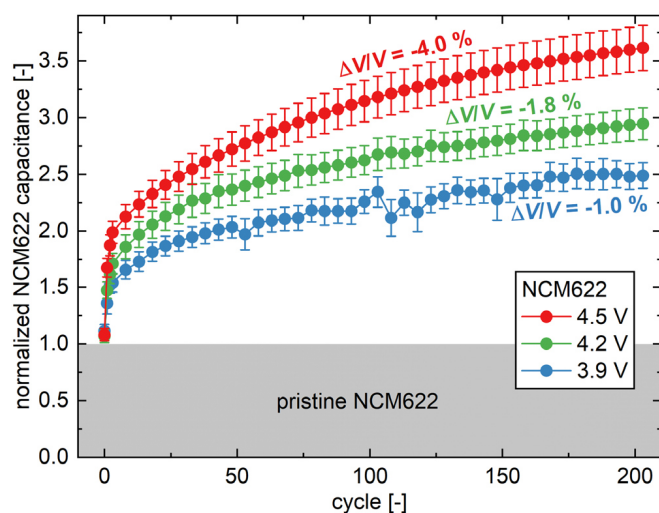
Figure 6. Capacitance contributed by the NCM622 particles in the NCM622 electrodes, normalized by their capacitance in the pristine NCM622 electrode vs. cycle number for the three upper cutoff potentials of 3.9 V (blue symbols), 4.2 V (green symbols), and 4.5 V (red symbols) vs. Li$^+$/Li. Data were extracted from Fig. 5, whereby the NCM622 capacitance contribution was obtained by subtracting the capacitance contribution of the VGCF electrode (dark gray area in Fig. 5b) from the overall NCM622 electrode capacitance (symbols in Fig. 5b). The error bars are determined by the laws of error propagation (see supporting information), using the average capacitances and their minimum/maximum values given by Fig. 5b. The relative volume change of the unit cell upon delithiation as measured by XRD[7,61,62] (i.e. $\Delta V/V$) for the three different upper cutoff potentials is specified in the figure.

electronic resistance and thus the overpotential at higher C-rates.[26] The effect of oxygen release on particle cracking and capacity fading will be discussed further in Part II of this study. To conclude, we believe that the capacity fading at 3.9 V vs. Li$^+$/Li is solely attributed to a loss of electronic connection of some NCM622 active material fragments; at 4.2 V, some fragments become totally isolated electronically, and at 4.5 V, particle breakage and oxygen release lead to both material loss as well as resistance growth.

Since the specific capacitance against cycle number described in Fig. 5b is composed of the contributions of the NCM622 active material, the conductive carbon, and the binder, we estimate the capacitance contribution from the NCM622 active material particles by subtracting the specific capacitance of the VGCF electrode in the same manner as done for the evaluation of the data in Fig. 3d. This assumes that the capacitance of the VGCF electrode can be subtracted by considering the weight fractions of the VGCF/PVDF components in the NCM622 electrode (10 wt%), and that their capacitance does not change over cycling (a reasonable assumption, as the VGCF fibers experience no ion (de)intercalation during cycling in this voltage region). Based on this, we can determine the relative change of the capacitance of the NCM622 particles over the cycling experiment (see Fig. 5a) normalized that of the pristine NCM622 particles, namely by taking the ratio of the difference of the capacitance at a given cycle and the capacitance of the VGCF electrode (illustrated by the blue arrow for cycle #133 in Fig. 5b) over this difference after the conditioning cycle (represented by the black arrow in Fig. 5b). Figure 6 shows the thus estimated normalized capacitance changes of the NCM622 particles over cycling for the three different upper cutoff potentials of 3.9 V (blue symbols), 4.2 V (green symbols), and 4.5 V (red symbols); the error bars are based on the minimum/maximum values of the measured electrode capacitances (see Fig. 5b) and the error propagation when equating capacitance differences and equating their ratio (explained in more detail in the supporting information).

Since the NCM622 particle capacitance is expected to be directly proportional to their electrochemically accessible surface area (i.e. to

the NCM622 particle area in contact with the electrolyte), the evolution of the normalized NCM622 particle capacitance shown in Fig. 6 should be directly proportional to the cracking-induced increase in the specific NCM622 surface area over the course of cycling, if a constant surface area normalized double layer capacitance is assumed. As shown in Fig. 6, the evolution of the normalized NCM622 particle capacitance and, presumably, of its electrochemically active specific surface area rapidly increases within the first three formation cycles (cycles #0 to #3) and then more gradually over the subsequent cycles, following the trend shown in Fig. 5b. This behavior coincides nicely with the results obtained by acoustic emission experiments on transition metal oxides as well as on silicon, all showing that the cracking of the active material particles appears predominantly during the first few cycles.[63–65] The total increase of the normalized NCM622 capacitance scales approximately with the relative volume change of the unit cell ($\Delta V/V$) measured through XRD,[7,61,62] and specified in Fig. 6 for the different upper cutoff potentials: (i) for 3.9 V vs. Li$^+$/Li, where $\Delta V/V$ during NCM622 delithiation amounts to -1.0 %, the NCM622 capacitance increased by 149 % over 203 cycles; (ii) for 4.2 V, where $\Delta V/V$ amounts to -1.8 %, the NCM 622 capacitance increased by 195 %; and, (iii) for 4.5 V, where $\Delta V/V$ amounts to -4.0 %, it increased by 261 %. If the relative increase in capacitance were indeed equal to a relative increase in specific surface area, an increase by 261 % (i.e. by a factor of ~3.6) would imply an approximate decrease of the effective NCM622 particle diameter by ~3.6 (based on a simple cubic approximation, where the specific surface area would be inversely proportional to the length of the cube, if the total volume is kept constant), which in turn would imply an increase of the number of particles by a factor of ~50 (corresponding to the area change to the third power). Considering that the approximate size of the primary crystallites in the ~5–10 μm secondary agglomerates of the pristine NCM622 particles (see Fig. 3a) is ~0.1–0.5 μm, the above estimated increase in the number of particles would suggest that a significant fraction of the interfaces between the primary crystallites would be exposed to the electrolyte after this cycling procedure to 4.5 V due to crack formation. Assuming a mean diameter of roughly spherical primary crystallites of ~0.2 μm, their complete separation and the full exposure of their surface area to the electrolyte would correspond to a specific surface area of ~6 m^2/g$_{AM}$, which is ~20-fold higher than that of the pristine NCM622 material. As the maximum experimentally determined surface area increase upon cycling (see Fig. 6) is only ~3.6-fold, this suggests that a few hundred cycles within the here considered upper cutoff potentials does not lead to a complete disintegration of the secondary particle agglomerates.

Kr-BET surface area of cycled NCM622 electrodes.—To verify that an increase of the specific surface area of the NCM622 electrodes and particles is indeed the origin for their increased capacitance upon cycling, the surface area of cycled electrodes was measured by Kr-BET and compared with the observed capacitance increase. For this, the cells cycled to 4.5 V vs. Li$^+$/Li for which the first 203 cycles are shown in Fig. 5c (red symbols) were cycled for another 100 cycles (for cycling and capacitance data over 303 cycles, see Fig. S3); after 303 cycles, the cells were disassembled and the NCM622 electrodes were harvested and washed prior to the Kr-BET measurement. The specific capacitance was extracted from the impedance spectra of the pristine and the cycled NCM622 electrodes in blocking conditions (i.e. after a potential hold at 2.55 V vs. Li$^+$/Li), either by fitting of the *R-Q* element (hatched bars in Fig. 7) or by using the value of the imaginary impedance at 180 mHz according to Eq. 6 (solid bars in Fig. 7).

The specific capacitance of the NCM622 electrodes calculated from the 180 mHz point increases from 0.12 F/g$_{electrode}$ in their pristine state (solid bar on the left-hand side of Fig. 7) to 0.34 F/g$_{electrode}$ after 303 cycles to 4.5 V (solid bar on the right-hand side of Fig. 7). Both determination methods for the electrode capacitance, the exact *R-Q* fit (hatched bars) as well as the 180 mHz approximation (solid bars),
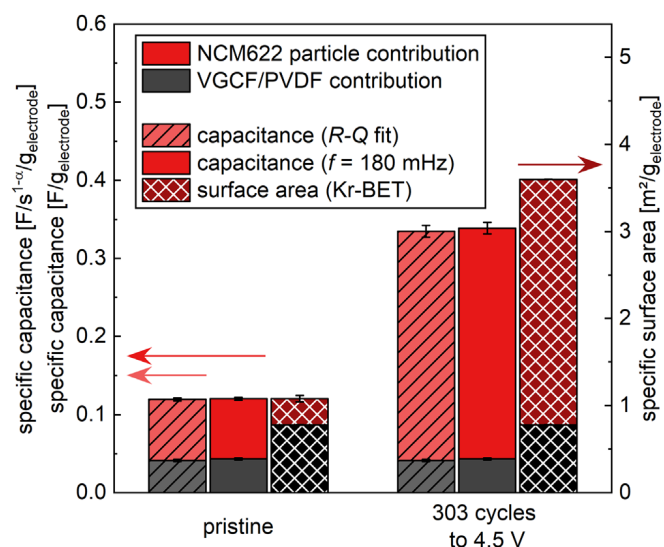
Figure 7. Effect of charge/discharge cycling on NCM622 electrodes for an upper cutoff potential of 4.5 V vs. Li$^+$/Li after 303 cycles, continuing the cycling shown in Fig. 5c (red symbols) for another 100 cycles (for cycling and capacitance data, see Fig. S3): Specific capacitances (left axis) of pristine electrodes (left-hand set of bars) and after the 203 cycles to 4.5 V vs. Li$^+$/Li (right-hand set of bars) were obtained either by fitting an *R-Q* element at frequencies between 100 mHz and 1 Hz (hatched bars) or by using the imaginary impedance at 180 mHz according to Eq. 6 (solid bars). BET surface area (right axis) of pristine and cycled NCM622 electrodes (cross-hatched bars) measured by Kr-BET. The contributions to capacitance and specific surface area by the NCM622 particles are colored in red and were obtained by subtracting the weight-fraction-normalized contributions from the VGCF electrodes (colored in black). All values are calculated from the mean of two nominally identical cells (capacitances) or two nominally identical electrodes (Kr-BET) and the error bars correspond to the minimum/maximum value of two measurements.

result in a very similar increase of the NCM622 electrode capacitance (left axis) over the 303 cycles, namely by 180 % and 182 %, respectively. This good agreement is expected, as the corresponding phase angles always exceed $\alpha = 0.85$, which was the requirement for the 180 mHz approximation (see Eq. 6) to be valid. Assuming that the contribution of the VGCF/PVDF components to the electrode capacitance remains constant upon cycling, the weight-fraction-normalized contribution from the VGCF electrode (i.e. 0.043 ± 0.001 F/g$_{electrode}$ or 0.041 ± 0.001 F/s$^{1-\alpha}$/g$_{electrode}$, constituting ~36 % of the total capacitance of the pristine NCM622 electrode) can be subtracted from the NCM622 electrode capacitance to obtain the NCM622 contribution to the capacitance (red colored parts of the bars in Fig. 7). Comparing the red colored segments of the hatched and solid bars for the pristine NCM622 electrode (left-hand side of Fig. 7) with those for the cycled NCM622 electrodes (right-hand side), a cycling-induced increase of the NCM622 capacitance contribution by ~280 % (i.e. by a factor of ~3.8) can be deduced.

The increase in NCM622 electrode and particle capacitance over the 303 cycles to 4.5 V vs. Li$^+$/Li will now be compared to the measured changes in the specific surface area determined by Kr-BET. The NCM622 electrode Kr-BET increases from 1.08 m^2/g (cross-hatched bar on the left-hand side of Fig. 7) to 3.6 m^2/g after 303 cycles (cross-hatched bar on the right-hand side). Subtracting the weight-fraction-normalized contribution of the VGCF/PVDF components to the specific surface area as explained in the discussion of Fig. 3d (i.e. 0.78 m^2/g$_{electrode}$, constituting ~72 % of the total specific surface area of the pristine NCM622 electrode), the specific surface area contribution of the NCM622 particles in the pristine NCM622 electrode can again be estimated to be 0.30 m^2/g$_{electrode}$ (corresponding to the Kr-BET area measured for pristine NCM622 active material). Here it should be noted that while in the case of the capacitance measurements in the non-intercalating electrolyte (10 mM TBATFSI in EC:

EMC 3:7 w/w) the ratio of the capacitance contribution of the NCM622 particles and the VGCF/PVDF components reflects the ratio of their Kr-BET areas (namely ~1:3 in both cases, see Fig. 3d), for the measurements in the intercalating LP57 electrolyte this ratio is ~2:1 for the capacitance contributions (hatched and solid bars on the left-hand side of Fig. 7) and ~1:3 for the Kr-BET area contributions (cross-hatched bar on the left-hand side of Fig. 7). This, we believe, can be explained by different dependencies of the capacitances of different materials (viz., NCM622 and VGCF) on the composition of the electrolyte. Assuming that the specific surface area of the VGCF/PVDF components will not be affected by cycling the electrodes, the specific surface area contribution of the NCM622 particles to the specific surface area of the electrode after 303 cycles can be estimated to be 2.82 $m^2/g_{electrode}$. This implies an estimated increase of the specific surface area of the NCM622 particles by 840 % (i.e. by a factor of ~9.4) over the 303 cycles.

Surprisingly, this estimated increase of the Kr-BET area of the NCM622 particles over the 303 cycles is ~2.5-fold higher than the above deduced capacitance increase of the NCM622 particles which was only a factor of ~3.8. This deviation might result from an unequal sensitivity of both methods towards the detectable surface area: As the size of krypton atoms is ~0.2 nm, pores which are larger than ~0.2 nm will contribute to the measured Kr-BET area, while only pores larger than ~1 nm will be accessible to the electrolyte (based on an estimated diameter of ~1 nm for solvated lithium ions) and will thus be able to contribute to the capacitance. Thus, the most likely explanation for the higher increase in Kr-BET area compared to the capacitance of NCM622 particles upon cycling would be the presence of very small pores or cracks in the cycled NCM622 particles, which are large enough to be detectable by Kr-BET, but too small for the wetting with electrolyte. If this assumption is true, the capacitance is a more meaningful measure for the electrochemically active surface area of an electrode as compared to the surface area obtained by Kr-BET, since the capacitance actually reflects the surface area in contact with electrolyte, which is the relevant area for the charge-transfer reaction as well as for possible side reactions, such as the attack of HF or dissolution of transition metals. The Kr-BET measurement also includes pores with a size between 1 nm and 0.2 nm, which, however, do not contribute to charge transfer and/or side reactions that require electrolyte contact. In addition to the different sensitivity of Kr-BET and capacitance, it cannot be excluded that the washing procedure which was applied to the cycled electrodes after disassembly of the cell prior to the BET measurements might have altered the obtained results as well, leading to the discrepancy between the surface area increase of the both techniques (note that such a washing step was not used for acquiring the data shown in Fig. 3d, where Kr-BET and capacitance measurements are essentially identical).

Additionally, the possible formation of a cathode electrolyte interphase (CEI) during cycling cannot be excluded; if it were to form, it could, in principle, change the areal capacitance (i.e. the capacitance normalized to the surface area of the electrode or of the cathode active material) and thereby compromise our here assumed direct correlation between the measured capacitance and the exposed surface area. However, the independently obtained evidence for crack formation and surface area increase by FIB-SEM and Kr-BET, respectively, prove that particle cracking and surface area increase indeed occur upon either mechanical compression or during cycling. In our view, the simplified assumption that the areal capacitance remains constant during crack formation (as stated in the theoretical considerations) seems to be a reasonable approximation. Nevertheless, the here suggested minor role of the changes in the areal capacitance of a cathode active material by the possible formation of a CEI upon cycling (or of an anode active material by the SEI formation upon cycling) is required to be investigated.

Summarizing the findings in this section, one can state that it was shown that electrochemical cycling of the NCM622 active material significantly increases its capacitance, which is most pronounced during the first few charge/discharge cycles. The capacitance

increase is dependent on the chosen cutoff potential, since this defines the extent of volume change of the unit cells, that ultimately causes the cracking of the NCM secondary agglomerates. This has an important consequence for studies and analyses which involve a normalization of a measured property/signal to the specific surface area of the active material, which could lead to erroneous conclusions in cases where the specific surface area of cycled and/or compressed/calendered active materials increases substantially over that of the pristine active materials. Examples where this would be critical are rate tests where the current normalized to the surface area is crucial for the evaluation of the rate capability, the analysis of the charge-transfer resistance over the course of cycling, or the estimation of the thickness of a surface spinel or rock-salt structure from the amount of evolved gases.

Visual investigation of cycled NCM electrodes.—Figure 8 presents the cross sections of pristine NCM622 electrodes as well as of the ones harvested from cells cycled to 4.2 V vs. Li^+/Li after a first charge cycle at C/10, after the subsequent first discharge cycle at C/10 including a CV hold at 2.55 V vs. Li^+/Li, and in the charged state after the 203 cycles shown in Fig. 5 (according to the protocol shown in Fig. 2). The uncompressed pristine electrode (see Fig. 8a), as discussed before in the context of mechanical compression effects (see Fig. 3a), does not show any cracks through the secondary agglomerates. When the NCM622 electrode is charged in the very first cycle at C/10 to 4.2 V vs. Li^+/Li (see Fig. 8b), numerous cracks appear that are induced by the lattice volume contraction as well as by the anisotropic change of the lattice parameters *a* and *c*.[6,7] These cracks appear mainly in the radial direction of the particles, creating pathways that connect the outer part of the particles with the inner voids of the NCM622 particles. The largest of these newly formed pores show more than 1 μm in length, but no more than ~100 nm in width; however, the formed cracks are clearly wide enough to be penetrated by the carbonate-based electrolyte (i.e. wider than 1 nm).

At the end of the very first charge/discharge cycle including a final CV hold at 2.55 V vs. Li^+/Li, the FIB-SEM image depicted in Fig. 8c indicates that the NCM622 particles seem to have almost fully and reversibly expanded into their original state, i.e. that the cracks that had been visible in the charged state shown in Fig. 8b have largely been closed again. However, from the impedance analysis in the fully discharged state (i.e. after a 1 h CV hold at 2.55 V vs. Li^+/Li) at the end the very first charge/discharge cycle to 4.2 V vs. Li^+/Li, it was proven that the electrochemically active surface area has already increased by 47 % (second green symbol from the left in Fig. 6). This increase in area must originate from irreversibly opened cracks or pores that are large enough for electrolyte penetration (i.e. with a width of more than 1 nm), created either mechanically due to the volume change upon (de)lithiation or through the decomposition of residual lithium salts by protic species.[59] These cracks must, however, be too small to be visible in the FIB-SEM image (Fig. 8c), whereby it must be considered that if there were one single crack reaching to the center of the particle, the entire inner void volumes would be connected ionically and would thus substantially increase the electrochemically active surface area and capacitance.

The FIB-SEM image in Fig. 8d shows an NCM622 electrode in the charged state after 203 cycles to 4.2 V vs. Li^+/Li, revealing obvious irreversible cracks which must have formed due to the repeated volume change upon (de)lithiation. Compared to the first charge (see Fig. 8b), large cracks which cannot close anymore upon lithiation have formed in almost all NCM particles. Some particle fragments have even displaced from their original position in the secondary agglomerate, resulting in a permanent and irreversible surface area increase that must be accompanied by poor electronic contacting of some parts within the secondary agglomerate, since for some of the fragments only point contacts seem to provide an electronic pathway; some particle fragments might even be electronically fully isolated.[6,16,25–27] As mentioned above, the surface area of NCM622 cycled to 4.2 V vs. Li^+/Li for more than 200 cycles
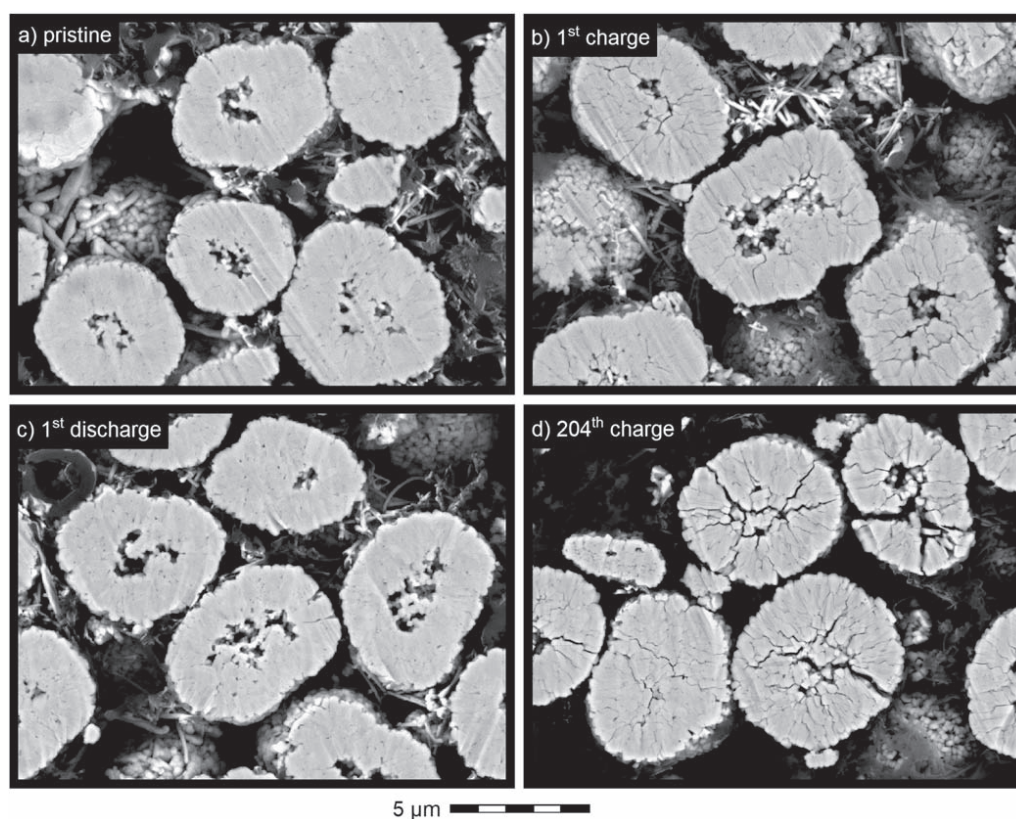
Figure 8. Visual investigation of particle cracking in uncompressed NCM622 electrodes upon charge/discharge cycling by cross-sectional FIB-SEM in backscattering mode at 10 kV. (a) Pristine electrode. (b) Partially delithiated/charged NCM622 electrode after the first charge at C/10 to 4.2 V vs. Li$^+$/Li. (c) Fully-lithiated/discharged NCM622 electrode at 0 %SOC after the first charge/discharge cycle at C/10 to 4.2 V vs. Li$^+$/Li followed by a 1 h CV hold at 2.55 V vs. Li$^+$/Li. (d) Partially delithiated/charged electrode at 4.2 V vs. Li$^+$/Li after the 203 cycles shown in Fig. 5.

increases by ∼200 % (green symbols in Fig. 6), corresponding to four complete cuts through the center of a sphere.

In summary, the FIB-SEM images, revealing the formation of cracks in the NCM622 secondary agglomerates and the formation of some almost completely isolated particle fragments upon repeated charge/discharge cycling, are consistent with the observed increase in NCM622 capacitance and Kr-BET surface area. While the latter two methods allow a more easy quantification of the extent of cracking, the FIB-SEM images also reveal that at least over the initial cycles, the cracking of the secondary NCM622 agglomerates seems to be partially reversible until larger and larger cracks are being formed over extended charge/discharge cycling. The additional electrochemically active surface area exposed through particle cracking has both detrimental and beneficial effects: On the one hand, these freshly created interfaces are expected to enhance side reactions and thus to lead to a loss of cyclable lithium and a loss of active material, reducing the battery cycle life. On the other hand, the formed cracks should facilitate the lithium-ion transport to the primary crystallites in the core of the secondary particles via fast transport through the lithium-ion conducting electrolyte (rather than through the solid phase), which will likely improve the rate capability of polycrystalline NCMs; since most of the cracking occurs within the first few cycles, the high rate capability of polycrystalline NCMs is likely due to their relatively high specific surface area (i.e. several times larger than what one would deduce from the BET area of the pristine materials). This latter aspect, when considering the case of all-solid-state batteries, however, is expected to have rather detrimental effects on performance and particularly on rate capability: As ion-conducting solid electrolytes or polymer electrolytes will not be able to intrude into the cracks formed in the NCM secondary particles, the transport of lithium ions into the interior of the secondary particles would be substantially hindered by the formation of cracks, so that crack formation would be expected

to lead to a decrease of their capacity, particularly at higher C-rates. This indeed has been observed for all-solid-state batteries, e.g. based on polymer electrolytes as shown in the study of M. M. Besli.[66]

Electrochemical cycling of LFP and LTO.—To exclusively prove that the change in the unit cell volume leads to particle cracking and an increased electrochemical surface area, cycling experiments equivalent to the ones done for NCM622 were performed for two other active materials, namely LFP and LTO. LFP experiences a volume change of $\Delta V/V = -6.8$ % upon full delithiation,[62] causing stress and strain more than one order of magnitude higher as compared to LTO, which has a volume change of only $+0.2$ %;[61] moreover, for both of these active materials, the crystal structure is maintained upon cycling, since phenomena such as oxygen release have not been reported in contrast to NCM active materials. Furthermore, using LTO and LFP, intraparticular cracking can be investigated from a more fundamental perspective, since both materials are usually made up of individual primary crystallites instead of secondary agglomerates; therefore, an increase in capacitance would then correspond to a cracking of the primary particles rather than a convoluted effect resulting from a combination of intraparticular and interparticular cracking.

Figure S4 depicts the specific discharge capacity for both LFP and LTO working electrodes cycled according to the protocol shown in Fig. 2 against a pre-lithiated, capacitively oversized LTO as the counter electrode in Swagelok T-cells with a µ-RE (i.e. a GWRE). At C/10, LFP (green open symbols) provides 150 mAh/g$_{AM}$ and loses 4 mAh/g$_{AM}$ over 203 cycles, whereas LTO (yellow open symbols) exhibits 154 mAh/gAM with a capacity loss of 2 mAh/g$_{AM}$ over 203 cycles, proving stable cycling for both materials over 203 cycles. However, both show a lower discharge capacity at 1C, by ∼20 mAh/g$_{AM}$ for LFP (green filled symbols) and by ∼40 mAh/g$_{AM}$ for LTO (yellow filled symbols). For LFP, the discharge capacity of
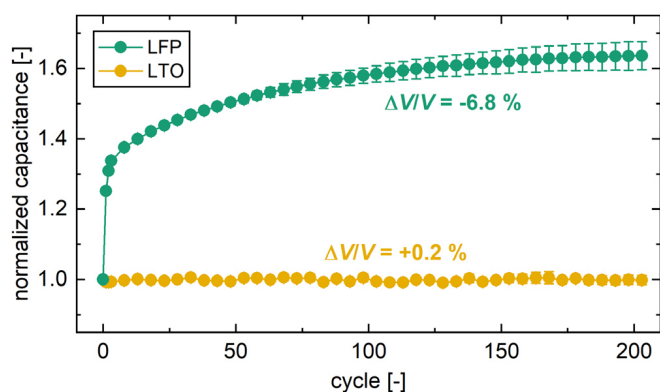
Figure 9. Capacitance of LTO and LFP working electrodes over extended charge/discharge cycling, determined from the imaginary impedance at a frequency of 180 mHz of the working electrodes under blocking conditions (using Eq. 6), normalized to the capacitance of the conditioning cycle (cycle #0). For this, pseudo full-cells were assembled in Swagelok T-cells with 60 µl LP57, two glass fiber separators, and a µ-RE (i.e. a GWRE) using LTO or LFP as working electrode and pre-lithiated, capacitively oversized LTO as the counter electrode. Following the procedure introduced in the experimental section and depicted in Fig. 2b, the cells were cycled at 25 °C, applying cutoff potentials of 1.05 and 2.05 V vs. Li$^+$/Li for LTO and 2.95 and 3.80 V vs. Li$^+$/Li for LFP. Impedance spectra of the working electrode were recorded after a potential hold at 2.55 V vs. Li$^+$/Li for both materials, applying an amplitude of 15 mV from 100 kHz to 100 mHz. The values shown here are calculated from the mean of two nominally identical cell pairs. The error bars correspond to the minimum/maximum value of two cells. The relative volume change of the unit cell upon delithiation as measured by XRD[7,61,62] (i.e. ΔV/V) is specified in the figure for both materials.

125 mAh/g$_{AM}$ at 1C is reasonable.[67,68] For LTO, these losses can be attributed to a limited electronic conductivity through the electrode, since these electrodes were not compressed before cell assembly as compared to LFP. However, during the cycles at C/10, the full capacity was exchanged and, therefore, the entire volume change of the respective unit cell was achieved for both materials at least in these low-current cycles.

The capacitance upon cycling normalized to the value after the conditioning cycle (cycle #0) is depicted in Fig. 9 for both materials. The initial specific capacitance is 1.65 F/g$_{electrode}$ for the LFP electrode and 0.14 F/g$_{electrode}$ for the LTO electrode (data not

shown). The capacitance of LTO, measured at 0 %SOC or full delithiation, shows no change over more than 200 charge/discharge cycles (green symbols). The relatively small volume change upon (de)lithiation of LTO, also often referred to as a zero strain material,[69] is not large enough to affect the mechanical stability of the material, and thus the formation of cracks has not been reported for LTO, which is reflected by the constant value of the electrode capacitance upon cycling.

For LFP, however, the capacitance of the electrode (yellow symbols, measured at 0 %SOC or full lithiation) increases by 25 % already after the first full cycle; over 203 cycles, the capacitance increases by a total of 64 % to 2.69 F/g$_{electrode}$. This surface area increase is expected to arise from the fracturing of the LFP particles, originating from the relatively large volume change of −6.8 % upon (de)lithiation, creating such large stress and strain that even the primary LFP crystallites are known to fracture.[67,70] In order to obtain the contribution of the capacitance of LFP to the total capacitance of the electrode, the contribution of C65 is subtracted from the capacitance of the LFP electrode, similarly done as for Figs. 3 and 6. However, since the weight fractions of C65 and PVDF in the LFP electrode are not 1:1, but 4:3, the calculations were adjusted in the following way: It was assumed that only C65 contributes to the capacitance of the C65/PVDF electrode, resulting in 3.5 F/g$_{C65}$. With this, the capacitance of C65 in the LFP electrode of 0.14 F/g$_{electrode}$ can be subtracted by considering the weight fraction of C65 in the LFP electrode (3 wt%) and assuming that its capacitance does not change over cycling (a reasonable assumption, as the C65 particles experience no ion (de)intercalation during cycling in this voltage region). With these assumptions, the capacitance of the LFP particles only increases by 71 % over 203 cycles. Gabrisch et al.[67] showed that LFP already forms first cracks upon a single chemical delithiation to 50 %SOC (corresponding to 0.25 charge/discharge cycles) due to the material's volume change, which explains the sudden increase in capacitance after the first charge/discharge cycle. Upon repeated cycling of LFP, some particles separate into two or more fragments, as found by TEM and SEM,[67,70] which can now by quantified in situ by our impedance-based analysis.

In summary, as illustrated by the overview in Table II, high surface area materials such as LFP, VGCF, and C65 result as expected in a relatively high specific capacitance as compared to LTO and NCM. Furthermore, the increase in capacitance upon cycling increases with relative volume change upon (de)lithiation, which is a general measure of particle cracking.

Table II. Overview of the major results. Relative unit cell volume change, specific capacitance of pristine electrodes (extracted from the capacitance at 2.55 V vs. Li$^+$/Li as shown in Fig. S2), capacitance increase of the various working electrodes after 203 cycles compared to the pristine electrodes, the active material surface area increase after having subtracted the contribution of conductive carbon to the electrode capacitance, as well as the capacity retention at C/10 and 1C. The specific capacitance and its increase are referred to the pristine material for NCM622 at 2.55 V vs. Li$^+$/Li and to cycle 0 for LTO and LFP. The relative volume change in the unit cell of each active material is taken from XRD measurements obtained from literature sources.[7,61,62] The error bars correspond to the minimum/maximum value of two cells.

		Electrode material						
	Units	NCM622 (3.9 V)	NCM622 (4.2 V)	NCM622 (4.5 V)	LTO	LFP	VGCF only	C65 only
Relative volume change	%	−1.0[7]	−1.8[7]	−4.0[7]	+0.2[61]	−6.8[62]	—	—
Spec. electrode capacitance (pristine)	F/g	0.12 ± 0.00	0.12 ± 0.00	0.12 ± 0.00	0.14 ± 0.00	1.65 ± 0.01	0.43 ± 0.01	1.73 ± 0.03
Electrode capacitance after 203 cycles	F/g	0.24 ± 0.00	0.27 ± 0.00	0.32 ± 0.01	0.14 ± 0.00	2.69 ± 0.06	—	—
Electrode capacitance gain over 203 cycles	%	+96	+125	+168	±0	+64	—	—
Active material surface area increase	%	+149	+195	+261	±0	+68	—	—
Capacity retention at C/10 over 203 cycles	%	99.6	88.5	80.8	—	—	—	—
Capacity retention at 1C over 199 cycles	%	94.4	84.8	78.5	—	—	—	—

Conclusions

In this paper, a novel in situ method based on impedance was introduced to monitor cracking of active material particles upon charge/discharge cycling. First, the analysis of impedance spectra in blocking conditions was illustrated from a theoretical point of view, showing that the electrode capacitance can be easily extracted at a frequency of 180 mHz to provide a measure of electrode surface area. The direct correlation of surface area and capacitance was validated by Kr-BET surface area measurements, and the cracking behavior of the NCM622 particles was observed by FIB-SEM. Over 200 cycles, the NCM622 active material showed a surface area increase of up to ∼261 % (i.e. by a factor of ∼3.6), depending on the upper cutoff potential. All studies in which electrochemical or analytical results are normalized to the surface area of an active material must consider this increase in surface area upon cycling, whereby the major gains in electrochemically active surface area are shown to occur during the first few cycles.

This novel method is highly beneficial as compared to post mortem Kr-BET measurements, symmetric cell measurements with harvested electrodes, or post mortem FIB-SEM analysis, since it can continuously track the surface area of a battery electrode in situ upon cycling at any point during extended cycle life tests. Therefore, this approach provides a powerful analytical tool to quantify particle cracking, thus facilitating quality management in CAM production. Moreover, it enables the monitoring of particle cracking originating from electrode calendering in cell production; thereby, the integrity of core–shell particles can be ensured, e.g. for NCMs synthesized with a radial gradient of the nickel content as well as for coated or gas-treated CAMs. Complementary studies specifically investigating the effects associated with the release of oxygen on the morphological integrity will be reported in Part II.

CrediT Authorship Contribution Statement

Stefan Oswald: Methodology, Investigation, Writing—Original Draft. Daniel Pritzl: Methodology, Supervision, Writing—Review & Editing. Morten Wetjen: Methodology, Supervision, Writing—Review & Editing. Hubert A. Gasteiger: Conceptualization, Supervision, Writing—Review & Editing.

Acknowledgments

ORCID

Stefan Oswald https://orcid.org/0000-0001-6402-7833
Daniel Pritzl https://orcid.org/0000-0002-9029-107X
Morten Wetjen https://orcid.org/0000-0002-2357-1151
Hubert A. Gasteiger https://orcid.org/0000-0001-8199-8703

References

1. D. Andre, S. J. Kim, P. Lamp, S. F. Lux, F. Maglia, O. Paschos, and B. Stiaszny, *J. Mater. Chem. A*, **3**, 6709 (2015).
2. S. T. Myung, F. Maglia, K. J. Park, C. S. Yoon, P. Lamp, S. J. Kim, and Y. K. Sun, *ACS Energy Lett.*, **2**, 196 (2017).
3. R. Schmuch, R. Wagner, G. Hörpel, T. Placke, and M. Winter, *Nat. Energy*, **3**, 267 (2018).
4. H. Noh, S. Youn, C. Seung, and Y. Sun, *J. Power Sources*, **233**, 121 (2013).
5. R. Jung, M. Metzger, F. Maglia, C. Stinner, and H. A. Gasteiger, *J. Electrochem. Soc.*, **164**, A1361 (2017).
6. A. O. Kondrakov, A. Schmidt, J. Xu, H. Geßwein, R. Mönig, P. Hartmann, H. Sommer, T. Brezesinski, and J. Janek, *J. Phys. Chem. C*, **121**, 3286 (2017).
7. L. De Biasi, A. O. Kondrakov, H. Geßwein, T. Brezesinski, P. Hartmann, J. Janek, L. de Biasi, A. O. Kondrakov, H. Geßwein, T. Brezesinski, P. Hartmann, and J. Janek, *J. Phys. Chem. C*, **121**, 26163 (2017).
8. Y. Mao, X. Wang, S. Xia, K. Zhang, C. Wei, S. Bak, Z. Shadike, X. Liu, Y. Yang, R. Xu, P. Pianetta, S. Ermon, E. Stavitski, K. Zhao, Z. Xu, F. Lin, X.-Q. Yang, E. Hu, and Y. Liu, *Adv. Funct. Mater.*, **29**, 1900247 (2019).
9. M. Lang, M. S. D. Darma, K. Kleiner, L. Riekehr, L. Mereacre, M. Ávila Pérez, V. Liebau, and H. Ehrenberg, *J. Power Sources*, **326**, 397 (2016).
10. H. R. Kim, S. G. Woo, J. H. Kim, W. Cho, and Y. J. Kim, *J. Electroanal. Chem.*, **782**, 168 (2016).
11. J. M. Lim, T. Hwang, D. Kim, M. S. Park, K. Cho, and M. Cho, *Sci. Rep.*, **7**, 39669 (2017).
12. H.-H. Ryu, K.-J. Park, C. S. Yoon, and Y.-K. Sun, *Chem. Mater.*, **30**, 1155 (2018).
13. P. Yan, J. Zheng, J. Liu, B. Wang, X. Cheng, Y. Zhang, X. Sun, C. Wang, and J. G. Zhang, *Nat. Energy*, **3**, 600 (2018).
14. S. Watanabe, M. Kinoshita, T. Hosokawa, K. Morigaki, and K. Nakura, *J. Power Sources*, **258**, 210 (2014).
15. H. Kim, S. Lee, H. Cho, J. Kim, J. Lee, S. Park, S. H. Joo, S. H. Kim, Y.-G. Cho, H.-K. Song, S. K. Kwak, and J. Cho, *Adv. Mater.*, **28**, 4704 (2016).
16. H. Liu, M. Wolf, K. Karki, Y. S. Yu, E. A. Stach, J. Cabana, K. W. Chapman, and P. J. Chupas, *Nano Lett.*, **17**, 3452 (2017).
17. P. C. Tsai, B. Wen, M. Wolfman, M. J. Choe, M. S. Pan, L. Su, K. Thornton, J. Cabana, and Y. M. Chiang, *Energy Environ. Sci.*, **11**, 860 (2018).
18. U. H. Kim, D. W. Jun, K. J. Park, Q. Zhang, P. Kaghazchi, D. Aurbach, D. T. Major, G. Goobes, M. Dixit, N. Leifer, C. M. Wang, P. Yan, D. Ahn, K. H. Kim, C. S. Yoon, and Y. K. Sun, *Energy Environ. Sci.*, **11**, 1271 (2018).
19. H. H. Sun and A. Manthiram, *Chem. Mater.*, **29**, 8486 (2017).
20. J. Wandt, A. T. S. Freiberg, A. Ogrodnik, and H. A. Gasteiger, *Mater. Today*, **21**, 825 (2018).
21. A. T. S. Freiberg, M. K. Roos, J. Wandt, R. De Vivie-Riedle, and H. A. Gasteiger, *J. Phys. Chem. A*, **122**, 8828 (2018).
22. J. A. Gilbert, I. A. Shkrob, and D. P. Abraham, *J. Electrochem. Soc.*, **164**, A389 (2017).
23. S. Solchenbach, G. Hong, A. T. S. Freiberg, R. Jung, and H. A. Gasteiger, *J. Electrochem. Soc.*, **165**, A3304 (2018).
24. R. Jung, F. Linsenmann, R. Thomas, J. Wandt, S. Solchenbach, F. Maglia, C. Stinner, M. Tromp, and H. A. Gasteiger, *J. Electrochem. Soc.*, **166**, A378 (2019).
25. J. H. Kim, S. J. Kim, T. Yuk, J. Kim, C. S. Yoon, and Y. K. Sun, *ACS Energy Lett.*, **3**, 3002 (2018).
26. F. Friedrich, B. Strehle, A. T. S. Freiberg, K. Kleiner, S. J. Day, C. Erk, M. Piana, and H. A. Gasteiger, *J. Electrochem. Soc.*, **166**, A3760 (2019).
27. F. P. McGrogan, S. R. Bishop, Y.-M. Chiang, and K. J. Van Vliet, *J. Electrochem. Soc.*, **164**, A3709 (2017).
28. C. Schilcher, C. Meyer, and A. Kwade, *Energy Technol.*, **4**, 1604 (2016).
29. J. Kim, H. Lee, H. Cha, M. Yoon, M. Park, and J. Cho, *Adv. Energy Mater.*, **8**, 1702028 (2017).
30. A. Manthiram, J. C. Knight, S. T. Myung, S. M. Oh, and Y. K. Sun, *Adv. Energy Mater.*, **6**, 1501010 (2016).
31. J. Pan, Y. Sun, P. Wan, Z. Wang, and X. Liu, *Electrochem. Commun.*, **7**, 857 (2005).
32. Y. K. Sun, S. T. Myung, B. C. Park, J. Prakash, I. Belharouak, and K. Amine, *Nat. Mater.*, **8**, 320 (2009).
33. J. Li, J. Camardese, R. Shunmugasundaram, S. Glazier, Z. Lu, and J. R. Dahn, *Chem. Mater.*, **27**, 3366 (2015).
34. B. B. Lim, S. T. Myung, C. S. Yoon, and Y. K. Sun, *ACS Energy Lett.*, **1**, 283 (2016).
35. Z. Sun, D. Wang, Y. Fan, L. Jiao, F. Li, T. Wu, D. Han, and L. Niu, *RSC Adv.*, **6**, 103747 (2016).
36. H. Kim, M. G. Kim, H. Y. Jeong, H. Nam, and J. Cho, *Nano Lett.*, **15**, 2111 (2015).
37. J. Zheng, J. Zhang, P. Yan, C. Wang, W. Zhao, S. Chen, and W. Xu, USA Pat. US2017/0338471A1 (2017).
38. G. Liu, M. Li, N. Wu, L. Cui, X. Huang, X. Liu, Y. Zhao, H. Chen, W. Yuan, and Y. Bai, *J. Electrochem. Soc.*, **165**, A3040 (2018).
39. H. Li, J. Li, X. Ma, and J. R. Dahn, *J. Electrochem. Soc.*, **165**, A1038 (2018).
40. S. Solchenbach, D. Pritzl, E. J. Y. Kong, J. Landesfeind, and H. A. Gasteiger, *J. Electrochem. Soc.*, **163**, A2265 (2016).
41. D. Pritzl, A. E. Bumberger, M. Wetjen, J. Landesfeind, S. Solchenbach, and H. A. Gasteiger, *J. Electrochem. Soc.*, **166**, A582 (2019).
42. G. J. Brug, A. L. G. van den Eeden, M. Sluyters-Rehbach, and J. H. Sluyters, *J. Electroanal. Chem.*, **176**, 275 (1984).
43. J. Bisquert, G. Garcia-Belmonte, P. Bueno, E. Longo, and L. O. S. Bulhões, *J. Electroanal. Chem.*, **452**, 229 (1998).
44. U. Rammelt and G. Reinhard, *Electrochim. Acta*, **35**, 1045 (1990).
45. B. Hirschorn, M. E. Orazem, B. Tribollet, V. Vivier, I. Frateur, and M. Musiani, *Electrochim. Acta*, **55**, 6218 (2010).
46. M. E. Orazem, I. Frateur, B. Tribollet, V. Vivier, S. Marcelin, N. Pébère, A. L. Bunge, E. A. White, D. P. Riemer, and M. Musiani, *J. Electrochem. Soc.*, **160**, C215 (2013).
47. O. Haik, S. Ganin, G. Gershinsky, E. Zinigrad, B. Markovsky, D. Aurbach, and I. Halalay, *J. Electrochem. Soc.*, **158**, A913 (2011).
48. J. Landesfeind, D. Pritzl, and H. A. Gasteiger, *J. Electrochem. Soc.*, **164**, A1773 (2017).

49. N. Ogihara, S. Kawauchi, C. Okuda, Y. Itou, Y. Takeuchi, and Y. Ukyo, *J. Electrochem. Soc.*, **159**, 1034 (2012).
50. N. Ogihara, Y. Itou, T. Sasaki, and Y. Takeuchi, *J. Phys. Chem. C*, **119**, 4612 (2015).
51. J. Landesfeind, J. Hattendorff, A. Ehrl, W. A. Wall, and H. A. Gasteiger, *J. Electrochem. Soc.*, **163**, A1373 (2016).
52. J. E. B. Randles, *Discuss. Faraday Soc.*, **1**, 11 (1947).
53. C. Ho, I. D. Raistrick, and R. A. Huggins, *J. Electrochem. Soc.*, **127**, 343 (1980).
54. M. Ebner, F. Geldmacher, F. Marone, M. Stampanoni, and V. Wood, *Adv. Energy Mater.*, **3**, 845 (2013).
55. S. Meini, M. Piana, H. Beyer, J. Schwämmlein, and H. A. Gasteiger, *J. Electrochem. Soc.*, **159**, A2135 (2012).
56. D. R. Gallus, R. Schmitz, R. Wagner, B. Hoffmann, S. Nowak, I. Cekic-Laskovic, R. W. Schmitz, and M. Winter, *Electrochim. Acta*, **134**, 393 (2014).
57. D. C. Grahame, *Chem. Rev.*, **41**, 441 (1947).
58. M. Gaberscek, J. Moskon, B. Erjavec, R. Dominko, and J. Jamnik, *Electrochem. Solid-State Lett.*, **11**, A170 (2008).
59. A. T. S. Freiberg, J. Sicklinger, S. Solchenbach, and H. A. Gasteiger, *Electrochim. Acta*, **346**, 136271 (2020).
60. R. Jung, P. Strobl, F. Maglia, C. Stinner, and H. A. Gasteiger, *J. Electrochem. Soc.*, **165**, A2869 (2018).
61. S. Scharner, W. Weppner, and P. Schmid-Beurmann, *J. Electrochem. Soc.*, **146**, 857 (1999).
62. A. K. Padhi, K. S. Nanjundaswamy, and J. B. Goodenough, *J. Electrochem. Soc.*, **144**, 1188 (1997).
63. T. Ohzuku, H. Tomura, and K. Sawai, *J. Electrochem. Soc.*, **144**, 3496 (1997).
64. K. Rhodes, N. Dudney, E. Lara-Curzio, and C. Daniel, *J. Electrochem. Soc.*, **157**, A1354 (2010).
65. A. Tranchot, H. Idrissi, P.-X. Thivel, and L. Roué, *J. Power Sources*, **330**, 253 (2016).
66. M. M. Besli, S. Xia, S. Kuppan, Y. Huang, M. Metzger, A. K. Shukla, G. Schneider, S. Hellstrom, Christensen, M. M. Doeff, and Y. Liu, *Chem. Mater.*, **31**, 491 (2019).
67. H. Gabrisch, J. Wilcox, and M. M. Doeff, *Electrochem. Solid-State Lett.*, **11**, A25 (2008).
68. V. Sharova, A. Moretti, T. Diemant, A. Varzi, R. J. Behm, and S. Passerini, *J. Power Sources*, **375**, 43 (2018).
69. N. Nitta, F. Wu, J. T. Lee, and G. Yushin, *Mater. Today*, **18**, 252 (2015).
70. D. Wang, X. Wu, Z. Wang, and L. Chen, *J. Power Sources*, **140**, 125 (2005).

Supporting Information

Novel Method for Monitoring the Electrochemical Capacitance by In Situ Impedance Spectroscopy as Indicator for Particle Cracking of Nickel-Rich NCMs: Part I. Theory and Validation

Stefan Oswald*,z, Daniel Pritzl, Morten Wetjen, and Hubert A. Gasteiger**

Chair of Technical Electrochemistry, Department of Chemistry and Catalysis Research Center,

Technical University of Munich, D-85748 Garching, Germany

zE-mail: Stefan.Oswald@tum.de

*Electrochemical Society Student Member.

**Electrochemical Society Fellow.

Realization of blocking conditions for LTO and LFP - In order to be able to apply the developed method for extracting an electrode's capacitance from an impedance spectrum, blocking conditions are required, which are achieved through a semi-infinite charge-transfer resistance at full (de)lithiation. Similar as for NCM622, an analogous procedure is applied to LFP and LTO, as described in **Figure 2a** and **Figure 4**, to prove that blocking conditions can be achieved for both active materials. In this experiment, impedance spectra of both LFP and LTO working electrodes are recorded at different SOCs between 0 %SOC and 100 %SOC (here, 0 %SOC corresponds to full lithiation of LFP and full delithiation of LTO); this is possible for LTO and LFP since both are structurally stable at both full lithiation as well as at full delithiation, in contrast to nickel-rich layered oxides. As it can be seen in **Figure S1a**, the capacitive branch of the constant-phase element dominates the impedance spectra at low frequency for LFP, both at 0 %SOC (which was used to collect the impedance spectra during the long-term cycling experiments) as well as at 100 %SOC. For LTO, shown in **Figure S1b**, blocking conditions are achieved at 0 %SOC, corresponding to full delithiation (at 2.55 V vs. Li$^+$/Li). (Note that at 100 %SOC, blocking conditions for LTO could not be achieved since the potential of 1.05 V vs. Li$^+$/Li is presumably not sufficiently low in order to provide complete lithiation of the material. The choice of the lower cutoff for LTO was limited by the reduction potential of the electrolyte in order to avoid the effect of SEI formation on the impedance spectra and the extracted capacitance.) Therefore, the capacitance can be extracted using the developed method by approximating the capacitance from the imaginary impedance at 180 mHz according to **Equation 6**. During the cycling experiments shown in **Figure 9**, the impedance spectroscopy is performed after a potential hold of 1 h at 2.55 V vs. Li$^+$/Li for both LTO and LFP.
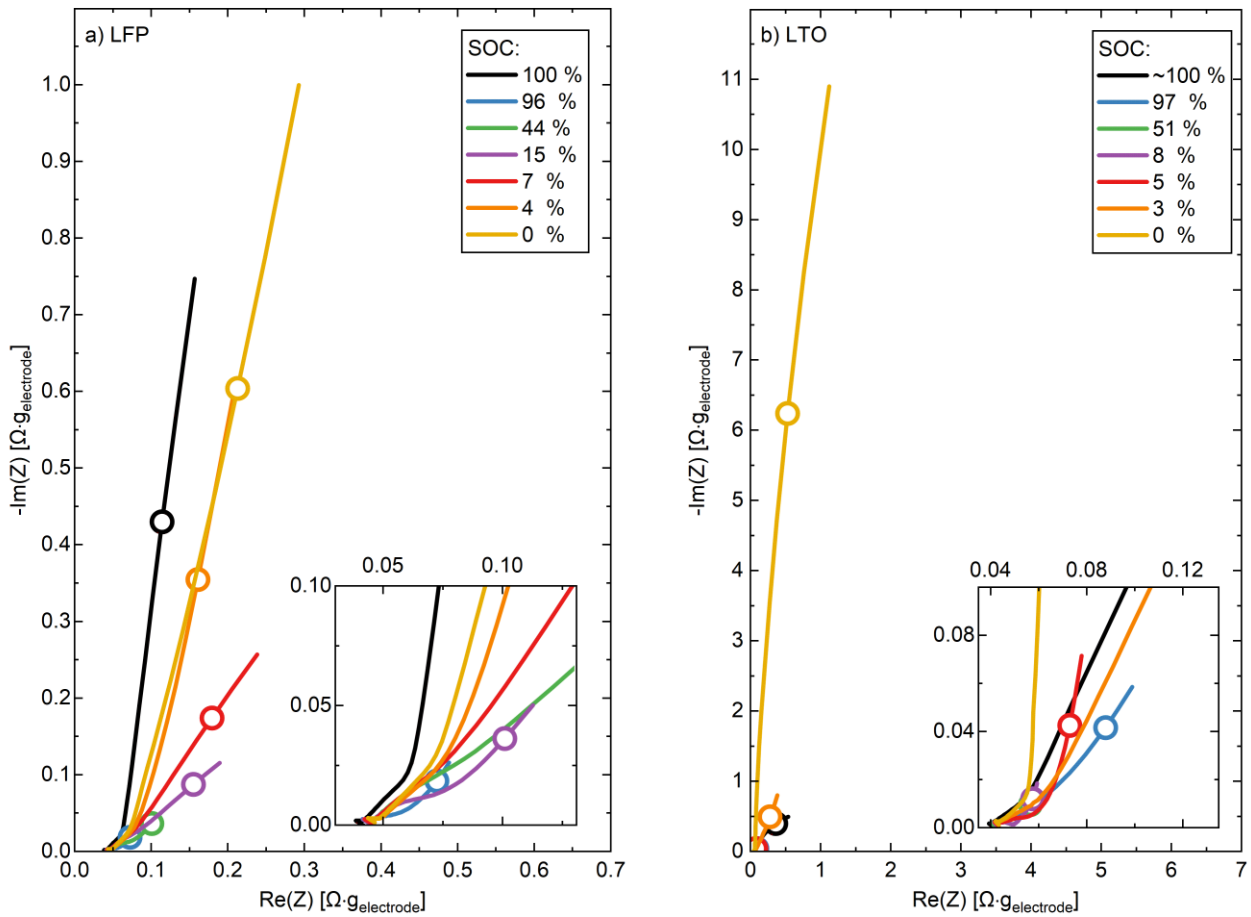
Figure S1: Realization of blocking conditions, shown for selected impedance spectra of **a)** LFP and **b)** LTO working electrodes in pseudo full-cells with 60 µl LP57 and capacitively oversized LTO counter electrodes that were pre-lithiated to 30 %SOC for LFP and 90 %SOC for LTO. Analogous to the procedure depicted in **Figure 2a**, the working electrode potential-controlled impedance spectroscopy (PEIS, with 15 mV amplitude and from 100 kHz to 100 mHz) was conducted with these cells using a µ-RE (i.e., a GWRE) at different SOCs between 0 %SOC and 100 %SOC. For LFP, blocking conditions are realized at 0 %SOC (corresponding to 2.55 V vs. Li$^+$/Li) as well as at 100 %SOC (corresponding to 3.80 V vs. Li$^+$/Li). For LTO, blocking conditions are achieved at 0 %SOC (corresponding to 2.55 V vs. Li$^+$/Li). The frequency points at 180 mHz are indicated by open circles.

Specific capacitance of pristine electrode constitutents – In **Figure S2**, the specific capacitance of pristine NCM622 electrodes as well as of electrodes containing only conductive carbon and binder in LP57 electrolyte is shown dependent on the applied potential which is set between 3.05 V vs. Li^+/Li and 2.55 V vs. Li^+/Li. Over the entire potential range, the capacitance of the VGCF electrode (VGCF:PVDF 8:2 w/w) and of the C65 electrode (C65:PVDF 1:1 w/w) varies less than 20 %, the variation of the capacitance of the NCM622 electrode of 12 % is even lower. This shows that the potential does not have a drastic effect on the measured capacitance for a pristine NCM622 electrode, either when measured at 2.55 V vs. Li^+/Li during cycling or in a symmetric cell setup in OCV at roughly 3.0 V vs. Li^+/Li. Therefore, the discrepancy of a factor of roughly two, which is observed for the specific capacitance of pristine NCM electrodes in either LP57 or an electrolyte containing 10 mM TBATFSI, is not due to the different electrode potential, but must be attributed to a changed double layer capacitance of the NCM active material in different electrolytes.

In LP57 electrolyte and at 2.55 V vs. Li^+/Li, where the capacitance is extracted during the cycling experiments, the VGCF electrode and the C65 electrode exhibit 0.43 $F/g_{electrode}$ and 1.7 $F/g_{electrode}$, respectively; the NCM electrode shows 0.12 $F/g_{electrode}$. These values are required in **Figure 5** and **Figure 6** to subtract the contribution of VGCF and PVDF from the specific capacitance of the entire NCM electrode, in order to obtain the contribution of the active material only and, subsequently, quantify its surface area increase.
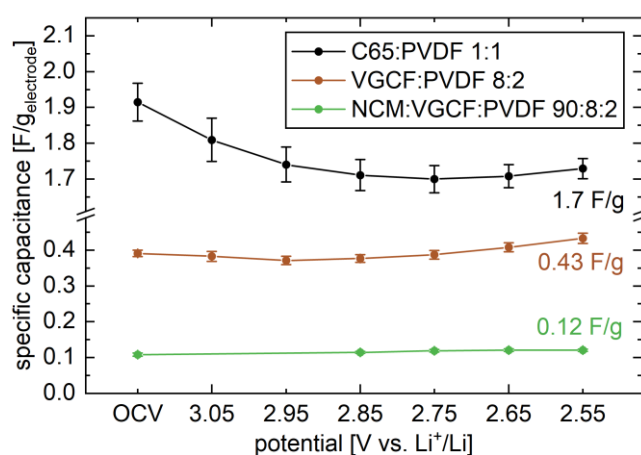
Figure S2: Potential dependence of the specific capacitance of pristine NCM622, VGCF, and C65 working electrodes in pseudo full-cells with 60 µl LP57 and capacitively oversized LTO counter electrodes that were pre-lithiated to 30 % SOC. The working electrode potential-controlled impedance spectroscopy (PEIS, with 15 mV amplitude and from 100 kHz to 100 mHz) was conducted with these cells using a µ-RE (i.e. a GWRE) at different potentials between 3.05 V and 2.55 V vs. Li^+/Li, approached by a discharge at C/10 followed by a constant voltage step of 1 h. The capacitance was extracted from the imaginary impedance at a frequency of 180 mHz and normalized to the electrode mass. The values shown here are calculated from the mean of two identical cell pairs; the error bars correspond to the minimum/maximum value of two cells.

Charge/discharge cycling of NCM622 electrodes - Except for the shown number of cycles, **Figure S3** is identical to **Figure 5b and 5c**. The latter show only 203 cycles, since the cells cycled to 3.9 V and 4.2 V were only tested for 203 cycles; the cells with an upper cutoff voltage of 4.5 V vs. Li$^+$/Li were cycled to 303 cycles, after which the NCM622 electrodes were harvested, washed, and investigated by Kr-BET.
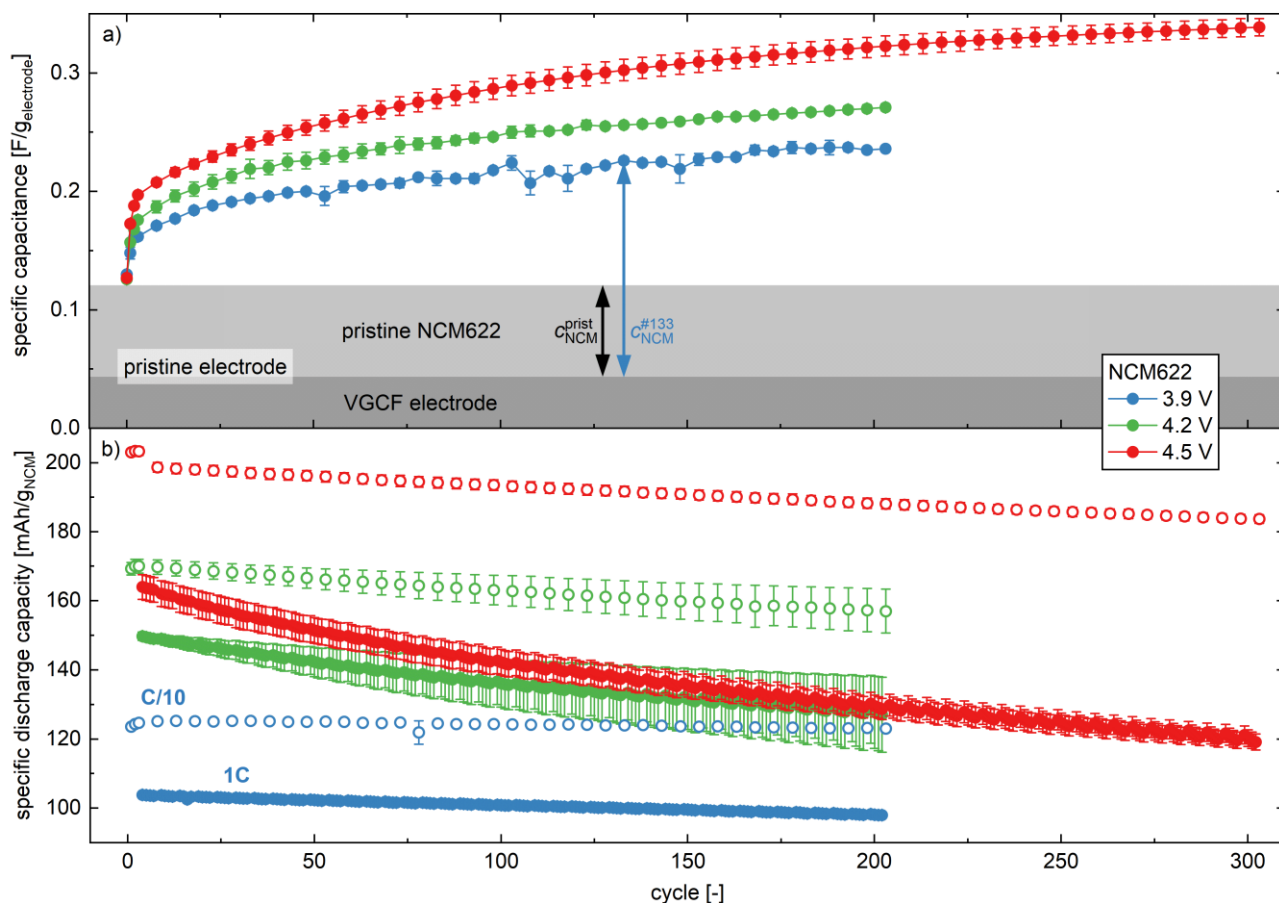
Figure S3: Electrochemical cycling of NCM622 in pseudo full-cells with 60 µl LP57, two glass fiber separators, and a µ-RE (i.e., a GWRE) using an uncompressed NCM622 working electrode and pre-lithiated, capacitively oversized LTO as the counter electrode. Following the procedure depicted in **Figure 2b**, NCM622 was cycled at 25 °C to different upper cutoff potentials of 3.9 V (blue lines/symbols), 4.2 V (green lines/symbols), or 4.5 V (red lines/symbols) vs. Li$^+$/Li. Impedance spectra of the NCM622 working electrodes were recorded in blocking conditions after a potential hold at 2.55 V vs. Li$^+$/Li, applying an amplitude of 15 mV from 100 kHz to 100 mHz. The specific capacitance and the specific discharge values shown here are calculated from the mean of two nominally identical cells, with the error bars corresponding to the minimum/maximum value of two cells. **a)** Specific capacitance of the NCM622 working electrode extracted from the imaginary impedance at a frequency of 180 mHz in blocking conditions (see **Equation 6**). The sum of the gray areas indicates the specific capacitance of the pristine uncompressed NCM622 working electrode, and the dark gray area shows the specific capacitance of a VGCF electrode multiplied by 0.1 (see text). **b)** Specific discharge capacity normalized to the active material mass vs. cycle number following the procedure shown in **Figure 2b**. The open circles show the discharge capacity at C/10 (after a CCCV charge at C/10), and the solid circles at 1C (after a CCCV charge at 1C).

5

Rules of error propagation - When calculating the specific capacitance of only the NCM622 particles normalized by the capacitance of the pristine NCM622, the following equation is applied:

$$\frac{c_{\text{NCM}}^{\text{cycled}}}{c_{\text{NCM}}^{\text{pristine}}} = \frac{c_{\text{electrode}}^{\text{cycled}} - 0.1 \cdot c_{\text{VGCF}}}{c_{\text{electrode}}^{\text{pristine}} - 0.1 \cdot c_{\text{VGCF}}}$$

In order to calculate the error of the ratio of the two specific capacitance values, the rules of error propagation are applied. The error of sums and differences is calculated in the following way:

$$a = \pm x \pm y \pm z \quad \Rightarrow \quad \Delta a = \sqrt{(\Delta x)^2 + (\Delta y)^2 + (\Delta z)^2}$$

The error of products and quotients is calculated in the following way:

$$a = \frac{x \cdot y}{z} \quad \Rightarrow \quad \Delta a = a \cdot \sqrt{\left(\frac{\Delta x}{x}\right)^2 + \left(\frac{\Delta y}{y}\right)^2 + \left(\frac{\Delta z}{z}\right)^2}$$

First, one determines the error in the difference between the measured capacitance of the cycled NCM622 electrode (with error) and the VGCF capacitance (with error) as well as the error in the difference between the capacitance of the pristine NCM622 electrode (with error) and the VGCF electrode (with error):

$$c_{\text{NCM}} = c_{\text{electrode}} - 0.1 \cdot c_{\text{VGCF}}$$

$$\Rightarrow \quad \Delta c_{\text{NCM}} = \sqrt{\left(\Delta c_{\text{electrode}}\right)^2 + \left(0.1 \cdot \Delta c_{\text{VGCF}}\right)^2}$$

The relative error is obtained by dividing the equation by the capacitance:

$$\frac{\Delta c_{\text{NCM}}}{c_{\text{NCM}}} = \frac{\sqrt{\left(\Delta c_{\text{electrode}}\right)^2 + \left(0.1 \cdot \Delta c_{\text{VGCF}}\right)^2}}{c_{\text{electrode}} - 0.1 \cdot c_{\text{VGCF}}}$$

Subsequently, one takes the ratio of the two differences and computes their error. Finally, we obtain the relative error of the normalized capacitance of the NCM only:

$$\Delta\left(\frac{c_{\text{NCM}}^{\text{cycled}}}{c_{\text{NCM}}^{\text{pristine}}}\right) = \frac{c_{\text{NCM}}^{\text{cycled}}}{c_{\text{NCM}}^{\text{pristine}}} \cdot \sqrt{\left(\frac{\Delta c_{\text{NCM}}^{\text{cycled}}}{c_{\text{NCM}}^{\text{cycled}}}\right)^2 + \left(\frac{\Delta c_{\text{NCM}}^{\text{pristine}}}{c_{\text{NCM}}^{\text{pristine}}}\right)^2} =$$

$$= \frac{c_{\text{NCM}}^{\text{cycled}}}{c_{\text{NCM}}^{\text{pristine}}} \cdot \sqrt{\left(\frac{\sqrt{\left(\Delta c_{\text{electrode}}^{\text{cycled}}\right)^2 + \left(0.1 \cdot \Delta c_{\text{VGCF}}\right)^2}}{c_{\text{electrode}}^{\text{cycled}} - 0.1 \cdot c_{\text{VGCF}}}\right)^2 + \left(\frac{\sqrt{\left(\Delta c_{\text{electrode}}^{\text{pristine}}\right)^2 + \left(0.1 \cdot \Delta c_{\text{VGCF}}\right)^2}}{c_{\text{electrode}}^{\text{pristine}} - 0.1 \cdot c_{\text{VGCF}}}\right)^2}$$

Electrochemical cycling of LFP and LTO – In **Figure S4**, the specific discharge capacity is depicted for the cycled cells shown in **Figure 9** using LTO or LFP as working electrode, illustrating that the cycling performance of the cells is as one would expect. Furthermore, these data show that the entire available capacity was exchanged at C/10 and that a large fraction of it was exchanged at 1C, so that both active materials experienced close to the full volume change of the respective unit cell. A detailed discussion of the data is found in the main text in the respective section where the electrochemical behavior of LFP and LTO is treated.
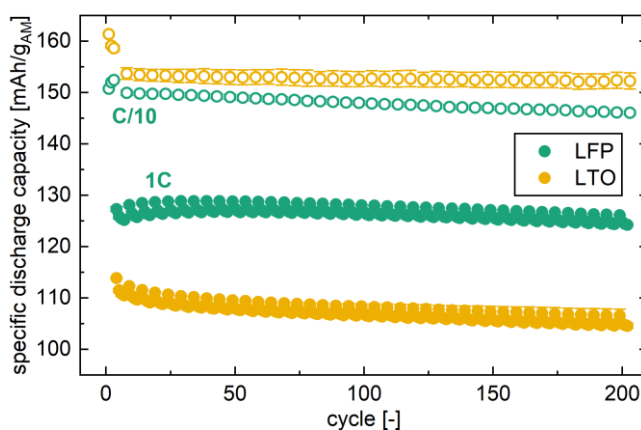
Figure S4: Specific discharge capacity of LTO and LFP during electrochemical cycling. For this, pseudo full-cells were assembled in Swagelok T-cells with 60 µl LP57, two glass fiber separators, and a µ-RE (i.e. a GWRE) using LTO or LFP as working electrode and pre-lithiated, capacitively oversized LTO as the counter electrode. Following the procedure introduced in the experimental section and depicted in **Figure 2b**, the cells were cycled at 25 °C, applying cutoff potentials of 1.05 and 2.05 V vs. Li$^+$/Li for LTO and 2.95 and 3.80 V vs. Li$^+$/Li for LFP. The values shown here are calculated from the mean of two identical cell pairs. The error bars correspond to the minimum/maximum value of two cells.

3.2 Effect of Oxygen Release Dependent on Particle Morphology

The article "Novel Method for Monitoring the Electrochemical Capacitance by In Situ Impedance Spectroscopy as Indicator for Particle Cracking of Nickel-Rich NCMs: Part II. Effect of Oxygen Release Dependent on Particle Morphology" was submitted to the peer-reviewed *Journal of the Electrochemical Society* in September 2021 and published online in December 2021 [252]. It is available as an open-access article and distributed under the terms of the Creative Commons Attribution Non-Commercial No Derivatives 4.0 License. A permanent link to this article can be found under https://doi.org/10.1149/1945-7111/ac3905. The main findings of this paper were presented by Stefan Oswald at the Electrochemistry Undercover 2020 Meeting of the *Gesellschaft deutscher Chemiker* in a virtual format in September 2020.

This article is a follow-up study on the newly developed impedance-based method to quantify particle cracking (see Chapter 3.1) and investigates the effect of composition (i.e., NCM622 vs. NCM851005) and particle morphology (i.e., PC vs. SC NCM) on the structural and morphological stability at high state of charge. To elucidate the structural stability of the partially delithiated NCM crystal lattice at high SOC, the three materials are charged to $5.0\,V_{Li}$ while the evolved gases O_2 and CO_2 are monitored by OEMS. Even though the release of lattice oxygen, being the indicator for the structural instability of the NCMs, starts at different potentials of $\sim$4.5 and $\sim$4.2 V_{Li} for NCM622 and NCM851005, respectively, their onset in terms of degree of delithiation coincides at $\sim$80 %SOC, as previously reported by Jung et al. [119]. In addition to particle cracking due to the repeated volume change upon (de)lithiation, the two PC NCMs exhibit a sudden increase in capacitance at $\sim$80 %SOC. After being cycled to various upper cutoff potentials, EIS measurements in the discharged state show an NCM capacitance increase by a factor of 4x to 5x for both NCM622 and NCM851005, while this increase was verified for NCM851005 by ex situ surface area measurements using Kr-BET. In contrast, the SC NCM851005 does not show a significant increase in capacitance, neither at low nor at high SOC (up to $5.0\,V_{Li}$). Additionally, at high SOC, the loss of specific discharge capacity, which indicates the degradation of the NCM active materials and which is most pronounced for the SC NCM, occurs simultaneously both with the release of lattice oxygen as well as with the cracking of the PC particles.

Interestingly, the surface-area-normalized capacitance of $\sim$28 F_{NCM}/cm^2_{NCM} was essen-

tially identical for both NCM622 and NCM851005 and did not change upon formation of the oxygen-depleted surface layer at high SOC. As a consequence, the specific NCM capacitance determined by EIS (in units of F_{NCM}/g_{NCM}) can be translated directly into a physical surface area (in units of m^2/g_{NCM}). Therefore, the novel impedance-based method is not only able to track relative changes of the electrode or NCM surface area but can also quantify the specific surface area of NCM materials in absolute values (after the subtraction of the contribution of the other components in the electrode). However, the dependence of the surface-area-normalized capacitance on, e.g., the potential or the electrolyte composition (i.e., the concentration and type of salt or the used solvents) has to be considered.

By comparing cycled PC and SC NCM particles after extended cell cycling by FIB-SEM, various reports have claimed the enhanced morphological stability of the SC materials [141, 180, 253]. In contrast, the cracking of the primary crystallites at the surface or in the bulk of the particles has been observed as well, both after extended cycling [254–256] but also already after the first charge [179, 257]. The results obtained in this study illustrate that the increase of the surface area in contact with the electrolyte is suppressed (or, at least, significantly diminished) for SC NCM crystallites since they do not crack even when cycled to $5.0\,V_{Li}$. However, it must be noted that the morphological stability is expected to not only depend on the upper cutoff potential but also on other operating conditions, such as the amount of charge/discharge cycles, the temperature, and the applied C-rate, as well as the material properties, such as primary particle size, composition, and preexisting stacking faults of the crystal structure. The consequences of the distinct particle morphologies on the fundamental properties and on the cycling performance are further elucidated in Chapter 4.

Author contributions

S.O., D.P., and M.W. developed the concept of the measurements based on an increasing upper cutoff potential. S.O. collected the SEM images, performed the OEMS, BET, and impedance measurements, and analyzed the data. S.O. wrote and H.A.G. edited the manuscript. All authors discussed the results and commented on the manuscript.

Novel Method for Monitoring the Electrochemical Capacitance by In Situ Impedance Spectroscopy as Indicator for Particle Cracking of Nickel-Rich NCMs: Part II. Effect of Oxygen Release Dependent on Particle Morphology

Stefan Oswald,[*,z] Daniel Pritzl, Morten Wetjen, and Hubert A. Gasteiger[**]

Chair of Technical Electrochemistry, Department of Chemistry and Catalysis Research Center, Technical University of Munich, D-85748 Garching, Germany

Nickel-rich NCMs ($LiMO_2$, with M = Ni, Co, and Mn) are increasingly commercialized as cathode active materials for lithium-ion batteries due to their high specific capacity. However, the available capacity is limited due to their structural instability at high state of charge, causing the formation of a resistive surface layer upon release of lattice oxygen, observed at different upper cutoff potentials depending on the NCM composition. To understand the impact of this instability, the correlation of oxygen release, capacity fading, and particle cracking was investigated as a function of state of charge for three nickel-rich NCMs, differing either in composition (i.e., in transition metal ratio) or in morphology (i.e., in primary crystallite size). First, the onset of the release of lattice oxygen was identified by on-line electrochemical mass spectrometry (OEMS). In electrochemical cycling experiments, the NCM capacitance was tracked in situ by impedance spectroscopy (EIS) using a micro-reference electrode while the upper cutoff potential was increased every third cycle stepwise from 3.9 V to 5.0 V. Hereby, the effect of the degree of delithiation on the discharge capacity and on the particle integrity (tracked via its surface area) was examined, both for poly- and single-crystalline NCMs.

The demand for nickel-rich layered lithium nickel cobalt manganese oxides (NCMs, $Li_{1+\delta}Ni_xCo_yMn_zO_2$, $x+y+z+\delta = 1$, and $0 < \delta < 0.01$) as attractive cathode active materials (CAMs) for lithium-ion batteries is constantly growing, owed to their high theoretical specific capacity of ~275 mAh/g_{NCM}.[1,2] As the material is required to endure thousands of charge/discharge cycles in applications such as electric vehicles or portable electronics, the used capacity of nickel-rich NCMs, easily controlled by the applied upper cutoff potential (typically set between 4.2 V and 4.4 V in graphite/NCM full-cells, depending on the NCM composition),[3] has to be limited to ~80–85 % of the theoretical capacity; otherwise, an accelerated capacity loss is observed during long-term cycling to higher states of charge (SOCs).[3–5]

This drawback, diminishing the practical energy density, is owed to the instability of the NCM layered structure at high degrees of delithiation, appearing beyond the H2-H3 phase transition at ~75 %SOC.[3,5–7] Above this limit, the release of lattice oxygen, detected by mass spectrometry for various NCM compositions,[3,8–10] is accompanied by the formation of a surface-near resistive oxygen-depleted layer, shown previously by microscopy (HR-TEM),[5,11–14] spectroscopy (EELS),[12] and diffraction (XRD and SAED).[12,14–16] This degradation of the surface-near structure of NCMs does not only add significant overpotentials during cycling, resulting in the loss of capacity and energy density,[3] but the released (singlet) oxygen also decomposes the electrolyte components.[17,18] In this reaction, protic species such as HF are produced,[17,18] initiating the dissolution of the transition metals from the NCM[19] and the redeposition on the anode that causes additional lithium loss in the SEI.[20] Since the phase transformation is mainly restricted to the surface-near regions of the NCM crystallites, reported to reach layer thicknesses of up to 20 nm,[3,11,14,16] the fraction of converted material, the extent of induced side reactions, and their impact on the battery performance depend directly on the specific surface area of the CAM (i.e., on the electrochemically active surface area) and, therefore, on the particle morphology of the CAM.

In part I of this study,[21] we successfully developed an in situ method for tracking the surface area of a battery electrode by its capacitance, obtained non-destructively from electrochemical impedance spectroscopy (EIS). With this novel tool, we showed that the surface area of a polycrystalline (PC) NCM622 increased continuously upon charge/discharge cycling, resulting from the crack formation of the secondary NCM agglomerates caused by the anisotropic change of the lattice parameters *a* and *c* upon (de)lithiation.[5,7,22–24]

Aiming to suppress the NCM surface area increase and, thereby, reduce the parasitic side reactions with the electrolyte that scale with exposed surface area, the interest for NCM particles with a monolithic structure and larger primary crystallites, so-called *single-crystalline* (SC) NCMs,[25] is growing, as they are expected to be less prone to particle cracking.[26–28] By comparing PC and SC NCM523, Li et al.[29] previously presented a significantly improved long-term cycling stability for SC NCM523 at elevated temperatures: at 40 °C, the single-crystalline NCM lasted for 300 cycles, before the capacity degraded to 90 % of its initial value, even without electrolyte additives; for the polycrystalline NCM, however, the same state of health was reached already after 150 cycles.[29] According to the study of Harlow et al., battery cells (using a similar SC NCM523 material) could deliver more than 1000 charge/discharge cycles at 40 °C, and even up to 10,000 cycles at 20 °C, before 90 % of the initial capacity was reached.[30] If it were possible to show that the surface area of SC NCMs was maintained upon cycling, the improved performance of SC NCMs[27,29] could be clearly assigned to the stability of their morphology and, therefore, to their ability to retain a low exposed surface area over the course of cycling.

In this paper, the correlation of lattice oxygen release, capacity fading, and particle cracking is investigated as a function of the state of charge for three nickel-rich NCMs, differing either in composition (i.e., in transition metal ratio: nickel content of 60 % vs 85 %) or in morphology (i.e., in primary crystallite size: PC vs SC). First, the onset of the release of lattice oxygen is identified by on-line electrochemical mass spectrometry (OEMS). In electrochemical

*Electrochemical Society Student Member.
**Electrochemical Society Fellow.
zE-mail: Stefan.Oswald@tum.de

cycling experiments, the NCM electrode capacitance is tracked in situ by impedance spectroscopy (EIS) using a micro-reference electrode (μ-RE) while the upper cutoff potential is increased every third cycle stepwise from 3.9 V to 5.0 V. Hereby, the effect of a high degree of delithiation on the discharge capacity as well as on the particle integrity, tracked by the NCM specific surface area via Kr-BET, is illuminated, both for poly- and single-crystalline NCMs. As the two NCM morphologies exhibit an entirely different integrity of the CAM particles at high state of charge, the underlying mechanisms causing the surface area increase are discussed. From the detected amounts of evolved gases as well as from the evolution of the specific surface areas of the CAMs, the thickness of the oxygen-depleted surface layer is estimated for each material.

Experimental

Scanning electron microscopy.—The morphology of the cathode active material powders was investigated via top-view scanning electron microscopy (SEM) using a tabletop microscope (JCM-6000, JEOL, Japan) in secondary electron mode and applying an acceleration voltage of 15 kV.

Electrode preparation.—For cell cycling, NCM electrodes were prepared from three NCM powders (as presented in the SEM pictures of Fig. 2): polycrystalline NCM622 referred to as *PC-60* ($Li_{1.01}(Ni_{0.6}Co_{0.2}Mn_{0.2})_{0.99}O_2$, 0.32 m^2_{BET}/g_{NCM} measured by Kr-BET), polycrystalline NCM851005 referred to as *PC-85* ($Li_{1.01}(Ni_{0.85}Co_{0.10}Mn_{0.05})_{0.99}O_2$, 0.27 m^2_{BET}/g_{NCM}), and single-crystalline NCM851005 referred to as *SC-85* ($Li_{1.01}(Ni_{0.85}Co_{0.10}Mn_{0.05})_{0.99}O_2$, 0.51 m^2_{BET}/g_{NCM}); all CAMs were received from BASF SE, Germany. The three NCM powders were each mixed at a mass ratio of 90:8:2 with vapor-grown carbon fibers (VGCF-H, 12.4 m^2_{BET}/g_{VGCF}, Showa Denko, Japan) and polyvinylidene difluoride (PVDF, Kynar HSV 900, Arkema, France) as well as N-methyl-2-pyrrolidone (NMP, anhydrous, Sigma Aldrich, Germany) in a planetary mixer (Thinky Corp., USA) for 17 min, using a four-step sequential mixing procedure.

For on-line electrochemical mass spectrometry (OEMS) measurements, the slurries (with a solid content of 80 wt%) were coated on a stainless-steel mesh (316 grade, 26 μm aperture, 25 μm wire diameter, The Mesh Company, UK) with a doctor blade using an automatic coater (RK PrintCoat Instruments, United Kingdom). The electrode sheets were then dried in a convection oven at 50 °C for 5 h before electrodes with a diameter of 14 mm were punched out, having a loading of 8.0 ± 2.0 mg_{NCM}/cm^2; this corresponds to a theoretical areal capacity of 2.2 ± 0.6 mAh/cm^2. For the counter electrodes, LFP electrodes with a diameter of 15 mm were punched out from commercially available LFP electrode sheets (LFP on aluminum, 3.5 mAh/cm^2, Custom Cells, Germany).

For the cycling experiments in Swagelok T-cells, the slurries (with a solid content of 63 wt%) were coated onto the rough side of an aluminum foil (18 μm, MTI, USA) with a box-type coating bar (Erichsen, Germany) using the automated coater. All electrode sheets were then dried in a convection oven at 50 °C for 5 h before electrodes with a diameter of 10.95 mm were punched out, having a loading of 8.7 ± 1.0 mg_{NCM}/cm^2; this corresponds to a theoretical areal capacity of 2.4 ± 0.3 mAh/cm^2. For the counter electrodes, LTO electrodes with a diameter of 10.95 mm were punched out from commercially available LTO electrode sheets (LTO on aluminum, 3.5 mAh/cm^2, Custom Cells, Germany).

To avoid any cracking of the NCM particles during electrode preparation, the NCM electrodes were not compressed or calendered. They were dried in a Büchi oven at 120 °C under dynamic vacuum for at least 6 h and then transferred without exposure to air to an argon-filled glove box (<1 ppm O_2 and H_2O, MBraun, Germany), where all cells were assembled.

On-line electrochemical mass spectrometry.—In preparation of the on-line electrochemical mass spectrometry (OEMS) experiments, the capacitively oversized LFP electrodes (15 mm,

3.5 mAh/cm^2) were pre-delithiated in coin cells (Hohsen, Japan) using two glass fiber separators, one H2013 polyolefin separator (Celgard, USA) facing the LFP electrode, and 100 μl of LP57 electrolyte (1 M LiPF$_6$ in EC:EMC 3:7 w/w, <20 ppm H_2O, BASF, Germany). For this, they were delithiated against metallic lithium (450 μm thick and 15 mm in diameter, Rockwood Lithium, USA) to ~90 % SOC at a specific current of 30 mA/g_{LFP} for 4.5 h, after having performed one full formation cycle at 30 mA/g_{LFP} between 3.0 V and 4.0 V vs. Li$^+$/Li. After pre-delithiation, the LFP electrodes were harvested from the cells and used without washing as the counter electrode in the OEMS cells for the gas evolution experiments. The pre-delithiated, capacitively oversized LFP electrodes are used because they: i) provide a stable potential of ~3.45 V vs. Li$^+$/Li over a wide SOC window (3.40 V used at 90 %SOC for the end of lithiation), ii) provide a sufficiently large capacity to take up the lithium from the investigated NCM working electrodes, and iii) exhibit no gas evolution due to the absence of electrolyte decomposition reactions at their operating potential (as compared to typical anodes such as lithium metal or graphite forming an SEI including gas evolution[3,20,31]).

For the OEMS experiments, a pre-delithiated LFP counter electrode was placed on the bottom of the custom-made OEMS cell hardware, then covered by two H2013 polyolefin separators (24 mm, Celgard, USA) that were wetted with 100 μl of LP57 electrolyte (1 M LiPF$_6$ in EC:EMC 3:7 w/w, <20 ppm H_2O, BASF, Germany); finally, an NCM electrode was placed on top of the stack. The electrode stack was then compressed by a spring in the sealed OEMS cell. The assembled cells were positioned in a climate chamber (CTS, Germany) at 25 °C and connected to a potentiostat (SP-300, BioLogic, France) and the mass spectrometer system (HiQuad QMH 400–1, Pfeiffer Vacuum, Germany), which has been described in detail elsewhere.[32]

The cells were held at OCV for 4 h before they were charged in constant-current mode (CC) to 5.0 V vs. Li$^+$/Li (corresponding to 1.6 V vs. the pre-delithiated, capacitively oversized LFP counter electrode) at a *C*-rate of *C*/15 (referenced to the theoretical capacities of 276.5 mAh/g_{NCM} for PC-60 and of 275.0 mAh/g_{NCM} for PC-85 and SC-85). The traced mass signals were first normalized to the ion current of the ^{36}Ar isotope to correct for fluctuations of pressure and temperature, and then the signals for O_2 and CO_2 were converted to concentrations using a calibration gas (argon with 2000 ppm of H_2, O_2, C_2H_4, and CO_2 each, Westfalen, Germany) and considering a cell volume of ~11 cm^3. For details on the calibration procedure, see Tsiouvaras et al.[32]

T-cell assembly.—In preparation of the cycling experiments in Swagelok T-cells (adapted and reprinted here from part I of this study[21]), capacitively oversized LTO electrodes (3.5 mAh/cm^2) were pre-lithiated to ~10 %SOC in spring-compressed T-cells with two glass fiber separators that were wetted with 60 μl of LP57 (1 M LiPF$_6$ in EC:EMC 3:7 w/w, <20 ppm H_2O, BASF, Germany) and a metallic lithium counter electrode (450 μm thick and 11 mm in diameter, Rockwood Lithium, USA). This was done at a specific current of 30 mA/g_{LTO} for 0.5 h, after having performed one full formation cycle at 30 mA/g_{LTO} between 1.2 V and 2.0 V vs. Li$^+$/Li. After pre-lithiation, the LTO electrodes were harvested from the cells. They were then used without washing as the counter electrode in the pseudo full-cells for the electrochemical cycling tests; note that pseudo full-cell here refers to a cell with a given working electrode (NCM electrodes in this work) and a capacitively oversized, pre-lithiated LTO electrode. The pre-lithiated, capacitively oversized LTO counter electrodes are used because they provide: i) a stable half-cell potential of 1.55 V vs. Li$^+$/Li over a wide SOC window, ii) a sufficiently large capacity to take up the lithium from the investigated NCM working electrodes, and iii) a sufficient excess of lithium to compensate for any lithium consumed by side reactions during cycling, so that the NCM working electrode can be fully lithiated for the EIS measurements that are being conducted in blocking conditions (see below).

For the electrochemical cycling tests, spring-compressed T-cells with capacitively oversized pre-lithiated LTO as the counter electrode and the different NCM-based cathodes (with PC-60, PC-85, or SC-85) as working electrodes were assembled using two glass fiber separators and 60 μl of LP57. Between the two separators, a micro-reference electrode (μ-RE) was inserted, namely a gold-wire reference electrode (GWRE) based on the setup described by Solchenbach et al.[33] The GWRE was lithiated in situ at 150 nA over 1 h from the LTO counter electrode before cycling, which establishes a constant GWRE potential of 0.31 V vs. Li^+/Li[33] that remained stable for more than 800 h (note that the GWRE lithiation charge of ∼0.15 μAh is negligible compared to the capacity of the counter electrode). For details about the cell setup and the preparation of the gold wire, please refer to the original publication.[33]

To record the potential curves of the first charge for the three NCMs (shown in the appendix), spring-compressed Swagelok T-cells with lithium metal as the reference and counter electrode (so-called *half-cells*) and working electrodes based on PC-60, PC-85, or SC-85 were assembled using three glass fiber separators (two between working and counter electrode and one on the lithium metal reference electrode) and 90 μl of LP57 electrolyte.

Impedance spectroscopy.—All electrochemical impedance spectra were included directly into the cycling procedure of a multi-channel potentiostat VMP3 (BioLogic, France) and recorded in a climate chamber (Binder, Germany) at 25 °C in potentiostatic mode (PEIS), with an amplitude of 15 mV for 8 points per decade from 100 kHz to 100 mHz, including a data point at a frequency of 180 mHz. This results in an acquisition time of ∼10 min per PEIS. Each EIS spectrum consists of a full-cell spectrum (between working and counter electrode) and, by using a μ-RE (i.e., the GWRE), also of the half-cell spectrum (i.e., between the working electrode and the μ-RE).

T-cell testing.—All electrochemical cycling tests including the PEIS were performed in a climate chamber (Binder, Germany) at 25 °C, using a multi-channel potentiostat (VMP3, Biologic, France). Before cell cycling, the GWRE was lithiated using the pre-lithiated, capacitively oversized LTO counter electrode (see above). To acquire EIS spectra under blocking conditions, characterized by a semi-infinite charge-transfer resistance, the NCM working electrode is cycled to the fully discharged state (corresponding to ∼5 %SOC due to the irreversible capacity of the NCM materials in the first cycle) at a potential of 2.55 V vs. Li^+/Li, i.e., to full lithiation of the NCM working electrodes, where the working electrode potential was then held for 1 h prior to taking EIS spectra. The long-term cycling procedure is shown exemplarily for a PC-85 working electrode in Fig. 1: it was initiated by an OCV phase of 10 h, during which a PEIS was taken every 1 h (red open circles in Fig. 1). Then, in order to determine the electrode capacitance for the *pristine* NCM, the NCM working electrode was discharged to the lower cutoff potential of 2.55 V vs. Li^+/Li at a specific current of 18.4 mA/g_{NCM} for PC-60 and 21.4 mA/g_{NCM} for PC-85 and SC-85 (both corresponding to ∼C/10 when referenced to the specific capacity obtained for an upper cathode potential of 4.2 V vs. Li^+/Li) in CC mode (orange line in Fig. 1), where a constant voltage (CV) hold of 1 h was performed, followed by a PEIS. During *conditioning* (black line in Fig. 1), the electrodes were charged at C/10 in CC mode for 1 h, then discharged to the lower cutoff potential of 2.55 V vs. Li^+/Li at C/10 in CC mode, where a CV hold of 1 h was performed, followed by a PEIS (marked by the #0 point in Figs. 1 and 4). Since nickel-rich CAMs are commonly slightly overlithiated (by up to 1 %) in the synthesis process, the conditioning step was included in the procedure to ensure comparable impedance spectra for each cycle, namely by assuring that similar SOCs are obtained by the potential hold of 1 h at 2.55 V vs. Li^+/Li, especially when comparing different NCM active materials.

For the subsequent *cycling* (blue lines in Fig. 1), three charge/discharge cycles were executed, with a charge to the initial upper
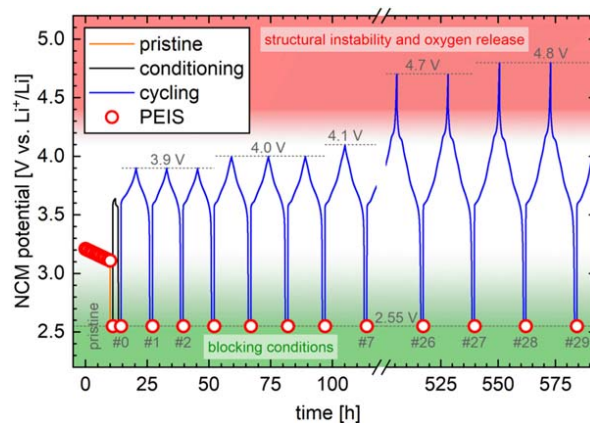
Figure 1. Cycling procedure shown exemplarily for a PC-85 working electrode in a pseudo full-cell with a pre-lithiated, capacitively oversized LTO counter electrode and a gold-wire reference electrode, whereby all potentials are shown vs. Li^+/Li, based on a potential of 1.55 V vs. Li^+/Li of the LTO counter electrode (analogous procedures were used for PC-60 and SC-85 working electrodes). The long-term cycling procedure consists of an initial OCV phase of 10 h, the discharge to blocking conditions of the pristine electrode (orange line), a conditioning step (black line), and the cycling to an upper cutoff potential which increases every three cycles from initially 3.9 V to 5.0 V vs. Li^+/Li (blue line), with the intermittent acquisition of EIS spectra (red circles) under blocking conditions at the points marked with #0, #1, etc.

cutoff potential of the NCM electrode of 3.9 V vs. Li^+/Li at C/10 with a CV hold until the current dropped to below 0.1 mA (∼C/20, CCCV mode), and with a discharge to the lower cutoff potential of 2.55 V vs. Li^+/Li at C/10 with a final CV hold of 1 h before a PEIS was recorded (marked by the #1, #2, and #3 points in Figs. 1 and 4). This set of three cycles was then repeated while increasing the upper cutoff potential (of the cell and, therefore, for the NCM electrode) by 100 mV for each set after every third cycle, finishing with three cycles to 5.0 V vs. Li^+/Li (corresponding to cycle #34, #35, and #36). The impedance spectra taken in blocking conditions are numbered by the full cycles the cell had performed up to that point (e.g., #6 after the three cycles to 4.0 V vs. Li^+/Li). For the surface area determination by Kr-BET, additional cells with PC-85 electrodes were stopped after cycle #9 and cycle #30, corresponding to charge/discharge cycling up to 4.1 V and 4.8 V vs. Li^+/Li, respectively.

To allow for the assignment of the applied potential to a state of charge (or degree of delithiation) for each of the three NCMs, the NCM electrodes assembled in half-cells were charged against the potential of a metallic lithium reference electrode in constant-current mode (CC) to 5.0 V vs. Li^+/Li at a specific current of 18.4 mA/g_{NCM} (corresponding to a C-rate of C/15 when referenced to the theoretical capacities of 276.5 mAh/g_{NCM} for PC-60 and of 275.0 mAh/g_{NCM} for PC-85 and SC-85), using a battery cycler (Series 4000, Maccor, USA).

Cell disassembly.—After cycling, the electrodes were harvested from the pseudo full-cells under inert atmosphere to determine their specific surface area by Kr-BET. Any residue of the conductive salt was removed from the electrodes in a three-step sequential washing procedure: first, they were washed for 5 min in 5 ml EC:EMC 3:7 w/w (Gelon Lib, China), followed by a soaking step of 24 h in 1 ml DMC (anhydrous, ≥99 %, Sigma Aldrich, USA) and, finally, a washing step of 5 min in 5 ml DMC.

Surface area analysis.—The surface area of the NCM powders as well as of the pristine and of the harvested and washed PC-85 electrodes was determined by krypton gas physisorption measurements at 77 K, as previously presented by Friedrich et al. and Oswald et al.,[14,21] measuring at 13 points between
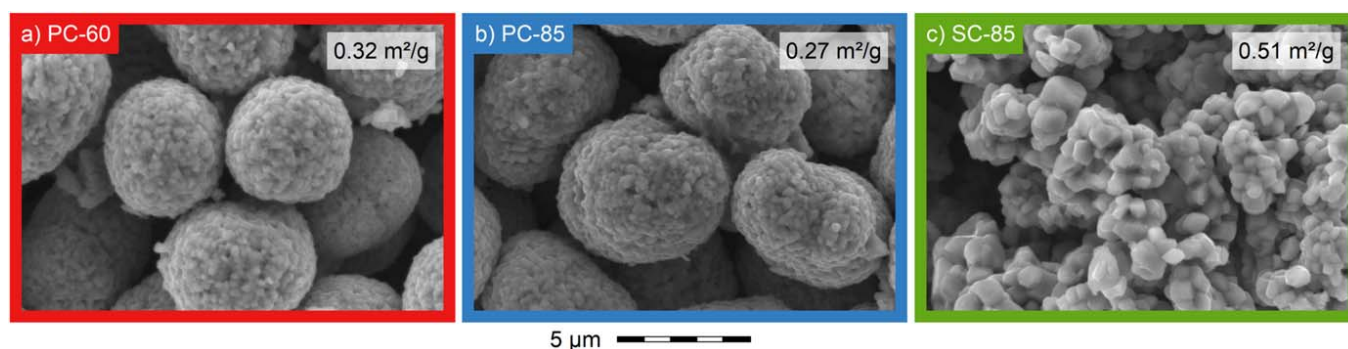
Figure 2. Visual investigation of the particle morphology of the three pristine NCM powders by top-view SEM in secondary electron mode at 15 kV. **a)** Polycrystalline NCM622 (PC-60). **b)** Polycrystalline NCM851005 (PC-85). **c)** Single-crystalline NCM851005 (SC-85). The specific surface area obtained by Kr-BET is displayed for each material in the respective panel.

$0.01 \leqslant p/p_0 \leqslant 0.30$, using an autosorb iQ (Quantachrome Instruments, USA). Comparative N_2-BET measurements for the pristine materials (VGCF and NCM powders) are within ±10 % of the specific surface areas obtained by krypton physisorption (also referred to as Kr-BET). The advantage of the measurement with krypton is a superior sensitivity of this method, since only ca. 1/100th of the total surface area is required for the physisorption measurements, so that Kr-BET areas can be obtained electrodes with a diameter of 11 mm, whereby an approximately 100-fold larger electrode area would be required for meaningful N_2-BET measurements. Prior to Kr-BET measurements, both powder samples as well as samples of pristine or harvested and washed electrodes were dried at 120 °C under vacuum for 6 h.

Results and Discussion

Visual investigation of pristine NCM powders.—To be able to understand and interpret the results of their later electrochemical characterization, at first, the morphology of the three NCM cathode active material (CAM) powders is examined, based on the representative SEM pictures depicted in Fig. 2. The polycrystalline (PC) NCM622 powder (PC-60, labeled in red color), as shown in Fig. 2a, consists of spherical secondary agglomerates (∼5–10 μm in diameter, obtained by a visual investigation) with a relatively narrow particle size distribution (as one would expect for CAM powders synthesized in a batch process). The secondary particles themselves are comprised of numerous primary crystallites (∼0.1–0.5 μm). As shown in Fig. 2b, the polycrystalline NCM851005 powder (PC-85, labeled in blue color), which has an increased nickel content of 85 % as compared to PC-60 with 60 %, has a similar particle morphology. In contrast to the polycrystalline materials, the single-crystalline NCM851005 (SC-85, labeled in green color), shown in Fig. 2c, has the same transition metal composition as PC-85 but consists of much larger primary crystallites (∼0.5–2.0 μm), which are randomly agglomerated or sintered, without having a well-defined secondary structure as compared to the polycrystalline CAMs.

Upon (de)lithiation, the NCM materials experience a significant unit cell volume change,[7,22] what results in stress and strain throughout the secondary particles, leading to cracking of the agglomerates and a surface area increase of the NCM particles.[21] Since the absolute strain would be larger for bigger particles, one could expect different behavior of smaller and larger particles contributing to the measured surface area increase during the electrochemical investigation. However, due to the relatively narrow secondary particle size distribution of the two PC materials as well as due to the similar particle size and, therefore, specific surface area, any possible influence of different particle sizes on the evolution of the morphology of the materials can be excluded. Furthermore, as the ink preparation did not include any harsh mixing procedures like ball-milling (a planetary mixer was used here), and as the electrodes were not compressed or calendered, the particle morphology of the powders was not altered during the electrode

preparation. For these reasons, a comparison of the two polycrystalline NCMs (PC-60 and PC-85) allows to examine the effect of the composition (i.e., the transition metal ratio and the nickel content) on the gas evolution and the increase in surface area. In contrast, the investigation of the polycrystalline and single-crystalline nickel-rich materials that have the same composition (PC-85 and SC-85) allows to elucidate the effect of NCM particle morphology on the surface area increase upon cycling and on the associated gas evolution. Additionally, a comparison of these two materials should make it possible to discriminate between the particle cracking of the primary and of the secondary NCM particles, as SC-85 consists only of primary crystallites without a well-defined secondary structure, so that a surface area increase would only occur upon cracking of the primary particles.

Oxygen release at high state of charge.—As morphological changes of NCM particles cannot only be caused through the repeated unit cell volume change upon long-term charge/discharge cycling (see part I of this study[21]), but may also be caused by the release of lattice oxygen at high state of charge[3] (SOC, note that the SOC is defined in this work as the degree of delithiation x in $Li_{1-x}MO_2$), we next investigate the onset and the amount of O_2 and CO_2 gas evolution of the three NCMs by on-line electrochemical mass spectrometry (OEMS) as a function of the degree of delithiation (note that the evolution of CO was below 1 $\mu mol_{CO}/g_{NCM}$ and will thus not be discussed here). In Fig. 3a, the potential profiles of the first charge of the three NCMs to 5.0 V vs. Li^+/Li in an OEMS cell are depicted as a function of time and SOC, respectively. The voltage curve of PC-60 (red) appears above the ones of the nickel-rich equivalents PC-85 (blue) and SC-85 (green); therefore, more capacity is extracted at the same potential for the nickel-rich materials—or, in other words, a lower cutoff potential is required to reach the same SOC. Since PC-85 and SC-85 have the same composition, the voltage profiles are essentially identical, especially in the range between 50 %SOC and 90 %SOC, which is relevant for this work. As the nickel content of PC-85 and SC-85 comes relatively close to the one of a pure layered lithium nickel oxide (LNO, $LiNiO_2$), a first evidence of a plateau at 4.2 V vs. Li^+/Li of the potential curve can be seen, indicating the H2-H3 phase transition,[5–7] which is reported to be the cause for the release of lattice oxygen.[3]

The onset and the amount of molecular oxygen (O_2) released from the NCM (quantified via mass spectrometry by the mass-over-charge ratio $m/z = 32$) is analyzed from Fig. 3b. Upon charging of the NCMs, the oxygen levels remain zero up to ∼80 %SOC, at which point all three materials start to evolve oxygen almost independently of nickel content, as stated by Jung et al. in previous reports.[3,9] The onset of the oxygen evolution for PC-60 seems to be shifted to lower SOCs by ∼5–10 %SOC as compared to PC-85 and SC-85; this observation will be subject of future studies. Nevertheless, most of the oxygen is released above ∼80 %SOC
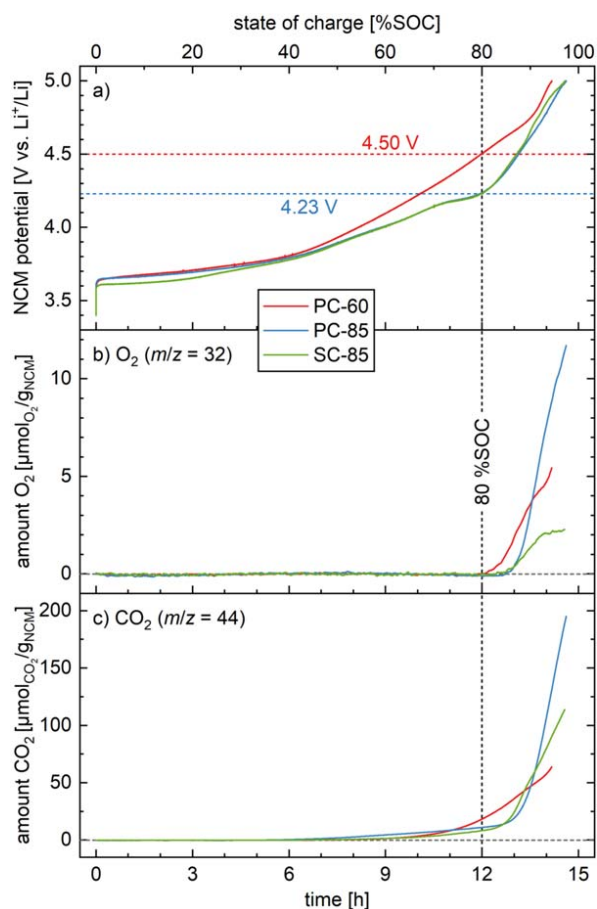
Figure 3. Electrochemical data and gas evolution of OEMS cells assembled with PC-60 (red), PC-85 (blue), and SC-85 (green) as working electrodes, using delithiated, capacitively oversized LFP as counter electrode, two Celgard H2013 separators, and 100 μl LP57 electrolyte. The cells were charged at 25 °C to 5.0 V vs. Li^+/Li (corresponding to a cell voltage of 1.6 V) in constant current mode at 18.4 mA/g_{NCM} (corresponding to C/15 when referenced to ∼275 mAh/g_{NCM}) while the gas evolution was recorded by mass spectrometry. All data are shown as a function of both time (lower x-axis) and state of charge (referenced to ∼275 mAh/g_{NCM}; upper x-axis). **a)** NCM potential vs. Li^+/Li (calculated from the cell voltage and the potential of 3.40 V vs. Li^+/Li for LFP during the end of its lithiation). **b)** and **c)** Total amounts of evolved oxygen (O_2, mass-over-charge ratio $m/z = 32$) and carbon dioxide (CO_2, $m/z = 44$) in the OEMS cell, respectively, which were normalized to the NCM mass. The horizontal dashed lines mark the potential at which 80 %SOC are reached for PC-60 (red) as well as for PC-85 and SC-85 (blue).

for the two different NCM compositions, corresponding to 4.50 V vs. Li^+/Li for PC-60 and 4.23 V vs. Li^+/Li for PC-85 and SC-85. For PC-85 and SC-85, the value of ∼80 %SOC nicely coincides with the end of the plateau at 4.2 V vs. Li^+/Li (see intersection of the horizontal green and blue lines with the vertical dashed black line in Fig. 3a), at which point the H2-H3 phase change is completed. The amount of detected oxygen rises with increasing degree of delithiation, which indicates an increasing destabilization of the layered oxide lattice structure, causing the transformation to the oxygen-depleted surface structure. At 5.0 V vs. Li^+/Li, corresponding to ∼100 %SOC ideally, the total amount of oxygen from PC-60 in this experiment amounts to 5.4 μmol$_{O_2}$/g_{NCM}, which is approximately half the amount as compared to the value for PC-85 with 11.7 μmol$_{O_2}$/g_{NCM} and approximately twice as much as compared to SC-85 with 2.5 μmol$_{O_2}$/g_{NCM}. Even though the evolution of oxygen almost vanishes before the upper potential limit at ∼4.8 V for the single-crystalline material (see green line in Fig. 3b), it must be noted that the release of lattice oxygen does not seem to be

completed yet as the increase of CO_2 continues for all three NCM materials.

Due to the reaction of the (singlet) oxygen released from the NCM lattice with the electrolyte, a large fraction of it is detected as carbon dioxide (CO_2, $m/z = 44$), what is depicted in Fig. 3c. The CO_2 signal of the three NCMs remains zero until ∼40 %SOC, corresponding to ∼3.8 V vs. Li^+/Li for all three NCMs. This potential is sufficiently high to initiate the electrochemical oxidation of alcohols such as ethylene glycol or ethanol[8,34] and other unwanted trace impurities remaining in the electrolyte from the synthesis of the carbonate-based solvents. One product of this process are protons (H^+) which chemically decompose lithium carbonate (Li_2CO_3) that remains on the NCM particles (from the lithium excess typical for the synthesis of the active material), resulting in the formation of lithium ions, water, and carbon dioxide.[34] Furthermore, the produced water in the electrolyte reacts with the conducting salt $LiPF_6$, which again generates protons,[35] resulting in an autocatalytic cycle decomposing Li_2CO_3 and evolving CO_2.[34] Therefore, we believe that the CO_2 detected above ∼3.8 V vs. Li^+/Li and prior to the onset potential for oxygen evolution predominantly stems from the electrochemical oxidation of electrolyte impurities and the chemical decomposition of Li_2CO_3. Up to ∼80 %SOC (corresponding to 12 h in the experiment), 18.6 μmol$_{CO_2}$/g_{NCM} of CO_2 were detected for PC-60, 11.2 μmol$_{CO_2}$/g_{NCM} for PC-85, and 8.5 μmol$_{CO_2}$/g_{NCM} for SC-85. Assuming that these amounts of CO_2 would indeed be due to the decomposition of Li_2CO_3, this would require a minimum Li_2CO_3 impurity level of the NCMs ranging between 0.06–0.14 wt%, which is within typical values.

At ∼80 %SOC, a sharply increasing slope of the CO_2 signals of PC-85 and SC-85 (corresponding to a change in CO_2 production rate) is observed. This SOC coincides with the O_2 release from the NCM lattice in the near-surface region of the NCM particles, which is why we assign most of the released CO_2 above ∼80 %SOC to the chemical oxidation of electrolyte.[8] At the end of charge, 64 μmol$_{CO_2}$/g_{NCM} of CO_2 were detected for PC-60, 195 μmol$_{CO_2}$/g_{NCM} for PC-85, and 114 μmol$_{CO_2}$/g_{NCM} for SC-85. The cause for the differing gas amount of the three NCMs will be discussed in a later section, where we estimate the thickness of the oxygen-depleted surface layer.

In summary, the release of reactive lattice oxygen from the surface-near regions of the NCM particles accompanied by a CO_2 evolution is almost independent of nickel content and occurs at an SOC of ∼80 %; at this SOC, however, the NCM cathode potential is lower for a nickel-rich NCM.

Charge/discharge cycling with increasing upper cutoff potential.—In the following, the effect of the state of charge (SOC) on the discharge capacity and on the morphology of the NCM active materials is investigated. For this, the upper cutoff potential of the NCM working electrode is increased stepwise by 0.1 V every third cycle, inducing structural and morphological changes which are illuminated through the measurement of the electrode capacitance in the discharged state (i.e., under blocking conditions). Aiming to track the behavior of fully intact NCM particles, electrodes that were not compressed or calendered were cycled, as the mechanical compression could lead to the partial breakage of the secondary agglomerates already before the measurement.[21] To ensure electronic connection throughout the entire electrode even without compression or calendering, vapor-grown carbon fibers with a length of 15 μm were used as conductive additive.

The specific discharge capacity of all three NCMs, depicted in Fig. 4a, increases after each set of three cycles, i.e., with each increase in the upper cutoff potential of the NCM working electrode. For lower cutoff potentials, the delivered capacity is higher for the nickel-rich materials PC-85 and SC-85 as compared to PC-60, consistent with the NCM charge curves shown in Fig. 3a and in Fig. A·2. When cycling to upper cutoff potentials that are below the onset of lattice oxygen release at ∼80 %SOC (marked by a vertical
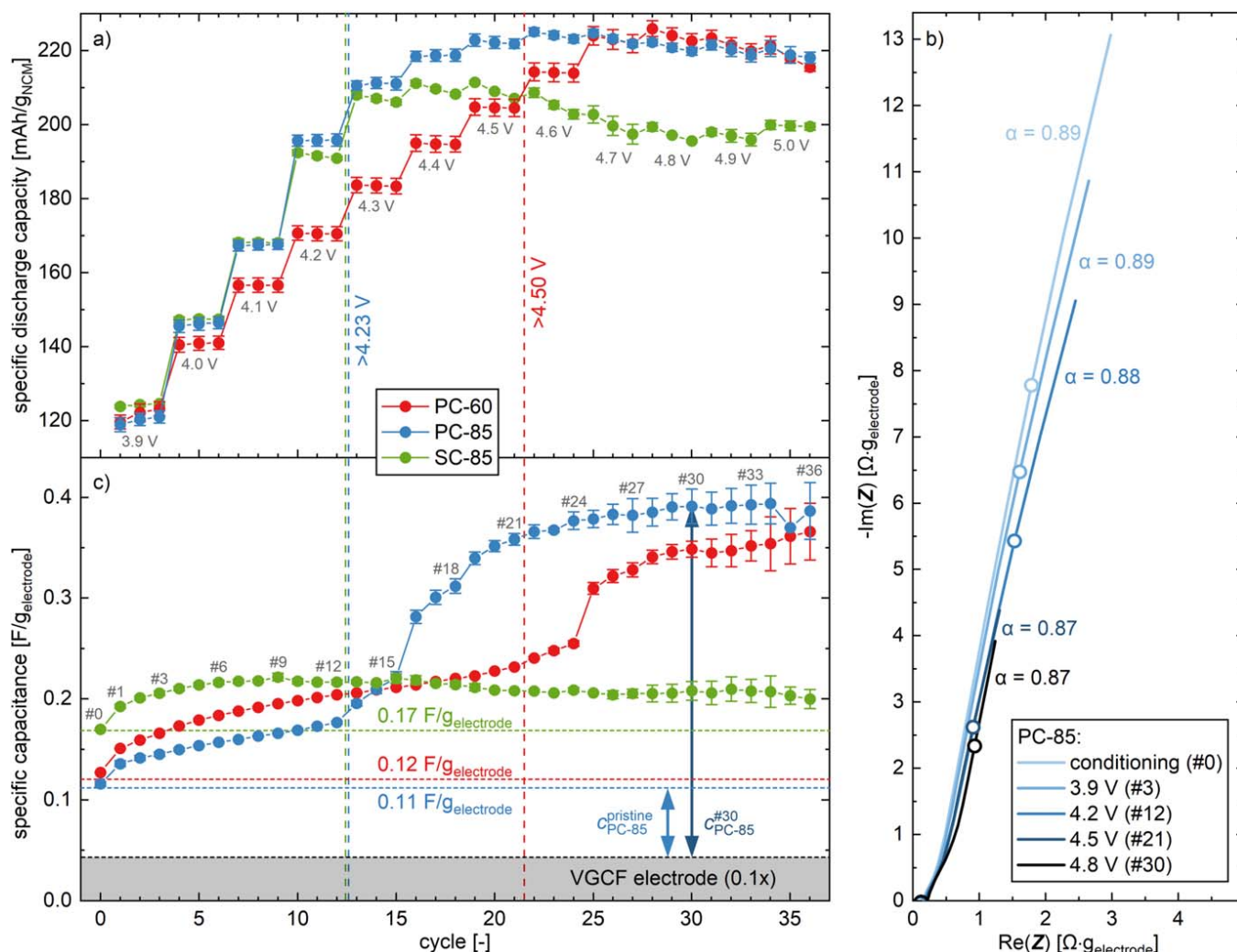
Figure 4. Electrochemical cycling data of PC-60 (red), PC-85 (blue), and SC-85 (green) as working electrodes in pseudo full-cells with a μ-RE (i.e., a GWRE), using pre-lithiated, capacitively oversized LTO as the counter electrode, two glass fiber separators and 60 μl LP57 electrolyte. Following the procedure depicted in Fig. 1, the cells were cycled at 25 °C to a selected upper cutoff potential of the NCM electrode that was increased every three cycles by 0.1 V starting at 3.9 V vs. Li^+/Li. The current applied for cell cycling was 18.4 mA/g_{NCM} for PC-60 and 21.4 mA/g_{NCM} for PC-85 and SC-85 (this corresponds to C/10 when referenced to the specific capacity obtained for an upper cathode potential of 4.2 V vs. Li^+/Li). Impedance spectra of the NCM working electrodes were recorded in blocking conditions after a potential hold of 1 h at 2.55 V vs. Li^+/Li (15 mV amplitude, from 100 kHz to 100 mHz). The vertical dashed lines mark the cycle at which ∼80 %SOC (extracted from Fig. 3) are exceeded for each of the three NCMs (4.50 V for PC-60, and 4.23 V for PC-85 and SC-85), marking the onset of the release of lattice oxygen. The specific capacitance and the specific discharge values are calculated from the mean of two nominally identical cells, with the error bars corresponding to the minimum/maximum values. **a)** Specific discharge capacity for the respective upper cutoff potential normalized to the NCM mass as a function of cycle number. **b)** Selected impedance spectra in blocking conditions of the PC-85 working electrode after the conditioning cycle (referred to as #0), after the three cycles to 3.9 V (referred to as #3), 4.2 V (#12), 4.5 V (#21), and 4.8 V (#30) (see also Fig. 1), while the respective frequency points at 180 mHz are indicated by empty circles. **c)** Specific capacitance of the NCM working electrode extracted from the imaginary impedance at 180 mHz in blocking conditions as a function of cycle number. The horizontal dashed lines indicate the pristine capacitance value of each of the three NCM working electrodes before the conditioning step (#0). The gray area marks the specific capacitance of the VGCF electrode multiplied by 0.1.

dashed line for each material), the discharge capacity stays constant during each set of three cycles. As the upper cutoff potential exceeds the onset potential for lattice oxygen release by more than ∼0.1 V, the discharge capacity starts to fade within each set of three consecutive cycles. For PC-60 (red symbols), the discharge capacity at 4.7 V decreases by 2 mAh/g_{NCM} in the course of three cycles (see cycle #25 to #27) and by 4 mAh/g_{NCM} at 4.8 V (see cycle #28 to #30). A similar capacity fading behavior is observed for PC-85 (blue symbols) and SC-85 (green symbols), but already starting at ∼4.2 V. Additionally, the discharge capacity fading of the SC-85 material within each set of three cycles decreases significantly above ∼4.2 V, namely by 2 mAh/g_{NCM} at 4.3 V (from cycle #13 to #15) and by 4 mAh/g_{NCM} at 4.5 V (from cycle #19 to #21), while no such fading is observed for these potentials for the PC-85 material. Overall, independent of the upper cutoff potential, the discharge capacity of the polycrystalline NCMs does not exceed 225 mAh/g_{NCM}

(or 211 mAh/g_{NCM} for the single-crystalline NCM), corresponding to ∼82 %SOC. Taking into account the initial irreversible capacity of these NCMs of ∼12 mAh/g_{NCM} or ∼5 %SOC (for all NCMs in cycle #0), the structural instability of the NCMs apparently limits the accessible SOC to ∼87 %SOC for the polycrystalline NCMs (or ∼81 %SOC for the single-crystalline NCM). The impact of the compositions and morphologies of the three NCMs on the here observed onset of the capacity fading as well as on the differences in (maximum) discharge capacity will be further examined when discussing Fig. 6.

To track the effect of a high SOC on the morphological stability of the three NCMs, the electrode capacitance was measured in situ from the recorded impedance spectra as a function of the upper cutoff potential. All spectra of the working electrode were collected via the μ-RE (i.e., the gold-wire reference electrode[33] (GWRE)) after each cycle in the fully discharged state at an NCM potential of

2.55 V vs. Li$^+$/Li. As the charge transfer of NCMs is impeded in the fully discharged/lithiated state, resulting in a semi-infinite value of the charge-transfer resistance (so-called *blocking conditions*), the impedance is dominated by the capacitive contribution of the electrochemical double layer at the electrode/electrolyte interface.[21,36] Assuming that the surface-area-normalized capacitance is distinct, constant, and uniformly distributed for each of the electrode components (i.e., the active material and the conductive carbon), the capacitance contribution of each of the electrode materials would be proportional to their respective surface area, an assumption that was proven by Kr-BET in part I of this study.[21] There, we had also shown that the electrode capacitance does not necessarily have to be extracted from a fit of the entire impedance spectrum, but that the impedance of the individual frequency point at 180 mHz is sufficient to accurately determine the electrode capacitance (see below).[21] For more details about the developed method and the applied analysis, please refer to the original publication.

Prior to charge/discharge cycling, it was verified that the impedance spectra of the NCM working electrodes are stable over time during the initial OCV phase of 10 h (data not shown), so that any time-dependent effects on the impedance can be excluded. Figure 4b shows five selected impedance spectra of the same PC-85 working electrode after the conditioning cycle (referred to as #0), and after the 3rd cycle at the here selected upper cutoff potentials of 3.9 V, 4.2 V, 4.5 V, and 4.8 V (referred to as #3, #12, #21, and #30, respectively). First, it is observed that blocking conditions are achieved in all instances upon the full lithiation of the NCM particles through a potential hold of 1 h at 2.55 V vs. Li$^+$/Li. The very small semicircle at high frequencies (see Fig. 4b) is due to a contact resistance at the interface between the NCM electrode and the aluminum current collector, as shown previously for uncompressed LFP,[33,37] LiNi$_{0.5}$Mn$_{1.5}$O$_4$,[38] and NCM622[21] electrodes. Similar to part I of this study, where we investigated the impedance of NCM622 electrodes under blocking conditions, the phase angle (extracted from an *R-Q* fit of the frequency points between 0.1 Hz and 1 Hz) of $\alpha = 0.89$ for the conditioned PC-85 electrode (see spectrum #0 in Fig. 4b) only decreases negligibly to 0.87 after the third cycle at 4.8 V (cycle #30). As the phase angle does not decrease below $\alpha = 0.85$ even at 5.0 V (data not shown), the theoretical considerations discussed in part I of this study still apply, and the electrode capacitance can be extracted from the impedance at 180 mHz with an error of less than ±1 % as compared to the value extracted from the fit.[21]

As shown in Fig. 4b, the length of the capacitive branch decreases considerably with increasing cycle number (and, therefore, with increasing upper cutoff potential), also illustrated by the decreasing value of the imaginary impedance at 180 mHz (marked by the empty circles), which decreases from 7.8 $\Omega \cdot g_{electrode}$ for the conditioned PC-85 electrode (see cycle #0) to values of 6.5 $\Omega \cdot g_{electrode}$ after 3.9 V (#3), 5.4 $\Omega \cdot g_{electrode}$ after 4.2 V (#12), 2.6 $\Omega \cdot g_{electrode}$ after 4.5 V (#21), and to 2.3 $\Omega \cdot g_{electrode}$ after 4.8 V (#30). As the imaginary impedance is inversely proportional to the capacitance of a purely capacitive circuit element, its decreasing contribution corresponds here to an increasing value of the capacitance. Quantitatively, the electrode capacitance is obtained from the imaginary part of the electrode impedance $\mathbf{Z}_{\omega_0}$ at the selected frequency of $f_0 = 180$ mHz (with $\omega_0 = 2 \cdot \pi \cdot f_0$) using Eq. 1, previously derived in part I of this study[21]:

$$Q \approx \frac{1}{\omega_0 \cdot (-\mathrm{Im}(\mathbf{Z}_{\omega_0}))} \qquad [1]$$

The thus obtained capacitance values can then be normalized by the electrode mass and are depicted in units of F/g$_{electrode}$ in Fig. 4c. The pristine capacitance (shown as horizontal dashed line) is found to be 0.12 F/g$_{electrode}$ for PC-60, 0.11 F/g$_{electrode}$ for PC-85, and 0.17 F/g$_{electrode}$ for SC-85, and is essentially identical with the values

obtained for the conditioned electrode (data points at cycle #0). Contained in these electrode capacitance values is the capacitance contribution from the conductive carbon and the binder (here referred to as inert components), which was identified to be 0.43 ± 0.01 F/g$_{electrode}$ for an electrode containing exclusively VGCF and PVDF (4:1 w/w).[21] As only 10 wt% of the NCM electrode consist of VGCF and PVDF, the contribution of the inert components to the NCM electrode capacitance is thus 0.043 ± 0.001 F/g$_{electrode}$ and is marked by the gray area in Fig. 4c. By subtracting this contribution of the inert components from the NCM electrode capacitance, the capacitance of the NCM only can be obtained. Exemplarily for the PC-60 working electrode, the NCM capacitance equates to 0.07 F$_{NCM}$/g$_{electrode}$, corresponding to 0.08 F$_{NCM}$/g$_{NCM}$, considering that the NCM content in the electrode is 90 wt% ($m_{NCM} = 0.9 \cdot m_{electrode}$). Analogously, values of 0.09 F$_{NCM}$/g$_{NCM}$ and 0.14 F$_{NCM}$/g$_{NCM}$ are obtained for PC-85 and SC-85, respectively.

By dividing the thus determined NCM capacitances by the specific surface areas (S_{BET}) of the pristine NCM powders obtained through krypton gas physisorption measurements (in the following referred to as Kr-BET), the surface-area-normalized NCM capacitances equate to 27 μF$_{NCM}$/cm$^2_{NCM}$ for PC-60, 29 μF$_{NCM}$/cm$^2_{NCM}$ for PC-85, and 28 μF$_{NCM}$/cm$^2_{NCM}$ for SC-85. By the same approach, a surface-area-normalized capacitance of 4.4 μF$_{VGCF}$/cm$^2_{VGCF}$ was determined for VGCF (12.4 m^2/g). Even though the NCMs show a six-fold higher areal capacitance as compared to VGCF, the results are in agreement with literature data for aqueous systems: for carbon, a typical electrode material in supercapacitors, the surface-area-normalized capacitance has been reported to be $\sim$2–10 μF/cm^2,[39–41] while the values for metals and metals oxides are typically $\sim$15–60 μF/cm^2.[42–46] For a Ni/NiO-based system, being rather similar in composition to the here used nickel-rich NCMs, Liu et al. found a surface-area-normalized capacitance of $\sim$25 μF/cm^2.[43] Even though the reported values for the double-layer capacitance were measured in aqueous systems only, they are similar to the ones we have measured here in the LP57 electrolyte, likely due to similar values of the dielectric constant of water ($\varepsilon_r \approx 80$) and the here used carbonate-based solvents ($\varepsilon_r \approx 65$–95).[47] As it is assumed that the determined values of $\sim$28 μF$_{NCM}$/cm$^2_{NCM}$ and 4.4 μF$_{VGCF}$/cm$^2_{VGCF}$ remain constant during the course of the experiment, this correlation allows for the determination of the specific surface area of the CAM powder from the measured electrochemical capacitance.

The evolution of the capacitance of the NCM electrode is depicted in Fig. 4c for the three NCMs as a function of cycle number (and, hence, of upper cutoff potential). After the conditioning step (corresponding to cycle #0), during which $\sim$10 % of the lithium were deintercalated to ensure a similar lithium content for all subsequent impedance measurements in blocking conditions, the capacitance of the three NCMs is insignificantly higher (<6 %) as for the pristine electrodes. During the first nine full cycles (cycle #1 to #9) to relatively low upper cutoff potentials ($\leqslant 4.1$ V vs. Li$^+$/Li), the electrode capacitance then increases continuously, what we assign to the repeated unit cell volume change of the NCM materials upon (de)lithiation.[7,21,22] As the crystal planes of the numerous primary crystallites are oriented arbitrarily, and as the change of the lattice parameters *a* and *c* is anisotropic, the repeated (de)lithiation induces stress and strain in the agglomerates, leading to crack formation primarily between the primary crystallites of the polycrystalline materials. The penetration of the electrolyte into the cracks is then accompanied by an increase in the NCM/electrolyte interface, which leads to the observed capacitance increase. This is observed even for the single-crystalline material that has no hierarchical secondary agglomerates, so that it is likely due to the (partial) separation of the adhered/sintered primary crystallites. After three cycles to 4.1 V, the capacitance of the PC-60 electrode has increased to 0.20 F/g$_{electrode}$, to 0.17 F/g$_{electrode}$ for PC-85, and to 0.22 F/g$_{electrode}$ for SC-85; when considering only the NCM contribution to the capacitance (i.e., in units of F$_{NCM}$/g$_{NCM}$, shown in Fig. A·1 in the Appendix), the NCM capacitance change between the

pristine electrodes and the electrodes after the third cycle to 4.1 V (cycle #9) is 2.0x for the PC-60, 1.8x for the PC-85, and 1.4x for the SC-85 electrodes.

The capacitance of the single-crystalline material remains at this value, even when cycled to upper cutoff potentials of 5.0 V (cycle #9 to #36 of the green curve in Figs. 4c and A·1), at which the release of lattice oxygen is known to lead to a reconstruction of the surface-near region into a rock-salt-type structure, implying the morphological stability of the (primary) single-crystalline particles even at a nearly full delithiation. In contrast, the electrode capacitance of the polycrystalline materials is increased abruptly as soon as the upper cutoff potential exceeds the onset of oxygen release (marked by the blue and red dashed vertical lines in Fig. 4c). Most of this increase is completed within nine cycles, corresponding to an additional ~0.3 V above the onset potential of the lattice oxygen release for both polycrystalline materials. For PC-85 (blue curve), the slope of the capacitance curve starts to increase at 4.3 V vs. Li^+/Li (oxygen release at ~4.23 V, see Fig. 3). When cycled to 4.4 V, a sudden jump in the capacitance is observed, which further increases during the subsequent cycles, however, then reaches a stable value of ~0.40 $F/g_{electrode}$ during the final nine cycles (cycle #30 in Fig. 4c). A similar behavior is observed for PC-60 (red curve), however, occurring at a higher cycle number: the change in electrode capacitance increases at a potential of ~4.5 V (oxygen release at ~4.50 V, see Fig. 3) and an abrupt increase is observed subsequently when cycling to 4.7 V. During the final nine cycles, the capacitance of PC-60 stabilizes at a value of ~0.35 $F/g_{electrode}$. The quantitative analysis of the NCM capacitance in contrast to the here examined electrode capacitance will be performed later when discussing Fig. 6 and Table I.

Validation of the surface area increase by Kr-BET.—To confirm that the shown increase in capacitance of the NCM electrodes induced by the increase of the upper cutoff potential is in fact corresponding to an increase of the specific surface area of the electrode, the Kr-BET surface area (hatched bars in Fig. 5, plotted vs. the right y-axis) is determined for PC-85 electrodes in the pristine state, for those cycled to 4.1 V vs. Li^+/Li, and for those cycled to 4.8 V; these are then compared to the electrode capacitance (solid bars, plotted vs. the left y-axis) at the respective point in the cycling procedure (extracted from Fig. 4c: pristine value from horizontal dashed line, #9 for 4.1 V, and #30 for 4.8 V). For this comparison, it is assumed that the contribution of VGCF and PVDF (black bars) remains constant during the experiment. This assumption is reflected in Fig. 5 by scaling the y-axes for the capacitance (left y-axis) and for the specific surface area (right y-axis) such that all values for the VGCF electrodes are at the same position for both y-axes. To obtain the contribution of the NCM only (blue bars in Fig. 5), 1/10th of the determined values for specific capacitance and the specific surface area of the electrode containing VGCF and PVDF only (i.e., 0.1x of 0.43 $F/g_{electrode}$ and 0.1x of 7.8 $m^2/g_{electrode}$) is subtracted from the respective values obtained for the NCM electrodes, as they comprise 10 wt% of VGCF and PVDF. It is obvious that the relative contribution of NCM differs depending on the used method: for the pristine electrodes, the NCM capacitance of 0.07 $F/g_{electrode}$ contributes 61 % to the total electrode capacitance of 0.11 $F/g_{electrode}$ (see left solid bars), whereas the NCM surface area of 0.22 $m^2/g_{electrode}$ contributes only 22 % to the total electrode surface area of 1.00 $m^2/g_{electrode}$ (see left cross-hatched bars). Therefore, the contribution of the NCM to the total electrode capacitance, as depicted in Fig. 5, is six times larger than its contribution to the electrode specific surface area. This is explained by the ~6-fold higher surface-area-normalized capacitance of NCM (28 $\mu F_{NCM}/cm^2_{NCM}$) as compared to VGCF (4.4 $\mu F_{VGCF}/cm^2_{VGCF}$), as already discussed in the previous section (listed also in the 5th row of Table I), whereas the ratio of the surface area determined by Kr-BET corresponds to the actual physical surface area, independent of the type
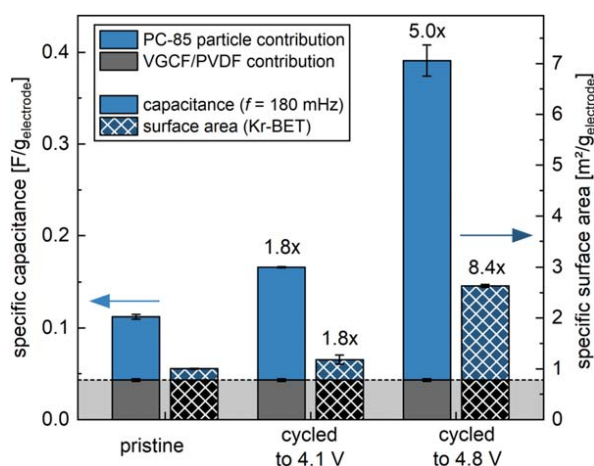

Figure 5. Comparison of the effect of the upper cutoff potential on the capacitance and on the Kr-BET surface area of discharged PC-85 electrodes: specific capacitance (left axis, extracted from the blue data in Fig. 4c) of pristine electrodes (corresponding to the blue horizontal dashed line and blue arrow in Fig. 4c, left-hand set of bars), after three cycles to 4.1 V vs. Li^+/Li (after a total of nine cycles, middle set of bars), and after three cycles to 4.8 V vs. Li^+/Li (after a total of 30 cycles, corresponding to the dark blue arrow in Fig. 4c, right-hand set of bars), which were obtained by using the imaginary impedance at 180 mHz according to Eq. 1 (solid bars). Specific surface area (right axis) of pristine and cycled PC-85 electrodes (cross-hatched bars) measured by Kr-BET. The contributions to capacitance and specific surface area by the PC-85 particles are colored in blue and were obtained by subtracting the weight-fraction-normalized contributions from the VGCF electrodes (colored in black). The left (capacitance) and right axis (surface area) are scaled such that the values for the VGCF electrodes are at the same position for both axes. All values are calculated from the mean of two nominally identical cells (capacitance) or two nominally identical electrodes (Kr-BET), and the error bars correspond to the minimum/maximum values. The numbers above the bars mark the increase of the NCM contributions to the electrode capacitance and specific surface area compared to the ones of the pristine electrodes.

of material. Even though the areal capacitance differs between the two electrode components, the relative increase of the contribution of the NCM only can be compared for each of the two properties.

Upon cycling, the NCM capacitance contribution to the electrode (blue solid bars) increases from 0.07 $F/g_{electrode}$ in the pristine state to 0.12 $F/g_{electrode}$ for the electrodes cycled to 4.1 V, corresponding to a change by a factor of ~1.8x, consistent with the increase of the NCM specific surface area (blue hatched bars) by the same factor, namely from 0.22 $m^2/g_{electrode}$ to 0.40 $m^2/g_{electrode}$. This suggests a direct proportionality between capacitance and specific surface area. When cycling to 4.8 V, the NCM contribution to capacitance and surface area further increases to values of 0.35 $F/g_{electrode}$ and 1.85 $m^2/g_{electrode}$, respectively, corresponding to an increase by a factor of ~5.0x and ~8.4x, respectively, as compared to the pristine state. The at first sight unexpected difference between these two factors in this case could be caused by the different domain sizes measured by the two methods: very small micropores and very thin cracks within the (primary and/or secondary) NCM particles[48–50] induced by the release of lattice oxygen will increase the surface roughness on an atomic scale and will contribute to the Kr-BET surface area (diameter of a krypton atom: ~0.2 nm) but might be too small to be detected by the capacitance measurement (diameter of a solvated lithium ion: ~1.0 nm), as already discussed in part I of this study.[21] The specific surface area of the PC-85 electrode of 1.85 $m^2/g_{electrode}$ after cycling to 4.8 V corresponds to 2.05 m^2/g_{NCM}, which may be compared to the Kr-BET area of an NCM811 material with the same initial BET area and a similar particle morphology, which after a few cycles to 4.5 V vs. Li^+/Li also substantially increased to ~1.8 m^2/g_{NCM}.[16] In addition, the

overestimation of the CAM surface area obtained by Kr-BET could stem from additional surface area contributed by a porous organic surface layer on the positive electrode (often referred to as *cathode-electrolyte interphase* or *CEI*);[51] the formation of such a phase would result from the electrochemical oxidation of the solvents in the electrolyte at high potentials[8] or via chemical electrolyte oxidation by singlet oxygen released at high SOCs[17,18] and, therefore, lead to an overestimation of the Kr-BET surface area of the electrode cycled to 4.8 V.

Summarizing the findings in this section, one can state that electrochemical cycling beyond the limit of oxygen release at high SOCs does increase the NCM specific surface area to greater extent (~8.4-fold at 4.8 V for PC-85) as compared to cycling to lower SOCs (~1.8-fold at 4.1 V for PC-85).

Simultaneity of lattice oxygen release, capacity fading, and surface area increase.—Since it was found by Jung et al. that the onset of the release of lattice oxygen occurs at ~80 %SOC for NCMs with a wide range of nickel content, i.e., that it is largely a function of the degree of delithiation, the analysis of the cycling data as a function of the degree of delithiation x (as in $Li_{1-x}MO_2$, with M = Ni, Co, Mn) or state of charge (in units of %SOC) will provide further insights when examining the correlation between oxygen release, capacity fading, and capacitance increase. By the analysis of the potential curves from NCM half-cells charged to 5.0 V vs. Li^+/Li at the essentially same mass specific current density as those used in Fig. 4 (see Fig. A·2 in the appendix), each one of the applied upper cutoff potentials (i.e., 3.9 V, 4.0 V, …, 5.0 V vs. Li^+/Li) can be assigned to its respective degree of delithiation x, whereby $x = 1$ corresponds to a specific capacity of ~275 mAh/g_{NCM} or to an SOC of 100 %SOC. Thus, Fig. 6a shows the oxygen evolution as a function of the SOC either in units of mAh/g_{NCM} (upper x-axis) or in percent (lower x-axis) with the onset of the lattice oxygen release at ~80 %SOC being marked by the dashed vertical line, whereby the data are taken from Fig. 3a. Figure 6b is based on the specific discharge capacity data shown in Fig. 4a, plotting the value for the third cycle at each upper cutoff potential setpoint as a function of its degree of delithiation x or its SOC that is expected based on the first charge curves shown in Fig. A·2 in the Appendix (note that ideally the difference between the actual discharge capacity and the thus obtained x or SOC value corresponds to the irreversible capacity of the first cycle of the NCM active material). The data of the specific NCM capacitance shown in Fig. 4c were re-plotted analogously in Fig. 6c as a function of SOC.

Below ~85 %SOC, the specific discharge capacity of the three NCMs increases linearly, as depicted in Fig. 6b, corresponding to a linear relation between the charge capacity (x-axis, converted from the upper cutoff potential from the first charge curve) and the discharge capacity (y-axis, measured for each set of three cycles shown in Fig. 4a), indicating a stable cycling performance and, therefore, sufficient integrity of the NCMs in this SOC range. When the SOC exceeds the onset of lattice oxygen release by more than ~5 %SOC, the discharge capacity decreases as compared to the linear behavior observed for upper cutoff potentials that do not lead to delithiation degrees that are higher than ~80 %SOC. As we used pre-lithiated LTO as counter electrode, providing a substantial lithium reservoir, the specific discharge capacity decrease at >80 %SOC cannot be caused by a loss of cyclable lithium in the cell (also confirmed by the potential profile of the LTO counter electrode vs. the reference electrode, which stays on its plateau at 1.55 V vs. Li^+/Li (data not shown)), but instead must be assigned to an NCM material loss and/or a significant overpotential growth of the NCM working electrode. This capacity loss can be explained by the surface reconstruction of the NCM particles into a resistive rock-salt-type surface layer upon the release of lattice oxygen, which according to previous studies with NCM811[14,16] leads to i) a cathode active material loss, as the layered structure is converted into an inactive rock-salt-type phase, and ii) an increase in the cathode impedance, caused by an increased charge-transfer resistance on the
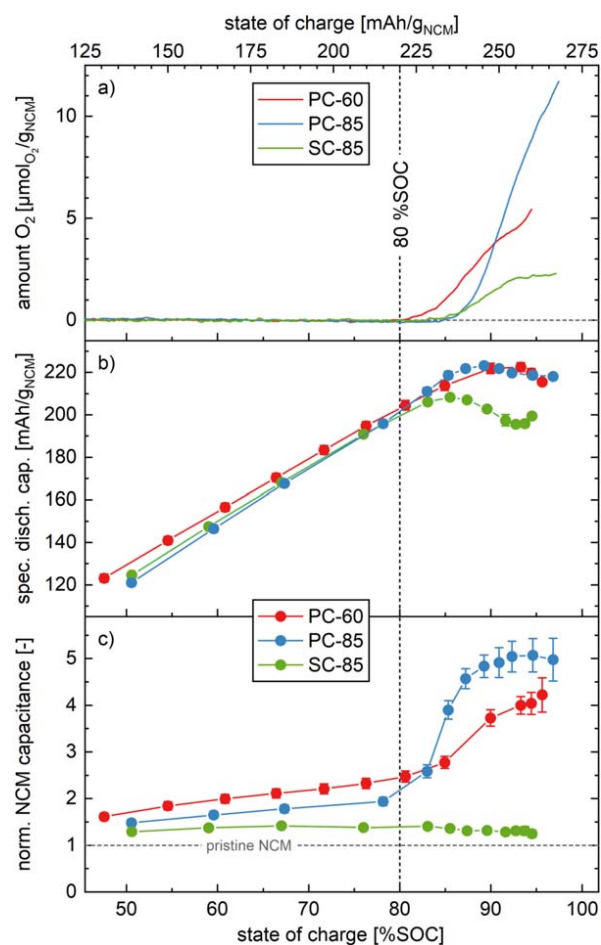

Figure 6. Comparison of the electrochemical characteristics of the three NCMs plotted as a function of SOC (at the top in mAh/g_{NCM}, at the bottom in units of %SOC corresponding to the degree of delithiation x in $Li_{1-x}MO_2$), where the value for ~80 %SOC is marked by the vertical dashed line. The relation between upper cutoff potential of the NCM electrode for the cycling data in Fig. 4 and the SOC was extracted from the potential curves of the first charge of the NCM half-cells charged to 5.0 V vs. Li^+/Li at the essentially identical rate of 18.4 mA/g_{NCM} (see Fig. A·2 in the Appendix). **a)** Amount of oxygen normalized to the NCM mass that is detected during a CC charge at 18.4 mA/g_{NCM} to 5.0 V vs. Li^+/Li (same data as in Fig. 3b). **b)** Specific discharge capacity of the cells cycled to an increasing upper cutoff potential of the NCM electrode. The here plotted data correspond to those obtained in the third cycle of each upper cutoff potential shown in Fig. 4a. **c)** Capacitance contributed by the NCM particles in the NCM electrodes, normalized by their capacitance of the pristine NCM. The here plotted data correspond to those obtained in the third cycle of each upper cutoff cathode potential shown in Fig. 4c, whereby the NCM capacitance contribution to the total electrode capacitance was obtained by subtracting the capacitance contribution of the VGCF electrode (the thus obtained NCM capacitances are normalized by the NCM mass and shown in Fig. A·1 in the Appendix). The error bars are determined by the laws of error propagation (see supporting information of part I of this study),[21] using the average capacitances and their minimum/maximum values given by Fig. 4c.

surface of the primary crystallites, a reduced electronic conductivity through the NCM secondary particles, or a combination of both. Due to these effects, the maximum discharge capacity of the two polycrystalline materials is limited to a value of ~223 mAh/g_{NCM}, which is reached at ~4.8 V vs. Li^+/Li for PC-60 (corresponding to ~93 %SOC, red curve in Fig. 6b) and at ~4.6 V vs. Li^+/Li for PC-85 (corresponding to ~89 %SOC, blue curve). Even though the single-crystalline SC-85 has essentially the same composition as the polycrystalline PC-85, it reaches its maximum discharge capacity already at ~4.4 V vs. Li^+/Li (corresponding to ~85 %SOC, green curve) at a ~15 mAh/g_{NCM} lower specific discharge capacity

($\sim$208 mAh/g_{NCM}), which is attributed to the difference in morphology and will be discussed below in the context of Fig. 7. After the capacity fading of SC-85 starting at $\sim$80 %SOC, a small increase of the discharge capacity is observed above 94 %SOC (or 4.8 V): here, we assume that the oxygen-depleted surface layer is limited in its thickness (and, therefore, in its resistance) due to the sluggish solid-state diffusion of oxygen in the NCM lattice, even though the upper cutoff potential is increased. If the growth of the surface resistance stagnates while the driving force to (de)intercalate lithium ions is increased, the increasing upper cutoff potential results in the extraction of more lithium ions and in the increase the discharge capacity for the cycles to 4.9 V and 5.0 V.

The NCM capacitance depicted in Fig. 6c is obtained by the subtraction of the contribution of the inert components VGCF and PVDF from the electrode capacitance (for details, see Figs. 4c and 5 in the previous sections and Fig. A·1 in the appendix), normalized by its pristine value, and depicted as a function of SOC. In this representation, the NCM capacitance of the two polycrystalline materials increases suddenly when charged to >80 %SOC, simultaneously with the release of lattice oxygen and the levelling-off/drop of the discharge capacity curve in Fig. 6b. Compared to their pristine state, the capacitance of the PC-60 and PC-85 active materials determined at the end of the experiment after cycling to 5.0 V vs. Li$^+$/Li changed by $\sim$4.2x and $\sim$5.0x, respectively, while that of the SC-85 active material changed by $\sim$1.2x only, illustrating the morphological stability of single-crystalline NCMs even at high degrees of delithiation.

For the possible formation of an organic layer on the NCM surface at high potential, as discussed in the previous section on the validation by Kr-BET, no effect is visible of the capacitance measurements of the NCMs: SC-85 shows a stable capacitance (after the formation of a few cycles is completed, see green data in Figs. 4 and 6) up to an upper cutoff potential of 5.0 V vs. Li$^+$/Li, where a significant amount of electrolyte oxidation occurs for the here used organic electrolyte.[8] We believe that it would be a curious coincidence if the effect of hypothetical particle cracking of the single-crystalline NCM (leading to an increase in the capacitance) and the effect of an organic surface layer on the capacitance would cancel each other out perfectly for each measurement point at each upper cutoff potential. Therefore, we believe that there is no impact of a possible CEI formation on the surface-area-normalized capacitance of the NCMs in this experiment.

Under the reasonable assumption that the surface-area-normalized capacitance ($\sim$28 μF_{NCM}/cm$^2_{NCM}$) determined for the pristine materials (see Table I) remains constant, the specific surface area calculated from the capacitance (S_{EIS}) can be estimated for the NCM materials at any point of the procedure. At 5.0 V (cycle #36 in Fig. 4c or in Fig. A·1), the specific surface area $S^{\#36}_{EIS}$ is estimated to be $\sim$1.3 m^2/g_{NCM} for both polycrystalline materials (PC-60 and PC-85), whereas it is only half as large for the single-crystalline material (SC-85) that equates to 0.63 m^2/g_{NCM}. If one assumes spherical NCM particles and takes into account the NCM crystallographic density of $\rho_{NCM} \approx 4.63$ g/cm^3, the specific surface areas obtained after cycling to 5.0 V vs. Li$^+$/Li ($S^{\#36}_{EIS}$) correspond to a particle diameter of $d^{\#36}_p \approx 1.0$ μm for PC-60 and PC-85, and to 2.0 μm for SC-85, when calculated from the specific surface area S by Eq. 2:

$$d = \frac{6}{S \cdot \rho_{NCM}} \qquad [2]$$

The fact that the estimated diameter values for the cycled polycrystalline NCMs are still much larger than the primary crystallite size ($\sim$0.1–0.5 μm, see Fig. 2) suggests that not all primary particles within the secondary agglomerates have been exposed to the electrolyte after the cycling procedure to 5.0 V vs. Li$^+$/Li. However, here one has to consider that the capacitance measurements are taken in the fully lithiated state of the NCM particles, where initially formed cracks between the primary

particles might be sealed again; such a phenomenon was observed for polycrystalline NCM811, which after a few cycles to 4.5 V vs. Li$^+$/Li had a Kr-BET area of $\sim$1.8 m^2/g in the fully lithiated state and $\sim$3.2 m^2/g in the charged state.[16]

To summarize the findings in this section, we were able to show that capacity loss and lattice oxygen release occur simultaneously above $\sim$80 %SOC for the three different NCM materials, independent of their composition and morphology. Furthermore, the lattice oxygen release also induces a sudden increase in the specific surface area of polycrystalline NCMs, whereas the morphology of the single-crystalline materials seems to be maintained, as inferred from in situ capacitance measurements.

Capacity loss in dependence of the NCM particle morphology.—When cycled to high state of charge, the observed capacity of SC-85 (207 mAh/g_{NCM} at 4.5 V in cycle #21, see Fig. 4a or Fig. 6b) is significantly diminished when compared to PC-85 (222 mAh/g_{NCM}), and since these materials have the identical composition, the observed difference must stem from the difference in particle morphology. To illuminate this effect further, the potential curves of charge and discharge as well as the respective specific differential capacity curves (often referred to as dq/dV plot) are presented in Fig. 7, both extracted from the electrochemical cycling data shown in Figs. 4 and 6.

During cycle #9 with an upper cutoff potential of the NCM electrode of 4.1 V vs. Li$^+$/Li, which corresponds to $\sim$69 %SOC and is thus still below the onset potential of the lattice oxygen release for both PC-85 and SC-85 (detected at 4.23 V or $\sim$80 %SOC), the potential curves (see Fig. 7a) and the specific differential capacities (see Fig. 7b) coincide, yielding the same discharge capacity of 186 mAh/g_{NCM}.

In contrast, after three cycles to 4.5 V vs. Li$^+$/Li (cycle #21, corresponding to $\sim$89 %SOC), the features of the potential curve of the single-crystalline SC-85 material (green), shown in Fig. 7c, are not only shifted to lower capacities by $\sim$15 mAh/g_{NCM} as compared to PC-85 (blue), e.g., when comparing the position of the plateau at $\sim$4.2 V, but the entire curve also shows a $\sim$40 mV higher overpotential as compared to PC-85, which can also be seen by the shift of all dq/dV features of SC-85 during both charge and discharge (see Fig. 7d). Furthermore, the capacity which is contributed during the H2-H3 phase transition (marked by the plateau in Fig. 7c or the peak in Fig. 7d at $\sim$4.2 V) is significantly smaller for the single-crystalline SC-85 material. When increasing the upper cutoff potential of the NCM electrode to 4.8 V vs. Li$^+$/Li (cycle #30, $\sim$94 %SOC), these differences between the poly- and the single-crystalline NCM increase: the potential curve of SC-85 is shifted by $\sim$20 mAh/g_{NCM} to lower capacities and it has a $\sim$100 mV higher overpotential for both charge and discharge as compared to the PC-85 material (see Fig. 7e), which becomes clear when comparing the shift of the dq/dV features (see Fig. 7f); at the same time, the H2-H3 feature disappears almost completely for the charge of the SC-85 material. Overall, a loss of the discharge capacity of 24 mAh/g_{NCM} is observed for SC-85 (196 mAh/g_{NCM}) as compared to PC-85 (220 mAh/g_{NCM}).

When cycled to 4.8 V vs. Li$^+$/Li in cycle #30, a potential difference of $\sim$210 mV is observed between the charge and discharge curve at 137.5 mAh/g_{NCM} (corresponding to $\sim$50 % SOC) for SC-85 in Fig. 7e, whereas only $\sim$60 mV or $\sim$30 % of the value of SC-85 are detected for PC-85. If we assume that the overpotential for charge and discharge are identical for the SC-85 material (i.e., $\sim$105 mV), this corresponds to a mass specific electrode resistance of $\sim$4.9 $\Omega \cdot g_{NCM}$ when considering the applied current of 21.4 mA/g_{NCM}; for the given NCM loading of 8.7 mg$_{NCM}$/cm$^2_{electrode}$, this translates to a very large areal resistance of $\sim$0.56 k$\Omega \cdot$cm$^2_{electrode}$. At the current state, we assign this resistance to the NCM charge-transfer reaction, which is significantly hindered by the formation of an oxygen-depleted surface layer. A similar resistance increase of an oxygen-depleted surface layer was previously shown by Pritzl et al., inducing the oxygen

release and the subsequent resistance increase through washing and heating.[52] In principal, the difference in overpotential of PC-85 and SC-85 and the subsequent capacity loss could stem from the difference in morphology, as, according to the above analysis of the capacitance data, the polycrystalline PC-85 material provides a ∼2-fold higher specific surface area as compared to the single-crystalline SC-85 when charged to high SOCs (∼1.3 m^2/g_{NCM} vs. ∼0.63 m^2/g_{NCM}, as discussed above): at a ∼2-fold higher specific surface area and at the same applied specific current (in units of mA/g_{NCM}), the surface-area-normalized current density (in units of mA/m^2_{NCM}) for the polycrystalline PC-85 material would be ∼50 % lower; this appears as a ∼2-fold lower charge-transfer resistance and thus a ∼2-fold lower overpotential for PC-85, assuming that the surface and bulk properties of the two NCM851005 materials with regards to the (de)lithiation kinetics are the same. Here, however, it must be considered that the exposed NCM surface area for a polycrystalline NCM can be up to ∼2-fold larger in its delithiated state compared to its lithiated state in which the capacitance measurements were made, as demonstrated for a polycrystalline NCM811 by means of Kr-BET.[16] If this were to apply also to the here used PC-85 material, which has the same particle morphology as the NCM811 material of the latter study, it would predict an up to ∼4-fold higher surface area. As the total charge-transfer resistance of an active material scales inversely with its total active material surface area, the resistance and, therefore, the overpotential is increased ∼4-fold at the same specific current for the single-crystalline SC-85 as compared to the polycrystalline PC-85 material. Within this uncertainty, the observed differences in overpotential between the PC-85 and the SC-85 material could be explained entirely by the differences in exposed surface area.

Furthermore, the suppressed H2-H3 phase transition of SC-85, seen in Fig. 7f at ∼4.2–4.3 V, might be caused by a mechanism mainly occurring at high SOC: Xu et al.[53] showed that the lattice mismatch of the layered bulk structure and the oxygen-depleted (rock-salt-type) surface layer hinders the development of the H3 phase in the bulk of the primary particles and, therefore, the extraction of lithium above ∼75 %SOC. This lattice mismatch, which occurs only at high SOCs, induces an additional kinetic hindrance of the H2-H3 phase transition in the NCM during charge. Due to the ∼4-fold lower surface area of the single-crystalline material as well as its respectively larger primary crystallite size, this effect might emerge to a higher extent for SC-85, limiting the capacity obtained from the H2-H3 phase transition at ∼4.2–4.3 V. In discharge, however, the H2-H3 phase transition of SC-85 delivers a similar (differential) capacity as the one of PC-85, which can only be explained by the higher charge capacity of SC-85 above 4.3 V (30 mAh/g_{NCM} for SC-85 between 4.3 V and the end of the CV hold at 4.8 V as compared to 19 mAh/g_{NCM} for PC-85, see Fig. 7e), as also the differential charge capacity of SC-85 above 4.3 V is permanently increased as compared to the one PC-85 (see Fig. 7f). This observation shows that the H2-H3 phase transformation of SC-85 does take place when cycled to 4.8 V vs. Li⁺/Li but is kinetically hindered during charge (i.e., during delithiation), which is why the H2-H3 feature in the dq/dV is diminished while its capacity is delivered at higher potentials.

In the end, the combination of the ∼4-fold higher overpotential caused by the difference in surface area as well as the suppressed H2-H3 transition enhance the loss of discharge capacity for the single-crystalline SC-85 material when cycled to high SOC. However, one should note that in actual commercial battery cells with single-crystalline NCMs such high cathode potential cutoffs of 4.8 V vs. Li⁺/Li would not be used for nickel-rich NCMs, so that the here observed very large increase in overpotentials and the associated large capacity losses would not be observed. The effect of the morphology on the long-term cycling performance of the here used materials in full-cells will be discussed in an independent publication.

Based on the results of this section, we conclude that stable cycling of conventional NCMs is limited to degrees of delithiation
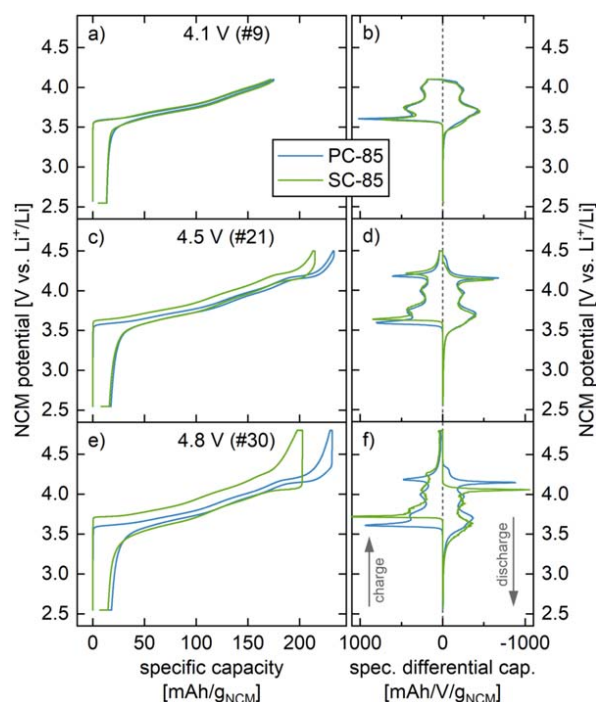

Figure 7. Comparison of the (dis)charge curves of PC-85 (blue) and SC-85 (green). The potential curves, showing the NCM potential vs. Li⁺/Li as a function of the specific capacity, were extracted from the electrochemical cycling data shown in Fig. 4, here depicted in separate panels for the third cycle to **a)** 4.1 V (#9), **c)** 4.5 V (#21), and **e)** 4.8 V (#30). The respective specific differential capacity (often referred to as dq/dV plot) as a function of the NCM potential, derived from the potential curves, is presented in separate panels for the same cycles to **b)** 4.1 V (#9), **d)** 4.5 V (#21), and **f)** 4.8 V (#30). Here, the charge is shown on the positive x-axis (left half of the right panels) and the discharge on the negative one (right half); also, the x- and y-axis are switched as compared to the conventional representation for an easier comparison with the potential curves. Distinct redox features or phase transitions appear as peaks, corresponding to plateau-like regions in the potential profiles. The NCM potential was calculated from the full-cell potential, based on the potential of 1.55 V vs. Li⁺/Li of the pre-lithiated, capacitively oversized LTO which was used as counter electrode.

<85 %SOC, independent of their composition or morphology. However, single-crystalline NCM particles having a concentration gradient of the transition metals (as previously reported for polycrystalline NCMs)[54,55] with a nickel-rich core (e.g., a nickel content of >85 %) and a surface layer region with a lower nickel content (e.g., 60 % nickel) could circumvent this limit: if such a material could be synthesized, and if it cycled without cracking of the primary crystallites (not exposing the nickel-rich core to the electrolyte), one could delithiate this material to an upper cutoff potential of 4.50 V (stability limit of NCM622 at ∼80 %SOC or 220 mAh/g_{NCM622}, see Figs. 3 and A·2); in contrast, the nickel-rich core would have delivered 240 mAh/$g_{NCM851005}$ (for NCM851005, 87 %SOC of its theoretical capacity, see Fig. A·2) or 257 mAh/g_{LNO} (for LNO, 93 %SOC)[6] at this potential, which could increase the provided cathode energy density in future lithium-ion batteries by ∼10 % or even up to ∼17 %, respectively.

Mechanisms causing the surface area increase.—In the following, possible reasons for the surface area increase observed for the polycrystalline NCMs occurring simultaneously with the oxygen release at high SOC are discussed:

• The capacitance increase of the polycrystalline NCMs, associated with an increase in specific surface area (proven by Kr-BET measurements), could be caused by the cracking of the primary crystallites upon the release of lattice oxygen. It has been reported that the delamination/exfoliation of the layered NCM structure might

Table I. Overview of the experimental results. Pristine NCM and VGCF-only powders/electrodes: specific surface areas of the material powders measured by Kr-BET (S_{BET}) and respective particle diameters d_p (calculated from S_{BET}), specific NCM and VGCF electrode capacitance (measured by EIS, from Fig. 4c), specific NCM capacitance contribution to the electrodes (from Fig. A·1 in the Appendix), and surface-area-normalized capacitance of NCMs or VGCF (normalized by S_{BET}). Electrodes cycled to 5.0 V vs. Li$^+$/Li (cycle #36): specific electrode capacitance (measured by EIS, from Fig. 4c), specific NCM capacitance (from Fig. A·1 in the Appendix), specific surface area ($S_{EIS}^{\#36}$) calculated from the specific NCM capacitance and the surface-area-normalized capacitance of the pristine electrodes, NCM particle diameter ($d_p^{\#36}$) calculated from $S_{EIS}^{\#36}$, and specific surface area change (comparing S_{BET} and $S_{EIS}^{\#36}$). Also shown are the specific amounts of oxygen (O_2) and carbon dioxide (CO_2) as well as their sum (O_2+CO_2) detected by OEMS during a charge to 5.0 V and normalized by the NCM mass (from Fig. 3), from which the fraction of NCM converted from a layered structure to a rock-salt-type reconstructed surface phase (y) and the respective layer thickness (d_l) were calculated.

	Electrode material	Units	PC-60	PC-85	SC-85	Units	VGCF only
Pristine	Specific surface area S_{BET}	m$^2_{NCM}$/g$_{NCM}$	0.32	0.27	0.51	m$^2_{VGCF}$/g$_{VGCF}$	12.4
	Particle diameter d_p (from S_{BET})	μm	4.0	4.8	2.6	–	–
	Specific electrode capacitance	F/g$_{electrode}$	0.12	0.11	0.17	F/g$_{electrode}$	0.43
	Specific material capacitance	F$_{NCM}$/g$_{NCM}$	0.09	0.08	0.14	F$_{VGCF}$/g$_{VGCF}$	0.54
	Surface-area-norm. capacitance	μF$_{NCM}$/cm$^2_{NCM}$	27	29	28	μF$_{VGCF}$/cm$^2_{VGCF}$	4.4
At 5.0 V vs. Li$^+$/Li (cycle #36)	Specific electrode capacitance	F/g$_{electrode}$	0.37	0.39	0.20		
	Specific NCM capacitance	F$_{NCM}$/g$_{NCM}$	0.36	0.38	0.17		
	Specific surface area $S_{EIS}^{\#36}$	m$^2_{NCM}$/g$_{NCM}$	1.34	1.33	0.63	–	
	Particle diameter $d_p^{\#36}$ (from $S_{EIS}^{\#36}$)	μm	1.0	1.0	2.0		
	Specific surface area change	–	4.2x	5.0x	1.2x		
	Detected specific O_2 amount	μmol$_{O_2}$/g$_{NCM}$	5.4	11.7	2.5		
	Detected specific CO_2 amount	μmol$_{CO_2}$/g$_{NCM}$	64.1	195.2	114.0		
	Detected specific O_2+CO_2 amount	μmol$_{O_2+CO_2}$/g$_{NCM}$	69.5	206.9	116.6	–	
	Oxygen-depleted fraction y	–	0.013	0.040	0.023		
	Rock-salt-type layer thickness d_l	nm	1.0	3.0	3.6		

be favored by the formation of a rock-salt-type phase which initiates the delamination of the layers either from the surface, from the bulk, or from nanopores of the primary crystallites.[49,50,56] Since the capacitance of the single-crystalline SC-85 material only changes by a factor of less than ∼1.4x, which could be explained by cracking of the interfaces between the large single-crystals (see Fig. 2c), a significant contribution from the cracking of the primary crystallites to the capacitance increase of the polycrystalline NCMs (with numerous primary crystallites forming secondary agglomerates) upon lattice oxygen release seems unlikely. However, it must be noted that the cells are cycled in this experiment for 36 cycles only, all at rather slow rates and only at 25 °C. As an accelerated degradation of the cell performance is typically observed during long-term cycling at higher rates and elevated temperatures, the potential cracking of the primary crystallites under harsher conditions can occur and has indeed been observed.[57,58]

• Under the here examined conditions, an irreversible opening of the void spaces between the primary crystallites seems to be more likely than the cracking of the primary particles. Here, it has to be noted that the capacitance is measured in the discharged state only, therefore, tracking only irreversibly opened pores; it was observed previously that small cracks are able to re-seal upon lithiation.[16,59] Upon the release of lattice oxygen, the near-surface region of the NCM particles reconstruct into an oxygen-depleted surface layer around each of the primary crystallites that are exposed to the electrolyte.[14] This phase, often reported to be a rock-salt-type phase,[60] has a primitive cell volume which is significantly reduced as compared to the layered structure. For LNO, being similar to the nickel-rich NCMs, the primitive cell volume decreases by 54 % when the structure is converted from LiNiO$_2$ ($V = 39.3$ Å^3)[6,7,61] to NiO ($V = 18.2$ Å^3),[62,63] a much larger volume change compared to that which occurs upon (de)lithiation (only ∼9 %).[7,61] Through this reduction of the material volume upon surface reconstruction, mechanical stresses are likely induced that lead to crack formation between the primary particles, which in turn leads to the penetration of the secondary agglomerates by the electrolyte and to the here observed increase of the capacitance and the Kr-BET.

• Finally, the released lattice oxygen partially reacts with the organic electrolyte components, forming protic species by the chemical oxidation of, e.g., ethylene carbonate (EC).[3,17,18] Lithium compounds like lithium carbonate and lithium oxide that may have remained on the surface of the primary crystallites from the synthesis, would then be chemically decomposed by the protons in the electrolyte, exposing the primary crystallites and increasing the surface area of polycrystalline NCMs.[34]

From the presented data, we expect a combination of the latter two mechanisms to cause the surface area increase at high state of charge. The apparent surface area increase observed for polycrystalline NCMs might give rise to capacity fading in full-cells, caused by loss of electronic contact in the secondary agglomerate[14,64,65] as well as by enhanced side reactions, including gas evolution,[3] electrolyte oxidation,[8,18] proton generation,[34] transition metal dissolution with subsequent deposition on the anode leading to additional SEI growth and loss of cyclable lithium,[19,20,66] as well as loss of active material.[14] For commercial cells, single-crystalline materials with an appropriate particle size are expected to provide an improved long-term performance, as they maintain their specific surface area upon cycling.

Estimation of the thickness of the oxygen-depleted surface layer.—Even though the pristine specific surface area of the SC-85 material (0.51 m^2/g$_{NCM}$) is larger as compared to PC-85 (0.27 m^2/g$_{NCM}$), smaller amounts (∼50 %) of molecular oxygen (O_2) and carbon dioxide (CO_2) are detected for the former (see Fig. 3). This can only be explained through a significant surface area increase of PC, if one assumes a similar film thickness of the oxygen-depleted surface layer, what seems reasonable based on the identical NCM composition. As the surface area increase of polycrystalline NCMs at high state of charge (see Fig. 6) has not been considered for the estimation of the

oxygen-depleted surface layer thickness, previous studies may have significantly overestimated its thickness. With the precise in situ quantification of the specific surface area of the NCM particles, a more reliable value for the oxygen-depleted surface layer thickness is now provided based on the detected amounts of O_2 and CO_2.

In contrast to the O_2 evolution, the generation of CO_2 is not only caused by the release of (singlet) oxygen and its chemical reaction with the electrolyte, but also partially by the decomposition of Li_2CO_3 and the electrochemical oxidation of electrolyte components at 5.0 V vs. Li^+/Li, prohibiting to discriminate the CO_2 amounts caused by the release of lattice oxygen from the other mechanisms. By taking the sum of the amounts of O_2 and CO_2 (in units of $\mu mol_{O_2+CO_2}/g_{NCM}$) released at 5.0 V to represent the total amount of released lattice oxygen, an upper limit of the released lattice oxygen and, hence, of the thickness of the oxygen-depleted surface layer can be determined. As shown in Fig. 3 and summarized in Table I, the total amounts of the evolved gases are 69.5 $\mu mol_{O_2+CO_2}/g_{NCM}$ for PC-60, 206.9 $\mu mol_{O_2+CO_2}/g_{NCM}$ for PC-85, and 116.6 $\mu mol_{O_2+CO_2}/g_{NCM}$ for SC-85. If the surface reconstruction of the layered structure to a rock-salt-type phase occurs according to the following reaction,

$$Li_{1-x}MO_2 \rightarrow (1-y)\,Li_{\frac{1-x}{1-y}}MO_2 + y\,MO + \frac{y}{2}\,O_2 \qquad [3]$$
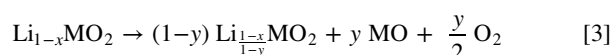
0.5 mol_{O_2} are released per 1 mol_{NCM} that is reconstructed into a rock-salt-type phase. From Eq. 3, together with the above assumption that the actual amount of released lattice oxygen is represented by the sum of detected O_2 and CO_2 (0.5 $mol_{O_2+CO_2}$), the fraction y of the NCM material that was converted to a rock-salt-type surface layer can be calculated from the ratio of the detected gas amounts (in $\mu mol_{O_2+CO_2}/g_{NCM}$) and the gas amounts calculated for a complete conversion to a rock-salt-type phase (0.5 $mol_{O_2+CO_2}/mol_{NCM}$), taking into account the NCM molar mass (M_{NCM} = 96.9 g_{NCM}/mol_{NCM} for PC-60 and 97.5 g_{NCM}/mol_{NCM} for PC-85 and SC-85).

For PC-60, the observed 69.5 $\mu mol_{O_2+CO_2}/g_{NCM}$ correspond to a converted fraction y = 0.013, whereas values of 0.040 and 0.022 are obtained for PC-85 and SC-85, respectively. As previously done by Jung et al. using a spherical approximation,[3] the thickness of the oxygen-depleted surface layer d_l can be estimated by Eq. 4, taking the ratio of the volume of the entire particle (V_p) and the one of the oxygen-depleted layer (V_l):

$$y = \frac{1}{0.46}\frac{V_l}{V_p} = \frac{1}{0.46}\frac{((d_p)^3 - (d_p - d_l)^3)}{d_p^3} \qquad [4]$$

Here, the estimated particle diameter $d_p^{\#36}$ of the three NCMs at 5.0 V (see Table I) is taken into account as well as the required correction factor of 0.46 which considers the volume difference of $Li_{1-x}MO_2$ and MO, as, e.g., for LNO (as the lattice parameters for rock-salt-type phase of the various NCMs are not available), the primitive cell volume of the rock-salt-type phase is only 46 % as compared to the one of the layered phase (see discussion above). For PC-60, a rock-salt-type layer thickness of the exposed primary crystallites of 1.0 nm is obtained when charged once to 5.0 V, whereas for PC-85 and SC-85, both having a higher nickel content, similar film thicknesses of 3.0 nm and 3.6 nm are estimated, respectively. Hereby, one should note that the film thicknesses of the polycrystalline NCMs would be overestimated by a factor of 4.2x or 5.0x, respectively, if the surface area increase at high SOC would not be taken into account. We believe that the increased film thickness of PC-85 and SC-85 as compared to PC-60 is caused by the increased nickel content, destabilizing the layered structure due to the high reactivity of Ni^{4+}, as this has been assigned multiple times to, e.g., a decreased thermal stability as well as an increased reactivity towards moisture.[4,61,67–69] Further, a higher solid-state

diffusion of oxygen in the structure of layered oxides with a higher nickel content could lead to more lattice oxygen being released upon delithiation to high SOC, what has not yet been reported to the best of our knowledge.

In summary, we were able to calculate the thicknesses of the oxygen-depleted surface layer, which were larger for NCMs with a higher nickel content and similar for NCMs with the same NCM composition, independent of the particle morphology when the gas amounts detected by OEMS were normalized to the surface area obtained by the capacitance measurements upon cycling.

Conclusions

The correlation of oxygen release, capacity fading, and particle cracking was investigated as a function of state of charge for three nickel-rich NCMs, differing either in composition (i.e., in transition metal ratio) or in morphology (i.e., in primary crystallite size of the poly- and single-crystalline NCMs). First, the onset of the release of lattice oxygen was observed at ~80 %SOC by OEMS, independent of the nickel content. In electrochemical cycling experiments, during which the NCM electrode capacitance was tracked by EIS while the upper cutoff potential was increased every third cycle stepwise from 3.9 V to 5.0 V, a fading of the discharge capacity occurred at high degree of delithiation when the onset of oxygen release was exceeded by ~10 %SOC. Simultaneously, the specific surface area of the polycrystalline NCMs increased suddenly at high SOC to more than 400 % of the pristine one, which was determined by the capacitance extracted from the impedance spectra using a micro-reference electrode (μ-RE) and validated through Kr-BET measurements of cycled electrodes. In contrast, the specific surface area of the single-crystalline NCM changed by less than 40 %, even after complete delithiation, highlighting the morphological stability of single-crystalline cathode active materials.

The lower specific surface area retained by the single-crystalline material upon cycling, however, enhanced the detrimental effect of the resistive oxygen-depleted surface layer formed upon release of lattice oxygen, leading to lower discharge capacities at high SOC compared to the polycrystalline materials. Owing to the morphological integrity of the crystallites of the single-crystalline NCM, its long-term cycling performance in full-cells with commonly used upper cutoff potentials, however, is expected to be improved, as the side reactions that consume cyclable lithium are diminished due to its lower specific surface area upon cycling. From the detected amounts of evolved gases and the determined specific surface areas, the thickness of the reconstructed rock-salt-type surface layer was estimated to be ~3-4 nm for NCM851005, independent of the particle morphology, and ~1 nm for NCM622. To enable a broader accessibility of this powerful and non-destructive impedance-based method tracking the NCM particle cracking in situ, a simplified cell setup – without reference electrode and without the need for a pre-lithiated LTO electrode – will be introduced in part III of this study.

CRediT Authorship Contribution Statement

Stefan Oswald: Methodology, Investigation, Writing—Original Draft. Daniel Pritzl: Methodology, Writing—Review & Editing. Morten Wetjen: Methodology, Writing—Review & Editing. Hubert A. Gasteiger: Conceptualization, Supervision, Writing—Review & Editing.

Acknowledgments

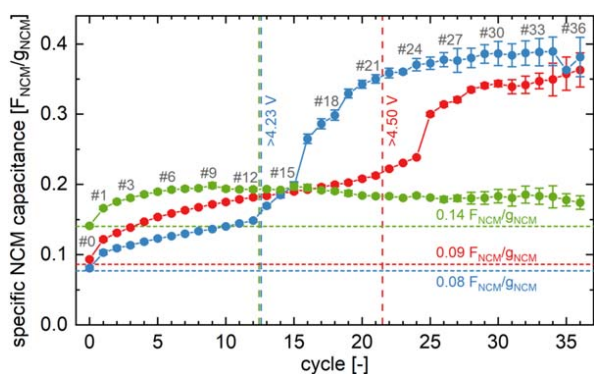**Figure A·1.** Specific NCM capacitance of PC-60 (red), PC-85 (blue), and SC-85 (green) as working electrodes (in units of F_{NCM}/g_{NCM}) as a function of cycle number, calculated from the specific electrode capacitance in Fig. 4c by subtracting $1/10^{th}$ of the contribution of the VGCF electrode (0.1x of 0.43 F/$g_{electrode}$) and subsequently normalized by the NCM mass. The horizontal dashed lines indicate the pristine NCM capacitance value of each of the three NCM materials before the conditioning step (#0), whereas the vertical dashed lines mark the cycle at which ∼80 %SOC (extracted from Fig. 3) are exceeded for each of the three NCMs (4.50 V for PC-60, and 4.23 V for PC-85 and SC-85), marking the onset of the release of lattice oxygen observed in Fig. 3. The error bars are determined by the laws of error propagation (see supporting information of part I of this study),[21] using the average capacitances and their minimum/maximum values given in Fig. 4c.

Appendix

To be able to quantify the relative increase of the capacitance of the NCM materials only, the contribution of the inert electrode components VGCF and PVDF are excluded: therefor, $1/10^{th}$ of the VGCF electrode (0.1x of 0.43 F/$g_{electrode}$) was subtracted from the electrode capacitance values for each NCM material and cycle number (both shown in Fig. 4c). The obtained NCM capacitance (in units of $F_{NCM}/g_{electrode}$) was normalized by the NCM mass in the electrode (resulting in units of F_{NCM}/g_{NCM}), considering that the NCM content in the electrode is 90 wt% ($m_{NCM} = 0.9 \cdot m_{electrode}$), and depicted as a function of cycle number in Fig. A·1.

To allow for a better interpretation of the cycling data in Fig. 4 showing the specific discharge capacity and the specific electrode capacitance as a function of cycle number with increasing upper cutoff potentials of the NCM electrode, the latter was converted into the respective degree of delithiation (x in $Li_{1-x}MO_2$, with M = Ni, Co, Mn) or state of charge (SOC), with the resulting plot being depicted in Fig. 6. For this conversion, the required relation between upper cutoff potential (i.e., 3.9 V, 4.0 V, …, 5.0 V vs. Li^+/Li) and the SOC was extracted from the potential curves of the first charge for each of the three NCMs under the essentially identical charging current, which are shown in Fig. A·2.
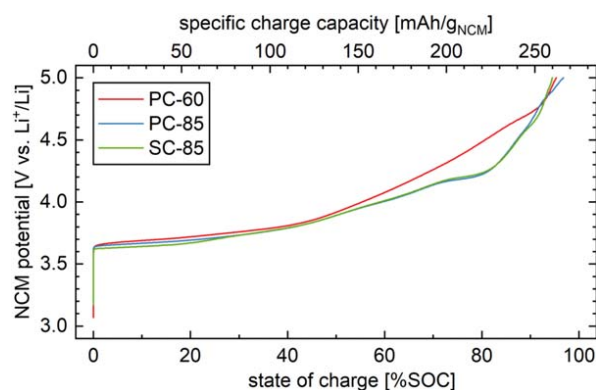
Figure A·2. Potential curves of the first charge of the three NCMs as a function of the specific charge capacity (in units of mAh/g_{NCM} at the top) or state of charge (in %SOC at the bottom, corresponding to the degree of delithiation x in $Li_{1-x}MO_2$), respectively. Cells were assembled with PC-60 (red), PC-85 (blue), or SC-85 (green) as working electrodes in T-cells with 90 µl LP57, and lithium metal as counter electrode and reference electrode (with three glass fiber separators, two placed between the working and the counter electrode as well as one toward the reference electrode). Controlled by the reference electrode potential, the NCM electrodes were charged at 25 °C to 5.0 V vs. Li^+/Li at a current of 18.4 mA/g_{NCM} (corresponding to a C-rate of C/15 when referenced to the theoretical capacity of ∼275 mAh/g_{NCM}).

ORCID

Stefan Oswald ⓘ https://orcid.org/0000-0001-6402-7833
Daniel Pritzl ⓘ https://orcid.org/0000-0002-9029-107X
Morten Wetjen ⓘ https://orcid.org/0000-0002-2357-1151
Hubert A. Gasteiger ⓘ https://orcid.org/0000-0001-8199-8703

References

1. N. Nitta, F. Wu, J. T. Lee, and G. Yushin, *Mater. Today*, **18**, 252 (2015).
2. W. Li, E. M. Erickson, and A. Manthiram, *Nat. Energy*, **5**, 26 (2020).
3. R. Jung, M. Metzger, F. Maglia, C. Stinner, and H. A. Gasteiger, *J. Electrochem. Soc.*, **164**, A1361 (2017).
4. H.-J. Noh, S. Youn, C. S. Yoon, and Y.-K. Sun, *J. Power Sources*, **233**, 121 (2013).
5. H.-H. Ryu, K.-J. Park, C. S. Yoon, and Y.-K. Sun, *Chem. Mater.*, **30**, 1155 (2018).
6. H. Li, N. Zhang, J. Li, and J. R. Dahn, *J. Electrochem. Soc.*, **165**, A2985 (2018).
7. H. Li, A. Liu, N. Zhang, Y. Wang, S. Yin, H. Wu, and J. R. Dahn, *Chem. Mater.*, **31**, 7574 (2019).
8. R. Jung, M. Metzger, F. Maglia, C. Stinner, and H. A. Gasteiger, *J. Phys. Chem. Lett.*, **8**, 4820 (2017).
9. R. Jung, P. Strobl, F. Maglia, C. Stinner, and H. A. Gasteiger, *J. Electrochem. Soc.*, **165**, A2869 (2018).
10. D. Streich, C. Erk, A. Guéguen, P. Müller, F.-F Chesneau, and E. J. Berg, *J. Phys. Chem. C*, **121**, 13481 (2017).
11. D. P. Abraham, R. D. Twesten, M. Balasubramanian, I. Petrov, J. McBreen, and K. Amine, *Electrochem. Commun.*, **4**, 620 (2002).
12. S. Watanabe, M. Kinoshita, T. Hosokawa, K. Morigaki, and K. Nakura, *J. Power Sources*, **258**, 210 (2014).

13. S. K. Jung, H. Gwon, J. Hong, K. Y. Park, D. H. Seo, H. Kim, J. Hyun, W. Yang, and K. Kang, *Adv. Energy Mater.*, **4**, 1300787 (2014).
14. F. Friedrich, B. Strehle, A. T. S. Freiberg, K. Kleiner, S. J. Day, C. Erk, M. Piana, and H. A. Gasteiger, *J. Electrochem. Soc.*, **166**, A3760 (2019).
15. J. Choi and A. Manthiram, *J. Electrochem. Soc.*, **152**, 1714 (2005).
16. B. Strehle, F. Friedrich, and H. A. Gasteiger, *J. Electrochem. Soc.*, **168**, 050512 (2021).
17. J. Wandt, A. T. S. Freiberg, A. Ogrodnik, and H. A. Gasteiger, *Mater. Today*, **21**, 825 (2018).
18. A. T. S. Freiberg, M. K. Roos, J. Wandt, R. De Vivie-Riedle, and H. A. Gasteiger, *J. Phys. Chem. A*, **122**, 8828 (2018).
19. R. Jung, F. Linsenmann, R. Thomas, J. Wandt, S. Solchenbach, F. Maglia, C. Stinner, M. Tromp, and H. A. Gasteiger, *J. Electrochem. Soc.*, **166**, A378 (2019).
20. S. Solchenbach, G. Hong, A. T. S. Freiberg, R. Jung, and H. A. Gasteiger, *J. Electrochem. Soc.*, **165**, A3304 (2018).
21. S. Oswald, D. Pritzl, M. Wetjen, and H. A. Gasteiger, *J. Electrochem. Soc.*, **167**, 100511 (2020).
22. L. de Biasi, A. O. Kondrakov, H. Geßwein, T. Brezesinski, P. Hartmann, and J. Janek, *J. Phys. Chem. C*, **121**, 26163 (2017).
23. A. O. Kondrakov, A. Schmidt, J. Xu, H. Geßwein, R. Mönig, P. Hartmann, H. Sommer, T. Brezesinski, and J. Janek, *J. Phys. Chem. C*, **121**, 3286 (2017).
24. W. Li, H. Y. Asl, Q. Xie, and A. Manthiram, *J. Am. Chem. Soc.*, **141**, 5097 (2019).
25. Y. Kim, *Appl. Mater. Interfaces*, **4**, 2329 (2012).
26. Q. Liu, M. Li, N. Wu, L. Cui, X. Huang, X. Liu, Y. Zhao, H. Chen, W. Yuan, and Y. Bai, *J. Electrochem. Soc.*, **165**, A3040 (2018).
27. G. Qian, Y. Zhang, L. Li, R. Zhang, J. Xu, Z. Cheng, S. Xie, H. Wang, Q. Rao, Y. He, Y. Shen, L. Chen, M. Tang, and Z.-F. Ma, *Energy Storage Mater.*, **27**, 140 (2020).
28. E. Trevisanello, R. Ruess, G. Conforto, F. H. Richter, and J. Janek, *Adv. Energy Mater.*, **2003400** (2021).
29. J. Li, A. R. Cameron, H. Li, S. Glazier, D. Xiong, M. Chatzidakis, J. Allen, G. A. Botton, and J. R. Dahn, *J. Electrochem. Soc.*, **164**, A1534 (2017).
30. J. E. Harlow, X. Ma, J. Li, E. Logan, Y. Liu, N. Zhang, L. Ma, S. L. Glazier, M. M. E. Cormier, M. Genovese, S. Buteau, A. Cameron, J. E. Stark, and J. R. Dahn, *J. Electrochem. Soc.*, **166**, A3031 (2019).
31. R. Bernhard, M. Metzger, and H. A. Gasteiger, *J. Electrochem. Soc.*, **162**, A1984 (2015).
32. N. Tsiouvaras, S. Meini, I. Buchberger, and H. A. Gasteiger, *J. Electrochem. Soc.*, **160**, A471 (2013).
33. S. Solchenbach, D. Pritzl, E. J. Y. Kong, J. Landesfeind, and H. A. Gasteiger, *J. Electrochem. Soc.*, **163**, A2265 (2016).
34. A. T. S. Freiberg, J. Sicklinger, S. Solchenbach, and H. A. Gasteiger, *Electrochim. Acta*, **346**, 136271 (2020).
35. U. Heider, R. Oesten, and M. Jungnitz, *J. Power Sources*, **81–82**, 119 (1999).
36. J. Landesfeind, D. Pritzl, and H. A. Gasteiger, *J. Electrochem. Soc.*, **164**, A1773 (2017).
37. M. Gaberscek, J. Moskon, B. Erjavec, R. Dominko, and J. Jamnik, *Electrochem. Solid-State Lett.*, **11**, A170 (2008).
38. D. Pritzl, A. E. Bumberger, M. Wetjen, J. Landesfeind, S. Solchenbach, and H. A. Gasteiger, *J. Electrochem. Soc.*, **166**, A582 (2019).
39. O. Barbieri, M. Hahn, A. Herzog, and R. Kötz, *Carbon*, **43**, 1303 (2005).
40. H. Ji, X. Zhao, Z. Qiao, J. Jung, Y. Zhu, Y. Lu, L. L. Zhang, A. H. MacDonald, and R. S. Ruoff, *Nat. Commun.*, **5**, 3317 (2014).
41. J. Chmiola, G. Yushin, Y. Gogotsi, C. Portet, P. Simon, and P. L. Taberna, *Science*, **313**, 1760 (2006).
42. L. Ramaley and C. G. Enke, *J. Electrochem. Soc.*, **112**, 947 (1965).
43. K. C. Liu and M. A. Anderson, *J. Electrochem. Soc.*, **143**, 124 (1996).
44. T. Pajkossy and D. M. Kolb, *Electrochim. Acta*, **46**, 3063 (2001).
45. P. S. Germain, W. G. Pell, and B. E. Conway, *Electrochim. Acta*, **49**, 1775 (2004).
46. T. Pajkossy and D. M. Kolb, *Electrochim. Commun.*, **9**, 1171 (2007).
47. R. P. Seward and E. C. Vieira, *J. Phys. Chem.*, **62**, 127 (1957).
48. M. M. Besli, A. K. Shukla, C. Wei, M. Metzger, J. Alvarado, J. Boell, D. Nordlund, G. Schneider, S. Hellstrom, C. Johnston, J. Christensen, M. M. Doeff, Y. Liu, and S. Kuppan, *J. Mater. Chem.*, **7**, 12593 (2019).
49. P. Yan, J. Zheng, M. Gu, J. Xiao, J. G. Zhang, and C. M. Wang, *Nat. Commun.*, **8**, 14101 (2017).
50. H. Zhang, F. Omenya, P. Yan, L. Luo, M. S. Whittingham, C. Wang, and G. Zhou, *ACS Energy Lett.*, **2**, 2607 (2017).
51. K. Edström, T. Gustafsson, and J. O. Thomas, *Electrochim. Acta*, **50**, 397 (2004).
52. D. Pritzl, T. Teufl, A. T. S. Freiberg, B. Strehle, J. Sicklinger, H. Sommer, P. Hartmann, and H. A. Gasteiger, *J. Electrochem. Soc.*, **166**, A4056 (2019).
53. C. Xu, K. Märker, J. Lee, A. Mahadevegowda, P. J. Reeves, S. J. Day, M. F. Groh, S. P. Emge, C. Ducati, B. L. Mehdi, C. C. Tang, and C. P. Grey, *Nat. Mater.*, **20**, 84 (2021).
54. Y.-K. Sun, S.-T. Myung, B.-C. Park, J. Prakash, I. Belharouak, and K. Amine, *Nat. Mater.*, **8**, 320 (2009).
55. Z. Sun, D. Wang, Y. Fan, L. Jiao, F. Li, T. Wu, D. Han, and L. Niu, *RSC Adv.*, **6**, 103747 (2016).
56. S. Ahmed, A. Pokle, S. Schweidler, A. Beyer, M. Bianchini, F. Walther, A. Mazilkin, P. Hartmann, T. Brezesinski, J. Janek, and K. Volz, *ACS Nano*, **13**, 10694 (2019).
57. F. Zhang, S. Lou, S. Li, Z. Yu, Q. Liu, A. Dai, C. Cao, M. F. Toney, M. Ge, X. Xiao, W.-K. Lee, Y. Yao, J. Deng, T. Liu, Y. Tang, G. Yin, J. Lu, D. Su, and J. Wang, *Nat. Commun.*, **11**, 3050 (2020).
58. P. Teichert, H. Jahnke, and E. Figgemeier, *J. Electrochem. Soc.*, **168**, 090532 (2021).
59. R. Ruess, S. Schweidler, H. Hemmelmann, G. Conforto, A. Bielefeld, D. A. Weber, J. Sann, M. T. Elm, and J. Janek, *J. Electrochem. Soc.*, **167**, 100532 (2020).
60. S. Schweidler, L. De Biasi, G. Garcia, A. Mazilkin, P. Hartmann, T. Brezesinski, and J. Janek, *ACS Appl. Energy Mater.*, **2**, 7375 (2019).
61. M. Bianchini, M. Roca-Ayats, P. Hartmann, T. Brezesinski, and J. Janek, *Angew. Chemie - Int. Ed.*, **58**, 10434 (2019).
62. M. A. Peck and M. A. Langell, *Chem. Mater.*, **24**, 4483 (2012).
63. F. Fiévet, P. Germi, F. de Bergevin, and M. Figlarz, *J. Appl. Crystallogr.*, **12**, 387 (1979).
64. J. H. Kim, S. J. Kim, T. Yuk, J. Kim, C. S. Yoon, and Y.-K. Sun, *ACS Energy Lett.*, **3**, 3002 (2018).
65. C. Tian, Y. Xu, D. Nordlund, F. Lin, J. Liu, Z. Sun, Y. Liu, and M. Doeff, *Joule*, **2**, 464 (2018).
66. J. A. Gilbert, I. A. Shkrob, and D. P. Abraham, *J. Electrochem. Soc.*, **164**, A389 (2017).
67. S. M. Bak, E. Hu, Y. Zhou, X. Yu, S. D. Senanayake, S. J. Cho, K. B. Kim, K. Y. Chung, X. Q. Yang, and K. W. Nam, *ACS Appl. Mater. Interfaces*, **6**, 22594 (2014).
68. J. Sicklinger, M. Metzger, H. Beyer, D. Pritzl, and H. A. Gasteiger, *J. Electrochem. Soc.*, **166**, A2322 (2019).
69. R. Jung, R. Morasch, P. Karayaylali, K. Phillips, F. Maglia, C. Stinner, Y. Shao-Horn, and H. A. Gasteiger, *J. Electrochem. Soc.*, **165**, A132 (2018).

3.3 Development of a Simplified Measurement Setup

The article "Novel Method for Monitoring the Electrochemical Capacitance by In Situ Impedance Spectroscopy as Indicator for Particle Cracking of Nickel-Rich NCMs: Part III. Development of a Simplified Measurement Setup" was submitted to the peer-reviewed *Journal of the Electrochemical Society* in March 2022 and published online in May 2022 [205]. It is available as an open-access article and distributed under the terms of the Creative Commons Attribution Non-Commercial No Derivatives 4.0 License. A permanent link to this article can be found under https://doi.org/10.1149/1945-7111/ac67b3. The main findings of this paper were presented by Stefan Oswald in an oral presentation as Paper #A02-0368 at the 241st Meeting of the *Electrochemical Society* in Vancouver, Canada, in June 2022.

As the impedance-based approach developed in Chapter 3.1 relies on an intricate setup using a GWRE as well as a pre-lithiated LTO counter electrode, what limits the broad application of the method, this article deals with the stepwise simplification thereof. It is found that the capacitance of the working electrode can be determined even without GWRE if the impedance of the counter electrode (in particular, at 180 mHz) is negligible as compared to the one of the working electrode in blocking conditions. This prerequisite is typically fulfilled by counter electrodes based on active materials such as graphite, LTO, and LFP, which are required to be capacitively oversized and partially lithiated to allow for the full lithiation of the working electrode. Even though lithium-metal electrodes exhibit an impedance contribution to the entire cell which cannot be neglected, the impedance of lithium at 180 mHz is more than 10x smaller as compared to the NCM in fully lithiated state. Therefore, the capacitance of the NCMs can be determined in standard coin cells without μ-RE when choosing a suitable counter electrode. The use of half-cells, however, is limited to ∼10 charge/discharge cycles since the lithium-metal counter electrode affects the capacitance of the NCM electrode, what is attributed to cross-talk phenomena. Finally, it could be demonstrated that the impedance-based capacitance determination does not require the use of an impedance analyzer but that, by implementing a sine-like current perturbation of 180 mHz, the capacitance can be extracted by a single-point impedance using a standard battery tester without explicit impedance capabilities. Through these simplifications, the surface area changes of NCMs upon cycling can be determined by implementing a single-point impedance into the standard testing protocols of coin

half-cells at battery cyclers.

A variety of literature articles have reported the beneficial nature of a customized morphology or microstructure (i.e., the size and shape of the primary crystallites) on the (chemo)mechanical stability of NCM particles [171, 172, 180, 253, 257, 258]. Other approaches to preserve the morphological integrity include the doping (using elements such as Al, B, and W) and coating/infusion of the CAMs by other elements/materials (e.g., by Li_3PO_4) [171, 172, 175, 255, 259, 260]. The evaluation of the success of this approach is typically based on the visual analysis by FIB-SEM. The here developed simplified method provides a convenient tool, which allows for the quantitative evaluation of the impact of the synthesis conditions on the (chemo)mechanical stability during operation. Exemplarily, Riewald et al. demonstrated through this approach that the irreversible capacity of LNO in the first cycle scales with the LNO capacitance and is thus directly linked to the exposed surface area and the size of the primary crystallites, resulting from the synthesis conditions [91, 92]. Due to its simplicity, the method also enables the large-scale screening of the effect of cycling conditions (e.g., operation temperature, applied C-rate, and upper cutoff potential) on the surface area changes of newly developed CAMs and can serve as quality management tool in CAM production.

Author contributions

S.O. and F.R. designed the experiments, performed the electrochemical measurements, and analyzed the data. S.O. validated the impedance measurements in half-cells, while F.R. implemented the impedance measurements at the battery cycler. S.O. and F.R. wrote and H.A.G. edited the manuscript. All authors discussed the results and commented on the manuscript. S.O. and F.R. contributed equally to this work as co-shared first authors.

Novel Method for Monitoring the Electrochemical Capacitance by In Situ Impedance Spectroscopy as Indicator for Particle Cracking of Nickel-Rich NCMs: Part III. Development of a Simplified Measurement Setup

Stefan Oswald,[1,=,*,z] Felix Riewald,[1,2,=] and Hubert A. Gasteiger[1,**]

[1]Technical University of Munich, Chair of Technical Electrochemistry, Department of Chemistry and Catalysis Research Center, Garching, Germany
[2]BASF SE, New Battery Materials and Systems, Ludwigshafen, Germany

As the optimization of the electrochemical performance of lithium-ion batteries by the adjustment of the composition of the cathode active materials (CAMs) has come to a limit, the focus has shifted to the modification of the morphological aspects. However, new methodologies for the quantification of characteristics such as particle size, particle cracking, and surface area change are needed. A previously reported impedance-based method allows for monitoring the capacitance of CAMs in the positive electrodes as indicator for their surface area but relies on a sophisticated cell setup. In this study, we deduce a stepwise simplification of the capacitance measurements from the setup using a gold-wire reference electrode to a conventional coin half-cell setup, which is commonly used in industry as testing platform for the initial benchmarking of newly developed CAMs. Additionally, it is shown that the CAM capacitance does not have to be extracted from a full impedance spectrum that requires an impedance analyzer, but that it can be obtained solely from a low-frequency single-point impedance measurement, which can be performed with a simple battery cycler. The working principle of this approach is validated using four different cell and electrochemical test hardware configurations (potentiostat, battery cycler) over several charge/discharge cycles.

As many technical challenges of the 21st century center on cheap and efficient energy storage, the demand for lithium-ion batteries (LIBs) is not expected to stop soon. LIBs provide a good trade-off between energy and power density, efficiency, safety, and cost.[1–3] The limitation in energy density as well as the lion's share of cost ($\sim$50 %) of such a battery still lie in the cathode active material (CAM).[2–4] Currently, layered lithium transition metal oxides ($LiMO_2$) are the most widely used CAMs for transportation applications. For NCM ($Li_{1+\delta}Ni_xCo_yMn_zO_2$, $x+y+z+\delta = 1$, and $0 < \delta < 0.01$), a representative of commercially used CAMs, the transition metal ratio has been adjusted towards higher nickel contents, providing more specific capacity at a fixed cutoff potential, while decreasing the raw materials' cost due to the reduced cobalt content.[5,6]

However, the optimization of cell performance through the composition has come to a limit, as recent reports on newly developed and implemented CAMs with an ultra-high nickel content have repeatedly crossed the mark of 90 mol% nickel.[7–11] More innovative approaches pursue the modification of the particle morphology, which often include the tailoring of the primary crystallite size as well as of their shape and arrangement in secondary particle agglomerates.[12–16] This approach targets to diminish the various side reactions and degradation mechanisms that frequently scale with the CAM surface area, such as the electrochemical electrolyte oxidation at elevated potential ($\geqslant$4.5 V_{Li}),[17] the chemical electrolyte oxidation by released lattice oxygen,[18–22] the formation of a resistive oxygen-depleted surface layer,[23–26] as well as the dissolution of transition metals (and their subsequent re-deposition on the anode).[27–31] Due to the anisotropic change of lattice parameters and the resulting change in unit cell volume upon (de)lithiation, mechanical fracture of the secondary particle structure occurs, leading to an increase of the interface area between CAM and electrolyte, which is therefore much higher during cell operation as compared to the pristine state.[25,32–36]

The combination of these factors heavily influences the long-term cycling stability of actual cells.[14,26,37,38]

Therefore, the morphology and the accessible surface area has become a more and more important characteristic and descriptor for CAMs. So far, however, the morphological changes upon cycling are investigated mainly by means of post mortem analyses. For the analysis of cycled electrodes, typical approaches include the non-quantitative scanning electron microscopy and transmission electron microscopy of cross sections prepared by focused-ion beam milling (FIB-SEM/-TEM)[10,39–41] as well as the surface area determination via (Kr-)BET.[25,26,34,42] All of these are tedious and destructive, and a convenient tool for in situ CAM surface area tracking upon cycling is required.

Recently, a non-intrusive in situ impedance-based method has been reported, which monitors the CAM's capacitance as indicator for its electrochemically active surface area and can be directly included into the electrochemical cycling procedure.[34,36] However, this requires a rather sophisticated and intricate Swagelok T-cell setup with a micro-reference electrode (μ-RE; e.g., a gold-wire reference electrode (GWRE)[43]) as well as an impedance analyzer. Thus, it is not well suited neither for the use in an industrial setting (e.g., by CAM developers) nor for high-throughput screening, which is typically needed in material development.

In this study, we deduce a stepwise simplification of the capacitance measurements from a μ-RE setup to a conventional coin half-cell setup, which is the most used testing platform in industry for the benchmarking of new active materials. Additionally, it is shown that the capacitance does not have to be extracted from a full impedance spectrum provided by an impedance analyzer, but that it can be obtained solely from a low-frequency single-point impedance measurement, which can be performed with a conventional battery cycler without impedance capability.

Experimental

Electrode preparation.—For cell cycling, NCM electrodes were prepared from polycrystalline NCM851005 powder ($Li_{1.01}Ni_{0.85}Co_{0.10}Mn_{0.05}O_2$, 0.2 m^2_{BET}/g_{NCM} (determined by N_2-BET), BASF SE, Germany). To avoid contamination of the material by

=These authors contributed equally to this work.
*Electrochemical Society Student Member.
**Electrochemical Society Fellow.
zE-mail: Stefan.Oswald@tum.de

Table I. Overview of the four cell and test hardware configurations used for cell cycling studies of the NCM working electrodes, stating: the abbreviated label specifying a given configuration, the cell type, the type of counter electrode, how the impedance was measured and whether acquired as cell or as NCM cathode impedance, as well as the type of test hardware. Coin cells were assembled with 95 µl LP57 electrolyte and one glass fiber separator; T-cells with a µ-RE (GWRE) were assembled with 60 µl LP57 electrolyte and two glass fiber separators.

Label	Cell type	Counter electrode	Measured impedance	Test hardware
Z_{NCM}-LTO-B	T-cell w. µ-RE[43]	pre-lithiated LTO	NCM (spectrum)	Biologic
Z_{cell}-LTO-M	Coin cell	pre-lithiated LTO	cell (180 mHz point only)	Maccor
Z_{cell}-Li-B	Coin cell	lithium metal	cell (spectrum)	Biologic
Z_{cell}-Li-M	Coin cell	lithium metal	cell (180 mHz point only)	Maccor

moisture, all steps were performed in a dry room (at a room temperature of 20 °C and a dew point below −40 °C). The NCM powder was mixed at a mass ratio of 94:3:3 with conductive carbon (C65, carbon black SuperC65, 64 m^2_{BET}/g, TIMCAL, Switzerland) and polyvinylidene difluoride (PVDF, Solef5130, Solvay, Germany) as well as N-methyl-2-pyrrolidone (NMP, anhydrous, BASF SE, Germany) at a solid content of 61 wt% in a planetary centrifual mixer (ARE250, Thinky Corp., Japan). In a first step, C65, PVDF, and NMP were mixed for 30 min before the NCM powder was added and mixed for a subsequent 10 min.

The slurries were coated onto aluminum foil (20 µm, Nippon, Japan) with a box-type coater (wet-film-thickness: 100 µm, width: 6 cm, Erichsen, Germany) using an automatic coating table (5 mm/s, Coatmaster 510, Erichsen, Germany). All electrode sheets were then dried in a vacuum oven at 120 °C for 12 h before being calendered to a target value of 3.0 g_{NCM}/cm^3 (corresponding to an electrode thickness of 24 µm and a porosity of 32 %), using a laboratory calender (CA5, Sumet, Germany) with non-heated rolls (i.e., at room temperature) and a line pressure of 30 N/mm. Cathode working electrodes (WEs) with a diameter of 11 mm and 14 mm were punched out, having a loading of 7.5 ± 1.0 mg_{NCM}/cm$^2_{WE}$ (the CAM loading of individual electrodes was determined with an accuracy of ±0.01 mg_{NCM}/cm$^2_{WE}$). For the counter electrodes, LTO ($Li_4Ti_5O_{12}$) electrodes with a diameter of 11 mm and 15 mm were punched out from commercially available LTO electrode sheets (LTO on aluminum, 3.5 mAh/cm^2, Custom Cells, Germany). All electrodes were vacuum-sealed and transferred without further exposure to air to an argon-filled glove box (<1 ppm O_2 and H_2O, Jacomex, Germany) where all cells were assembled.

Cell assembly.—In preparation of the cycling experiments, capacitively oversized LTO electrodes (3.5 mAh/cm^2, Ø 11 mm for Swagelok T-cells and Ø 15 mm for CR2032-type coin cells) were pre-lithiated in coin cells to a state of charge (SOC) of ∼10 %SOC, using a single glass fiber separator (Ø 17 mm, 675 µm nominal thickness, GF/D, VWR, Germany), 95 µl of LP57 electrolyte (1 M LiPF$_6$ in EC:EMC 3:7 w/w, <20 ppm H_2O, BASF SE, Germany), and a metallic lithium counter electrode (Ø 16 mm, 580 µm thickness, Gelon, China): after one full formation cycle at 30 mA/g_{NCM} between 1.2 V_{Li} and 2.0 V_{Li}, the LTO electrodes where lithiated to ∼10 %SOC at a specific current of 30 mA/g_{LTO} for 0.5 h. After pre-lithiation, the LTO electrodes were harvested from the cells and used as the counter electrode (CE) in the pseudo full-cells for the electrochemical cycling tests (note that pseudo full-cell here refers to a cell with a specific working electrode and a capacitively oversized, pre-lithiated LTO counter electrode). As it was discussed previously,[34] the use of a pre-lithiated, capacitively oversized LTO counter electrode provides: i) a stable half-cell potential of 1.55 V_{Li} over a wide SOC window; ii) a sufficiently large capacity to take up the lithium from the investigated NCM working electrodes; and, iii) an excess of lithium to compensate any lost lithium due to side reactions during cycling, thereby allowing to fully lithiate the working electrodes for the EIS measurements (i.e., for bringing the working electrodes into so-called blocking conditions).

For the electrochemical cycling tests with a µ-RE, spring-compressed Swagelok T-cells with capacitively oversized, pre-lithiated LTO as the counter electrode (Ø 11 mm) and NCM as the

working electrode (Ø 11 mm) were assembled using two glass fiber separators (Ø 11 mm, 240 µm nominal thickness, GF/A, VWR, Germany) and 60 µl of LP57 electrolyte. Between the two separators, a µ-RE was placed, namely a gold-wire reference electrode (GWRE) based on the setup described by Solchenbach et al.,[43] whereby the GWRE was lithiated in situ at 150 nA over 1 h from the LTO counter electrode before cycling (note that the GWRE lithiation charge of ∼0.15 µAh is negligible compared to the capacity of the counter electrode). This establishes a constant GWRE potential of 0.31 V_{Li}, which remains stable for more than 450 h. For details about the cell setup and the preparation of the gold wire, please refer to the original publication.[43]

For the electrochemical cycling tests without µ-RE, coin cells (CR2032, Hohsen Corp., Japan) with either capacitively oversized pre-lithiated LTO (Ø 15 mm) or lithium metal (Ø 16 mm) as counter electrode and NCM as working electrode (Ø 14 mm) were assembled using one GF/D type glass fiber separator and 95 µl of LP57 electrolyte. An overview of the configuration of the various cells with an NCM working electrode is displayed in Table I. In addition, symmetric coin cells using lithium metal (Ø 16 mm) for both electrodes were assembled using one glass fiber separator (Ø 17 mm, 240 µm nominal thickness, GF/A, VWR, Germany) and 95 µl of LP57 electrolyte, what allowed to determine the impedance of lithium metal electrodes upon stripping and plating during extended cell cycling. No pretreatment was carried out on the lithium metal surface before cell assembly.

Impedance spectroscopy.—All electrochemical impedance spectra (EIS) were included directly into the cycling procedure and recorded in a climate chamber (Binder, Germany) at 25 °C. For the experiments performed with a multi-channel potentiostat VMP3 (BioLogic, France), all spectra were recorded in potentiostatic mode (PEIS), with an amplitude of 15 mV for 8 points per decade from 100 kHz to 100 mHz, including a data point at a frequency of 180 mHz. This results in an acquisition time of ∼10 min per PEIS. For the T-cells, each EIS spectrum consists of a full-cell spectrum (between working and counter electrode) and, by using a GWRE, also of the half-cell spectrum (i.e., between the working and the micro-reference electrode). Note that measurements with the GWRE potentially contain artifacts at frequencies over 30 kHz;[44] however, as this work is focused on the low frequency region of the impedance spectra, in particular on the 180 mHz point, the impedance spectra obtained with the GWRE can be used without restrictions.

For the cycling experiments performed with a multi-channel battery cycler (Series 4000, Maccor, USA), the impedance was recorded for a single frequency point in galvanostatic mode (GEIS). For this purpose, an alternating current was simulated by applying a sine-like current-step function changing the current every 100 ms. Thus, the duration of a single sine-like current excitation was set to 5.6 s, resulting in a frequency of 178.56 mHz, which will be rounded to 180 mHz in the following for better readability. The current amplitude corresponded to a rate of C/50 (4 mA/g_{NCM}) for all battery cells. The sine-like current perturbation was repeated for 40 periods, resulting in a total duration of 224 s. The current perturbation and the voltage response of period 10 to 30 were fitted to a sine curve. The

resulting fitting parameters were then used to calculate the complex impedance.

For comparison of the impedance recorded with the potentiostat and with the battery cycler, three replicas each of a 1 mF electrolytic capacitor (±20 % tolerance, KEMET, USA) and a 10 mF super-capacitor (−20 %/+80 % Tolerance, KEMET, USA) were tested by PEIS using the Biologic potentiostat (by the parameters described above) as well as by a single-point GEIS measured at the Maccor battery cycler at a frequency of 180 mHz. For the latter, the current amplitudes were set to 0.02 mA (1 mF) and to 0.2 mA (10 mF), respectively. Before each measurement, the capacitors were left to rest in the climate chamber for at least 2 h for temperature equilibration.

Cell testing.—All electrochemical cycling tests were performed in a climate chamber (Binder, Germany) at 25 °C, using either a multi-channel potentiostat with full EIS capabilities (VMP3, Biologic, France) or a multi-channel battery cycler without integrated impedance capabilities (Series 4000, Maccor, USA), applying similar charge/discharge procedures. When using T-cells with a μ-RE, the GWRE was lithiated using the pre-lithiated, capacitively oversized LTO counter electrode (see above) prior to starting any cycling procedures. Throughout this study, voltages are given either in terms of the cell voltage in case of NCM/Li and Li/Li cells (labeled as V_{Li}) or, in the case of NCM/LTO cells, as cell voltage corrected for the potential difference between the LTO electrode and a lithium metal electrode ($V_{Li} \equiv V_{NCM/LTO} + 1.55$ V).

To acquire EIS spectra under so-called *blocking conditions*, represented by a semi-infinite charge-transfer resistance, the NCM working electrode is cycled to the fully discharged state at a potential of 2.55 V_{Li}, i.e., to nearly full lithiation (that this results in blocking conditions is shown in a previous study[34]).

The long-term cycling procedure (shown exemplarily in Fig. 4a for the first few cycles of Z_{cell}-Li-M, using lithium as counter electrode and cycled at the Maccor battery cycler, see Table I) was initiated by an open circuit voltage (OCV) phase of 2 h. To identify the *pristine* value of the NCM electrode capacitance, the NCM working electrode was discharged at C/10 ($\equiv$20 mA/g_{NCM} or ~0.15 mA/cm²$_{WE}$) from OCV to the lower cutoff potential of 2.55 V_{Li} (shown as the first step from OCV to "pristine" in Fig. 4a), where a constant voltage (CV) hold was performed (referred to as CCCV mode, always with either a 1 h CV hold when using the Biologic potentiostat or until the current dropped below C/250 when using the Maccor battery cycler), followed by an EIS. During *conditioning* (shown as the steps from "pristine" over point A to point B in Fig. 4a), the electrodes were charged at C/10 in constant current (CC) mode for 1 h, then discharged to the lower cutoff potential of 2.55 V_{Li} at C/10 in CC mode, where again a CV hold of 1 h (Biologic) or until the current dropped below C/250 (Maccor) was performed (shown as the step from point B to #0 in Fig. 4a), followed by an EIS (point #0 for cycle 0). Since nickel-rich CAMs are commonly slightly overlithiated (by up to 1 %) in the synthesis process, the conditioning step was included in the procedure to ensure comparable impedance spectra for each cycle, namely by assuring that similar SOCs are obtained by the potential hold at 2.55 V_{Li} (especially critical when comparing different NCM active materials). For the consecutive *formation*, three charge/discharge cycles are executed, with a charge to the upper cutoff potential of 4.3 V_{Li} at C/10 (in CC mode), and with a discharge to a lower cutoff potential of 2.55 V_{Li} at C/10 with a final CV hold before an EIS was recorded (marked by the #1 point in Fig. 4a for the first formation cycle, referred to as cycle 1). The formation was followed by an extended *cycling* procedure that consisted of five cycles per set: (i) cycling four times at 1C ($\equiv$200 mA/g_{NCM} or ~1.5 mA/cm²$_{WE}$) in CCCV mode (either for 30 min or until the current drops below C/10 at 4.3 V_{Li}) for charge and in CC mode to 3.0 V_{Li} for discharge; (ii) a fifth cycle performed at C/10, followed by a CV hold at 2.55 V_{Li} and an EIS (i.e., identical to the formation cycles). This set of five cycles was repeated for 65 charge/discharge

cycles. The impedance spectra taken in blocking conditions are numbered by the number of full cycles that the electrodes had performed up to that point (e.g., #8 after three formation cycles and one set of five cycles).

A similar cycling procedure was applied for the symmetric lithium-lithium cells cycled with the Biologic potentiostat (shown in Fig. A·1): After an OCV period of 1 h and an initial PEIS at OCV in the pristine state, the cells were charged for 1 h and discharged for 1 h at a current of 0.30 mA (corresponding to 0.15 mA/cm²$_{Li}$ (similar to the areal current of 0.18 mA/cm²$_{WE}$ in the NCM cells), mimicking the conditioning step of the NCM cells (C/10) with lithium metal counter electrode), both charge and discharge followed by a rest step of 1 h and a PEIS. During three formation cycles, the cells were charged for 10 h and discharged for 10 h at a current of 0.30 mA, while both charge and discharge were completed by a 1 h OCV period and a PEIS. During cycling, the cells were charged for 1 h and discharged for 1 h, both at a current of 3.0 mA for four cycles (mimicking the cycling of the NCM cells at 1C) and at a current of 0.30 mA for a single charge/discharge cycle, whereby after each set of four cycles at 3.0 mA and one cycle of 0.30 mA, an OCV period of 1 h and a PEIS is added, similar to the formation cycles. This set of five cycles was repeated for 65 charge/discharge cycles. The impedance spectra are numbered by the number of full cycles that the cell had performed up to that point (e.g., #8 after three formation cycles and one set of five cycles).

Results and Discussion

Comparison of impedance contributions.—As proven in part I of this study,[34] the capacitance of the electrochemical double layer of the components of a battery electrode is proportional to their respective electrochemically active surface areas. To be able to extract the cathode electrode capacitance, it is required to increase the charge-transfer resistance to semi-infinite values (i.e., into blocking conditions). To achieve this, the NCM electrodes were fully lithiated, resulting in a capacitive branch of the electrode/electrolyte interface dominating the impedance spectra for medium to low frequencies (<100 Hz), a region in which contributions of other effects (e.g., of the pore resistance) are negligible.[45,46] Further, it was demonstrated that it is not necessary to extract the electrode capacitance from a fit of the impedance data by an equivalent circuit, but that it is possible to calculate the electrode capacitance Q from the imaginary impedance $\text{Im}(\mathbf{Z}_{\omega_0})$ of a single frequency point at $\omega_0 = 180$ mHz using the following formula:[34]

$$Q \approx \frac{1}{\omega_0 \cdot (-\text{Im}(\mathbf{Z}_{\omega_0}))} \quad [1]$$

This approximation for the electrode capacitance is possible solely since, at this frequency of 180 mHz, the imaginary impedance of a constant-phase element (CPE) and, therefore, of the extracted capacitance does not vary significantly with the phase angle α (error of <1 % if $\alpha > 0.85$). As it was shown in part I of this study, frequencies in the range of 160 to 220 mHz are suitable to be used with Eq. 1, while the optimal value depends on the expected/determined values for the phase angle of the investigated electrode as well as on the desired accuracy.[34] In this study, the value of 180 mHz is used for better comparability with the previous reports.

The imaginary impedance of an NCM electrode with a loading of ~10 mg/cm²$_{WE}$ at 180 mHz was reported to be on the order of $-\text{Im}(\mathbf{Z}_{NCM}) = 700$–1000 Ω·cm²$_{WE}$ in the pristine state and on the order of $-\text{Im}(\mathbf{Z}_{NCM}) = 200$-300 Ω·cm²$_{WE}$ after 200 cycles to 4.5 V_{Li} or after being cycled to high states of charge (SOCs),[34,35] depending on mass loading and electrode composition. In order to utilize this method in a cell configuration without reference electrode, where only the impedance of the entire cell can be determined instead of the individual electrode impedances that are accessible with a μ-RE, the relative contributions of the imaginary impedance of working
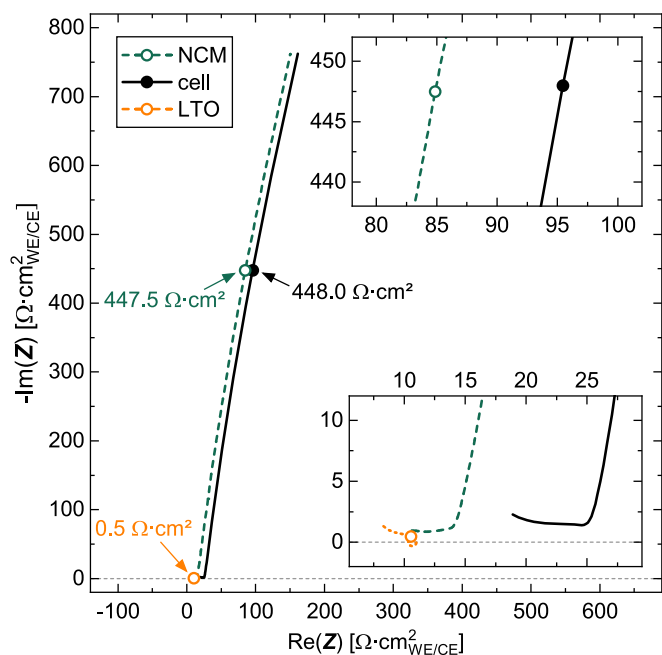
Figure 1. Nyquist plot of the impedance data acquired with the Z_{NCM}-LTO-B cell (see Table I) after the conditioning step (corresponding to cycle #0, following the procedure displayed in Fig. 4a), showing the impedance spectra of the NCM working electrode (dark green), of the capacitively oversized pre-lithiated LTO counter electrode (orange), as well as of the entire cell (black), all normalized to the geometrical surface area of the cell (0.94 $cm^2_{WE/CE}$). The frequency points at 180 mHz are indicated by circles and the respective values of the imaginary impedance are marked by the arrows. The insets magnify the region near the frequency point of 180 mHz for the cell and NCM impedance (upper panel) and for the LTO impedance (lower panel). Pseudo full-cells were assembled with 60 μl LP57, two glass fiber separators, and a μ-RE, and cycled at 25 °C. Impedance spectra were acquired between 100 kHz and 100 mHz (15 mV amplitude) with the NCM working electrode being in blocking conditions, achieved after a potential hold of 1 h at 2.55 V_{Li}.

and counter electrode need to be evaluated for the frequency point of 180 mHz.

Figure 1 shows the impedance spectra acquired with the Z_{NCM}-LTO-B cell (see Table I) at 2.55 V_{Li} for cycle #0 (after the conditioning step), presenting the impedance of the entire cell (black line) as well as the one of the individual contributions of the NCM (dashed dark green line) and the LTO electrode (dashed orange line). Both the cell impedance as well as the NCM impedance show a capacitive branch, whereby the cell impedance is mainly shifted to larger real impedance values by ∼10 $\Omega \cdot cm^2$; the imaginary impedance at 180 mHz (marked by the circles in Fig. 1), however, is similar for both, namely -Im(Z_{cell}) = 448.0 $\Omega \cdot cm^2_{WE/CE}$ for the entire cell and -Im(Z_{NCM}) = 447.5 $\Omega \cdot cm^2_{WE}$ for the NCM electrode only. The difference in the real as well as in the imaginary impedance is solely owed to the additional contribution of the LTO counter electrode, which at 180 mHz has impedance values of Re(Z_{LTO}) = 10.6 $\Omega \cdot cm^2_{CE}$ and -Im(Z_{LTO}) = −0.5 $\Omega \cdot cm^2_{CE}$. The impedance loop observed for the impedance spectrum of the LTO counter electrode originates from the inherent difference of anode and cathode impedance of more than three orders of magnitude, which induces artifacts when utilizing a μ-RE.[47]

As the contribution of the LTO counter electrode is not altered significantly upon cycling (<0.1 $\Omega \cdot cm^2_{CE}$ in imaginary direction and <0.5 $\Omega \cdot cm^2_{CE}$ in real direction, data not shown), and as the negative imaginary impedance of the NCM working electrode at 180 mHz does not decrease below 200 $\Omega \cdot cm^2_{WE}$ in all of the measurements presented in this study (as well as in the ones of part I and part II of this study), the relative contribution of the imaginary impedance of the LTO counter electrode in comparison to the one of the entire cell

does not exceed 0.3 %. This finding allows for a reasonably accurate estimation of the capacitance of the NCM electrode from the impedance measurement of the entire cell, enabling the elimination of the μ-RE for the setup with an LTO counter electrode.

Since a full lithiation of the NCM active material is required to achieve blocking conditions for the NCM working electrode,[34] a lithium reservoir is needed in the counter electrode. Therefore, counter electrodes such as pre-lithiated graphite or LTO, pre-delithiated LFP, or even lithium metal might fulfill these prerequisites. However, the magnitude of their imaginary impedance value at 180 mHz needs to be sufficiently low to assure that their contribution to the total impedance of the entire cell is negligible. Due to the lithium loss upon solid-electrolyte interphase (SEI) formation, the use of pristine graphite is here therefore not possible.

Impedance of lithium metal.—As half-cells are easy to build and most used for the initial characterization of active materials, lithium metal is investigated as possible counter electrode for the capacitance measurements in a coin cell without reference electrode. To mimic the cycling procedure to which the lithium metal electrode is subjected in the later discussed NCM/Li cells, a similar protocol with corresponding areal currents is applied to the symmetric Li/Li cells. This procedure includes "C/10" cycles at 0.30 mA ($\equiv$ 0.15 mA/cm^2_{Li}) and "$1C$" cycles at 3.0 mA ($\equiv$ 1.5 mA/cm^2_{Li}), as it is depicted in Fig. A·1 (note that, even though no value for the cell capacity was assigned for the symmetric Li/Li cells, the C-rates in quotation marks refer to the corresponding C-rates that would be applied in an NCM/Li cell based on the mass loading of the NCM electrodes used in this study).

Figure 2 presents the impedance spectra of lithium metal cycled in a symmetric cell with LP57 electrolyte, divided by a factor of 2 to obtain the impedance of one electrode from the symmetric cell setup and normalized to the geometric surface area of one lithium metal electrode (2.0 cm^2_{Li}), resulting in the areal impedance of one lithium metal electrode only (including 50 % of the separator resistance). The spectrum of the pristine cell (black) shows a large semicircle at high to medium frequencies, with an apex of -Im(Z) = 60 $\Omega \cdot cm^2_{Li}$ at 376 Hz, and a substantially smaller semicircle at low frequencies that is partially overlapped by the large semicircle; the large semicircle is typically attributed to the charge transfer through a compact SEI and the small semicircle potentially stems from the diffusion of lithium ions through a porous SEI.[48] The observed high-frequency resistance (HFR, measured at 100 kHz) of 10 $\Omega \cdot cm^2_{Li}$ is due to the ohmic resistance of the electrolyte in the porous separator.[45] The frequency point at 180 mHz (marked by the empty circle) shows an imaginary impedance of -Im(Z) = 2.7 $\Omega \cdot cm^2_{Li}$.

After the conditioning step at 0.30 mA ("C/10") (dark blue, corresponding to cycle #0), the imaginary impedance contribution of the apex of the large semicircle has reduced in magnitude by 38 % to -Im(Z) = 37 $\Omega \cdot cm^2_{Li}$, what we assign to an increasing surface area of the lithium metal electrodes upon formation of dendrites and cavities.[48,49] This trend further continues during the repeated lithium stripping and plating of the subsequent cycles at 3.0 mA ("$1C$"). Up to cycle #8 (turquoise), the negative imaginary impedance maximum has already decreased to -Im(Z) = 4.4 $\Omega \cdot cm^2_{Li}$, whereas the HFR stays constant. Starting at cycle #28 (green), only one full semicircle is visible in the applied frequency range, whereas the onsets of two other ones appear at lower and higher frequency: for both cycle #28 and #48 (dark green), the visible semicircle shows a negative imaginary impedance maximum of -Im(Z) = 2.0 $\Omega \cdot cm^2_{Li}$ and 2.2 $\Omega \cdot cm^2_{Li}$, respectively, which then increases to -Im(Z) = 8.6 $\Omega \cdot cm^2_{Li}$ for cycle #68 (brown). The HFR, however, initially undergoes a slight increase (cycle #3: 10 $\Omega \cdot cm^2_{Li}$; #8: 11 $\Omega \cdot cm^2_{Li}$; #28: 20 $\Omega \cdot cm^2_{Li}$) but then starts to significantly rise in the following cycles (#48: 47 $\Omega \cdot cm^2_{Li}$; #68: 205 $\Omega \cdot cm^2_{Li}$).

This behavior is reflected in the lithium/lithium cell voltage extracted from the measured voltage profile shown in Fig. A·1, which, even though the applied currents are constant for the "$1C$" and "C/10" cycles, respectively, starts to increase drastically starting after cycle
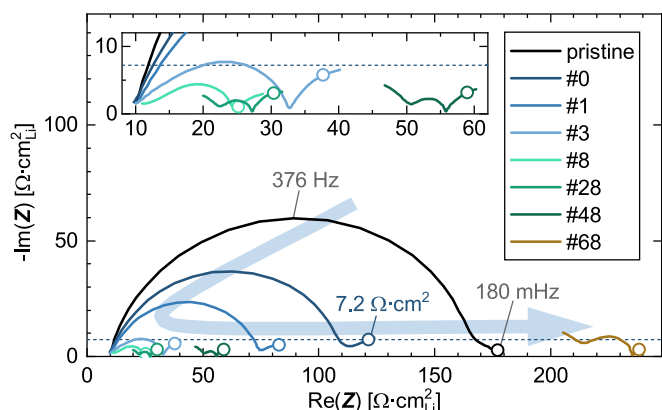
Figure 2. Nyquist plot of the impedance spectra of a symmetric lithium/lithium cell upon cycling at 25 °C (following the procedure displayed in Fig. A·1), whereby the impedance values were divided by a factor of 2 to obtain the value of one electrode only and were further normalized to the geometrical surface area of one lithium metal electrode (2.0 cm²$_{Li}$). The frequency points at 180 mHz are indicated by empty circles, and the imaginary impedance of 7.2 Ω·cm² is marked by the horizontal dashed dark blue line. The inset magnifies the low-impedance region of the spectra between cycle #3 and #48. Coin cells were assembled with lithium metal as both electrodes, with 95 μl LP57 electrolyte, and one glass fiber separator.

#28: At "*C*/10" (≡ 0.30 mA or 0.15 mA/cm²$_{Li}$), the cell voltage required to drive the applied current decreases during the three formation cycles from ~0.05 V during the conditioning to ~0.02 V during cycle #3, correlating with the initial impedance decrease. Starting at cycle #28, the cell voltage starts to increase from 0.01 V to a maximum of 0.11 V in cycle #68. This overpotential increase is even better visible for the "1*C*" cycles (≡ 3.0 mA or 1.50 mA/cm²$_{Li}$): here, the overpotential increases from 0.16 V (#7) to 0.20 V (#27), to 0.38 V (#47), all the way to 1.34 V (#67).

When calculating the effective lithium/lithium cell resistance from the potential drop of 0.073 V (from -0.119 V to −0.046 V) after 1 s at the end of "discharge" for cycle #68 at a current of 0.30 mA (as it is done for direct current internal resistance (DCIR) measurements), a value of 243 Ω is obtained. This equates to an areal cell resistance of 486 Ω·cm²$_{Li}$ (based on the area of the lithium electrodes of 2.0 cm²$_{Li}$) or, if referenced to the resistance of only one of the two lithium electrodes, to 243 Ω·cm²$_{Li}$. As the lowest frequency of 100 mHz in the EIS measurements shown in Fig. 2 corresponds to a time constant of $T = 1/\omega = 1/2\pi f \approx 1.6$ s, the above determined effective cell resistance is in good agreement with the measured low-frequency resistance (LFR, measured at 100 mHz) of 240 Ω·cm²$_{Li}$ for cycle #68 (see brown spectrum in Fig. 2).

We assign the initial decrease of the magnitude of the real and imaginary impedance to the increase of the surface area upon plating and stripping of lithium metal, i.e., to the commonly observed formation of a porous or mossy lithium surface.[48,50,51] In addition, however, the repeated deposition and stripping of lithium upon cycling continuously produces a fresh lithium metal surface, concomitant with a continuous reduction of electrolyte components for the formation of the SEI. Therefore, we believe that the drastic increase of the HFR is caused by the decomposition of the alkyl carbonate electrolyte solvents, resulting in large amounts of porous SEI and eventually leading to electrolyte dry-out.[52,53]

Nevertheless, the magnitude of the imaginary impedance value at a frequency of 180 mHz (marked by the empty circles in Fig. 2) never exceeds the value of 7.2 Ω·cm²$_{Li}$ (marked by the horizontal dashed dark blue line) that is observed for cycle #0 during the entire cycling procedure up to cycle #68. Therefore, the contribution of a lithium metal counter electrode to the imaginary impedance at 180 mHz of an NCM/Li cell is <4 % for the here observed imaginary

impedance of the NCM working electrode of >200 Ω·cm²$_{WE}$. In turn, this means that the NCM capacitance determined from the cell impedance by using -Im(Z_{cell}) at 180 mHz in Eq. 1 (i.e., not requiring a reference electrode) would differ by <4 % from the more accurate NCM capacitance value determined from -Im(Z_{NCM}) at 180 mHz that can only be obtained for a cell setup with a μ-RE. Thus, a reasonably accurate quantification of a CAM working electrode can be obtained from the cell impedance of a CAM/Li half-cell, if the negative imaginary impedance at 180 mHz is on the order of >200 Ω·cm²$_{WE}$ (assuming similarly sized working and counter electrode sizes).

Validation of battery cycler impedance by commercial capacitors.—Due to the higher price and the limited availability of potentiostats built for impedance spectroscopy as compared to conventional battery cyclers that usually have no built-in impedance capability, it would be convenient to be able to measure the impedance at the frequency point of 180 mHz using a simple battery cycler, as this would allow for a reasonably accurate quantification of the CAM capacitance from CAM/Li half-cells during the screening of new CAMs. For this purpose, an alternating current was simulated at the Maccor battery cycler by applying a sine-like current-step function with which the current is changed every 100 ms. To validate this approach, the impedance of two types of commercially available capacitors was obtained with the Maccor battery cycler and compared to the precise value determined with the Biologic potentiostat, both depicted in Fig. 3.

Figure 3a shows the measurement data obtained by the Maccor battery cycler (empty circles) and the mathematical fit (line) of the current-step based perturbation (blue) with an amplitude of 0.02 mA and a frequency of 180 mHz applied to one of the electrolytic capacitors. The respective voltage response (red) is delayed as compared to the current and shows an amplitude of ~19 mV oscillating around an OCV of −40 mV. To calculate the complex impedance of the received signal, data processing was done by fitting the modulated current and the voltage response to a sine curve. This was done by first subtracting a baseline from the signal to account for voltage drifts by calculating a floating average of the voltage with the bandwidth of one sine period (target value: 180 mHz, effectively 5.6 s at 178.56 mHz). After subtraction, the current and the voltage were fitted to Eqs. 2 and 3, respectively, using an applied frequency of $\omega_0 = 2\pi f_0 = 2\pi \cdot 178.58$ Hz, yielding the fitting parameters for the current amplitude (I_0), the voltage amplitude (U_0), as well as the phase of current (φ_I) and voltage (φ_U). The relative phase shift was calculated by $\varphi_0 = \varphi_U - \varphi_I$.

$$I(t) = I_0 \cdot \sin(\omega_0 t + \varphi_I) \quad [2]$$

$$U(t) = U_0 \cdot \sin(\omega_0 t + \varphi_U) \quad [3]$$

From the fit in Fig. 3a, the relative phase shift φ_0 of the two curves was identified to correspond to −1.39 s for the electrolytic capacitor, equating to approximately −π/2 or −90° (precisely −89.4°), considering the duration of a period of 5.56 s. From the fitting parameters I_0, U_0, and φ_0, the real and the imaginary impedance were calculated by the following formula:

$$\boldsymbol{Z} = \frac{|U_0|}{|I_0|} \cdot e^{i\varphi_0} = \frac{|U_0|}{|I_0|} \cdot \cos(\varphi_0) + i \cdot \frac{|U_0|}{|I_0|} \cdot \sin(\varphi_0)$$
$$= \text{Re}(\boldsymbol{Z}) + i \cdot \text{Im}(\boldsymbol{Z}) \quad [4]$$

The calculated impedance values at 180 mHz obtained for the electrolytic capacitors by the Maccor battery cycler are depicted in Fig. 3b (empty triangles), together with the impedance spectra collected using the Biologic potentiostat (line), including the respective value at 180 mHz (empty circles). The impedance of the electrolytic capacitors consists of a vertical line through the origin (corresponding to a phase shift of $\varphi_0 = -90°$, as it would be expected for an ideal parallel-plate
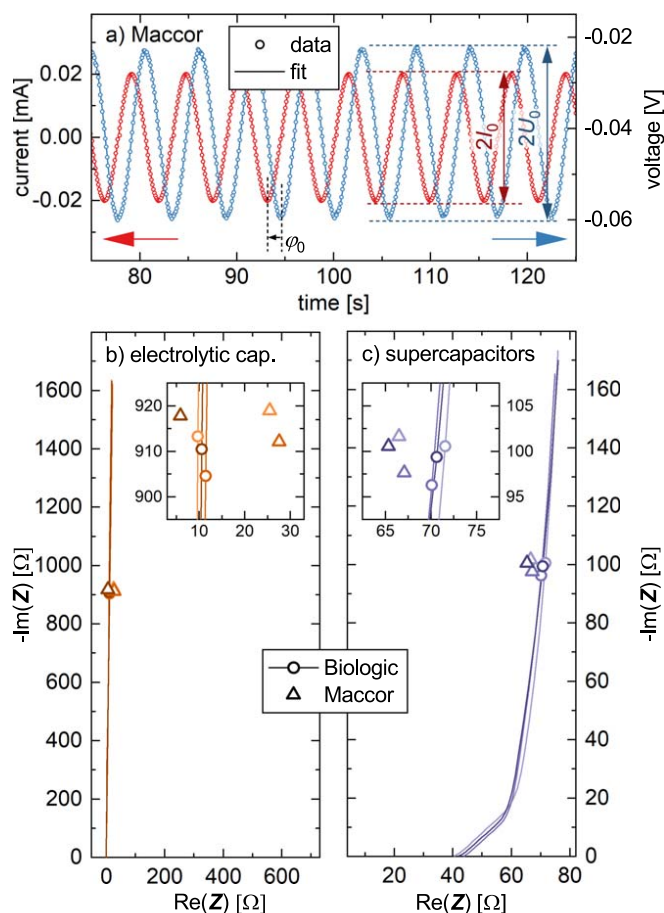
Figure 3. Impedance data of three replicas each of a 1 mF electrolytic capacitor as well as of a 10 mF supercapacitor at OCV and 25 °C, determined by PEIS with an amplitude of 15 mV from 100 kHz to 100 mHz using the Biologic potentiostat as well as by a single-point GEIS at 180 mHz with an amplitude of 0.02 mA for the electrolytic capacitor and 0.2 mA for the supercapacitor using the Maccor battery cycler. **a)** Measurement data (empty circles) and mathematical fit (line) of the current-step-based perturbation (blue) and the voltage response (red) of an electrolytic capacitor measured at 180 mHz with the Maccor battery cycler. The relative phase shift as well as the twofold amplitudes of current (I_0) and voltage (U_0) are marked by the dashed lines and the arrows. Nyquist plots of **b)** the electrolytic capacitors (three shades of ocher) and of **c)** the supercapacitors (three shades of violet), showing the PEIS data (Biologic, lines) including the frequency point at 180 mHz (empty circle) as well as the GEIS data at 180 mHz (Maccor battery cycler, empty triangles).

capacitor). The impedance obtained at the Biologic potentiostat at 180 mHz shows a real value of $\text{Re}(\mathbf{Z}) = 10.5 \pm 0.9\ \Omega$ and an imaginary value of $-\text{Im}(\mathbf{Z}) = 909 \pm 4\ \Omega$, which we believe to be more precise owed to an instrument architecture that is optimized for impedance measurements. At the Maccor battery cycler, the impedance shows a real value of $\text{Re}(\mathbf{Z}) = 16.8 \pm 10.9\ \Omega$ and an imaginary value of $-\text{Im}(\mathbf{Z}) = 915 \pm 3\ \Omega$. The larger scatter of the real value is attributed to small errors in the obtained phase shift: As the value of the real impedance is relatively small at a phase angle of around $\pm 90°$ whereas the imaginary value is relatively large, small deviations of the phase angle lead to a large relative error of the real impedance value, as it is proportional to $\cos(\varphi_0)$. In contrast, the obtained imaginary value (proportional to $\sin(\varphi_0)$) is not affected significantly by small errors in the phase angle, as already discussed in part I of this study.[34]

In turn, however, if a relatively large shift of the capacitive branch in the real direction would occur (possibly due to, e.g., a large contact resistance of uncompressed electrodes, ohmic resistances of the setup, etc.), the phase angle of the impedance vector φ_0 for the 180 mHz point would become smaller (i.e., $0 < \varphi_0 \ll \pi/2$). Hence, a certain

error in the determination of the phase angle at the Maccor could lead to significant deviations of the extracted imaginary impedance value and, therefore, of the capacitance. Even though this seems unlikely in practical cases, as the real part of an electrode/cell should be low for a proper application, the extent of this compromise is dependent on the parameters of the systems and on the precision of the measurement. To exclude any erroneous interpretation of the collected impedance data, it is recommended to evaluate both imaginary and real value of the impedance at 180 mHz to be able to estimate any introduced errors.

By using Eq. 1, the capacitance of the electrolytic capacitors is obtained from the frequency points at 180 mHz, yielding similar values of 0.972 ± 0.003 mF (standard deviation based on three capacitor replicas) using the Maccor battery cycler and of 0.980 ± 0.004 mF using the Biologic potentiostat. The deviation between the measured values and the nominal value of 1 mF is well within the tolerance of the specified capacity of the electrolytic capacitor ($\pm 20\ \%$).

The impedance spectra of the three replicas of the supercapacitors (depicted in Fig. 3c) include a high-frequency resistance (owed to the ohmic resistance of the electrolyte), a 45° line at medium frequencies (attributed to the ionic electrolyte resistance within the pores of the carbon electrodes),[45] as well as a capacitive branch at low frequencies in the form of a constant-phase element with a phase angle of $\alpha \approx 0.95$.[54] It thus exhibits similar features as one would observe with porous battery electrodes.[46,55] The obtained imaginary values at a frequency of 180 mHz are $-\text{Im}(\mathbf{Z}) = 100 \pm 2\ \Omega$ using the Biologic potentiostat and $-\text{Im}(\mathbf{Z}) = 98 \pm 2\ \Omega$ using the Maccor battery cycler; based on Eq. 1, the resulting values for the capacitance of the supercapacitors are 9.0 ± 0.2 mF using the Biologic potentiostat and 8.9 ± 0.2 mF using the Maccor battery cycler. The deviation between these measured capacitances and the nominal value of 10 mF is well within the specified product tolerance of $-20\ \%/+80\ \%$.

To summarize the above discussion, it can be stated that the relative error of the capacitance values obtained from the current-step-based simulated sine-form current perturbation at 180 mHz with the Maccor battery cycler as compared to the capacitance values obtained with the Biologic potentiostat is found to be $<1.5\ \%$ for both types of capacitors. This demonstrates the feasibility and the validity of the here developed method to determine the cell capacitance with a simple battery cycler by simulating a sine-form current perturbation at 180 mHz using a current-step based procedure that can be easily programmed.

Application in a simplified coin half-cell setup.—After investigation of the applicability of a two-electrode setup with a lithium metal anode for the determination of the NCM electrode capacitance as well as the possibility of conducting the measurement with a simple battery cycler, a "real" cell system will be investigated next. Figure 4a shows the initial OCV, the initial EIS in the pristine state, the conditioning, and the first formation cycle of a coin half-cell with an NCM851005 cathode and a lithium metal anode, conducted with the Maccor battery cycler. After the initial OCV phase, the cell was discharged to 2.55 V_{Li}, where a CV step was applied until the current dropped below $C/250$ (~ 0.0073 mA/cm$^2_{\text{WE}}$). Under the assumption that the residual current at this point is approximately constant over the time frame of several tens of seconds, a sine curve with a current amplitude (i_0) corresponding to $C/50$ (0.036 mA/cm$^2_{\text{WE}}$) was modulated on top of the residual current (marked by *pristine*, with a variation of the current between 0.044 and -0.029 mA/cm$^2_{\text{WE}}$). After the initial PEIS, the cell was charged to ~ 10 %SOC (marked by A), then (Z_{cell}-Li-M, see Table I) discharged to 2.55 V_{Li} (B), where another CV hold at 2.55 V_{Li} (B) and a PEIS (marked by cycle #0) was performed. The cell was then charged (C) and discharged at $C/10$ (first formation cycle, ending at D) before the capacitance test was repeated after another CV hold at 2.55 V_{Li} (marked by cycle #1). Figure 4b shows the enlarged view of the applied current modulation at 180 mHz (via the current-step procedure) and the voltage response after the first formation cycle (cycle #1). Although the average current
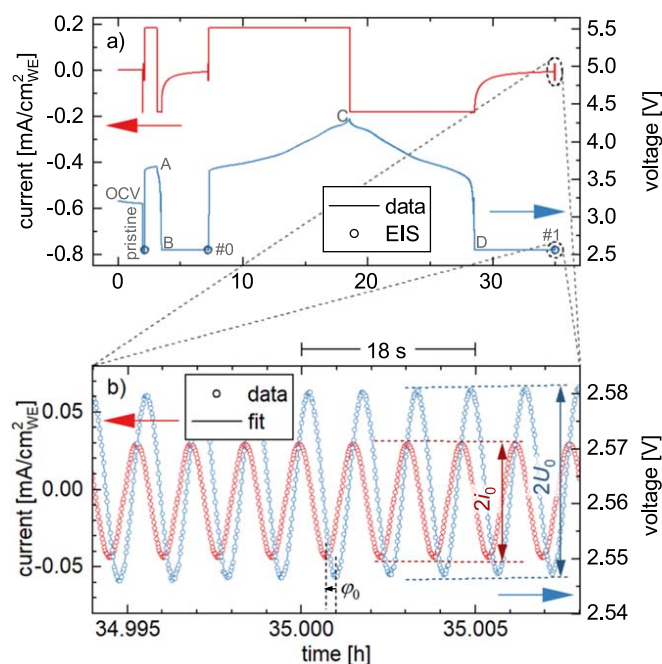
Figure 4. Current and potential profile of the initial cycling in a coin NCM/Li half-cell (Z_{cell}-Li-M, see Table I) measured with the Maccor battery cycler using a current-step simulated sine-form current perturbation with 180 mHz. **a)** Area-normalized current (red, left axis) and voltage (blue, right axis) of the conditioning and first formation cycle. After an OCV period of 2 h, the cell is brought into blocking conditions by discharging to 2.55 V_{Li} in CCCV mode (until the current dropped below $C/250$), after which the capacitance measurement is performed (see main text). In a conditioning step, the cell is then charged to ∼10 %SOC (marked by A), before the cell is again discharged to 2.55 V_{Li} (B), where the capacitance is again determined (marked as cycle #0). The cell is then charged to 4.3 V_{Li} (C) and again discharged (D) for a full formation cycle after which the capacitance is again determined (cycle #1). **b)** Enlarged view of the current perturbation at the end of the first formation cycle. The measured values are shown as empty circles, with the fitted sine curves being shown as solid lines. The area-normalized current amplitude (i_0), the voltage amplitude (U_0), and the phase shift (φ_0) are indicated by arrows.

(i.e., the time-averaged current over the cycles shown in Fig. 4b) is not perfectly zero due to the residual current (of less than $C/250$) (see above), a sine wave voltage response with an amplitude of $U_0 = 17$ mV (between 2.54 V_{Li} and 2.58 V_{Li}, see blue symbols/line) is observed. This value is in good accordance with the voltage amplitude of $U_0 = 15$ mV that was chosen for the PEIS measurements with the Biologic potentiostat, validating the chosen dimension of the current perturbation. The phase shift between current and voltage resulting from the fits of current and voltage to Eqs. 2 and 3, respectively (solid red and blue lines in Fig. 4b) amounts to $\varphi_0 = -62.6°$ (corresponding to a time shift of −0.97 s).

For the 180 mHz impedance measurement performed at the Maccor battery cycler, the current instead of the voltage is controlled, as this turned out to be more feasible for the experiment at this instrument, possibly due to the much faster instrument response rates in galvanostatic operation mode. To get reproducible results for the specific capacitance of the electrodes, the applied current perturbation must be sufficiently small to induce only minor changes (below ±50 mV) on the electrode potential of the previous CV phase, as the double layer capacitance of the electrochemically active materials (CAM, Li, conductive carbon) is potential dependent. Thus, the perturbation current is modulated on top of the base current at the end of the CV phase to stay in the potential range of 2.55 V_{Li}, as otherwise the perturbation would be modulated on top of the OCV relaxation curve. This base current (here: 0.0073 mA/cm$^2_{WE}$) is assumed to stay constant over the

measurement range (40 sine periods à 5.6 s, in total 224 s). However, the residual current at the end of the CV step after the first cycle (cycle #1) still changes at a rate of ∼0.001 μA/s·cm$^2_{WE}$ during impedance measurement at 180 mHz shown in Fig. 4b (corresponding to ∼0.2 μA/cm$^2_{WE}$ over the 40 sine waves). This, in combination with limitations in the hardware of the battery cycler (latency when switching between charge and discharge) leads to a slight drift in the voltage during measurement. This shift was <0.01 V for all performed measurements and was accounted for by the baseline subtraction of the floating average.

Additionally, the difference of time spent at 2.55 V_{Li} in the CV step prior to an impedance measurement needs to be discussed, as the impedance measurements were performed either in potentiostatic mode (PEIS) with the Biologic potentiostat or in galvanostatic mode (GEIS) with the Maccor battery cycler: the average time to reach the cutoff criterion of $C/250$ at 2.55 V_{Li} for the GEIS measurements is on the order of 5 h, in comparison to the 1 h CV hold at 2.55 V_{Li} performed before the PEIS measurements, increasing the experimental time for a set of 5 cycles by ∼15 %. In theory, this longer duration might affect the measurement due to phenomena like calendar aging of the NCM and the lithium metal within the cell.[56,57] In comparison to other occurrences like the continuous SEI growth during lithium metal plating and stripping, this impact is assumed to be negligible.

Similar to conventional EIS measurements performed over the whole frequency range, the single-point GEIS measurement using a current-step-based sine wave modulation is determined by a series of experimental parameters: the voltage where blocking conditions are achieved (here: 2.55 V_{Li}), the time/current over which this voltage is held before the low-frequency modulation happens (here: until the current drops below $C/250$), the applied frequency of the alternating current (here: 180 mHz), and its amplitude (here: $C/50$). Those parameters can be varied and adapted to the individual case as long as certain boundary conditions are still met, e.g., the charge-transfer resistance still being semi-infinitely large. The base current on which the alternating current is applied can be further reduced to decrease the overall measurement time if no severe voltage drift during modulation is observed. The frequency was chosen due to the mathematically small deviation of the constant-phase element in comparison to the behavior of an ideal capacitor, but can be varied in a certain range if this factor is regarded.[34] The amplitude can be adapted to the measured voltage response, so that a proper signal-to-noise ratio is achieved, should however not be increased in a way that the SOC is significantly varied over the range of a single sine excitation. In our view, it might be advantageous if material developers would use battery cyclers having an implemented option to include (potentiostatic and/or galvanostatic) single-frequency impedance points (at relatively low frequency of ∼180 mHz) in testing protocols.

Comparison of the different NCM cell configurations.—Finally, a direct comparison of the capacitance data with different cell and test hardware configurations was realized. When transferring the formerly established approach to determine the CAM capacitance using a T-cell setup with a μ-RE and operated with an impedance-capable potentiostat[34] into an approach based on coin half-cells operated with a simple battery cycler, the impact of the following changes made must be evaluated: (i) moving from a cell setup with a μ-RE to a two-electrode setup without μ-RE; (ii) replacing the pre-lithiated LTO counter electrode with a lithium metal counter electrode; and, (iii) conducting the impedance measurement with a common battery cycler without explicit impedance capability (Series 4000, MACCOR) rather than with a PEIS-capable potentiostat (VMP3, Biologic). Table I gives an overview of the cells built for this purpose.

Figure 5a shows the Nyquist plot of all cell combinations at 2.55 V_{Li} after the initial conditioning step (cycle #0). The cathode impedance spectrum measured by the T-cell setup with μ-RE at the Biologic potentiostat (cell Z_{NCM}-LTO-B; as originally described in
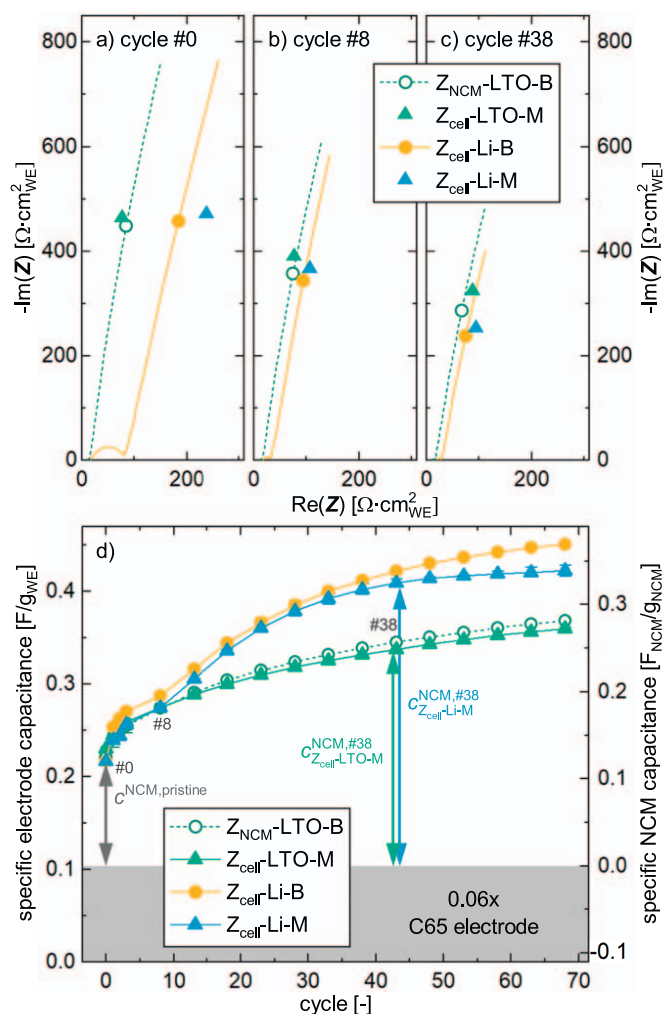
Figure 5. Impedance spectra and specific capacitance vs. cycle number for the four different combinations of cell setups and measurement modes, all based on an NCM working electrode (specified in Table I). Nyquist plots recorded in blocking conditions shown after **a)** initial conditioning (cycle #0), **b)** after cycle # 8, and **c)** after cycle #38. For the cells measured at the Biologic potentiostat, the measurement over the whole frequency range is given by the dashed dark green line (T-cell with μ-RE and LTO anode: Z_{NCM}-LTO-B) and by the yellow solid line (coin cell with a lithium metal anode: Z_{cell}-Li-B), with the 180-mHz frequency points highlighted as circles. For the measurements done at the Maccor battery cycler using a current-step-based sine wave modulation at 180 mHz, the impedance at 180 mHz is given as green triangle for the coin cell with the LTO anode (Z_{cell}-LTO-M) and as blue triangle for the coin cell with the lithium metal anode (Z_{cell}-Li-M). **d)** Specific electrode capacitance in units of F/g_{WE} (left y-axis) and the specific NCM capacitance in units of F_{NCM}/g_{NCM} (right y-axis), both as a function of the cycle number, shown for the NCM working electrode for the T-cell with μ-RE or for the entire cell for the coin cells. The gray box indicates the contribution of the binder-carbon mixture of 0.104 F/$g_{electrode}$ to the total capacitance. The specific capacitance of the NCM (right y-axis) was obtained by subtracting the contribution of C65 and PVDF from the value of the entire electrode, schematical shown by the arrows in cycle #0 and #38, and subsequently normalizing it to the NCM mass contribution (of 94 wt%) in the electrode. The values of the capacitance shown here are calculated from the mean of two identical cell pairs and the error bars correspond to the minimum/maximum value of two measurements.

part I and part II of this study[34,36]) is shown in dark green, mainly consisting of a capacitive branch, whereby the empty circle highlights the 180-mHz frequency point. For the NCM851005 working electrode, a real impedance of Re(Z_{NCM}) = 84.9 $\Omega \cdot cm^2_{WE}$ and an imaginary impedance of -Im(Z_{NCM}) = 447.5 $\Omega \cdot cm^2_{WE}$ is obtained ($\varphi_0 = -79°$) at 180 mHz. This can now be compared to the pseudo

full-cell impedance measured at 180 mHz at the Maccor potentiostat in a two-electrode coin cell setup, still employing a pre-lithiated LTO anode (green triangle, cell Z_{cell}-LTO-M). By fitting the voltage response to the current perturbation with a frequency of 180 mHz, a real impedance of Re(Z_{cell}) = 77.3 $\Omega \cdot cm^2_{WE}$ and an imaginary impedance of -Im(Z_{cell}) = 462.8 $\Omega \cdot cm^2_{WE}$ is obtained ($\varphi_0 = -81°$), being reasonably close to the one of the μ-RE setup, as expected from the observations made in Fig. 1. When comparing these data with the cell impedance of the coin half-cell, where lithium metal is employed as counter electrode (cell Z_{cell}-Li-B, measured with the Biologic potentiostat, yellow line), a shift of the capacitive branch at low frequencies to higher real impedance values is observed, caused by an additional semicircle feature at high frequencies. This is consistent the measured impedance of the pristine symmetrical lithium/lithium cell shown in Fig. 2: As the impedance of the complete cell is measured, the impedance response is a superposition of the lithium metal and the NCM impedance; therefore, a higher value is determined for the real part, namely Re(Z_{cell}) = 184.0 $\Omega \cdot cm^2_{WE}$. However, due to the small contribution of the real impedance to the imaginary impedance at the 180-mHz point (see yellow circle in Fig. 2), the effect of replacing the LTO counter electrode with a lithium counter electrode on the imaginary part of the impedance is only minor, resulting in a value of -Im(Z_{cell}) = 456.3 $\Omega \cdot cm^2_{WE}$ which is very close to the value that was obtained with the T-cell with a μ-RE (Z_{NCM}-LTO-B) that yielded a value of -Im(Z_{NCM}) = 447.5 $\Omega \cdot cm^2_{WE}$. Finally, the blue triangle depicts the 180-mHz point for the same coin half-cell setup measured with the Maccor battery cycler (cell Z_{cell}-Li-M). Even though the real part is shifted to higher values with Re(Z_{cell}) = 237.8 $\Omega \cdot cm^2_{WE}$, the imaginary part of -Im(Z_{cell}) = 469.9 $\Omega \cdot cm^2_{WE}$ again fits well with the values obtained from the other configurations. The observed shift in the real part is hereby assumed to originate from the lithium metal anode impedance, which is expected to stem from cell-to-cell variations occuring for the initially low surface area of the employed lithium foil, where small differences in the NCM loading determines the amount of exchanged charge (and thus freshly plated lithium surface), and can therefore have a significant impact on the measured impedance. Likewise, deviations in the areal resistance can also originate from varying areal loadings of the NCM active material itself, which, however, will be eliminated for Fig. 5d when normalizing the capacitance to the electrode mass.

Furthermore, it must be considered that a single-point impedance is not sufficient to determine whether the CAM is in blocking conditions, i.e., whether the 180-mHz point lies on the capacitive branch in the Nyquist depiction or whether it lies on another semicircular feature in the case that the semi-infinite charge-transfer resistance might not be reached. For NCMs, no deviation of the capacitive behavior was observed so far; however, it is recommended to measure an impedance spectrum over the whole frequency range to understand the impedance behavior of the CAM that is being investigated before going forward with single-point measurements using a battery cycler.

Figures 5b and 5c show the Nyquist plots after cycle #8 and #38, respectively. For all cells, a continuous decrease of the negative imaginary contribution of the 180-mHz point is observed, coinciding with the cycling-induced increase of the capacitance of the CAM by particle fracture and, therefore, of the surface area. Similar to the lithium/lithium cell impedance shown in Fig. 2, a decrease of the real part of the cell impedance at lower frequencies as well as of the semicircle is observed for the half-cell setups. Although the values measured with the Biologic potentiostat and the Maccor battery cycler coincide well in all cases, the decrease of the negative imaginary contribution to the impedance at 180 mHz undergoes a stronger decrease for the cells measured vs. a lithium metal counter electrode: from cycle #0 to #38, the imaginary part decreases from -Im(Z_{NCM}) = 447.5 $\Omega \cdot cm^2_{WE}$ to -Im(Z_{NCM}) = 285.6 $\Omega \cdot cm^2_{WE}$ for the Z_{NCM}-LTO-B cells as well as from -Im(Z_{cell}) = 456.3 $\Omega \cdot cm^2_{WE}$ to -Im(Z_{cell}) = 237.4 $\Omega \cdot cm^2_{WE}$ for the Z_{cell}-Li-B cells. This will be further discussed in the following.

Figure 5d shows the evolution of the specific capacitance of the NCM electrode (left y-axis) as well as of the NCM active material only (right y-axis), as determined from the imaginary impedance as a function of cycle number for all four examined cell and test hardware configurations. The values for the specific electrode capacitance were calculated by Eq. 1 using the imaginary cell impedance or NCM impedance (in case of cell Z_{NCM}-LTO-B) at 180 mHz. After conditioning (cycle #0), all measurements are in good agreement. Exemplarily for the Z_{NCM}-LTO-B cell, a specific capacitance of 0.221 ± 0.008 F/g_{WE} is obtained which then increases to a value of 0.255 ± 0.007 F/g_{WE} over the three formation cycles (green empty circles in Fig. 5d, left y-axis). To determine the capacitance of the NCM active material only, from which the relative surface area increase of the NCM CAM can be deduced, the contribution of conductive carbon and binder to the capacitance must be subtracted. The latter was estimated by the measurement of a model electrode without NCM, as outlined in part I of this study; for the present study, the contribution by the conductive carbon and the binder is 0.104 ± 0.002 F/g, corresponding to 6 % of the capacitance of the C65/PVDF electrode (with a composition of C65:PVDF of 1:1 w/w) of 1.729 ± 0.028 F/g, since the NCM electrode comprises 6 wt% of the C65/PVDF mixture.[34] After this subtraction of the contribution of the conductive carbon and the normalization by the mass of the active material, a value for the NCM specific capacitance of 0.125 ± 0.005 F_{NCM}/g_{NCM} is determined (plotted vs. the right y-axis in Fig. 5d). By using the value for the surface-area-normalized capacitance for NCMs of ~ 28 $\mu F_{NCM}/cm^2_{NCM}$ in LP57 at 2.55 V_{Li} determined in part II of this study,[36] the obtained value for the specific NCM capacitance can be converted to a specific surface area of ~ 0.4 m^2_{BET}/g_{NCM}, which is approximately twice as large as compared to the value of the pristine NCM powder determined by N_2-BET. This difference is attributed to the cracking and the concomitant surface area increase of the secondary NCM agglomerates due to the mechanical forces during calendering, as reported previously.[34,35,58] It should be noted that, for carbons, the surface-area-normalized capacitance (e.g., of VGCF or C65) with typical values between 4 and 10 $\mu F/cm^2$ is significantly smaller.[34,59]

During the first three cycles, an increase of the capacitance value to 0.161 ± 0.003 F_{NCM}/g_{NCM} is observed for all four cell setups what equals an increase of ~ 30 % as compared to the initial NCM capacitance. Depending on the upper cutoff potential, the capacitance increase of an NCM622 CAM evaluated in the first part of this study varied from ~ 50 % (3.9 V) to ~ 100 % (4.5 V),[34] which is much higher as compared to the NCM851005 used in this study. When comparing different CAMs, a higher tendency for particle fracture would be expected for compositions that have a higher nickel content, as the degree of delithiation that is reached up to a set voltage, and thus the anisotropic volume contraction, increases.[32,40,60] However, in part I of this study,[34] uncalendered electrodes were used for the determination of the capacitance evolution upon cycling; here, however, the NCM851005 electrodes were calendered before use, which is always done for electrodes used in commercial cells to maximize the energy density. Due to this compression, the mechanical cracking of the polycrystalline particles increases the electrode surface area already before cell assembly, as this was shown in part I of this study,[34] what is partially responsible for the smaller relative surface area increase upon cycling of the here examined NCM851005 cathodes compared to the NCM622 cathodes that had been uncalendered. Additionally, the size and the shape of the NCM primary crystallite as well as the morphology of the secondary NCM particle agglomerates have an impact on the relative surface area increase upon cycling.

Next to the differences in mechanical processing of the electrode tapes or the CAM type, other factors might affect the capacitance that is determined initially for the pristine cell: Commercial CAMs are frequently washed to remove residual lithium salts such as Li_2CO_3 and LiOH,[61,62] which remain from the synthesis procedure or form during improper storage of the materials.[63–66] Said washing, e.g.,

impacts the surface area accessible for the electrolyte by opening initially clogged pores within the secondary particle agglomerates. Even though the pristine capacitance varies for differently prepared CAMs and electrodes thereof, a quantitative comparison of the capacitance upon cycling is still reasonable: as the areal capacitance of NCM materials was identified to be 25 $\mu F/cm^2_{CAM}$ independent of nickel content or particle morphology, as shown in part II of this study,[36] the determination of the NCM capacitance directly provides the surface area of the active material in the cell, which is in many cases directly proportional to the various side reactions of the positive electrode, such as oxygen release, electrolyte decomposition, formation of a resistive oxygen-depleted surface layer, and transition metal dissolution, as discussed in the introduction. Therefore, this method provides a powerful tool for the large-scale investigation and optimization of CAMs in material development.

When considering the capacitance evolution over the measured range of 68 cycles, no significant difference between the two test hardware configurations (Biologic vs. Maccor) as well as between the electrode setups (with and without μ-RE) is observed for the cells with an LTO counter electrode, with the estimated NCM capacitance being 0.282 ± 0.005 F_{NCM}/g_{NCM} (cells Z_{NCM}-LTO-B in Fig. 5d, right y-axis) and 0.273 ± 0.005 F_{NCM}/g_{NCM} (cells Z_{cell}-LTO-M), i.e., differing by <4 %. However, a divergence of the cells with a lithium metal counter electrode in comparison to those with an LTO counter electrode develops after cycle #8: while the NCM capacitance values of the NCM/Li cells up to cycle #38 agree reasonably well with each other (0.328 ± 0.006 F_{NCM}/g_{NCM} for Z_{cell}-Li-B vs. 0.318 ± 0.007 F_{NCM}/g_{NCM} for Z_{cell}-Li-M after 38 cycles), they are substantially higher than those obtained for the NCM/LTO cells (0.250 ± 0.001 F_{NCM}/g_{NCM} for Z_{NCM}-LTO-B vs. 0.242 ± 0.001 F_{NCM}/g_{NCM} for Z_{cell}-LTO-M after 38 cycles). Upon further cycling of the NCM/Li cells, the NCM capacitance values obtained with the Maccor battery cycler are slightly lower compared to those obtained with the Biologic potentiostat (e.g., in cycle #68, 0.339 ± 0.007 F_{NCM}/g_{NCM} for Z_{cell}-Li-M vs. 0.370 ± 0.006 F_{NCM}/g_{NCM} for Z_{cell}-Li-B). At the cycle number where the divergence of the data measured with the two different test hardware configurations (Maccor battery cycler vs. Biologic potentiostat) initiates, the impedance of the lithium metal anode already starts to significantly rise, as depicted in Figs. 2 and A·1. Although it is not clear if the deviation between the two test hardware configurations is correlated to this impedance rise, the limitations of the CAM/Li half-cells upon extended cycling become obvious, indicating that the capacitance measurement in half-cells should be restricted up to a certain number of cycles, or exchanged accumulated charge per area of the lithium metal anode, respectively.

For the above discussed reasons (i.e., the minor contribution of the lithium metal anode to the imaginary part of the impedance), the larger increase of specific NCM capacitance of the NCM/Li cells starting at cycle #8 cannot be ascribed to a cell-to-cell variation nor to a measurement artifact but originates from a real increase of the CAM's surface area. Even if the lithium metal anode would develop a significant contribution to the imaginary impedance, an increasing imaginary impedance would indicate a drop in capacitance following Eq. 1 instead of the measured increase. As the lithium metal electrode can barely decrease to lower values, as no imaginary impedance of $-Im(\mathbf{Z}) < 0$ is expected (see Fig. 2), the additional increase in the capacitance is, therefore, assigned to a true decrease of the imaginary impedance of the cathode. Here, cross-talk phenomena between the lithium metal anode and the CAM that do not come into play for the LTO anodes must be considered,[67] whereby an apparent difference between an LTO and a Li counter electrode is that no SEI is formed on an LTO electrode due to its significantly higher electrode potential of 1.55 V_{Li} and that it does not form any additional surface area as no lithium plating can occur. Indeed, it is expected that impurities like alkoxides, soluble electrolyte reduction products, and/or detached SEI components, all originating from the lithium metal surface of the counter

electrode, can be oxidized at the cathode potential, leading to the formation of protons within the electrolyte.[68] Said protons can hydrolyze residual Li_2CO_3 impurities in CAMs that stem from synthesis or storage.[69] If said Li_2CO_3 residuals sit at the grain boundaries between the primary particle crystallites of the secondary NCM agglomerates, the dissolution process is hypothesized to lead to a capacitance increase as a result of pore opening and a concomitant increase of the electrolyte percolation within the secondary agglomerates.

Although it can only be hypothesized on the contribution of the electrolyte to the increased surface area, a clear difference in the coulombic efficiency can be seen when comparing cells with LTO vs. those with a lithium metal counter electrode, as shown in Fig. A·2b. The oxidation of the impurities formed at the counter electrode and oxidized on the cathode electrode would be expected to provide additional electrons on the cathode side, what would result in a higher charge or lower discharge capacity for each cycle. While the coulombic efficiency of the NCM/LTO cells averages >0.995 over the whole cycle range, a lower coulombic efficiency of ~0.98 is measured for the NCM/Li cells, indicating parasitic side reactions on the NCM cathode. In fact, the coulombic efficiency continuously decreases during the cycling of the NCM/Li cells, which coincides with the increase of lithium metal surface area by plating and stripping operation, facilitating said parasitic reactions, which thus could explain said continuous decrease of the coulombic efficiency by increasing the extent of a parasitic current. In addition, when investigating the discharge capacities depicted in Fig. A·2a, a slightly steeper capacity fading is observed for the cells with a lithium metal counter electrode as compared to the ones with an LTO counter electrode, starting at around cycle #20 and indicating a faster NCM degradation for the NCM/Li cells, possibly originating from the above described cross-talk phenomenon.

Overall, these observations indicate a distortion of the capacitance and the coulombic efficiency when NCM electrodes are tested for many cycles in a half-cell setup. To reduce the effect of the cross-talk to a minimum, we therefore suggest limiting the amount of half-cell cycles to <10. This approach was already applied successfully to evaluate the effect of the morphology on the electrochemical behavior of $LiNiO_2$.[70] When seeking to evaluate the morphological stability that would be exhibited by a given active material over extended charge/discharge cycling in a full-cell, it is recommended to avoid the use of lithium metal counter electrodes, as this would lead to cross-talk-induced artefacts (see above). For this purpose, the counter electrode should instead be based on other active materials that also satisfy the prerequisites of a relatively low imaginary contribution at low frequencies (of ~180 mHz) and a sufficient lithium reservoir to fully lithiate the working electrode upon discharge to induce blocking conditions (e.g., graphite, LTO, or LFP, all capacitively oversized and used in a partially lithiated state).

In principle, the developed approach should also be applicable for other active materials including anode active materials, if they can be brought into blocking conditions. Of course, the same prerequisites apply, i.e., a counter electrode with a relatively low imaginary impedance contribution at low frequencies (of ~180 mHz) is required. Throughout this study, in addition to the different NCM compositions and morphologies, the capacitance of conductive carbons (i.e., VGCF and C65) was determined;[34] furthermore, the particle cracking of LFP was quantified by the here presented impedance-based method by monitoring its increasing capacitance upon charge/discharge cycling, while, in contrast, the capacitance of LTO was observed to remain constant in a similar experiment.[34] For graphite active materials, the application of this method does not seem interesting, as no surface area increase due to particle cracking is expected. For silicon, being a possible alternative for graphite on the negative electrode, the evaluation of the capacitance could provide a quantification of the surface area increase induced by the large volume change upon lithiation; however, this approach does not appear to be straightforward since the SEI formation of silicon would likely alter the surface-

area-normalized capacitance as well as decrease the electronic conductivity of the silicon electrode.[71,72] In general, monitoring the change of the electrochemical capacitance of anode active materials is expected to be possible using a suitable electrode composition (e.g., using conductive carbons such as VGCF ensuring the sufficient electronic connection of the active material); however, for the operation of electrodes at potentials below the reduction potential of the electrolyte components, the concomitant (possibly continuous) SEI formation must be considered for the meaningful application of this method.

In general, if the parameters of any type of working electrode were to deviate strongly from the typically used values that had been chosen for this study (such as the mass loading of the electrode, its porosity, its contact resistance, the electronic conductivity through the electrode, its initial specific surface area, the ratio of the capacitance contribution of the active material and the other components, etc.), however, the approach using the single-point frequency at 180 mHz in a half-cell for the determination of the capacitance would have to be reevaluated. Exemplarily, in the case of an increased mass loading of the working electrode (or, similarly, an increased specific surface area of the active material powder), the imaginary impedance would decrease due to the increased total surface area, which would consequently increase the relative contribution of the counter electrode to the imaginary impedance, inducing a larger relative error of the capacitance determined for the working electrode. In general, the potential user of the here presented method is advised to thoroughly analyze and fully understand the impedance response of the investigated active materials and electrodes before this simplified method is applied.

Conclusions

In this study, we deduced a stepwise simplification of the experimental design to monitor particle cracking through the evolution of the capacitance of a NCM851005 CAM from the sophisticated, but intricate setup in T-cells with a micro-reference electrode to a conventional coin (half-)cell setup. For the latter, no μ-RE electrode is required if the impedance of the counter electrode is negligible as compared to the investigated CAM working electrode. This prerequisite is met for electrodes such as (pre-lithiated) LTO and likely even for pre-lithiated graphite. Even though lithium metal showed a relatively large impedance, it is still suitable for the use as counter electrode, as its contribution to the imaginary cell impedance at 180 mHz is small as compared to the one of the examined NCM working electrode.

Additionally, it was shown that the NCM capacitance does not have to be extracted from a full impedance spectrum provided by an impedance analyzer but can be obtained by solely a low-frequency single-point impedance measurement performed with a simple battery cycler without explicit impedance capabilities, whereby a sine-like current perturbation at 180 mHz is generated by a stepwise but rapid change of the applied current. The measurement of two types of commercial capacitors resulted in a deviation of <1 % between the two methods.

Each step of the transformation was validated in cycling experiments using four different cell and test hardware configurations: No deviation in the specific NCM capacitance was found for cells without a reference electrode as well as for the single-point impedance measurement at the battery cycler for at least 68 cycles. However, it could be shown that cross-talk phenomena increase the capacitance and, consequently, the electrochemically active surface area of the NCM CAM when cycled against a lithium metal counter electrode for extended cycling. These occurring side reactions with NCM/lithium cells were also expressed in the decrease of the coulombic efficiency in contrast to NCM/LTO cells (i.e., pseudo full-cells).

Even though we suggest limiting the analysis of the capacitance in half-cells to ~10 charge/discharge cycles due to pronounced cross-talk phenomena as compared to NCM/LTO cells, the data
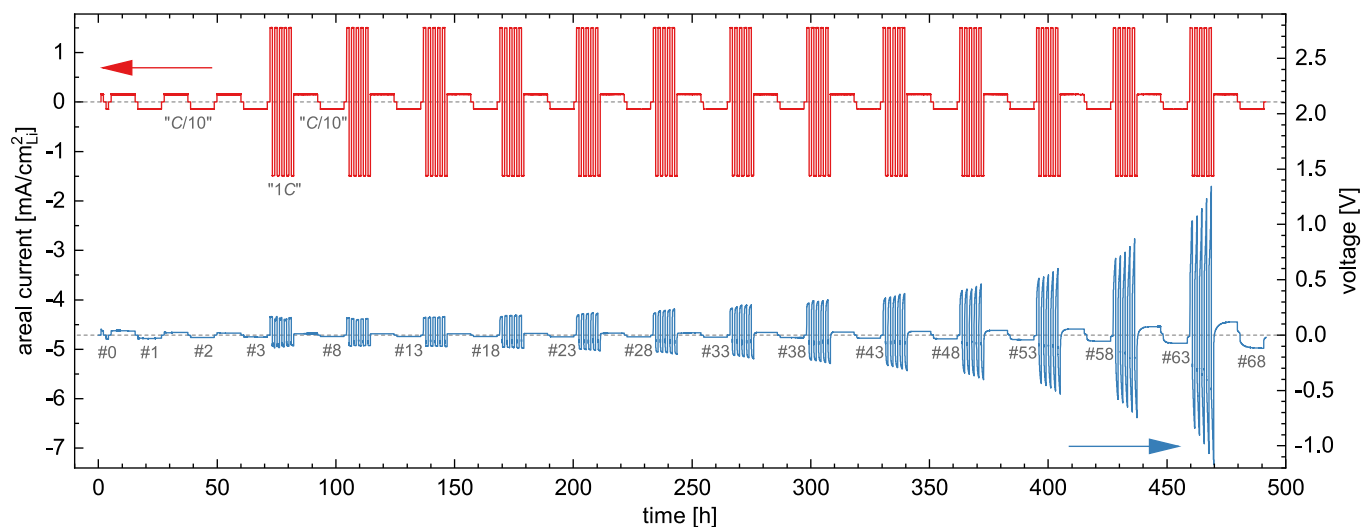
Figure A·1. Cycling data of the symmetric lithium/lithium cell presented in Fig. 2, showing its areal current (red, left axis) and cell voltage profile (blue, right axis). For the "$C/10$" cycles, 0.30 mA or 0.15 mA/cm$^2_{Li}$ (when normalized to the geometric surface area of the lithium metal electrodes) were applied during symmetric cell cycling, whereas for the "$1C$" cycles, a current of 3.0 mA or 1.50 mA/cm$^2_{Li}$ was set. The "$C/10$" cycles are labeled with the respective cycle number. The cell voltages given in the figure represent the cell potential at the end of the last of the four cycles at 3.0 mA.

acquired by the here proposed method and setup can give valuable information about the chemomechanical stability of CAM particles. Therefore, the capacitance method, which is now applicable in combination with the developed simplified cell and test hardware setup, provides a powerful in situ tool to monitor the surface evolution of CAMs, using only standard testing procedures and instrumentation.

CRediT Authorship Contribution Statement

Stefan Oswald: Methodology, Investigation, Writing—Original Draft. Felix Riewald: Methodology, Investigation, Writing—Original Draft. Hubert A. Gasteiger: Conceptualization, Supervision, Writing—Review & Editing.

Appendix

Cycling data of the symmetric lithium/lithium coin cell.—Figure A·1 shows the areal current and potential profiles of the symmetric lithium metal cell discussed in Fig. 2. Even though the same two currents (i.e., 0.30 mA and 3.0 mA) were applied repeatedly over 68 cycles, the cell voltage initially decreases during the first few cycles and later increases again. At cycle #28, the cell voltage starts to increase drastically, which is in good agreement with the LFR extracted from the impedance data being recorded after each slow cycle and presented in Fig. 2.

Cycling data of the different NCM cell configurations.—Figure A·2 shows the coulombic efficiencies and specific discharge capacities of the four different cell configurations during the aging cycles at $1C$ that were used in this study. For all samples, the discharge capacity shown in Fig. A·2a starts at 185.5 ± 1.9 mAh/g$_{NCM}$ in cycle #4 and decreases to 172.8 ± 3.0 mAh/g$_{NCM}$ in cycle #68. Although the capacity retention is similar for all samples, the coulombic efficiency depicted in Fig. A·2b differs depending on the selected counter electrode: it stays on a stable level for the cells with pre-lithiated LTO anodes, viz. at >0.995 (pseudo full-cells, dark green empty circles and green triangles), but continuously decreases for the cells with lithium metal as anode, viz., from 0.995 to 0.97
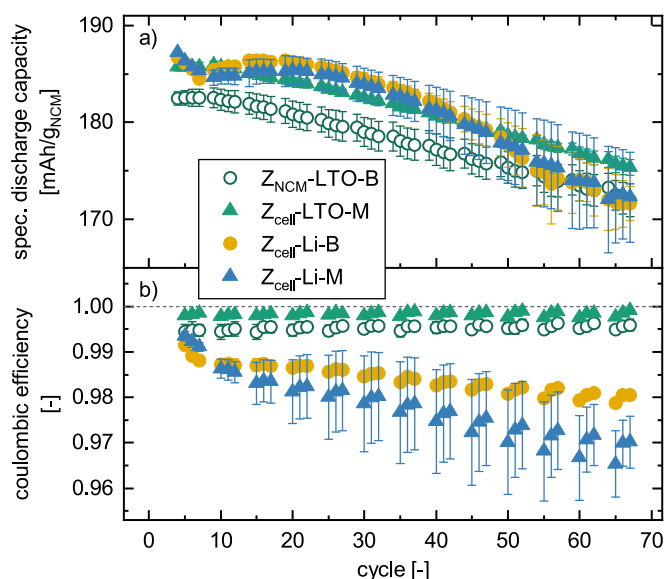

Figure A·2. a) Specific discharge capacity and **b)** coulombic efficiency as a function of the cycle number during the $1C$ cycles for the data depicted in Fig. 5. Green empty circles depict the T-cell setup with a μ-RE and a pre-lithiated LTO anode measured with the Biologic potentiostat (Z$_{NCM}$-LTO-B), green triangles show the coin-cell setup with pre-lithiated LTO anodes measured with the Maccor battery cycler (Z$_{cell}$-LTO-M), yellow circles represent coin half-cells with lithium metal anode measured with the Biologic potentiostat (Z$_{cell}$-Li-B), and blue triangles show the half-cell setup measured with the Maccor battery cycler (Z$_{cell}$-Li-M). The first cycle of each set of four $1C$ cycles was omitted in the presentation of the coulombic efficiency, as the ratio of charge and discharge capacity is affected simply by the change of C-rate from $C/10$ to $1C$. The values shown here are calculated from the mean of two identical cells, and the error bars correspond to the minimum/maximum value of two measurements.

(yellow circles and blue triangles), indicating parasitic side reactions during cell cycling.

ORCID

Stefan Oswald ⓘ https://orcid.org/0000-0001-6402-7833
Felix Riewald ⓘ https://orcid.org/0000-0001-9002-3633
Hubert A. Gasteiger ⓘ https://orcid.org/0000-0001-8199-8703

References

1. O. Gröger, H. A. Gasteiger, and J.-P. Suchsland, *J. Electrochem. Soc.*, **162**, A2605 (2015).
2. W. Li, E. M. Erickson, and A. Manthiram, *Nat. Energy*, **5**, 26 (2020).
3. R. Schmuch, R. Wagner, G. Hörpel, T. Placke, and M. Winter, *Nat. Energy*, **3**, 267 (2018).
4. D. Andre, S.-J. Kim, P. Lamp, S. F. Lux, F. Maglia, O. Paschos, and B. Stiaszny, *J. Mater. Chem. A*, **3**, 6709 (2015).
5. S.-T. Myung, F. Maglia, K.-J. Park, C. S. Yoon, P. Lamp, S.-J. Kim, and Y.-K. Sun, *ACS Energy Lett.*, **2**, 196 (2017).
6. H.-J. Noh, S. Youn, C. S. Yoon, and Y.-K. Sun, *J. Power Sources*, **233**, 121 (2013).
7. U. H. Kim et al., *Energy Environ. Sci.*, **11**, 1271 (2018).
8. J. Li and A. Manthiram, *Adv. Energy Mater.*, **9**, 1902731 (2019).
9. C. S. Yoon, H.-H. Ryu, G.-T. Park, J.-H. Kim, K.-H. Kim, and Y.-K. Sun, *J. Mater. Chem. A*, **6**, 4126 (2018).
10. J.-H. Kim, H.-H. Ryu, S. J. Kim, C. S. Yoon, and Y.-K. Sun, *ACS Appl. Mater. Interfaces*, **11**, 30936 (2019).
11. Q. Xie and A. Manthiram, *Chem. Mater.*, **32**, 7413 (2020).
12. Y. Kim, *ACS Appl. Mater. Interfaces*, **4**, 2329 (2012).
13. J. Li, A. R. Cameron, H. Li, S. Glazier, D. Xiong, M. Chatzidakis, J. Allen, G. A. Botton, and J. R. Dahn, *J. Electrochem. Soc.*, **164**, A1534 (2017).
14. J. E. Harlow et al., *J. Electrochem. Soc.*, **166**, A3031 (2019).
15. Y.-K. Sun, S.-T. Myung, B.-C. Park, J. Prakash, I. Belharouak, and K. Amine, *Nat. Mater.*, **8**, 320 (2009).
16. J. Langdon and A. Manthiram, *Energy Storage Mater.*, **37**, 143 (2021).
17. R. Jung, M. Metzger, F. Maglia, C. Stinner, and H. A. Gasteiger, *The Journal of Physical Chemistry Letters*, **8**, 4820 (2017).
18. R. Jung, M. Metzger, F. Maglia, C. Stinner, and H. A. Gasteiger, *J. Electrochem. Soc.*, **164**, A1361 (2017).
19. J. Wandt, A. T. S. Freiberg, A. Ogrodnik, and H. A. Gasteiger, *Mater. Today*, **21**, 825 (2018).
20. D. Streich, C. Erk, A. Guéguen, P. Müller, F.-F. Chesneau, and E. J. Berg, *The Journal of Physical Chemistry C*, **121**, 13481 (2017).
21. L. Giordano, P. Karayaylali, Y. Yu, Y. Katayama, F. Maglia, S. Lux, and Y. Shao-Horn, *The Journal of Physical Chemistry Letters*, **8**, 3881 (2017).
22. A. T. S. Freiberg, M. K. Roos, J. Wandt, R. de Vivie-Riedle, and H. A. Gasteiger, *The Journal of Physical Chemistry A*, **122**, 8828 (2018).
23. D. P. Abraham, R. D. Twesten, M. Balasubramanian, I. Petrov, J. McBreen, and K. Amine, *Electrochem. Commun.*, **4**, 620 (2002).
24. S. Venkatraman and A. Manthiram, *Chem. Mater.*, **15**, 5003 (2003).
25. F. Friedrich, B. Strehle, A. T. S. Freiberg, K. Kleiner, S. J. Day, C. Erk, M. Piana, and H. A. Gasteiger, *J. Electrochem. Soc.*, **166**, A3760 (2019).
26. B. Strehle, F. Friedrich, and H. A. Gasteiger, *J. Electrochem. Soc.*, **168**, 050512 (2021).
27. S. Solchenbach, G. Hong, A. T. S. Freiberg, R. Jung, and H. A. Gasteiger, *J. Electrochem. Soc.*, **165**, A3304 (2018).
28. J. Wandt, A. Freiberg, R. Thomas, Y. Gorlin, A. Siebel, R. Jung, H. A. Gasteiger, and M. Tromp, *J. Mater. Chem. A*, **4**, 18300 (2016).
29. R. Jung, F. Linsenmann, R. Thomas, J. Wandt, S. Solchenbach, F. Maglia, C. Stinner, M. Tromp, and H. A. Gasteiger, *J. Electrochem. Soc.*, **166**, A378 (2019).
30. Z. Ruff, C. Xu, and C. P. Grey, *J. Electrochem. Soc.*, **168**, 060518 (2021).
31. L. M. Thompson, J. E. Harlow, A. Eldesoky, M. K. G. Bauer, J. H. Cheng, W. S. Stone, T. Taskovic, C. R. M. McFarlane, and J. R. Dahn, *J. Electrochem. Soc.*, **168**, 020532 (2021).
32. L. de Biasi, A. O. Kondrakov, H. Geßwein, T. Brezesinski, P. Hartmann, and J. Janek, *The Journal of Physical Chemistry C*, **121**, 26163 (2017).
33. A. O. Kondrakov, A. Schmidt, J. Xu, H. Geßwein, R. Mönig, P. Hartmann, H. Sommer, T. Brezesinski, and J. Janek, *The Journal of Physical Chemistry C*, **121**, 3286 (2017).
34. S. Oswald, D. Pritzl, M. Wetjen, and H. A. Gasteiger, *J. Electrochem. Soc.*, **167**, 100511 (2020).
35. S. Oswald, M. Bock, and H. A. Gasteiger, *J. Electrochem. Soc.*, **169**, 050501 (2022).
36. S. Oswald, D. Pritzl, M. Wetjen, and H. A. Gasteiger, *J. Electrochem. Soc.*, **168**, 120501 (2021).
37. S. Oswald, M. Bock, and H. A. Gasteiger, *manuscript in preparation*.
38. L. de Biasi, B. Schwarz, T. Brezesinski, P. Hartmann, J. Janek, and H. Ehrenberg, *Adv. Mater.*, **31**, 1900985 (2019).
39. S. Watanabe, M. Kinoshita, T. Hosokawa, K. Morigaki, and K. Nakura, *J. Power Sources*, **258**, 210 (2014).
40. H.-H. Sun and A. Manthiram, *Chem. Mater.*, **29**, 8486 (2017).
41. J.-H. Kim, S. J. Kim, T. Yuk, J. Kim, C. S. Yoon, and Y.-K. Sun, *ACS Energy Lett.*, **3**, 3002 (2018).
42. E. Trevisanello, R. Ruess, G. Conforto, F. H. Richter, and J. Janek, *Adv. Energy Mater.*, **11**, 2003400 (2021).
43. S. Solchenbach, D. Pritzl, E. J. Y. Kong, J. Landesfeind, and H. A. Gasteiger, *J. Electrochem. Soc.*, **163**, A2265 (2016).
44. S. Solchenbach, *PhD Thesis*, Technical University of Munich (2018).
45. J. Landesfeind, J. Hattendorff, A. Ehrl, W. A. Wall, and H. A. Gasteiger, *J. Electrochem. Soc.*, **163**, A1373 (2016).
46. J. Landesfeind, D. Pritzl, and H. A. Gasteiger, *J. Electrochem. Soc.*, **164**, A1773 (2017).
47. R. Morasch, B. Suthar, and H. A. Gasteiger, *J. Electrochem. Soc.*, **167**, 100540 (2020).
48. S. Drvarič Talian, J. Bobnar, A. R. Sinigoj, I. Humar, and M. Gaberšček, *The Journal of Physical Chemistry C*, **123**, 27997 (2019).
49. K. N. Wood, E. Kazyak, A. F. Chadwick, K.-H. Chen, J.-G. Zhang, K. Thornton, and N. P. Dasgupta, *ACS Central Science*, **2**, 790 (2016).
50. J. Wandt, C. Marino, H. A. Gasteiger, P. Jakes, R.-A. Eichel, and J. Granwehr, *Energy Environ. Sci.*, **8**, 1358 (2015).
51. R. Weber, J.-H. Cheng, A. J. Louli, M. Coon, S. Hy, and J. R. Dahn, *J. Electrochem. Soc.*, **166**, A3250 (2019).
52. G. Bieker, M. Winter, and P. Bieker, *Phys. Chem. Chem. Phys.*, **17**, 8670 (2015).
53. L. Yang, C. Smith, C. Patrissi, C. R. Schumacher, and B. L. Lucht, *J. Power Sources*, **185**, 1359 (2008).
54. G. J. Brug, A. L. G. van den Eeden, M. Sluyters-Rehbach, and J. H. Sluyters, *J. Electroanal. Chem. Interfacial Electrochem.*, **176**, 275 (1984).
55. D. Pritzl, J. Landesfeind, S. Solchenbach, and H. A. Gasteiger, *J. Electrochem. Soc.*, **165**, A2145 (2018).
56. D. T. Boyle, W. Huang, H. Wang, Y. Li, H. Chen, Z. Yu, W. Zhang, Z. Bao, and Y. Cui, *Nat. Energy*, **6**, 487 (2021).
57. H.-H. Ryu, G.-T. Park, C. S. Yoon, and Y.-K. Sun, *Small*, **14**, 1803179 (2018).
58. R. Sim, S. Lee, W. Li, and A. Manthiram, *ACS Appl. Mater. Interfaces*, **13**, 42898 (2021).
59. J. Chmiola, G. Yushin, Y. Gogotsi, C. Portet, P. Simon, and P. L. Taberna, *Science*, **313**, 1760 (2006).
60. W. Li, H. Y. Asl, Q. Xie, and A. Manthiram, *JACS*, **141**, 5097 (2019).
61. I. Hamam, N. Zhang, A. Liu, M. B. Johnson, and J. R. Dahn, *J. Electrochem. Soc.*, **167**, 130521 (2020).
62. D. Pritzl, T. Teufl, A. T. S. Freiberg, B. Strehle, J. Sicklinger, H. Sommer, P. Hartmann, and H. A. Gasteiger, *J. Electrochem. Soc.*, **166**, A4056 (2019).
63. I. A. Shkrob, J. A. Gilbert, P. J. Phillips, R. Klie, R. T. Haasch, J. Bareño, and D. P. Abraham, *J. Electrochem. Soc.*, **164**, A1489 (2017).
64. J. Sicklinger, M. Metzger, H. Beyer, D. Pritzl, and H. A. Gasteiger, *J. Electrochem. Soc.*, **166**, A2322 (2019).
65. R. Jung, R. Morasch, P. Karayaylali, K. Phillips, F. Maglia, C. Stinner, Y. Shao-Horn, and H. A. Gasteiger, *J. Electrochem. Soc.*, **165**, A132 (2018).
66. Z. Chen, J. Wang, J. Huang, T. Fu, G. Sun, S. Lai, R. Zhou, K. Li, and J. Zhao, *J. Power Sources*, **363**, 168 (2017).
67. J. Langdon and A. Manthiram, *Adv. Funct. Mater.*, **31**, 2010267 (2021).
68. B. Strehle, S. Solchenbach, M. Metzger, K. U. Schwenke, and H. A. Gasteiger, *J. Electrochem. Soc.*, **164**, A2513 (2017).
69. A. T. S. Freiberg, J. Sicklinger, S. Solchenbach, and H. A. Gasteiger, *Electrochim. Acta*, **346**, 136271 (2020).
70. F. Riewald, P. Kurzhals, M. Bianchini, H. Sommer, J. Janek, and H. A. Gasteiger, *J. Electrochem. Soc.*, **169**, 020529 (2022).
71. U. Kasavajjula, C. Wang, and A. J. Appleby, *J. Power Sources*, **163**, 1003 (2007).
72. M. Wetjen, D. Pritzl, R. Jung, S. Solchenbach, R. Ghadimi, and H. A. Gasteiger, *J. Electrochem. Soc.*, **164**, A2840 (2017).

4 Implications of the Particle Morphology of Nickel-Rich NCMs

The rising demand for SC CAMs for today's LIBs and the increasing number of literature reports on this class of materials highlight the importance of the morphology of the active material morphology. Not only the synthesis and processing of monolithic particles has become a trending topic [176, 177, 183, 190, 261–263], but also the understanding of their electrochemical properties has emerged: based on previous results, the SC morphology mostly outperforms the conventional PC analog in cycling and storage experiments, especially at elevated temperatures [179, 180, 257]. This advantage is often attributed to the absence of particle cracking, what could then result in a reduced active material loss and impedance build-up as well as less electrolyte oxidation, gas evolution, transition metal dissolution, or other unwanted side reactions in general. In contrast, other studies present a similar or even an inferior performance for cells based on SC CAMs [141, 256, 264]. On that account, deeper understanding and knowledge on the electrochemical properties and degradation mechanisms of the different NCM morphologies is required.

After having demonstrated the improved morphological stability of SC NCMs in Chapter 3.2, the two articles presented in this chapter elucidate the implications of this finding on the electrochemical properties depending on the particle morphology. First, the fundamental physical and electrochemical properties of PC and SC NCM622 are investigated regarding surface area changes as a function of the SOC and their effect on the (de)lithiation kinetics, the gas evolution, and the thermal stability. Second, the impact of the CAM morphology and the electrode properties on the capacitance determination are elucidated. Third, PC and SC NCM851005 materials are compared in extended full-cell cycling experiments, elucidating the effect of morphology, upper cutoff potential, and temperature on capacity loss, impedance build-up, and particle cracking.

4.1 Cracking, Gassing, Rate Capability, and Thermal Stability

The article "Elucidating the Implications of Morphology on Fundamental Characteristics of Nickel-Rich NCMs: Cracking, Gassing, Rate Capability, and Thermal Stability of Poly- and Single-Crystalline NCM622" was submitted to the peer-reviewed *Journal of the Electrochemical Society* in January 2022 and published online in May 2022 [265]. It is available as an open-access article and distributed under the terms of the Creative Commons Attribution Non-Commercial No Derivatives 4.0 License. This paper is part of the *Focus Issue In Honor of John Goodenough: A Centenarian Milestone*. A permanent link to this article can be found under https://doi.org/10.1149/10.1149/1945-7111/ac5f7f. The main findings of this paper were presented by Stefan Oswald as Paper #A01-0144 at the PRiME 2020 Meeting of the *Electrochemical Society* in a virtual format in October 2020.

To assess the influence of particle morphology and primary particle size, the three NCM622 CAM powders are first investigated visually by SEM, illuminating their distinct morphological properties: i) spherical PC secondary agglomerates (with a diameter of $\varnothing$ 5–10 µm) consisting of primary particles ($\varnothing$ 0.2–1.0 µm), ii) small monolithic crystallites ($\varnothing$ 0.2–1.0 µm), and iii) large monolithic crystallites ($\varnothing$ 2–8 µm). By gas physisorption experiments using Kr-BET to determine the surface area of charged electrodes, a significantly increased surface area (by a factor of 3.0x) of the PC CAM reveals substantial particle cracking induced by the volume change of the material upon delithiation already after the first charge; in contrast, the two SC NCMs maintain their surface area even when charged. By SOC-dependent measurements of the capacitance of the NCM, as introduced in Chapter 3.2, the (chemo)mechanical stability of the SC NCM can be demonstrated even for high SOCs while, for the PC NCM, the surface area increases at $5.0\,\mathrm{V_{Li}}$ to 6.5x of its pristine value, corresponding to $\sim$70 % of the primary crystallite surface area being exposed to the electrolyte. In accordance, both the gas evolution at 90 %SOC, monitored by OEMS, as well at high temperatures of 325 °C, tracked by the mass loss in TGA experiments, do not scale with the pristine NCM surface area but with the surface area determined in the charged state. As a drawback, however, the large SC particles exhibit an inferior rate capability as compared to the PC ones, which benefit from particle cracking and electrolyte penetration enhancing the diffusion of lithium ions through the liquid phase.

The implications of particle cracking on the (de)lithiation kinetics are further illumi-

nated by a series of articles published by the group of Prof. Jürgen Janek at Justus-Liebig-Universität, Gießen, Germany. The here observed difference in rate capability between PC and SC CAMs (despite a similar specific surface area in the pristine state) can also be expressed by the SOC-dependent apparent diffusion coefficient, as it was investigated by Trevisanello et al. through GITT measurements [266]: over a wide region of the SOC window, the apparent diffusion coefficient remains constant for the SC NCMs, while the one of the PC NCMs increases with increasing SOC, which is explained by particle cracking, the increase in surface area, and the consequent shortening of the diffusion paths in the solid phase. Nevertheless, particle cracking only has a beneficial effect if the electrolyte can penetrate the pores, which is not the case in all-solid-state batteries. For systems using a solid-state electrolyte, Ruess et al. observed that the apparent diffusion coefficient of PC NCM particles behaves like the one of SC particles in liquid electrolyte since particle cracking reduces the lithium diffusion between primary particles and thus the rate capability [145]. Furthermore, Conforto et al. demonstrated that the capacity retention during extended cycling in solid-state batteries is significantly improved for SC CAMs since active material is disconnected ionically and/or electronically [144]. Even though particle cracking in the first cycle is beneficial to the kinetics of PC NCMs in liquid electrolytes, its effect during long-term cycling still needs to be evaluated and compared to the one of SC materials.

Author contributions

S.O. and M.B. prepared the electrode sheets, assembled the half-cells, performed the rate test, and conducted the SEM measurements. S.O. performed the ball-milling of the PC NCM and the BET, TGA, OEMS, and impedance experiments. S.O. analyzed the data. S.O. wrote and H.A.G. edited the manuscript. All authors discussed the results and commented on the manuscript.

Elucidating the Implications of Morphology on Fundamental Characteristics of Nickel-Rich NCMs: Cracking, Gassing, Rate Capability, and Thermal Stability of Poly- and Single-Crystalline NCM622

Stefan Oswald,[*,z] Moritz Bock,[*] and Hubert A. Gasteiger[**]

Technical University of Munich, Chair of Technical Electrochemistry, Department of Chemistry and Catalysis Research Center, Garching, Germany

Nickel-rich NCM (LiMO$_2$, with M = Ni, Co, and Mn) cathode active materials for lithium-ion batteries are being increasingly commercialized due to their high specific capacity. Since the particle cracking of conventional polycrystalline NCMs is reported to be a major failure mechanism, the demand for single-crystalline materials is rising, as they are believed to provide superior cycle life. To gain comprehensive insights into the implications of NCM particle morphology on the electrochemical performance, the fundamental properties of these two material classes will be examined in this study. Krypton physisorption experiments and capacitance measurements reveal considerable differences in the change of the NCM surface area upon compression, delithiation, and charge/discharge cycling, depending on the material's morphology. Here, a polycrystalline NCM622 exhibits changes of its specific surface area of up to 650 % when cycled to a high state of charge, while the one of a single-crystalline NCM622 remains essentially unaffected. Consequently, the difference in morphology and, therefore, in exposed NCM surface area leads to differences in the extent of gassing at high degrees of delithiation (determined via on-line electrochemical mass spectrometry), in the rate capability (evaluated in half-cell discharge rate tests), and in the thermal stability (assessed by thermogravimetric analysis).

Owing to their high specific capacity and their technological maturity, ternary layered lithium transition metal oxides (LiMO$_2$) such as NCMs (M = Ni$_x$Co$_y$Mn$_z$, $x+y+z = 1$) have already been commercialized as cathode active materials (CAMs) for lithium-ion batteries.[1,2] In particular, nickel-rich NCM compositions are cost-effective and deliver practical discharge capacities of >200 mAh/g$_{NCM}$.[3–5] With increasing nickel content, however, the capacity gain is often accompanied by a shorter cycle life due to undesired side reactions at the NCM/electrolyte interface, resulting, e.g., from (i) the decomposition of residual lithium salts leftover from the synthesis[6,7] or of surface contaminants formed during improper storage,[8–10] all present in greater amounts on nickel-rich materials,[7,10] as well as from (ii) the reaction of released (singlet) oxygen at high degrees of delithiation from the NCM lattice with the electrolyte,[11,12] which occurs at lower potentials for higher nickel content.[13,14] These processes degrade the NCM active material upon charge/discharge cycling and increase the cell impedance, eventually leading to cell failure.[10,15]

One additional reported failure mechanism of conventional polycrystalline NCMs is the cracking of the secondary agglomerates due to the anisotropic volume change of the NCM unit cell of up to −8 % upon (de)lithiation,[16–18] causing stress and strain throughout the NCM particle,[16] what results in the formation of pores and cracks between the NCM primary crystallites and, therefore, in an increase of the NCM surface area that is in contact with the electrolyte.[19–21] This does not only enhance surface-area-dependent side reactions but also impairs the electrical contact across a secondary agglomerate upon its fragmentation into primary crystallites.[22,23]

To overcome this issue, more and more attention has been dedicated to the development of an improved particle morphology.[2,24] One way to minimize the occurring side reactions and resistances lays in the reduction of the specific surface area

through a greater primary crystallite size, being known in the literature under the designation *single-crystals*,[24–26] describing relatively large primary crystallites without a regular secondary structure and (ideally) without agglomeration, which are expected to maintain their pristine surface area upon cycling.[14,20,27] The expected integrity of the single-crystalline particle morphology could be the origin of the improved capacity retention observed during extended charge/discharge cycling experiments reported in recent studies.[27–30] However, the synthesis of single-crystalline NCMs is more demanding and, therefore, more expensive when implemented in large-scale industrial processes. For example, the synthesis of single-crystalline layered transition metal oxides often includes higher calcination temperatures of up to 1000 °C, multi-step calcination procedures, a washing step to remove excess lithium salts and flux agents, as well as mechanical grinding to deagglomerate the sintered primary crystallites (e.g., by ball milling).[24]

To better understand the morphology-related (dis)advantages of single-crystalline NCMs, this study focuses on elucidating the intrinsic characteristics and the possible performance benefits of different NCM particle morphologies: a comparison of a polycrystalline and a single-crystalline NCM622 with similar pristine specific surface area ($\sim$0.3 m$^2_{NCM}$/g$_{NCM}$) allows for the discrimination of the effect of particle morphology, whereas a comparison of the rather large NCM622 single-crystals (with a size of $\sim$5 μm) with the tiny primary crystallites obtained by milling of the polycrystalline NCM622 (with $\sim$0.6 μm) exposes the effect of the difference in pristine surface area (of a factor of $\sim$8x) for single-crystalline materials. As one might expect on account of the very different morphologies and specific surface areas of these three materials, krypton physisorption experiments (referred to as Kr-BET) and capacitance measurements reveal considerable differences in the change of the NCM surface area upon compression, delithiation, and charge/discharge cycling. Consequently, the effect of the morphology on the extent of gassing at high state of charge (SOC) was determined via on-line electrochemical mass spectrometry (OEMS), the rate capability was evaluated in half-cell discharge rate test, and the thermal stability was assessed by thermogravimetric analysis (TGA). In summary, this report gives comprehensive insights into the fundamental properties of poly- and single-crystalline NCMs.

*Electrochemical Society Student Member.
**Electrochemical Society Fellow.
zE-mail: Stefan.Oswald@tum.de

Experimental

NCM622 active material powders.—Three different NCM622 ($LiNi_{0.6}Co_{0.2}Mn_{0.2}O_2$) active materials were used in this study. The polycrystalline NCM622 material (referred to as "PC," 0.32 m^2_{NCM}/g_{NCM} (measured by Kr-BET), BASF SE, Germany) was used as received.

In order to obtain an NCM622 material that consists mostly of individual primary crystallites, the secondary agglomerates of the polycrystalline NCM622 powder were crushed to obtain the individual primary particles by ball milling, similar to the procedure shown by Hou et al.:[31] The polycrystalline NCM622 powder was mixed with N-methyl-2-pyrrolidone (NMP, anhydrous, 99.5 %, Sigma-Aldrich) at a mass ratio of 4:1 and ground in a 45 ml zirconium oxide beaker using zirconium oxide balls (ZrO_2, 2 mm in diameter) for 2×5 min at 400 rpm and 2×5 min at 1000 rpm, using a planetary ball mill (Pulverisette 7, Fritsch, Germany), including rest periods of 2 min between each step. The mixture of NCM, NMP, and ZrO_2 balls was heated and dried in a tube furnace (Carbolite, Germany) under argon atmosphere (1 l/min), applying a temperature ramp of 0.75 K/min from room temperature to 150 °C and then at 0.33 K/min to 210 °C, where each of the two temperatures was held for 4 h. (The relatively flat temperature profile (including the slow temperature increase and the temperature hold) was chosen to avoid boiling, bubbling, and splashing of the NMP in the furnace during drying. Through the here chosen procedure, most of the solvent had evaporated before the boiling point of NMP (at ∼203 °C) was reached. Up to this point, however, no changes of the NCM particles regarding morphology, composition, or crystal structure were expected). Subsequently, the dried mixture of NCM powder and ZrO_2 balls was re-annealed by applying a temperature ramp of 10 K/min up to 525 °C in a gas atmosphere of 20 vol% oxygen in argon (1 l/min), holding it at 525 °C for 1 h before letting it cool down to room temperature. The resulting ball-milled NCM622 was separated from the ZrO_2 balls by sieving and then stored under inert conditions; this material, consisting of mostly individual primary NCM622 particles, will be referred to further on as "PC-bm" (2.25 m^2_{NCM}/g_{NCM}).

As a third NCM622 material, a directly synthesized single-crystalline NCM622 (referred to as "SC," 0.27 m^2_{NCM}/g_{NCM}, BASF SE, Shanghai, China) was used as received.

Scanning electron microscopy.—The morphology of the CAM powders was investigated via top-view scanning electron microscopy (SEM) using a tabletop microscope (JCM-6000, JEOL, Japan) in secondary electron mode and applying an acceleration voltage of 15 kV.

Electrode preparation.—For cell cycling, NCM electrodes were prepared from the three above described NCM622 powders that exhibit very different morphologies (described later in Fig. 1) and specific surface areas: the as-received polycrystalline NCM622 (PC), the ball-milled polycrystalline NCM622 (PC-bm), and the as-received single-crystalline NCM622 (SC). Targeting different experimental investigations (see below), three different electrode inks were prepared with each of the three NCM622 powders, using different mass ratios of active material, carbon black (C65, carbon black SuperC65, 64 m^2_{C65}/g_{C65}, TIMCAL, Switzerland), and polyvinylidene difluoride binder (PVDF, Solef, Solvay, Germany) binder as well as different solid contents in the NMP solvent: (i) with a mass ratio of 96:2:2 and a solid content of 80 wt%; (ii) with a mass ratio of 96:2:2 and a solid content of 63 wt%; and, (iii) with a mass ratio of 90:5:5 and a solid content of 52 wt%. The inks based on polycrystalline NCM622 (PC) were mixed in a planetary mixer (Thinky Corp., USA) for 17 min, using a four-step sequential mixing procedure. To avoid particle agglomeration, the inks based on the SC and PC-bm active materials were prepared using the planetary ball

mill with a ZrO_2 beaker (20 ml) and ZrO_2 balls (10 mm in diameter) by mixing 4×5 min at 400 rpm, including rest periods of 2 min between each step.

Due to the very high specific surface area of the PC-bm material, uncompressed electrodes with a composition of 96:2:2 resulted in significant overpotentials during electrochemical testing, even when cycled at a slow rate of *C*/20, as the amount of conductive carbon of 2 wt% in the electrode was not sufficient to allow for a complete and homogeneous electrical contacting of the PC-bm particles. Therefore, PC-bm electrodes were compressed, even in experiments in which uncompressed electrodes were used for the SC and PC materials, as described in the following paragraphs. However, since the PC-bm material consists mostly of separated primary crystallites, as will be further discussed later, the mechanical compression of the electrodes is expected to have no effect on the pristine CAM surface area. In the following, we will describe the different electrode compositions and electrode compressions used for the different experimental procedures.

On-line electrochemical mass spectrometry (OEMS) measurements: The NCM slurries with a mass ratio of 96:2:2 and a solid content of 80 wt% were coated onto a stainless steel mesh (316 grade, 26 μm aperture, 25 μm wire diameter, The Mesh Company, United Kingdom) with a doctor blade, using an automated coater (RK PrintCoat Instruments, United Kingdom). The electrode sheets were then dried in a convection oven at 50 °C for 5 h before electrodes with a diameter of 14 mm were punched out, having a mass loading in the range of 10.0 ± 1.8 mg_{NCM}/cm^2. For the counter electrodes, lithium iron phosphate (LFP) electrodes with a diameter of 15 mm were punched out from commercially available LFP electrode sheets (LFP on aluminum, 3.5 mAh/cm^2, Customcells, Germany). While the PC and the SC electrodes were used uncompressed to avoid mechanically induced particle cracking, the PC-bm electrodes were compressed at 100 MPa for 30 s using a manual hydraulic press (Specac, United Kingdom) to minimize electrical contact resistances (see above). Data with these NCM electrodes are shown in Figs. 4 and A·5.

Cycling experiments in coin cells and T-cells: The NCM inks were coated onto the rough side of an aluminum foil (18 μm, MTI, USA) with a box-type coating bar (Erichsen, Germany), using the automated coater. All NCM electrode sheets were then dried in a convection oven at 50 °C for 5 h before punching out electrodes for the different types of experiments:

• The electrodes used for the Kr-BET and TGA measurements as well as for the potential curves of the first charge were prepared from the inks with an NCM:C65:PVDF mass ratio of 96:2:2 (with a solid content of 63 wt%). They were punched out to diameter of 14 mm (for the use in coin cells) and had a mass loading of 12.5 ± 1.5 mg_{NCM}/cm^2. The PC and SC electrodes were used uncompressed while the PC-bm electrodes were compressed at 100 MPa for 30 s, if not stated otherwise. Data with these NCM electrodes are shown in Figs. 2, 6, A·2, and A·4.

• The electrodes used for the discharge rate tests were prepared from the inks with an NCM:C65:PVDF mass ratio of 90:5:5 (with a solid content of 52 wt%). They were punched out to a diameter of 10.95 mm (for the use in T-cells) and had a mass loading of 12.5 ± 0.5 mg_{NCM}/cm^2. The electrodes for all three NCM materials were compressed at 200 MPa for 30 s. Data with these NCM electrodes are shown in Figs. 5 and A·6.

• The electrodes used for the NCM capacitance measurements in T-cells were prepared from the inks with an NCM:C65:PVDF mass ratio of 96:2:2 (with a solid content of 63 wt%). They were punched out to a diameter of 10.95 mm and had a loading of 8.5 ± 0.5 mg_{NCM}/cm^2. These electrodes with all three NCM materials were used both uncompressed and compressed at 100 MPa for 30 s. Data with these NCM electrodes are shown in Figs. 3 and A·3.

Two types of counter electrodes are used in these experiments: either LTO electrodes, punched out at a diameter of 10.95 mm from commercially available LTO electrode sheets (LTO on aluminum,

3.5 mAh/cm^2, Customcells, Germany), or lithium metal electrodes (450 μm thick, Rockwood Lithium, USA) with a diameter of 11 mm in T-cells or 15 mm in coin cells.

C65/PVDF electrodes: To serve as a background reference material for the determination of the NCM specific surface area as well as for the evaluation of the NCM thermal stability, slurries without active material containing only C65 and PVDF at a mass ratio of 1:1 were mixed with NMP in the planetary centrifugal mixer, and coatings on aluminum foil were prepared as described above. For the Kr-BET and TGA measurements, uncompressed C65 electrodes with a diameter of 14 mm and a mass loading of 3.2 mg/cm^2 were used.

All electrodes were dried in a Büchi oven at 120 °C under dynamic vacuum for at least 6 h and then transferred without exposure to air to an argon-filled glove box (<1 ppm O_2 and H_2O, MBraun, Germany) where all cells were assembled.

On-line electrochemical mass spectrometry.—In preparation of the on-line electrochemical mass spectrometry (OEMS) experiments (reprinted here from a previous publication[14] for the sake of completeness), capacitively oversized LFP electrodes (15 mm in diameter, 3.5 mAh/cm^2) were pre-delithiated in coin cells (Hohsen, Japan) using two glass fiber separators (16 mm in diameter), one polyolefin separator (17 mm in diameter, H2013, Celgard, USA) facing the LFP electrode (preventing that glass fibers adhere to the LFP electrodes and get transferred to the OEMS cell), and 100 μl of LP57 electrolyte (1 M $LiPF_6$ in EC:EMC 3:7 w/w, <20 ppm H_2O, BASF, Germany). For this, they were pre-delithiated in coin half-cells against metallic lithium (450 μm thick and 15 mm in diameter, Rockwood Lithium, USA) to ∼90 %SOC at a specific current of 30 mA/g$_{LFP}$ for 4.5 h, after having performed one full formation cycle at 30 mA/g$_{NCM}$ between 3.0 and 4.0 V$_{Li}$ (note that throughout this article potentials referenced to the Li$^+$/Li redox potential are denoted as V$_{Li}$; similarly, V$_{LFP}$ and V$_{LTO}$ are used for the cell potential of the OEMS cells with LFP as counter electrode as well as for the pseudo full-cells with LTO as counter electrode, respectively). After pre-delithiation, the LFP electrodes were harvested from the cells and used without washing as the counter electrode in the OEMS cells for the gas evolution experiments. As described previously,[14] the pre-delithiated, capacitively oversized LFP electrodes are used because they: (i) provide a stable potential of ∼3.45 V$_{Li}$ over a wide SOC window, (ii) provide a sufficiently large capacity to take up the lithium from the investigated NCM working electrodes, and (iii) exhibit no gas evolution due to the absence of electrolyte decomposition reactions at their operating potential (as compared to typical anodes such as lithium metal or graphite forming an SEI, accompanied by gas evolution[15,32,33]). To later choose the end of charge potential of the NCM electrodes in the OEMS experiments, the LFP potential at ∼10 %SOC is used: during the re-lithiation in here-mentioned half-cells, a potential of 3.40 V$_{Li}$ was observed.

For the OEMS experiments, a pre-delithiated LFP counter electrode was placed on the bottom of the custom-made OEMS cell hardware, then covered by two polyolefin separators (24 mm in diameter, H2013, Celgard, USA) that were wetted with 100 μl of LP57 electrolyte, and finally an NCM electrode (14 mm in diameter, NCM:C65:PVDF mass ratio of 96:2:2, with the PC-bm electrode compressed at 100 MPa and the PC and SC electrodes uncompressed) was placed on top of the stack in the spring-compressed OEMS cells. The assembled cells were positioned in a climate chamber (CTS, Germany) at 25 °C and connected to a potentiostat (SP-300, BioLogic, France) and the mass spectrometer system (HiQuad QMH 400–1, Pfeiffer Vacuum, Germany), which has been described in detail elsewhere.[34]

The cells were held at OCV for 4 h before they were charged in constant-current mode (CC) to 4.08 V$_{Li}$ (corresponding to 0.68 V$_{LFP}$ against the pre-delithiated, capacitively oversized LFP counter electrode) at a C-rate of C/5 (corresponding to 55 mA/g$_{NCM}$, referenced to the theoretical capacity of 276.5 mAh/g$_{NCM}$ of NCM622), where they were held for one hour in constant-voltage mode (CV), before they were discharged to ∼3.0 V$_{Li}$ (corresponding to −0.4 V$_{LFP}$). After two full cycles to 4.08 V$_{Li}$, three cycles were executed with a higher upper cutoff potential of 4.73 V$_{Li}$ (corresponding to 1.33 V$_{LFP}$). Each of the five CV steps was followed by a OCV period of 10 min.

The traced mass signals were normalized to the ion current of the ^{36}Ar isotope in order to correct for fluctuations of pressure and temperature, and the signals for O_2 and CO_2 were then converted to concentrations using a calibration gas (Ar with 2000 ppm of H_2, O_2, C_2H_4, and CO_2 each, Westfalen, Germany) and considering a cell volume of ∼11 cm^3, as introduced by Strehle et al. and Jung et al. for the gassing of (LMR-)NCM.[15,35] For details on the calibration procedure, see Tsiouvaras et al.[34]

Impedance spectroscopy.—All electrochemical impedance spectra were included directly into the cycling procedure of a multi-channel potentiostat VMP3 (BioLogic, France) and recorded in a climate chamber (Binder, Germany) at 25 °C in potentiostatic mode (PEIS), with an amplitude of 15 mV for 8 points per decade from 100 kHz to 100 mHz, including a data point at a frequency of 180 mHz. This results in an acquisition time of ∼10 min per PEIS. Each EIS spectrum consists of a full-cell spectrum (between working and counter electrode) and, by using a micro-reference electrode (μ-RE, i.e., a gold-wire reference electrode (GWRE)[36]), also of the half-cell spectrum (i.e., between the working electrode and the μ-RE).

Coin cell assembly and testing.—All electrochemical cycling tests (of both coin and Swagelok T-cells) were performed in a climate chamber (Binder, Germany) at 25 °C, using a battery cycler (Series 4000, Maccor, USA) for cell cycling or a multi-channel potentiostat (VMP3, Biologic, France) for cell cycling with PEIS.

For the Kr-BET surface area determination as well as for the TGA, NCM electrodes (14 mm in diameter, NCM:C65:PVDF mass ratio of 96:2:2, with the PC-bm electrodes compressed at 100 MPa and the PC and SC electrodes uncompressed) as well as C65 electrodes (14 mm in diameter, C65:PVDF mass ratio of 1:1, uncompressed) were assembled in coin cells (CR2032, Hohsen, Japan) using two glass fiber separators (16 mm in diameter), one polyolefin separator (17 mm in diameter, H2013, Celgard, USA) facing the NCM or C65 electrode, and 100 μl of LP57 electrolyte cycled against metallic lithium as counter electrode (15 mm in diameter).

For Kr-BET, the coin half-cells with lithium counter and NCM working electrodes were cycled at a C-rate of C/20 (corresponding to 13.8 mA/g$_{NCM}$ referenced to the theoretical capacity of 276.5 mAh/g$_{NCM}$ of NCM622). After an initial OCV phase of 1 h, the cells were charged to 3.9 V$_{Li}$ or to 4.4 V$_{Li}$, where the potential was held for 1 h, followed by an OCV phase of 1 h. Additional cells were cycled to 4.4 V$_{Li}$ and, subsequently, discharged to 2.55 V$_{Li}$, applying a potential hold of 1 h at both potentials, resulting in a total time of the experiment of 32 h. This procedure is shown in Fig. A·2 in the Appendix. To investigate the influence of the storage of the electrode in the electrolyte on the electrode surface area, additional cells with NCM or C65 electrodes were held at OCV for 24 h.

For thermal analysis via TGA, the coin half-cells with NCM electrodes were first held at OCV for 1 h and then charged at C/15 (corresponding to 18.3 mA/g$_{NCM}$ referenced to the theoretical capacity of 276.5 mAh/g$_{NCM}$ of NCM622) to 4.1 V$_{Li}$, where the potential was held for 1 h, followed by another OCV phase of 1 h (this procedure is also shown in Fig. A·2).

To record the potential charge curves of the three NCMs, coin half-cells with lithium metal as the counter electrode (15 mm in diameter) and PC, PC-bm, and SC as working electrodes (14 mm in diameter, NCM:C65:PVDF mass ratio of 96:2:2, with the PC-bm electrodes compressed at 100 MPa and the PC and SC electrodes

uncompressed) were assembled using two glass fiber separators (16 mm in diameter) and 100 μl of LP57 electrolyte. To allow for the assignment of the applied potential to an SOC (i.e., to a degree of delithiation of the NCM material) for each of the three NCMs, the coin half-cells were charged in constant-current mode to 5.0 V_{Li} at a C-rate of C/20 (corresponding to 13.8 mA/g_{NCM}).

T-cell assembly and testing.—In preparation of the cycling experiments in T-cells (Swagelok, USA) with μ-RE (adapted and reprinted here from a previous publication[14] for the sake of completeness), capacitively oversized LTO electrodes (10.95 mm in diameter, 3.5 mAh/cm²) were pre-lithiated in spring-compressed T-cells using two glass fiber separators (11 mm in diameter) and 60 μl of LP57 electrolyte against metallic lithium (450 μm in thickness and 11 mm in diameter, Rockwood Lithium, USA) to ~10 %SOC at a specific current of 30 mA/g_{LTO} for 0.5 h, after having performed one full formation cycle at 30 mA/g_{LTO} between 1.2 V_{Li} and 2.0 V_{Li}. After pre-lithiation, the LTO electrodes were harvested from the cells and used as the counter electrode in the pseudo full-cells for the electrochemical cycling tests (note that pseudo full-cell here refers to a cell with a specific working electrode and a capacitively oversized, pre-lithiated LTO electrode). As it was already discussed in a previous publication,[19] the pre-lithiated, capacitively oversized LTO are used because they provide: (i) a stable half-cell potential of 1.55 V_{Li} over a wide SOC window, (ii) a sufficiently large capacity to take up the lithium from the investigated NCM working electrodes, and (iii) a sufficient excess of lithium to compensate for any lithium consumed by side reactions during cycling, so that the NCM working electrode can be fully lithiated for the EIS measurements that are being conducted in blocking conditions (see below). Due to the stable half-cell potential of 1.55 V_{Li} of the LTO counter electrode, the NCM working electrode potential could be controlled by the cell voltage.

For the electrochemical cycling tests, spring-compressed T-cells with capacitively oversized pre-lithiated LTO as the counter electrode and NCM as working electrode (10.95 mm in diameter, NCM:C65:PVDF mass ratio of 96:2:2, with all NCM electrodes examined both uncompressed and compressed at 100 MPa) were assembled using two glass fiber separators (11 mm in diameter) and 60 μl of LP57 electrolyte. Between the two separators, a micro-reference electrode (μ-RE) was inserted, namely a gold-wire reference electrode (GWRE) based on the setup described by Solchenbach et al.[36] Prior to the experiments, the GWRE was lithiated in situ at 150 nA over 1 h from the LTO counter electrode before cycling, which establishes a constant GWRE potential of 0.31 V_{Li}[36] that remained stable for more than 800 h (note that the GWRE lithiation charge of ~0.15 μAh is negligible compared to the capacity of the counter electrode). For details about the cell setup and the preparation of the gold wire, please refer to the original publication.[36]

To acquire EIS spectra under blocking conditions, represented by a very large or quasi-infinite charge-transfer resistance, the working electrode is cycled to the fully discharged state (corresponding to ~5 %SOC due to the irreversible capacity of the first cycle) at a potential of 2.55 V_{Li} for all active materials (corresponding to a cell voltage of 1.00 V_{LTO} in the pseudo full-cells), i.e., to full lithiation for the NCM working electrodes, where the working electrode was then held for 1 h prior to taking EIS spectra (for further details, see Ref. [19]). The long-term cycling procedure (adapted and reprinted here from a previous publication[14] for the sake of completeness), was initiated by an OCV phase of 10 h, during which a PEIS was taken every 1 h. To identify the *pristine* value of the electrode capacitance (cycle #0), the NCM working electrode was discharged to the lower cutoff potential of 2.55 V_{Li} at C/10 (corresponding to 27.7 mA/g_{NCM}) in CC mode, where a CV hold of 1 h was performed, followed by a PEIS. During *conditioning* (cycle #1), the electrodes were charged at C/10 in CC mode for 1 h, then discharged to the lower cutoff potential of 2.55 V_{Li} at C/10 in CC mode, where a CV

hold of 1 h was performed, followed by a PEIS. Since nickel-rich CAMs are commonly slightly overlithiated (by up to 1 %) in the synthesis process, the conditioning step was included in the procedure to ensure comparable impedance spectra for each cycle, namely by assuring that similar SOCs are obtained by the potential hold of 1 h at 2.55 V_{Li}, especially when comparing different NCM active materials.

For the subsequent *cycling*, three charge/discharge cycles are executed, with a charge to the initial upper cutoff potential of 3.9 V_{Li} at C/10 followed by a CV hold until the current dropped to below 0.1 mA (~C/20, CCCV mode), and with a discharge to the lower cutoff potential at C/10 followed by a CV hold of 1 h before recording a PEIS (corresponding to cycle #2, #3, and #4). This set of three cycles is then repeated while increasing the upper cutoff potential by 0.1 V for each set after every third cycle, finishing with three cycles to 5.0 V_{Li} (corresponding to cycle #35, #36, and #37). The impedance spectra taken in blocking conditions are numbered by the cycles the cell had performed up to that point (e.g., #7 after the three cycles to 4.0 V_{Li}).

To record the charge curves of the first charge of the three NCMs (shown in Fig. A·4 in the Appendix), coin half-cells with lithium metal as the counter electrode (15 mm in diameter) and PC, PC-bm, and SC as working electrodes (14 mm in diameter, NCM:C65:PVDF mass ratio of 96:2:2, with the PC-bm compressed at 100 MPa and the PC and SC electrodes uncompressed) were assembled using two glass fiber separators (11 mm in diameter) and 100 μl of LP57 electrolyte. To allow for the assignment of the applied potential to an SOC (i.e., to a defined degree of delithiation) for each of the three NCMs, the coin half-cells were charged in constant-current mode (CC) to 5.0 V_{Li} at a C-rate of C/20 (corresponding to 13.8 mA/g_{NCM}).

For the discharge rate tests, spring-compressed T-cells with a lithium metal reference (6 mm in diameter) and a lithium metal counter electrode (11 mm in diameter) as well as NCM-based working electrodes (10.95 mm in diameter, NCM:C65:PVDF mass ratio of 90:5:5, all NCM electrodes compressed at 200 MPa) were assembled using three glass fiber separators (11 mm in diameter, two between working and counter electrode and one on the lithium metal reference electrode) and 90 μl of LP57 electrolyte. The NCM electrodes were cycled between 3.0 V_{Li} and 4.1 V_{Li} measured against the potential of the lithium metal reference electrode. After an initial OCV phase of 1 h, the cells were charged in CCCV mode, with a CV step for 1 h or until the current dropped to below C/20, and were then discharged in CC mode. The applied discharge C-rates (referenced to the theoretical capacity of 276.5 mAh/g_{NCM} of NCM622) were increased from C/100 to C/50, C/20, C/10, C/5, C/2, 1C, 2C, 5C, 10C, 20C, while each rate was applied for three cycles. For C-rates between C/100 and C/2, the charge currents were set to be the same as the ones for discharge, and set to C/2 for all other rates. After the rate test, another 14 cycles with a charge rate of C/2 and a discharge rate of 1C as well as three cycles at C/10 for both charge and discharge were appended.

Cell disassembly.—In several experiments, the NCM electrodes were harvested from charged or discharged coin half-cells under inert atmosphere to determine their specific surface area by Kr-BET as well as their thermal stability by TGA. Any residue of the conductive salt was removed from the electrodes in a three-step sequential washing procedure: first, they were washed for 5 min in 5 ml EC:EMC 3:7 w/w (Gelon Lib, China), followed by a soaking step of 24 h in 1 ml DMC (anhydrous, ⩾99 %, Sigma Aldrich, USA) and, finally, a washing step of 5 min in 5 ml DMC.

Surface area analysis.—The surface area of the active material powders and of the pristine as well as of the harvested and washed electrodes was determined by krypton gas physisorption measurements at 77 K (adapted and reprinted here from previous publications[14,19,21,23] for the sake of completeness), measuring at
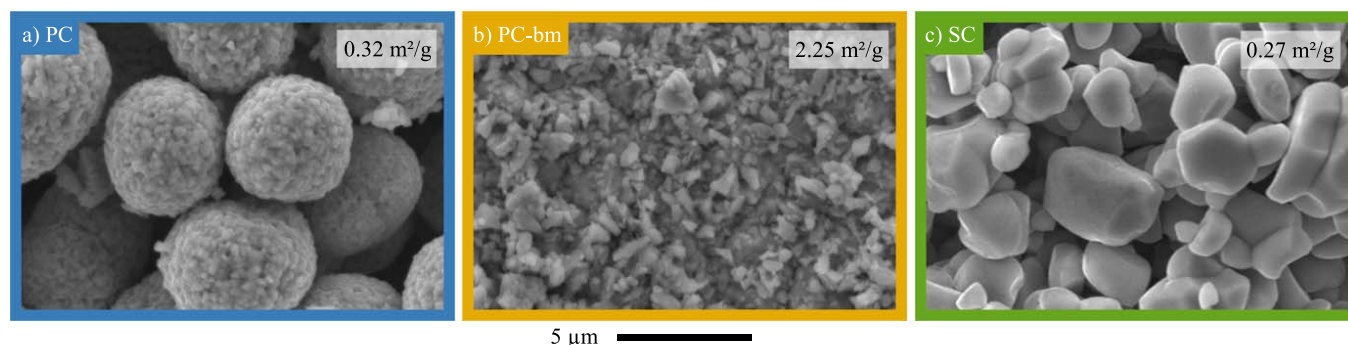
Figure 1. Visual investigation of the particle morphology of the three pristine NCM622 powders by top-view SEM in secondary electron mode at 15 kV. **a)** Polycrystalline NCM (PC). **b)** Ball-milled polycrystalline NCM (PC-bm). **c)** Single-crystalline NCM (SC). The specific surface area obtained by Kr-BET is displayed for each material in the respective panel.

13 points between $0.01 \leqslant p/p_0 \leqslant 0.30$, using an autosorb iQ (Quantachrome Instruments, USA). Comparative N_2-BET measurements for the pristine materials (C65 and NCM powders) are within ±10 % of the specific surface areas obtained by krypton physisorption (also referred to as Kr-BET, referring to the original publication by Brunauer, Emmett, and Teller[37]). The advantage of the measurement with krypton is a superior sensitivity of this method, since only ca. 1/100 of the total surface area is required for krypton compared to nitrogen physisorption measurements, so that Kr-BET areas can be obtained for electrodes with 14 mm in diameter, whereas an approximately 100-fold larger electrode area would be required for meaningful N_2-BET measurements. Prior to Kr-BET measurements, both powder samples as well as samples of pristine or harvested and washed electrodes were dried at 120 °C under vacuum for 6 h. (It has to be noted that these conditions are common, both for the outgassing of samples for BET measurements as well as for the drying of battery electrodes. No Kr-BET measurements were performed with non-dried electrodes, as this would not lead to reliable surface area measurements).

Thermal analysis.—To investigate the thermal stability of charged electrodes by thermogravimetric analysis (TGA), the pristine as well as the washed and harvested electrodes were dried at 120 °C under dynamic vacuum for 6 h. To avoid contact to ambient atmosphere during the transfer to the TGA device (TGA/DSC 1, Mettler Toledo, USA), the electrodes were placed in crimped, airtight aluminum crucibles (Mettler Toledo, USA), which were opened by a needle right before the start of the TGA measurement. First, the measurement cell with the sample was flushed at 25 °C for 5 min under an argon flow rate of 200 ml/min, which was then reduced to 50 ml/min for another 5 min at 25 °C. Subsequently, the sample was heated under a constant argon flow rate of 50 ml/min applying a temperature ramp of 5 K/min from 25 °C to 325 °C, while the mass of the sample was recorded.

Results and Discussion

Visual investigation of pristine NCM622 powders.—In advance to the electrochemical investigations, the morphology of the three NCM622 CAM powders is examined by SEM and BET surface area measurements with krypton gas (Kr-BET). The as-received pristine polycrystalline NCM622 powder (PC, marked in blue color) displayed in Fig. 1a consists of spherical secondary particles with a diameter of 5–10 μm, each comprising thousands of primary crystallites. Kr-BET yields a specific surface area of $0.32~\mathrm{m^2_{NCM}/g_{NCM}}$ for PC, which (based on a spherical approximation of solid spheres with a single diameter $d = 6/(A_{BET} \cdot \rho)$) would correspond to an average diameter of $d \approx 4~\mu m$, using the crystallographic NCM622 density of $\rho = 4.78~\mathrm{g/cm^3}$,[17] suggesting that mostly the external surface area of the secondary particle agglomerates of the pristine PC material is accessible to the electrolyte. For

the pristine ball-milled polycrystalline NCM622 (PC-bm, yellow) shown in Fig. 1b, most of the secondary agglomerates of the polycrystalline NCM622 have been completely separated into their primary particles, showing individual crystallites with a size of 0.2–1.0 μm, while only a few agglomerates with a size of ∼2 μm remain (see also the magnification in Fig. A·1 in the Appendix). If compared to the original polycrystalline material, this separation of the secondary agglomerates into its primary crystallites results in an 8-fold increase of the specific surface area to $2.25~\mathrm{m^2_{NCM}/g_{NCM}}$, corresponding to an average particle size of 0.6 μm (for the spherical approximation). In contrast to the as-received polycrystalline NCM622, the *single-crystalline* NCM622 (SC, green) consists of individual monolithic particles without significant agglomeration, with a particle size ranging from 2–8 μm, as displayed in Fig. 1c, exhibiting a specific surface area of $0.27~\mathrm{m^2_{NCM}/g_{NCM}}$, very similar to that of the PC material.

Therefore, the three NCM622 materials used in this study allow for the discrimination of the effect of particle morphology (polycrystalline vs. single-crystalline) for a similar pristine specific surface area when comparing the PC and SC materials, whereas the comparison of the PC-bm and SC materials allows to examine the effect of the difference in pristine specific surface area (with an ∼8-fold difference) for a similar single-crystalline particle morphology (i.e., without significant secondary agglomerates).

NCM surface area during the first charge/discharge cycle.—Due to their secondary structure, polycrystalline NCM particles experience cracking upon long-term cycling, caused by the repeated volume change of the NCM unit cell upon (de)lithiation and, more importantly, by the anisotropic change of the lattice parameters a and c that induces stress and strain throughout the secondary particle agglomerate.[16,17,19] Particle cracking increases the surface area, facilitating unwanted side reactions as well as the loss of electrical contact between the separated primary crystallites, both leading to a decrease in cell capacity. In a previous publication,[19] SEM analysis of the cross section of an NCM electrode cut by a focused ion beam (FIB-SEM) showed that this chemo-mechanical effect does not only lead to cracking upon extended charge/discharge cycling, but also induces the reversible formation of cracks through the polycrystalline particle in its charged state already in the very first cycle. For single-crystalline materials, however, no (reversible) surface area change is expected upon (de)lithiation due to their monolithic nature having no secondary structure. To quantify the extent of the surface area change of the three active materials during the first charge/discharge cycle, Kr-BET measurements of pristine, stored, and cycled electrodes are performed. To illustrate the procedure, the respective voltage profiles of the stored and cycled PC electrodes are depicted in Fig. A·2.

As mechanical compression of the electrodes affects the integrity of the CAM particles,[19] it was intended to use uncompressed electrodes. However, it was found that the electrochemical

performance of the PC-bm material is very poor when only 2 wt% C65 were used for electrode preparation, as this is too low for the very high specific surface area of PC-bm (2.25 m^2_{NCM}/g_{NCM}) and thus results in significant overpotentials during cycling (data not shown). At the same time, increasing the carbon content in the electrode was not possible due to the high specific surface area of C65, as it would then be the main contributor to the electrode surface area, thereby masking any changes in the CAM surface area. For this reason, the electrodes based on the PC-bm material had to be compressed, but, since the primary crystallites of the PC-bm material were already mostly separated, no change of its specific surface area is expected upon electrode compression. A change of the surface area of the PC-bm material could be excluded by Kr-BET measurements of pristine (un)compressed PC-bm electrodes, which exhibited similar specific surface area values of 2.81 ± 0.03 $m^2/g_{electrode}$ for the uncompressed electrodes (data not shown) and 2.92 ± 0.05 $m^2/g_{electrode}$ for the electrodes compressed at 100 MPa (see Fig. 2a), respectively (note that the error values of the specific surface areas correspond to the minimum/maximum values determined from the separate measurement of two electrodes and are always below ± 0.07 $m^2/g_{electrode}$ or below ± 0.07 m^2_{NCM}/g_{NCM}). Even though we illustrated that the specific surface area and, therefore, the integrity of the PC-bm primary crystallites was maintained despite the mechanical compression at 200 MPa, the integrity is certainly dependent on the applied compressing force and may be affected negatively at higher compressive forces. The advanced mechanical stability of the single-crystalline material as compared to the polycrystalline equivalent is discussed in detail in Fig. 3. For the materials with relatively low specific surface area (i.e., PC and SC), no compression was required, and uncompressed electrodes were used for this experiment.

The measured values of the electrodes obtained by Kr-BET are depicted in Fig. 2a (left y-axis): in the pristine state, the specific surface areas are determined to be 1.20 ± 0.03 $m^2/g_{electrode}$, 2.92 ± 0.05 $m^2/g_{electrode}$, and 1.17 ± 0.03 $m^2/g_{electrode}$ for the PC, PC-bm, and SC electrodes, respectively. For the electrodes charged to 3.9 V_{Li} or to 4.4 V_{Li}, it is observed already in this representation that there is a relatively small increase of the specific surface area of the SC and PC-bm electrodes, while the one of the PC electrodes exhibits a significant increase.

To allow for a quantitative analysis of the surface area change of the NCM active material only, the contribution of C65 and PVDF, which is assumed to remain constant, is subtracted by considering the specific surface area of a C65 electrode (C65:PVDF 1:1 w/w) of 17.9 ± 0.4 $m^2/g_{electrode}$: as the NCM electrodes comprise 2 wt% of C65 and 2 wt% of PVDF, the conductive carbon and binder are assumed to contribute 0.72 ± 0.01 $m^2/g_{electrode}$ to the NCM electrode (corresponding to 4 % of the measured value of the C65 electrode and as marked by the gray area in Fig. 2a). Subtracting this value provides a good estimate of the contribution of the NCM active material to the specific surface area of the electrode and, when normalized by the mass of the NCM in the electrode ($m_{NCM} = 0.96 \cdot m_{electrode}$), of the specific surface area of the NCM material. The latter is displayed on the right y-axis of Fig. 2a in units of m^2_{NCM}/g_{NCM}. For the further discussion, this latter contribution of the NCM only will be considered.

The pristine NCM surface area of 2.30 ± 0.05 m^2_{NCM}/g_{NCM} extracted from the PC-bm electrode (left-most yellow symbol in Fig. 2a) agrees well with the one of 2.25 m^2_{NCM}/g_{NCM} of the PC-bm powder (dashed yellow line). For the PC and SC materials, however, the NCM surface areas in the electrodes of 0.50 ± 0.04 and 0.47 ± 0.04 m^2_{NCM}/g_{NCM} (left-most blue and green symbols) are noticeably larger than the 0.32 and 0.27 m^2_{NCM}/g_{NCM} of the pristine powders (dashed blue and green lines), respectively. The difference for these two NCMs with a low specific surface area could stem from an underestimation of the contribution of C65 and PVDF in the NCM electrode: based on the specific surface area of the C65 powder of 64 m^2_{C65}/g_{C65}, one would expect a value of at least 32 $m^2/g_{electrode}$ for the C65 electrode with PVDF, as 50 wt% are

Figure 2. Specific surface area of PC (blue), PC-bm (yellow), and SC (green) electrodes obtained by Kr-BET measurements at different states of charge. Electrodes were used in the pristine state or harvested from stored or cycled cells. Coin half-cells were assembled using lithium metal as counter electrode, 100 μl of LP57 electrolyte, two glass fiber separators, and one polyolefin separator facing the NCM electrode. Cells were either stored at OCV for 24 h, charged to 3.9 V_{Li} or to 4.4 V_{Li}, or discharged to 2.55 V_{Li} after one full cycle to 4.4 V_{Li}, as depicted by the exemplary potential profiles in Fig. A·2. Electrodes were harvested, washed in carbonate-based solvents, and subsequently dried. **a)** Specific electrode surface area (in units of $m^2/g_{electrode}$, left y-axis) and specific NCM surface area (in units of m^2_{NCM}/g_{NCM}, right y-axis), whereby the latter was obtained by the subtraction of the contribution of the C65 electrode (gray area, multiplied by 0.04). The horizontal dashed lines indicate the expected surface area obtained from Kr-BET measurements of the NCM powders (plotted on the right y-axis). The error bars correspond to the minimum/maximum value of two measurements. **b)** NCM surface area normalized to the value of the pristine NCM surface area, calculated from the values of the right axis of Fig. 2a. The error bars are determined by the laws of error propagation taking into account the error value of the C65 electrode.

contributed by the C65. From the value of 17.9 ± 0.4 $m^2/g_{electrode}$ which was actually measured, however, we conclude that the binder might agglomerate C65 particles and/or cover its surface and/or its pores, resulting in a lower electrode surface area as expected from the powder values. When an NCM electrode is prepared, the binder is distributed between NCM and C65, reducing the covering effect of the binder on the carbon and therefore, possibly increasing the contribution of the C65 to the surface area of the NCM electrode. This increase would result in the observed overestimation of the NCM specific surface area and an underestimation of its relative increase upon charge; therefore, the determined NCM specific surface area increase represents a lower limit only.

To assure that the mere exposure of the electrodes to the electrolyte does not affect the Kr-BET measurement (e.g., through the decomposition of residual lithium salts such as Li_2CO_3 in pores of the polycrystalline particles by HF impurities),[23,38] all electrodes were also stored with electrolyte in the cell at OCV for 24 h, then harvested, washed, and subjected to Kr-BET measurements. In this experiment, the surface area

of the C65 electrode remains constant at 18.0 ± 0.7 m^2/g$_{electrode}$ (data not shown), which is why it is assumed to also be unchanged throughout the following experiments. The stored NCM electrodes exhibit NCM surface areas of 0.41 ± 0.02 m$^2_{NCM}$/g$_{NCM}$, 2.33 ± 0.02 m$^2_{NCM}$/g$_{NCM}$, and 0.51 ± 0.07 m$^2_{NCM}$/g$_{NCM}$ for the PC, PC-bm, and SC electrodes, respectively (see second set of symbols from the left in Fig. 2a), which are essentially identical with the values obtained for the pristine electrodes within the measurement error.

After the charge to 3.9 V$_{Li}$ (corresponding to 49 %SOC, see Fig. A·4 in the Appendix), the specific surface area of the SC material remains unchanged (showing a value of 0.50 ± 0.02 m$^2_{NCM}$/g$_{NCM}$) and that of the PC-bm material increases only slightly (to 2.44 ± 0.07 m$^2_{NCM}$/g$_{NCM}$). In contrast to these two single-crystalline materials, the specific surface area of the polycrystalline PC material increases drastically (to 1.26 ± 0.05 m$^2_{NCM}$/g$_{NCM}$). This value corresponds to a $\sim$2.5-fold specific surface area increase as compared to the pristine PC material, which is depicted in Fig. 2b. These trends continue when the electrodes are charged to 4.4 V$_{Li}$ (corresponding to 76 %SOC, see Fig. A·4): the specific surface areas of both the SC and PC-bm materials increase slightly to 0.65 ± 0.02 and 2.68 ± 0.04 m$^2_{NCM}$/g$_{NCM}$, respectively, while the one of the PC material increases further to 1.48 ± 0.02 m$^2_{NCM}$/g$_{NCM}$, corresponding to a $\sim$3-fold increase over the pristine PC material. Additionally, this experiment shows that the specific surface area of the PC material after its first charge to 4.4 V$_{Li}$ reaches 55 % of the specific surface area of the pristine PC-bm, what implies that more than half of the surface area of the primary crystallites in the polycrystalline secondary particle agglomerates is exposed to the electrolyte already during the very first charge.

Discharging again to 2.55 V$_{Li}$ after the initial charge to 4.4 V$_{Li}$, the NCM materials show specific surface areas which are similar to the ones in their pristine state: 0.49 ± 0.02 m$^2_{NCM}$/g$_{NCM}$ for PC, 2.55 ± 0.02 m$^2_{NCM}$/g$_{NCM}$ for PC-bm, and 0.48 ± 0.02 m$^2_{NCM}$/g$_{NCM}$ for SC. This is in contrast to a previous study, where we found that the specific capacitance of a polycrystalline NCM622 increases by $\sim$50 % and by $\sim$70 % after a first full cycle to 4.2 V$_{Li}$ and 4.5 V$_{Li}$, respectively,[19] so that one would have expected a similar increase in NCM specific surface area. This suggests that for the here performed ex situ surface area determination by Kr-BET, it is possible that small pores are closed/clogged due to the washing and drying procedure of the harvested electrodes.

De Biasi et al. showed that NCM622 experiences a volume change of its unit cell of -0.8 % as well as a change of the ratio of its *a* and *c* lattice parameters of $+3.3$ % for a charge to 3.9 V$_{Li}$, whereas a charge to 4.4 V$_{Li}$ induces a volume change of -3.0 % and an *a/c* change of $+1.9$ %. Apparently, these structural changes are responsible for the up to $\sim$3-fold specific surface area of the here investigated polycrystalline NCM622 (PC) observed in the charged state, which can be induced by cracking of the primary crystallites and/or by a gradual separation of the primary crystallites in the secondary particle agglomerates. The former is expected to be minor due to the much lower specific surface area increase of the single-crystalline materials (SC and PC-bm, see Fig. 2a), so that the major effect must be the formation of cracks between the primary crystallites in the secondary particle agglomerates, in which case the specific surface area increase should depend on the size, shape, and orientation of the primary crystallites, as suggested by Kim et al.[39] Similar increases in the specific surface area in the charged state were also observed for NCM811 by Trevisanello et al.,[20] who showed by Kr-BET that the NCM811 specific surface area changes by $\sim$3.5-fold and $\sim$4.5-fold when charged to 3.9 V$_{Li}$ ($\sim$50 %SOC) and 4.2 V$_{Li}$ ($\sim$75 %SOC), respectively. Our study shows that this process seems to be reversible, as the specific surface area of the PC material discharged after one full cycle is similar to the one observed for the pristine material, suggesting that the initially formed cracks close again in the discharged state.

The reversible change of the specific surface area by a factor of $\sim$1.4 between the charged state at 4.4 V$_{Li}$ and the subsequent discharged state, however, cannot likely be explained by reversible opening and closing of cracks between primary particles, as very few

particles are fused together (see Fig. 1). However, the reversible gliding of the (003) planes, previously observed by scanning tunneling electron microscopy (STEM) and in situ atomic force microscopy (AFM) in a study by Bi et al. for a nickel-rich NCM,[40] could roughen the surface area of single-crystalline materials in the charged state and, therefore, be the origin of the (relatively small) reversible change in surface area. This would also explain the small reversible change in specific surface area observed for the PC-bm material ($\sim$1.2-fold).

Overall, the behavior of the specific NCM surface area as a function of its state of charge differs significantly depending on the NCM particle morphology: polycrystalline materials increase their surface (reversibly) already during the first charge, whereas the surface area of single-crystalline materials remains almost constant. While the absolute value of the specific surface area of PC material in its pristine state is similar to the one of the SC material, its drastic specific surface area increase upon charge is expected to promote a larger amount of released lattice oxygen at high state of charge, an improved rate capability, as well as a decreased thermal stability.

Morphological stability at high state of charge.—To investigate the effect of the SOC on the particle integrity for the poly- and single-crystalline morphologies, the NCMs are cycled at slow rates while the upper cutoff potential is increased stepwise by 0.1 V every three cycles, using the exact procedure introduced in a previous publication.[14] Any induced morphological changes that increase the electrode surface area can be followed through the measurement of the NCM capacitance in the fully discharged state, i.e., in blocking conditions.

It was shown previously that the release of lattice oxygen from NCMs due to structural instabilities which are often attributed to the H2-H3 phase transition at high degrees of delithiation, viz., at/above $\sim$80 %SOC, has a negative effect on the discharge capacity;[7,15,41] additionally, these processes are accompanied by a sudden increase of the specific surface area of polycrystalline NCMs at high SOCs.[14] To better illustrate this behavior, the measured specific discharge capacity and electrode capacitance data (depicted in Fig. A·3 as a function of cycle number) are plotted as a function of SOC in Fig. 3. The latter is determined from an analysis of the potential curves collected in half-cells charged to 5.0 V$_{Li}$ (see Fig. A·4), allowing to assign each one of the applied upper cutoff potentials (i.e., 3.9, 4.0, …, and 5.0 V$_{Li}$) to its respective SOC (corresponding to the degree of delithiation *x* in Li$_{1-x}$MO$_2$, as introduced previously.[14] For the PC-bm material, however, only the pristine and the conditioned electrode (i.e., after a C/10 charge of 1 h and subsequent discharge to 2.55 V$_{Li}$) could be analyzed, since the impedance spectra obtained after subsequent cycling were corrupted by additional features, as discussed below in more detail.

The specific discharge capacity depicted in Fig. 3a increases linearly with SOC for both the PC and SC materials, up to a degree of delithiation of $\sim$80 %SOC (i.e., up to an upper cutoff potential of 4.5 V$_{Li}$ in cycle #22). During these first 22 cycles, the SC material consistently delivers $\sim$10 mAh/g$_{NCM}$ less discharge capacity as compared to the PC material, what we assign to a kinetic limitation caused by the much lower specific surface area that is accessible to the electrolyte in the charged state even after one cycle (see Fig. 2a); this difference is further analyzed below in the discussion on the rate capability in Fig. 5. At 4.5 V$_{Li}$ (or $\sim$80 %SOC), the PC material reaches a discharge capacity of 202 ± 3 mAh/g$_{NCM}$ compared to only 185 ± 2 mAh/g$_{NCM}$ for the SC material (note that the error values of the specific capacities as well as of the specific capacitances correspond to the minimum/maximum values determined from the measurement of two cells). Above 80 %SOC (i.e., starting at 4.6 V$_{Li}$ in cycle #25), the discharge capacity does not follow its observed linear increase with SOC anymore and even decreases significantly, particularly in the case of the SC material: while the PC material delivers its maximum discharge capacity of 216 ± 2 mAh/g$_{NCM}$ at 4.7 V$_{Li}$, the maximum discharge capacity of 185 ± 3 mAh/g$_{NCM}$ is already reached at 4.5 V$_{Li}$ (#28) for the SC material. We assign this

earlier and larger decrease in discharge capacity of the SC material to its almost an order of magnitude larger primary crystallite size: while the release of lattice oxygen near/beyond ∼80 %SOC is known to form a resistive, oxygen-depleted surface layer on NCMs,[15,23] the specific surface area of the SC material remains at lower values as compared to the PC material, both when charged (see Fig. 2) and/or when electrodes are mechanically compressed during preparation (see Fig. 3b), what results in a higher surface-area-normalized current at a given *C*-rate and, therefore, in a higher overpotential during cycling. This effect (amongst others) decreases the capacity of single-crystalline CAMs at high SOCs, as we had previously observed and analyzed in more detail for NCM851005 in similar experiments.[14] Overall, a high SOC is detrimental for the discharge capacity of NCMs, especially for SC materials with larger primary crystallite size.

To track the effect of a high SOC on the morphological stability of the three NCMs, the electrode capacitance was measured in situ from the recorded impedance spectra as a function of the upper cutoff potential (reprinted here from a previous publication for the sake of completeness[14]). All spectra of the working electrode were collected via the μ-RE (i.e., the gold-wire reference electrode[36] (GWRE)) after each cycle in the fully discharged state at an NCM potential of 2.55 V_{Li}. As the charge transfer of NCMs is impeded in the fully discharged/lithiated state, resulting in a very large or quasi-infinite value of the charge-transfer resistance (so-called *blocking conditions*), the impedance is dominated by the capacitive contribution of the electrochemical double layer at the electrode/electrolyte interface.[19,42] Assuming that the surface-area-normalized capacitance is distinct, constant, and uniformly distributed for each of the electrode components (i.e., the active material and the conductive carbon), the capacitance contribution of each of the electrode materials would be proportional to their respective surface area, what was proven by Kr-BET in previous publications.[14,19] There, we had also shown that the electrode capacitance does not necessarily have to be extracted from a fit of the entire impedance spectrum, but that the impedance of the individual frequency point at 180 mHz under blocking conditions is sufficient to accurately determine the electrode capacitance (for more details, see Ref. 19). Quantitatively, the electrode capacitance is obtained from the capacitive branch of the NCM electrode impedance spectrum in blocking conditions, which was achieved for all recorded impedance spectra through the full lithiation of the NCM particles by a potential hold of 1 h at 2.55 V_{Li}. From the spectra, the value of the imaginary part of the electrode impedance Z_{ω_0} at the selected frequency of $f_0 = 180$ mHz (with $\omega_0 = 2 \cdot \pi \cdot f_0$) yields the electrode capacitance Q by means of Eq. 1:[19]

$$Q \approx \frac{1}{\omega_0 \cdot (-\text{Im}(Z_{\omega_0}))} \quad [1]$$

The thus obtained capacitance values can then be normalized by the electrode mass (in units of $F/g_{electrode}$) serving as a measure for the specific electrode surface area.

Unfortunately, in case of the uncompressed PC-bm electrodes, the impedance spectra showed an additional semicircle (of ∼1 kΩ·cm²$_{electrode}$) at high to medium frequencies (at around 100 kHz to 1 Hz) in their discharged state only; this feature was absent for the compressed PC-bm electrodes in their pristine state but developed also there upon cycling (with a somewhat smaller value ranging from 0.1–1 kΩ·cm²$_{electrode}$). We assign these observations to the relatively large surface area of the PC-bm material (of 2.25 m²$_{NCM}$/g$_{NCM}$) and the resulting low carbon-to-surface-area ratio in combination with the poor electrical conductivity of NCM at full lithiation,[43] which seems to result in a growing contact resistance upon cycling as well as a poor electrical conductivity through the electrode at low SOC (note that a similar behavior was also observed for an LNMO (LiNi$_{0.5}$Mn$_{1.5}$O$_4$) cathode when using 1.5 wt% rather than 5 wt% of conductive carbon[44]). An increase of
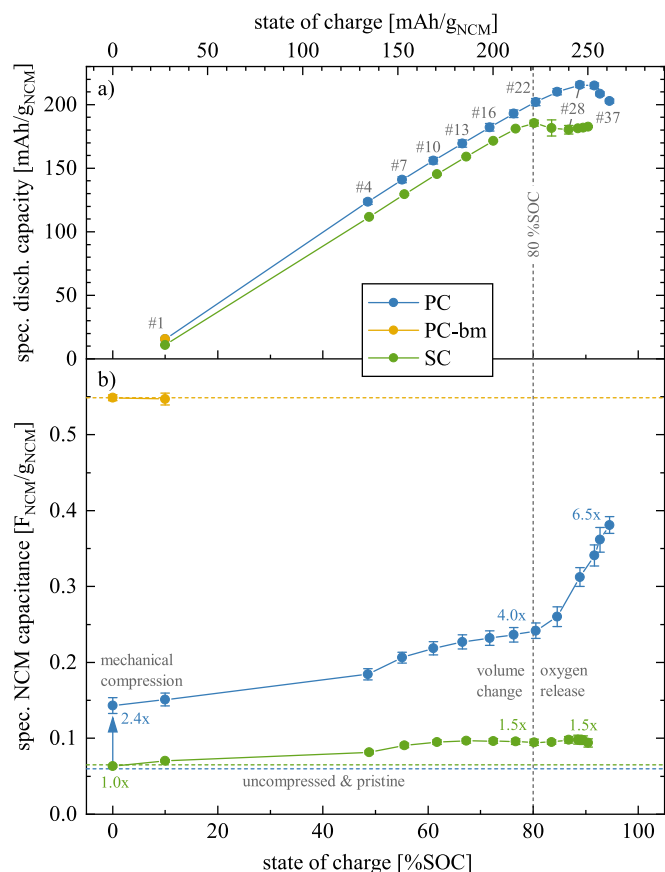
Figure 3. Electrochemical cycling data as a function of SOC for PC (blue), PC-bm (yellow), and SC (green) as working electrodes (all compressed at 100 MPa) in pseudo full-cells with 60 μl LP57, two glass fiber separators, and a μ-RE, using pre-lithiated, capacitively oversized LTO as the counter electrode. Following a previously developed procedure,[14] the cells were cycled at 25 °C and at C/10 to an upper cutoff potential which was increased every three cycles by 0.1 V, starting at 3.9 V_{Li}. Impedance spectra of the NCM working electrodes were recorded in blocking conditions after a potential hold of 1 h at 2.55 V_{Li} (15 mV amplitude, from 100 kHz to 100 mHz), from which the electrode capacitance was extracted. The obtained capacity and capacitance data are depicted in Fig. A·3 as a function of cycle number and then presented here for every third cycle as a function of SOC (top x-axis in mAh/g$_{NCM}$, bottom x-axis in terms of the degree of delithiation *x* in Li$_{1-x}$MO$_2$), which was calculated for each NCM material from the applied upper cutoff potential using the potential curves of the first charge depicted in Fig. A·4. The vertical gray dashed line marks the value of ∼80 %SOC (extracted from Fig. A·4), and the gray numbers mark the cycle for which the data were extracted from Fig. A·3. The specific capacitances and the specific discharge capacities represent the mean of two nominally identical cells, with the error bars corresponding to the minimum/maximum value of two cells. **a)** Specific discharge capacity delivered at a given SOC and normalized by the NCM mass. **b)** Specific NCM capacitances (in units of F$_{NCM}$/g$_{NCM}$). Derived from the specific capacitance of the NCM working electrodes (in units of F/g$_{electrode}$, as depicted in Fig. A·3b) determined from the imaginary impedance at 180 mHz in blocking conditions, with a subsequent subtraction of the contribution of the C65 electrode and a normalization to the NCM mass. The blue and green horizontal dashed lines indicate the capacitance value of the pristine uncompressed PC and SC electrodes, respectively, and the yellow dashed line the one of the compressed pristine PC-bm electrode. The blue and green numbers indicate the relative change of the capacitance at selected SOCs as compared to the pristine uncompressed electrode. The error bars are determined by the laws of error propagation (see supporting information of a previous publication[19]), using the average capacitances and their minimum/maximum values given by Fig. A·3b.

the carbon content in the electrode would alleviate this problem but was not feasible for the analysis of the NCM capacitance since the excessively high capacitance contribution from the high-surface-area

carbon would not allow anymore to quantify the NCM capacitance at higher carbon content (due to the high specific surface area of carbon compared to that of the NCMs, as discussed in detail for the Kr-BET measurements).

For the PC and SC materials, the effect of electrode compression during fabrication of the polycrystalline and single-crystalline morphologies is analyzed in the pristine state (shown at 0 %SOC), comparing both uncompressed and compressed electrodes for the PC and SC materials. As the determination of the capacitance of the uncompressed PC-bm electrode was not possible (see above), and as the primary crystallites of PC-bm were already separated mechanically during ball milling, the effect of compression as well as the effect of charge/discharge cycling on the electrode surface area is assumed to be negligible for PC-bm electrodes; therefore, the results of the PC-bm material are only depicted for compressed electrodes in their pristine and conditioned state, representing the value of the capacitance expected for the fully exposed primary crystallite surface area of the PC material.

The measured specific electrode capacitance of the three NCM morphologies is displayed in Fig. A·3b as a function of cycle number. In the pristine uncompressed state (electrodes having a thickness of $46 \pm 3 \, \mu m$ and a porosity of 59 %), the capacitance amounts to $0.127 \pm 0.001 \, F/g_{electrode}$ and $0.131 \pm 0.001 \, F/g_{electrode}$ for the PC and SC electrodes, respectively (shown in Fig. A·3b as green and blue horizontal dashed lines); in the pristine compressed state (electrodes having a thickness of $37 \pm 3 \, \mu m$ and a porosity of 49 %), the capacitance is increased to $0.207 \pm 0.010 \, F/g_{electrode}$ for PC but remained unchanged with a value of $0.130 \pm 0.001 \, F/g_{electrode}$ for the SC material (shown in Fig. A·3b as green and blue symbols at 0 %SOC, respectively), while the one of the PC-bm material is $0.596 \pm 0.004 \, F/g_{electrode}$ (yellow horizontal dashed line and yellow symbol at 0 %SOC).

For a quantitative analysis of the capacitance of the NCM active material only, the contribution of C65 and PVDF is subtracted: for the C65 electrode (with a composition of C65:PVDF of 1:1 w/w), a specific capacitance of $1.729 \pm 0.028 \, F/g_{electrode}$ was previously obtained.[19] As the NCM electrode comprises 4 wt% of the carbon-binder mixture at the same C65:PVDF ratio, a capacitance value of $0.069 \pm 0.001 \, F/g_{electrode}$ (corresponding to 4 % of the measured value of the C65 electrode, and displayed as the gray area in Fig. A·3b) is subtracted from the capacitance value of the electrode, resulting in the value of the NCM only, which is subsequently normalized to the NCM mass in the electrode, as done in a similar manner above for the Kr-BET measurements. Through this approach, capacitance values of the NCM only in the pristine uncompressed electrode of $0.060 \pm 0.001 \, F_{NCM}/g_{NCM}$ and $0.065 \pm 0.001 \, F_{NCM}/g_{NCM}$ are obtained for the PC and SC material, respectively (shown in Fig. 3b as green and blue horizontal dashed lines). In the pristine compressed state, the NCM capacitance amounts to $0.143 \pm 0.010 \, F_{NCM}/g_{NCM}$ for the PC material, $0.549 \pm 0.003 \, F_{NCM}/g_{NCM}$ for the PC-bm material, and $0.064 \pm 0.001 \, F_{NCM}/g_{NCM}$ for the SC material. When comparing the NCM capacitance values of the pristine electrodes (uncompressed for the PC and SC materials, and compressed for the PC-bm material), a ratio of 1:0.93:8.5 is observed for PC:PC-bm:SC, which agrees reasonably well (within an error of <20 %) with the ratio of the specific surface areas of the pristine powders of 1:0.82:7.0 obtained by Kr-BET (see Fig. 1). This illustrates nicely that the in situ determined capacitance is a reasonably good measure of the CAM specific surface area determined by ex situ Kr-BET and demonstrates the convenience and relevance of the capacitance-based in situ determination of any changes in the CAM specific surface area.

Upon electrode compression (at 100 MPa for 30 s), the NCM capacitance of the PC material changes by a factor of 2.4x from a value of $0.060 \pm 0.001 \, F_{NCM}/g_{NCM}$ to $0.143 \pm 0.010 \, F_{NCM}/g_{NCM}$. The same increase was observed already for the same polycrystalline NCM622 material in a previous publication (also 2.4-fold when

compressed to 100 MPa), where this capacitance change was verified through Kr-BET measurements and further explained by FIB-SEM images, which clearly identified the appearance of partially cracked secondary particles.[19] For the SC material, however, the capacitance remains unchanged at $0.064 \pm 0.001 \, F_{NCM}/g_{NCM}$ upon compression. As the capacitance and, therefore, the specific surface area of the single-crystalline materials is unaffected, particle cracking by mechanical compression (at least for pressures up to 100 MPa) can be excluded, highlighting the mechanical stability of the primary crystallites in contrast to that of the secondary particle agglomerates in the polycrystalline material, as it was already shown qualitatively in a previous study.[45]

During the conditioning cycle to 10 %SOC (see cycle #1 in Fig. 3b), the NCM capacitance of the PC-bm material remains unchanged as compared to its compressed and pristine state (yellow symbols and dashed yellow line). For the compressed PC and SC materials, however, a slight increase of the capacitance is observed during conditioning, which then continues for both materials during the subsequent cycles (blue and green symbols, respectively): For the SC material, the evolution of the NCM capacitance does not exceed a value of $0.098 \pm 0.006 \, F_{NCM}/g_{NCM}$, corresponding to an increase of not more than 1.5x over the entire SOC range, which is already reached when cycled to 67 %SOC (#13 or 4.2 V_{Li}). The PC material, however, shows an enhanced and steady NCM capacitance increase during the cycling up to 80 %SOC (cycle #22 or 4.5 V_{Li}), yielding a capacitance of $0.242 \pm 0.010 \, F_{NCM}/g_{NCM}$, i.e., 4.0x larger than in its pristine and uncompressed state. This steady increase is interrupted by a sudden rise of the capacitance when cycled beyond 80 %SOC (marked by the vertical gray dashed line), which reaches $0.381 \pm 0.011 \, F_{NCM}/g_{NCM}$ when cycled up to 95 %SOC (#37 or 5.0 V_{Li}). The possible causes for this increase are the change of the unit cell volume of the oxygen-depleted surface layer and/or the decomposition of residual lithium salts[38] in the pores, as already discussed in detail in our previous publication.[14]

Most importantly, it must be noted that the NCM capacitance (and thus its specific surface area) of the PC material does not only rise by a factor of 6.5x when cycled to high SOCs as compared to its pristine and uncompressed state, but that it reaches 69 % of the NCM capacitance value of the PC-bm material for which the secondary agglomerates were almost fully separated into their primary crystallites. This implies that two thirds of the primary crystallite surface area of the polycrystalline NCM622 material are exposed to the electrolyte already after a few cycles to high SOC. In contrast, the single-crystalline material shows a resilience toward particle cracking—not only to cracking upon mechanical compression as discussed above, but additionally to cracking both upon repeated volume change during (de)lithiation as well as upon oxygen release at high SOCs. Here it should be noted, however, that the cracking of the primary crystallites of single-crystalline CAMs has been observed under more harsh conditions, namely over the course of long-term cycling at higher rates and elevated temperatures.[46–48]

Structural stability and gas evolution at high state of charge.— To illuminate the effect of particle morphology on the gassing behavior, the three NCM materials are cycled consecutively to two different upper cutoff potentials, one below the onset of the release of lattice oxygen and one above, while the amounts of evolved oxygen (O_2, determined at the mass-over-charge ratio of $m/z = 32$) and carbon dioxide (CO_2, $m/z = 44$) were tracked, as depicted in Fig. 4. To avoid any effect on the integrity of the NCM particles upon mechanical compression, uncompressed PC and SC electrodes were investigated, while the PC-bm electrode had to be compressed at 100 MPa (this should not alter the PC-bm specific surface area, as already discussed above).

During the first two cycles to 4.08 V_{Li} (corresponding to a degree of delithiation of 60 %SOC when converted using the charge curve in Fig. A·4), the potential curves shown in Fig. 4a as a function of time coincide for all three NCMs; only during the first hour of the

initial charge (i.e., up to ~20 %SOC), the overpotential of the PC electrode (blue curve in Fig. 4a) is higher as compared to that of the PC-bm electrode (yellow), while that of the SC electrode (green) is even more pronounced, appearing in the form of an initial potential spike. A similar behavior was also observed in half-cells during the first charge at $C/20$ (i.e., a quarter of the here used C-rate), where the SC electrode requires the highest overpotential and the PC-bm electrode the lowest, as seen in Fig. A·4, albeit to a smaller extent due to the lower applied specific current. This difference in the initial charge overpotential is believed to originate from the effect of the different particle morphologies of the three CAMs, which will be discussed in detail for the discharge rate test in Fig. 5. In addition, as the charge-transfer resistance of NCMs becomes very large at both ends of the SOC window,[23] the observed morphology-dependent overpotential is particularly pronounced in the pristine and, therefore, fully lithiated state at the beginning of the first charge; it decreases to negligible values at intermediate SOC values, as reflected in the data of Figs. 4a and A·4. In conclusion, the observed initial charge overpotential is more pronounced for smaller specific CAM surface areas, for very low/high SOCs, and for faster C-rates. Additionally, no relaxation of the potential is observed during the 10 min OCV phases (following the 1 h CV hold) at the upper cutoff potential of the first two cycles, which implies a negligible overpotential in the intermediate SOC range for the applied current if cycled below the onset of oxygen release.

For the subsequent three cycles to 4.73 V_{Li} (or 90 %SOC), the potential curves in Fig. 4a start to differ depending on the particle morphology: the required time per cycle is smallest for the SC material, followed by the PC-bm material, and longest for the PC material, which is also reflected in the discharge capacities discussed below in Fig. 4b. Additionally, a significant potential drop appears after the CV hold once the potential was cycled into the oxygen release region: for the fifth and last cycle, the NCM potential drop during the OCV phase of 10 min amounts to 38 and 42 mV for the PC-bm and the PC material, respectively, while the OCV drop amounts to 119 mV for the SC material. This finding coincides with the previous observation of a pronounced capacity loss of single-crystalline materials due to the impedance build-up at high SOCs (see green data points in Fig. 3a for the NCM622 SC material as well as a previous publication for an NCM851005 SC material[14]) on account of the formation of an oxygen-depleted surface layer, in combination with the relatively low and constant specific surface area of the single-crystalline material (see Figs. 2 and 3b).

When considering the discharge capacities that are depicted in Fig. 4b, a similar picture emerges: during the first two cycles to 4.08 V_{Li}, the PC-bm material delivers with 146 mAh/g_{NCM} the highest capacity, followed by the PC material with 143 mAh/g_{NCM}, while the SC material provides only 138 mAh/g_{NCM}. These values coincide well with the determined discharge capacities at the identical C-rate of $C/5$, shown in Fig. 5 for the discharge rate test in half-cells to an upper cutoff potential of 4.1 V_{Li}. As the upper cutoff potential is increased to 4.73 V_{Li}, the discharge capacities increase to 217 mAh/g_{NCM}, 210 mAh/g_{NCM}, and 204 mAh/g_{NCM} for the PC, the PC-bm, and the SC material, respectively (see Fig. 4b). During these three cycles to 4.73 V_{Li}, all materials suffer from a fading of the discharge capacity in the range of 6–12 mAh/g_{NCM}. When comparing the first two and the last three cycles in Fig. 4b, an increased difference in the discharge capacity of the PC and the SC material becomes apparent, which we assign to the pronounced impedance build-up of the SC material, supporting the arguments of the above discussion. For the PC-bm material, the lower discharge capacity obtained at high upper cutoff potential as compared to the one of the PC material is believed to result from the relatively high surface area (of 2.25 m$^2_{NCM}$/g_{NCM}) of the pristine powder in combination with the relatively low conductive carbon content (of 2 wt%) in the electrode: When the electrical conductivity of lithium layered oxides of roughly $10^{-1}-10^{0}$ S/cm for LiNiO$_2$ (LNO, being a semiconductor)[49–51] is compared to the one of the respective rock-salt structure of NiO with $10^{-7}-10^{-5}$ S/cm (being an
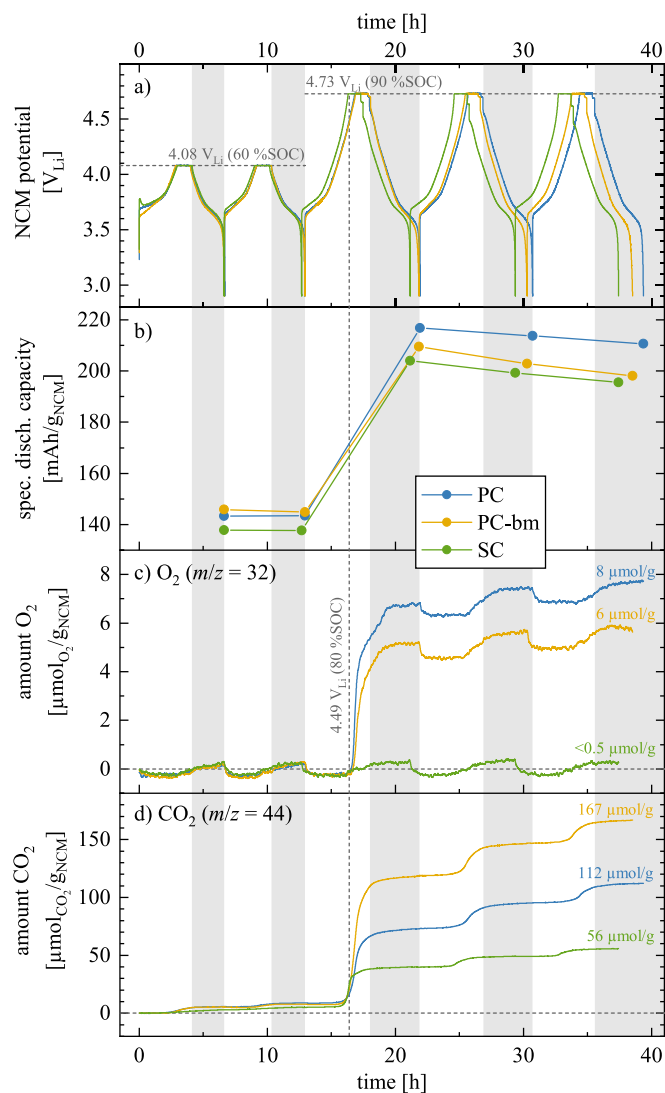
Figure 4. Cycling and gas evolution data as a function of time for OEMS cells assembled with PC (blue), PC-bm (yellow), and SC (green) as working electrodes (uncompressed for PC and SC; compressed at 100 MPa for PC-bm), using delithiated, capacitively oversized LFP as counter electrode, two Celgard H2013 separators, and 100 μl LP57 electrolyte. The cells were cycled at 25 °C at $C/5$ (corresponding to 55.3 mA/g_{NCM} when referenced to the theoretical NCM622 capacity of 276.5 mAh/g_{NCM}), with a 1 h CV hold at the upper potential cutoff followed by a 10 min OCV phase, recording the gas evolution by mass spectrometry: (i) two cycles to an NCM potential of 4.08 V_{Li} (corresponding to 0.68 V_{LFP} cell voltage or to a degree of delithiation of 60 %SOC (determined from the potential curve in Fig. A·4)); (ii) three cycles to 4.73 V_{Li} (corresponding to 1.33 V_{LFP} cell voltage or to 90 %SOC). **a)** NCM cathode potential vs. Li$^+$/Li. **b)** Specific discharge capacity for each of the five cycles. **c)** & **d)** Total amount of evolved oxygen (determined at $m/z = 32$) and carbon dioxide (at $m/z = 44$) in the OEMS cell, both normalized to the NCM mass (in units of μmol$_{gas}$/g_{NCM}). The vertical light gray areas accentuate each NCM discharge/lithiation period (marked for the PC material). The vertical gray dashed line marks the onset of the O$_2$ evolution of PC at a potential of 4.49 V_{Li}, corresponding to a degree of delithiation of ~80 %SOC. The numbers represent the gas amounts obtained at the end of the experiment.

insulator),[52,53] the latter has an at least four orders of magnitude lower conductivity. If the electrical conductivity of the NCM622 material were to be in the same range as the one of LNO, and if the electrical conductivity of the corresponding oxygen-depleted (rock-salt-type) near-surface layer formed upon lattice oxygen release were also to be lower by several orders of magnitude, the electron transport across the NCM electrode thickness would have to rely on the conductive carbon, which seems, however, not sufficient for the

PC-bm particle morphology. This is supported by the fact that rate capability of the PC-bm based electrodes is actually superior to that of the PC and SC electrodes when the amount of conductive carbon in the electrode is increased to 5 wt% (demonstrated below in Figs. 5 and A·6). The lower carbon content of 2 wt% is apparently sufficient for the PC and SC electrodes, explained by the fact that their pristine specific surface areas are ∼8-fold lower compared to the PC-bm material, so that 2 wt% of carbon seem to suffice for good electrical conduction across the electrode thickness.

During the cycling experiment, the specific amounts of evolved oxygen are monitored for each NCM material and depicted in Fig. 4c. Apart from the apparent release of lattice oxygen initially observed for the first cycle to 4.73 V_{Li} (i.e., for the third of the five cycles) for the PC (blue line) and the PC-bm (yellow) material, a periodic increase and decrease of the oxygen signal is observed, which is visible best for the SC (green) material: it decreases to around −0.5 $\mu mol_{O_2}/g_{NCM}$ during charge, and then increases to around +0.5 $\mu mol_{O_2}/g_{NCM}$ during discharge (corresponding to a fluctuation of the apparent O_2 concentration of ±20 ppm), which is not only visible for all of the five cycles, but also similar in its extent, independent of the upper cutoff potential. At first sight, one explanation could be the potential-dependent consumption and production of oxygen by the reversible reaction of lithium oxide to/from lithium peroxide, as it is known from lithium-air battery research,[54–56] e.g., happening for residual lithium oxide on the surface of the NCMs, as previously suggested by Yabuuchi et al.[57] This, however, would result in a release of molecular oxygen at potentials >4.0 V_{Li} (i.e., during charge),[54–56] whereas the opposite is observed in this experiment (i.e., a decrease of the oxygen signal at high potential). Furthermore, NCM622 should not evolve any oxygen when cycled to only 4.08 V_{Li} (i.e., to 60 %SOC), putting in question whether the signals at $m/z = 32$ really derive from oxygen.

In principle, it could be possible that a fluctuating concentration of the electrolyte solvents in the gas phase (i.e., ethylene carbonate (EC) or ethyl methyl carbonate (EMC)) could affect the signals at $m/z = 32$. Due to the four orders of magnitude higher vapor pressure of the linear carbonate,[58] this affect would be dominant for EMC, which has its main MS signal at $m/z = 77$ and, due to the fragmentation pattern in the MS, minor signals at, e.g., $m/z = 32$ (∼20 % of the one at $m/z = 77$) and at $m/z = 44$ (∼20 %), as shown by Strehle et al.[59] Looking at the signal of $m/z = 77$ multiplied by 20 % (corresponding to the expected signal contribution at $m/z = 32$) as well as the signal of $m/z = 44$, both signals show a similarly fluctuating behavior, changing simultaneously as the one at $m/z = 32$ (note that all ion currents were normalized to the signal at $m/z = 36$ of the ^{36}Ar isotope, see Fig. A·5). Since EMC is expected to be the only substance which can be detected in this experiment on the signal at $m/z = 77$, we assign the apparent O_2 signal fluctuation of ±0.5 $\mu mol_{O_2}/g_{NCM}$ to a fluctuation of the EMC background signal (note that the fluctuation of the $m/z = 44$ signal cannot be observed in the representation of Fig. 4d due to the relatively high CO_2 evolution during this experiment, which is at least two orders of magnitude higher than the fluctuation of the signal).

The possible origin of a fluctuating EMC signal can be found by a closer examination of the time dependence of the fluctuation of the apparent oxygen signal for all three NCM materials: the increase of the apparent oxygen signal subsequent to the charge phase does not initiate at lower potentials but initiates with the beginning of the CV hold at high potential. During this potential hold of 1 h, the charge current drops quickly to below 10 mA/g_{NCM} (corresponding to ∼C/20; data not shown). From this observation one can conclude that the repeated change of the apparent oxygen signal at $m/z = 32$ at least correlates with the extent and the direction of the applied current, even in the low potential region where no evolution of oxygen should yet have occurred. One possible explanation might be a small fluctuation of the local salt concentration in the NCM working electrode that faces the OEMS inlet (note that the cathode current

collector is a porous stainless steel mesh to allow for fast access of the evolved gases to the mass spectrometer inlet), due to the salt concentration gradient generated in electrochemical cells when a current is drawn.[60,61] This effect predicts an increase of the lithium salt concentration in the NCM working electrode during charge, due to the delithiation of the NCM active material, particularly at the interface between electrolyte and the gas phase of the OEMS cell (i.e., furthest away from the cathode/separator interface); during discharge (or NCM lithiation), however, the lithium salt concentration is predicted to be decreased at that interface. As a higher (or lower) salt concentration should result in a decreased (or increased) vapor pressure of the EMC solvent, the OEMS mass signals at $m/z = 77$ and $m/z = 32$ should also fluctuate, decreasing during charge and increasing during discharge, exactly as observed for the $m/z = 32$ signal in Fig. 4c. From this, we conclude that the apparent fluctuation of the OEMS signal at $m/z = 32$, with an amplitude corresponding to approximately ±0.5 $\mu mol_{O_2}/g_{NCM}$, is due to an alternating partial pressure of the EMC solvent in the OEMS cell. Nevertheless, the proper quantification and interpretation of the evolved oxygen is not affected, as the change of the background with ±0.5 $\mu mol_{O_2}/g_{NCM}$ is periodic and at least an order of magnitude lower than the oxygen evolved at ∼80 %SOC from the PC and PC-bm materials.

Considering that the fluctuations of the signal at $m/z = 32$ of roughly ±0.5 $\mu mol_{O_2}/g_{NCM}$ are not related to changes in the oxygen concentration, the data in Fig. 4c would suggest that no oxygen is evolved for the SC material even at >80 %SOC. For the PC and PC-bm materials, however, a significant amount of oxygen (i.e., far above the background fluctuation) is evolved in the first cycle to 4.73 V_{Li}, initiating as the potential increases above ∼4.5 V_{Li} (corresponding to a degree of delithiation of ∼80 %SOC); in subsequent cycles, smaller but still visible amounts of oxygen are evolved whenever the potential increases above ∼4.5 V_{Li}. This is attributed to the release of lattice oxygen from the layered oxide due to the reported structural instabilities of NCMs at high degrees of delithiation.[15] At the end of the fifth and final charge/discharge cycle, ∼8 and ∼6 $\mu mol_{O_2}/g_{NCM}$ of oxygen are detected for the PC and PC-bm material, respectively, while none (<0.5 $\mu mol_{O_2}/g_{NCM}$) is observed for the SC material.

However, as the major fraction of the released (singlet) oxygen reacts with the solvents in the electrolyte and is mainly detected as carbon dioxide,[11,12,15] the absence of oxygen evolution in case of the SC material does not at all imply that there is no lattice oxygen release. Further insights into the lattice oxygen release can therefore be gained by examining the CO_2 signal. During the first two cycles to 4.08 V_{Li}, carbon dioxide is detected at potentials greater than ∼3.8 V_{Li}, as shown in Fig. 4d, and at the end of the first two cycles amounts to ∼9 $\mu mol_{CO_2}/g_{NCM}$ for the PC material, ∼8 $\mu mol_{CO_2}/g_{NCM}$ for the PC-bm material, and ∼5 $\mu mol_{CO_2}/g_{NCM}$ for the SC material. As we do not expect any lattice oxygen release from the NCM at this potential or SOC, these relatively low amounts of CO_2 must mainly stem from the electrochemical oxidation of trace impurities in the carbonate-based electrolyte (e.g., alcohols such as ethanol or ethylene glycol)[13,62] as well as from the subsequent chemical decomposition of residual lithium salts (e.g., Li_2CO_3), which remain on the NCM particles due to the slight lithium excess that is typically used in the synthesis of (nickel-rich) active materials[7] and that are decomposed by the protic species originating from the oxidation of the electrolyte.[38]

Simultaneously with the release of oxygen from the PC and PC-bm materials, a significant rise of the carbon dioxide amount is observed for all three materials during the first cycle to 4.73 V_{Li} (or 90 %SOC, respectively), as shown in Fig. 4d. The onset of the strong CO_2 evolution at high potentials, however, appears to occur slightly before the onset of the oxygen evolution, which in part can be explained by a rapid reaction of released lattice oxygen with the electrolyte to yield CO_2, so that at low oxygen evolution rates no molecular oxygen (or only in the form of CO_2) escapes from the

electrolyte into the gas phase (a more detailed analysis will be subject to future studies). For the subsequent two cycles to 4.73 V_{Li}, the carbon dioxide amount rises stepwise for all three materials when the NCM is charged above ∼80 %SOC. At the end of the fifth and final cycle, 112 $\mu mol_{CO_2}/g_{NCM}$ of carbon dioxide are detected for the PC material, 167 $\mu mol_{CO_2}/g_{NCM}$ for the PC-bm material, and 56 $\mu mol_{CO_2}/g_{NCM}$ for the SC material. Even though the identical CO_2 evolution profiles for all three materials suggest that the CO_2 evolution of the SC material at high potentials originates from the release of lattice oxygen it is, at first sight, surprising that no molecular oxygen is detected for this material (see green curve in Fig. 4c). This could be rationalized by considering that the SC material shows only a minor increase in specific surface area upon cycling (see green data points in Fig. 3b) and thus insignificant cracking, so that its entire surface area from which the lattice oxygen is released is in contact with the electrolyte, which might facilitate a rapid reaction of released oxygen (e.g., in form of singlet oxygen) with the electrolyte so that no oxygen can escape into the gas phase where it would be detected by OEMS. In case of the PC material, however, lattice oxygen can also be released into tiny pores or cracks in the secondary agglomerates that are not filled with electrolyte, where then the unreactive triplet oxygen can be formed and escape into the gas phase. This is further supported by the lower overall amount of evolved oxygen for the PC-bm material (for which most of its surface area is already exposed) as compared to the PC material, even though it yields the highest total amount of evolved gas, consistent with the expectation that higher specific surface areas lead to more electrolyte decomposition.[14]

At the end of the five cycles of the OEMS experiment, a total gas amount (i.e., the sum of oxygen and carbon dioxide) of 120 $\mu mol_{O_2+CO_2}/g_{NCM}$ is observed for the PC material, 173 $\mu mol_{O_2+CO_2}/g_{NCM}$ for the PC-bm material, and 56 $\mu mol_{O_2+CO_2}/g_{NCM}$ for the SC material, resulting in a ratio of the total gas amounts of 1:1.44:0.47 for PC:PC-bm:SC. This proportion is also reasonably closely reflected in the ratio of the NCM surface areas of 1:1.75:0.31 for PC:PC-bm:SC, which is deduced from the capacitance measurements at 4.7 V_{Li} (see Fig. 3b). The minor differences in these ratios could stem from the fact that the capacitance measurements are performed in the discharged state, while the gas release occurs at high SOC, where additional surface area is exposed (see Fig. 2). Furthermore, the capacitance measurements were performed for compressed PC and SC electrodes, while uncompressed electrodes were used for the OEMS experiments to exclude mechanically induced cracking, as the resulting surface area increase of the NCMs would lead to additional gassing. Despite these minor differences, the here made observation clearly suggest that - apart from the oxidation of electrolyte impurities and the chemical decomposition of residual lithium salts[38] - the gas evolution from the NCMs is not governed by the surface area of the pristine NCM powders but mainly by the surface area of the primary crystallites and, therefore, by their particle size. The here observed reduced gassing of single-crystalline CAMs would be advantageous for the use in commercial cells, as indeed reported previously by Li et al. for single-crystalline NCM523.[63]

Rate capability.—The performance of the three NCM materials is investigated regarding their discharge rate capability. To exclude the effect of electrical resistances through the electrode and/or from the electrode to the current collector, the conductive carbon content was increased to 5 wt% for this rate test (as compared to typical values of ∼2 wt%); for the same purpose, the electrodes were additionally compressed at 200 MPa. By this, we expect to better elucidate the morphology-specific performance of the NCMs only.

The specific discharge capacity as a function of cycle number is depicted in Fig. A·6: during the first 33 cycles of the procedure, a discharge rate test is performed, cycling the NCM cathode potential
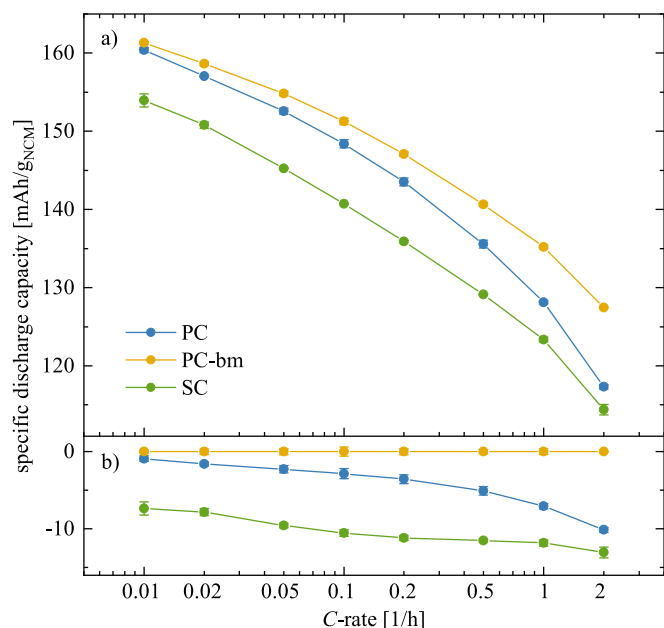
Figure 5. Discharge rate capability of PC (blue), PC-bm (yellow), and SC (green) materials. Cells were assembled with PC, PC-bm, or SC working electrodes in T-cells with 90 μl LP57 electrolyte, a lithium metal reference electrode, and a lithium metal counter electrode (with three glass fiber separators, two placed between working and counter electrode as well as one towards the reference electrode). Controlled by the reference electrode potential, the NCM electrodes were cycled between 3.0 V_{Li} and 4.1 V_{Li} at 25 °C, applying discharge rates of C/100, C/50, C/20, C/10, …, 2C (all referenced to the theoretical capacity of 276.5 mAh/g_{NCM}). The C-rate applied during the respective charge (in CCCV mode, with a CV step at the upper cutoff potential for 1 h, or until the current dropped below C/20) was either identical to the discharge rate (for C/2 or slower) or set to C/2 (for C/2 or faster). **a)** Specific discharge capacity as a function C-rate, while latter is plotted on a logarithmic scale. The data are extracted from the cycling data shown in Fig. A·6, depicting the third data point of each set of three cycles at the respective C-rate. **b)** Deviation of the discharge capacity of the respective NCM material to the one of the PC-bm material. The error bars correspond to the minimum/maximum value of two measurements.

between 3.0 and 4.1 V_{Li} and increasing the discharge rate every third cycle from C/100 to 20C. Up to 2C, the PC-bm (yellow) material shows the best performance, followed by the PC (blue) material, and then by the SC (green) material. The fact that the discharge capacity of the three NCMs becomes quasi-identical for C-rates of 5C and higher suggests that at such high rates cell-related resistances become dominant (e.g., the ohmic resistance of the separator and concentration overpotentials), so that we limit our analysis of the rate capability in Fig. 5 to rates up to only 2C. During each set of three cycles, the discharge capacity remains constant (see Fig. A·6), indicating stable cycling of the three materials. This is further supported by the subsequent 14 cycles at 1C, during which the discharge capacity does not decrease (see Fig. A·6), which is expected since the upper cutoff potential of 4.1 V_{Li} (or 61 %SOC) is still below the onset potential for the release of lattice oxygen.

To better compare the rate capabilities of the different NCM materials, the specific discharge capacities (taken from the third cycle of each set of three cycles with the same discharge rate) are evaluated in Fig. 5a as a function of the applied C-rate, which is plotted on a logarithmic scale. At C/100, the PC-bm and PC material deliver a similar capacity of 161 mAh/g_{NCM} and 160 mAh/g_{NCM}, respectively, while the SC material provides only 154 mAh/g_{NCM}, even at this very low rate (note that the error values of the specific capacities correspond to the minimum/maximum values determined from the measurement of two cells and are always below ±2.3 mAh/g_{NCM}, and even below ±0.9 mAh/g_{NCM} when excluding the cycles at C-rates of 5C or higher. If an error value is below ±0.5 mAh/g_{NCM}, it is omitted).

At C/10, the discharge capacity provided by the PC-bm material is diminished to 151 mAh/g$_{NCM}$, while that of the PC material amounts to 148 ± 1 mAh/g$_{NCM}$, followed by that of the SC material with 141 mAh/g$_{NCM}$. When the applied rate is increased to 1C, the PC-bm delivers 135 mAh/g$_{NCM}$, the PC material delivers 128 mAh/g$_{NCM}$, and the SC material delivers 123 mAh/g$_{NCM}$. The data in Fig. 5b thus show that the difference of the discharge capacity of the PC and the PC-bm materials grows with increasing C-rate, while the discharge capacity between the PC and SC materials shrinks continuously, until a difference of only 3 mAh/g$_{NCM}$ remains at 2C. The here observed dependence of the rate capability on the particle morphology can be explained as follows:

- Small and deagglomerated primary crystallites: The highest rate performance is determined for PC-bm, which consists of small and separated primary crystallites, having a high specific surface area (at any SOC) already in its pristine state (see Fig. 2). As each primary crystallite is in contact with electrolyte as well as with the conductive carbon (assured by the higher carbon content of 5 wt%), the particle and electrode morphology ensure optimal ionic and electrical connectivity, so that the area specific current density (referenced to the total NCM surface area) is lowest at any given C-rate for the PC-bm material, leading to the lowest charge-transfer overpotential. Furthermore, due to the relatively small NCM particle size, overpotentials due to solid-state diffusion of lithium through the NCM must also be the lowest of the three materials.

- Polycrystalline secondary agglomerates: In contrast, the smaller specific surface area of the secondary agglomerates of PC material (in its pristine state) should give rise to significant kinetic limitations. However, due to the volume change upon (de)lithiation[17] and the resulting crack formation between the primary crystallites during the first charge (see Fig. 2),[19] the fast lithium-ion diffusion through the liquid electrolyte penetrating the formed cracks allows for discharge capacities similar to the ones of the PC-bm material, analogous to the effect previously reported by Trevisanello et al. on the basis of galvanostatic polarization and relaxation experiments.[20] Note that this effect is only advantageous with liquid electrolytes, as solid electrolytes do not penetrate into the formed cracks and as the cracks additionally hinder the solid-state diffusion of lithium through the NCM particle.[64] In contrast, as the conductive carbon is only located on the exterior surface of the secondary agglomerates and not in its interior, as all the pores are still closed during ink preparation, the PC material suffers at high C-rates from a reduced electrical connection of the primary crystallites in the center of the secondary agglomerates - in particular in the charged state, where some primary particles are expected to be (partially) electrically isolated. This is expected to result in an heterogeneity of SOC over the radius of the secondary particles, as previously observed by Kim et al. by atomic force microscopy,[22] leading to a loss in rate capability, as suggested by Friedrich et al.[23] As the formation of cracks grows continuously during extended cycling,[19] these opposing effects with regards to rate capability are expected to become more pronounced after long-term charge/discharge cycling: (i) the favorable increase of the interfacial area between electrolyte and CAM (lowering the area specific current density and thus the charge-transfer resistance) and of the faster lithium ion diffusion through the electrolyte phase within the secondary particle agglomerate (effectively lowering the solid-state lithium diffusion overpotential); (ii) the unfavorable increase of the electrical connectivity across the secondary particle agglomerate, leading to an apparent decrease in rate capability.

- Single-crystals with μm-scale dimensions: In case of the SC material, the individual SC particles are expected to be well connected both ionically and electrically, similar to the PC-bm material. As the SC particles do not form cracks (see Fig. 2) into which electrolyte can penetrate and thereby increase the apparent lithium diffusion coefficient,[20] the kinetics of (de)lithiation rely on the solid-state diffusion of the lithium through the NCM. Since the lithium has to diffuse over comparatively long distances for the

larger primary crystallites of the SC material, the (de)lithiation rates are diminished.[65] Additionally, the ∼4.5-fold lower specific surface area of the SC compared to the PC-bm materials (see right y-axis in Fig. 2a) increases the area specific current density and, consequently, the charge-transport overpotentials by the same factor. This is in reasonably good agreement with the difference in rate capability at low C-rates: the discharge capacity of the SC material at C/100 (154 mAh/g$_{NCM}$; see Fig. 5a) is already reached by the PC-bm material at a ∼6-fold higher C-rate (i.e., at ∼0.06C). Furthermore, the kinetic limitation is also reflected in the higher first-cycle irreversible capacity of the SC compared to the PC-bm material, i.e., for the material with the larger primary crystallites (see Fig. A·6), as it was observed similarly by Riewald et al. for LNO.[66] Therefore, the discharge capacity of the SC material is diminished as compared to the one of the PC-bm material at all C-rates.

Thermal stability in the charged state.—In a final experiment, the thermal stability of the NCM materials in the charged state is evaluated by thermogravimetric analysis (TGA), which is often used as an indicator for the safety of electrode active materials in large cells. Delithiated NCMs are prone to the thermally induced decomposition of the layered transition metal oxide to a spinel- or rock-salt-type structure[67] at much lower temperatures (around 200–350 °C, depending on transition metal ratio and degree of delithiation)[7,67,68] as compared to the fully lithiated materials (with decomposition temperatures ≫500 °C), which is accompanied by heat evolution and the release of lattice oxygen,[7,67–69] initiating the combustion of the organic electrolyte and eventually a thermal runaway in larger battery packs.[70]

In the following, the onset and the extent of the thermal decomposition of delithiated NCM electrodes were evaluated by their relative mass loss upon heating under argon flow, as depicted in Fig. 6. For this, the electrodes were charged once to 4.1 V$_{Li}$, what resulted in a degree of delithiation of ∼62 %SOC for the three NCM622 materials. To exclude any influence of the decomposition of the conductive carbon and/or the binder in the electrode, an electrode solely consisting of C65 and PVDF (see black curve in Fig. 6) was investigated using the same procedure: up to 325 °C, however, the C65/PVDF electrode exhibits a mass loss of only ∼0.70 wt%, what would correspond to a negligible mass loss of not more than ∼0.03 wt% in the NCM electrodes, when taking into account the relative contribution of C65 and PVDF of 4 wt%. The observed thermal stability of the C65/PVDF electrode is consistent with the previously observed onset temperatures of the thermal oxidation reaction of C65[38] as well as of PVDF[71] since neither of the two decomposes at temperatures below 350 °C (even in oxygen-containing atmosphere).

Up to 140 °C, the mass changes observed for the three NCM electrodes are within ±0.07 wt%, corresponding to ±15 μg for the used electrodes with a mass of ∼20 mg; therefore, we assign the observed variations of the sample mass (under argon flow) to the fluctuation of the background signal between the different measurements. Starting at temperatures of 140–160 °C, however, a significant mass loss of all three NCM electrodes initiates, with the rate of the mass loss increasing with increasing temperatures. This temperature range for the onset of a significant mass loss from the NCM electrodes coincides well with the reported onset temperatures of the thermal runaway in heating experiments for commercial graphite/NCM full-cells.[70,72] At the final temperature of 325 °C, the total mass loss of the PC-bm and the PC electrodes amounts to 2.38 wt% and 1.59 wt%, respectively, while the total mass loss of the SC electrode is only 1.11 wt%.

Based on the results of previous studies,[7,67] we assume that the mass loss of the delithiated NCM electrodes is mainly driven by its thermal decomposition which is accompanied by the release of lattice oxygen. For the full transformation from the layered and partially delithiated MO$_2$ to the rock-salt-type MO phase which is expected to occur for the complete decomposition of NCM622 at temperatures of ∼550 °C (measured for 75 %SOC),[67] a mass loss of the NCM material of 17.8 wt% would be expected; this value corresponds to a maximum mass loss of the electrode of 17.1 wt% when considering
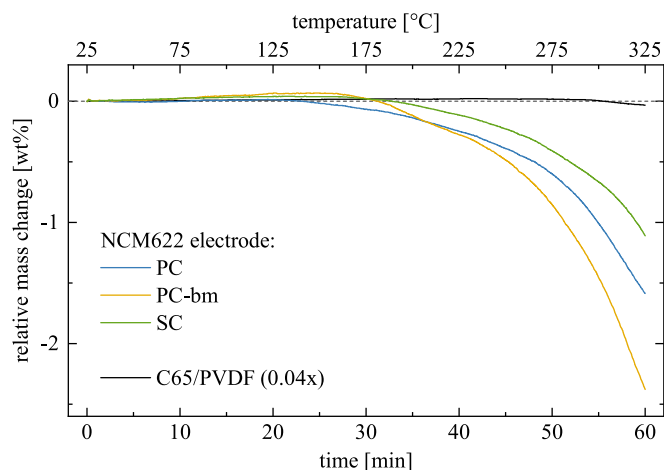
Figure 6. Relative electrode mass change during thermogravimetric analysis of a C65/PVDF electrode (1:1 w/w, black line) as well as of charged PC (blue), PC-bm (yellow), and SC (green) electrodes (96:2:2 w/w) as a function of experiment time (lower x-axis) and temperature (upper x-axis), performed under argon flow of 60 ml/min while ramping the temperature at 5 K/min from 25 °C to 325 °C. Beforehand, the electrodes were charged in coin half-cells at 25 °C to 4.1 V_{Li} (corresponding to ∼62 %SOC, as determined from Fig. A·4) in CCCV mode (see Fig. A·2), then harvested from the cells, washed in three steps using carbonate-based solvents, and finally dried at 120 °C under dynamic vacuum. The signal of the C65/PVDF electrode is scaled according to the mass contribution (of 4 wt%) in the charged and heated NCM electrodes.

the NCM content of 96 wt% in the electrode. The measured mass loss of 2.38 wt% for the PC-bm electrode thus suggests that only ∼14 wt% of the layered phase of the PC-bm material are decomposed up to 325 °C in the performed TGA experiment (and even less for PC and SC). Due to this minor part, we suggest that, from the onset temperature of the transformation of the layered oxide structure up to 325 °C, mainly oxygen from the surface region of the primary crystallites is evolved, while the bulk of the delithiated NCM requires higher temperatures to decompose, possibly due to the limited solid-state diffusion of oxygen through the NCM lattice. This is further expressed in the ratio of the respective mass loss of 1:1.5:0.7 up to 325 °C for the PC:PC-bm:SC electrodes, which shows a similar trend as the ratio of the surface areas of 1:1.94:0.39 for the electrodes charged to 3.9 V_{Li} (see Fig. 2). The investigation of the proposed mechanism, however, needs to be subject of future studies using temperature-resolved diffraction and/or spectroscopic techniques. In summary, larger NCM primary crystallites (with a smaller specific surface area) exhibit a diminished mass loss upon heating and, therefore, are expected to release less oxygen improving their thermal stability as well as the safety of large-format battery cells and packs.

Conclusions

We investigated the effect of three different NCM622 particle morphologies on the electrochemically active surface area, the discharge capacity as a function of the upper cutoff potential, the gassing during the initial cycles, the rate capability, and the thermal stability. These properties were evaluated for: (i) a polycrystalline NCM622 composed of secondary agglomerates with a size of ∼5–10 μm ("PC"), (ii) the same material almost completely separated by ball milling into its primary crystallites with a final particle size of ∼0.2–1.0 μm ("PC-bm"), and (iii) a single-crystalline NCM622 material composed of monolithic particles with a size of ∼2–8 μm. For the pristine powders, the specific surface area determined by krypton physisorption (Kr-BET) was ∼0.3 m^2_{NCM}/g_{NCM} for the PC and SC materials, while it was ∼8-fold larger for the PC-bm material. This allowed to independently examine the effect of specific surface area for the same morphology (SC vs. PC-bm materials) and the effect of poly- vs. single-crystalline morphologies for a similar specific surface area (PC vs. SC materials).

Even though the specific surface area of the PC and SC materials was similar for the pristine CAM powders, Kr-BET measurements revealed a ∼3-fold higher specific surface area of the PC material in the charged state of the first cycle, while that of the SC material remained essentially unaffected. Similar observations were made by in situ monitoring the NCM electrode capacitance via impedance spectroscopy, showing that the capacitance of SC electrodes remained essentially constant, both upon compression and even after full delithiation, highlighting the (chemo)mechanical stability of single-crystalline CAMs, while the capacitance of the PC electrodes changed by 240 % upon mechanical compression and by 650 % when cycled to 5.0 V_{Li}. Here, the specific surface area and the capacitance of the PC material reached ∼70 % of the values obtained for the PC-bm material (for which most primary crystallites of the PC material had been separated into individual particles). This finding demonstrates that most of the surface area of the primary crystallites which compose the secondary agglomerates of the polycrystalline NCM is accessible to the electrolyte after the material has been delithiated to a high state of charge (SOC), elucidating the fragile integrity for the polycrystalline morphology. This observation also explains the more than 2-fold higher gassing of the PC material when charged to 4.7 V_{Li} (∼90 %SOC) as compared to the SC material; as the gassing is found to be roughly proportional to the electrochemically active surface area, the highest amount of gas was evolved by the PC-bm material.

Discharge rate tests in half-cells revealed the impact of the NCM particle morphology and the electrochemically active surface area on the rate capability: (i) the highest rate capability was found for the PC-bm material, owing both to its very high specific surface area that lowers the charge-transfer overpotentials and to its small particle size that allows for efficient solid-state lithium diffusion; (ii) the SC material showed the lowest rate capability, as it maintained a low specific surface area, leading to large charge-transport resistances; (iii) the rate capability of the PC material was inferior to that of the PC-bm material, presumably due to the poor electrical connection of primary crystallites within the secondary agglomerates upon particle cracking. This illustrates the dependence of the delivered capacity on the lithium diffusion in the solid and the liquid phase (poor for the large SC primary crystallites) as well as on electrical resistances inside the NCM particles (affecting the PC particles negatively).

Additionally, it was found that the morphology does not affect the decomposition temperature of the NCM materials for the same degree of delithiation, investigated up to 325 °C by TGA; however, the relative mass loss (expected to be induced by the decomposition of the delithiated layered structure and the release of surface-near lattice oxygen) as a function of temperature is more pronounced for an NCM with a higher surface area.

In addition to this safety aspect, the observed stable surface area of single-crystalline CAMs is expected to have a positive impact on the gas evolution and on surface-area-dependent side reactions with the electrolyte, on the cathode impedance, and, therefore, on the capacity retention in full-cells. However, as a larger particle size is also accompanied by disadvantages such as a decreased rate capability as well as an increased sensitivity to the formation of a resistive rock-salt-type surface layer, the optimal particle size of single-crystalline NCMs needs to be determined in future studies.

CRediT Authorship Contribution Statement

Stefan Oswald: Methodology, Supervision, Investigation, Writing—Original Draft. Moritz Bock: Investigation, Writing—Review & Editing. Hubert A. Gasteiger: Conceptualization, Writing—Review & Editing.
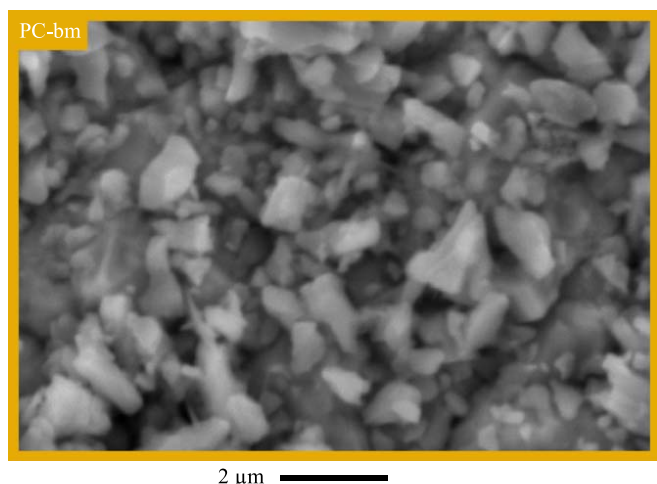
Acknowledgments

Figure A·1. Magnified representation of the SEM image shown in Fig. 1b illuminating the particle morphology of the pristine PC-bm powder by top-view SEM in secondary electron mode at 15 kV.
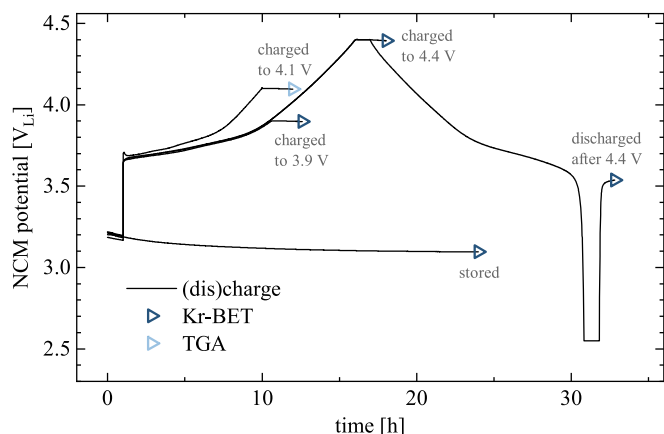

Figure A·2. Potential curves (black lines) of the PC electrodes stored or (dis)charged for Kr-BET (dark blue triangles) and TGA measurements (light blue triangles). Coin-half cells were assembled using uncompressed PC electrodes, lithium metal as counter electrode, 100 μl LP57 electrolyte, and two glass fiber separators as well as one Celgard separator facing the NCM electrode. At 25 °C, they were either stored for 24 h or cycled galvanostatically at a *C*-rate of *C*/20 for the Kr-BET measurements and *C*/15 for the TGA experiments (when referenced to the theoretical capacity of 276.5 mAh/g_{NCM} of NCM622), all including a CV step of 1 h at the respective approached potential (CCCV mode) and an OCV period of 1 h, prior to being harvested.

Appendix

Magnified SEM image of PC-bm.—For a better visual investigation, the magnified SEM image of the pristine PC-bm (obtained by ball milling of the polycrystalline NCM622) is shown in Fig. A·1. It is observed that most of the secondary agglomerates of the polycrystalline NCM622 have been completely separated into their primary particles, showing individual crystallites with a size of 0.2–1.0 μm, while only a few agglomerates with a size of ∼2 μm remain.

Cycling procedures for Kr-BET and TGA measurements.—Prior to the SOC-dependent surface area determination via Kr-BET and the evaluation of the thermal stability in TGA experiments, the NCM electrodes were either stored for 24 h or cycled galvanostatically to the respective potentials of 3.9, 4.1, or 4.4 V_{Li}, or to fully discharged state at 2.55 V_{Li} after one charge/discharge cycle to an upper cutoff potential of 4.4 V_{Li}. The potential profiles of the respective cycling procedures are depicted in Fig. A·2.
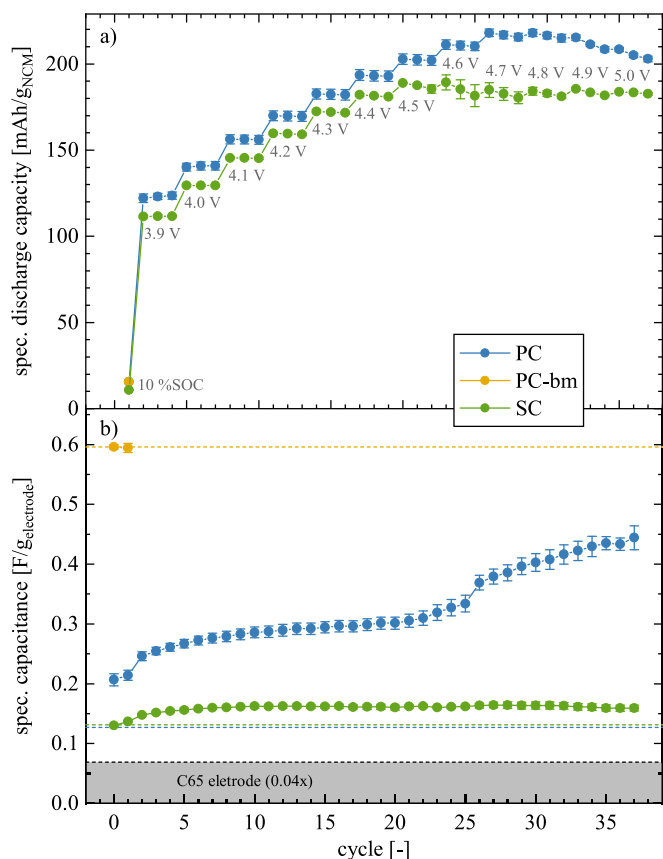
Figure A·3. Electrochemical cycling data as a function of cycle number for PC (blue), PC-bm (yellow), and SC (green) electrodes, as described in detail in Fig. 3. **a)** Specific discharge capacity. The gray labels indicate the applied upper cutoff potential vs. Li$^+$/Li. **b)** Specific electrode capacitance. The gray area marks the specific capacitance of the C65 electrode multiplied by its relative mass contribution (of 4 wt%, or 0.04x) in the NCM electrodes. The horizontal dashed lines correspond to the respective specific electrode capacitance in pristine state (uncompressed for PC and SC, compressed at 100 MPa for PC-bm). The error bars correspond to the minimum/maximum value of two measurements.

Capacitance measurements as a function of cycle number.—The data of specific discharge capacity and specific capacitance obtained in the electrochemical cycling experiments in pseudo-full cells are depicted here as a function of cycle number, for which the upper cutoff potential is increased every three cycles by 0.1 V. Here, the discharge capacity (in Fig. A·3a) increases with increasing upper cutoff potential but stays constant within each set of three cycles up to an upper cutoff potential of 4.3 V_{Li}. Up to cycle #16 (or 4.3 V_{Li}), the specific discharge capacity of SC is lower by ∼10 mAh/g_{NCM} as compared to PC, what is in accordance with the observed discharge capacities in the rate capability test *C*/10, as depicted in Figs. 5 and A·6. Starting at cycle #17 (or 4.4 V_{Li}), the discharge capacities stagnate even though the upper cutoff potential is increased, what is more pronounced for SC than for PC. The specific electrode capacitance (in Fig. A·3b) increases for the compressed PC electrodes as compared to the uncompressed ones, while the one of SC remains unchanged upon compression. The capacitance upon cycling remains almost constant for SC, however, increases significantly for PC, especially above 4.3 V_{Li}. This data is discussed in detail as a function of SOC in Fig. 3.

Potential curves of the first charge.—To allow for a better interpretation of the cycling data in Fig. A·3, showing the specific discharge capacity and the specific capacitance as a function of cycle number with increasing upper cutoff potentials of the NCM electrode, the latter were converted into the respective degree of delithiation (*x* in Li$_{1-x}$MO$_2$, with M = Ni, Co, and Mn) or SOC, with the resulting plot being depicted in Fig. 3. For this conversion, the required relation
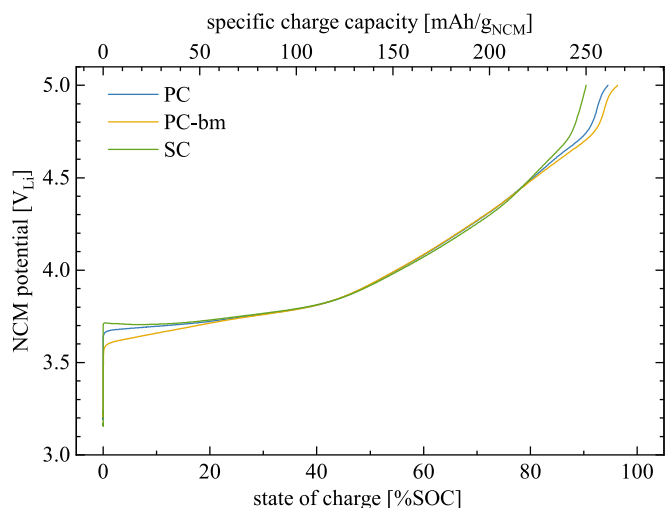
Figure A·4. Potential curves of the first charge of the three NCMs as a function of the specific capacity (top x-axis, in units of mAh/g$_{NCM}$) or SOC (bottom x-axis, in %SOC), respectively. PC (blue), PC-bm (yellow), or SC (green) as working electrodes in T-cells with 90 µl of LP57 electrolyte and lithium metal as counter electrode and reference electrode (with three glass fiber separators, two placed between working and counter electrode as well as one facing the reference electrode). Controlled by the reference electrode potential, the NCM electrodes were charged at 25 °C to 5.0 V$_{Li}$ at C/20 (corresponding to a current of 13.8 mA/g$_{NCM}$ when referenced to the theoretical capacity of 276.5 mAh/g$_{NCM}$).
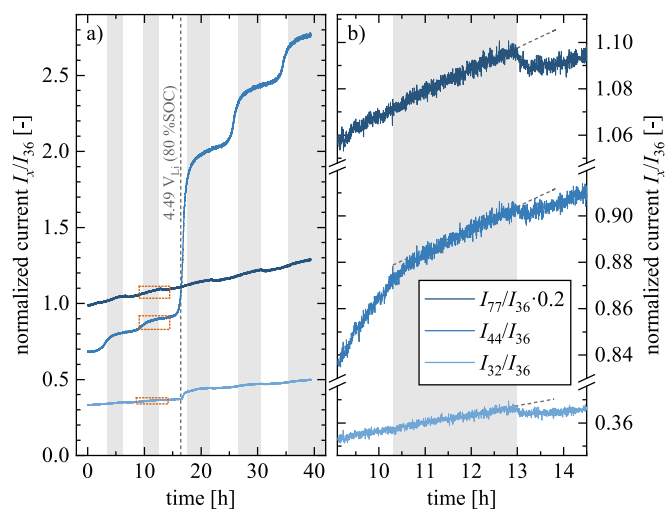
Figure A·5. Gas evolution data as a function of time from the OEMS experiment with the PC material, as presented in Fig. 4. **a)** Ion currents I_x/I_{36} of the mass traces at $m/z = 32$, 44, and 77, all normalized to the signal at $m/z = 36$ of the ^{36}Ar isotope. The signal at $m/z = 77$ is multiplied by 0.2 since the contribution of EMC to the other two signals is only ~20 % (see main text). The vertical light gray areas accentuate each NCM discharge/lithiation period. The vertical gray dashed line marks the onset of the O$_2$ evolution at a potential of 4.49 V$_{Li}$, corresponding to a degree of delithiation of ~80 %SOC. **b)** Magnification of the areas marked by the dotted orange frame in Fig. A·5a. The gray dashed lines are extrapolated from the ion current data of the NCM discharge/lithiation period and serve as a guide to the eye.

between upper cutoff potential (i.e., 3.9, 4.0, ..., 5.0 V$_{Li}$) and the SOC was extracted from the potential curves of the first charge for each of the three NCMs under the essentially identical charging current, which are shown in Fig. A·4. The morphology-dependent overpotentials observed <20 %SOC and >80 %SOC are particularly pronounced in these SOC regions due to the well-known increase in charge-transfer resistance at low/high degree of delithiation[23] as well as due to the formation of a resistive oxygen-depleted surface layer caused by the oxygen release at >80 %SOC.[15]
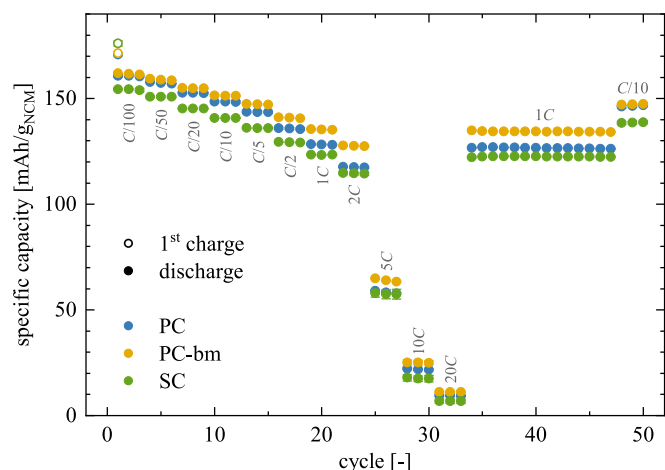
Figure A·6. Specific capacity of the discharge rate test as a function of cycle number for PC (blue), PC-bm (yellow), and SC (green) in half-cells, applying an upper cutoff potential of 4.1 V$_{Li}$, as described in detail in Fig. 5. The empty circles mark the charge capacity of the first cycle while the filled circles represent the discharge capacity of each cycle. The gray labels indicate the applied discharge C-rate. After the rate test, another 14 cycles with a charge rate of C/2 and a discharge rate of 1C as well as three cycles at C/10 for both charge and discharge were appended. The error bars correspond to the minimum/maximum value of two measurements.

Effect of EMC fragmentation on MS signals.—In the OEMS experiment depicted in Fig. 4, an apparent fluctuation of the oxygen signal at $m/z = 32$ is observed, changing repeatedly with the direction and the extent of the applied electrical current. To prove that this fluctuation originates from the contribution of EMC on the mass trace of oxygen due to its fragmentation, the signals of $m/z = 32$, 44, and 77 are depicted in Fig. A·5. Here, the signal at $m/z = 77$ is multiplied by 0.2 since the contribution of EMC to the other two signals is only ~20 % (see main text). From the data, it can be observed that all three signals repeatedly show a small, but visible decrease and increase (see Fig. A·5a). In particular, the drop of the ion current appearing after the switch from discharge to charge, or from NCM lithiation to delithiation, respectively, occurs simultaneously for all three mass traces in the magnified representation (see Fig. A·5b). Since EMC is expected to be the only contribution from the electrochemical system to the signal at $m/z = 77$, the apparent fluctuation of the O$_2$ and the CO$_2$ signals is owed to a change in the concentration of EMC vapor in the OEMS cell.

Discharge capacities from rate test as a function of cycle number.—To evaluate the rate capability of the three NCMs, a discharge rate test with C-rates between C/100 and 20C was performed in half-cells to an upper cutoff potential of 4.1 V$_{Li}$. For all three NCMs, stable cycling is observed within each set of three cycles at the respective C-rate as well as during the 14 cycles at 1C, as depicted in Fig. A·6. This data is discussed in detail as a function of C-rate in Fig. 5.

ORCID

Stefan Oswald ⓘ https://orcid.org/0000-0001-6402-7833
Moritz Bock ⓘ https://orcid.org/0000-0002-9516-853X
Hubert A. Gasteiger ⓘ https://orcid.org/0000-0001-8199-8703

References

1. R. Schmuch, R. Wagner, G. Hörpel, T. Placke, and M. Winter, *Nat. Energy*, **3**, 267 (2018).
2. W. Li, E. M. Erickson, and A. Manthiram, *Nat. Energy*, **5**, 26 (2020).
3. H.-H. Ryu, K.-J. Park, C. S. Yoon, and Y.-K. Sun, *Chem. Mater.*, **30**, 1155 (2018).
4. C. S. Yoon, H. H. Ryu, G. T. Park, J. H. Kim, K. H. Kim, and Y.-K. Sun, *J. Mater. Chem. A*, **6**, 4126 (2018).
5. W. Xue et al., *Nat. Energy*, **6**, 495 (2021).
6. J. Paulsen and J. Kim, *USA Pat.*, US2014/0054495A1 (2014).
7. H.-J. Noh, S. Youn, C. S. Yoon, and Y.-K. Sun, *J. Power Sources*, **233**, 121 (2013).

8. N. V. Faenza, L. Bruce, Z. W. Lebens-Higgins, I. Plitz, N. Pereira, L. F. J. Piper, and G. G. Amatucci, *J. Electrochem. Soc.*, **164**, A3727 (2017).
9. R. Jung, R. Morasch, P. Karayaylali, K. Phillips, F. Maglia, C. Stinner, Y. Shao-Horn, and H. A. Gasteiger, *J. Electrochem. Soc.*, **165**, A132 (2018).
10. J. Sicklinger, M. Metzger, H. Beyer, D. Pritzl, and H. A. Gasteiger, *J. Electrochem. Soc.*, **166**, A2322 (2019).
11. J. Wandt, A. T. S. Freiberg, A. Ogrodnik, and H. A. Gasteiger, *Mater. Today*, **21**, 825 (2018).
12. A. T. S. Freiberg, M. K. Roos, J. Wandt, R. De Vivie-Riedle, and H. A. Gasteiger, *J. Phys. Chem. A*, **122**, 8828 (2018).
13. R. Jung, M. Metzger, F. Maglia, C. Stinner, and H. A. Gasteiger, *J. Phys. Chem. Lett.*, **8**, 4820 (2017).
14. S. Oswald, D. Pritzl, M. Wetjen, and H. A. Gasteiger, *J. Electrochem. Soc.*, **168**, 120501 (2021).
15. R. Jung, M. Metzger, F. Maglia, C. Stinner, and H. A. Gasteiger, *J. Electrochem. Soc.*, **164**, A1361 (2017).
16. A. O. Kondrakov, A. Schmidt, J. Xu, H. Geßwein, R. Mönig, P. Hartmann, H. Sommer, T. Brezesinski, and J. Janek, *J. Phys. Chem. C*, **121**, 3286 (2017).
17. L. De Biasi, A. O. Kondrakov, H. Geßwein, T. Brezesinski, P. Hartmann, and J. Janek, *J. Phys. Chem. C*, **121**, 26163 (2017).
18. W. Li, H. Y. Asl, Q. Xie, and A. Manthiram, *J. Am. Chem. Soc.*, **141**, 5097 (2019).
19. S. Oswald, D. Pritzl, M. Wetjen, and H. A. Gasteiger, *J. Electrochem. Soc.*, **167**, 100511 (2020).
20. E. Trevisanello, R. Ruess, G. Conforto, F. H. Richter, and J. Janek, *Adv. Energy Mater.*, **11**, 2003400 (2021).
21. B. Strehle, F. Friedrich, and H. A. Gasteiger, *J. Electrochem. Soc.*, **168**, 050512 (2021).
22. J. H. Kim, S. J. Kim, T. Yuk, J. Kim, C. S. Yoon, and Y.-K. Sun, *ACS Energy Lett.*, **3**, 3002 (2018).
23. F. Friedrich, B. Strehle, A. T. S. Freiberg, K. Kleiner, S. J. Day, C. Erk, M. Piana, and H. A. Gasteiger, *J. Electrochem. Soc.*, **166**, A3760 (2019).
24. J. Langdon and A. Manthiram, *Energy Storage Mater.*, **37**, 143 (2021).
25. X. Han, Q. Meng, T. Sun, and J. Sun, *J. Power Sources*, **195**, 3047 (2010).
26. Y. Kim, *Appl. Mater. Interfaces*, **4**, 2329 (2012).
27. X. Fan, G. Hu, B. Zhang, X. Ou, J. Zhang, W. Zhao, H. Jia, L. Zou, P. Li, and Y. Yang, *Nano Energy*, **70**, 104450 (2020).
28. J. E. Harlow et al., *J. Electrochem. Soc.*, **166**, A3031 (2019).
29. G. Qian et al., *Energy Storage Mater.*, **27**, 140 (2020).
30. S. Klein, P. Bärmann, O. Fromm, K. Borzutzki, J. Reiter, Q. Fan, M. Winter, T. Placke, and J. Kasnatscheew, *J. Mater. Chem. A*, **9**, 7546 (2021).
31. J. Hou, A. Freiberg, T.-H. Shen, R. Girod, J. Gonthier, S.-J. Kim, F. Maglia, H. A. Gasteiger, and V. Tileli, *J. Phys.: Energy*, **2**, 034007 (2020).
32. R. Bernhard, M. Metzger, and H. A. Gasteiger, *J. Electrochem. Soc.*, **162**, A1984 (2015).
33. S. Solchenbach, G. Hong, A. T. S. Freiberg, R. Jung, and H. A. Gasteiger, *J. Electrochem. Soc.*, **165**, A3304 (2018).
34. N. Tsiouvaras, S. Meini, I. Buchberger, and H. A. Gasteiger, *J. Electrochem. Soc.*, **160**, A471 (2013).
35. B. Strehle, K. Kleiner, R. Jung, F. Chesneau, M. Mendez, H. A. Gasteiger, and M. Piana, *J. Electrochem. Soc.*, **164**, A400 (2017).
36. S. Solchenbach, D. Pritzl, E. J. Y. Kong, J. Landesfeind, and H. A. Gasteiger, *J. Electrochem. Soc.*, **163**, A2265 (2016).
37. S. Brunauer, P. H. Emmett, and E. Teller, *J. Am. Chem. Soc.*, **60**, 309 (1938).
38. A. T. S. Freiberg, J. Sicklinger, S. Solchenbach, and H. A. Gasteiger, *Electrochim. Acta*, **346**, 136271 (2020).
39. U. H. Kim, G. T. Park, B. K. Son, G. W. Nam, J. Liu, L. Y. Kuo, P. Kaghazchi, C. S. Yoon, and Y.-K. Sun, *Nat. Energy*, **5**, 860 (2020).
40. Y. Bi et al., *Science*, **370**, 1313 (2020).
41. H. Li, A. Liu, N. Zhang, Y. Wang, S. Yin, H. Wu, and J. R. Dahn, *Chem. Mater.*, **31**, 7574 (2019).
42. J. Landesfeind, D. Pritzl, and H. A. Gasteiger, *J. Electrochem. Soc.*, **164**, A1773 (2017).
43. R. Amin and Y.-M. Chiang, *J. Electrochem. Soc.*, **163**, A1512 (2016).
44. D. Pritzl, A. E. Bumberger, M. Wetjen, J. Landesfeind, S. Solchenbach, and H. A. Gasteiger, *J. Electrochem. Soc.*, **166**, A582 (2019).
45. G. Li, Y. Wen, B. Chu, L. You, L. Xue, X. Chen, T. Huang, and A. Yu, *ACS Sustain. Chem. Eng.*, **9**, 11748 (2021).
46. F. Zhang et al., *Nat. Commun.*, **11**, 3050 (2020).
47. P. Teichert, H. Jahnke, and E. Figgemeier, *J. Electrochem. Soc.*, **168**, 090532 (2021).
48. Y. Liu, J. Harlow, and J. Dahn, *J. Electrochem. Soc.*, **167**, 020512 (2020).
49. T. A. Hewston and B. L. Chamberland, *J. Phys. Chem. Solids*, **48**, 97 (1987).
50. J. Molenda, P. Wilk, and J. Marzec, *Solid State Ionics*, **146**, 73 (2002).
51. M. Bianchini, M. Roca-Ayats, P. Hartmann, T. Brezesinski, and J. Janek, *Angew. Chemie - Int. Ed.*, **58**, 10434 (2019).
52. K. V. Rao and A. Smakula, *J. Appl. Phys.*, **36**, 2031 (1965).
53. J. G. Aiken and A. G. Jordan, *J. Phys. Chem. Solids*, **29**, 2153 (1968).
54. T. Ogasawara, A. Débart, M. Holzapfel, P. Novák, and P. G. Bruce, *J. Am. Chem. Soc.*, **128**, 1390 (2006).
55. S. A. Freunberger, Y. Chen, N. E. Drewett, L. J. Hardwick, F. Bardé, and P. G. Bruce, *Angew. Chemie - Int. Ed.*, **50**, 8609 (2011).
56. K. U. Schwenke, S. Meini, X. Wu, H. A. Gasteiger, and M. Piana, *Phys. Chem. Chem. Phys.*, **15**, 11830 (2013).
57. N. Yabuuchi, K. Yoshii, S.-T. Myung, I. Nakai, and S. Komaba, *J. Am. Chem. Soc.*, **133**, 4404 (2011).
58. M. Metzger, C. Marino, J. Sicklinger, D. Haering, and H. A. Gasteiger, *J. Electrochem. Soc.*, **162**, A1123 (2015).
59. B. Strehle, S. Solchenbach, M. Metzger, K. U. Schwenke, and H. A. Gasteiger, *J. Electrochem. Soc.*, **164**, A2513 (2017).
60. A. J. Bard and L. R. Faulkner, *Electrochemical Methods - Fundamentals and Applications* (Wiley, New York, NY) (2001).
61. L. O. Valøen and J. N. Reimers, *J. Electrochem. Soc.*, **152**, A882 (2005).
62. R. Jung, P. Strobl, F. Maglia, C. Stinner, and H. A. Gasteiger, *J. Electrochem. Soc.*, **165**, A2869 (2018).
63. J. Li, A. R. Cameron, H. Li, S. Glazier, D. Xiong, M. Chatzidakis, J. Allen, G. A. Botton, and J. R. Dahn, *J. Electrochem. Soc.*, **164**, A1534 (2017).
64. R. Ruess, S. Schweidler, H. Hemmelmann, G. Conforto, A. Bielefeld, D. A. Weber, J. Sann, M. T. Elm, and J. Janek, *J. Electrochem. Soc.*, **167**, 100532 (2020).
65. A. C. Wagner, N. Bohn, H. Geßwein, M. Neumann, M. Osenberg, A. Hilger, I. Manke, V. Schmidt, and J. R. Binder, *ACS Appl. Energy Mater.*, **3**, 12565 (2020).
66. F. Riewald, P. Kurzhals, M. Bianchini, H. Sommer, J. Janek, and H. A. Gasteiger, *J. Electrochem. Soc.*, **169**, 020529 (2022).
67. S. M. Bak, E. Hu, Y. Zhou, X. Yu, S. D. Senanayake, S. J. Cho, K. B. Kim, K. Y. Chung, X. Q. Yang, and K. W. Nam, *ACS Appl. Mater. Interfaces*, **6**, 22594 (2014).
68. M. M. Besli et al., *J. Mater. Chem.*, **7**, 12593 (2019).
69. J. Kasnatscheew, S. Röser, M. Börner, and M. Winter, *ACS Appl. Energy Mater.*, **2**, 7733 (2019).
70. X. Feng, M. Ouyang, X. Liu, L. Lu, Y. Xia, and X. He, *Energy Storage Mater.*, **10**, 246 (2018).
71. J. Qian, C. Fu, X. Wu, X. Ran, and W. Nie, *e-Polymers*, **18**, 541 (2018).
72. Z. Wang, H. Yang, Y. Li, G. Wang, and J. Wang, *J. Hazard. Mater.*, **379**, 120730 (2019).

4.2 Effect of Electrode Properties on the Capacitance Determination

As described in the previous Chapter 4.1, the capacitance of the small SC NCM622 material (labeled PC-bm in the article [265]) could not be determined as a function of the cycle number, or the upper cutoff potential, respectively, since it was prevented by a large unidentified feature in the impedance spectrum in blocking conditions (i.e., in the fully discharged state at $2.55\,V_{Li}$). This semicircle-like contribution was present in uncompressed state but appeared also for the compressed electrodes with increasing cycle number. In this chapter, first, the origin of this feature is elucidated before the implications of the findings on the capacitance determination and the electrode design in general are discussed.

Effect of NCM Particle Size and Conductive Carbon Content

The data for the specific discharge capacity and the specific electrode capacitance, depicted in Figure 4.1 as a function of cycle number, are adapted from Figure A·3 from the article presented in Chapter 4.1 [265] and completed by the ones of PC-bm and PC-bm-90/5/5, while the latter comprises $5\,wt\%$ of both C65 and PVDF, as compared to only $2\,wt\%$ each for the other three electrodes used in the article. For the discussion of the data for the PC and the SC electrodes, the reader is referred to the original publication [265]. In Figure 4.1a, the discharge capacities of both PC-bm and PC-bm-90/5/5 electrodes, which were compressed at $100\,MPa$ and cycled by the same protocol as the PC and SC electrodes [265], exhibit similar values as for the PC electrodes, until the upper cutoff potential exceeds $\sim 4.5\,V_{Li}$, at which point the discharge capacity of both decreases as compared to the PC electrode (note that the discharge capacities were recorded in pseudo-full cells with a lithium reservoir in the LTO counter electrode; therefore, the capacity loss does not stem from loss of lithium inventory but solely from the degradation of the NCM). Even though the PC-bm CAM has a relatively large specific surface area of $2.25\,m^2/g_{NCM}$, it shows a reasonable cycling performance in this experiment for both electrode compositions.

The specific capacitance, which was extracted from the 180-mHz point, is presented in Figure 4.1b, exposing a larger initial capacitance of the PC-bm-90/5/5 electrode as compared to the PC-bm electrode due to the increased content in surface area contributed by the increased amount of high-surface-area carbon (as depicted by the
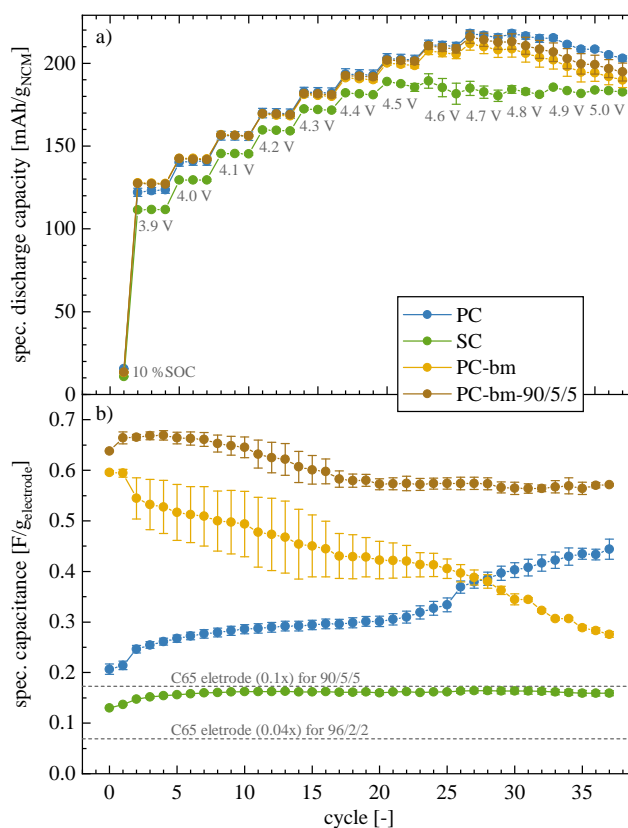
Figure 4.1 a) Specific discharge capacity (in units of mAh/g_{NCM}) and b) specific electrode capacitance (in $F/g_{electrode}$) of four NCM622 materials (PC (blue), SC (green), PC-bm (yellow) and PC-bm-90/5/5 (brown), all compressed at 100 MPa for 30 s) as a function of cycle number. The experimental setup, the cycling procedure, and the data for the PC and the SC electrodes were extracted from Figure 3 in Chapter 4.1 [265] and completed by the data for the PC-bm and the PC-bm-90/5/5 electrodes. Similar to the PC and the SC electrodes, the PC-bm electrode comprises 2 wt% of both C65 and PVDF, while the PC-bm-90/5/5 electrode contained 5 wt% of each of the two components. The gray dashed horizontal lines at 0.069 and 0.17 $F/g_{electrode}$ mark the contribution of the C65 electrode to the total capacitance of the electrode for a composition of 96/2/2 (0.04x of the value of 1.7 $F/g_{electrode}$ for the C65 electrode, see Chapter 3.1 [224]) and 90/5/5 (0.1x), respectively.

two horizontal gray dashed lines in Figure 4.1); furthermore, Figure 4.1b shows a decreasing capacitance for both the PC-bm and the PC-bm-90/5/5 electrodes with increasing cycle number. Reasons for a decrease in capacitance may include: i) the decrease in electrode surface area (e.g., due to the loss of active material, however, appearing unlikely due to the reasonable discharge capacity observed in Figure 4.1); ii) the change of the surface-area-normalized capacitance (e.g., due to the formation of an interphase on the electrode, however, being unlikely as shown previously [252]); or iii) the convolution of the capacitive branch with another feature, which might increase the imaginary impedance at 180 mHz significantly.

To illuminate the origin of this capacitance decrease, the impedance spectra of the
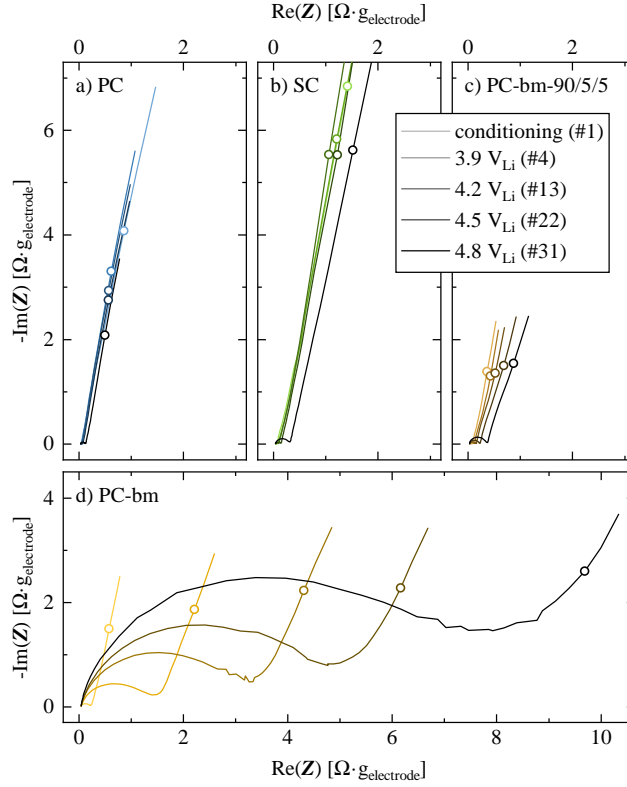
Figure 4.2 Impedance spectra (in units of $\Omega \cdot g_{\text{electrode}}$) of the four NCM622 electrodes of a) PC, b) SC, c) PC-bm-90/5/5, and d) PC-bm. The impedance spectra are extracted from the cycling data presented in Figure 4.1 for the selected cycle numbers #1, #4, #13, #22, and #31, corresponding to the conditioning step to 10 %SOC and the cycles to an upper cutoff potential of 3.9, 4.2, 4.5, and 4.8 V_{Li} (presented from light to dark colors). The impedance of the NCM electrodes is recorded in the fully lithiated state at 2.55 V_{Li} and the respective frequency points at 180 mHz are indicated by open symbols.

four electrode configurations are depicted in Figure 4.2 as a function of the cycle number and, therefore, also of the upper cutoff potential. The impedance spectra of the PC electrode (see Figure 4.2a) exhibit a capacitive branch in the form of a tilted straight line, as it would be expected for a CPE of an electrode in blocking conditions, which decreases in length with increasing upper cutoff potential; simultaneously, the impedance point at 180 mHz is shifted to lower imaginary impedance values, resulting in the capacitance increase seen in Figure 4.1. A similar shape is observed for the impedance data of the SC electrode (see Figure 4.2b), which, however, show higher imaginary values and remain essentially constant starting at cycle #4 (both originating from the (chemo)mechanical stability of SC). For the PC-bm-90/5/5 electrode (see Figure 4.2c), the impedance spectra exhibit the capacitive branch of the CPE, similar as for the PC and the SC electrode. At first sight, the only noticeable difference is the decrease to lower imaginary values (due to the 8-fold surface area of the CAM and the
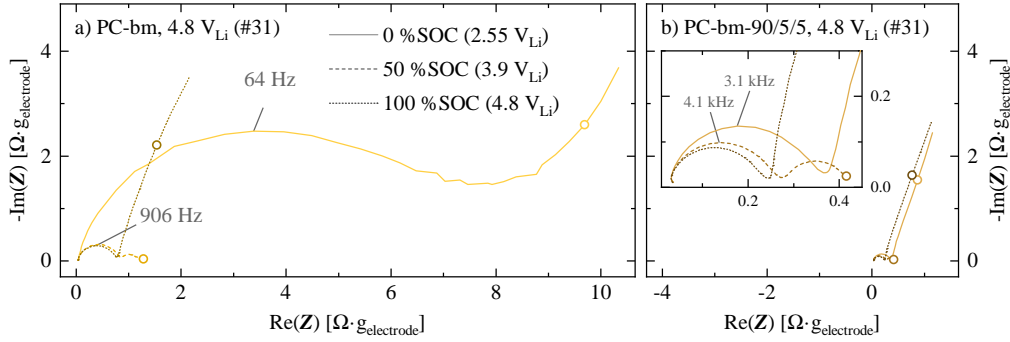
Figure 4.3 Impedance spectra of a) the PC-bm electrode and b) the PC-bm-90/5/5 electrode as a function of SOC extracted from the cycling data presented in Figure 4.1 for the selected cycle number #31 to an upper cutoff potential $4.8\,\mathrm{V_{Li}}$. The spectra were recorded at three different chemical SOCs (corresponding to $\mathrm{Li_1MO_2}$ for 0 %SOC and to $\mathrm{Li_0MO_2}$ for 100 %SOC) of: i) ~100 %SOC after charging to $4.8\,\mathrm{V_{Li}}$ (dark dotted line, after resting in OCV for 1 h); ii) ~50 %SOC after discharging to $3.9\,\mathrm{V_{Li}}$ (dashed line, after OCV); and iii) ~0 %SOC after discharging to $2.55\,\mathrm{V_{Li}}$ (light solid line, held in CV mode). The respective frequency points at 180 mHz are indicated by open symbols, while the apex frequency of the semicircles is given for selected impedance spectra.

increased C65 content), however, a slight curvature of the originally straight line after conditioning can be observed, which could originate from a semicircle-like feature being convoluted with the CPE and which grows with increasing cycle number. This shape change could stem from the growth of an additional contribution in the impedance spectrum, which simultaneously shifts the imaginary impedance at 180 mHz to higher values. When examining the impedance data of the PC-bm electrode (see Figure 4.2d), only the first spectrum after conditioning appears to be similar to the ones observed for the other electrodes. However, starting already at cycle #4 (to $3.9\,\mathrm{V_{Li}}$), an additional semicircle-like feature with an extent of $\sim 1.5\,\Omega \cdot \mathrm{g_{electrode}}$ occurs, which grows continuously with cycle number to $\sim 7\,\Omega \cdot \mathrm{g_{electrode}}$ at cycle #31 (to $4.8\,\mathrm{V_{Li}}$). This feature could contribute to the observed increase in imaginary impedance of the 180-mHz point of the PC-bm and the PC-bm-90/5/5 electrode. Even though the PC-bm electrode exhibits this unexpectedly large impedance contribution in blocking conditions, it shows typical discharge capacities similar to the ones of the other materials; if this large impedance would be present over the entire SOC window, significant overpotentials (which were not observed when comparing the potential curves of the PC-bm and the PC-bm-90/5/5 electrodes, data not shown) would diminish the available capacity. Therefore, the unassigned feature is likely only present in the fully discharged state.

To prove this hypothesis, PEIS is recorded at three different SOCs during cycle #31 (to $4.8\,\mathrm{V_{Li}}$): i) at ~100 %SOC after charging to $4.8\,\mathrm{V_{Li}}$ (after resting in OCV for 1 h), ii) at ~50 %SOC after discharging to $3.9\,\mathrm{V_{Li}}$ (after OCV), and iii) at ~0 %SOC after

discharging to $2.55\,V_{Li}$ (held in CV mode). The resulting data, depicted in Figure 4.3a, show blocking conditions at low frequencies for both the fully lithiated as well as the fully delithiated state (i.e., ∼0 %SOC (light solid line) and ∼100 %SOC (dark dotted line), respectively); at ∼50 %SOC (dashed line), a semicircle is observed at medium to low frequencies, resulting from the impedance of the electrode in non-blocking state, corresponding to the convolution of charge-transfer resistance, ionic pore resistance, and electronic resistance through the electrode (see Figure 2.4). Furthermore, the data expose that the observed unassigned feature is much larger in the discharged state; for the two other impedance spectra, a relatively small semicircle of $<1\,\Omega \cdot g_{electrode}$ remains. When taking into account the extent of the semicircle in fully discharged state of ∼$7\,\Omega \cdot g_{electrode}$, or ∼$600\,\Omega$, respectively, and its apex frequency of $64\,Hz$, a capacitance of ∼$4\,\mu F$ can be calculated using Equation 2.8. For a typical surface-area-normalized capacitance of an electrochemical double layer of $4\,\mu F \cdot cm^2_{electrode}$, the obtained surface area equates to ∼$1\,cm^2_{electrode}$, which corresponds the geometrical surface area of the investigated electrodes. Therefore, the observed feature is assigned to be the contact resistance of the electrode [267], which shows a strong dependence on the SOC of the CAM. Furthermore, it grows continuously, either with time or cycle number (see Figure 4.2d). In contrast, the contact resistance of PC-bm-90/5/5 remains at smaller values (see Figure 4.2c) and does not depend as strongly on the SOC as for PC-bm (see Figure 4.3b).

Implications of the electronic conductivity of an electrode

The observed dependence likely stems from the electronic conductivity of the CAM which changes with degree of delithiation: Amin et al. showed that the electronic conductivity of NCMs varies by five orders of magnitude between ∼10^{-2} and ∼$10^{-7}\,S/cm$ for the charged and discharged state, respectively, being lowest in the fully lithiated state [225]. If the electronic current from the electrode to the current collector (or vice versa) has to pass mainly through the CAM (which is expected to be the case for high-surface-area CAMs with relatively low amounts of conductive carbon, as it is the case for the PC-bm electrode), the corresponding resistance depends on the electronic conductivity of the CAM. The feature dominating the impedance spectrum of the PC-bm electrode is not pronounced for the PC-bm-90/5/5 electrode since latter comprises a 2.5-fold amount of conductive carbon in the electrode, providing a sufficient amount of conductive carbon to guide the current rather through the carbon

than through the NCM.

This decrease in electronic conductivity of the CAM is not only induced by its full lithiation but can also stem from a decomposition of the layered structure to a rock-salt-type phase on the surface of the particles, e.g., by the release of lattice oxygen at high SOC. LNO, for example, exhibits an electronic conductivity of 10^{-1} to 10^0 S/cm [268, 269], while the electronic conductivity of its rock-salt phase NiO is only 10^{-7} to 10^{-5} S/cm [270, 271]. If this increasing resistance shows also as a contact resistance of an electrode, it is expected to be independent of the SOC of the layered-oxide core since the rock-salt-type phase would remain independent of the degree of (de)lithiation and insulate the particle.

The electronic conductivity of the NCM does not only affect the contact resistance but also the conductivity through the entire electrode if the ratio of conductive carbon to CAM surface area is not sufficiently large, what would lead to overpotentials, capacity loss, and an inhomogeneous (de)lithiation of the electrode. Furthermore, the same can be expected for the electronic conductivity within a PC agglomerate since no conductive carbon is present in the pores which form upon (de)lithiation. Here, the electronic rail of the transmission line model (see Figure 2.4) cannot be neglected anymore, what is often done for typical battery electrodes (see Chapter 2.4). This resistance, e.g., due to an insufficient amount of conductive carbon or due to particle cracking, could lead to a (partial) disconnection of active material. Consequently, if the resistance is too large to be overcome by an applied voltage difference of typically only $\sim$10 mV switching between "charge" and "discharge" on the order of a few seconds, it could result in a decrease of the capacitance determined by EIS (at 180 mHz) in the fully discharged state, what could be misinterpreted as a surface area decrease or material loss. Since the high resistance caused by the SOC-dependent electronic conductivity of the NCM is not observed over the entire SOC window but only in the fully discharged state, the available capacity during charge/discharge cycling is barely affected.

In some cases, it might be interesting to monitor the capacitance (e.g., as a function of the cycle number) as a measure for the loss of active material by the disconnection of CAM particles (if it is not convoluted with a simultaneous capacitance increase, e.g., due to particle cracking). In the case of the impedance measurement, the time scales as well as the applied potentials are 100x smaller as compared to the charge/discharge capacity measurement. Therefore, it is expected that the impedance measurement is much more sensitive to introduced resistances in the electrode and could, therefore,

show a significant capacitance decrease, even for small resistances and even before any significant capacity decrease (due to material loss) is observed, what could also explain the decrease in capacitance in Figure 4.1b. In conclusion, for an observed decrease in capacitance, it remains challenging to discriminate between the effect of (relatively small) resistances within the electrode limiting the exchanged currents during EIS and an actual loss of active material, which affects the available capacity. The proper determination of the electrode capacitance can be improved either by a suitable electrode composition diminishing electronic resistances within the electrode (e.g., by a sufficient amount of conductive carbon, ideally long carbon fibers such as VGCF or carbon nanotubes (CNTs)) or by determining the capacitance at even lower frequencies (e.g., between 1 and 10 mHz, however, requiring an *R-Q* fit of the impedance data) for which the electronic resistances can be overcome.

In summary, to enable the proper determination of the capacitance of an electrode, a suitable type and sufficient amount of conductive carbon is required to ensure the electronic conductivity into and through the electrode.

4.3 Performance of Poly- and Single-Crystalline NCMs in Full-Cells

The manuscript with the title "The Implications of Particle Morphology on the Capacity Retention, Side Reactions, and Impedance Build-Up of Nickel-Rich NCMs in Full-Cells: Poly- vs. Single-Crystalline NCM851005" is currently in preparation and will be submitted in Summer 2023. The main findings of this paper were presented by Stefan Oswald as Paper #A03-0368 at the 240th Meeting of the *Electrochemical Society* in a virtual format in October 2021.

After having elucidated the effect of different NCM particle morphologies on its fundamental properties in Chapter 4.1, this article generates important insights into the impact of the NCM particle morphology on the long-term cycling performance: therefor, PC and SC NCM851005 are cycled for more than 200 charge/discharge cycles in coin full-cells with LP57 against graphite, both at 25 and 45 °C, applying two different upper cutoff voltages of 4.1 and 4.4 V. While both an increased voltage as well as an increased temperature lead to an accelerated capacity fading for both CAMs, differences between the two materials are only observed at 4.4 V, where the discharge capacity at high C-rates and the resistance build-up are pronounced for the PC NCM. By using EIS and a µ-RE, the impedance contributions of both anode and cathode are quantified at 4.4 V and 45 °C: while the anode impedance is determined to be relatively small and constant, the cathode impedance grows with cycle number. Since the CAM surface area of the PC NCM increased significantly upon calendering, charging, and cycling as compared to the SC NCM, what is determined by Kr-BET and would result in a smaller charge-transfer resistance, the pronounced electrode resistance of the PC NCM can only originate from the diminished electronic conductivity within the electrode due to particle cracking. For other typical degradation phenomena, such as the increased gas evolution or the increased transition metal dissolution of PC NCMs, no significant impact on the performance was observed in this experiment. Hence, the superior performance of SC CAMs, in particular at higher C-rates, stems from the maintained integrity due to their particle morphology, suppressing the impedance build-up upon particle cracking.

This study highlights the importance of identifying the origin of the capacity loss of a battery upon operation: The contributions of lithium inventory loss, material loss, and resistance build-up can be deconvoluted, e.g., through a procedure applying various C-rates, via the use of a reference electrode to track the half-cell potentials, by in

situ electrochemical impedance spectroscopy to monitor the individual contributions of each half-cell to the total impedance, or by the post mortem analysis of the electrodes against lithium metal. Through this set of methods, the findings of this study do not only suggest that SC NCMs eliminate particle cracking even upon extended cycling under harsh conditions but that most primary particles remain connected both ionically and electronically in contrast to their PC analog, what reduces the impedance of the cathode for SC by a factor of 3x. In addition to the enhanced rate capability enabling cells for high-power applications, SC NCMs are also expected to provide a higher energy density in commercial cells since higher electrode densities are obtained upon calendering for the solid spheres, enabling electrode densities of up to $3.9\,\mathrm{g/cm^3}$, exceeding the one of PC NCMs [184, 272]. Even though the synthesis of SC NCMs is more complex due to the calcination at higher temperatures of up to $1000\,\mathrm{^\circ C}$ as well as the additional washing and deagglomeration steps [161], the spent effort is rewarded by LIBs with a lifetime of more than 10,000 cycles or 25 years, if the upper cutoff voltage and the electrolyte additives are chosen properly [43, 273].

Overall, SC NCMs enable significant improvements in power, energy, and cycle life of LIBs; nevertheless, the open question regarding their optimal particle size, naturally depending on the requirements of the respective application, needs to be answered in future studies.

Author contributions

S.O. and M.B. prepared the electrode sheets, built the half- and full-cells, and conducted the SEM, BET, and EIS measurements. S.O. performed the OEMS experiments. S.O. and M.B. designed the experiments and analyzed the data. S.O. and M.B. wrote the manuscript. S.O. and M.B. contributed equally to this work as co-shared first authors.

The Implications of Particle Morphology on the Capacity Retention, Side Reactions, and Impedance Build-Up of Nickel-Rich NCMs in Full-Cells: Poly- vs. Single-Crystalline NCM851005

Stefan Oswald[=,*,z], Moritz Bock[=,*], and Hubert A. Gasteiger[**]

Chair of Technical Electrochemistry, Department of Chemistry and Catalysis Research Center, School of Natural Sciences, Technical University of Munich, Garching, Germany

[z]E-mail: Stefan.Oswald@tum.de

[=]These authors contributed equally to this work.

[*]Electrochemical Society Student Member.

[**]Electrochemical Society Fellow.

Abstract

The rising interest in single-crystalline NCMs ($LiMO_2$, M = Ni, Co, Mn) has generated numerous publications which feature promising results in terms of cycle life improvement when compared to the conventional polycrystalline analog. To elucidate the effect of the two morphologies on the capacity retention and the internal resistance, this study aims to discriminate the effect of different degradation phenomena of polycrystalline (PC) and single-crystalline (SC) NCM851005 ($LiNi_{0.85}Co_{0.10}Mn_{0.05}O_2$) in coin full-cells cycled against graphite anodes. The impact of the particle morphology is analyzed over the course of more than 200 charge/discharge cycles for two temperatures of 25 and 45 °C, applying two upper cutoff voltages of 4.1 or 4.4 V. The morphology-dependent surface area changes, resulting mainly from the well-known tendency of PC NCMs towards particle cracking upon calendering, charging, and extended cycling, are quantified via krypton-gas physisorption and their consequences regarding the amount of gas evolution, transition metal dissolution, loss of lithium inventory, and resistance build-up are analyzed. In particular, the pronounced cathode impedance of PC, investigated by electrochemical impedance spectroscopy using a micro-reference electrode in full-cells, exposes the impact of particle cracking and the induced electronic resistances within a secondary agglomerate on the rate capability.

1

Introduction

Over the past 25 years, the production capacity of lithium-ion batteries (LIBs) has been rising exponentially, reaching almost 1,000 GWh in 2021, while their price (in US$/kWh) has dropped by an order of magnitude.[1] Until 2010, this trend was mainly driven by the growing market of portable electronics, while it is now dominated by the rise of electric vehicles (EVs).[2] Exemplarily, the share of yearly registered EVs in Germany doubled within one year to reach 26 % of all passenger cars in 2021.[3] In the next years, their advance is expected to continue since a carbon-neutral mobility sector, which is desired to be accomplished in most countries until 2035 or 2050, relies purely on electric propulsion. In this context, future LIBs need to fulfill requirements regarding social and environmental aspects as well as availability, scalability, and cost.

With regard to cost, the raw materials and the processing of cathode active materials (CAMs) are still the largest contributor, accounting for ~50 % of the cell's cost.[2,4] The layered oxide cobalt-based $LiCoO_2$ (LCO), employed in the first commercial LIB by Sony in 1991, continues to dominate the market of portable electronics but does not fulfill the given requirements for the growing demands of the EV market.[5,6] To reduce (or even eliminate) cobalt, the partial (or complete) replacement by nickel and manganese since the early 2000s opened the field of so-called NCMs ($LiMO_2$, M = Ni, Co, and Mn),[7,8] while nickel-rich NCMs (of more than 90 mol% nickel) have emerged as promising candidate for high-energy EV applications.[2,9,10]

Nickel-rich NCMs do not only fulfill the market's requirements but also provide a higher reversible capacity of more than 200 mAh/g, which is delivered at a lower potential.[11,12] On the downside, nickel-rich NCMs require a more complex synthesis due to their tendency towards lithium/nickel mixing,[9,13,14] form unwanted contaminants when exposed to humid atmosphere,[15–18] and are structurally and thermally less stable. For the latter, the instability manifests in the release of lattice oxygen and the formation of a rock-salt-type surface layer, either upon heating of delithiated NCMs (above ~140 °C)[11,19–21] or at high degrees of delithiation (above ~80 % SOC).[12,20,22–26] Additionally, the change of the lattice parameters *a* and *c* results in an anisotropic volume change of the NCM unit cell, which increases with the degree of delithiation and is, therefore, more pronounced for nickel-rich NCMs.[11,27,28] For the conventional polycrystalline (PC) NCMs, consisting of spherical secondary agglomerates with thousands of randomly oriented primary crystallites, this volume-change-induced strain induces the formation of cracks within the agglomerates and deteriorates the integrity of the NCM particles.[25,28–32] Particle cracking does not only result in the electronic disconnection of fragments,[33] but also exposes fresh surface area: already within the first charge, the NCM surface area can increase by a factor of 10.[20,34,35] This surface area increase gives rise to parasitic side reactions, such as pronounced oxygen release[20,36] and transition metal (TM) dissolution,[37–41] compromising the performance and the safety of LIBs.

In contrast, single-crystalline (SC) NCMs comprising monolithic crystallites without secondary structure[42,43] have been found to not only maintain the pristine surface area upon operation, even when charged to high degrees of delithiation,[20,26,34,44] but also allow for higher electrode densities due to the absence of the intraparticular pore volume and, therefore, for higher energy densities.[43,45–47] Depending on the application's requirements, the NCM surface area can be conveniently adjusted by the particle size through different synthesis parameters, mainly controlled by the calcination time and/or temperature.[30,43,48] While smaller SC particles provide kinetic advantages due to the higher electrochemically active surface area, an improved cycle life is expected for larger SC particles due to diminished side reactions on their smaller specific surface area and, therefore, a reduced loss of lithium inventory. This development of SC NCM cathodes has peaked in LIBs with a cycle life of more than 25 years or 1,000,000 km, as presented for NCM523 by Harlow et al. in 2019.[49]

Even though tremendous progress has been achieved in terms of lifetime, the mechanisms behind the differences in battery performance are often convoluted and complex, and a deeper understanding of the impact of particle morphology is still lacking. So far, a variety of studies has compared the cycle life of PC and SC, which have often attested an improved capacity retention for SC NCM,[30,31,47,50] while also the opposite, i.e., the superiority of PC NCM, has been observed.[36,44,51]

To elucidate the effect of the two morphologies on the capacity retention and the internal resistance, this study aims to discriminate the effect of different degradation phenomena of polycrystalline (PC) and single-crystalline (SC) NCM851005 ($LiNi_{0.85}Co_{0.10}Mn_{0.05}O_2$) in coin full-cells cycled against graphite anodes. Since the unwanted side reactions such as loss of lithium inventory, gas evolution, formation of a resistive surface layer, particle cracking, and electrolyte oxidation are accelerated at elevated temperature and/or higher upper cutoff potential, the impact of the particle morphology is analyzed over the course of more than 200 charge/discharge cycles for two temperatures of 25 and 45 °C, applying two upper cutoff voltages of 4.1 or 4.4 V. The morphology-dependent surface area changes, resulting mainly from the well-known tendency of PC NCMs towards particle cracking upon calendering, charging, and extended cycling, are quantified via krypton-gas physisorption and new insights regarding the amount of gas evolution, TM dissolution, loss of lithium inventory, and resistance build-up are generated.

Experimental

NCM active material powders – Two different NCM851005 active materials were used in this study: a polycrystalline NCM851005 material (referred to as "PC", $LiNi_{0.85}Co_{0.10}Mn_{0.05}O_2$, BASF SE, Germany) as

well as a single-crystalline NCM851005 ("SC", from BASF SE, Shanghai, China) were used as received. Both NCMs were not doped, coated, nor washed during their synthesis.

Scanning electron microscopy – The morphology of the two NCM powders as well as of the respective electrodes (prepared as described below) was investigated via top-view scanning electron microscopy (SEM, JSM-IT200, JEOL, Japan) in secondary electron mode, applying an acceleration voltage of 5 kV.

Titration – To quantify the amount of carbonate species on the surface of the two NCMs, 1 g of NCM was mixed in a high-density-polyethylene (HDPE) bottle with 5 ml of deionized water (H_2O, 18 MΩ/cm, Merck MilliPore Milli-Q, USA) in a water-to-CAM ratio of 5:1 (H_2O:CAM w/w) and stirred at 500 rpm using a magnetic stirring bar for 60 min. After the washing, the water was separated by vacuum filtration using a membrane filter (cellulose acetate, 0.2 µm pore size, Whatman, United Kingdom) and the washing solution was collected in an HDPE bottle. For the titration, 0.5 ml of the collected washing solution were pipetted into a PE beaker, diluted with 10 ml of H_2O, and stirred with a magnetic stirring bar. To obtain the titration curve, an acidic titrant solution of 10 mM hydrochloric acid (HCl, Sigma-Aldrich) in H_2O was added stepwise with a resolution dV_{HCl} of the added titrant volume of 0.1 ml using an automated titrator (TitroLine 7000, SI Analytics, Xylem Inc., USA) until a pH of 3.5 was reached, while recording the pH as a function of time and added acid volume.

Electrode preparation – Graphite electrodes were prepared from graphite powder (T311, 3.2 m^2_{Gra}/g$_{Gra}$, SGL Carbon GmbH, Germany) using a mass ratio of 97:1.5:1.5 of active material, sodium carboxymethyl cellulose (Na-CMC, M_w = ~90,000, Sigma-Aldrich, USA), and styrene-butadiene rubber (SBR, 40 wt% emulsion in water, Zeon, Japan) as well as ultra-pure water (H_2O, 10 MΩ·cm, Milli-Q IQ 7005, Millipore, Merck, Germany) with a final solid content of 55 wt%. The ink was mixed in a planetary centrifugal mixer (ARV-310, Thinky Corp., USA) for 22 min, using a three-step sequential mixing procedure, while the SBR binder was added before the last mixing step of 2 min at low rotation speed. The graphite ink was coated onto the rough side of a copper foil (12 µm, MTI, USA) with a box-type coating bar (Erichsen, Germany), using an automated coater (RK PrintCoat Instruments, United Kingdom). The electrode sheets were then dried at room temperature for 5 h. Uncompressed graphite electrodes with a diameter of 10.95 mm and 15 mm were punched out from the prepared sheets, having a mass loading in the range of 5.9 ± 0.7 mg$_{Gra}$/cm², which were then used in uncompressed state.

NCM electrodes were prepared from the two above described NCM851005 powders that exhibit very different morphology (described later in **Figure 1**) and specific surface area: a polycrystalline NCM851005 (PC, 0.27 m^2_{NCM}/g$_{NCM}$ (measured by Kr-BET)) and a single-crystalline NCM851005 (SC, 0.51 m^2_{NCM}/g$_{NCM}$). Targeting different experimental investigations (see below), two different electrode inks were prepared with each of the two NCM851005 powders, using a mass ratio of 96:2:2 of active material,

carbon black (C65, carbon black SuperC65, 64 m^2_{C65}/g_{C65}, TIMCAL, Switzerland), and polyvinylidene difluoride binder (PVDF, Solef 5130, Solvay, Germany) with N-methyl-2-pyrrolidone (NMP, anhydrous, Sigma-Aldrich, Germany) as dispersing agent. For the OEMS measurements, a solid content of the ink of 80 wt% was chosen, while for all other measurements a solid content of 63 wt% was used. The inks based on PC were mixed in the planetary mixer for 17 min, using a sequential mixing procedure. To deagglomerate the primary particles, the inks based on SC were prepared using a planetary ball mill (Pulverisette 7, Fritsch, Germany) with a ZrO_2 beaker (20 ml) and ZrO_2 balls (10 mm in diameter) by mixing 4x5 min at 400 rpm, including rest periods of 2 min between each step.

On-line electrochemical mass spectrometry (OEMS) measurements): The NCM inks with a solid content of 80 wt% were coated onto a stainless steel mesh (316 grade, 26 μm aperture, 25 μm wire diameter, The Mesh Company, United Kingdom) with a doctor blade, using the automated coater. The electrode sheets were then dried in a convection oven at 50 °C for 5 h before electrodes with a diameter of 14 mm were punched out, having a mass loading in the range of 10.8 ± 0.2 mg_{NCM}/cm^2. For the counter electrodes, lithium iron phosphate (LFP) electrodes with a diameter of 15 mm were punched out from commercially available LFP electrode sheets (LFP on aluminum, 3.5 mAh/cm^2, Customcells, Germany). The electrodes for OEMS were used uncompressed.

Cycling experiments in coin cells and T-cells: The NCM inks with a solid content of 63 wt% were coated onto the rough side of an aluminum foil (16 μm, MTI, USA) with a box-type coating bar (Erichsen, Germany), using the automated coater. The electrode sheets were then dried in a convection oven at 50 °C for 5 h before they were calendered at 100 °C to a porosity of 39 % (corresponding to ~30 μm in thickness) using a lab calender (GK 300 L, Saueressig, Germany). Electrodes with a diameter of 10.95 mm as well as 14 mm were punched out from uncompressed as well as from calendered sheets, having a mass loading in the range of 8.2 ± 0.5 mg_{NCM}/cm^2.

All electrodes were dried in a Büchi oven at 120 °C under dynamic vacuum for at least 6 h and then transferred without exposure to air to an argon-filled glove box (<1 ppm O_2 and H_2O, MBraun, Germany) where all cells were assembled.

On-line electrochemical mass spectrometry – In preparation of the on-line electrochemical mass spectrometry (OEMS) experiments (reprinted here from previous publications[20,26] for the sake of completeness), capacitively oversized LFP electrodes (Ø 15 mm, 3.5 mAh/cm^2) were pre-delithiated in coin cells (Hohsen, Japan) using two glass fiber separators (Ø 16 mm, glass microfiber filter, 691, VWR, Germany, dried for 6 h at 300 °C under dynamic vacuum), one polyolefin separator (Ø 17 mm, H2013, Celgard, USA) facing the LFP electrode (preventing that glass fibers adhere to the LFP electrodes and get transferred to the OEMS cell), and 100 μl of LP57 electrolyte (1 M $LiPF_6$ in EC:EMC 3:7 w/w, <20 ppm

5

H_2O, BASF, Germany). For this, they were delithiated in coin half-cells against metallic lithium (Ø 15 mm, 450 μm thick, Rockwood Lithium, USA) to ~90 %SOC at a specific current of 30 mA/g_{LFP} for 4.5 h, after having performed one full formation cycle at 30 mA/g_{NCM} between 3.0 and 4.0 V_{Li} (note that throughout this article potentials referenced to the Li^+/Li redox potential are denoted as V_{Li}; similarly, V_{Gra} is used for the cell potential of the full-cells with graphite as counter electrode). After pre-delithiation, the LFP electrodes were harvested from the cells and used without washing as the counter electrode in the OEMS cells for the gas evolution experiments. As described previously,[20,26] the pre-delithiated, capacitively oversized LFP electrodes are used because they: i) provide a stable potential of ~3.45 V_{Li} over a wide SOC window, ii) provide a sufficiently large capacity to take up the lithium from the investigated NCM working electrodes, and iii) exhibit no gas evolution due to the absence of electrolyte decomposition reactions at their operating potential (as compared to typical anodes such as lithium metal or graphite forming an solid-electrolyte interphase (SEI), accompanied by gas evolution[23,52,53]). To later calculate the end of charge potential of the NCM electrodes in the OEMS experiments, the LFP potential at ~10 %SOC is used: during the relithiation in here-mentioned half-cells, a potential of 3.40 V_{Li} was observed.

For the OEMS experiments, a pre-delithiated LFP counter electrode was placed on the bottom of the custom-made OEMS cell hardware, then covered by two polyolefin separators (Ø 24 mm, H2013, Celgard, USA) that were wetted with 100 μl of LP57 electrolyte, and finally an NCM mesh electrode (Ø 14 mm) was placed on top of the stack in the spring-compressed OEMS cells. The assembled cells were positioned in a climate chamber (T-40/25, CTS, Germany) at 25 °C and connected to a potentiostat (SP-300, BioLogic, France) and the mass spectrometer system (HiQuad QMH 400-1, Pfeiffer Vacuum, Germany), which has been described in detail elsewhere.[54]

The cells were held at OCV for 4 h before they were charged in constant-current mode (CC) to 4.14 V_{Li} (corresponding to 0.74 V_{LFP} against the pre-delithiated, capacitively oversized LFP counter electrode) at a C-rate of C/5 (corresponding to 55 mA/g_{NCM}, referenced to the theoretical capacity of 275 mAh/g_{NCM} of NCM851005), where they were held for one hour in constant-voltage mode (CV), before they were discharged to ~3.0 V_{Li} (corresponding to -0.4 V_{LFP}). After two full cycles to 4.14 V_{Li}, three cycles were executed with a higher upper cutoff potential of 4.62 V_{Li} (corresponding to 1.22 V_{LFP}). Each of the five CV steps was followed by an OCV period of 10 min.

The traced mass signals were normalized to the ion current of the ^{36}Ar isotope in order to correct for fluctuations of pressure and temperature, and the signals for O_2 and CO_2 were then converted to concentrations using a calibration gas (Ar with 2000 ppm of H_2, O_2, C_2H_4, and CO_2 each, Westfalen, Germany) and considering a cell volume of ~11 cm^3, as introduced by Strehle et al. and Jung et al. for the gassing of (LMR-)NCM.[23,55] For details on the calibration procedure, see Tsiouvaras et al.[54]

Coin cell assembly and testing – All electrochemical cycling tests (of both coin and Swagelok T-cells) were performed in a climate chamber (KB 115 or KB 720, Binder, Germany), using a battery cycler (Series 4000, Maccor, USA) for cell cycling. Two cells were built for each combination of NCM material, temperature, and upper cutoff voltage; the error bars in the figures represent the standard deviation of the two.

For the comparison of the long-term cycling behavior of the two NCM materials, full-cells with each PC and SC were assembled in coin cells (CR2032, Hohsen, Japan), using uncompressed graphite electrodes on copper foil as anode (Ø 15 mm) and calendered NCM electrodes on aluminum foil as cathode (14 mm in diameter), with two glass fiber separators (Ø 16 mm) and 100 µl of LP57 electrolyte in between. Aiming to achieve a constant balancing factor between anode and cathode capacity, the mass of the graphite electrodes was adapted according to the mass of the NCM electrodes, taking into account their respective specific capacity at the two applied upper cutoff voltages of 4.1 V_{Gra} and 4.4 V_{Gra}, or NCM potentials of ~4.2 V_{Li} and ~4.5 V_{Li}, respectively. Therefor, the specific capacities of the first charge to each of the two potentials of 215 mAh/g_{NCM} and 245 mAh/g_{NCM}, respectively, were extracted from the potential curve depicted in **Figure A.2**. The areal capacity of the anode (in mAh/cm^2) was 1.1-fold oversized compared to the cathode when referenced to a capacity of 355 mAh/g_{Gra} of the graphite anode (corresponding to the approximate reversible discharge capacity of graphite during the first cycle in a half-cell (see **Figure A.1**), as compared to its theoretical capacity of 372 mAh/g_{Gra}).

The cycling performance of the full-cells was investigated both at 25 °C and 45 °C, applying an upper cutoff voltage of either 4.1 V_{Gra} or 4.4 V_{Gra}, while the lower cutoff voltage was held constant at 3.0 V_{Gra}. After an initial OCV phase of 2 h, the full-cells were cycled for five sets of 36 intermediate cycles (with a *C*-rate of *C*/3 for both charge and discharge, always referenced to the theoretical capacity of NCM851005 of 275 mAh/g_{NCM}), while each set was framed by a sequence of two slow cycles (*C*/15 for both charge and discharge) and two fast cycles at 2*C* (*C*/3 for the charge and 2*C* for the discharge), including a direct current internal resistance (DCIR) measurement after the two slow cycles, resulting in a total of 204 full cycles. Each charge (except for the ones for the DCIR measurements) was performed in CCCV mode (including a CV step at the respective upper cutoff voltage for 1 h or until the current dropped below *C*/20) while each discharge was performed in CC mode (without CV step). For the DCIR measurements that followed the two slow cycles and were not considered for the cycle count, the cells were charged in CC mode to 3.8 V_{Gra} (or ~3.9 V_{Li}) and then held at OCV for 1 h, before two discharge pulses of *C*/3 were applied for 1 s as well for 10 s (note that only the latter was analyzed in this study), including a OCV phase of 1 min in between them, before the cells were again discharged to 3.0 V_{Gra} in CC mode. For the final 204th full cycle, the cells were discharged in CCCV mode (including a CV step at 3.0 V_{Gra} for 1 h).

For the post mortem analysis of the cycled NCM electrodes (Ø 14 mm, cycled to 4.4 V at 45 °C) in a discharge rate test as well as by Kr-BET measurements, the NCM electrodes were harvested from the cycled coin full-cells (as described below) and reassembled without washing in coin half-cells with lithium counter and NCM working electrode, using two glass fiber separators (Ø 16 mm), one polyolefin separator (Ø 17 mm, H2013, Celgard, USA) facing the NCM electrode, and 100 µl of LP57 electrolyte. Additionally, identical cells with pristine PC or SC working electrode were assembled (both for the comparison to the cycled cells as well as for Kr-BET measurements of charged electrodes).

To determine the rate capability of the pristine and cycled electrodes, the cells with both PC or SC were cycled at 25 °C for five charge/discharge cycles between 3.0 V_{Li} and 4.5 V_{Li} (corresponding to ~4.4 V_{Gra} as it was used for the full-cells). The first four cycles consisted of a discharge rate test, in which each rate was applied for one cycle. The applied *C*-rates were *C*/15, *C*/3, *C*/3, and *C*/50 for the charge in CCCV mode (including a CV step at 4.5 V_{Li} for 1 h or until the current dropped below *C*/20), and *C*/15, *C*/3, 2*C*, and *C*/50 for the discharge in CC mode (all referenced to the theoretical capacity of 275 mAh/g$_{NCM}$ of NCM851005). The rate test was followed by a final charge to 4.1 V_{Li} at *C*/15 in CCCV mode (including a CV step at 4.1 V_{Li} for 1). Additionally, cells with pristine NCM electrodes were charged to 4.1 V_{Li} in the same way as in cycle five of the rate test. Subsequently, all cells charged to 4.1 V_{Li} were disassembled, before the harvested NCM electrodes were washed, dried, and analyzed by Kr-BET, as described below.

Cell disassembly – NCM electrodes were harvested from charged coin half-cells as well as from cycled coin full-cells under inert atmosphere to investigate their rate capability in post mortem cycling experiments as well as to determine their specific surface area by Kr-BET. To determine the surface area of the NCM electrode only, any residue of the conductive salt was removed in a three-step sequential washing procedure: first, they were washed for 5 min in 5 ml EC:EMC 3:7 w/w (Gelon Lib, China), followed by a soaking step of 24 h in 1 ml DMC (anhydrous, ≥99 %, Sigma Aldrich, USA) and, finally, a washing step of 5 min in 5 ml DMC. Additionally, graphite electrodes from cycled coin full-cells were harvested without washing.

Surface area analysis – The surface area of the active material powders and of the (uncompressed or calendered) pristine as well as of the (calendered) harvested and washed electrodes was determined by krypton-gas physisorption measurements (also referred to as Kr-BET)[56] at 77 K (adapted and reprinted here from previous publications[20,25,26,32,35] for the sake of completeness), measuring at 13 points between $0.01 \leq p/p_0 \leq 0.30$, using an autosorb iQ (Quantachrome Instruments, USA). The advantage of the measurement with krypton is a superior sensitivity of this method, since only ca. 1/100th of the total surface area is required for krypton compared to nitrogen physisorption measurements, so that Kr-BET areas can be obtained for electrodes with 14 mm in diameter, whereas an approximately 100-fold larger electrode area would be required for meaningful N_2-BET measurements. Prior to Kr-BET measurements, both powder

samples as well as samples of pristine or harvested and washed electrodes were dried at 120 °C under vacuum for 6 h.

Elemental analysis – The graphite electrodes harvested from the cycled coin full-cells without washing were scratched off from the copper current collector using the blade of a scalpel, before their elemental composition was analyzed by an external lab (Mikroanalytisches Labor Pascher, Germany). To determine the carbon content of the cycled graphite electrodes, the electrode powder was burned in an oxygen flow of 1200 °C while the resulting CO_2 was absorbed in sodium hydroxide solution, from which the carbon content was determined by the change of conductivity of the solution. For the quantification of lithium, nickel, cobalt, and manganese, the electrode powder was solubilized at 180 °C in a mixture of nitric acid and hydrochloric acid, from which the content of the four metals was determined via inductively coupled plasma atomic emission spectrometry (ICP-AES). The amounts were given in units of wt%, while the absolute errors of the measurements were 0.5 wt% for carbon, 0.002 wt% for nickel, and 0.0002 wt% for cobalt and manganese.

T-cell assembly and testing – To monitor the impedance spectra of anode and cathode in the full-cells during the long-term cycling procedure, full-cells with each PC and SC (similar to the ones assembled in coin cells, as described above) were assembled in T-cells (Swagelok, USA). Due to the change of the cell setup, the parameters were adapted as following: Graphite anodes and NCM cathodes (Ø 10.95 mm for both) were assembled with two glass fiber separators (Ø 11 mm) and 60 µl of LP57 electrolyte. The balancing factor of 1.1:1 between anode and cathode was maintained for the areal capacities (in mAh/cm²) of the two electrodes. To monitor the impedance spectra of both the graphite anode as well as of the NCM cathode individually, a micro-reference electrode (µ-RE, i.e., a gold-wire reference electrode (GWRE)[57]) was placed between the two glass fiber separators of the T-cells.

The T-cells were cycled at 45 °C to an upper cutoff voltage of 4.4 V_{Gra}, using the identical procedure as described above for the coin full-cells; additionally, an electrochemical impedance spectrum was recorded directly after each DCIR measurement at 3.8 V_{Gra}. The spectra were recorded by a multi-channel potentiostat (VMP3, BioLogic, France) in a climate chamber (Binder, Germany) after an equilibration time of 2 h at 45 °C in potentio mode (PEIS), with an amplitude of 15 mV for 8 points per decade from 100 kHz to 10 mHz, including a data point at a frequency of 18 mHz. This results in an acquisition time of ~1 h per PEIS. Each EIS spectrum consists of a full-cell spectrum (between working and counter electrode) and, by using the µ-RE, also of the two half-cell spectra (i.e., between the working electrode and the µ-RE, as well as between the counter electrode and the µ-RE). It must be noted that for measurements with the GWRE, the impedance spectra are only shown up to 31 kHz due to artefacts at higher frequencies.[58]

9

To record the potential curves of the first two cycles of graphite (shown in **Figure A.1** in the appendix), spring-compressed T-cells with a lithium-metal reference electrode (Ø 6 mm) and a lithium-metal counter electrode (Ø 11 mm) and with uncompressed graphite working electrodes (Ø 10.95 mm) were assembled using three glass fiber separators (Ø 11 mm, two between working and counter electrode and one on the lithium-metal reference electrode) and 90 µl of LP57 electrolyte. Controlled by the reference electrode potential, the graphite electrode was cycled at 25 °C three times at $C/15$ (corresponding to a specific current of 24.8 mA/g_{Gra} when referenced to the theoretical capacity of graphite of 372 mAh/g_{Gra}), charging (or lithiating) the graphite to 0.01 V_{Li} in CCCV mode (including a CV step at 0.01 V_{Li} for 1 h or until the current dropped below $C/20$), and discharging (or delithiating) it in CC mode.

To record the potential curves of the first charge of the three NCMs (shown in **Figure A.2** in the appendix), similar T-cells as described above for graphite were assembled, however, using calendered NCM-based working electrodes (Ø 10.95 mm). To allow for the assignment of the applied potential to a state of charge (i.e., to a defined degree of delithiation) for each of the three NCMs, the T-cells were charged at 25 °C in constant-current mode (CC) to 5.0 V_{Li} at a C-rate of $C/15$ (corresponding to a specific current of 18.3 mA/g_{NCM} when referenced to the theoretical capacity of NCM851005 of 275 mAh/g_{Gra}).

Results and Discussion

Visual investigation of the pristine NCM powders and electrodes – In advance to the electrochemical investigations, the morphology of the two NCM851005 cathode active material (CAM) powders as well as of the respective (uncompressed or calendered) electrodes is evaluated through representative images obtained by scanning electron microscopy (SEM) as well as through BET surface area measurements with krypton-gas physisorption (Kr-BET). The pristine polycrystalline NCM851005 powder (PC, marked in blue color) displayed in **Figure 1a** consists of spherical secondary particles with a diameter of 5 to 10 µm, each comprising thousands of primary crystallites with a size of 0.2 to 1.0 µm. The Kr-BET measurement of the PC NCM powder yields a specific surface area of 0.27 m^2_{NCM}/g_{NCM}, which (based on a spherical approximation of solid spheres with a single diameter $d = 6/(A_{BET} \cdot \rho)$) would correspond to an average diameter of $d \approx 5$ µm, using the crystallographic density of NCM851005 of $\rho = 4.80$ g/cm^3,[27] suggesting that mostly the external surface area of the secondary particle agglomerates of the pristine PC material is accessible to the electrolyte. The uncompressed PC electrode, shown in **Figure 1b**, exhibits intact secondary agglomerates, similar to the ones of the powder. This also reflects in the similar values of the specific NCM surface area of the pristine PC powder of 0.27 m^2_{NCM}/g_{NCM} and the one of the PC electrode of 0.31 m^2_{NCM}/g_{NCM}, latter determined from the specific surface area of the electrode (note that the

determination of the Kr-BET values of the NCM from the ones of the electrodes is explained and discussed in detail below in **Figure 4**). Further, the network of conductive carbon and binder, visible in the image of the electrode, provides electric connection between the polycrystalline agglomerates; however, it must be noted that not all primary crystallites are connected equally, as the carbon/binder network is not expected to penetrate the agglomerates, only reaching (some of) the outmost primary crystallites, as carbon and binder cover the agglomerates' surface only partially (these observations will gain relevance when discussing the impedance data in **Figure 7**). During calendering, some of the secondary agglomerates form noticeable cracks due to the mechanical forces of the compression, which are shown in **Figure 1c**. This disintegration of the primary crystallites induces an increase of the NCM surface area by 83 % to 0.56 m^2_{NCM}/g_{NCM} (see **Figure 4**). These findings have already been correlated previously by (FIB-)SEM,[32,59–61] Kr-BET,[32] and capacitance-based measurements.[20,32,59]
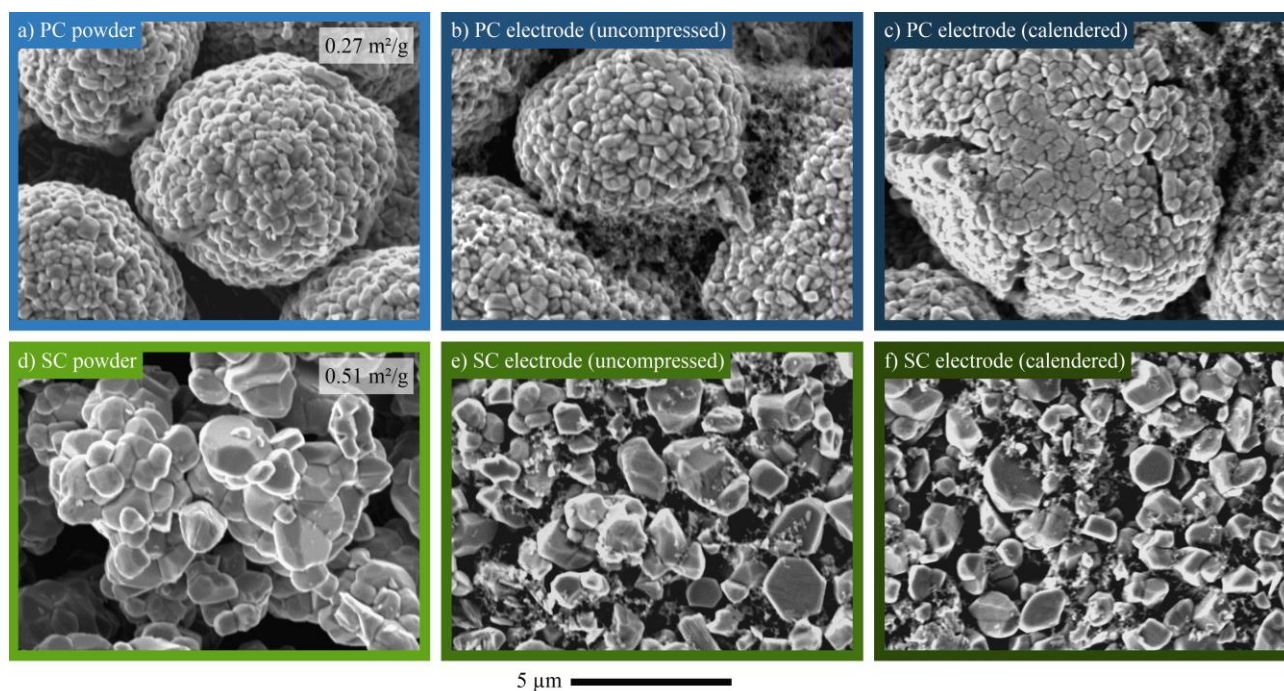
Figure 1: Visual investigation of the particle morphology of the pristine NCM851005 powders (**Figures 1a** and **1d**) of PC (blue, **Figures 1a** to **1c**) and SC (green, **Figures 1d** to **1f**) as well as of the respective uncompressed (darker colors, **Figures 1b** and **1e**) or calendered (darkest colors, **Figures 1c** and **1f**) electrodes. Representative images collected by top-view scanning electron microscopy in secondary electron mode using an acceleration voltage of 5 kV. The specific surface area of the two pristine NCM powders obtained by Kr-BET is displayed for each material in the respective panel.

In contrast to the polycrystalline NCM, the pristine single-crystalline NCM851005 (SC, green), displayed in **Figure 1d,** consists of randomly agglomerated, sintered primary particles without regular secondary ordering, having a primary particle size ranging from 0.2 to 3.0 µm and exhibiting a specific surface area of 0.51 m^2_{NCM}/g_{NCM}. During the ink preparation of the SC powder, the ink mixing in a ball mill resulted in the complete separation of the agglomerated particles into individual monolithic primary particles without

11

significant agglomeration, as presented in **Figure 1e**. If compared to the pristine SC powder, this separation is accompanied by an increase of the NCM specific surface area of 180 % to 1.42 m^2_{NCM}/g_{NCM} (see **Figure 4**), corresponding to an average particle size of 0.9 µm (for the spherical approximation), which coincides well with the primary crystallite size of the SC material. Additionally, it is observed for the SC electrode that the carbon/binder network is homogeneously distributed between all primary crystallites. The subsequent calendering of the SC electrode results in the occasional cracking of the primary particles, as seen in **Figure 1f**; overall, however, the mechanical compression does not affect the integrity of most SC particles, which was already shown by previous publications[20,61] and is also expressed in the relatively small increase of the NCM surface area by 11 % to 1.57 m^2_{NCM}/g_{NCM} (see **Figure 4**).

Based on the visual investigation of the two materials, the two very different morphologies of the NCM851005 materials used in this study allow for the discrimination of the effect of the (polycrystalline vs. single-crystalline) particle morphology on the cycling performance in full-cells.

Full-cell aging upon charge/discharge cycling – To investigate the influence of the two different NCM morphologies on the cell aging, coin full-cells with graphite anode and PC or SC NCM cathodes were cycled at a *C*-rate of *C*/3 (corresponding to 91.7 mA/g_{NCM} based on the theoretical capacity of 275 mAh/g_{NCM}) to an upper cutoff voltage of 4.1 V_{Gra} or 4.4 V_{Gra} (corresponding to an NCM potential of ~4.2 V_{Li} and ~4.5 V_{Li}, respectively), both at 25 °C or 45 °C. To distinguish between the overpotential-induced capacity loss due to resistance build-up and the loss of lithium inventory (LLI) due to side reactions as well as the LAM, the cycling procedure included check-up sequences consisting of two cycles with a *C*-rate of *C*/15 for charge and discharge followed by a DCIR measurement at 3.8 V_{Gra} (or ~3.9 V_{Li}, corresponding to ~50 % SOC, see **Figure A.2**) and two cycles with a *C*-rate of *C*/3 for the charge and 2*C* for the discharge. The cells are evaluated in terms of capacity retention and cell resistance build-up, as depicted in **Figure 2**, before post-mortem experiments illuminated the extent of LLI, the surface area increase induced by particle cracking, and the amount of TM dissolution and redeposition.
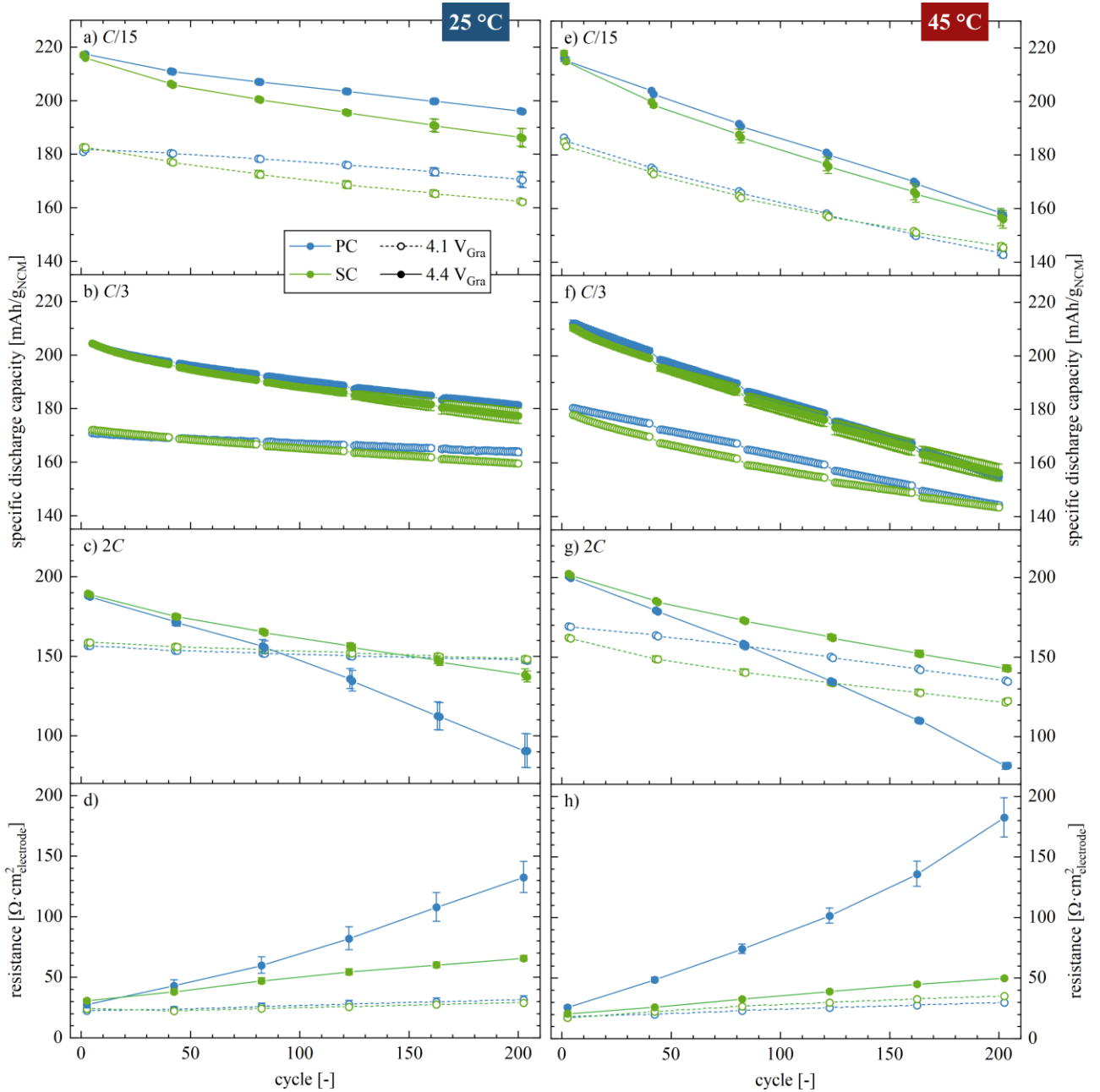
Figure 2: Cycling data of PC (blue) and SC (green) cycled in coin full-cells over 204 cycles **a) – d)** at 25 °C and **e) – h)** at 45 °C presenting the specific discharge capacity for the applied *C*-rates of *C*/15, *C*/3 and 2C (based on the theoretical capacity of 275 mAh/g_{NCM}) as well as the cell resistance, both as a function of cycle number. The resistance is extracted from a DCIR pulse of *C*/3 for 10 s at 3.8 V_{Gra}. The coin cells were assembled using NCM cathodes with a mass loading of 8.2 mg$_{NCM}$/cm², graphite anodes (with an areal balancing factor of 1.1:1, based on 372 mAh/g_{Gra} and 215 mAh/g_{NCM} or 245 mAh/g_{NCM} for 4.1 V_{Gra} and 4.4 V_{Gra}, respectively), two glass fiber separators, and 100 µl LP57 electrolyte. The error bars correspond to the minimum/maximum value of two cells.

Cycling at 25 °C: In **Figures 2a** to **2d**, the discharge capacities and resistances are depicted for PC (blue symbols) and SC (green) cycled at 25 °C, both to 4.1 V_{Gra} (open symbols and dashed line) and 4.4 V_{Gra} (closed symbols and solid line). At begin of test (BOT, corresponding to the first cycle with a *C*-rate of *C*/15), PC NCM yields a discharge capacity of 181 mAh/g_{NCM} when cycled to 4.1 V_{Gra} at a *C*-rate of *C*/15. For the higher *C*-rates of *C*/3 and 2C, the available capacity is reduced to 171 mAh/g_{NCM} and 157 mAh/g_{NCM}, respectively. The discharge capacities of SC NCM at BOT are similar to the ones of PC within a range of

±2 mAh/g$_{NCM}$ for all *C*-rates. However, upon cycling, SC NCM exhibits a lower capacity retention of 89 %SOH (state of health, based on the discharge capacity of the second cycle with a *C*-rate of *C*/15) as compared to PC NCM with 94 %SOH for the check-up cycles at the end of test (EOT, corresponding to cycle 202 with a *C*-rate of *C*/15). This difference is particularly visible at *C*/15, whereas for the cycles applying the highest discharge *C*-rate of 2*C*, negligible differences are discernible within the error range. At slow *C*-rates, the effect of resistance-induced overpotentials should play a minor role as their contribution scales with the applied current. The loss of active material (LAM) or LLI likely dominates the capacity at slow rates. In contrast, the discharge capacity at high *C*-rates is expected to correlate with the cell resistance, determined by Ohm's law for a current-pulse-induced voltage drop. In **Figure 2d**, the DCIRs of PC and SC NCM are depicted for the discharge pulses of 10 s at 3.8 V$_{Gra}$. After the formation, the cell resistance normalized to the geometric surface area of the electrode of 1.54 cm$^2_{electrode}$ is similar for both PC and SC NCM with 23 Ω·cm$^2_{electrode}$ and 24 Ω·cm$^2_{electrode}$, respectively. Throughout the 204 cycles, the cell resistances rise to 31 Ω · cm$^2_{electrode}$ and 29 Ω · cm$^2_{electrode}$ for PC and SC NCM, respectively, resulting in a relative increase of ~40 % and ~20 % upon cycling. However, the absolute values of the cell resistances remain similar, which is in agreement with the negligible differences of accessible discharge capacity in the cycles with the highest *C*-rate of 2*C*.

By charging to the higher cell voltage of 4.4 V$_{Gra}$ and, therefore, to a higher degree of delithiation of the NCM, it becomes obvious from the potential curve of the first charge in a NCM half-cell depicted in **Figure A.2** that the charge capacity is increased from 215 mAh/g$_{NCM}$ to 240 mAh/g$_{NCM}$ for both materials. The resulting discharge capacity of the discharge in the coin full-cells with graphite anode and NCM cathode cycled to 4.4 V$_{Gra}$ is increased as well to 217 mAh/g$_{NCM}$ for both NCM materials. However, by extracting more lithium from the NCM structure, the capacity fades more severely as compared to the cells cycled to 4.1 V$_{Gra}$; this accelerated degradation was previously observed by Kondrakov et al. for NCM811[62] as well as by Jung et al. for NCM111, NCM622 and NCM811, attributing the capacity loss to a degradation of the cathode active material decomposition of the layered structure upon release of lattice oxygen.[23] For the higher upper cutoff potential, the capacity retention at EOT is 90 %SOH and 86 %SOH for PC and SC, respectively. In the first cycle with a *C*-rate of *C*/3, both PC and SC NCM exhibit a discharge capacity of 204 mAh/g$_{NCM}$. Upon cycling, a similar fading as in the *C*/15 checkup cycles is observed, with a slightly lower accessible discharge capacity at *C*/3 of 177 mAh/g$_{NCM}$ for SC NCM compared to PC NCM with 181 mAh/g$_{NCM}$. The largest differences between PC and SC NCM cycled to 4.4 V$_{Gra}$ are observed in the cycles with a fast discharge *C*-rate of 2*C*. Beside the same initial discharge capacity of 189 mAh/g$_{NCM}$ for both materials, PC NCM shows a severe capacity loss of 99 mAh/g$_{NCM}$ upon cycling, resulting in a remaining capacity of 48 % of the initial discharge capacity at 2*C*. In contrast, SC NCM still exhibits

137 mAh/g$_{NCM}$ after 204 cycles, which is 72 % of the initial discharge capacity at 2*C*. This observation is accompanied by a drastic increase of cell resistance of +382 % for PC referenced to the initial value compared to an increase of +113 % for SC. Through Ohm's law, the cell resistance of 66 Ω·cm^2$_{electrode}$ and 132 Ω·cm^2$_{electrode}$ for SC and PC NCM electrodes during the final cycles with a *C*-rate of 2*C* (corresponding to 4.4 mA/cm^2$_{NCM}$) translates to an overpotential of 290 mV and 580 mV, respectively, which then results in the lower discharge capacity of PC.

Cycling at 45 °C: Cycling of full-cells at elevated temperatures promotes their aging due to the accelerated side reactions.[35,49,63,64] To investigate the influence of the NCM morphology under enhanced aging conditions, the two used NCM materials are cycled at 45 °C, both to 4.1 and 4.4 V$_{Gra}$. The discharge capacities and resistances of the coin full-cells with graphite anode and NCM cathode cycled at 45 °C are shown in **Figures 2e** to **2h**. Due to the elevated temperature, the initial discharge capacities of PC and SC are increased to 186 mAh/g$_{NCM}$ and 183 mAh/g$_{NCM}$, respectively. However, the accelerated aging manifests in a decreased capacity retention in the *C*/15 check-up cycles of 77 %SOH for PC and 79 %SOH for SC after 202 cycles. The observed capacities at a *C*-rate of *C*/3 is quite similar for both materials with a slightly steeper fading in the first 80 cycles for SC, but both materials still reach 143 mAh/g$_{NCM}$ after 200 cycles. During the cycles at a *C*-rate of 2*C*, a discrepancy of ~15 mAh/g$_{NCM}$ is observed with a lower rate capability for SC when cycled to 4.1 V$_{Gra}$. In addition, the DCIR of the cells with SC NCM is 5 Ω·cm^2$_{electrode}$ larger than for PC NCM after 202 cycles. When cycled to the higher upper cutoff potential of 4.4 V$_{Gra}$, the initial capacities at an elevated temperature of 45 °C are increased as compared to the cells cycled at 25 °C, while the state of health is diminished to ~73 %SOH within 202 cycles, independent of the morphology of the here used CAMs. The capacity fading in the *C*/3 cycles follows a similar trend for both materials. In contrast, the discharge capacities during the 2*C* cycles are identical only at BOT; within the 202 cycles, however, the rate capability of PC drastically decreases as compared to SC, what also shows in the approximately fourfold resistance of 182 Ω·cm^2$_{electrode}$ of PC as compared to 50 Ω·cm^2$_{electrode}$ of SC. For the cells cycled to 4.4 V$_{Gra}$ at 45 °C, the individual contributions to the cell resistance are deconvoluted using a μ-RE and discussed in **Figure 7**.

The cycling data obtained for PC and SC NCM in full-cells cycled to two upper cutoff potentials at two temperatures are summarized by the following three conclusions:

- At elevated temperatures of 45 °C, the capacity fading is more pronounced for both NCM materials as compared to 25 °C, diminishing the capacity retention even at slow *C*-rates.
- For the cutoff potential of 4.1 V$_{Gra}$, both NCM materials exhibit a similar cycling performance, independent of temperature.

15

- When the cutoff potential is increased to 4.4 V_{Gra}, the cell resistance grows more rapidly, compromising the rate capability, what is most pronounced for PC, in particular, at 45 °C.

Contributions to the capacity loss: To analyze the capacity losses of the cells cycled under the harshest conditions, the charge and discharge capacities of the full-cells cycled to 4.4 V_{Gra} at 45 °C (already discussed in the previous section in **Figure 2**) are summarized on the left side of **Figure 3**. For both PC (blue) and SC (green), the discharge capacity at BOT (cycle 1) of 217 mAh/g_{NCM} is significantly lower than the respective charge capacity of 247 mAh/g_{NCM}, resulting in a first-cycle coulombic efficiency (CE) of 88 %. This low CE cannot be caused by the LLI upon formation of the solid-electrolyte interphase (SEI), as the CE of the graphite anode is above 95 % in the first cycle (see **Figure A.1**), but is due to the irreversible capacity (IRC) of the NCM (see discussion below). Furthermore, the charge and discharge capacities are depicted for the final cycle at C/15 (cycle 202): here, the difference between the first discharge capacity at BOT and the last discharge capacity at EOT originates from the aging over the course of 202 cycles in the full-cells. However, from the full-cell data, it's not trivial to determine the different contributions to the capacity fade, ranging from LLI over LAM to resistance build-up. Therefore, the full-cells were disassembled after 204 cycles at 45 °C to 4.4 V_{Gra} in fully discharged state (after a CV hold of 1 h at 3.0 V_{Gra}) before the NCM cathodes were reassembled using fresh electrolyte and a lithium-metal counter electrode.
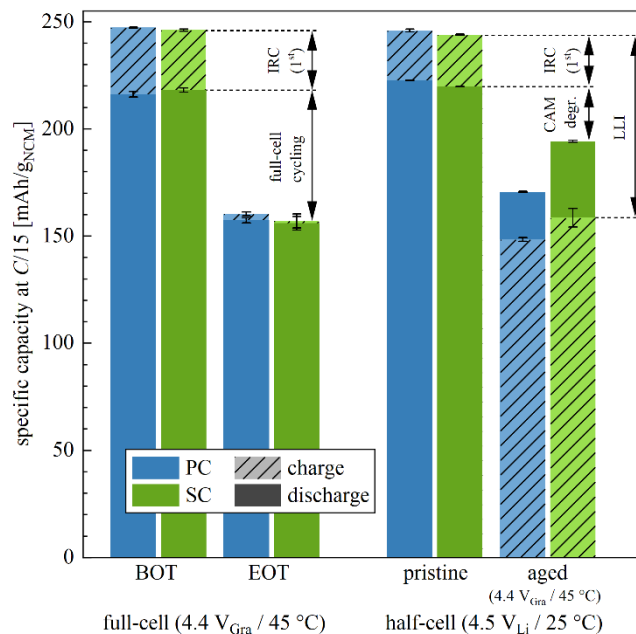
Figure 3: Overview of charge (patterned) and discharge (plain) capacities of the PC (blue) and SC (green) coin full-cells cycled to 4.4 V_{Gra} at 45 °C for BOT (cycle 1) and EOT (cycle 202) (left, extracted from the cycling data in **Figure 2**) as well as of coin half-cells with fresh and aged NCM electrodes at 25 °C (right, extracted from **Figure A.3**), all recorded at a C-rate of C/15. The first-cycle irreversible capacity (IRC (1st)) as well as the CAM degradation (including both the loss of active material as well as the resistance build-up) and the loss of lithium inventory (LLI) are marked by the black arrows. The error bars correspond to the minimum/maximum value of two cells.

The cells with aged NCM electrodes as well as the ones with pristine PC and SC NCM electrodes are analyzed in four charge/discharge cycles at a *C*-rate of *C*/15, *C*/3, 2*C*, and *C*/50, as displayed in **Figure A.3**. It has to be noted that the applied upper cutoff potential in the half-cell of 4.5 V_{Li} is chosen to represent the potential of 4.4 V_{Gra} in the full-cell, what might induce slight discrepancies in the observed capacity between full- and half-cells, as the graphite potential is below 0.08 V_{Li} at the end of charge (see **Figure A.1**); furthermore, the full-cells were cycled at 45 °C while the half-cell experiments were performed at 25 °C, what might lead to small differences in the obtained capacities. For the pristine NCMs, however, the initial charge capacities of 246 mAh/g_{NCM} for PC and 244 mAh/g_{NCM} for SC agree well with the observed values for the full-cells. The capacities of the pristine NCM of 223 mAh/g_{NCM} for PC and 220 mAh/g_{NCM} for SC obtained during the first discharge correspond to the respective available NCM capacities, also for the full-cells. The first-cycle CE of both pristine NCMs at *C*/15 in the half-cell is only 90 % (see **Figure 3**), caused by the poor solid-state diffusion and a subsequent kinetically impeded intercalation of lithium at high degree of lithiation (i.e., low SOC).[65,66] Since the CE of the half- and the full-cells are similar, and since the CE of the graphite is much higher, the first-cycle CE in the full-cells must be governed by the first-cycle IRC of the NCM.

As the aged full-cells are disassembled in fully discharged state at EOT, the available capacities in the half-cell upon charging at *C*/15 of 148 and 158 mAh/g_{NCM} for PC and SC, respectively, are either limited by the LAM of the NCM or by the LLI in the full-cells. Since the subsequent discharge capacity of PC and SC yields 171 and 194 mAh/g_{NCM}, respectively, more lithium is inserted into the NCM structure during discharge than extracted during charge (enabled by the large lithium reservoir of the lithium metal in the reassembled half-cell). Hence, the LAM of the cathode can be excluded as dominating source of capacity loss in the full-cell and, therefore, the difference of the first charge capacity of the full-cell (or the essentially identical first-charge capacity of the pristine NCM in the half-cells, respectively) and the one in the half-cell with the aged NCMs is assigned to the LLI (as labeled by the black arrow in **Figure 3**). Furthermore, the difference between the first-cycle discharge capacity in the half-cell of the pristine and the aged NCM is attributed to the CAM degradation, which includes both the LAM of the NCM as well as the resistance build-up. The capacity loss due to CAM degradation of PC NCM accounts to 52 mAh/g_{NCM}, which is twofold as compared to the one of SC NCM with 26 mAh/g_{NCM}. At *C*/50, however, the discharge capacity of both PC and SC even reaches 189 and 204 mAh/g_{NCM}, respectively, being significantly increased by an additional 18 and 10 mAh/g_{NCM}, respectively, as compared to the one at *C*/15 (see **Figure A.3**). This difference observed even at these slow rates is caused by the large resistance build-up of the NCMs, especially pronounced for PC (as already discussed for **Figure 2** and deconvoluted below in **Figure 7**), what caused the decreased rate capability as compared to SC.

17

In summary, the analysis of the aged NCM electrodes in half-cells reveals that the observed capacity loss of the full-cells cycled to 4.4 V_{Gra} at 45 °C is owed at fast rates to the degradation of the NCM by the growth in resistance, which is further discussed in **Figure 7**; at slow rates, however, the capacity decrease is dominated by the LLI. The apparent LLI is attributed to a continuous SEI decomposition and reformation on the anode side, what is accelerated at elevated temperatures. The authors are aware that the here used standard LP57 electrolyte does not contain SEI-stabilizing additives such as vinylene carbonate (VC) or fluoroethylene carbonate (FEC), which are expected to diminish LLI to provide an improved full-cell performance. To compare the effect of the NCM morphology on the electrochemical properties, however, the performed analyses of the CAMs are valid and meaningful.

Evolution of the NCM surface area – After significant differences in the rate capability and the cell resistance of PC and SC were observed in full-cells when cycled to 4.4 V_{Gra}, the performance of the NCM (at high *C*-rates) seems to be governed by its particle morphology. Depending on its morphology, it has been reported that the changes of the NCM surface area upon delithiation deviate strongly,[20,26,34] what is expected to affect the extent of typical side reactions at the interface, such as electrolyte oxidation,[64,67] gas evolution,[23,26] and TM dissolution.[37–39] To quantify the extent of the surface area change of the two active materials during processing, delithiation, and extended cycling, Kr-BET measurements of pristine, calendered, charged, and aged electrodes are performed.

The uncompressed pristine PC (grey and blue column in **Figure 4**, left y-axis) and SC (grey and green) electrodes exhibit a specific surface area of 1.01 and 2.08 $m^2/g_{electrode}$, respectively. To allow for a quantitative analysis of the surface area change of the NCM active material only (reprinted here from previous publications[20,26] for the sake of completeness), the contribution of C65 and PVDF, which is assumed to remain constant, is subtracted by considering the specific surface area of a C65 electrode (C65:PVDF 1:1 w/w) of 17.9 ± 0.4 $m^2/g_{electrode}$: as the NCM electrodes comprise 2 wt% of C65 and 2 wt% of PVDF, the conductive carbon and binder are assumed to contribute 0.72 ± 0.01 $m^2/g_{electrode}$ to the NCM electrode (corresponding to 4 % of the measured value of the C65 electrode, as marked by the gray area in **Figure 4**). The subtraction of this value provides a good estimate of the contribution of the NCM active material to the specific surface area of the electrode and, when normalized by the mass of the NCM in the electrode ($m_{NCM} = 0.96 \cdot m_{electrode}$), of the specific surface area of the NCM material. The latter is displayed on the right y-axis of **Figure 4** in units of m^2_{NCM}/g_{NCM}. For the further discussion, the contribution of the NCM only will be considered.
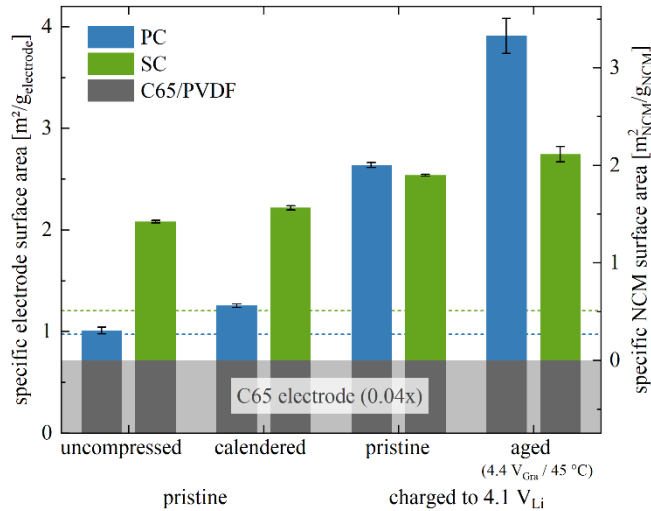
Figure 4: Specific surface area of PC (blue and gray) and SC (green and gray) electrodes obtained by Kr-BET measurements. Electrodes were measured either in the pristine (uncompressed or calendered) state or harvested from cells charged to 4.1 V_{Li}. Coin half-cells were assembled using lithium metal as counter electrode, 100 µl of LP57 electrolyte, two glass fiber separators, and one polyolefin separator facing the NCM electrode. The working electrodes in these cells were either pristine NCM electrodes or the ones harvested after being aged over 204 cycles in full-cells to 4.4 V_{Gra} at 45 °C (after having performed the subsequent post mortem rate test in half-cells additionally). All cells were charged to 4.1 V_{Li} at C/15 in CCCV mode (including a CV step at 4.1 V_{Li} for 1). The electrodes were harvested, washed in carbonate-based solvents, and subsequently dried. Specific electrode surface area (in units of m^2/$g_{electrode}$, left y-axis) and specific NCM surface area (in units of m^2_{NCM}/g_{NCM}, right y-axis), whereby the latter was obtained by the subtraction of the contribution of the C65 electrode (gray area, multiplied by 0.04). The horizontal dashed lines indicate the expected surface area obtained from Kr-BET measurements of the NCM powders (plotted on the right y-axis). The error bars correspond to the minimum/maximum value of two measurements.

The NCM surface area of the uncompressed pristine PC electrode of 0.31 m^2_{NCM}/g_{NCM} (blue column in **Figure 4**) is in good agreement with the surface area of 0.27 m^2_{NCM}/g_{NCM} of the PC powder. Therefore, it is expected that the integrity of its secondary agglomerates is not (significantly) altered by the mixing procedure (in the planetary centrifugal mixer), as already observed visually by SEM in **Figure 1b**. Upon compression by calendering, however, the NCM surface area is increased by 1.8x (here consistently referenced to the NCM surface area in the pristine electrode) to 0.56 m^2_{NCM}/g_{NCM}, what is attributed to the crack formation due to the applied mechanical force, as seen in **Figure 1c** as well as reported previously.[20,32,61] During the first charge/delithiation of the NCM to 4.1 V_{Li} (corresponding to 67 %SOC, see **Figure A.2**), an increase of the surface area to 2.00 m^2_{NCM}/g_{NCM} is observed. This increase arises from the anisotropic volume change of -1.9 % for NCM851005, determined by de Biasi et al. through X-ray diffraction (XRD),[27] which leads to crack formation between the primary crystallites of the secondary agglomerates of PC, in particular at elevated temperatures,[68] as it was already observed visually[32] and quantified[20] for NCM622. For the PC electrodes harvested from the full-cells (cycled for 204 cycles to 4.4 V_{Li} at 45 °C, depicted in **Figure 2**), the NCM surface area (determined at 4.1 V_{Li}) increases even further to 3.33 m^2_{NCM}/g_{NCM} due to the repeated volume change upon (de)lithiation; consequently, this surface area equates to a particles size of ~0.4 µm as compared to ~5 µm for the pristine powder (based on the spherical approximation, as discussed for **Figure 1**) due to compression, delithiation, and extended cycling. Based

on the visual investigation by SEM (see **Figure 1a**), showing a primary crystallite size of 0.2 to 1.0 µm, most of the surface area of the primary crystallites is exposed after cycling. Similar values of 1.8 to 3.6 m^2_{NCM}/g_{NCM} were determined previously by Strehle et al. for polycrystalline NCM811 (in the discharged state) after being cycled to 4.5 V_{Li} at 45 °C for 250 to 700 cycles.[35] As the surface area determination by krypton-gas physisorption was performed ex situ, a possible closing/clogging of pores due to the washing and drying of the harvested electrodes, as it was discussed in a previous article,[20] may even lead to an underestimation of the determined surface area of the charged PC NCM.

In contrast to PC, the NCM surface area of the uncompressed pristine SC electrode (green column in **Figure 4**) of 1.42 m^2_{NCM}/g_{NCM} is threefold higher as compared to the pristine SC powder, what originates from the deagglomeration of the primary crystallites during the ball-mill-based slurry preparation, as already observed visually in **Figure 1e**. This value corresponds to a particle size of ~0.9 µm, what is in good agreement with the particle size of 0.2 to 3.0 µm determined visually in **Figure 1e**, implying the exposure of most of the surface area of the SC primary crystallites during ink preparation. Upon calendering of the electrode, the surface area increases only marginally to 1.56 m^2_{NCM}/g_{NCM}, highlighting the mechanical stability of the primary crystallites, what has also been reported previously by impedance-based capacitance measurements,[20] suppressing the crack formation within primary particles (see **Figure 1f**). During the first charge to 4.1 V_{Li}, the NCM surface area of SC rises slightly to 1.90 m^2_{NCM}/g_{NCM}, what might stem from the volume-change-induced separation of few primary crystallites which had not been deagglomerated during ink mixing. After 204 cycles in full-cells, the NCM surface area of SC rises only marginally to 2.11 m^2_{NCM}/g_{NCM} (corresponding to a particle size of 0.6 µm), indicating the suppression of significant crack formation of the primary crystallites despite the repeated volume change of -7.1 % during delithiation to 4.4 V_{Gra}, or ~4.5 V_{Li}, respectively.[27] Overall, the surface area of SC does not exceed an increase of 1.5x as compared to the pristine electrode, even during extended charge/discharge cycling to a high cutoff potential at elevated temperature.

Resulting from its primary crystallite size, SC shows a relatively high initial specific surface area in the pristine electrode, which, however, remains relatively unaffected during processing and cycling. Even though PC exhibits a relatively low surface area before compression and cycling due to its agglomerated nature, it reveals a poor (chemo)mechanical integrity of the secondary agglomerates, resulting in a >50 % higher surface area of PC as compared to SC which gets exposed to the electrolyte in the full-cells. The impact of the increased surface area of PC on gas evolution and TM dissolution is illuminated in the following.

Structural stability and gas evolution at high state of charge – The release of lattice oxygen degrades the NCM materials at high SOC[23], while its onset SOC depends on the NCM composition.[12] Due to the

subsequent chemical oxidation of the electrolyte, however, the released oxygen is not only detected mainly in the form of carbon dioxide but the products of this process contain protic species which may be detrimental for the battery.[67,69,70] In an earlier work, the dependence of the particle morphology on the detected gas amounts and the resulting rock-salt layer thickness was shown for: i) NCMs with various nickel content and particle morphology which were charged once to 5.0 V_{Li};[26] and for ii) three different NCM622 materials with a fundamentally different particle morphology which were cycled in a similar procedure as applied in this work.[20] Hence, the absolute amount of evolved gas is determined mainly by the accessible surface area of the cathode active material.[20,26,47] Since the two materials investigated in this work have different particle morphology and specific surface area after the powders are processed during ink mixing into an electrode (0.31 m^2_{NCM}/g_{NCM} and 1.42 m^2_{NCM}/g_{NCM} for PC and SC, respectively, as discussed for **Figure 4**), the gas evolution during electrochemical cycling is quantified via on-line electrochemical mass spectrometry (OEMS). Therefor, uncompressed PC and SC electrodes are cycled for two consecutive cycles to an upper cutoff potential of 4.22 V_{Li} (corresponding to a degree of delithiation of ~70 %SOC when converted using the charge curve in **Figure A.2**), where no oxygen release is expected, followed by three cycles to 4.62 V_{Li} (~90 %SOC) above the onset of oxygen release. As the evolved gases consist for the most part of molecular oxygen (O_2) and carbon dioxide (CO_2), the mass traces of $m/z = 32$ and $m/z = 44$ are evaluated and converted to $\mu mol/g_{NCM}$.

The potential curves of PC (blue curve) and SC (green) as a function of time depicted in **Figure 5a** show negligible differences during the first two cycles to 4.14 V_{Li}, except for an additional initial overpotential of PC of ~50 mV which diminishes after ~1.5 hours (corresponding to ~30 %SOC) and is only present in the first cycle. This observation can be attributed: i) to the lower surface area of the pristine PC particles resulting in a higher surface-area-normalized current density as compared to the SC particles, or ii) to a higher amount of surface impurities on the PC material such as lithium or TM hydroxides or carbonates, which can induce an initial resistance in the first cycle.[17,18] During the subsequent three cycles to 90 %SOC, additional overpotentials arise which manifest in increasing OCV drops after the CV step at the end of charge of 56 mV for PC and 75 mV for SC in the fifth cycle and the suppressed H2-H3 phase transition at ~4.2 V_{Li}. Both effects are pronounced for the SC material what is attributed to the larger primary crystallite size for this particle morphology[20,26] since a rock-salt-type surface reconstruction leads to kinetic limitations mainly occurring at high SOC, as previously described by Xu et al.[71]
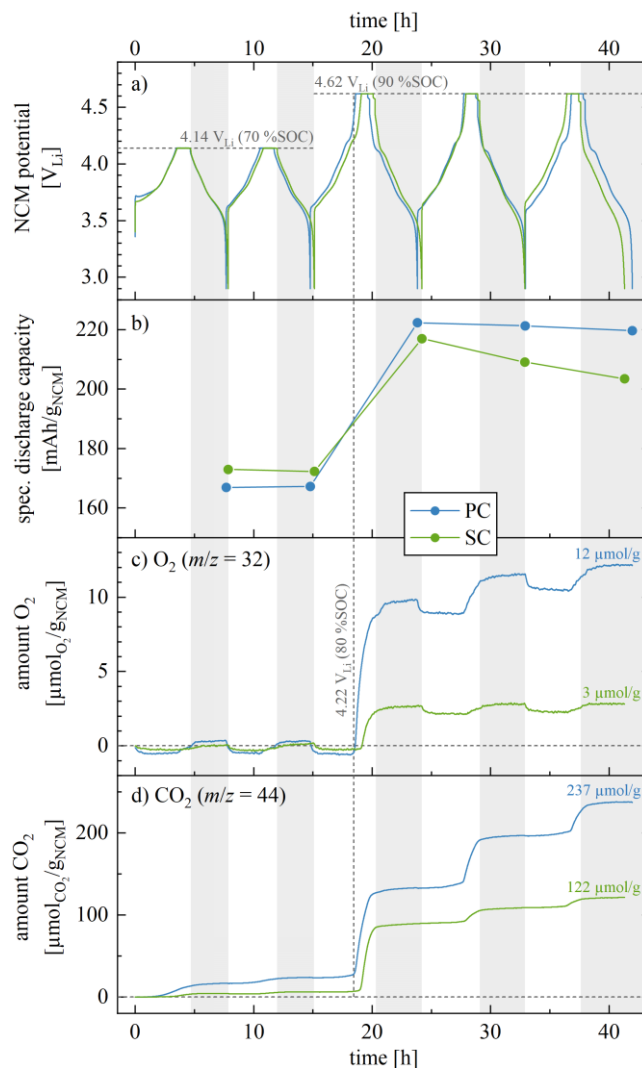
Figure 5: Cycling and gas evolution data as a function of time for OEMS cells assembled with PC (blue) and SC (green) as working electrodes (both uncompressed), using delithiated, capacitively oversized LFP as counter electrode, two Celgard H2013 separators, and 100 µl of LP57 electrolyte. The cells were cycled at 25 °C at $C/5$ (corresponding to 55 mA/g_{NCM} when referenced to the theoretical capacity of NCM851005 of 275 mAh/g_{NCM}), with a 1 h CV hold at the upper potential cutoff followed by a 10 min OCV phase, recording the gas evolution by mass spectrometry: i) two cycles to an NCM potential of 4.14 V_{Li} (corresponding to 0.74 V_{LFP} cell voltage or to a degree of delithiation of 70 %SOC (determined from the potential curve in **Figure A.2**)); ii) three cycles to 4.62 V_{Li} (corresponding to 1.22 V_{LFP} cell voltage or to 90 %SOC). **a)** NCM cathode potential vs. Li$^+$/Li. **b)** Specific discharge capacity for each of the five cycles. **c)** & **d)** Total amount of evolved oxygen (determined at $m/z = 32$) and carbon dioxide (at $m/z = 44$) in the OEMS cell, both normalized to the NCM mass (in units of $\mu mol_{gas}/g_{NCM}$). The vertical light gray areas accentuate each NCM discharge/lithiation period (marked for the SC material). The vertical gray dashed line marks the onset of the O$_2$ evolution of SC at a potential of 4.22 V_{Li}, corresponding to a degree of delithiation of ~80 %SOC. The numbers represent the gas amounts obtained at the end of the experiment.

The respective discharge capacities of PC, depicted in **Figure 5b**, yield values of 167 mAh/g_{NCM} for the first two cycles to 70 %SOC, which is 6 mAh/g_{NCM} lower than for SC. When charged to 90 %SOC (above the onset of oxygen release), the discharge capacity of PC is increased to 222 mAh/g_{NCM}, what sightly decreases to 220 mAh/g_{NCM} within three cycles. The mentioned overpotentials result in relatively lower capacity for SC of 217 mAh/g_{NCM} in the third cycle which then decreases to 204 mAh/g_{NCM} causing a capacity fading of 6 % within three cycles.

Since the surface reconstruction above ~80 %SOC from layered to rock-salt-type phase is induced by the release of lattice oxygen, which reacts partially with the electrolyte to CO_2, the gas signals of $m/z = 32$ and $m/z = 44$ are depicted in **Figure 5c** and **5d**, respectively. During the first two cycles to 4.22 V_{Li} (corresponding to 70 %SOC), no oxygen evolution is observed; however, a fluctuation of the oxygen signal results in a repeated change of ±0.5 $\mu mol_{O_2}/g_{NCM}$ for both materials. This fluctuation is attributed to a change in the background signal of volatile electrolyte components, namely EMC, dependent on the extent and the direction of the applied current, as discussed in detail in a previous work.[20] In contrast, CO_2 is detected in the first two cycles for both materials, as shown in **Figure 5d**. For PC, the total amount of CO_2 after two cycles is determined to be 24 $\mu mol_{CO_2}/g_{NCM}$ which is fourfold as compared to SC with 6 $\mu mol_{CO_2}/g_{NCM}$. This difference likely stems from the (electro)chemical decomposition of an increased amount of surface impurities on PC,[72] as no oxygen release of the NCM is expected up to 70 %SOC.[23,26] This observation matches with the previously discussed overpotential within the first two hours.

When charged above 80 %SOC (dotted vertical grey line for SC), a sharp increase in the O_2 and CO_2 signals is detected for both materials. During the third cycle, more gas is released for PC, namely 10 $\mu mol_{O_2}/g_{NCM}$ and 109 $\mu mol_{CO_2}/g_{NCM}$, as compared to SC, showing 3 $\mu mol_{O_2}/g_{NCM}$ and 84 $\mu mol_{CO_2}/g_{NCM}$. For PC, O_2 is detected even during the discharge of the third cycle (see blue data after 21 h in **Figure 5c**). In the subsequent cycles, there is a stepwise increase in the gas amounts when the NCMs are charged above 80 %SOC, which is more pronounced for PC, while the increase becomes smaller with each cycle. After five cycles, the sum of evolved oxygen and carbon dioxide is two times higher for PC with a total of 249 $\mu mol_{O_2+CO_2}/g_{NCM}$ implying more side reactions under harsh cycling conditions compared to 125 $\mu mol_{O_2+CO_2}/g_{NCM}$ for SC.

It has to be considered, however, that CO_2 may also originate from the (chemical) decomposition of carbonate species (e.g., lithium carbonate and transition metal carbonates) from the surface of the NCMs, which get oxidized either electrochemically at high potential[73] or chemically in the presence of protons.[72] Assuming that all carbonate species are present in the form of lithium carbonate (Li_2CO_3), the titration of the washing solution by HCl[74,75] reveals a carbonate content of 1.0 and 0.3 wt% of Li_2CO_3 for PC and SC NCM, respectively, which correspond to 136 and 40 $\mu mol_{Li_2CO_3}/g_{NCM}$. In general, the reduced carbonate content of SC as compared to PC may stem: i) from a less effective washing after synthesis since the carbonate species within the pores of the secondary agglomerate remain for short washing times, or ii) from the longer times and higher temperatures applied during the synthesis of SC[43], promoting the sublimation and thus removal of residual lithium species (i.e., lithium oxide) from the surface.[76] Upon oxidation, each Li_2CO_3 is converted to one CO_2; thus, to estimate the gas amount which stems exclusively from the release of lattice oxygen, the gas amounts need to be corrected by the carbonate content. Assuming that all

carbonate species are decomposed at high state of charge, 113 $\mu mol_{O_2+CO_2}/g_{NCM}$ are expected to be evolved from the lattice of PC after three cycles, while only 85 $\mu mol_{O_2+CO_2}/g_{NCM}$ remain for SC.

Overall, the OEMS experiments reveal a strong dependence of the gas evolution on the NCM particle morphology since, after two cycles to the lower SOC and three cycles to the higher SOC, a 1.3-fold gas evolution (i.e., the sum of O_2 and CO_2) is observed for PC as compared to SC. Assuming a similar thickness of the oxygen-depleted surface layer,[47] which was reported for the two here used materials,[26] a higher gas evolution of the SC material would have been expected considering the fivefold specific surface area of the uncompressed SC electrodes (see **Figure 7**). However, for PC NCM, the cracking of the secondary agglomerates increases the accessible surface area (see **Figure 4**), either when charged to high SOCs or over the course of extensive charge/discharge cycling.[26,32] Therefore, the pronounced gas release of PC during the fourth and fifth cycle can be attributed to the repeated exposure of fresh surface area to the electrolyte due to particle cracking. As the gas evolution from SC is reduced as compared to the one from PC, and as the amount of products formed upon the chemical electrolyte oxidation such as HF are expected to scale with the amount of released gas, the dissolution of TMs which are etched by HF from the NCM might depend on the particle morphology. Consequently, the amount of TMs redeposited on the graphite anode is quantified.

Extent of transition metal dissolution and redeposition – The dissolution of TM ions from NCMs and their subsequent diffusion through the electrolyte and redeposition at the negative electrode has been identified to accelerate LLI due to the pronounced formation of SEI.[39,53,77] In particular, deposited manganese ions seem to drive the consumption of lithium ions as well as the gas evolution.[38,39,53] Delacourt et al. proposed an insufficient passivating SEI layer due to a higher electronic conductivity of manganese-containing SEIs[77] whereas Solchenbach et al. observed a catalytic conversion of the SEI decreasing lithium inventory.[53] As the TM dissolution does not only increase with the upper cutoff potential of the NCM but also with the operating temperature,[37–39,41,78] in this study, the extent of TM dissolution and redeposition is quantified for the full-cells with PC or SC cycled for 204 cycles to 4.4 V_{Gra} at 45 °C, elucidating the effect of the NCM particle morphology.

Since the TM ions deposit at low potential,[39] and since only minor amounts of TM ions are expected to remain dissolved in the electrolyte,[41] the extent of TM dissolution is determined by the elemental analysis of the graphite anode. For the cells assembled with PC (blue, see **Figure 6**), 530, 23, and 50 $\mu g_{TM}/g_{NCM}$ of nickel, cobalt, and manganese were detected on the negative electrode, respectively, while, for SC (green), only 226, 9, and 21 $\mu g_{TM}/g_{NCM}$ were found (all normalized to the amount of NCM in the cell). By taking into account the molar mass of 58.69, 58.93, and 54.94 mol/g_{TM} of nickel, cobalt, and manganese,

respectively, as well as the one of 97.47 mol/g_{NCM} of the NCM, the obtained values translate to 880, 38, and 89 ppm for PC and to 375, 15, 38 ppm for SC, respectively (note that ppm is defined as the ratio between the detected TM amount on the graphite electrode and the total amount of NCM in the cell in units of $\mu mol_{TM}/mol_{NCM}$). It becomes obvious that, even though both NCM materials are composed of a molar ratio of 85:10:05 for Ni:Co:Mn, the detected amounts expose a ratio of 85:04:09 for both SC and PC. This reduced cobalt content as compared to the one of manganese possibly originates from an inhomogeneous distribution of the TMs within the active material particles from their synthesis; however, a preferential dissolution of nickel and manganese from the NCM as compared to cobalt could also induce this discrepancy, as previously reported,[38,41,79,80] resulting in a remaining cobalt-rich NCM surface; furthermore, a possibly selective (electro)chemical reactivity of the TM ions with the (SEI of the) negative electrode cannot be excluded. Even though minor amounts of TM ions might remain in a dissolved from in the electrolyte,[41] in sum, however, at least 1008 and 428 ppm of TMs must have been dissolved from the PC and SC NCM, respectively.
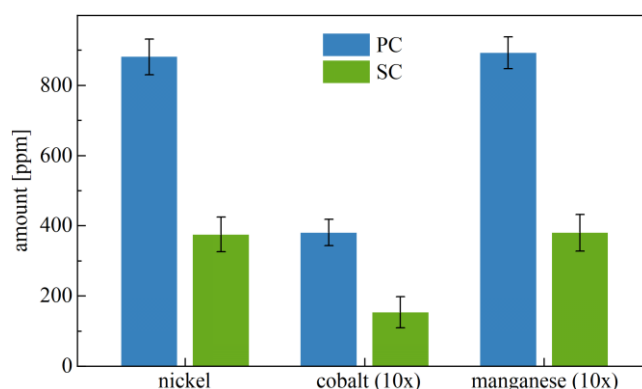
Figure 6: Amount of nickel, cobalt, and manganese in units of ppm (defined as $\mu mol_{TM}/mol_{NCM}$) detected in graphite anodes and normalized to the amount of NCM in the cell. Graphite electrodes were harvested from full-cells with PC or SC after 204 cycles to 4.4 V_{Gra} at 45 °C (as depicted in **Figure 2**) and scraped off from the current collector before the transition metal content was analyzed by ICP-AES. The amounts of cobalt and manganese are magnified by 10x. The error bars correspond to the minimum/maximum value of two measurements while the absolute errors for each element are considered by the laws of error propagation.

Most importantly, however, the detected amount of each TM is significantly reduced by 0.4x for SC as compared PC, as it was previously observed by Klein et al. semi-quantitatively through EDX.[40] This discrepancy is explained by the difference in surface area of the NCMs of 0.6x after cell cycling, as observed by Kr-BET in **Figure 4**. To estimate the number of monolayers of dissolved NCM, the fraction of dissolved active material of $y = 0.1$ mol% for PC (with a particle diameter of $d_p = 0.4$ µm after cycling as discussed for **Figure 4**) is converted to the thickness d_l of the dissolved surface layer. Using a spherical approximation and the ratio y of surface layer volume V_l to particle volume V_p, **Equation 1** (adapted from a previous study[26])

$$y = \frac{V_l}{V_p} = \frac{\left(\left(d_p\right)^3 - \left(d_p - d_l\right)^3\right)}{d_p^3} \tag{1}$$

yields a layer thickness of 1.3 Å for PC. Since the dissolution is assumed to occur on various crystal facets, for simplicity, a cubic NCM unit cell with an edge length of 3.2 Å is assumed on average (corresponding to the actual cell volume of 33.7 Å^3 per LiMO$_2$ unit[27]). For PC, this equates to the dissolution of 0.4x of one monolayer of the NCM materials, while for SC (with a calculated particle size of 0.6 µm after cycling and a detected TM amount of 0.04 mol%) a similar sub-monolayer value of 0.8 Å or 0.3x of a monolayer is obtained. Thompson et al. showed that, for NCM523/graphite full-cells which were cycled under even harsher conditions to 4.4 V$_{Gra}$ at 55 °C for 750 cycles, less than 0.1 % of the TMs were dissolved and redeposited on the negative electrode.[81] Therefore, it appears that, even though the cycling was performed in this study at a relatively high upper cutoff potential and at elevated temperatures amplifying the dissolution reaction, the TM dissolution is limited to less than one monolayer for both NCM materials and that, therefore, the extent of TM dissolution is determined by the exposed NCM surface area. Even though Thompson et al. attributed the low detected amounts to effective electrolyte additives,[81] this upper limit could also stem (since no electrolyte additives were used in this study) from a fluorinated passivation layer on the NCM surface, which is formed upon attack of HF, assumed to cause the TM dissolution, and which suppresses an ongoing dissolution reaction.

To evaluate the impact of the TM dissolution on the capacity loss in full-cells to previous studies, the detected TM amounts are converted to a TM concentration in the electrolyte. Based on the molar mass of NCM of 97.47 g/mol$_{NCM}$, the NCM mass loading of 8.2 mg$_{NCM}$/cm^2, the electrode diameter of 14 mm, and the total electrolyte amount of 100 µl, the detected TM amount of 1008 ppm for PC translates to a concentration of 1.3 mmol$_{TM}$/l. As previously reported by Jung et al., a TM concentration of 60 mmol$_{TM}$/l inserted into the cell through the electrolyte itself (being 50x higher as compared to the value in this study) lead to a capacity loss of less than 100 mAh/g$_{NCM}$ over the course of 202 cycles for all three TM ions, at least at 25 °C.[39] Even though the influence of the temperature on the SEI formation and lithium consumption by the TMs remains unclear, it appears as the TM dissolution cannot be responsible for the entire capacity decrease through LLI of almost 100 mAh/g$_{NCM}$, observed in **Figure 2** and **3**. Furthermore, even though the calculated TM concentration of 0.6 mmol$_{TM}$/l for SC (based on the value of 428 ppm) is less than half of the one of PC, and since the capacity loss in the full-cell at *C*/15 is very similar for both materials when cycled to 4.4 V$_{Gra}$ at 45 °C, the role of the TM dissolution on the capacity loss seems to be minor. The expectedly small effect of the TM ions on the capacity loss is further illustrated by the relatively small coverage of TM ions on the graphite active material: by taking into account the specific capacities of 245 mAh/g$_{NCM}$ of the two NCMs and 355 mAh/g$_{Gra}$ of graphite, the balancing factor of 1.1:1, the specific

surface area after cycling of 3.33 m²/g_{NCM} for PC and 2.11 m²/g_{NCM} for SC, as well as the one of graphite of 3.2 m^2_{Gra}/g_{Gra}, the amount of dissolved TMs is converted into a TM coverage of 0.5x and 0.2x of a monolayer on the graphite active material for the cells with PC and SC, respectively; this sub-monolayer amount seems to be easily covered by a typical SEI of ~10 nm or ~25x monolayers.

In contrast, the integrity of the SEI could be compromised by the volume change of the graphite by more than 10 % during (de)lithiation;[5,82] however, since the capacity loss of the full-cells cycled at 25 °C (see **Figure 2a**) and 45 °C (see **Figure 2e**) is significantly different by a factor of ~2x, even though the graphite experiences the same volume change in both cases, the regeneration of the mechanically ruptured SEI is excluded as dominant process for the lithium consumption. Therefore, we believe that the operation at elevated temperatures harms the intrinsic (chemical) stability of the SEI what induces the lithium loss, as it was observed for calendar aging during storage experiments.[83,84]

Overall, the TM deposition on the graphite (as well as the gas evolution of the NCM) is determined by the surface area of the NCM and, therefore, by its particle morphology, while the impact of the lithium consumption by TMs in the SEI seems to be minor, likely due to the relatively small quantities of less than one monolayer of NCM. To understand the effect of the deposited TMs on the impedance of the graphite electrode and, therefore, on the one of the full-cell, the evolution of the individual impedance contributions of both graphite and NCM is monitored in the following.

Evolution of the impedance of graphite and NCM – The observed differences in the DCIR of 2x to 4x between PC and SC occurring during cycling in the full-cells cycled to 4.4 V_{Gra} (see closed symbols in **Figure 2d** and **Figure 2h**) seem to be induced by the two distinct particle morphologies. To identify the cause for this difference, similar full-cells were assembled in T-cells cycled using the same procedure. The T-cells showed a similar cycling performance over 204 cycles (see **Figure A.4**) as the coin cells presented in **Figure 2**. The use of T-cells allowed the use of a lithiated gold wire as µ-RE, as previously introduced by Solchenbach et al.,[57] to deconvolute the impedance of the graphite and the NCM electrode upon cycling at 45 °C. The impedance is recorded at 3.8 V_{Gra} (or ~3.9 V_{Li}) what corresponds to ~50 %SOC (see **Figure A.2**), where the charge-transfer resistance is at its lowest value.[25]

The impedance spectra of the graphite anodes (red) cycled both against PC (blue) and SC (green) are depicted in **Figure 7a** and **Figure 7d**, respectively, both showing a similar behavior: the pristine spectrum (black dotted line) starts at the high-frequency resistance (HFR, determined at 31 kHz) of 3 $\Omega \cdot cm^2_{electrode}$ (note that the resistances are given as the absolute values of the impedance vector |Z| if not stated otherwise), which is mainly caused by the ohmic resistance of the electrolyte, a 45° line induced by the ionic pore resistance of the electrode, and a capacitive blocking branch (extending to 30 $k\Omega \cdot cm^2_{electrode}$ at 10 mHz,

data not shown), as reported previously for graphite with inhibited charge transfer (e.g., in delithiated state).[85,86] After the two formation cycles (solid dark red line), the spectrum consists of a semicircle-like feature caused both by the charge-transfer (and the SEI) resistance as well as the ionic pore resistance at low frequencies, which cannot be deconvoluted in a straight forward manner,[87] as well as a low-frequency branch which is attributed to the solid-state diffusion in the graphite active material.[88] Upon cycling (solid red line, from dark to light red with increasing cycle number), the impedance of the semicircle-like feature slightly increases, however, the low-frequency impedance R_{LF}^{anode} (LFR, determined at 18 mHz) never exceeds 7 $\Omega \cdot cm^2_{electrode}$. Upon extended cycling, loops appear in the spectra which may occur when the impedance of two electrodes with a significant impedance mismatch is determined by the GWRE[89]. Due to this effect on the impedance of the graphite anode, its impedance data cannot be analyzed reliably but the relative contribution to the total cell impedance can still be estimated. The large impedance of the NCM electrode, inducing this mismatch and the loops, is discussed in the following.
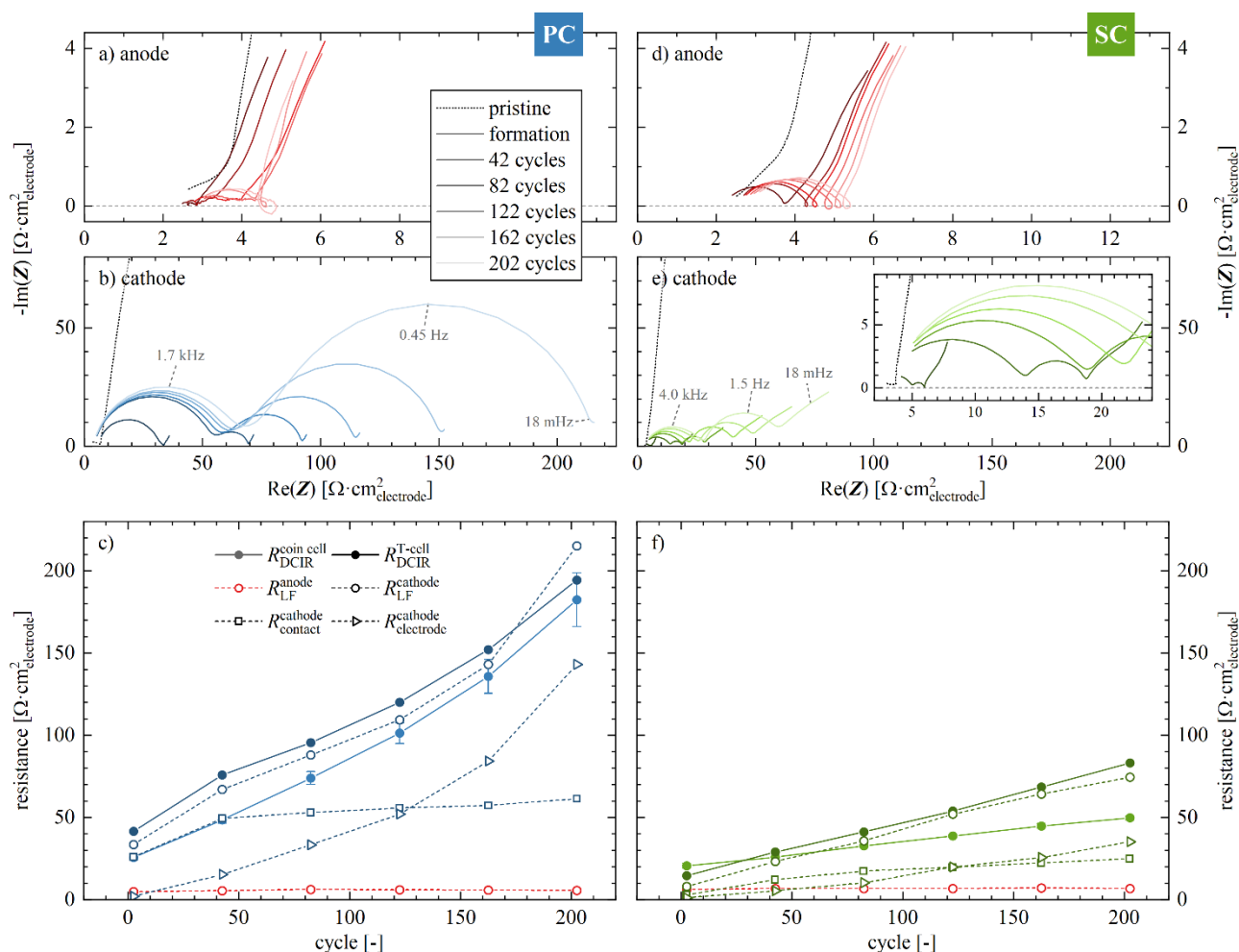
Figure 7: Impedance spectra and resistance contributions of **a) – c)** PC (blue) and **d) – f)** SC (green) in full-cells depicted as a function of cycle number. The T-cells were assembled using NCM cathodes with a mass loading of 8.2 mg$_{NCM}$/cm², graphite anodes (with an areal balancing factor of 1.1:1, based on 372 mAh/g$_{Gra}$ and 245 mAh/g$_{NCM}$), two glass fiber separators, a μ-RE (i.e., a GWRE), and 60 μl LP57 electrolyte. The T-cells were cycled over 204 cycles to 4.4 V$_{Gra}$ at 45 °C according to the same cycling procedure as the coin cells in **Figure 2**, however, including an additional PEIS after each DCIR in OCV with an

amplitude of 15 mV from 100 kHz to 100 mHz. The impedance spectra are recorded using a µ-RE (i.e., a GWRE) and normalized by the geometric area of the electrodes of 0.94 $cm^2_{electrode}$, both for **a)** & **d)** the graphite anodes (red) as well as **b)** & **e)** the NCM cathodes. The dotted black line represents the impedance spectrum of the pristine cell, while the solid lines show the impedance spectra at 3.8 V_{Gra} (or ~50 % SOC, respectively), while their color becomes lighter with increasing cycle number (i.e., after formation and subsequently for cycle 42, 82, 122, 162, and 202). **c)** & **f)** The resistances of both the coin cells $R_{DCIR}^{coin\,cell}$ (extracted from **Figure 2h**) as well as the T-cells R_{DCIR}^{T-cell} are extracted from a DCIR pulse of $C/3$ for 10 s at 3.8 V_{Gra} (note that the cycling performance of the two cell types is compared in **Figure A.4**). The low-frequency resistances of both the anode R_{LF}^{anode} as well as of the cathode $R_{LF}^{cathode}$ are extracted from the absolute impedance $|\mathbf{Z}|$ at the frequency point of 18 mHz. The contact resistance $R_{contact}^{cathode}$ as well as the electrode resistance $R_{electrode}^{cathode}$ of the NCM electrodes are extracted from an individual fit of each of the two semicircles by an equivalent circuit consisting of a resistor connected in series with a parallel circuit of a capacitor and a resistor (see main text). The error bars of the resistance of the coin cells correspond to the minimum/maximum value of two cells, while only one cell was assembled per NCM material for the T-cells with µ-RE.

The impedance of the PC electrode (blue), depicted in **Figure 7b**, shows a capacitive branch in the fully lithiated, pristine state (extending to 5 kΩ·$cm^2_{electrode}$ at 10 mHz, data not shown).[32,90] After the two formation cycles (solid dark blue line), one semicircle occurs which originates from the contact resistance $R_{contact}^{cathode}$ of the electrode, which could be assigned by the apex frequency of 3 kHz[91], as well as a short low-frequency branch, which is attributed to the solid-state diffusion of the NCM active material.[88] At this point, the LFR of the NCM of 35 Ω·$cm^2_{electrode}$ already exceeds the one of the graphite anode by a factor of 5x (note the different scales of the impedance representation of anode and cathode). After 42 cycles (solid blue line, from dark to light blue with increasing cycle number), the contact resistance further increases while also a second semicircle appears in the spectrum, which is attributed to the electrode resistance, which combines the contributions of charge-transfer resistance of the NCM, the ionic pore resistance of the liquid phase, and the electronic resistance through the solid part of the electrode.[90] During the subsequent cycling, the extent of both semicircles increases strictly monotonically, until, after 202 cycles, an $R_{LF}^{cathode}$ of 215 Ω·$cm^2_{electrode}$ is reached. For the SC electrode (green), shown in **Figure 7e**, the data exhibits similar features as for PC as well as the evolution thereof, however, at smaller values: even after 202 cycles, $R_{LF}^{cathode}$ does not exceed 75 Ω·$cm^2_{electrode}$ for SC.

For a convenient quantitative analysis of the resistances, their individual contributions are depicted for PC and SC as a function of cycle number in **Figure 7c** and **Figure 7f**, respectively. First, the DCIR (closed circles and solid line) obtained from the coin full-cells $R_{DCIR}^{coin\,cell}$ (blue), extracted from **Figure 2h**, is displayed and compared to the one obtained from the T-cells R_{DCIR}^{T-cell} (dark blue): Even though the T-cells show slightly higher DCIR values of 42 Ω·$cm^2_{electrode}$ after the two formation cycles as compared to 26 Ω·$cm^2_{electrode}$ for the coin cells, what possibly originates from the different cell setups, both increase concurrently to 194 Ω·$cm^2_{electrode}$ and 182 Ω·$cm^2_{electrode}$ over the course of 202 cycles, respectively, what highlights the comparability of the results from coin and T-cells. The LFR (open circles and dashed line) of the graphite anode R_{LF}^{anode} (red), extracted from the T-cell data in **Figure 7a**, remains almost unaffected by the cycling at values below 7 Ω·$cm^2_{electrode}$, while the one of the NCM cathode $R_{LF}^{cathode}$ (dark blue),

extracted from the T-cell data in **Figure 7b**, coincides relatively well with the total resistance of the cell $R_{\text{DCIR}}^{\text{T-cell}}$. From this observation, it becomes clear that (the evolution of) the cell resistance is determined primarily by the NCM, while the contribution of the graphite anode is less than 3 %.

By the individual fit of each of the semicircles in **Figure 7b** applying an equivalent circuit consisting of a resistor connected in series with a parallel circuit of a capacitor and a resistor (while latter is then depicted and discussed), the contributions of the contact resistance $R_{\text{contact}}^{\text{cathode}}$ (open squares and dashed line) as well as of the electrode resistance $R_{\text{electrode}}^{\text{cathode}}$ (open triangles and dashed line) are quantified (see **Figure 7c**). $R_{\text{contact}}^{\text{cathode}}$ after formation of 26 $\Omega \cdot \text{cm}^2_{\text{electrode}}$ is doubled to 49 $\Omega \cdot \text{cm}^2_{\text{electrode}}$ during the next 40 cycles, which remains relatively constant subsequently until EOT. In contrast, the relatively small $R_{\text{electrode}}^{\text{cathode}}$ of 2 $\Omega \cdot \text{cm}^2_{\text{electrode}}$ after formation increases continuously; it exceeds $R_{\text{contact}}^{\text{cathode}}$ after 160 cycles before it reaches 143 $\Omega \cdot \text{cm}^2_{\text{electrode}}$ after 202 cycles, being more than twice as large as compared to $R_{\text{contact}}^{\text{cathode}}$. The same analysis performed for SC in **Figure 7f** reveals similar behavior of the individual resistances as for PC: $R_{\text{LF}}^{\text{anode}}$ remains below 7 $\Omega \cdot \text{cm}^2_{\text{electrode}}$ over 202 cycles, while $R_{\text{LF}}^{\text{anode}}$ increases from 8 to 75 $\Omega \cdot \text{cm}^2_{\text{electrode}}$. $R_{\text{contact}}^{\text{cathode}}$ is limited to 25 $\Omega \cdot \text{cm}^2_{\text{electrode}}$, while $R_{\text{electrode}}^{\text{cathode}}$ increases steadily to 35 $\Omega \cdot \text{cm}^2_{\text{electrode}}$ after 202 cycles.

The initial $R_{\text{contact}}^{\text{cathode}}$ of PC, which appears only after the formation and is 10x larger than the one of SC, might stem from the morphology-dependent contact of the cathode active material with the current collector. This difference can be explained if one assumes that each NCM particle creates one contact point with the current collector, and that SC with a particle diameter of 0.9 µm as compared to PC with 5 µm (as discussed for **Figure 4**) could bring 30x more (secondary) particles to the same surface area of the current collector, what would decrease the contact resistance in an inversely proportional manner. Since the PC particles are deformed when pressed on the current collector due to the mechanical force upon calendering, of course, more contact points are established which is why the value of 30x overestimates the actual one of 10x. Additionally, the release of lattice oxygen increased by 2x for PC as compared to SC due to the higher NCM surface area (see **Figure 5**) oxidizes a larger amount of electrolyte components and consequently forms more HF, what could then transform the Al_2O_3 layer of the aluminum current collector to a thicker AlF_3 layer, possibly compromising the electronic conductivity and, therefore, leading to the pronounced increase of $R_{\text{contact}}^{\text{cathode}}$.[91,92]

The electrode resistance $R_{\text{electrode}}^{\text{cathode}}$ (comprising electronic and ionic resistances as well as the NCM charge-transfer resistance) is barely detectable after the two formation cycles for both PC and SC electrodes, even though the resistive oxygen-deficient surface layer has already formed as the majority of the released lattice

oxygen evolves in the first charge to high SOC (see **Figure 5**); therefore, it seems unlikely that the continuous increase in $R_{\text{electrode}}^{\text{cathode}}$ over 202 cycles results from the increased resistance of the decomposed phase. Additionally, $R_{\text{electrode}}^{\text{cathode}}$ of PC is more than twice as large as the one of SC, even though the NCM surface area is 50 % larger for PC than for SC after 202 cycles (see **Figure 4**), what should result in a decreased charge-transfer resistance, as it is proportionally to the surface area of the active material. Since, to the best of our knowledge, it has not been reported that the ionic pore resistance of the NCM electrode is compromised upon extended cycling, we assign the pronounced increase in $R_{\text{electrode}}^{\text{cathode}}$ of PC mainly to a growing electronic resistivity within the NCM electrode. We believe that the cracking of the NCM agglomerates upon extended cycling[32] diminishes the electronic connection of the resulting fragments, as previously shown by scanning spreading resistance microscopy,[33] since no conductive carbon is present within the secondary particle.[20] Furthermore, due to the formation of the oxygen-deficient surface layer, the poor electrical conductivity of this structure, e.g., of NiO with 10^{-7} to 10^{-5} S/cm (being an insulator),[93,94] as compared to lithium layered oxides of roughly 10^{-1} to 10^{0} S/cm, e.g., for $LiNiO_2$ (LNO, being a semiconductor)[95–97], is expected to impair the electronic conductivity even further due to the absence of the conductive carbon. Since most of the SC crystallites are separated during electrode preparation (see **Figure 1**), and since they do not crack significantly upon cycling (see **Figure 4**), the particles remain connected electrically; the observed increase in $R_{\text{electrode}}^{\text{cathode}}$ of SC is attributed to the continuous growth of the insulating surface film, which hinders both the electronic conductivity as well as the lithium (de)intercalation and solid-state diffusion. In this case, each NCM secondary agglomerate could be represented in an equivalent circuit by a transmission line model (TLM) with a poorly conductive electronic path (due to the absence of conductive carbon within the secondary particles) and a well conductive ionic path (due to the penetration of the electrolyte and its short diffusion lengths);[98] in contrast, the entire (well designed) electrode typically constitutes of a TLM with a well conductive electronic path (due to the sufficient amount of carbon) and a poorly conductive ionic path (due to the long and tortuous diffusion lengths); [85,90] the complete equivalent circuit would then comprise a TLM where each NCM particle is represented by a TLM itself. Interestingly, after more than 202 cycles under the harshest conditions, $R_{\text{electrode}}^{\text{cathode}}$ of PC of 143 $\Omega \cdot cm^2_{\text{electrode}}$ is 4.1x as compared to the one of 35 $\Omega \cdot cm^2_{\text{electrode}}$ of SC, while the NCM surface area of PC of 0.31 $m^2_{\text{NCM}}/g_{\text{NCM}}$ of the uncompressed electrode is 4.6x as compared to the one of 1.42 $m^2_{\text{NCM}}/g_{\text{NCM}}$ of SC. Due to this similarity, it seems likely that the charge-transfer reaction of the aged NCM particles may mainly take place on surface which was already exposed in the pristine state and is, therefore, connected electronically by the conductive carbon, while the crystallites within the agglomerates are isolated by particle cracking and the formation of the oxygen-depleted, resistive surface layer, what is represented graphically in **Scheme 1** for the two NCM morphologies.
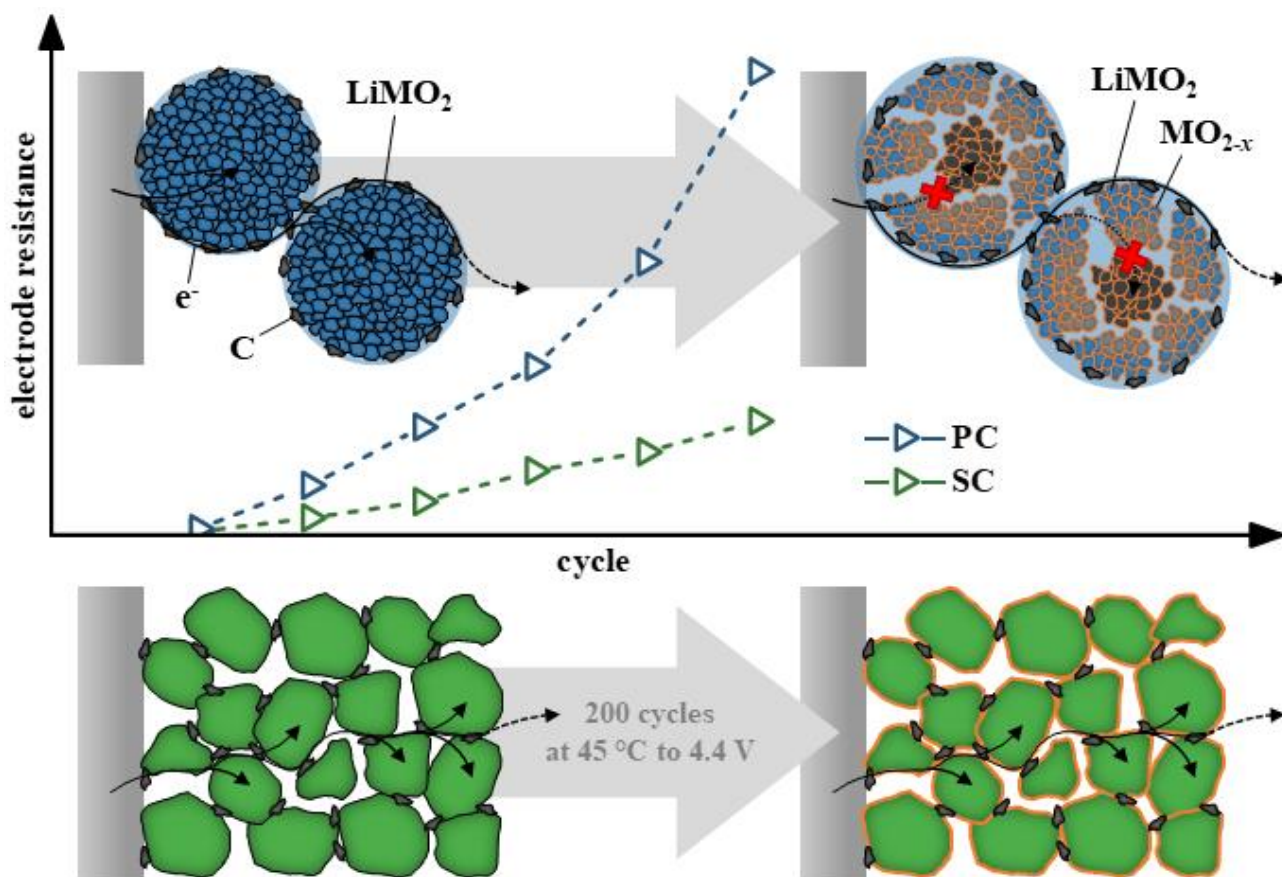
Scheme 1: Graphical presentation of the combined effect of oxygen release, the formation of an insulating oxygen-deficient surface layer, and particle cracking on the electronic conductivity of the NCM electrode depending on the particle morphology. The electrode before (left) and after (right) aging consists of a current collector (light gray), the NCM active materials PC (blue) or SC (green), and carbon additives (dark gray). The electronic pathways are illustrated by the black lines. The schematic of the electrode resistance $R_{electrode}^{cathode}$ as a function of cycle number is extracted from **Figure 7**.

Conclusions

By comparing polycrystalline (PC) and single-crystalline (SC) NCM851005 by cycling experiments in graphite full-cells, this study elucidated the impact of the cathode particle morphology on the capacity retention. While the capacity loss due to the elevated temperature of 45 °C was similar both for PC and SC simply due to loss of lithium inventory (LLI) on the anode side, the higher voltage of 4.4 V_{Gra} exposed a fivefold full-cell resistance for PC after more than 200 charge/discharge cycles as compared to SC. Consequently, the initial discharge capacity of 200 mAh/g_{NCM} of both materials at $2C$ drops to 41 % for PC, but remained at 71% for SC. Even though the surface area of PC NCM in the uncompressed electrode is only a fourth as compared to the one of SC, as determined by Kr-BET, it skyrocketed to the elevenfold

value due to particle cracking upon calendering, charging, and extended cycling; the one of SC grew only by 1.6x. Due to this morphological instability of the PC secondary agglomerates and the consequently exposed surface area, the evolved amounts of O_2 and CO_2 detected by on-line electrochemical mass spectrometry at high SOC reached a twofold value of 250 µmol/g$_{NCM}$ for PC as compared to 125 µmol/g$_{NCM}$ for SC. Consistently, the amounts of TMs deposited on the graphite anodes in the full-cell experiments, often hypothesized to be the cause for accelerated LLI, were also twice as high for PC, in accordance both with the gas amounts at high SOC as well as with the NCM surface area after 204 cycles; in this study, however, the LLI did not scale with the TM amounts detected on the anode. Interestingly, based on the detected amounts, not more than 0.1 % of the NCM dissolved, what corresponds to less than one monolayer, even after extended cycling under harsh conditions.

To identify the origin of the resistance build-up at 4.4 V$_{Gra}$, impedance spectroscopy in full-cells with an additional µ-RE revealed a constant and negligible contribution from the graphite anode whereas the impedance of the NCM cathode dominated the full-cell impedance already after formation. After 202 cycles, the cathode impedance of PC in the full-cells was threefold as compared to the one of SC. For both NCMs, the impedance was dominated by the electrode resistance, which is commonly simplified as charge-transfer resistance, but does also include the ionic pore resistance as well as electronic resistances in the solid phase. As a pure charge-transfer resistance would be less pronounced for PC due to the lower areal currents of the smaller primary crystallites, the higher electrode resistance of PC is assigned to the electronic resistance within a secondary agglomerate, where the conductivity is not improved by conductive additives. The electronic conductivity within a secondary agglomerate is not only impaired by cracking, but also due to the poor electronic conductivity of the oxygen-depleted phase which is formed at high SOC.

Due to morphology of PC, only the accessible surface of the secondary particles is connected electronically by the conductive additives during electrode manufacturing, while primary crystallites within the core of the agglomerates may get disconnected for high upper cutoff potentials; in contrast, all primary crystallites are connected electronically within an SC electrode, what is maintained upon cycling due to their monolithic morphology suppressing particle cracking. The mechanism inducing the significantly increased resistance of PC is represented graphically in **Scheme 1** for the two NCM morphologies.

CRediT authorship contribution statement

Stefan Oswald: Methodology, Supervision, Investigation, Writing - Original Draft. Moritz Bock: Methodology, Investigation, Writing - Original Draft. Hubert A. Gasteiger: Conceptualization, Supervision, Writing - Review & Editing.

Acknowledgment

Appendix

Graphite potential curves of the first two cycles – The potential curves of graphite of the first three cycles in **Figure A.1** do not only exhibit a reversible capacity of graphite of 346 mAh/g_{Gra} and the distinct plateaus apparent during (de)lithiation, but also the difference of charge and discharge capacity of the first cycle (black) of 16 mAh/g_{Gra}, or 4 %SOC (when normalized by the theoretical capacity of 372 mAh/g_{Gra}), respectively, due to the formation of the SEI. For the assumed reversible capacity of 355 mAh/g_{Gra}, the chosen balancing factor of 1.1:1 in the full-cells, as well the ratio of the geometric areas of the electrodes of 1.76:1.54 (see **Figure 2**), the graphite is lithiated up to 76 %SOC in the full-cells, what corresponds to ~0.075 V_{Li}. Hence, for the analysis of the aged NCM electrodes in half-cells (see **Figures 3** and **A.3**), the upper cutoff potential in the half-cell is corrected by 0.1 V as compared to the full-cell.
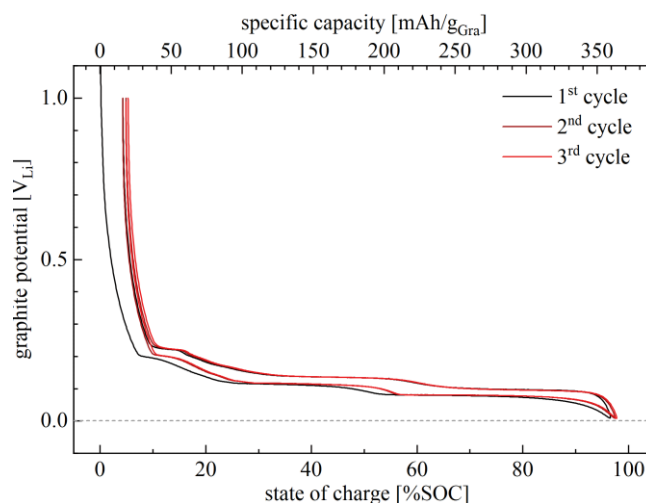
Figure A.1: Potential curves of the first three cycles of graphite as a function of the specific capacity (top x-axis, in units of mAh/g_{Gra}) or state of charge (bottom x-axis, in %SOC), respectively. Graphite as working electrodes in T-cells with 90 µl of LP57 electrolyte and lithium metal as counter electrode and reference electrode (with three glass fiber separators, two placed between working and counter electrode as well as one facing the reference electrode). Controlled by the reference electrode potential, the graphite electrode was cycled at 25 °C at a *C*-rate of *C*/15 (corresponding to a specific current of 24.8 mA/g_{Gra} when referenced to the theoretical capacity of graphite of 372 mAh/g_{Gra}), charging (or lithiating) the graphite to 0.01 V_{Li} in

CCCV mode (including a CV step at 0.01 V_{Li} for 1 h or until the current dropped below $C/20$), and discharging (or delithiating) it in CC mode.

NCM potential curves of the first charge – To allow for the conversion of the applied NCM potential to the respective degree of delithiation (x in $Li_{1-x}MO_2$, with M = Ni, Co, Mn) or state of charge (SOC), the required relation between potential and the SOC was extracted from the potential curves of the first charge for each of the two NCMs, which are shown in **Figure A.2**. The morphology-dependent differences observed <20 % SOC are attributed to the diminished kinetics of PC resulting from its larger charge-transfer resistance what is owed to its lower pristine surface area[20] before the secondary particles have cracked (see **Figures 1** and **6**). The differences above 90 % SOC are assigned to the increased surface area of PC at high SOC due to particle cracking[20,26] what scales the electrochemical oxidation of electrolyte, being observed in the potential curve in the form of additional capacity.
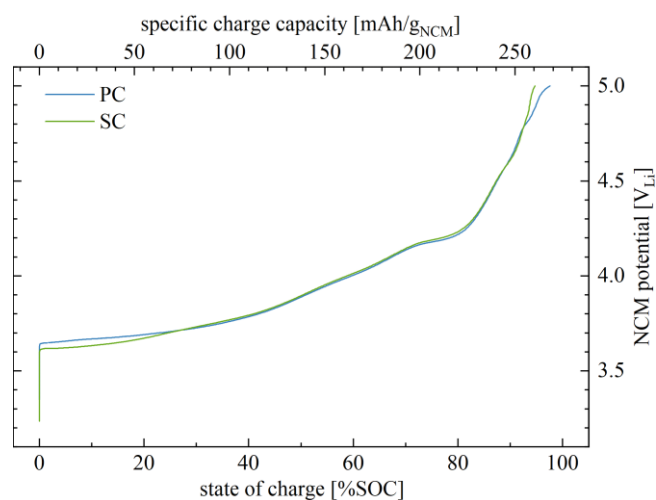
Figure A.2: Potential curves of the first charge of the two NCMs as a function of the specific capacity (top x-axis, in units of mAh/g_{NCM}) or state of charge (bottom x-axis, in % SOC), respectively. PC (blue) or SC (green) as working electrodes in T-cells with 90 µl of LP57 electrolyte and lithium metal as counter electrode and reference electrode (with three glass fiber separators, two placed between working and counter electrode as well as one facing the reference electrode). Controlled by the reference electrode potential, the NCM electrodes were charged at 25 °C to 5.0 V_{Li} at $C/15$ (corresponding to a current of 18.3 mA/g_{NCM} when referenced to the theoretical capacity of 275 mAh/g_{NCM}).

Discharge rate test in half-cells – To elucidate the capacity loss in the full-cells as well as the differences in the rate capability of the two NCM morphologies after aging (see **Figure 2**), pristine and aged NCM electrode were analyzed by a discharge rate test in half-cells. As depicted in **Figure A.3**, the rate capability of PC (blue) and SC (green) is similar for the pristine NCMs (closed symbols and solid lines), while the aged NCMs (open symbols and dashed lines) provide significantly less capacity, what is most pronounced for PC and analyzed in detail in **Figure 7**. The discharge capacity of the aged SC in the half-cells agrees well with the one in the full-cells at EOT, both being 122 mAh/g_{NCM}. For PC, however, the rate capability in the half-cells with aged NCM (see **Figure A.3**) seems to be even worse, as it does not deliver any capacity at 2C. This effect is explained by the additional overpotential caused by the polyolefin separator used in

35

the half-cells[85] as well as by the overpotential caused by the lithium-metal counter electrode.[99] The capacities of the first cycle of both the pristine and aged NCMs are discussed in detail for **Figure 3**.
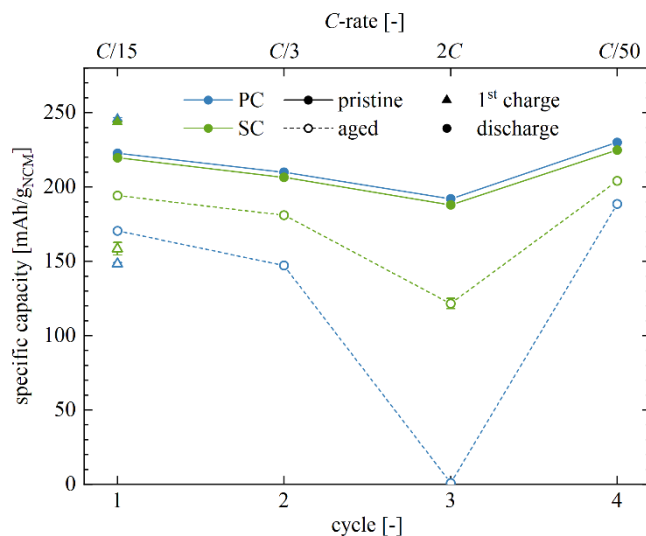
Figure A.3: Cycling data of PC (blue) and SC (green) cycled in coin half-cells at 25 °C over four cycles to 4.5 V_{Li}, presenting the specific charge capacity of the first cycle (triangles) and the discharge capacities (circles) of all four cycles for the applied C-rates of $C/15$, $C/3$, $2C$, and $C/50$ (based on the theoretical capacity of 275 mAh/g_{NCM}) as a function of cycle number. The coin cells were assembled using pristine (closed symbols and solid lines) or aged (open symbols and dashed lines) NCM cathodes with a mass loading of 8.2 mg$_{NCM}$/cm², lithium-metal counter electrodes, two glass fiber separators, and 100 µl LP57 electrolyte. The aged NCM electrodes were harvested from the coin full-cells after 204 cycles to 4.4 V_{Gra} at 45 °C (see **Figure 2**). The error bars correspond to the minimum/maximum value of two cells.

Cell performance in coin cells and T-cells – To elucidate the individual contributions to the resistance in the coin full-cells (see **Figure 2**), T-cells with µ-RE were assembled and cycled under the same conditions, while additionally the impedance of both electrodes was analyzed (see **Figure 7**). In **Figure A.4a**, the essentially coinciding discharge capacities as a function of the cycle number are directly compared for the cycles with a C-rate of $C/3$, while **Figure A.4b** exhibits the similar behavior of the cell resistance, each for PC (blue) and SC (green). Hence, the results and conclusions obtained from the impedance data of the T-cells can be utilized to explain the results obtained from the coin cells.
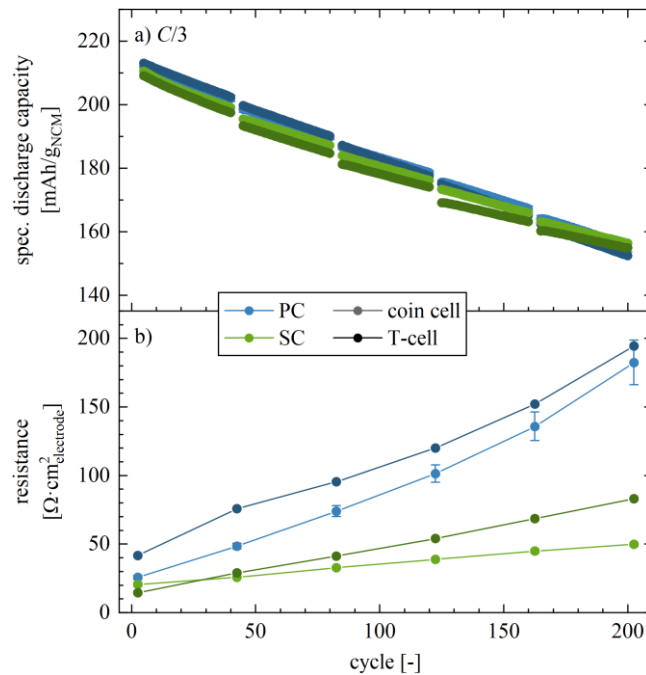
Figure A.4: Electrochemical cycling data of PC (blue) and SC (green) in coin-cells (medium colors, extracted from **Figure 2**) or T-cells with µ-RE (dark colors, extracted from **Figure 7**) cycled over 204 cycles at 45 °C to 4.4 V_{Gra}. **a)** Discharge capacity of the cycles with an applied *C*-rate of *C*/3. **b)** Cell resistance extracted from a DCIR pulse of *C*/3 for 10 s at 3.8 V_{Gra}. The error bars of the coin cells correspond to the minimum/maximum value of two cells, while only one cell was assembled per NCM material for the T-cells with µ-RE.

ORCID

Stefan Oswald https://orcid.org/0000-0001-6402-7833

Moritz Bock https://orcid.org/0000-0002-9516-853X

Hubert A. Gasteiger https://orcid.org/0000-0001-8199-8703

References

1. M. S. Ziegler and J. E. Trancik, *Energy Environ. Sci.*, **14**, 1635–1651 (2021).

2. W. Li, E. M. Erickson, and A. Manthiram, *Nat. Energy*, **5**, 26–34 (2020).

3. Kraftfahrtbundesamt, (2022).

4. R. Schmuch, R. Wagner, G. Hörpel, T. Placke, and M. Winter, *Nat. Energy*, **3**, 267–278 (2018).

5. N. Nitta, F. Wu, J. T. Lee, and G. Yushin, *Mater. Today*, **18**, 252–264 (2015).

6. S. Lee and A. Manthiram, *ACS Energy Lett.*, **7**, 3058–3063 (2022).

7. Z. Lu, D. D. MacNeil, and J. R. Dahn, *Electrochem. Solid-State Lett.*, **4**, A200–A203 (2001).

8. D. D. MacNeil, Z. Lu, and J. R. Dahn, *J. Electrochem. Soc.*, **149**, A1332–A1336 (2002).

9. S. T. Myung, F. Maglia, K. J. Park, C. S. Yoon, P. Lamp, S. J. Kim, and Y.-K. Sun, *ACS Energy Lett.*, **2**, 196–223 (2017).

10. F. Schipper, E. M. Erickson, C. Erk, J.-Y. Shin, F. F. Chesneau, and D. Aurbach, *J. Electrochem. Soc.*, **164**, A6220–A6228 (2017).

11. H.-J. Noh, S. Youn, C. S. Yoon, and Y.-K. Sun, *J. Power Sources*, **233**, 121–130 (2013).

12. S. Oswald and H. A. Gasteiger, *J. Electrochem. Soc.*, **170**, 030506 (2023).

13. E. Zhecheva and R. Stoyanova, *Solid State Ionics*, **66**, 143–149 (1993).

14. S. Albrecht, J. Kümpers, M. Kruft, S. Malcus, C. Vogler, M. Wahl, and M. Wohlfahrt-Mehrens, *J. Power Sources*, **119**–**121**, 178–183 (2003).

15. N. V. Faenza, L. Bruce, Z. W. Lebens-Higgins, I. Plitz, N. Pereira, L. F. J. Piper, and G. G. Amatucci, *J. Electrochem. Soc.*, **164**, A3727–A3741 (2017).

16. I. Shkrob, J. Gilbert, P. J. Phillips, R. Klie, R. T. Haasch, J. Bareño, and D. P. Abraham, *J. Electrochem. Soc.*, **164**, A1489–A1498 (2017).

17. R. Jung, R. Morasch, P. Karayaylali, K. Phillips, F. Maglia, C. Stinner, Y. Shao-Horn, and H. A. Gasteiger, *J. Electrochem. Soc.*, **165**, A132–A141 (2018).

18. J. Sicklinger, M. Metzger, H. Beyer, D. Pritzl, and H. A. Gasteiger, *J. Electrochem. Soc.*, **166**, A2322–A2335 (2019).

19. S. M. Bak, E. Hu, Y. Zhou, X. Yu, S. D. Senanayake, S. J. Cho, K. B. Kim, K. Y. Chung, X. Q. Yang, and K. W. Nam, *ACS Appl. Mater. Interfaces*, **6**, 22594–22601 (2014).

20. S. Oswald, M. Bock, and H. A. Gasteiger, *J. Electrochem. Soc.*, **169**, 050501 (2022).

21. S. Qian, A. T. S. Freiberg, F. Friedrich, and H. A. Gasteiger, Prep. (2023).

22. J. Choi and A. Manthiram, *J. Electrochem. Soc.*, **152**, A1714–A1718 (2005).

23. R. Jung, M. Metzger, F. Maglia, C. Stinner, and H. A. Gasteiger, *J. Electrochem. Soc.*, **164**, A1361–A1377 (2017).

24. D. Streich, C. Erk, A. Guéguen, P. Müller, F.-F. Chesneau, and E. J. Berg, *J. Phys. Chem. C*, **121**, 13481–13486 (2017).

25. F. Friedrich, B. Strehle, A. T. S. Freiberg, K. Kleiner, S. J. Day, C. Erk, M. Piana, and H. A. Gasteiger, *J. Electrochem. Soc.*, **166**, A3760–A3774 (2019).

26. S. Oswald, D. Pritzl, M. Wetjen, and H. A. Gasteiger, *J. Electrochem. Soc.*, **168**, 120501 (2021).

27. L. de Biasi, A. O. Kondrakov, H. Geßwein, T. Brezesinski, P. Hartmann, and J. Janek, *J. Phys. Chem.*

C, **121**, 26163–26171 (2017).

28. A. O. Kondrakov, A. Schmidt, J. Xu, H. Geßwein, R. Mönig, P. Hartmann, H. Sommer, T. Brezesinski, and J. Janek, *J. Phys. Chem. C*, **121**, 3286–3294 (2017).

29. S. Schweidler, L. de Biasi, G. Garcia, A. Mazilkin, P. Hartmann, T. Brezesinski, and J. Janek, *ACS Appl. Energy Mater.*, **2**, 7375–7384 (2019).

30. G. Qian, Y. Zhang, L. Li, R. Zhang, J. Xu, Z. Cheng, S. Xie, H. Wang, Q. Rao, Y. He, Y. Shen, L. Chen, M. Tang, and Z. F. Ma, *Energy Storage Mater.*, **27**, 140–149 (2020).

31. X. Fan, G. Hu, B. Zhang, X. Ou, J. Zhang, W. Zhao, H. Jia, L. Zou, P. Li, and Y. Yang, *Nano Energy*, **70**, 104450 (2020).

32. S. Oswald, D. Pritzl, M. Wetjen, and H. A. Gasteiger, *J. Electrochem. Soc.*, **167**, 100511 (2020).

33. J. H. Kim, S. J. Kim, T. Yuk, J. Kim, C. S. Yoon, and Y.-K. Sun, *ACS Energy Lett.*, **3**, 3002–3007 (2018).

34. E. Trevisanello, R. Ruess, G. Conforto, F. H. Richter, and J. Janek, *Adv. Energy Mater.*, 2003400 (2021).

35. B. Strehle, F. Friedrich, and H. A. Gasteiger, *J. Electrochem. Soc.*, **168**, 050512 (2021).

36. J. Hu, L. Li, Y. Bi, J. Tao, J. Lochala, D. Liu, B. Wu, X. Cao, S. Chae, C. Wang, and J. Xiao, *Energy Storage Mater.*, **47**, 195–202 (2022).

37. J. Wandt, A. Freiberg, R. Thomas, Y. Gorlin, A. Siebel, R. Jung, H. A. Gasteiger, and M. Tromp, *J. Mater. Chem. A*, **4**, 18300–18305 (2016).

38. J. A. Gilbert, I. A. Shkrob, and D. P. Abraham, *J. Electrochem. Soc.*, **164**, A389–A399 (2017).

39. R. Jung, F. Linsenmann, R. Thomas, J. Wandt, S. Solchenbach, F. Maglia, C. Stinner, M. Tromp, and H. A. Gasteiger, *J. Electrochem. Soc.*, **166**, A378–A389 (2019).

40. S. Klein, P. Bärmann, O. Fromm, K. Borzutzki, J. Reiter, Q. Fan, M. Winter, T. Placke, and J. Kasnatscheew, *J. Mater. Chem. A*, **9**, 7546–7555 (2021).

41. Z. Ruff, C. Xu, and C. P. Grey, *J. Electrochem. Soc.*, **168**, 060518 (2021).

42. Y. Kim, *ACS Appl. Mater. Interfaces*, **4**, 2329–2333 (2012).

43. J. Langdon and A. Manthiram, *Energy Storage Mater.*, **37**, 143–160 (2021).

44. H. H. Ryu, B. Namkoong, J. H. Kim, I. Belharouak, C. S. Yoon, and Y.-K. Sun, *ACS Energy Lett.*, **6**, 2726–2734 (2021).

45. F. Li, L. Kong, Y. Sun, Y. Jin, and P. Hou, *J. Mater. Chem. A*, **6**, 12344–12352 (2018).

46. D. Schreiner, T. Zünd, F. J. Günter, L. Kraft, B. Stumper, F. Linsenmann, M. Schüßler, R. Wilhelm,

A. Jossen, G. Reinhart, and H. A. Gasteiger, *J. Electrochem. Soc.*, **168**, 030507 (2021).

47. W. Zhao, L. Zou, L. Zhang, X. Fan, H. Zhang, F. Pagani, E. Brack, L. Seidl, X. Ou, K. Egorov, X. Guo, G. Hu, S. Trabesinger, C. Wang, and C. Battaglia, *Small*, **18** (2022).

48. H. Li, J. Li, X. Ma, and J. R. Dahn, *J. Electrochem. Soc.*, **165**, A1038–A1045 (2018).

49. J. E. Harlow, X. Ma, J. Li, E. Logan, Y. Liu, N. Zhang, L. Ma, S. L. Glazier, M. M. E. Cormier, M. Genovese, S. Buteau, A. Cameron, J. E. Stark, and J. R. Dahn, *J. Electrochem. Soc.*, **166**, A3031–A3044 (2019).

50. T.-Y. Zeng, X.-Y. Zhang, X.-Y. Qu, M.-Q. Li, P.-P. Zhang, M.-R. Su, A.-C. Dou, A. Naveed, Y. Zhou, and Y.-J. Liu, *Rare Met.* (2022).

51. G.-M. Han, Y.-S. Kim, H.-H. Ryu, Y.-K. Sun, and C. S. Yoon, *ACS Energy Lett.*, **7**, 2919−2926 (2022).

52. R. Bernhard, M. Metzger, and H. A. Gasteiger, *J. Electrochem. Soc.*, **162**, A1984–A1989 (2015).

53. S. Solchenbach, G. Hong, A. T. S. Freiberg, R. Jung, and H. A. Gasteiger, *J. Electrochem. Soc.*, **165**, A3304–A3312 (2018).

54. N. Tsiouvaras, S. Meini, I. Buchberger, and H. A. Gasteiger, *J. Electrochem. Soc.*, **160**, A471–A477 (2013).

55. B. Strehle, K. Kleiner, R. Jung, F. Chesneau, M. Mendez, H. A. Gasteiger, and M. Piana, *J. Electrochem. Soc.*, **164**, A400–A406 (2017).

56. S. Brunauer, P. H. Emmett, and E. Teller, *J. Am. Chem. Soc.*, **60**, 309–319 (1938).

57. S. Solchenbach, D. Pritzl, E. J. Y. Kong, J. Landesfeind, and H. A. Gasteiger, *J. Electrochem. Soc.*, **163**, A2265–A2272 (2016).

58. S. Solchenbach, thesis, Technical University of Munich (2018).

59. R. Sim, S. Lee, W. Li, and A. Manthiram, *ACS Appl. Mater. Interfaces*, **13**, 42898−42908 (2021).

60. K. Shishino, T. Yamada, K. Fujisawa, M. Motoi, T. Hatakeyama, and K. Teshima, *ACS Appl. Energy Mater.*, **5**, 2747–2757 (2022).

61. G. Li, Y. Wen, B. Chu, L. You, L. Xue, X. Chen, T. Huang, and A. Yu, *ACS Sustain. Chem. Eng.*, **9**, 11748–11757 (2021).

62. A. O. Kondrakov, H. Geßwein, K. Galdina, L. de Biasi, V. Meded, E. O. Filatova, G. Schumacher, W. Wenzel, P. Hartmann, T. Brezesinski, and J. Janek, *J. Phys. Chem. C*, **121**, 24381–24388 (2017).

63. R. Jung, P. Strobl, F. Maglia, C. Stinner, and H. A. Gasteiger, *J. Electrochem. Soc.*, **165**, A2869–A2879 (2018).

64. M. Metzger, P. Walke, S. Solchenbach, G. Salitra, D. Aurbach, and H. A. Gasteiger, *J. Electrochem.*

Soc., **167**, 160522 (2020).

65. J. Kasnatscheew, M. Evertz, B. Streipert, R. Wagner, R. Klöpsch, B. Vortmann, H. Hahn, S. Nowak, M. Amereller, A.-C. Gentschev, P. Lamp, and M. Winter, *Phys. Chem. Chem. Phys.*, **18**, 3956–3965 (2016).

66. K. Märker, P. J. Reeves, C. Xu, K. J. Griffith, and C. P. Grey, *Chem. Mater.*, **31**, 2545–2554 (2019).

67. R. Jung, M. Metzger, F. Maglia, C. Stinner, and H. A. Gasteiger, *J. Phys. Chem. Lett.*, **8**, 4820–4825 (2017).

68. S. Watanabe, M. Kinoshita, T. Hosokawa, K. Morigaki, and K. Nakura, *J. Power Sources*, **260**, 50–56 (2014).

69. J. Wandt, A. T. S. Freiberg, A. Ogrodnik, and H. A. Gasteiger, *Mater. Today*, **21**, 825–833 (2018).

70. A. T. S. Freiberg, M. K. Roos, J. Wandt, R. De Vivie-Riedle, and H. A. Gasteiger, *J. Phys. Chem. A*, **122**, 8828–8839 (2018).

71. C. Xu, K. Märker, J. Lee, A. Mahadevegowda, P. J. Reeves, S. J. Day, M. F. Groh, S. P. Emge, C. Ducati, B. Layla Mehdi, C. C. Tang, and C. P. Grey, *Nat. Mater.*, **20**, 84–92 (2021).

72. A. T. S. Freiberg, J. Sicklinger, S. Solchenbach, and H. A. Gasteiger, *Electrochim. Acta*, **346**, 136271 (2020).

73. S. E. Renfrew and B. D. McCloskey, *J. Am. Chem. Soc.*, **139**, 17853–17860 (2017).

74. W. M. Seong, Y. Kim, and A. Manthiram, *Chem. Mater.*, **32**, 9479–9489 (2020).

75. S. Oswald, R. Wilhelm, T. Kratky, G. Kieslich, S. Hallweger, L. Szentmiklósi, B. Maróti, I. Harsányi, and H. A. Gasteiger, *Prep.* (2024).

76. Y. Ikeda, M. Tamaki, G. Matsumoto, K. Amioka, and T. Mizuno, *Spectrochim. Acta*, **37B**, 647–658 (1982).

77. C. Delacourt, A. Kwong, X. Liu, R. Qiao, W. L. Yang, P. Lu, S. J. Harris, and V. Srinivasan, *J. Electrochem. Soc.*, **160**, A1099–A1107 (2013).

78. L. M. Thompson, J. E. Harlow, A. Eldesoky, M. K. G. Bauer, J. H. Cheng, W. S. Stone, T. Taskovic, C. R. M. McFarlane, and J. R. Dahn, *J. Electrochem. Soc.*, **168**, 020532 (2021).

79. S. J. Wachs, C. Behling, J. Ranninger, J. Möller, K. J. J. Mayrhofer, and B. B. Berkes, *ACS Appl. Mater. Interfaces*, **13**, 33075–33082 (2021).

80. W. Li, X. Liu, Q. Xie, Y. You, M. Chi, and A. Manthiram, *Chem. Mater.*, **32**, 7796–7804 (2020).

81. L. M. Thompson, W. Stone, A. Eldesoky, N. K. Smith, C. R. M. McFarlane, J. S. Kim, M. B. Johnson, R. Petibon, and J. R. Dahn, *J. Electrochem. Soc.*, **165**, A2732–A2740 (2018).

82. S. Schweidler, L. de Biasi, A. Schiele, P. Hartmann, T. Brezesinski, and J. Janek, *J. Phys. Chem. C*, **122**, 8829–8835 (2018).

83. M. Ecker, N. Nieto, S. Käbitz, J. Schmalstieg, H. Blanke, A. Warnecke, and D. U. Sauer, *J. Power Sources*, **248**, 839–851 (2014).

84. P. Keil, S. F. Schuster, J. WIlhelm, J. Travi, A. Hauser, R. C. Karl, and A. Jossen, *J. Electrochem. Soc.*, **163**, A1872–A1880 (2016).

85. J. Landesfeind, J. Hattendorff, A. Ehrl, W. A. Wall, and H. A. Gasteiger, *J. Electrochem. Soc.*, **163**, A1373–A1387 (2016).

86. D. Pritzl, J. Landesfeind, S. Solchenbach, and H. A. Gasteiger, *J. Electrochem. Soc.*, **165**, A2145–A2153 (2018).

87. R. Morasch, J. Keilhofer, H. A. Gasteiger, and B. Suthar, *J. Electrochem. Soc.*, **168**, 080519 (2021).

88. J. Moškon, J. Žuntar, S. Drvarič Talian, R. Dominko, and M. Gaberšček, *J. Electrochem. Soc.*, **167**, 140539 (2020).

89. R. Morasch, B. Suthar, and H. A. Gasteiger, *J. Electrochem. Soc.*, **167**, 100540 (2020).

90. J. Landesfeind, D. Pritzl, and H. A. Gasteiger, *J. Electrochem. Soc.*, **164**, A1773–A1783 (2017).

91. D. Pritzl, A. E. Bumberger, M. Wetjen, J. Landesfeind, S. Solchenbach, and H. A. Gasteiger, *J. Electrochem. Soc.*, **166**, A582–A590 (2019).

92. X. Zhang and T. M. Devine, *J. Electrochem. Soc.*, **153**, B375–B383 (2006).

93. K. V. Rao and A. Smakula, *J. Appl. Phys.*, **36**, 2031–2038 (1965).

94. J. G. Aiken and A. G. Jordan, *J. Phys. Chem. Solids*, **29**, 2153–2167 (1968).

95. T. A. Hewston and B. L. Chamberland, *J. Phys. Chem. Solids*, **48**, 97–108 (1987).

96. J. Molenda, P. Wilk, and J. Marzec, *Solid State Ionics*, **146**, 73–79 (2002).

97. M. Bianchini, M. Roca-Ayats, P. Hartmann, T. Brezesinski, and J. Janek, *Angew. Chemie - Int. Ed.*, **58**, 10434–10458 (2019).

98. R. Ruess, S. Schweidler, H. Hemmelmann, G. Conforto, A. Bielefeld, D. A. Weber, J. Sann, M. T. Elm, and J. Janek, *J. Electrochem. Soc.*, **167**, 100532 (2020).

99. S. Oswald, F. Riewald, and H. A. Gasteiger, *J. Electrochem. Soc.*, **169**, 040552 (2022).

5 Structural Stability of NCMs at High State of Charge

The article "The Structural Stability Limit of Layered Lithium Transition Metal Oxides Due to Oxygen Release at High State of Charge and Its Dependence on the Nickel Content" was submitted to the peer-reviewed *Journal of the Electrochemical Society* in December 2022 and published online in April 2023 [274]. It is available as an open-access article and distributed under the terms of the Creative Commons Attribution Non-Commercial No Derivatives 4.0 License. A permanent link to this article can be found under https://doi.org/10.1149/1945-7111/acbf80. The main findings of this paper were presented by Stefan Oswald in an oral presentation at the *Gordon Research Seminar* on Batteries as well as in a poster presentation at the *Gordon Research Conference* on Batteries, both in Ventura, California, USA, in June 2022.

Upon the electrochemical removal of all contained lithium ions, NCMs (also including LCO and LNO) provide a theoretical capacity of $\sim$275 mAh/g$_{\text{CAM}}$, which can in fact be delivered during the first charge to 5.0 V$_{\text{Li}}$. It is known, however, that charging NCMs to high potentials and completely delithiating the layered structure result in the degradation of the CAM and, therefore, in an irreversible loss of available capacity [135, 275]; furthermore, when NCMs are cycled repeatedly to high potentials/SOCs, the discharge capacity of NCMs decreases continuously with each charge/discharge cycle [125, 137, 276]. This capacity loss, which is induced by a combination of active material loss and impedance build-up [122, 148], is attributed to one of the following mechanisms (or a combination thereof, respectively):

○ At high potentials of >4.5 V$_{\text{Li}}$, the solvent molecules of the carbonate-based electrolyte start to get oxidized electrochemically (at least for LiPF$_6$-containing electrolytes at 25 °C) [31, 32]. The products of this process form protic species such as HF or gases such as CO$_2$, eventually compromising the cell performance, e.g., by decomposing the CAM through the dissolution of transition metals, by degrading the SEI resulting in additional lithium loss, or by causing safety risks due to the swelling of the cells.

○ At high degrees of delithiation, the layered structure becomes unstable and collapses forming an oxygen-depleted (spinel- or rock-salt-type) surface layer with a thickness of a few nanometers. This structural instability is accompanied by the release of lattice oxygen, what has been reported to occur at >80 %SOC independent of the NCM composition [119]. Due to the chemical reaction of the reactive released lattice oxygen, this process implicates similar reactions as for the electrochemical electrolyte oxidation.

Since NCMs cannot be delithiated electrochemically without increasing the potential, and since the onset potential of the release of lattice oxygen occurs at similar values as the onset of the electrochemical electrolyte oxidation, it is challenging to investigate the two mentioned degradation mechanisms individually to determine their respective onset potential/SOC.

This article aims to elucidate the stability limit and its origin for five commercially used layered oxide materials with varying transition metal composition (from purely cobalt-containing to purely nickel-containing, i.e., LCO, NCM111, NCM622, NCM851005, and LNO). First, the stability limit of each material is determined by charge/discharge cycling experiments in half-cells applying the approach of an increasing upper cutoff potential, as introduced in Chapter 3.2. Through two independent analyses of the specific discharge capacity of each CAM as a function of the upper cutoff potential, it is demonstrated that the onset of the capacity loss occurs at a higher SOC for CAMs having a higher nickel content. The enhanced stability window of the nickel-rich CAMs is substantiated in extended cycling experiments, comparing NCM111 and NCM851005 over the course of 200 cycles, which highlight the capacity loss and resistance increase of NCM111 at lower SOCs as compared to the nickel-rich CAM. The gas evolution analysis of the five CAMs by OEMS at high SOC reveals that the evolution of lattice oxygen from each CAM occurs at the same SOC as the one which induces the capacity loss. Since the electrochemical electrolyte oxidation occurs at higher potentials than the onset of the capacity loss, the CAM degradation is assigned purely to the structural instability of the delithiated CAMs and the concomitant oxygen release. Most importantly, however, the stability limit of the CAMs depends substantially on the CAM composition and varies between 65 and 86 %SOC for the here investigated materials.

Based on the results of this study, the rising use of nickel-rich CAMs in commercial LIBs and the gained increase in specific capacity, as discussed in Chapter 1.3, does not

stem from the limited stability of the electrolyte towards electrochemical oxidation but from the larger structural stability window of the CAM itself. Since the CAM typically contributes more than ~30 wt% to the mass of a commercial cell [21], the stability window, which is enlarged by more than ~30 % from 65 to 86 %SOC for nickel-rich NCMs, results in an expected gain of specific cell capacity of ~9 % by choosing a nickel-rich material. It has to be noted that this conclusion is based on the previously reported (and here determined) stability limit of the electrolyte of >4.5 V_{Li} [31, 201]; the theoretical/thermodynamic stability limit of the electrolyte components may actually be at lower potentials, depending on the composition of the electrolyte [32]. This effect may not be detectable in the performed experiments at 25 °C with a duration of a few hours, but could oxidize significant amounts of electrolyte during cell operation, either at elevated temperatures increasing the reaction kinetics or during the lifetime of the cell over many years. Nevertheless, the use of nickel-rich CAMs, shifting the distinct charge/discharge curve of the CAM to lower potentials to avoid the electrochemical oxidation of the electrolyte while, at the same time, extending the structural stability to higher SOCs, benefits the long-term performance in full-cells either way.

Author contributions

S.O. designed and performed the electrochemical and OEMS experiments and analyzed the data. S.O. wrote and H.A.G. edited the manuscript. All authors discussed the results and commented on the manuscript.

The Structural Stability Limit of Layered Lithium Transition Metal Oxides Due to Oxygen Release at High State of Charge and Its Dependence on the Nickel Content

Stefan Oswald[*,z] and Hubert A. Gasteiger[**]

Technical University of Munich, Chair of Technical Electrochemistry, Department of Chemistry and Catalysis Research Center, School of Natural Sciences, Garching, Germany

The composition of layered transition metal oxides ($LiMO_2$, M = Ni, Co, Mn) as cathode active materials (CAMs) is currently trending towards higher nickel contents, which can provide more capacity and energy. The origin of this performance improvement is often ascribed to the lower potential of nickel-rich CAMs, suppressing detrimental electrochemical electrolyte oxidation. In this study, it is shown that the stability limit of $LiMO_2$-based CAMs is not determined by the stability window of typical electrolytes in terms of potential but by the CAM composition, governing the structural stability at high degrees of delithiation. The latter is investigated for five CAMs with distinct composition (LCO, NCM111, NCM622, NCM851005, and LNO) as a function of upper cutoff potential and thus state of charge (SOC). Short-term cycling experiments with an increasing upper cutoff potential as well as extended cycling to selected SOCs reveal stability limits between 66 and 86 %SOC depending on the CAM composition. On-line electrochemical mass spectrometry (OEMS) does not only allow to exclude any impact of electrochemical electrolyte oxidation on the determined stability window of the CAMs but also illuminates the concurrence of capacity fade and lattice oxygen release, with the latter being the origin of the CAM degradation.

Layered lithium transition metal oxides ($LiMO_2$) are commercially available cathode active materials (CAMs) for lithium-ion batteries (LIBs), featuring a theoretical capacity of $\sim$275 mAh/g_{CAM}.[1–4] For the commercialization of the first LIBs, lithium cobalt oxide ($LiCoO_2$, LCO) was employed by Sony in 1991, which delivers a reversible capacity of 145 to 165 mAh/g_{CAM} at a relatively high mean discharge potential of $\sim$4.0 V_{Li}.[4–7] At the same time, lithium nickel oxide ($LiNiO_2$, LNO) was investigated as alternative to LCO, providing 160 to 200 mAh/g_{CAM} at a mean discharge potential of $\sim$3.8 V_{Li}.[4,8–11] To overcome the observed drawbacks of both LCO (i.e., the cost and availability of cobalt as well as the low capacity) and LNO (i.e., the more complex synthesis as well as its sensitivity towards exposure to ambient air), isostructural ternary compositions comprising nickel, cobalt, and manganese ($LiNi_aCo_bMn_cO_2$ with $a+b+c=1$, NCMs) were developed. $LiNi_{1/3}Co_{1/3}Mn_{1/3}O_2$ (NCM111) gained popularity in the 2000s, exchanging typically 160 to 180 mAh/g_{CAM} at an intermediate average discharge potential of $\sim$3.9 V_{Li}.[12–15] Aiming for a higher available capacity, the nickel content of NCMs was then increased continuously over the last decade,[4,16,17] now reaching up to 95 mol% of nickel and 200 to 220 mAh/g_{CAM}[18–20]; at the same time, however, the thermal stability deteriorates with increasing nickel content,[21–24] concomitant with an increasing sensitivity towards exposure to ambient air.[25,26]

The CAM composition (i.e., the type and amount of the transition metals) directly affects the electronic environment of the lithium ions in the CAM, defining the redox potentials for lithium (de)intercalation, what results in a distinct potential profile for the above listed CAMs.[3,27] Due to this property, more capacity is extracted from the CAM for an increased nickel content at the same applied upper cutoff potential, what is, above a certain capacity limit, detrimental for the capacity retention of nickel-rich CAMs.[21,22,24,28] Similarly, for a given nickel content, an increased upper cutoff potential allows for more capacity but ultimately leads to a degradation of the CAM above a certain potential and/or state of charge (SOC, defined here as the degree of delithiation x in $Li_{1-x}MO_2$, with 100 %SOC representing

complete delithiation).[14,28–32] In summary, the capacity retention of a layered lithium transition metal oxide depends both on its composition as well as on the applied upper cutoff potential, which determines the extent of delithiation.

The higher reversibly exchanged capacity observed for nickel-rich CAMs is often attributed to their lower potential profile, believed to mitigate the electrochemical oxidation of electrolyte components at high potential. While experiments on the electrochemical oxidation of typical LIB electrolytes as well as of their carbonate-based solvents on platinum or glassy-carbon electrode disks provide stability limits of 5.5 to 6.7 V vs. Li^+/Li,[33–35] experiments using practical porous battery electrodes (performed on pure carbon black (C65) or actual cathode electrodes) reveal a realistic oxidative stability limit of 4.4 to 4.9 vs. Li^+/Li.[36–41] Since these values overlap with the upper cutoff potentials typically applied to CAMs, the electrochemical electrolyte oxidation could possibly explain the capacity loss at high potential/SOC (e.g., of LCO and NCM111) as well as the higher stability of nickel-rich NCMs.

By an independent mechanism, however, the CAM crystal structure starts to degrade, too: At high degrees of delithiation, the surface of the CAM particles reconstructs to spinel- and/or rock-salt-type structures,[14,42–47] forming upon the release of lattice oxygen.[28,48–50] This process induces a degradation of the CAM (in the form of resistance build-up and/or CAM loss)[28,46,47,50] as well as a chemical electrolyte oxidation,[51,52] which can both be detrimental to the performance of LIBs. Due to the relatively small fractions of decomposed layered phase on the order of $\sim$1 mol% during the first charge,[28,50] it remains challenging to identify the precise onset of this lattice reconstruction in the near-surface region of the CAM particles by bulk-sensitive X-ray diffraction (XRD),[14,46,47] while visual transmission electron microscopy (TEM) or surface-sensitive spectroscopic (XAS/XPS) measurements are tedious and also sensitive to the preparation of the sample when performed ex situ.[42,45,53] By monitoring the gas evolution in differential/on-line electrochemical mass spectrometry experiments (DEMS/OEMS), the onset of the oxygen release has been reported to occur between 75 and 80 %SOC for LNO and NCMs, independent of their composition.[28,49,53,54]

However, due to the singular relationship between potential and SOC (i.e., the degree of delithiation) given by the potential curve for

*Electrochemical Society Student Member.
**Electrochemical Society Fellow.
zE-mail: Stefan.Oswald@tum.de

each CAM, the effect of potential and SOC on the degradation of layered lithium transition metal oxides cannot be investigated independently. To illuminate the mechanistic origin of the higher stability of nickel-rich NCMs at the same SOC (i.e., at equal capacity), this study investigates the structural stability of five CAMs with different composition as a function of either upper cutoff potential or of SOC. To assess the stability limit in cycling experiments, a half-cell test procedure with an increasing upper cutoff potential was applied, which revealed the stability of each CAM through the onset of capacity fading. Here, a higher stability limit in terms of SOC is found for nickel-rich CAMs. This is then substantiated for NCM111 and NCM851005 cathodes assembled in pseudo half-cells (i.e., cells with a pre-lithiated, capacitively over-sized lithium-titanate counter electrode), using a cycling procedure over 200 cycles, in which an increasing upper SOC of 60, 70, 80, and 90 %SOC is applied consecutively. To exclude any impact of electrochemical electrolyte oxidation on the determined stability window of the CAMs, OEMS experiments were first performed using C65 electrodes. Subsequently, OEMS experiments with LCO, NCM, and LNO working electrodes were used to quantify the SOC-dependent release of oxygen from the CAM lattice in dependence of the CAM composition.

Experimental

Electrode preparation.—Electrodes were prepared from five uncoated CAM powders that exhibit very different composition (i.e., transition metal ratio; for material specifications, see Table I): LCO, NCM111, NCM622, NCM851005, and LNO (ordered from high to low cobalt content, or from low to high nickel content, respectively). NCM851005 and LNO were not doped, coated, nor washed during their synthesis, while NCM622 received an aluminum doping of 0.3 mol% but was also not washed or coated; the treatments of LCO (442704, Sigma-Aldrich, USA) and NCM111 are unknown. Due to the relatively high reactivity of LNO with water (vapor), the preparation of the slurries and electrodes containing LNO was done under inert conditions in an argon-filled glovebox ($<$1 ppm O_2 and H_2O, MBraun, Germany). For the electrochemical experiments, electrodes were prepared from the five CAM powders, which were each mixed at a mass ratio of 96:2:2 with carbon black (C65, carbon black SuperC65, 64 m^2/g_{C65}, TIMCAL, Switzerland) and polyvinylidene difluoride (PVDF, Solef 5130, Solvay, Germany) with N-methyl-2-pyrrolidone (NMP, anhydrous, Sigma-Aldrich, Germany) as dispersing agent in a planetary centrifugal mixer (ARV-310, Thinky Corp., USA) for 17 min, using a sequential mixing procedure. Furthermore, a slurry without active material, containing only C65 and PVDF at a mass ratio of 1:1, was mixed with NMP (at a solid content of 20 wt%) by the same mixing procedure.

For the cycling experiments in Swagelok T-cells with a lithium-metal reference electrode (Li-RE), the slurries (with a solid content of 63 wt%) were coated onto the rough side of an aluminum foil (18 μm in thickness, MTI, USA) with a box-type coating bar (Erichsen, Germany) using an automated coater (RK PrintCoat Instruments, United Kingdom). All electrode sheets were then dried in a convection oven at 50 °C for 5 h before electrodes (Ø 10.95 mm) were punched out and compressed at 200 MPa for 30 s using a manual hydraulic press (Specac, United Kingdom). The CAM electrodes for the cycling experiments had a loading of 10.3 ± 1.0 mg_{CAM}/cm^2 what corresponds to a theoretical areal capacity of 2.8 ± 0.3 mAh/cm^2. Depending on the experiment, two different types of counter electrodes (CEs) were used: i) lithium-metal CEs (Li-CEs, Ø 11 mm, 450 μm in thickness, Rockwood Lithium, USA) to assemble half-cells for short-term cycling experiments with increasing upper cutoff potentials; and ii) partially pre-lithiated and capacitively oversized lithium-titanate (LTO, $Li_4Ti_5O_{12}$) CEs (LTO-CEs, Ø 10.95 mm, LTO on aluminum, 3.5 mAh/cm^2, Customcells, Germany) for extended cycling experiments in a so-called *pseudo full-cell* configuration (note that pseudo full-cell here refers to a cell with a specific WE and a pre-lithiated, capacitively oversized LTO or pre-delithiated LFP electrode).

For on-line electrochemical mass spectrometry (OEMS) measurements, CAM slurries with a higher solid content of 80 wt% (prepared as described above) as well as the C65 slurry (with a solid content of 20 wt%) were coated on a stainless-steel mesh (316 grade, 26 μm aperture, 25 μm wire diameter, The Mesh Company, UK) with a doctor blade using an automatic coater (see above). The electrode sheets were then dried in a convection oven at 50 °C for 5 h before electrodes (Ø 17 mm) were punched out and used uncompressed. The CAM electrodes for OEMS had a relatively high loading of 18.3 ± 1.8 mg_{CAM}/cm^2 what corresponds to a theoretical areal capacity of 5.0 ± 0.5 mAh/cm^2; they were assembled in a half-cell configuration with Li-CEs (Ø 17 mm). The C65 electrodes for OEMS had a loading of 8.8 mg_{C65}/cm^2; they were assembled either in a pseudo full-cell configuration with pre-delithiated lithium iron phosphate (LFP, $LiFePO_4$) CEs (LFP-CEs, Ø 17 mm, LFP on aluminum, 3.5 mAh/cm^2, Customcells, Germany) or in a half-cell configuration with Li-CEs (Ø 17 mm).

All electrodes (other than lithium metal) were dried in a Büchi oven at 120 °C under dynamic vacuum for at least 6 h and then transferred without exposure to air to an argon-filled glove box, where all cells were assembled.

T-cell assembly and testing.—All electrochemical cycling tests were performed in a climate chamber (KB 115 or KB 720, Binder, Germany) at 25 °C, using a battery cycler (Series 4000, Maccor, USA). Spring-compressed Swagelok T-cells with a Li-RE (Ø 6 mm) were assembled (for details see Fig. 1a in ref.[55]), and *C*-rates are consistently referenced to the respective theoretical capacity of each CAM, as depicted in Table I.

For recording the potential profiles as a function of SOC as well as for the cycling tests with increasing upper cutoff potential, half-

Table I. Material properties of the investigated CAMs (ordered from low to high nickel content, or from high to low cobalt content, respectively) including label, composition, theoretical capacity for the complete delithiation, particle morphology (determined by top-view scanning-electron microscopy, data not shown), specific surface area (obtained by Kr-BET), as well as the CAM supplier.

Active material	Composition	Theo. capacity	Morphology	Specific surface area	Supplier
LCO	$LiCoO_2$	273.8 mAh/g_{CAM}	single-crystalline	0.36 m^2_{BET}/g_{CAM}	Sigma-Aldrich
NCM111	$LiNi_{1/3}Co_{1/3}Mn_{1/3}O2$	277.9 mAh/g_{CAM}	polycrystalline	0.24 m^2_{BET}/g_{CAM}	BASF SE
NCM622	$LiNi_{0.6}Co_{0.2}Mn_{0.2}O_2$	276.5 mAh/g_{CAM}	polycrystalline	0.36 m^2_{BET}/g_{CAM}	BASF SE
NCM851005	$LiNi_{0.85}Co_{0.10}Mn_{0.05}O_2$	275.0 mAh/g_{CAM}	polycrystalline	0.27 m^2_{BET}/g_{CAM}	BASF SE
LNO	$LiNiO_2$	274.5 mAh/g_{CAM}	polycrystalline	0.31 m^2_{BET}/g_{CAM}	BASF SE

cells with a Li-CE (Ø 11 mm) and CAM-based working electrodes (CAM-WEs, Ø 10.95 mm) were assembled using three glass fiber separators (Ø 11 mm, glass microfiber filter, 691, VWR, Germany, two between WE and CE and one on the Li-RE) and adding 90 μl of LP57 electrolyte (1 M LiPF$_6$ in EC:EMC 3:7 w/w, <20 ppm H$_2$O, Gotion, China). To allow for the assignment of the applied potential to a state of charge (SOC, corresponding to the degree of delithiation x in Li$_{1-x}$MO$_2$, with 100 %SOC representing complete delithiation) from the respective potential profiles of the five CAMs, the half-cells were charged in constant-current mode (CC) to 5.0 V$_{Li}$ at a C-rate of C/15 (corresponding to ~18.3 mA/g$_{CAM}$). It has to be noted that, throughout this article, potentials referenced to either the Li-RE or to the Li-CE are denoted as V$_{Li}$.

For the half-cell cycling tests with increasing upper cutoff potential (adapted from a previous publication[50]), three charge/discharge cycles were executed, with a constant-current (CC) charge to the initial upper cutoff potential of the CAM-WE (NCMs, LCO, and LNO, see Table I) of 3.9 V$_{Li}$ at C/3 including a CV hold for 10 min or until the current dropped to below C/30 (CCCV mode), and with a CC discharge to the lower cutoff potential of 3.0 V$_{Li}$ at C/3 (corresponding to cycle 1, 2, and 3); each (dis)charge step was followed by an OCV (open-circuit voltage) phase of 10 min. This set of three cycles was then repeated while increasing the upper cutoff potential of the CAM electrode by 0.1 V for each set after every third cycle, finishing with three cycles to 5.0 V$_{Li}$ (corresponding to cycle 34, 35, and 36). Since the exchanged capacity of <5 mAh/g$_{CAM}$ is relatively small for LCO for an upper cutoff potential of 3.9 V$_{Li}$ (see Fig. A.2), the first three cycles to 3.9 V$_{Li}$ are omitted in the procedure for LCO.

In the extended cycling tests with T-cells in pseudo full-cell configuration, CAM-WEs were cycled using pre-lithiated, capacitively oversized LTO-CEs. To prepare the CEs (adapted and reprinted here from a previous publication[50] for the sake of completeness), capacitively oversized LTO electrodes (Ø 10.95 mm, 3.5 mAh/cm^2) were pre-lithiated in spring-compressed T-cells using two glass fiber separators (Ø 11 mm) and 60 μl of LP57 electrolyte against metallic lithium (Ø 11 mm, 450 μm in thickness, Rockwood Lithium, USA) to ~10 %SOC at a specific current of 30 mA/g$_{LTO}$ for 0.5 h, after having performed one full formation cycle at 30 mA/g$_{LTO}$ between 1.2 V$_{Li}$ and 2.0 V$_{Li}$. After pre-lithiation, the LTO electrodes were harvested from the cells without an additional washing step and used as the CEs in the pseudo full-cells for the electrochemical cycling tests.

For these extended cycling tests applying an increasing upper SOC (of 60, 70, 80, and 90 %SOC), spring-compressed T-cells with a Li-RE (Ø 6 mm), a pre-lithiated, capacitively oversized LTO-CE (Ø 10.95 mm), and an NCM111- or NCM851005-based CAM-WE (Ø 10.95 mm) were assembled using three glass fiber separators (Ø 11 mm, two between WE and CE and one on the Li-RE) and 90 μl of LP57 electrolyte. The pre-lithiated, capacitively oversized LTO electrodes are used because they provide: i) a stable half-cell potential of 1.55 V$_{Li}$ at which no solid-electrolyte interphase (SEI) is formed on LTO for the here used carbonate-based electrolytes, thereby suppressing any cross-talk of WE and CE caused by

electrolyte reduction products; ii) a sufficiently large capacity to take up the lithium from the investigated CAM-WEs; and, iii) a sufficient excess of lithium to compensate for any lithium consumed by side reactions during cycling, so that the delivered discharge capacity of the cell translated directly into the available capacity of the CAM only.

When cycling NCM111 and NCM851005, the lower cutoff potential, which was controlled against the Li-RE, was held constant at 3.0 V$_{Li}$ throughout the procedure, while the chosen upper cutoff potential (and thus the reached SOC) was increased for each set in a way that 60, 70, 80, and 90 %SOC were targeted for four sets of 50 cycles, respectively. The applied potential was determined from an analysis of the potential curves collected in half-cells charged to 5.0 V$_{Li}$ (see Fig. 1), allowing to assign each one of the targeted SOCs (i.e., 60, 70, 80, and 90 %SOC) to its respective upper cutoff potential, as introduced previously.[14] For NCM111, the upper cutoff potentials corresponding to each of the four targeted SOCs were identified to be 4.25, 4.44, 4.58, and 4.70 V$_{Li}$, while the ones for NCM851005 were 4.00, 4.14, 4.22, and 4.62 V$_{Li}$, respectively; the direct current internal resistance (DCIR) measurement was performed at 50 %SOC, corresponding to 4.05 and 3.89 V$_{Li}$ for NCM111 and NCM851005, respectively (see Table II).

The cycling procedure consisted of four sets of 50 cycles: Each set included 42 intermediate cycles (with a C-rate of C/3 for both charge and discharge) as well as a sequence of four full cycles before and after the intermediate cycles, which consisted of two slow cycles (C/15 for both charge and discharge), a DCIR measurement, and two fast cycles (C/3 for the charge and 3C for the discharge), resulting in a total of 50 full cycles per SOC and 200 full cycles for the entire experiment. Each charge (except for the ones for the DCIR measurements) was performed in CCCV mode (including a CV step at the respective upper cutoff voltage for 1 h or until the current dropped below C/30), while each discharge was performed in CC mode (without CV step). For the DCIR measurements, which followed the two C/15 cycles and were not considered for the total cycle count, the cells were charged at C/15 in CC mode to 50 %SOC and then held at OCV for 1 h, before a discharge pulse of C/3 was applied for 10 s, before the cells were again discharged at C/15 in CC mode.

On-line electrochemical mass spectrometry.—The gassing behavior of the various CAMs during the first charge was studied using either a home-mixed EC-only electrolyte or a home-mixed FEC-only electrolyte, both containing 1.5 M of lithium hexafluorophosphate salt (LiPF$_6$, dried at 120 °C for 3 days, Sigma-Aldrich, Germany) either in ethylene carbonate (EC, Gotion, China) or in fluoroethylene carbonate (FEC, Gotion, China), respectively. Even though pure EC is solid at room temperature, the EC-only electrolyte is liquid due to the melting point depression introduced by the addition of the salt. The OEMS half-cells were assembled with a Li-CE (Ø 17 mm, 450 μm in thickness, Rockwood Lithium, USA), which was placed on the bottom of the custom-made OEMS cell hardware,[56] then covered by two glass fiber separators (Ø 24 mm, glass microfiber filter, 691, VWR, Germany), which were wetted with 300 μl

Table II. Charge capacity and potential of NCM111 and NCM851005 corresponding to the respective SOCs of 50, 60, 70, 80, and 90 %SOC (defined as degree of delithiation x in Li$_{1-x}$MO$_2$, with, e.g., 90 %SOC corresponding to Li$_{0.1}$MO$_2$), extracted from the potential curves of the first charge in half-cells as depicted in Fig. 1. The potential corresponding to 50 %SOC is applied before the DCIR measurements, while the ones for 60, 70, 80, and 90 %SOC are used as upper cutoff potentials in the extended cycling tests shown in Fig. 4.

	NCM111		NCM851005	
State of charge	Capacity	Potential	Capacity	Potential
50 %SOC (DCIR)	139.0 mAh/g$_{CAM}$	4.05 V$_{Li}$	137.5 mAh/g$_{CAM}$	3.89 V$_{Li}$
60 %SOC	166.7 mAh/g$_{CAM}$	4.25 V$_{Li}$	165.0 mAh/g$_{CAM}$	4.00 V$_{Li}$
70 %SOC	194.5 mAh/g$_{CAM}$	4.44 V$_{Li}$	192.5 mAh/g$_{CAM}$	4.14 V$_{Li}$
80 %SOC	222.3 mAh/g$_{CAM}$	4.58 V$_{Li}$	220.0 mAh/g$_{CAM}$	4.22 V$_{Li}$
90 %SOC	250.1 mAh/g$_{CAM}$	4.70 V$_{Li}$	247.5 mAh/g$_{CAM}$	4.62 V$_{Li}$

of EC-only or FEC-only electrolyte (1.5 M LiPF$_6$ in EC or in FEC, respectively), and finally a CAM electrode (Ø 17 mm, 18.3 ± 1.8 mg$_{CAM}$/cm^2) was placed on top of the stack in the spring-compressed OEMS cells. The assembled cells were positioned in a climate chamber (T-40/25, CTS, Germany) at 25 °C and connected to a potentiostat (SP-300, BioLogic, France) and the mass spectrometer system (HiQuad QMH 400–1, Pfeiffer Vacuum, Germany), which has been described in detail elsewhere.[56] Subsequently, the cells were held at OCV for 4 h before they were charged in constant-current (CC) mode to 5.0 V$_{Li}$ at a C-rate of C/15 (corresponding to ~18.3 mA/g$_{CAM}$, referenced to the respective theoretical capacity of ~275 mAh/g$_{CAM}$, see Table I).

To study the potential-dependent gas evolution in the absence of chemical electrolyte oxidation, i.e., in the absence of lattice oxygen release, OEMS experiments were conducted with carbon-only electrodes (PVDF-bonded C65, Ø 17 mm, 8.8 mg$_{C65}$/cm^2). These cells were assembled as described above, with 300 μl of either EC-only or LP57 electrolyte, using either a Li-CE (Ø 17 mm) or a capacitively oversized, pre-delithiated LFP-CE (Ø 17 mm, 3.5 mAh/cm^2), and placing the C65 electrode on top. The LFP-CE was pre-delithiated in an OEMS cell with a lithium-metal electrode (Ø 17 mm, 450 μm in thickness, Rockwood Lithium, USA) prior to the actual OEMS experiment, using two different configurations depending on the electrolyte: i) two glass fiber separators (Ø 24 mm), one H2013 polyolefin separator (Ø 24 mm, Celgard, USA) facing the LFP electrode (to facilitate the separation of the delithiated LFP electrode and the separator), and 300 μl of LP57; or ii) two glass fiber separators only (i.e., no H2013 polyolefin separator), and 300 μl of EC-only electrolyte. The LFP electrodes were then delithiated to ~50 %SOC at a specific current of 30 mA/g$_{LFP}$ for 2.5 h, after having performed one full formation cycle at 30 mA/g$_{LFP}$ between 3.0 and 4.0 V$_{Li}$. After pre-delithiation, the LFP electrodes were harvested from the cells and used without washing as the LFP-CE in the OEMS cells for the gas evolution experiments. The pre-delithiated, capacitively oversized LFP electrodes are used because they: i) provide a stable potential of ~3.45 V$_{Li}$ over a wide SOC window, and ii) exhibit no gas evolution due to the absence of electrolyte decomposition reactions at their operating potential (as compared to typical anodes such as lithium metal or graphite forming an SEI including gas evolution[28,57,58]). It has to be noted that, in the following, the pseudo full-cell voltage with the LFP-CE was converted to the potential of the C65 electrode in units of V$_{Li}$ by adding 3.45 V. After connecting them to the OEMS (see above), the OEMS cells with the C65 WEs were held in constant-voltage (CV) mode at 3.0 V$_{Li}$ for 4 h before the potential was scanned linearly from 3.0 V$_{Li}$ to 5.5 V$_{Li}$, applying a voltage ramp of 2.5 mV/min, what resulted in a measurement duration of ~17 h within the voltage window from 3.0 to 5.0 V$_{Li}$, being comparable to the duration of ~15 h for the OEMS experiments with CAM-WEs (see above).

The simultaneously traced mass signals were normalized by the ion current of the ^{36}Ar isotope to correct for fluctuations of pressure and temperature, and the signals for O$_2$ and CO$_2$ were then converted to concentrations using a calibration gas (argon with 2000 ppm of O$_2$, CO$_2$, hydrogen (H$_2$), and ethylene (C$_2$H$_4$) each, Westfalen, Germany) and considering a cell volume of ~11 cm^3, as introduced by Strehle et al. and Jung et al. for the gassing of (LMR-)NCM.[28,59] For details on the calibration procedure, see Tsiouvaras et al.[56]

Results and Discussion

Potential curves for varying CAM composition.—To investigate the effect of the CAM composition on the potential profiles, the CAM potential (determined via a Li-RE, marked as V$_{Li}$) as a function of the specific capacity of the first slow charge (i.e., delithiation) at C/15 is depicted in Fig. 1. After cell assembly, the OCP (open-circuit potential) of the CAMs was ~3.1 V$_{Li}$ (data not shown). During the charge, the different potential curves show a clear trend as a function of the composition, as the CAMs with
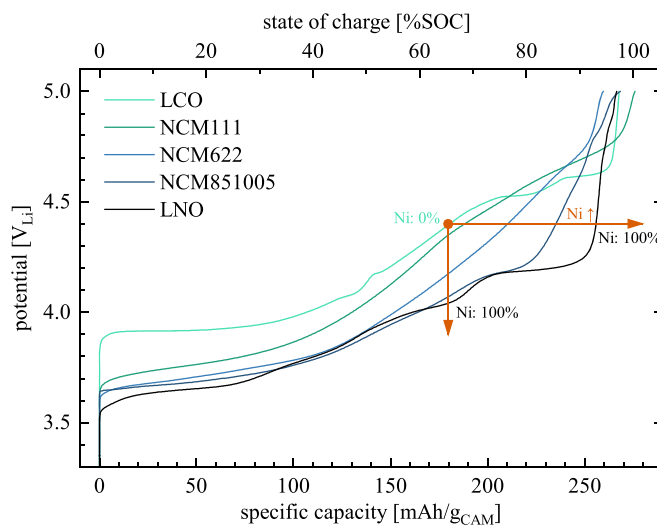

Figure 1. Potential curves of the first charge of the five CAMs measured vs. the Li-RE as a function of the specific capacity (bottom x-axis, in units of mAh/g$_{CAM}$) or SOC (top x-axis, in %SOC, calculated for a theoretical capacity of 275 mAh/g$_{CAM}$). LCO (mint green), NCM111 (elf green), NCM622 (blue), NCM851005 (dark blue), and LNO (black) WEs (10.3 ± 1.0 mg$_{CAM}$/cm^2) in T-cells with 90 μl of LP57 electrolyte and lithium metal as CE and RE. Controlled by the Li-RE potential, the NCM electrodes were charged at 25 °C to 5.0 V$_{Li}$ at C/15 (corresponding to a current of ~18.3 mA/g$_{CAM}$ when referenced to the theoretical capacity of ~275 mAh/g$_{CAM}$). The horizontal orange arrow indicates the increase of the specific capacity with increasing nickel content for a fixed CAM potential of 4.4 V$_{Li}$, while the vertical orange arrow marks the decrease of the potential with increasing nickel content for a fixed capacity of 180 mAh/g$_{CAM}$.

higher nickel content (and lower cobalt content, respectively) appear at lower potentials: From LCO (mint green data in Fig. 1) over NCM111 (elf green), NCM622 (blue), NCM851005 (dark blue) to LNO (black), a higher charge capacity is delivered at the same upper cutoff potential (e.g., at 4.4 V$_{Li}$, horizontal orange arrow); in other words, a lower upper cutoff potential is required to reach the same charge capacity (e.g., at 180 mAh/g$_{CAM}$, vertical orange arrow). However, it has to be noted that this statement is not entirely true in all SOC regimes, but this overall trend is observed for the majority of the SOC range. At the upper cutoff potential of 5.0 V$_{Li}$, all materials achieved a charge capacity between 260 and 275 mAh/g$_{CAM}$, corresponding to more than 95 % of the theoretical capacity.

For the two materials containing only one type of transition metal, i.e., LCO and LNO, the potential profiles exhibit various distinct potential plateaus, while the ones of the ternary NCMs are relatively smooth without obvious potential steps. These plateaus of LCO and LNO originate from phase transitions with distinct redox potentials during the delithiation of the layered structure, clearly apparent for both LCO[5,6,60,61] and LNO,[11,54,62,63] which can be detected by X-ray diffraction (XRD) as well as by computational modeling. To find the corresponding potentials and SOCs of these phase transitions, the potential curves of the two materials as well as the respective specific differential capacity curves (often referred to as dq/dV plots) are presented in Fig. A.1. As shown in these two representations of the first charge curve of LCO in Figs. A.1a and A.1b in the appendix, most of the charge capacity of LCO is delivered between 3.9 and 4.7 V$_{Li}$. The potentials of the five phase changes of LCO (discussed in more detailed for Fig. A.1) are determined from the plateaus in Fig. A.1a or from the peaks in Fig. A.1b, respectively, and occur at 3.92, 4.08, 4.18, 4.52, and 4.62 V$_{Li}$. The two phase changes (from the octahedral to the monoclinic phase (O3→M) and then back to the octahedral phase (M→O3)) at ~4.2 V$_{Li}$ (see Fig. A.1b) occur at 47 and 52 %SOC (extracted from the potential curves of the first charge of the LCO half-cells in Fig. A.1a). As depicted in Figs. A.1c and A.1d, most of the charge capacity from LNO is extracted between 3.5 and 4.3 V$_{Li}$,

accompanied by five phase changes at 3.66, 3.79, 3.94, 4.02, 4.19 V_{Li}. Since it will become relevant throughout this study, the three phase changes at 3.79, 4.02, and 4.19 V_{Li} are assigned to their respective SOCs of 39, 62, and 80 %SOC, with the latter being the H2→H3 phase transition, which is often observed to mark the stability limit of LNO.[10,11,62]

Charge/discharge cycling with increasing upper cutoff potential.—Even though it is desired to increase the upper cutoff potential to extract more capacity from a given CAM and thus increase the provided energy of the entire cell, the capacity retention is typically diminished when higher cutoff potentials are applied. To assess the performance of a battery cell in dependence of the used active materials and the applied cutoff potentials, typically, full- or half-cells are assembled and investigated in extended charge/discharge cycling experiments. For the long-term testing of these cells, a different (but fixed) upper and/or lower cutoff potential is then chosen for a given CAM, resulting in a set of experiments which are often time-consuming and possibly limited by the available resources for cycling experiments.[14,28,29,31,32,64–67] In contrast, it has been stated by Kasnatscheew et al.[37,68] that a single charge/discharge cycle in a half-cell is sufficient to evaluate the stability limit of CAMs by the irreversible capacity of the first cycle, what allows for much shorter experiments; at the same time, however, the assembly of at least one cell for each condition of a series of different upper cutoff potentials is required to determine the stability limit. In the present study, a different approach is pursued which allows to identify the stability limit of a given CAM from a single half-cell measurement (or for two, as done here to check for reproducibility), what is achieved by implementing a procedure with an increasing upper cutoff potential (which is increased after each set of three charge/discharge cycles), similarly as in our previous studies.[50,69]

For these experiments, the potential of the CAM is controlled against a Li-RE, which eliminates any overpotential contributions originating from the Li-CE. After several cycles, here starting at cycle 7, however, the Li-CE exhibits overpotentials of less than 15 mV (tracked against the Li-RE, data not shown) for the applied C-rate of C/3, what is expected to be sufficiently low to apply this method without a RE. Therefore, the applied method could also be used for large-scale screening of newly synthesized CAMs in coin half-cells without Li-RE, even though the use of a Li-RE is recommended.

For the chosen C-rate of C/3, the CAMs typically reached the current-based cutoff criterion of C/30 during the CV step at the end of charge within 5 to 10 min, at least, for the initial cycles. Only when the degradation of the CAM sets in at higher potentials, the resulting overpotentials and remaining currents would require a longer CV hold to reach the full charge capacity. Due to the deliberately chosen time-based end-of-charge criterion, i.e., due to the CV step which was limited to 10 min, the capacity loss of the degraded CAMs is magnified, what allows for a more precise determination of the onset of CAM degradation.

The specific discharge capacities of the five CAMs, cycled to increasingly higher upper cutoff potentials (after each set of three charge/discharge cycles), are depicted in Fig. 2a as function of the cycle number: As expected from the potential curves (see Fig. 1), the delivered capacity increases with increasing upper cutoff potential and, therefore, with cycle number for all used CAMs, while the nickel-rich materials deliver a higher capacity at a lower potential. At a certain point of the cycling procedure, however, the capacity starts to decrease, even though the upper cutoff potential is increased. Exemplarily for NCM851005 (dark blue), a discharge capacity of 106.4 mAh/g_{CAM} is observed for the third cycle to 3.9 V_{Li}, which then increases stepwise to 129.6, 150.3, 179.3, 195.1, 201.8, and 204.9 mAh/g_{CAM} for the respective cutoff potentials of 4.0 to 4.5 V_{Li}. The maximum discharge capacity of NCM851005 is then reached at 4.6 V_{Li} in cycle 22, delivering 207.5 mAh/g_{CAM}; beyond this point, the discharge capacity continuously decreases. At 5.0 V_{Li}, a discharge capacity of 199.8 mAh/g_{CAM} remains in
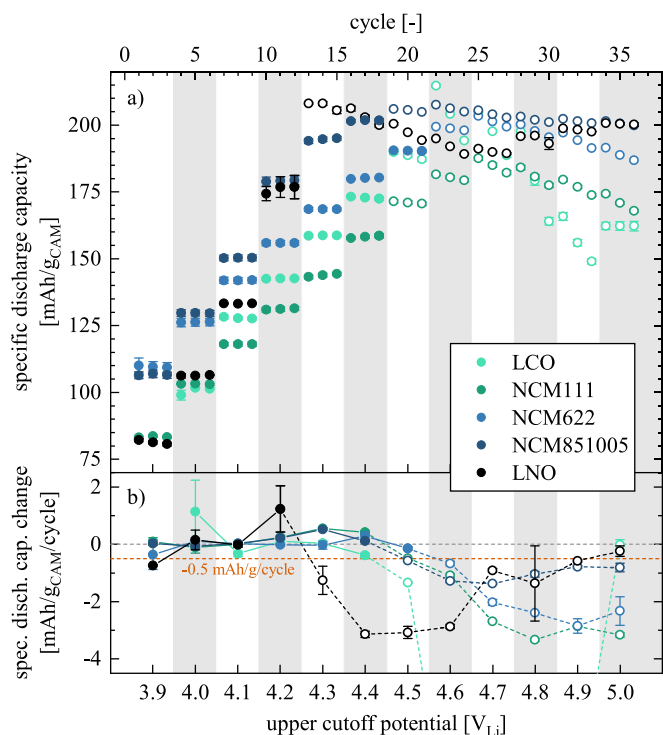

Figure 2. Cycling data of LCO (mint green), NCM111 (elf green), NCM622 (blue), NCM851005 (dark blue), and LNO (black) WEs (10.3 ± 1.0 mg$_{CAM}$/cm^2) to increasingly higher upper cutoff potentials controlled by a Li-RE (in T-cells with a Li-CE, three glass fiber separators, and 90 μl LP57 electrolyte). The cells were cycled at 25 °C and a C-rate of C/3 (corresponding to ~91.7 mA/g_{CAM}, based on the theoretical capacities listed in Table I) between the lower cutoff potential of 3.0 V_{Li} and an upper cutoff potential that was increased every three cycles by 0.1 V, starting at 3.9 V_{Li} and ending at 5.0 V_{Li} (marked by the alternating white and gray areas). The three cycles to 3.9 V_{Li} were omitted for LCO due to the minor capacity delivered at this potential. The data are presented as a function of cycle number (top x-axis) or upper cutoff potential (bottom x-axis). **a)** Specific discharge capacity normalized by the CAM mass. **b)** Change of the specific discharge capacity per cycle within a set of three cycles to the same upper cutoff potential (taken as half of the difference between the first and the third cycle of each set); the orange horizontal dashed line indicates a capacity change of -0.5 mAh/g_{CAM}/cycle, which is chosen to determine the stability of a given CAM (see main text). The closed symbols mark the cycles and thus the upper cutoff potentials exhibiting stable cycling for each CAM, while the open ones indicate the cycles after the capacity decay first exceeded -0.5 mAh/g_{CAM}/cycle. All values are based on two nominally identical cells, and the error bars represent the minimum/maximum values; the error of the capacity change was calculated using the laws of error propagation.

cycle 36. A similar behavior is observed for the four other CAMs as well, whereby the maximum capacity as well as the corresponding cycle depend on the CAM composition: For LCO (mint green), the maximum capacity of 214.8 mAh/g_{CAM} is delivered at 4.6 V_{Li} (cycle 22), while the maximum is reached at 4.7 V_{Li} (cycle 25) for NCM111 (elf green) with a value of 187.6 mAh/g_{CAM}, at 4.7 V_{Li} (cycle 25) for NCM622 (blue) with a value of 203.4 mAh/g_{CAM}, at 4.6 V_{Li} (cycle 22) for NCM851005 (dark blue) with a value of 207.5 mAh/g_{CAM}, and at 4.3 V_{Li} (cycle 13) for LNO (black) with a value of 208.1 mAh/g_{CAM}.

Even before the maximum of the discharge capacity is reached for each CAM, a capacity fade within the sets of three cycles to the same upper cutoff potential can be observed for certain conditions. To illustrate this loss as a function of upper cutoff potential, the change of the specific discharge capacity within a set of three cycles (in units of mAh/g_{CAM}/cycle) is depicted in Fig. 2b, which was calculated by taking half of the difference between the first and the third cycle of each set. For the first set of three cycles of each CAM to 3.9 V_{Li} (or to 4.0 V_{Li} for LCO), where the formation/equilibration

of the CAMs is performed, a relatively large scatter of the data is observed. After the first (three) formation cycles, the capacity change remains around 0 mAh/g_{CAM}/cycle. Surprisingly, an increase of the discharge capacity within a set of three cycles can be observed at 4.3 V_{Li} for NCM851005 and at 4.2 V_{Li} for LNO; the origin of this effect will be discussed for Fig. 3c. Starting at a certain upper cutoff potential, however, an obvious capacity fade within a set of three cycles can be observed in Fig. 2b, occurring first for LNO, then for LCO, followed by the three NCMs. By choosing a threshold of −0.5 mAh/g_{CAM}/cycle, the onset for significant capacity fading is determined (note that, for a practical specific discharge capacity of 200 mAh/g_{CAM}, a state of health of 80 %SOH, i.e., a remaining capacity of 160 mAh/g_{CAM}, would be reached after less than 80 cycles for a linear extrapolation of this threshold): For LCO, the final cycles before such a significant capacity fade occurs are thus found for an upper cutoff potential of 4.4 V_{Li}, while the chosen threshold results in the observation of stable cycling up to 4.4 V_{Li} for NCM111, up to 4.5 V_{Li} for NCM622, up to 4.4 V_{Li} for NCM851005, and up to only 4.2 V_{Li} for LNO (this will be summarized later in Table III). For a better visibility, the cycles with an upper cutoff potential below the onset of the observed capacity fade are presented in Fig. 2 as well as later in Fig. 3 by closed symbols, while the ones beyond this limit are marked by open symbols. Even though the applied procedure allows to quantify the onset of capacity fading, it has to be noted that the values for the specific discharge capacity which are obtained after the capacity starts to decrease within a set of three cycles are not comparable between the different CAMs, since the loss of capacity beyond the onset of the capacity decrease depends on various parameters, such as the temperature, the applied *C*-rate, the criterion which ends the CV phase during charge, the CAM composition as well as its particle morphology and surface area.

From Fig. 2, it becomes obvious that the onset potential of this capacity fade varies depending on the CAM composition. The here observed degradation of the CAMs is often ascribed to the intrinsic phase changes of the layered oxides at high degree of delithiation, which are typically accompanied by the release of lattice oxygen, the change of the unit cell volume, and the increase of their electrochemically active surface area due to the cracking of the secondary agglomerates. Even though these effects occur at different potentials depending on the CAM composition, they seem to have a similar onset of ∼80 %SOC when evaluated as a function of SOC (defined as the degree of delithiation or *x* in $Li_{1-x}MO_2$).[27,28,50,70]

To correct for the potential curves differing with the CAM composition, the recorded cycling data presented in Fig. 2 are analyzed in Fig. 3 by plotting the obtained discharge capacities as a function of SOC, i.e., the degree of delithiation. Therefor, each applied upper cutoff potential is converted to its respective SOC (top *x*-axis in Fig. 3 in mAh/g_{CAM}, and bottom *x*-axis in terms of the degree of delithiation *x* in $Li_{1-x}MO_2$, here based on a theoretical capacity of 275 mAh/g_{CAM}, which is extracted from the potential curves of the first charge depicted for each CAM in Fig. 1. Hereby, the obtained specific discharge capacities (presented in Fig. 2a) appear in Fig. 3a as a straight line with a slope of 1 (i.e., that the discharge capacity increases by 1 mAh/g_{CAM} when the degree of delithiation is increased (due to a higher applied upper cutoff potential) by 1 mAh/g_{CAM}), at least for the cycles which exhibited only insignificant capacity loss in Fig. 2b (marked by the closed symbols in Figs. 2 and 3). Starting with the cycles which showed capacity fading in Fig. 2b (marked by the open symbols in Figs. 2 and 3), the discharge capacities start to deviate from this straight line, showing smaller capacities than expected from a linear extrapolation of the closed symbols.

Furthermore, it becomes obvious that curves with the closed symbols do not overlap for the different CAMs. To provide a meaningful baseline for this shift, the gray dashed line (bisecting line, with a slope of 1 through the origin of the graph) in Fig. 3a represents the line of full reversibility, i.e., that the discharge
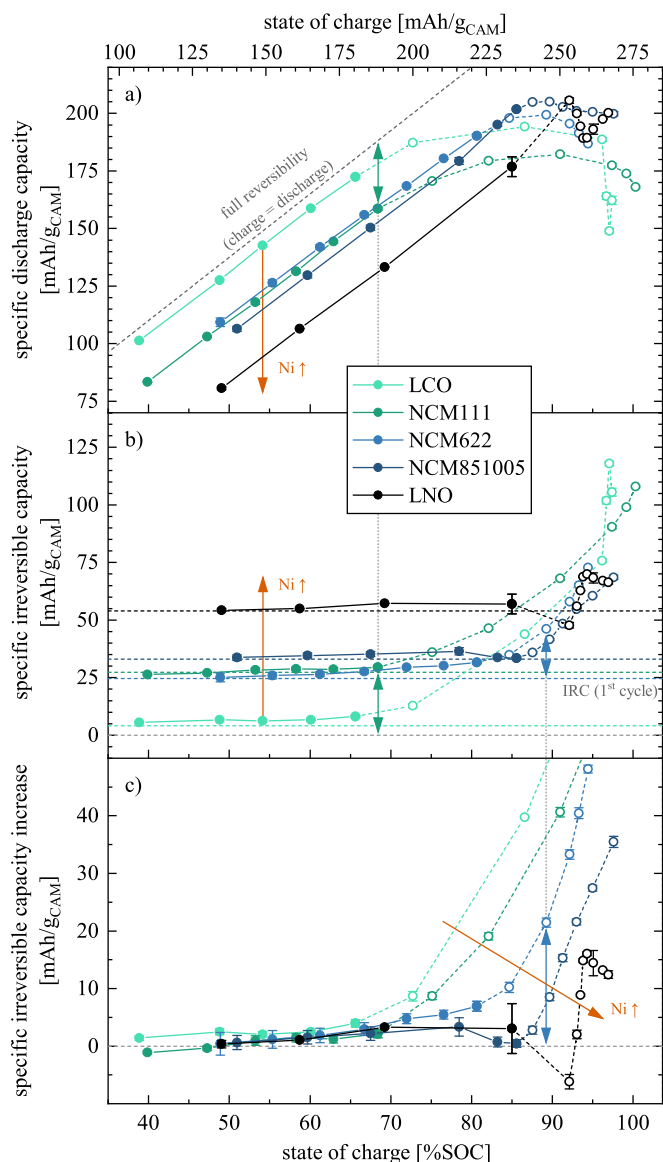

Figure 3. Electrochemical cycling data of LCO (mint green), NCM111 (elf green), NCM622 (blue), NCM851005 (dark blue), and LNO (black) as a function of SOC, extracted from the cycling data shown in Fig. 2a. The obtained capacity data is presented here for every third cycle as a function of SOC (top *x*-axis in mAh/g_{CAM}, and bottom *x*-axis in terms of the degree of delithiation *x* in $Li_{1-x}MO_2$, here based on a theoretical capacity of 275 mAh/g_{CAM}), which was calculated for each CAM from the applied upper cutoff potential using the potential curves of the first charge depicted in Fig. 1. The closed symbols mark the cycles and thus the SOCs exhibiting stable cycling for each CAM, while the open ones indicate the cycles with an SOC above the stability limit of the CAM, which is defined by the criterion in the form of the orange line in Fig. 2b. The orange arrows highlight the change of the specific capacities with the nickel content of the CAMs. **a)** Specific discharge capacity. The gray dashed line (bisecting line, with a slope of 1 through the origin of the graph) represents the line of full reversibility, i.e., that the discharge capacities for the respective SOC would appear on this line for a CAM which could (de)intercalate all lithium fully reversibly, i.e., without a first-cycle irreversible capacity loss. **b)** Specific irreversible capacity, calculated from the vertical difference between each data point in Fig. 3a and the line of full reversibility (gray dashed line in Fig. 3a), as indicated exemplarily for NCM111 by the elf green arrows. The horizontal dashed lines represent the first-cycle irreversible capacity of each CAM, i.e., the difference of the first charge and discharge capacity. **c)** Specific irreversible capacity increase, calculated from the vertical difference of each data point in Fig. 3b and the first-cycle irreversible capacity (horizontal dashed lines in Fig. 3b, which is extracted from Fig. A.2), as indicated exemplarily for NCM622 by the blue arrows. All values are calculated from the mean of two nominally identical cells, and the error bars correspond to the minimum/maximum values.

capacities for the respective SOC would appear on this line for a CAM which could (de)intercalate all lithium fully reversibly at any given SOC, i.e., in the absence of a first-cycle irreversible capacity loss. The (stable/closed) symbols of the cobalt-only LCO CAM appear relatively close to the line of full reversibility, while the NCMs are shifted to lower capacities for a higher nickel content at each SOC (indicated by the orange arrow in Fig. 3a), showing the largest offset and thus the smallest capacities for the nickel-only LNO CAM, what is ascribed to the different (lithiation) kinetics of the different CAMs (see discussion of Fig. 3b).

To obtain the irreversible fraction from the discharge capacities in Fig. 3a, the vertical difference of each data point and the line of full reversibility (or, speaking in practical terms, the difference of the SOC and the discharge capacity), indicated exemplarily for NCM111 by the elf green arrows in Figs. 3a and 3b, is plotted in Fig. 3b as a function of SOC. Through this conversion, the capacities in the stable regime of the SOC window (closed symbols) show constant capacities as a function of SOC for each CAM, while the ones in the unstable regime (open symbols) at higher SOC deviate to higher irreversible capacities.

In addition, the first-cycle irreversible capacity (IRC) loss, i.e., the difference of the first charge and first discharge capacity, is extracted from Fig. A.2 and depicted for each CAM in Fig. 3b as horizontal dashed lines, which overlap reasonably well with the closed symbols. Here, it should be noted that the irreversible contributions obtained for each CAM either from the first-cycle IRC (dashed lines) or from the discharge capacities and the subsequent transformation using the potential curve (solid symbols in Fig. 3b) are obtained independently; hence, their agreement supports the validity of the latter approach.

It has been previously shown that the first-cycle IRC of a CAM does not only depend on its composition[2,68,71–74] but is also affected, e.g., by the synthesis conditions[15,75,76] (controlling the particle morphology as well as the crystal structure), the particle morphology[15,69,76–78] (i.e., the size of the primary crystallites as well as of the secondary agglomerates), the operating temperature,[30,79] the applied C-rate,[80] the application of a CV step at the lower cutoff potential,[37,79] the upper cutoff potential,[12,68,80] and the compression of the electrode.[79] Nevertheless, a general trend is obvious for the various CAM compositions: Even though LCO is typically prepared as a single-crystalline material, what should lead to higher first-cycle IRCs due to the smaller electrochemically active surface area resulting from the larger primary crystallites and the absence of particle cracking,[15,50,69,76–78] the data in Figs. 3b and A.2 show relatively small first-cycle IRCs of ~5 mAh/g_{CAM}, as it was also observed by MacNeil et al.[72] Their study also showed that the substitution of cobalt with only 2.5 mol% nickel and/or manganese increases the first-cycle IRC significantly to values of more than 25 mAh/g_{CAM}; when the nickel and manganese contents are increased further, however, the first-cycle IRC depends only little on the composition.[72] Other studies have shown that, when the substitution of cobalt is pushed to cobalt contents of less than 20 mol%, the first-cycle IRC increases further with increasing nickel and/or manganese content.[2,71,73] For the nickel-only LNO CAM, first-cycle IRCs of 15 to 55 mAh/g_{CAM} are typically observed, depending on the synthesis conditions.[10,62,71,75,76,81] In this study, the cobalt-only LCO CAM (mint green horizontal dashed line in Fig. 3b) shows the smallest, almost negligible IRC of 4.1 mAh/g_{CAM} in the first charge/discharge cycle (to 4.0 V_{Li}), while, for the NCMs, the IRCs (all from the first cycle to 3.9 V_{Li}) amount to 27.4, 24.7, and 33.0 mAh/g_{CAM} for NCM111 (elf green), NCM622 (blue), and NCM851005 (dark blue), respectively, followed by LNO (black) with 53.9 mAh/g_{CAM}, all agreeing well with the results from previous reports.

To correct the data in Fig. 3b for the first-cycle IRC, the difference between the first-cycle IRC (horizontal dashed lines) and each data point in Fig. 3b, indicated exemplarily for NCM622 by the blue arrows, is plotted for each CAM in Fig. 3c as a function of SOC, exhibiting the specific irreversible capacity increase (in units of mAh/g_{CAM}). From this quantity, the onset SOC, i.e., the SOC at which the irreversible capacity increases beyond the first-

cycle IRC, as well as the extent of additional irreversible contributions to the discharge capacity can be determined. Since the CAMs were cycled against a Li-CE (providing sufficient lithium inventory to fully lithiate the CAMs), while the cutoff conditions were controlled using a Li-RE (excluding any overpotentials introduced by the Li-CE), any change in the discharge capacity solely stems from the CAM-WE. Therefore, the observed decrease of the discharge capacity arises from an active material loss and/or from an impedance build-up of the cathode, which may both originate, e.g., from a resistive (oxygen-depleted) surface layer,[28,82] from the development of cation disorder (i.e., transition metals migrating into the lithium layer),[83,84] from the formation of a non-intercalating (rock-salt-type) structure,[46,47] and/or from particle cracking that introduces electronic resistances or leads to a complete isolation of primary CAM particles within a secondary particle agglomerate.[50,85,86]

The specific irreversible capacity increase in Fig. 3c remains within ±5 mAh/g_{CAM} for the lower SOCs (or lower upper cutoff potentials), however, starts to deviate at higher SOCs for all CAMs. The onset of this deviation coincides well with the open symbols (describing the cycles exhibiting capacity loss of −0.5 mAh/g_{CAM}/cycle within a set of three cycles to the same upper cutoff voltage in Fig. 2); in contrast, the values for the capacity increase with closed symbols (describing the cycles exhibiting a negligible/small capacity loss in Fig. 2) remain within approximately ±5 mAh/g_{CAM} and reach an SOC of 180.5, 188.1, 221.8, 235.2, and 233.8 mAh/g_{CAM} for LCO, NCM111, NCM622, NCM851005, and LNO, respectively, which correspond to 66, 68, 80, 86, and 85 %SOC, respectively, when considering the theoretical capacities of the CAMs of ~275 mAh/g_{CAM}. Even though the analysis of the capacity loss within a set of three cycles (see Fig. 2) and the one of the irreversible capacity (see Fig. 3) were performed entirely independently, the obtained stability limits for each CAM are in good agreement, illuminating the higher stability limit of the nickel-rich CAMs (highlighted by the orange arrow in Fig. 3c).

For the two most nickel-rich CAMs NCM851005 and LNO, in addition to the rise of the specific irreversible capacity increase values at high SOCs (see Fig. 3c), an intermediate region with a small decrease of these values is observed: Between 78 and 85 %SOC, these values again decrease by 2.9 mAh/g_{CAM} for NCM851005, while a decrease of 9.2 mAh/g_{CAM} is observed for LNO at 92 %SOC. Since it was shown by Lee et al. that the nickel-rich (or cobalt-poor) materials exhibit slower kinetics during the lithiation,[71] and since it was observed by Riewald et al. that the lithiation kinetics of LNO suffer for a smaller electrochemically active surface area,[76] and since it was observed in previous studies that the CAM surface area increases suddenly at high SOC (>80 %SOC) upon the release of lattice oxygen,[50,69] we assign this decrease in the specific irreversible capacity increase values of Fig. 3c to effectively increased kinetics of the nickel-rich CAMs due to an increased surface area. This increase of the surface area available for charge transfer decreases the surface-area-normalized currents and thus the overpotentials of the cathode, providing more (lithiation) capacity. Similarly, an increase of the discharge capacity within a set of three cycles can be observed already at 4.3 V_{Li} (or 83 %SOC) for NCM851005 and at 4.2 V_{Li} (or 85 %SOC) for LNO (see Fig. 2b), which is ascribed to the same mechanism. This effect, however, is then counteracted by the degradation of the CAMs at high SOC.

Since the specific discharge energy accessible in the stable SOC region is not only determined by the delivered capacity but also by the mean discharge potential that depends on the distinct potential profile of each CAM, the discharge potential and the specific discharge energy are presented and discussed for each CAM in Fig. A.3.

Extended charge/discharge cycling with increasing upper state of charge.—So far, the observed degradation occurring at a higher SOC (or upper cutoff potential) for the nickel-rich CAMs was solely determined by three charge/discharge cycles to the chosen upper

cutoff potentials. Therefore, an extended cycling procedure was applied to cathodes with NCM111 and NCM851005, which, according to the analysis shown in Fig. 3, exhibited a different stability limit of 68 and 86 %SOC, respectively. In this experiment, presented in Fig. 4, the two CAMs were charged for the first set of 50 cycles to an upper cutoff SOC of 60 %SOC, which was successively increased for the following sets to 70, 80, and 90 %SOC (all controlled by the upper cutoff potential derived from Fig. 1 and listed in Table II). Since the CAMs were cycled against a pre-lithiated, capacitively oversized LTO-CE (avoiding the reduction of the electrolyte components to inhibit possible cross-talk phenomena[87,88] and providing sufficient lithium storage and inventory to fully (de)lithiate the CAMs), while the cutoff conditions were controlled using a Li-RE (excluding any overpotentials introduced by the LTO-CE), any change in the discharge capacity solely stems from the CAM-WE.

As depicted in Fig. 4a, NCM851005 (dark blue) exhibits relatively stable cycling for the upper SOCs of 60, 70, and 80 %SOC: During the first 50 cycles at C/15 to 60 %SOC (corresponding to an upper cutoff potential of 4.00 V_{Li}, see Table II), the initial discharge capacity of 143.2 mAh/g_{CAM} increases slightly to 144.7 mAh/g_{CAM} (possibly originating from enhanced kinetics due to the volume change and particle cracking over extended cycling,[50,86] similarly as described above for Fig. 3c), then decreases slightly from 173.0 to 170.9 mAh/g_{CAM} over the next 50 cycles to 70 %SOC (or 4.14 V_{Li}) as well as from 198.1 mAh/g_{CAM} to 195.5 mAh/g_{CAM} over the subsequent 50 cycles to 80 %SOC (or 4.22 V_{Li}). In contrast, over the course of the final 50 cycles to 90 %SOC (or 4.62 V_{Li}), a strong capacity fade from 219.7 to 194.9 mAh/g_{CAM} is observed. An analogous trend is observed for the cycles at C/3 (see Fig. 4b) and for the cycles at 3C (see Fig. 4c), albeit at the expected slightly lower capacities due to the increased C-rates. Over the first three sets of 50 cycles to 60, 70, and 80 %SOC, the resistance (DCIR recorded at the charge-transfer resistance minimum at 50 %SOC[46] and normalized by the geometric surface area of the electrode) increases slightly from 5.3 to 12.6 $\Omega \cdot cm^2_{electrode}$ for NCM851005 (see Fig. 4d). Only when the upper SOC is increased to 90 %SOC, the resistance grows significantly from 10.4 to 92.1 $\Omega \cdot cm^2_{electrode}$ over the 50 cycles, indicating the degradation of the NCM851005 CAM, which is consistent with the analysis in Fig. 3, where the irreversible degradation of NCM851005 was suggested to occur above 86 %SOC.

For NCM111 (elf green), the cycling experiment exposes a clear difference in the stability limit: At 60 %SOC (or 4.25 V_{Li}), the discharge capacity at C/15, shown in Fig. 4a, already decreases slightly from 147.4 to 144.6 mAh/g_{CAM}, whereby the overall capacity is slightly higher compared to the NCM851005 CAM, even though the degree of delithiation of 60 %SOC is the same for both CAMs. This is assigned to the smaller nickel content (or higher cobalt content, respectively) of NCM111 and thus the enhanced lithiation kinetics, as described above for Fig. 3b. At 70 %SOC (or 4.44 V_{Li}), however, the delivered capacity lays between 170.9 and 167.2 mAh/g_{CAM}, thus already below the one of the NCM851005, which could be the first indication for a degradation of the CAM. For the following cycles to 80 and 90 %SOC (or 4.58 V_{Li} and 4.70 V_{Li}, respectively), a significant fade of the discharge capacity from 182.9 to 170.6 mAh/g_{CAM} as well as from 183.4 to 157.1 mAh/g_{CAM} is observed, respectively. The trends observed at C/15 becomes even more clear for the increased C-rates of C/3 (see Fig. 4b) and 3C (see Fig. 4c), where relatively stable cycling is observed only for 60 %SOC, while an increased capacity fade manifests itself already at 70 %SOC. Over the first 50 cycles to 60 %SOC, the resistance of NCM111 increases slightly from 9.1 to 14.8 $\Omega \cdot cm^2_{electrode}$ (see Fig. 4d), while an accelerated resistance build-up is observed for the subsequent sets of 50 cycles: First, it rises from 14.3 to 29.0 $\Omega \cdot cm^2_{electrode}$ for 70 %SOC, then from 27.8 to 60.1 $\Omega \cdot cm^2_{electrode}$ for 80 %SOC, and finally from to 56.7 to 103.8 $\Omega \cdot cm^2_{electrode}$ for 90 %SOC. These data suggest that the stability limit for NCM111 is near 70 %SOC, consistent with the 68 %SOC deduced from the analysis shown in Fig. 3.
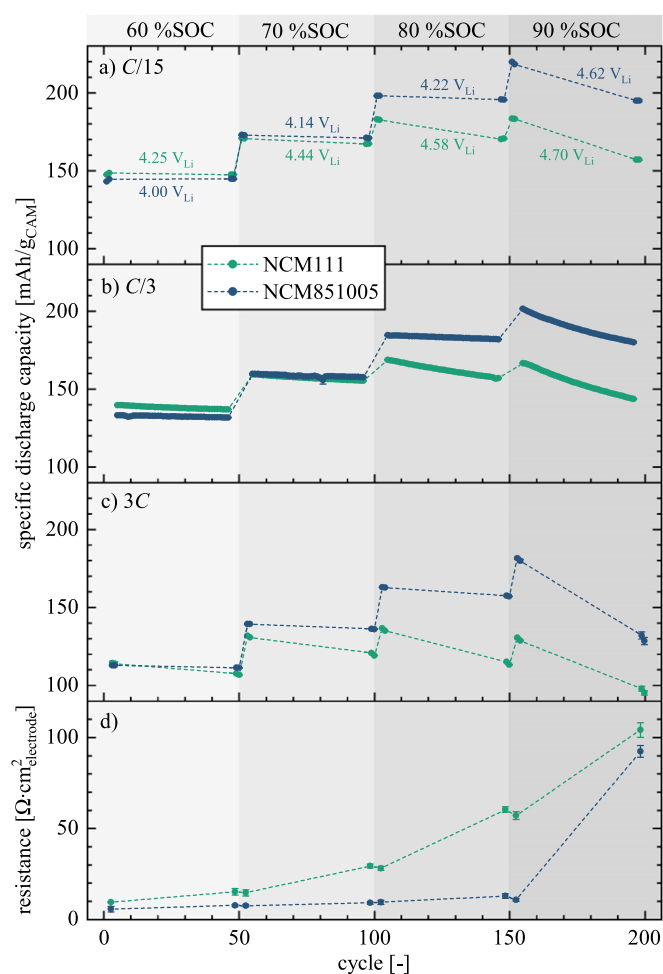

Figure 4. Electrochemical cycling data of NCM111 (elf green) and NCM851005 (dark blue) WEs (with a loading of 10.3 ± 1.0 mg$_{CAM}$/cm^2 and compressed at 200 MPa) in pseudo full-cells with a pre-lithiated, capacitively oversized LTO-CE, 90 μl LP57 electrolyte, and a Li-RE to control the CAM potential. The cells were cycled at 25 °C between the lower cutoff potential of 3.0 V_{Li} and a selected upper cutoff potential that was increased every 50 cycles to delithiate the CAM up to 60, 70, 80, and finally 90 %SOC (marked by the differently shaded gray areas), whereby the upper cutoff potentials for each SOC of both CAMs are given in Table II. While charge/discharge cycling was predominantly done at C/3, the procedure included two slow cycles at C/15, a DCIR measurement, and two fast cycles at 3C at the end as well as at the beginning of each set of 50 cycles (C-rates are based on the theoretical capacities presented in Table I). The shown specific discharge capacities are normalized by the CAM mass and shown as a function of cycle number at: **a)** C/15, **b)** C/3, and **c)** 3C. **d)** DCIR obtained from the potential difference during a 10 s discharge pulse at C/3 and 50 %SOC, with the latter being controlled for each CAM by the potential cutoff listed in Table II. All values are calculated from the mean of two nominally identical cells, and the error bars correspond to the minimum/maximum values.

In summary, the stability limits of 68 %SOC for NCM111 and 86 %SOC for NCM851005 deduced from Fig. 3 are supported by the extended cycling experiments in Fig. 4, which expose an upper limit for the structural stability of 70 %SOC for NCM111 and of 90 %SOC for NCM851005. Here, it must be noted, however, that the potential at any given SOC is always higher for the NCM111 CAM compared to the NCM851005 CAM (by 0.25 to 0.36 V for 60 to 80 %SOC and by 0.08 V at 90 %SOC), what might give rise to a more pronounced effect of electrochemical electrolyte oxidation for the NCM111, resulting in its stronger degradation at a given SOC. At 80 and 90 %SOC for NCM111 and at 90 %SOC for NCM851005, the selected upper cutoff potentials might exceed the stability limit of

the electrolyte components near $\sim$4.5 V_{Li} (as discussed below for Fig. A.5); therefore, the degradation of the CAM may not be driven solely by the intrinsic stability limit of the CAM but also by the electrochemical electrolyte oxidation at high potential. This point will be addressed in the following section.

Gas evolution at high state of charge.—To identify the impact of the oxidation of electrolyte components as well as the origin of the CAM degradation, the gas evolution of the different CAMs (see Figs. 5 and A.4) as well as of CAM-free C65 electrodes (see Fig. A.5 in the appendix) is investigated at high potential (i.e., at high SOC) by on-line electrochemical mass spectrometry (OEMS). For the amplification of the monitored gas signals, an EC-only electrolyte (1.5 M $LiPF_6$ in EC) was used due to its four orders of magnitude lower vapor pressure at room temperature as compared to the one of linear carbonates,[36] not only providing a lower background signal but also reducing the noise of the measurement (see Fig. A.5). For the same purpose, a relatively high mass loading of 18.3 $\pm$ 1.8 mg_{CAM}/cm^2 was used for the CAM electrodes, what resulted in a total amount of 41.5 $\pm$ 4.1 mg_{CAM} in the OEMS cells (note that the areal currents of $\sim$0.34 mA/cm^2 remain at reasonable values due to the relatively low C-rate of C/15). The respective potential curves recorded in the OEMS cells are depicted in Fig. 5a, very closely resembling the ones obtained in T-cells (see Fig. 1).

First, the detected consumption and evolution of carbon dioxide (CO_2) during the first charge of the CAMs is examined in Fig. 5b. During the charge of (nickel-rich) layered-oxide-based cathodes, CO_2 is typically evolved due to: i) the electrochemical oxidation of (carbonate-based) electrolyte components at high potentials above $\sim$4.5 V_{Li};[36,39,41] ii) the chemical electrolyte oxidation upon release of (singlet) oxygen from the CAM lattice at high SOCs;[28,39,49,51,52] and/or iii) the (electro)chemical decomposition of residual lithium salts.[89,90] In contrast to the positive electrode, the Li-CE is not expected to contribute to the CO_2 evolution, since EC, being the only solvent in the EC-only electrolyte, forms ethylene gas upon reduction but no CO_2.[91,92] The detected amounts of evolved CO_2 (mass-over-charge ratio $m/z = 44$) depicted in Fig. 5b as a function of time, however, show an initial consumption of CO_2 for all five CAMs during the first 5 to 10 h of the OEMS experiments. This decrease stems from the CO_2 reduction on the Li-CE due to its low redox potential, forming compounds such as lithium carbonate, lithium oxalate, and lithium formate.[92–94] For the NCMs, the evolution of CO_2 becomes apparent at potentials above $\sim$3.8 V_{Li} (corresponding to $\sim$40 %SOC), either originating directly from an electrochemical oxidation,[90,95] or from a chain of cause and effect as follows: Since alcohols such as ethylene glycol or ethanol[39,89] and other unwanted trace impurities remain in the electrolyte from the synthesis of the carbonate-based solvents, the formed protons (H^+), being one product of this oxidation process, then chemically decompose lithium carbonate (Li_2CO_3) that remains on the NCM particles (from the lithium excess typical for the synthesis of the active material), resulting in the formation of lithium ions, water, and carbon dioxide.[89] Furthermore, the produced water reacts with the ion-conducting salt $LiPF_6$ in the electrolyte, what again generates protons,[96] forming an autocatalytic cycle decomposing Li_2CO_3 and evolving CO_2.[89] Therefore, the CO_2 detected above $\sim$3.8 V_{Li} is assigned partially to the electrochemical oxidation of electrolyte impurities and the chemical decomposition of Li_2CO_3. In addition, for LNO, a step-wise increase of the CO_2 signal is observed at 39 and 62 %SOC; the origin of this effect is discussed below for Fig. 5d.

Beyond the reported limit for the release of lattice oxygen above 80 %SOC,[28] the evolution of CO_2 rises exponentially. For the full delithiation of the CAMs, reached at 5.0 V_{Li}, the detected CO_2 from LCO, NCM111, NCM622, NCM851005, and LNO amounts to 0, 23, 33, 139, and 78 $\mu mol_{CO_2}/g_{CAM}$, respectively (these, however, only represent a lower limit, as CO_2 is reduced simultaneously on the Li-CE). From these numbers, it becomes apparent that the amount of released CO_2 increases with the nickel content, which
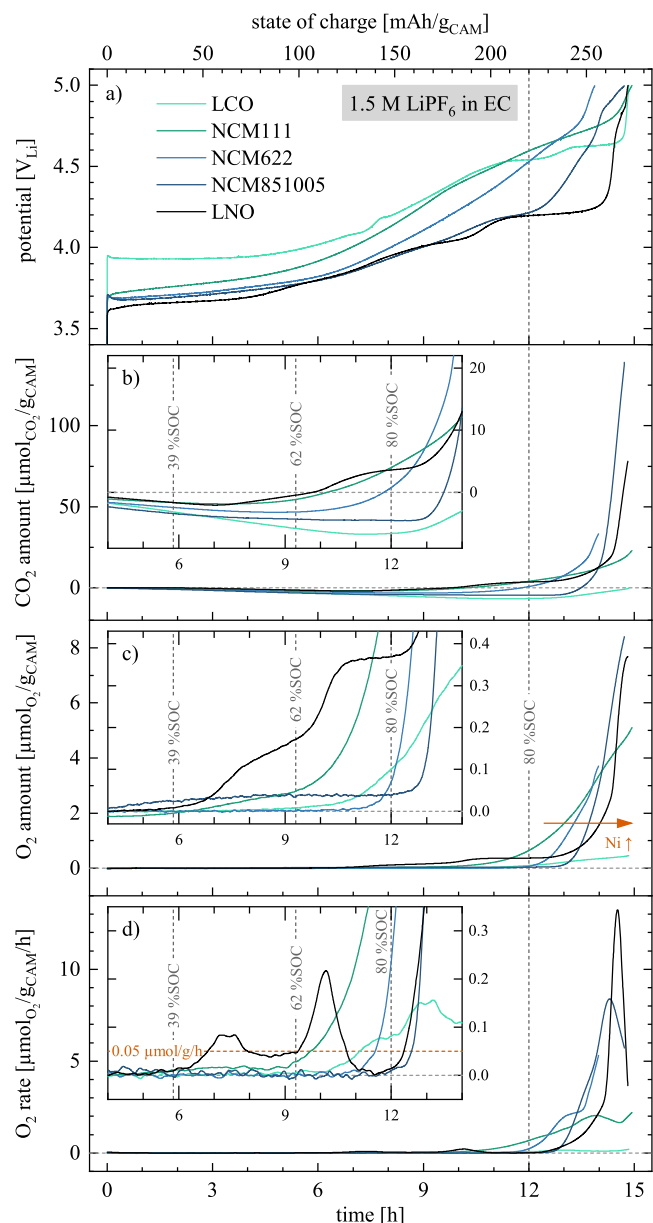

Figure 5. Electrochemical data and gas evolution measured in OEMS half-cells with LCO (mint green), NCM111 (elf green), NCM622 (blue), NCM851005 (dark blue), and LNO (black) WEs (18.3 $\pm$ 1.8 mg_{CAM}/cm^2, all uncompressed), using a Li-CE, two glass fiber separators, and 300 μl of EC-only electrolyte (1.5 M $LiPF_6$ in EC). The cells were charged at 25 °C to 5.0 V_{Li} in constant current mode at C/15 (corresponding to $\sim$18.3 mA/g_{CAM} when referenced to $\sim$275 mAh/g_{CAM}) while the gas evolution was recorded by mass spectrometry. All data are shown as a function of both time (lower x-axis) and SOC (in units of mAh/g_{CAM}, upper x-axis). **a)** CAM potential. **b)** and **c)** Total amounts of evolved carbon dioxide (CO_2, mass-over-charge ratio $m/z = 44$) and oxygen (O_2, $m/z = 32$), respectively, normalized by the CAM mass. The orange arrow highlights the shift in the onset of the O_2 evolution to higher SOCs with the nickel content of the CAM. **d)** O_2 evolution rate obtained from the time derivative of the data in Fig. 5c, with the orange horizontal dashed line in the inset marking the O_2 evolution rate of 0.05 $\mu mol_{O_2}/g_{CAM}/h$. The vertical dashed gray lines mark the SOCs of 39, 62, and 80 %SOC.

may originate from: i) increased amounts of residual lithium salts from the synthesis of nickel-rich CAM[22]; ii) the high reactivity of nickel-rich CAMs with water vapor and carbon dioxide in ambient atmosphere forming surface contaminants (such as Li_2CO_3)[26,97]; and/or, iii) the high reactivity of $Ni^{3+/4+}$ at high SOCs, increasing the amount of released reactive lattice oxygen (since the reactivity of

nickel has been already assigned multiple times to, e.g., a decreased thermal stability as well as an increased reactivity towards moisture[11,22,23,26,98]). For LNO, however, the observed CO_2 amount is reduced as compared to the one of NCM851005, what likely results from the preparation of the LNO-based electrodes in an argon-filled glovebox, thereby preventing the formation of Li_2CO_3 during electrode preparation[26,97] (note that the electrodes with the other CAMs were prepared under ambient atmosphere). Furthermore, due to the absence of manganese and its inhibiting effect on crystal growth, larger primary crystallites of LNO that have a lower specific surface area could lead to the reduced gas evolution. Due to the convolution of the manifold processes resulting in the release of CO_2, a determination of the onset of the electrochemical electrolyte oxidation as well as of the release of lattice oxygen from the CAMs is intricate.

Next, the evolution of molecular oxygen (O_2) is examined in Fig. 5c. Even though most of the released (reactive) lattice oxygen is observed in the form of CO_2 due to the chemical oxidation of the electrolyte, minor amounts (on the order of 5 to 10 % of the CO_2 signal) are still detected as O_2.[28,69] Due to the chosen experimental conditions (i.e., the high CAM mass and the low background signal of the EC-only electrolyte), the onset of the oxygen release may be determined rather accurately from the O_2 signal of the OEMS data. The five CAMs do no exhibit significant O_2 evolution within the first 6 h of the experiments, i.e., up to 40 %SOC. The highest amount of evolved O_2 after 6 h is observed for NCM851005, amounting to $\sim$0.04 $\mu mol_{O_2}/g_{CAM}$ (dark blue line in the inset of Fig. 5c; equating to $\sim$4 ppm of O_2 in the cell) or $\sim$0.15 $\mu mol_{O_2}/m^2_{CAM}$ considering its specific surface area (see Table I), which is $\sim$100-fold lower than the molar surface density of layered transition metal oxides ($\sim$15 $\mu mol_{O_2}/m^2_{CAM}$ for an approximate cubic unit cell with $a = 0.34$ nm); therefore, this amount of evolved O_2 could not lead to a significant surface reconstruction. It might either originate from the decomposition of minor amounts of surface species or from the release of occluded O_2 (remaining in the internal pores from the synthesis process) upon the onset of CAM particle cracking. Beyond 40 %SOC, LNO (black) shows a stepwise increase of the O_2 signal to 0.2 $\mu mol_{O_2}/g_{CAM}$ at 62 %SOC and 0.4 $\mu mol_{O_2}/g_{CAM}$ at 80 %SOC, subsequently merging into a significantly larger evolution of O_2. Since the two-step O_2 release of LNO below 80 %SOC appears simultaneously with the release of CO_2 (see Fig. 5b), this O_2 is assigned to stem from the release of lattice oxygen as well. For each of the other four CAMs, one single onset for the observed O_2 evolution at high SOC is observed, which accelerates with increasing degree of delithiation. For the full delithiation of the CAMs, reached at 5.0 V_{Li}, the detected O_2 from LCO, NCM111, NCM622, NCM851005, and LNO amounts to 0.5, 5.1, 3.7, 8.4, and 7.7 $\mu mol_{O_2}/g_{CAM}$, respectively.

To identify the onset of the O_2 release for each CAM more precisely, the presented total amounts of O_2 are converted to a respective O_2 evolution rate by the derivation of the data in Fig. 5c with respect to time. Since the resulting O_2 evolution rate, presented in Fig. 5d, exhibits a background noise of below $\pm$0.02 $\mu mol_{O_2}/g_{CAM}/h$, an experimentally reasonable detection criterion for the O_2 evolution rate should be 0.05 $\mu mol_{O_2}/g_{CAM}/h$ ($\sim$3 times the experimental noise, marked by the orange horizontal dashed line in Fig. 5d, corresponding to $\sim$5 ppm/h). From the O_2 evolution rate, the two additional stages of the O_2 evolution from LNO become apparent, as observed previously,[49,54] which closely coincides with the phase transitions identified by the dq/dV analysis in Fig. A.1d, occurring at 39 %SOC and 62 %SOC, respectively, but the release of O_2 ceases after each phase transition is completed. Even though oxygen is released below 80 %SOC for LNO, it does not induce a capacity loss in this lower SOC region, as presented in Figs. 2 and 3; therefore, the stability limit of LNO is correlated to the third (and final) stage of the O_2 evolution. By applying the above chosen detection criterion for the O_2 evolution rate, the third stage is determined to initiate at 82 %SOC, which

continues to evolve gas with increasing degree of delithiation, similar to the NCMs. For the three NCMs, the onset SOC increases with the nickel content, with onsets at 65, 77, and 84 %SOC determined for NCM111, NCM622, and NCM851005, respectively. In contrast to previous reports which state that no O_2 (neither in the form of O_2 nor CO_2) is evolved from LCO,[49] the evolution of O_2 is observed starting at $\sim$70 %SOC and reaching a rate of 0.05 $\mu mol_{O_2}/g_{CAM}/h$ at 74 %SOC. The maximum O_2 evolution rate is reached at 88 %SOC (or 4.61 V_{Li}) with 0.16 $\mu mol_{O_2}/g_{CAM}/h$, what is essentially identical to the value of 0.15 $\mu mol_{O_2}/g_{CAM}/h$ at 4.7 V_{Li} reported by Streich et al. in a DEMS setup.[48] Overall, however, the total amounts of evolved O_2 and CO_2 from LCO are significantly smaller as compared to the other CAMs, which is attributed to the expectedly small amounts of Li_2CO_3 on the LCO surface. In addition, due to the absence of crack formation during delithiation,[69,86] the single-crystalline morphology of the LCO particles does not only expose less CAM surface area from which lattice oxygen can evolve, but facilitates the direct reaction of the reactive (singlet) oxygen with the electrolyte, as there are no pores where (reactive) singlet oxygen can decay to (relatively unreactive) triplet oxygen without contact to electrolyte, what results in the favored evolution of CO_2.[51,52,69] From these observations, the evolution of O_2 from all five CAMs at high SOCs can be confirmed, starting between $\sim$4.2 V_{Li} for LNO and $\sim$4.5 V_{Li} for LCO (see Table III).

The gas evolution data reveals a similar onset SOC for each CAM, when FEC-only electrolyte is used instead of EC-only: As depicted in Fig. A.4 in the appendix, the onset SOCs are determined by the same criterion of 0.05 $\mu mol_{O_2}/g_{CAM}/h$ of the O_2 evolution rate, resulting in a stability limit of 72, 68, 76, 82, and 81 %SOC for LCO, NCM111, NCM622, NCM851005, and LNO, respectively.

To exclude the evolution of O_2 from the electrochemical oxidation of the electrolyte at these potentials, the gas evolution from C65 electrodes (without CAM) was monitored up to 5.5 V_{Li} (see Fig. A.5 in the appendix): With both used electrolytes (i.e., LP57 and 1.5 M $LiPF_6$ in EC), the evolution of CO_2 initiates above $\sim$4.5 V_{Li}, what also coincides with the oxidative currents occurring above this potential (see Figs. A.5a and A.5b). However, in this experiment, the O_2 signal does not exceed $\pm$0.12 $\mu mol_{O_2}/g_{C65}$ (or 0.002 $\mu mol_{O_2}/m^2_{C65}$) up to 5.2 V_{Li}, as presented in Fig. A.5c. As the here used CAM electrodes, based on CAMs with a specific surface area of $\sim$0.3 m^2/g_{CAM} and with 2 wt% of C65 (with a specific surface area of $\sim$64 m^2/g_{C65}), have a specific surface area of $\sim$1.2 $m^2/g_{electrode}$ (or $\sim$1.3 m^2/g_{CAM}, for 96 wt% CAM in the electrodes),[69] the maximum surface-area-normalized O_2 evolution rate determined from the C65 electrode (i.e., 0.002 $\mu mol_{O_2}/m^2_{C65}$) would translate to $\sim$0.0025 $\mu mol_{O_2}/g_{CAM}$, if it would originate only from the electrochemical oxidation of the electrolyte on the electrochemically active surface area. Since this value is negligible as compared to the O_2 amounts observed for the CAM electrodes up to 5.0 V_{Li} (see Fig. 5c), the evolved O_2 amounts must stem solely from the release of lattice oxygen from the CAMs.

Correlation of capacity loss and oxygen release.—Figure 6 compares the stability limits of the various CAMs obtained by the two different criteria, one based on the capacity fade (squares, from the cycling data in Fig. 2 and quantified as a function of SOC in Fig. 3) and one based on the onset of O_2 evolution (see Fig. 5 for EC-only (circles) and Fig. A.4 for FEC-only (triangles); note that, for LNO, this is defined as the onset of continuously increasing O_2 evolution beyond 12 h or 80 %SOC), plotted as a function of the nickel content. From this, it becomes obvious that, in contrast to a previous report by Jung et al., stating a stability limit of 80 %SOC for NCM111, NCM622, and NCM811,[28] the stability limit is a function of the composition of the CAM: It increases with increasing nickel content from $\sim$66 to $\sim$79, $\sim$85, and $\sim$84 %SOC for NCM111, NCM622, NCM851005, and LNO, respectively. For the NCMs as well as for LNO, the stability limits determined by these two independent methods coincide within an error of not more than

±3 %SOC (or ±8 mAh/g_{CAM}). For LCO, however, a larger deviation between the two values is obtained and, in contrast to the other CAMs, the stability limit obtained from the O_2 evolution (left-most open mint green circle for EC-only in Fig. 6, and open triangle for FEC-only) is 6 to 8 %SOC higher than the one obtained from the capacity fade (left-most mint green square). This difference is assigned to the relatively small absolute amounts of O_2 evolved from the single-crystalline LCO. Additionally, a smaller contribution of O_2 to the total gas amounts is expected for a single-crystalline CAM since the released oxygen is mainly detected as CO_2.[50,69] Therefore, it is assumed that the limit of the O_2 evolution would be found at a lower SOC for a polycrystalline LCO material, which would experience particle cracking during the first charge and thus expose a larger surface area, resulting in a larger total amount of released O_2.

Furthermore, the cracking of the polycrystalline CAMs results in an increase of the discharge capacity for the two most nickel-rich CAMs, as it was discussed for Figs. 2 and 3. This has an unwanted effect on the determination of the stability limits by charge/discharge cycling, as particle cracking is expected to shift the obtained stability limits of NCM851005 and LNO to higher values. Since this capacity increase, observed at 4.3 V_{Li} for NCM851005 and at 4.2 V_{Li} for LNO (see Fig. 2b), is expected to originate from oxygen release and the subsequent particle cracking, the stability limit of NCM851005 and LNO would be expected at lower SOC values. Based on these values, the stability limit in terms of potential is expected between 4.2 and 4.3 V_{Li} (or between 78 and 83 %SOC, when converted by the potential profile in Fig. 1) for NCM851005 and between 4.1 and 4.2 V_{Li} (or 69 and 85 %SOC) for LNO, in contrast to the values found by the criterion defined in Fig. 2 and listed in Table III. Therefore, the stability limit, especially of LNO due to its flat potential profile in the relevant region (see Fig. 1), cannot be determined unambiguously through the charge/discharge cycling experiment. In contrast, the stability limits of 82 %SOC for NCM851005 and 81 %SOC for LNO obtained by the onset of the O_2 release (see Fig. 5 and Table III) are expected to be reliable.

In general, the effect of the CAM particle morphology has to be considered when aiming to determine its stability limit: The investigation of polycrystalline CAMs or CAMs with a high specific surface area are beneficial for the determination of the stability limit by experiments monitoring the gas evolution at high SOC since they release larger gas amounts[50,69]; in contrast, the degradation of the discharge capacity at high SOCs is more pronounced for single-crystalline CAMs with a relatively large particle size.[50,69] For future experiments which intend to determine the stability limit of CAMs, it is expected that the most reliable results are obtained for single-crystalline CAMs with a relatively high specific surface area (i.e., of ~1 m^2), for which relatively large gas amounts are detected and the effect of particle cracking can be excluded.[50,69]

Based on this discussion, the stability limit of the CAMs which was determined by the O_2 evolution is likely overestimated, especially for LCO due to its single-crystalline particle morphology
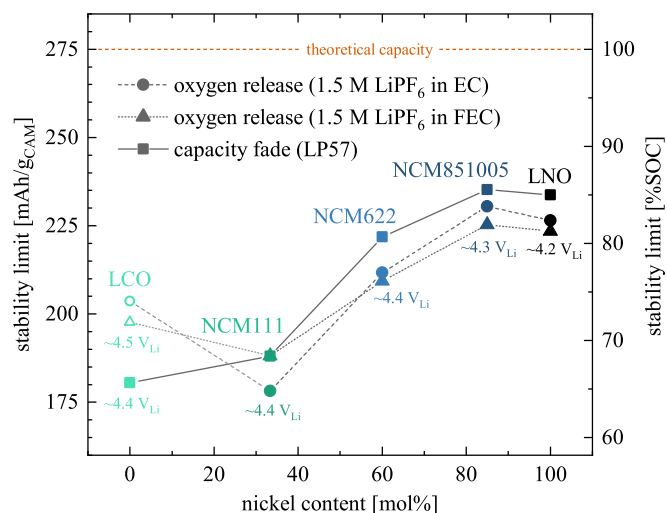
Figure 6. Overview of the determined stability limits of the five CAMs in terms of SOC (i.e., the degree of delithiation x in $Li_{1-x}MO_2$; depicted either in units of mAh/g_{CAM} on the left-hand y-axis or in %SOC based on a theoretical capacity of 275 mAh/g_{CAM} on the right-hand y-axis) as a function of the nickel content of the CAM. The squares mark the stability limit obtained from the cycling data analysis in LP57 shown in Figs. 2 and 3, applying the criterion of -0.5 mAh/g_{CAM}/cycle for the capacity change over a set of three cycles. The circles and the triangles indicate the stability limit obtained from the gas evolution data in EC-only electrolyte and in FEC-only electrolyte, respectively, presented in Figs. 5 and A.4, respectively, applying the criterion of 0.05 μmol_{O_2}/g_{CAM}/h to determine the onset of O_2 evolution (note that the circle and the triangle of LCO, obtained by the O_2 release in EC-only and FEC-only, respectively, is open since the onset SOC of the O_2 could not be determined reliably due to the relatively small absolute amounts of released O_2). The potentials given next to the symbols are extracted from the potential curves (see Fig. 1) at the respective SOC for a given CAM. The orange horizontal dashed line marks the theoretical capacity of 275 mAh/g_{CAM}.

with a relatively small surface area; similarly, an overestimation is also expected for the stability limit obtained by the charge/discharge cycling experiment, especially for the two most nickel-rich CAMs due their relatively flat potential profile in the relevant region between 4.1 and 4.2 V_{Li} and the effect of particle cracking. When considering the lowest stability limit of each CAM, values of 66, 65, 76, 82 and 81 %SOC are found for LCO, NCM111, NCM622, NCM851005, and LNO, respectively (see Table III). However, it must be noted that, in general, the stability limits stated in this study are expected to somewhat overestimate the actual values and to only provide their upper boundary since their determination relies on the detection i) of a small capacity loss within only three cycles, and ii) of relatively small amounts of released O_2.

The here determined values for the stability limits of the various CAMs, however, are in good agreement with the upper cutoff

Table III. Overview of the determined stability limits of the five CAMs in terms of upper cutoff potential as well as of SOC (i.e., the degree of delithiation x in $Li_{1-x}MO_2$). For the stability limit obtained from the cycling data, the criterion of −0.5 mAh/g_{CAM}/cycle for the capacity change over a set of three cycles is applied (from the cycling data in Fig. 2, given in terms of SOC in Fig. 3), while the one obtained from the gas evolution data at high SOC is determined by the criterion of 0.05 μmol_{O_2}/g_{CAM}/h for the O_2 evolution in either EC-only (see Fig. 5) or FEC-only electrolyte (see Fig. A.4).

	Capacity fade (LP57)		Oxygen release (EC-only)		Oxygen release (FEC-only)	
Active material	Potential	State of charge	Potential	State of charge	Potential	State of charge
LCO	4.4 V_{Li}	66 %SOC	4.51 V_{Li}	74 %SOC	4.49 V_{Li}	72 %SOC
NCM111	4.4 V_{Li}	68 %SOC	4.36 V_{Li}	65 %SOC	4.41 V_{Li}	68 %SOC
NCM622	4.5 V_{Li}	80 %SOC	4.42 V_{Li}	77 %SOC	4.40 V_{Li}	76 %SOC
NCM851005	4.4 V_{Li}	86 %SOC	4.33 V_{Li}	84 %SOC	4.26 V_{Li}	82 %SOC
LNO	4.2 V_{Li}	85 %SOC	4.19 V_{Li}	82 %SOC	4.19 V_{Li}	81 %SOC

potentials enabling stable cycling in practical cells (note that the listed potentials obtained in full-cell experiments were translated to V_{Li} by the graphite potential of ∼0.1 V_{Li}; furthermore, the values of the available capacity were not compared, as they are affected by the first-cycle IRC of the CAM and/or the irreversible losses of the SEI in full-cells): From long-term cycling experiments, the stability limit is reported to be ∼4.4 V_{Li} for LCO,[5,99] ∼4.5 V_{Li} for NCM111,[14,28,30] ∼4.4 V_{Li} for NCM622,[28] ∼4.3 V_{Li} for NCM851005,[27,100] and ∼4.1 V_{Li} for nickel-rich CAMs with nickel contents of 90 to 95 mol%,[31] all agreeing well with the stability limits found in this work (see Fig. 6 and Table III). Here, it must be noted that it is challenging to determine the exact SOC value for LNO since the onset of the degradation occurs during the potential plateau of the H2→H3 phase transition at ∼4.2 V_{Li}, which covers ∼55 mAh/g$_{CAM}$ (or ∼20 %SOC, respectively; see Fig. A.1) of the capacity of LNO. Based on our observations, however, even though there is an uncertainty in the determination of the exact SOC of the stability limit, the clear correlation of capacity fade and gas evolution hints towards the degradation of the CAMs solely induced by the release of lattice oxygen and the concomitant formation of a resistive oxygen-depleted layer at the exposed CAM particle surface.

However, even though previous studies have observed a beneficial effect of EC-free electrolytes on the long-term performance,[101] possibly owed to their reduced reactivity with the nickel-rich CAMs changing the extent of the release of lattice oxygen,[102] the stability limit of each CAM obtained by OEMS is essentially identical for both EC-only and FEC-only electrolyte. Based on these findings, the release of oxygen is not attributed to the extraction of the oxygen from the CAM lattice by the solvent molecules; instead, we believe that the CAM lattice becomes structurally unstable with increasing degree of delithiation, forms a spinel- or rock-salt-type structure, and releases the surplus lattice oxygen, independent of the used (cyclic or linear) carbonate-based electrolyte components. To exclude or demonstrate the impact of the used electrolyte components on the onset of the oxygen release, future studies should investigate the effect of linear carbonates on the stability limit of the CAMs as well as the role of carbonate-free electrolytes.

In principle, it could be argued that the electrochemical stability window of the electrolyte components is exceeded at higher SOCs for nickel-rich CAMs, as their potential curve is shifted to lower values (see Fig. 1), allowing to extract more capacity in the stability window of the electrolyte. For the increasing stability limit in terms of SOC, however, the corresponding upper cutoff potential is not the same for the five CAMs but decreases with increasing nickel content (see Fig. 6 and Table III). In addition, based on the current and gas evolution data presented in Fig. A.5, the stability window of the two electrolytes (i.e., LP57 and 1.5 M LiPF$_6$ in EC) extends to ∼4.5 V_{Li} (at least, at 25 °C). Since the structural stability limit of the CAMs (between 4.2 and 4.5 V_{Li}) is up to 300 mV lower than the oxidative stability limit of the electrolyte, a CAM degradation induced by the electrochemical oxidation of the electrolyte can be excluded. Furthermore, the determination of the structural stability limit by the O$_2$ evolution is completely independent from the electrochemical oxidation of the electrolyte since no O$_2$ is evolved from the C65 electrode for both LP57 as well as the EC-only electrolyte, even up to 5.2 V_{Li} (see Fig. A.5). These observations prove that the CAM degradation solely stems from the structural (in)stability of the CAMs upon delithiation.

For the CAMs containing only one type of transition metal, their structural instability at high SOC is often assigned to the CAM degradation induced by the phase transitions at ∼50 %SOC for LCO[5,6,60] and at ∼75 %SOC for LNO[31,54,63] (see Fig. A.1). Since the stability limits determined in this study occur at ∼65 %SOC for LCO (based on the capacity-fade criterion) and at ∼84 %SOC for LNO (i.e., ∼10 %SOC higher than the respective phase transformations for both CAMs), we ascribe the observed release of lattice oxygen, indicating the structural instability of the CAMs, likely to be induced by the respective phase transformations of each CAM.
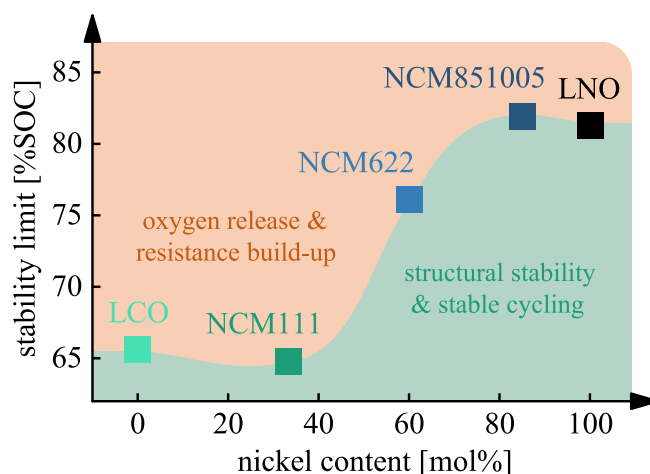
Scheme 1. Graphical summary of the key findings of this work, based on the results of the cycling data analysis summarized in Fig. 6 and depicting the structural stability limit as a function of the nickel content (here, the lowest SOC value is chosen from Table III for each CAM). The green region highlights the SOC window for which the CAMs are structurally stable, while oxygen release and impedance build-up occur in the orange region, all depending on the nickel content.

In the pristine state (i.e., at a degree of delithiation of 0 %SOC), the mean average oxidation state of the transition metals in all five CAMs is M^{3+} (due to the oxidation states of Li^{1+} and O^{2-}), while it is M^{4+} for the complete delithiation at 100 %SOC (if structure and stoichiometry are maintained). For LNO at 75 %SOC, nickel is in the state of Ni$^{3.75+}$ since the oxidation of oxygen starts to occur above 75 %SOC.[53] When oxygen is oxidized in the solid state due to the extraction of the lithium ions, it forms peroxo-like or molecular oxygen bonds, as it is also observed for lithium-rich NCMs, e.g., during the potential plateau of the first charge.[103–105] For this class of lithium-rich materials, it is known that oxygen can be reversibly oxidized and reduced in the bulk; in the surface-near regions, however, oxygen redox is directly correlated to the release of lattice oxygen.[59,105–107]

For the conventional/stoichiometric NCMs (i.e., LiMO$_2$) investigated in this study, manganese is expected to be present only in the form of Mn^{4+}, independent of the degree of delithiation.[108,109] Therefore, an increasing manganese content would reduce the oxidation state of the other transition metals in the pristine state; however, during delithiation, their oxidation state would increase more rapidly as compared to manganese-poor materials since nickel (and cobalt) would have to compensate for the exchanged charge. If one were to assume that oxygen redox and oxygen release initiate at Ni$^{3.75+}$ for these NCMs, an increasing manganese content would shift the onset of the oxygen release and the concomitant degradation of the CAMs to lower SOCs, as it was suggested previously by Streich et al. based on the DEMS measurements.[48] Exemplarily for NCM111 with a manganese content of 33 mol%, the onset would be shifted to 50 %SOC as compared to LNO with 75 %SOC, while the experimental values are ∼67 and ∼84 %SOC, respectively (see Figs. 2 and 5). For the mixture of nickel, cobalt, and manganese, however, a more thorough analysis of the oxidation states of nickel and cobalt as well as of the density of states of the transition metals would have to be performed. Nevertheless, the observed increased stability of nickel-rich (or manganese-poor) CAMs follows the nickel oxidation state, which is affected by the degree of delithiation as well as the overall CAM composition, as it is summarized graphically in Scheme 1.

Conclusions

The structural stability was investigated for five CAMs with different transition metal composition as a function of upper cutoff potential or SOC (defined as the degree of delithiation x in

Li$_{1-x}$MO$_2$), focusing on the impact of an increased nickel content (from LCO over the three NCMs to LNO). Due to the effect of the composition on the potential profile of the different CAMs, more capacity was extracted at the same potential for a higher nickel content. To assess the stability limit in cycling experiments, a test procedure using half-cells with a lithium-metal reference electrode and LP57 electrolyte (1 M LiPF$_6$ in EC:EMC) consisting of sets of three charge/discharge cycles to increasingly higher upper cutoff potentials was applied. This test revealed the stability of the CAMs through the onset of capacity fading within a given set of cycles (based on the criterion of -0.5 mAh/g$_{CAM}$/cycle), providing a convenient and fast tool to identify the stability limit of newly developed CAMs. Here, a higher stability limit in terms of SOC was found for nickel-rich CAMs since it increased from ~66 %SOC for LCO and ~65 %SOC for NCM111 to ~86 %SOC for NCM851005, while the stability limit in terms of potential varies between 4.2 and 4.5 V$_{Li}$. The independent analysis of the deviation of the observed discharge capacities from the potential profile of the first charge as a function of SOC provides further evidence for a significant difference in stability limit depending on the CAM composition. The different stability limits were then substantiated using a cycling procedure over 200 charge/discharge cycles, by which an increasing upper SOC of 60, 70, 80, and 90 %SOC (controlled by the upper cutoff potential) was applied to NCM111 and NCM851005, exhibiting capacity fading and resistance build-up at SOCs that were consistent with those found in the above described analysis, showing stable cycling up to ~70 %SOC for NCM111 and up to ~80 %SOC for NCM851005.

To exclude any impact of electrochemical electrolyte oxidation on the determined stability window of the CAMs, on-line electrochemical mass spectrometry (OEMS) experiments were first performed using C65 electrodes, yielding potentials for the onset of electrolyte oxidation for the LP57 electrolyte and an EC-only electrolyte (1.5 M LiPF$_6$ in EC) electrolyte of $\geqslant$4.5 V$_{Li}$ at 25 °C. Subsequently, OEMS experiments using CAM electrodes and either EC-only or FEC-only (1.5 M LiPF$_6$ in FEC) electrolyte revealed that the oxygen release from the CAM lattice in delithiated state occurs simultaneously with the onset of the capacity fade determined in the cycling experiments in LP57, i.e., at the same SOCs/potentials. Moreover, the results did not depend on the used electrolyte, i.e., the release of lattice oxygen occurred at the same SOCs/potentials for both EC-only and FEC-only electrolyte. For LCO and LNO, the oxygen release was assigned to the phase changes at 50 %SOC and 75 %SOC, respectively. Furthermore, additional (relatively small but significant) oxygen evolution appeared for LNO in two steps already at lower SOCs, coinciding with the phase transitions at 39 and 62 %SOC.

Due to these observations, the stability limit of the CAMs is ascribed to the release of lattice oxygen, inducing the degradation of the CAMs through the formation of a resistive oxygen-depleted surface layer. Since this degradation is not only a function of potential/SOC but also of the composition, nickel-rich NCMs will provide stable cycling with a higher available specific capacity and higher specific energy in commercial lithium-ion batteries. The data obtained in this study for (undoped, uncoated, and not post-treated) NCM851005 suggest a maximum available discharge capacity of 202 mAh/g$_{CAM}$ and specific energy of 778 Wh/g$_{CAM}$ in the stable regime of the SOC window below 4.4 V$_{Li}$.

CRediT Authorship Contribution Statement

Stefan Oswald: Methodology, Investigation, Writing - Original Draft. Hubert A. Gasteiger: Conceptualization, Writing - Review & Editing.

Acknowledgment

Appendix

Specific differential capacity of LCO and LNO.—To allow for the interpretation of the observed stability limits of LCO and LNO, the phase transitions of the two CAMs were illuminated by the dq/dV analysis of the first charge. The plateaus of the potential profiles, shown in Figs. A.1a and A.1c for LCO and LNO, respectively, transform to peaks when presented in terms of specific differential capacity in Figs. A.1b and A.1d. These peaks can be ascribed to the phase transitions for LCO[5,6,60,61,110] and LNO,[11,54,62,63] respectively. For both materials, five phase transitions are observed between the fully lithiated and fully delithiated state. The ones relevant for this study, occurring at 47 and 52 %SOC for LCO and at 39, 62, and 80 %SOC for LNO, are highlighted in Fig. A.1 by dashed lines, which are referred to in the discussion of the OEMS experiments shown in Figs. 5 and A.4.

Potential curves of the first (dis)charge.—To obtain the IRC of the first (dis)charge cycle for each of the five CAMs (marked by the horizontal dashed lines in Fig. 3b), the difference of the charge capacity and the discharge capacity of the first cycle was extracted from the
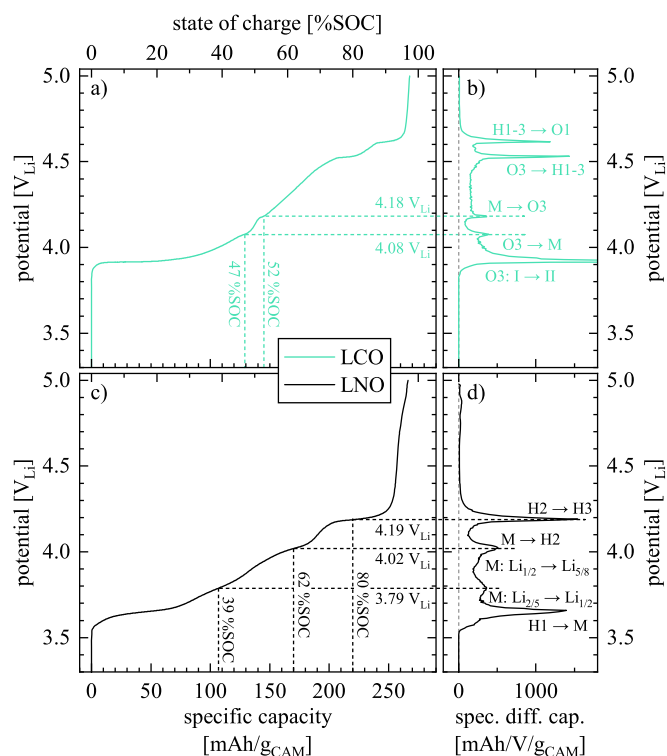

Figure A.1. Comparison of the first charge of LCO and LNO, showing the CAM potential (referenced to the Li-RE) as a function of the specific capacity (in units of mAh/g$_{CAM}$) or of the specific differential capacity (in units of mAh/V/g$_{CAM}$), all extracted from the data presented in Fig. 1: **a)** and **b)** for LCO (mint green); **c)** and **d)** for LNO (black). For the respective specific differential capacity (often referred to as dq/dV plot) as a function of the NCM potential, derived from the potential curves, the *x*- and *y*-axis are switched as compared to the conventional representation for an easier comparison with the potential curves. Distinct redox features or phase transitions appear as peaks, corresponding to plateau-like regions in the potential profiles. The horizontal dashed lines mark the potentials of selected phase transitions, which were converted to the respective SOCs by the potential curve and then indicated in terms of SOC by the vertical dashed lines. The experiments were conducted with CAM loadings of 10.3 ± 1.0 mg$_{CAM}$/cm^2 and in LP57 electrolyte.
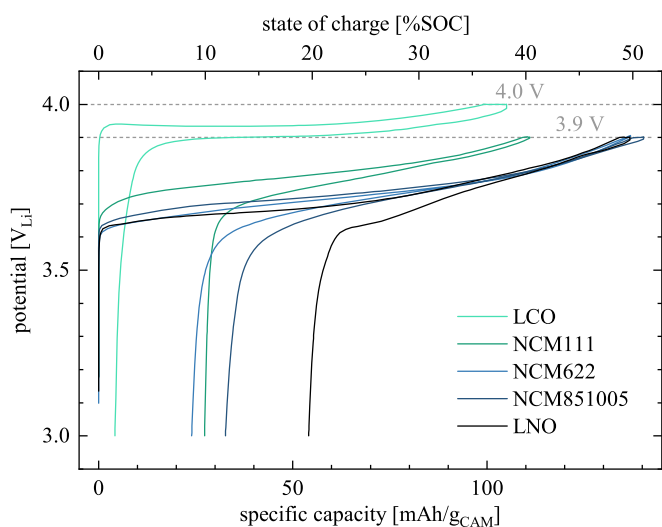
Figure A.2. Comparison of the first (dis)charge to 4.0 V_{Li} for LCO (mint green) and to 3.9 V_{Li} for NCM111 (elf green), NCM622 (blue), NCM851005 (dark blue), and LNO (black), showing the CAM potential recorded against the Li-RE as a function specific capacity (bottom *x*-axis, in units of mAh/g_{CAM}) or SOC (top *x*-axis, in %SOC, calculated for a theoretical capacity of 275 mAh/g_{CAM}), extracted from the experiments presented in Fig. 2, which were conducted with CAM loadings of 10.3 ± 1.0 mg$_{CAM}$/cm^2 in LP57 electrolyte.

data presented in Fig. A.2 (shown only for one cell for each CAM). The calculation of the mean values as well as of the experimental errors from the two cells of each CAM yields first-cycle IRCs of 4.1 ± 0.1, 27.4 ± 0.1, 24.7 ± 0.7, 33.0 ± 0.4, and 53.9 ± 0.2 mAh/g_{CAM} for LCO, NCM111, NCM622, NCM851005, and LNO, respectively; these are plotted as horizontal dashed lines in Fig. 3b.

Mean discharge voltage and specific discharge energy.—Since the available specific discharge energy of the CAM is not only defined by the discharge capacity but also by the discharge potential curve, the discharge potential as well as the specific discharge energy are calculated from the charge/discharge curves underlying the data presented in Fig. 2. The discharge potential is defined as the mean discharge potential averaged over the exchanged charge, which can be calculated by Eq. 1:

$$\bar{V}_{discharge} = \left. \frac{\int V(q)\, dq}{\int dq} \right|_{discharge} \qquad [1]$$

From Fig. A.3b, it becomes obvious that the mean discharge potential increases continuously with increasing SOC (i.e., as the upper cutoff potential is increased) for the stable regime of the SOC window (closed symbols), and then decreases upon CAM degradation (closed symbols) due the induced overpotentials. LCO shows the highest mean discharge potential over a wide SOC window, while the one of NCM111 is lower by ∼135 mV; the nickel-rich NCMs NCM622 and NCM851005 as well as LNO exhibit a similar mean discharge potential, which is ∼185 mV lower than the one of LCO.

The specific discharge energy, being the product of mean discharge potential and specific discharge capacity (shown in Fig. A.3a), is calculated by Eq. 2:

$$E_{discharge} = \left. \int V(q)\, dq \right|_{discharge} = \bar{V}_{discharge} \cdot q_{discharge} \qquad [2]$$

Even though the relatively high mean discharge potential of LCO increases its specific discharge energy, the maximum reversibly available energy (closed symbols in Fig. A.3c) of LCO does not exceed 688 Wh/kg_{CAM}, while the one of NCM111 amounts to 618 Wh/kg_{CAM}. With increasing nickel content, the available specific energy increases to 737, 778, and 686 Wh/kg_{CAM} for
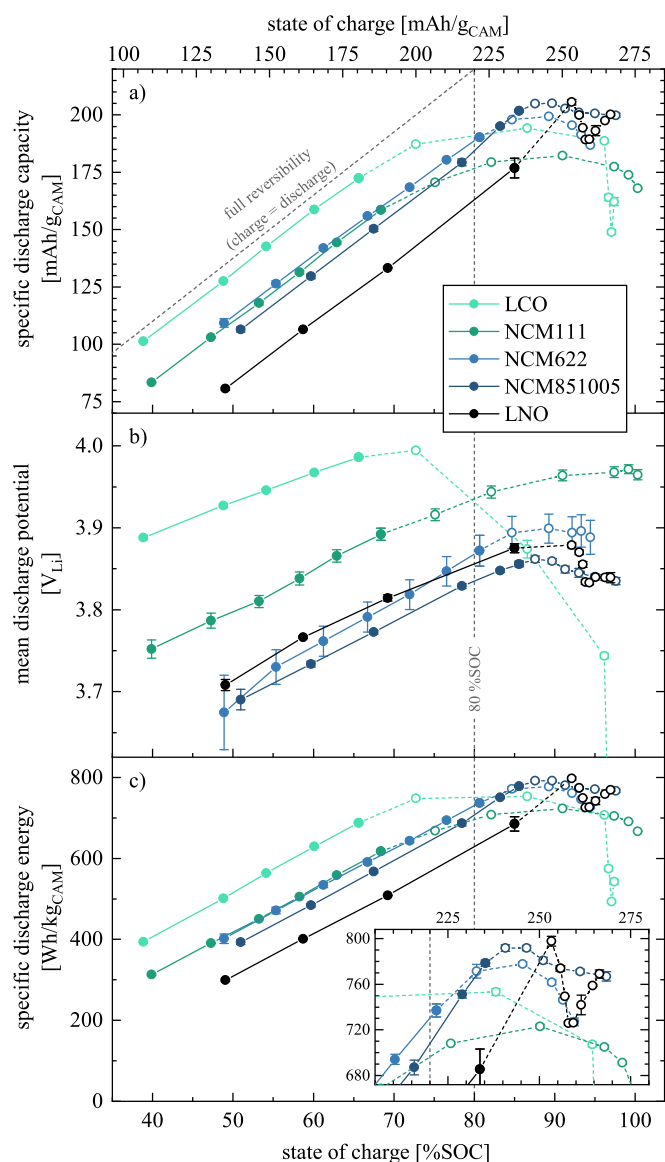
Figure A.3. Electrochemical cycling data of LCO (mint green), NCM111 (elf green), NCM622 (blue), NCM851005 (dark blue), and LNO (black) as a function of SOC, extracted from the cycling data shown in Fig. 2. The obtained specific discharge capacity, average discharge potential, and specific discharge energy are presented here for every third cycle as a function of SOC (similar to Fig. 3). **a)** Specific discharge capacity (same as in Fig. 3a). The gray dashed line (bisecting line, with a slope of 1 through the origin of the graph) represents the line of full reversibility, i.e., that the discharge capacities for the respective SOC would appear on this line for a CAM which could (de)intercalate all lithium fully reversibly at any given SOC, i.e., in the absence of any first-cycle IRC. **b)** Mean discharge voltage calculated using Eq. 1. **c)** Specific discharge energy calculated using Eq. 2. All values are calculated from the mean of two nominally identical cells, and the error bars correspond to the minimum/maximum values.

NCM622, NCM851005, and LNO, respectively. Similarly, de Biasi et al. showed that, when the upper cutoff is adjusted for various CAMs in a way that the same gravimetric energy is delivered, only the nickel-rich NCMs exhibited stable cycling,[27] what further supports our findings.

Gas evolution at high state of charge in FEC.—To investigate the effect of the electrolyte solvent on the onset SOC of the oxygen release from the CAM, similar experiments as presented in Fig. 5 are performed, however, using FEC-only electrolyte (1.5 M LiPF$_6$ in FEC) instead of EC-only electrolyte. The results for FEC-only, depicted in Fig. A.4, are essentially identical to the ones obtained in
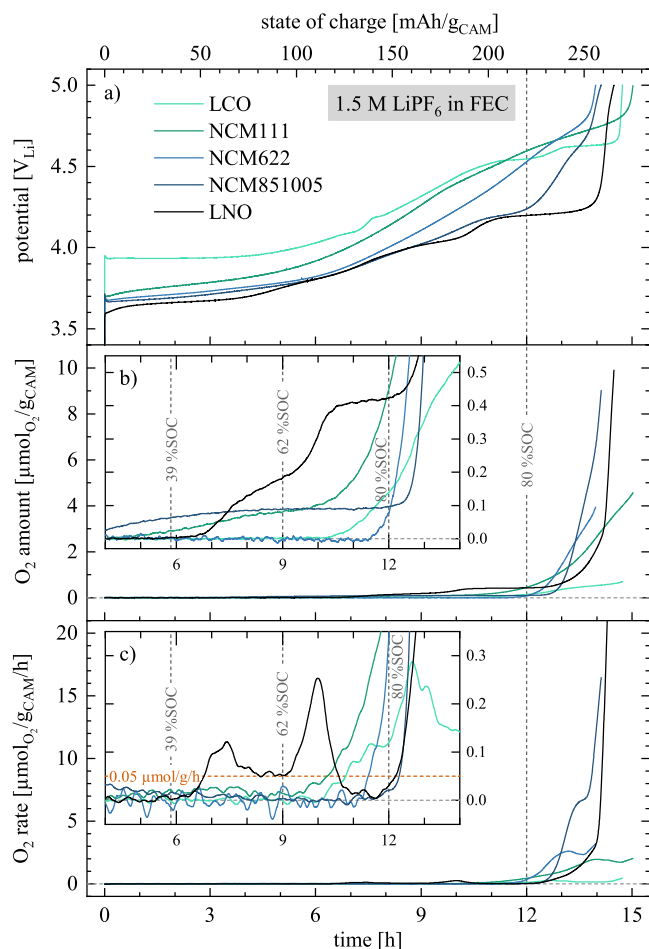
Figure A.4. Electrochemical data and gas evolution measured in OEMS half-cells using the same setup and procedure as for the experiments presented in Fig. 5. As the only difference, FEC-only electrolyte (1.5 M LiPF$_6$ in FEC) was used instead of the EC-only electrolyte. The amount of evolved CO$_2$ was not evaluated, since the reduction of FEC on the Li-CE produced significant amounts of CO$_2$. **a)** CAM potential. **b)** Total amounts of evolved oxygen (O$_2$, $m/z = 32$), respectively, normalized by the CAM mass. **c)** Oxygen evolution rate obtained from the time derivative of the data in Fig. A.4b, with the orange horizontal dashed line in the inset marking the oxygen evolution rate of 0.05 $\mu mol_{O_2}/g_{CAM}$/h. The vertical dashed gray lines mark the SOCs of 39, 62, and 80 %SOC.

Fig. 5 for EC-only: This similarity applies to the shape of the potential curves (see Fig. A.4a) as well as to the amounts (see Fig. A.4b), rates (see Fig. A.4c), and onset SOCs (see Fig. A.4c) of the O$_2$ evolution; furthermore, LNO exhibits the three-step oxygen evolution at ∼39, 62, and 80 %SOC, as already observed in Fig. 5. The onset SOCs of the four investigated CAMs are determined by the criterion of 0.05 $\mu mol_{O_2}/g_{CAM}$/h of the oxygen evolution rate, resulting in a stability limit of 68, 76, 82, and 81 %SOC for NCM111, NCM622, NCM851005, and LNO, respectively. The values are summarized in Table III and depicted in Fig. 6. The amount of evolved CO$_2$ was not evaluated as it was convoluted with the CO$_2$ evolution from the constant reduction of FEC upon plating of lithium on the Li-CE, resulting in more than 1,000 ppm/h of CO$_2$ (corresponding to ∼10 $\mu mol_{CO_2}/g_{CAM}$/h, data not shown), while this was absent for the experiments using EC-only electrolyte.

Electrochemical electrolyte oxidation.—To exclude any effects of the electrochemical oxidation of the electrolyte components and possible follow-up reactions on the performance and the gas evolution of the CAMs, the stability window of the two used electrolytes was investigated by OEMS experiments with C65 electrodes (consisting only of C65 carbon and PVDF binder). Here,
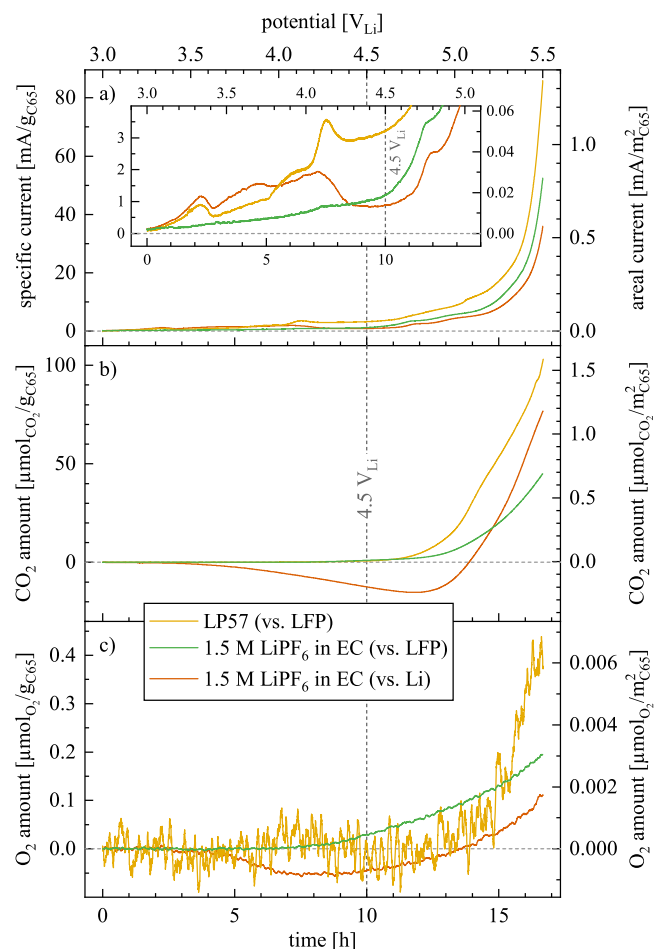
Figure A.5. Electrochemical data and gas evolution of OEMS cells assembled with C65/PVDF WE, using either a Li-CE or a pre-delithiated LFP-CE as well as 300 μl of either LP57 (1.0 M LiPF$_6$ in EC:EMC 3:7 w/w) or EC-only electrolyte (1.5 M LiPF$_6$ in EC). The potential of the cells was scanned at 25 °C from 3.0 to 5.5 V$_{Li}$ at 150 mV/h (corresponding to a duration of ∼13.3 h before a potential of 5.0 V$_{Li}$ was reached, what is comparable to the data presented in Figs. 5 and A.4 for a CC charge of the CAM electrodes) while the gas evolution was recorded by mass spectrometry. All data are shown as a function of both time (lower x-axis) and potential of the C65 electrode (top x-axis). **a)** Specific current (left-hand y-axis, normalized by the C65 mass) and surface-area-normalized current density (right-hand axis, normalized by 64 m$^2_{BET}$/g$_{C65}$). **b)** and **c)** Total amounts of evolved carbon dioxide (CO$_2$, $m/z = 44$) and oxygen (O$_2$, $m/z = 32$) in the OEMS cell, respectively, either normalized by the mass (left-hand y-axes) or the surface area (right-hand y-axes) of C65 in the cell. The vertical dashed gray line marks the potential of 4.5 V$_{Li}$.

the potential-dependent electrochemical electrolyte oxidation is tracked by the oxidative current and the evolving gases. By using C65-PVDF electrodes with a relatively high absolute surface area of ∼0.18 m$^2_{electrode}$ (based on the specific surface area of 17.9 m^2/g$_{electrode}$ of C65-PVDF electrodes[69] as well as the mass loading of ∼10 mg$_{C65}$ of the electrodes), the oxidation current and the gas evolution rates due to electrolyte oxidation are magnified compared to the CAM electrodes, which have a ∼3.5-fold lower overall surface area of ∼0.05 m$^2_{electrode}$. For the cell containing LP57 electrolyte and a pre-delithiated LFP-CE (yellow data in Fig. A.5), the current profile (see Fig. A.5a) yields an exchanged charge of 15.6 mAh/g$_{C65}$ up to 4.5 V$_{Li}$, what we ascribe to the electrochemical oxidation of impurities (e.g., alcohols such as ethylene glycol, ethanol, etc.), which typically remain from the synthesis of the carbonate-based solvents.[89] This is a reasonable assumption, as 15.6 mAh/g$_{C65}$ correspond to ∼0.43 mAh/g$_{electrolyte}$ (based on the C65 mass of ∼10 mg$_{C65}$, the electrolyte volume of 300 μl, and an LP57 electrolyte density of ∼1.2 g/ml), which, for a two-electron oxidation reaction of a given impurity (e.g., the oxidation of an alcohol to an

aldehyde), would require an impurity level of only ∼300 ppm (assuming a molecular weight of ∼50 g/mol, as it would be the case for ethanol or ethylene glycol).

For the EC-only electrolyte with LFP (green), the observed current is smaller than the one for LP57, yielding an exchanged charge of only 5.4 mAh/g_{C65} (or 0.12 mAh/$g_{electrolyte}$, based on the EC-only electrolyte density of ∼1.5 g/cm^3)[111] up to 4.5 V_{Li}, which is ascribed to the higher purity of the used EC (following the above given estimate, this would correspond to an impurity level of only ∼100 ppm). When LFP is replaced by a Li-CE (ocher), the observed currents are higher than for the measurements with an LFP-CE, likely due to the oxidation of soluble species on the C65 electrode, which are previously formed by the reduction of the electrolyte components on the Li-CE (this does not occur with an LFP-CE due to its high potential). Therefore, a ∼2-fold charge of 11.4 mAh/g_{C65} is exchanged up to 4.5 V_{Li}. Above 4.5 V_{Li}, the current increases rapidly for all three configurations, what is assigned to the electrochemical oxidation of the solvents, i.e., of EC (and EMC).[39]

The electrochemical oxidation of the components above 4.5 V_{Li} is also reflected by the CO_2 evolution (mass-over-charge ratio $m/z = 44$), which is displayed in Fig. A.5b: Up to 4.5 V_{Li}, essentially no CO_2 is detected, while it evolves rapidly above 4.5 V_{Li}. Only when a Li-CE is utilized, the CO_2 signal decreases over the course of the first 12 h up to ∼4.7 V_{Li} due to the reduction of CO_2 at the lithium potential, while it is subsequently dominated by the CO_2 evolution at high potentials.

By monitoring the O_2 signal ($m/z = 32$), as depicted in Fig. A.5c, it becomes obvious that the presence of linear carbonates (here EMC in LP57), that have an order of magnitude higher vapor pressure, negatively affects the signal-to-noise ratio.[36] Similar as for CO_2, a slight consumption of O_2 is observed for the setup comprising a Li-CE. For all three measurement configurations, a slight evolution of O_2 is observed at high potentials (initiating at above ∼4.5 V_{Li}), which is expected to originate from the oxidation of the electrolyte, since the C65 electrode should not contain oxygen (neither in C65 nor in PVDF). However, up to 5.2 V_{Li}, the O_2 signal does not exceed ±0.12 $\mu mol_{O_2}/g_{C65}$ (or 0.002 $\mu mol_{O_2}/m_{C65}^2$) up to 5.2 V_{Li}.

From these observations, significant electrochemical electrolyte oxidation can be excluded at 25 °C for potentials below 4.5 V_{Li}. In addition, its contribution to the O_2 signal in OEMS cells containing CAM is negligible up to 5.2 V_{Li} (see main text).

ORCID

Stefan Oswald ⓘ https://orcid.org/0000-0001-6402-7833
Hubert A. Gasteiger ⓘ https://orcid.org/0000-0001-8199-8703

References

1. K. Mizushima, P. C. Jones, P. J. Wiseman, and J. B. Goodenough, *Solid State Ionics*, **15**, 783 (1980).
2. Z. Lu, D. D. MacNeil, and J. R. Dahn, *Electrochem. Solid-State Lett.*, **4**, A200 (2001).
3. N. Nitta, F. Wu, J. T. Lee, and G. Yushin, *Mater. Today*, **18**, 252 (2015).
4. F. Schipper, E. M. Erickson, C. Erk, J.-Y. Shin, F. F. Chesneau, and D. Aurbach, *J. Electrochem. Soc.*, **164**, A6220 (2017).
5. J. N. Reimers and J. R. Dahn, *J. Electrochem. Soc.*, **139**, 2091 (1992).
6. G. G. Amatucci, J. M. Tarascon, and L. C. Klein, *J. Electrochem. Soc.*, **143**, 1114 (1996).
7. Y. Lyu et al., *Adv. Energy Mater.*, **11**, 2000982 (2021).
8. J. R. Dahn, U. von Sacken, and C. A. Michal, *Solid State Ionics*, **44**, 87 (1990).
9. J. R. Dahn, U. von Sacken, M. W. Juzkow, and H. Al-Janaby, *J. Electrochem. Soc.*, **138**, 2207 (1991).
10. T. Ohzuku, A. Ueda, and M. Nagayama, *J. Electrochem. Soc.*, **140**, 1862 (1993).
11. M. Bianchini, M. Roca-Ayats, P. Hartmann, T. Brezesinski, and J. Janek, *Angew. Chemie - Int. Ed.*, **58**, 10434 (2019).
12. T. Ohzuku and Y. Makimura, *Chem. Lett.*, **30**, 642 (2001).
13. M. H. Lee, Y. J. Kang, S. T. Myung, and Y.-K. Sun, *Electrochim. Acta*, **50**, 939 (2004).
14. J. Choi and A. Manthiram, *J. Electrochem. Soc.*, **152**, A1714 (2005).
15. J. Choi and A. Manthiram, *Electrochem. Solid-State Lett.*, **8**, C102 (2005).
16. S. T. Myung, F. Maglia, K. J. Park, C. S. Yoon, P. Lamp, S. J. Kim, and Y.-K. Sun, *ACS Energy Lett.*, **2**, 196 (2017).
17. W. Li, E. M. Erickson, and A. Manthiram, *Nat. Energy*, **5**, 26 (2020).
18. H.-H. Ryu, K.-J. Park, C. S. Yoon, and Y.-K. Sun, *Chem. Mater.*, **30**, 1155 (2018).
19. H. Li, M. Cormier, N. Zhang, J. Inglis, J. Li, and J. R. Dahn, *J. Electrochem. Soc.*, **166**, A429 (2019).
20. C. S. Yoon, H. H. Ryu, G. T. Park, J. H. Kim, K. H. Kim, and Y.-K. Sun, *J. Mater. Chem. A*, **6**, 4126 (2018).
21. Y.-K. Sun, D. J. Lee, Y. J. Lee, Z. Chen, and S.-T. Myung, *ACS Appl. Mater. Interfaces*, **5**, 11434 (2013).
22. H.-J. Noh, S. Youn, C. S. Yoon, and Y.-K. Sun, *J. Power Sources*, **233**, 121 (2013).
23. S. M. Bak, E. Hu, Y. Zhou, X. Yu, S. D. Senanayake, S. J. Cho, K. B. Kim, K. Y. Chung, X. Q. Yang, and K. W. Nam, *ACS Appl. Mater. Interfaces*, **6**, 22594 (2014).
24. C. S. Yoon, K. J. Park, U. H. Kim, K. H. Kang, H. H. Ryu, and Y.-K. Sun, *Chem. Mater.*, **29**, 10436 (2017).
25. I. Shkrob, J. Gilbert, P. J. Phillips, R. Klie, R. T. Haasch, J. Bareño, and D. P. Abraham, *J. Electrochem. Soc.*, **164**, A1489 (2017).
26. J. Sicklinger, M. Metzger, H. Beyer, D. Pritzl, and H. A. Gasteiger, *J. Electrochem. Soc.*, **166**, A2322 (2019).
27. L. de Biasi, A. O. Kondrakov, H. Geßwein, T. Brezesinski, P. Hartmann, and J. Janek, *J. Phys. Chem. C*, **121**, 26163 (2017).
28. R. Jung, M. Metzger, F. Maglia, C. Stinner, and H. A. Gasteiger, *J. Electrochem. Soc.*, **164**, A1361 (2017).
29. A. O. Kondrakov et al., *J. Phys. Chem. C*, **121**, 24381 (2017).
30. J. Kasnatscheew et al., *J. Power Sources*, **359**, 458 (2017).
31. H. Li, A. Liu, N. Zhang, Y. Wang, S. Yin, H. Wu, and J. R. Dahn, *Chem. Mater.*, **31**, 7574 (2019).
32. W. Li, X. Liu, Q. Xie, Y. You, M. Chi, and A. Manthiram, *Chem. Mater.*, **32**, 7796 (2020).
33. K. Xu, S. P. Ding, and T. R. Jow, *J. Electrochem. Soc.*, **146**, 4172 (1999).
34. O. Borodin, W. Behl, and T. R. Jow, *J. Phys. Chem. C*, **117**, 8661 (2013).
35. T. R. Jow, *Electrolytes for Lithium and Lithium-Ion Batteries* (Berlin, Springer) (2014).
36. M. Metzger, C. Marino, J. Sicklinger, D. Haering, and H. A. Gasteiger, *J. Electrochem. Soc.*, **162**, A1123 (2015).
37. J. Kasnatscheew et al., *Phys. Chem. Chem. Phys.*, **18**, 3956 (2016).
38. J. Kasnatscheew, B. Streipert, S. Röser, R. Wagner, I. Cekic Laskovic, and M. Winter, *Phys. Chem. Chem. Phys.*, **19**, 16078 (2017).
39. R. Jung, M. Metzger, F. Maglia, C. Stinner, and H. A. Gasteiger, *J. Phys. Chem. Lett.*, **8**, 4820 (2017).
40. D. Pritzl, S. Solchenbach, M. Wetjen, and H. A. Gasteiger, *J. Electrochem. Soc.*, **164**, A2625 (2017).
41. M. Metzger, P. Walke, S. Solchenbach, G. Salitra, D. Aurbach, and H. A. Gasteiger, *J. Electrochem. Soc.*, **167**, 160522 (2020).
42. D. P. Abraham, R. D. Twesten, M. Balasubramanian, I. Petrov, J. McBreen, and K. Amine, *Electrochem. commun.*, **4**, 620 (2002).
43. S. Venkatraman and A. Manthiram, *Chem. Mater.*, **15**, 5003 (2003).
44. S. Watanabe, M. Kinoshita, T. Hosokawa, K. Morigaki, and K. Nakura, *J. Power Sources*, **258**, 210 (2014).
45. L. Mu et al., *Nano Lett.*, **18**, 3241 (2018).
46. F. Friedrich, B. Strehle, A. T. S. Freiberg, K. Kleiner, S. J. Day, C. Erk, M. Piana, and H. A. Gasteiger, *J. Electrochem. Soc.*, **166**, A3760 (2019).
47. B. Strehle, F. Friedrich, and H. A. Gasteiger, *J. Electrochem. Soc.*, **168**, 050512 (2021).
48. D. Streich, C. Erk, A. Guéguen, P. Müller, F.-F. Chesneau, and E. J. Berg, *J. Phys. Chem. C*, **121**, 13481 (2017).
49. J. K. Papp, N. Li, L. A. Kaufman, A. J. Naylor, R. Younesi, W. Tong, and B. D. McCloskey, *Electrochim. Acta*, **368**, 137505 (2021).
50. S. Oswald, D. Pritzl, M. Wetjen, and H. A. Gasteiger, *J. Electrochem. Soc.*, **168**, 120501 (2021).
51. J. Wandt, A. T. S. Freiberg, A. Ogrodnik, and H. A. Gasteiger, *Mater. Today*, **21**, 825 (2018).
52. A. T. S. Freiberg, M. K. Roos, J. Wandt, R. De Vivie-Riedle, and H. A. Gasteiger, *J. Phys. Chem. A*, **122**, 8828 (2018).
53. N. Li, S. Sallis, J. K. Papp, J. Wei, B. D. McCloskey, W. Yang, and W. Tong, *ACS Energy Lett.*, **4**, 2836 (2019).
54. L. de Biasi, A. Schiele, M. Roca-Ayats, G. Garcia, T. Brezesinski, P. Hartmann, and J. Janek, *ChemSusChem*, **12**, 2240 (2019).
55. S. Solchenbach, D. Pritzl, E. J. Y. Kong, J. Landesfeind, and H. A. Gasteiger, *J. Electrochem. Soc.*, **163**, A2265 (2016).
56. N. Tsiouvaras, S. Meini, I. Buchberger, and H. A. Gasteiger, *J. Electrochem. Soc.*, **160**, A471 (2013).
57. R. Bernhard, M. Metzger, and H. A. Gasteiger, *J. Electrochem. Soc.*, **162**, A1984 (2015).
58. S. Solchenbach, G. Hong, A. T. S. Freiberg, R. Jung, and H. A. Gasteiger, *J. Electrochem. Soc.*, **165**, A3304 (2018).
59. B. Strehle, K. Kleiner, R. Jung, F. Chesneau, M. Mendez, H. A. Gasteiger, and M. Piana, *J. Electrochem. Soc.*, **164**, A400 (2017).
60. Z. Chen and J. R. Dahn, *Electrochim. Acta*, **49**, 1079 (2004).
61. A. J. Merryweather, C. Schnedermann, Q. Jacquet, C. P. Grey, and A. Rao, *Nature*, **594**, 522 (2021).
62. H. Li, N. Zhang, J. Li, and J. R. Dahn, *J. Electrochem. Soc.*, **165**, A2985 (2018).
63. M. Mock, M. Bianchini, F. Fauth, K. Albe, and S. Sicolo, *J. Mater. Chem. A*, **9**, 14928 (2021).

64. S. Watanabe, M. Kinoshita, T. Hosokawa, K. Morigaki, and K. Nakura, *J. Power Sources*, **260**, 50 (2014).
65. C. S. Yoon, D. W. Jun, S. T. Myung, and Y.-K. Sun, *ACS Energy Lett.*, **2**, 1150 (2017).
66. M. Wetjen, S. Solchenbach, D. Pritzl, J. Hou, V. Tileli, and H. A. Gasteiger, *J. Electrochem. Soc.*, **165**, A1503 (2018).
67. M. Graf, C. Berg, R. Bernhard, S. Haufe, J. Pfeiffer, and H. A. Gasteiger, *J. Electrochem. Soc.*, **169**, 020536 (2022).
68. J. Kasnatscheew, M. Evertz, R. Kloepsch, B. Streipert, R. Wagner, I. Cekic Laskovic, and M. Winter, *Energy Technol.*, **5**, 1670 (2017).
69. S. Oswald, M. Bock, and H. A. Gasteiger, *J. Electrochem. Soc.*, **169**, 050501 (2022).
70. W. Li, H. Y. Asl, Q. Xie, and A. Manthiram, *J. Am. Chem. Soc.*, **141**, 5097 (2019).
71. K.-K. Lee and K.-B. Kim, *J. Electrochem. Soc.*, **147**, 1709 (2000).
72. D. D. MacNeil, Z. Lu, and J. R. Dahn, *J. Electrochem. Soc.*, **149**, A1332 (2002).
73. N. Zhang, J. Li, H. Li, A. Liu, Q. Huang, L. Ma, Y. Li, and J. R. Dahn, *Chem. Mater.*, **30**, 8852 (2018).
74. Y. Liu, J. Harlow, and J. R. Dahn, *J. Electrochem. Soc.*, **167**, 020512 (2020).
75. P. Kurzhals, F. Riewald, M. Bianchini, H. Sommer, H. A. Gasteiger, and J. Janek, *J. Electrochem. Soc.*, **168**, 110518 (2021).
76. F. Riewald, P. Kurzhals, M. Bianchini, H. Sommer, J. Janek, and H. A. Gasteiger, *J. Electrochem. Soc.*, **169**, 020529 (2022).
77. R. Weber, C. R. Fell, J. R. Dahn, and S. Hy, *J. Electrochem. Soc.*, **164**, A2992 (2017).
78. S. Klein, P. Bärmann, O. Fromm, K. Borzutzki, J. Reiter, Q. Fan, M. Winter, T. Placke, and J. Kasnatscheew, *J. Mater. Chem. A*, **9**, 7546 (2021).
79. H. Zhou, F. Xin, B. Pei, and M. S. Whittingham, *ACS Energy Lett.*, **4**, 1902 (2019).
80. Y. Makimura and T. Ohzuku, *J. Power Sources*, **119–121**, 156 (2003).
81. F. Kong, C. Liang, L. Wang, Y. Zheng, S. Perananthan, R. C. Longo, J. P. Ferraris, M. Kim, and K. Cho, *Adv. Energy Mater.*, **9**, 1802586 (2019).
82. D. Pritzl, T. Teufl, A. T. S. Freiberg, B. Strehle, J. Sicklinger, H. Sommer, P. Hartmann, and H. A. Gasteiger, *J. Electrochem. Soc.*, **166**, A4056 (2019).
83. Y. Makimura, T. Sasaki, T. Nonaka, Y. F. Nishimura, T. Uyama, C. Okuda, Y. Itou, and Y. Takeuchi, *J. Mater. Chem. A*, **4**, 8350 (2016).
84. J. Choi and A. Manthiram, *Solid State Ionics*, **176**, 2251 (2005).
85. J. H. Kim, S. J. Kim, T. Yuk, J. Kim, C. S. Yoon, and Y.-K. Sun, *ACS Energy Lett.*, **3**, 3002 (2018).
86. S. Oswald, D. Pritzl, M. Wetjen, and H. A. Gasteiger, *J. Electrochem. Soc.*, **167**, 100511 (2020).
87. S. Oswald, F. Riewald, and H. A. Gasteiger, *J. Electrochem. Soc.*, **169**, 040552 (2022).
88. J. Langdon and A. Manthiram, *Adv. Funct. Mater.*, **31**, 2010267 (2021).
89. A. T. S. Freiberg, J. Sicklinger, S. Solchenbach, and H. A. Gasteiger, *Electrochim. Acta*, **346**, 136271 (2020).
90. S. E. Renfrew and B. D. McCloskey, *J. Am. Chem. Soc.*, **139**, 17853 (2017).
91. B. Zhang, M. Metzger, S. Solchenbach, M. Payne, S. Meini, H. A. Gasteiger, A. Garsuch, and B. L. Lucht, *J. Phys. Chem. C*, **119**, 11337 (2015).
92. K. U. Schwenke, S. Solchenbach, J. Demeaux, B. L. Lucht, and H. A. Gasteiger, *J. Electrochem. Soc.*, **166**, A2035 (2019).
93. S. Solchenbach, M. Wetjen, D. Pritzl, K. U. Schwenke, and H. A. Gasteiger, *J. Electrochem. Soc.*, **165**, A512 (2018).
94. A. Etxebarria, D. J. Yun, M. Blum, Y. Ye, M. Sun, K. J. Lee, H. Su, M. Á. Muñoz-Márquez, P. N. Ross, and E. J. Crumlin, *ACS Appl. Mater. Interfaces*, **12**, 26607 (2020).
95. N. Mahne, S. E. Renfrew, B. D. McCloskey, and S. A. Freunberger, *Angew. Chemie - Int. Ed.*, **57**, 5529 (2018).
96. U. Heider, R. Oesten, and M. Jungnitz, *J. Power Sources*, **81–82**, 119 (1999).
97. L. Hartmann, D. Pritzl, H. Beyer, and H. A. Gasteiger, *J. Electrochem. Soc.*, **168**, 070507 (2021).
98. R. Jung, R. Morasch, P. Karayaylali, K. Phillips, F. Maglia, C. Stinner, Y. Shao-Horn, and H. A. Gasteiger, *J. Electrochem. Soc.*, **165**, A132 (2018).
99. Y. Jiang, C. Qin, P. Yan, and M. Sui, *J. Mater. Chem. A*, **7**, 20824 (2019).
100. S. Schweidler, L. de Biasi, G. Garcia, A. Mazilkin, P. Hartmann, T. Brezesinski, and J. Janek, *ACS Appl. Energy Mater.*, **2**, 7375 (2019).
101. J. Xia, S. L. Glazier, R. Petibon, and J. R. Dahn, *J. Electrochem. Soc.*, **164**, A1239 (2017).
102. W. M. Dose, I. Temprano, J. P. Allen, E. Björklund, C. A. O'Keefe, W. Li, B. L. Mehdi, R. S. Weatherup, M. F. L. De Volder, and C. P. Grey, *ACS Appl. Mater. Interfaces*, **14**, 13206 (2022).
103. R. A. House, G. J. Rees, M. A. Pérez-Osorio, J. J. Marie, E. Boivin, A. W. Robertson, A. Nag, M. Garcia-Fernandez, K. J. Zhou, and P. G. Bruce, *Nat. Energy*, **5**, 777 (2020).
104. D. H. Seo, J. Lee, A. Urban, R. Malik, S. Kang, and G. Ceder, *Nat. Chem.*, **8**, 692 (2016).
105. W. E. Gent et al., *Nat. Commun.*, **8**, 2091 (2017).
106. M. M. Rahman and F. Lin, *Matter*, **4**, 490 (2021).
107. K. Luo et al., *Nat. Chem.*, **8**, 684 (2016).
108. W. S. Yoon, M. Balasubramanian, K. Y. Chung, X. Q. Yang, J. McBreen, C. P. Grey, and D. A. Fischer, *J. Am. Chem. Soc.*, **127**, 17479 (2005).
109. H. J. Shin, M. Kim, N. Kim, C. Jung, J. G. Chung, K. H. Kim, and W. S. Jeon, *J. Phys. Chem. Solids*, **148**, 109732 (2021).
110. Y. Takahashi, N. Kijima, K. Tokiwa, T. Watanabe, and J. Akimoto, *J. Phys. Condens. Matter*, **19**, 436202 (2007).
111. M. Metzger, B. Strehle, S. Solchenbach, and H. A. Gasteiger, *J. Electrochem. Soc.*, **163**, A1219 (2016).

6 Conclusion and Outlook

The overall goal of this PhD thesis was the thorough investigation and comprehensive understanding of degradation phenomena associated with layered lithium transition metal oxides used as cathode active material for lithium-ion batteries. This work focused on crucial processes including particle cracking (by FIB-SEM, Kr-BET, and EIS), the release of lattice oxygen in the near-surface region at high SOC (by OEMS) or upon heating (via TGA-MS), and the dissolution of transition metals (through elemental analysis). Furthermore, the impact of the particle morphology as well as of the NCM composition on these degradation phenomena was evaluated. The key results of this thesis are summarized by the graphical overview in Figure 6.1.

6.1 Summary of the Key Developments

In the first part (see Chapter 3), three studies introduced the development, validation, and application of a novel method which allows to track the surface area of an electrode and thus the particle cracking of an active material. For this approach, the capacitance of an electrode in blocking conditions, which was proven to be directly proportional to the electrochemically active surface area of the electrode by krypton-gas physisorption experiments, was extracted from the imaginary impedance at a frequency of 180 mHz using in situ electrochemical impedance spectroscopy. This powerful and convenient characterization tool is able to monitor the evolution of the surface area quantitatively without the need to disassemble the cell, in contrast to alternative post-mortem techniques such as microscopy or gas physisorption. By these means, the cracking of NCM particles was quantified upon mechanical compression (see Chapter 3.1), upon extended cycling for three upper cutoff potentials (see Chapter 3.1), or upon the release of lattice oxygen at high SOC (see Chapter 3.2). To allow for a broad accessibility of the impedance-based method, the originally introduced configuration (requiring a pre-lithiated lithium titanate (LTO) counter electrode as well as a micro-reference electrode (μ-RE)) was modified to enable its use with a conventional coin (half-)cell setup without μ-RE. Furthermore, it was shown that the capacitance does not have to

be extracted from a full impedance spectrum provided by an impedance analyzer but that it can be obtained solely from a low-frequency single-point impedance measurement, which can be performed using a conventional battery cycler, enabling an easy implementation in standard cycling procedures (see Chapter 3.3).

In the second part (see Chapter 4), three studies demonstrated the implications of the polycrystalline and the single-crystalline NCM particle morphology on the surface area changes upon mechanical compression, during the (de)lithiation within the first charge/discharge cycle, as well as at high SOC. Due to the observed absence of particle cracking for the SC NCM, the beneficial effect of the particle morphology was elucidated regarding the extent of gas evolution, the rate capability, and the thermal stability (see Chapter 4.1) as well as the transition metal dissolution, the impedance build-up, and the capacity retention in full-cells (see Chapter 4.3). In particular under harsh operating conditions, i.e., for a high upper cutoff potential and elevated temperatures, the aged SC NCM was superior after extended cycling regarding the rate capability due to the threefold internal cell resistance of the aged PC NCM. Furthermore, the effect of the electrode composition, i.e., the content of conductive carbon, on the contact resistance of an electrode as well as on the impedance-based determination of the capacitance of an electrode were evaluated and, consequently, the limitations of the developed impedance-based method were discussed critically (see Chapter 4.2).

In the final part (see Chapter 5), the structural stability was investigated for five CAMs with different composition as a function of upper cutoff potential or SOC. To assess the stability limit in cycling experiments, a test procedure with an increasing upper cutoff potential revealed the stability limit of the CAMs through the onset of capacity fading, providing a convenient tool to identify the stability limit of newly developed CAMs. Here, a higher stability limit in terms of SOC was found for nickel-rich CAMs, which was then substantiated by extended cycling experiments over 200 cycles to various SOCs as well as by OEMS measurements. OEMS revealed that the oxygen release from the CAM lattice in delithiated state occurs simultaneously with the onset of the capacity fade determined in the cycling experiments. Due to these observations, the structural stability limit of the CAMs was ascribed to the release of lattice oxygen, inducing the degradation of the CAMs through the formation of a resistive oxygen-depleted surface layer, resulting in loss of active material and impedance build-up.

In summary, the precise characterization and quantification of the degradation phenomena of different NCM morphologies and NCM compositions enables the optimization of the particle properties to improve the available capacity and the performance
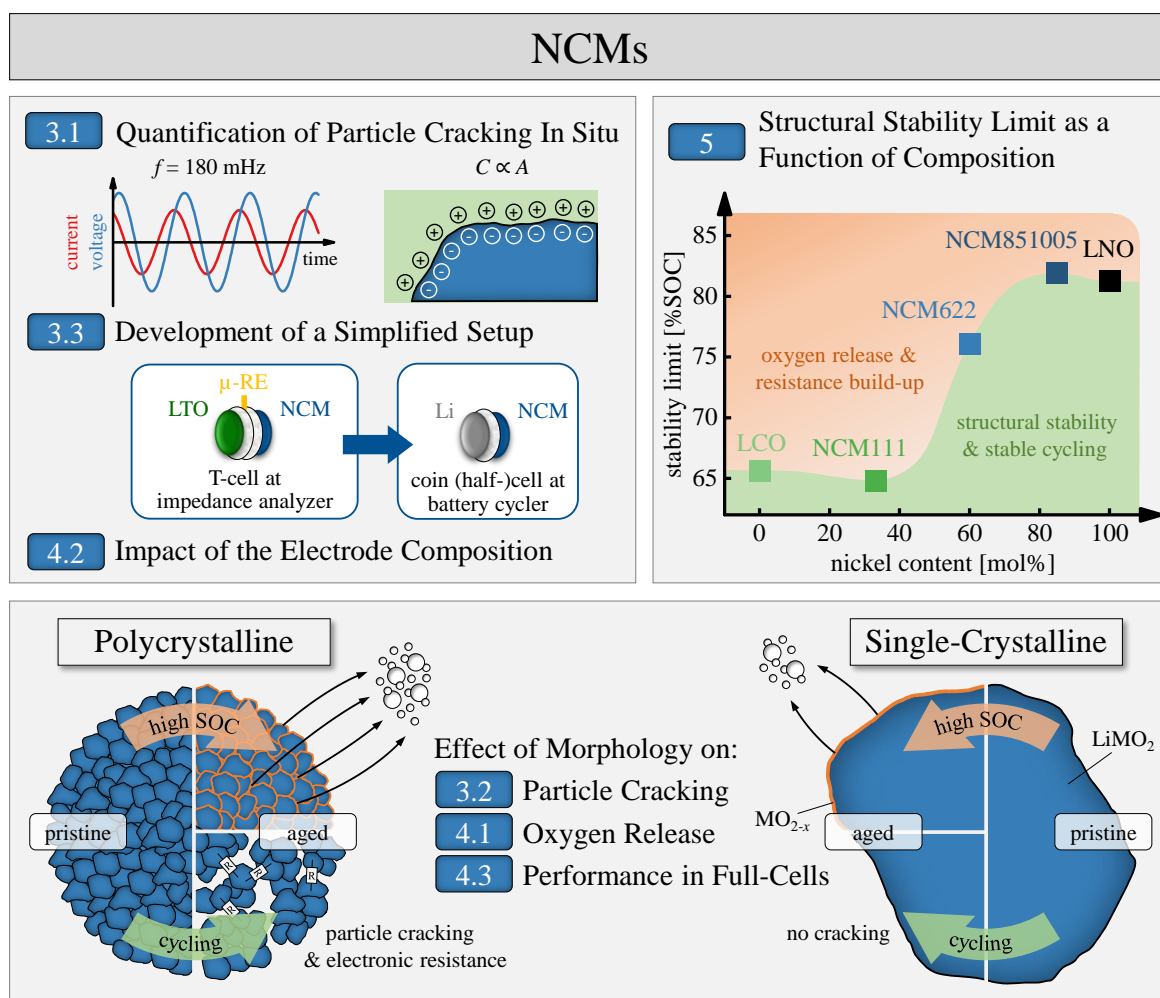
Figure 6.1 Graphical summary of the key results of this PhD thesis, with the numbers in the blue boxes referring to the respective chapters in this thesis. To quantify particle cracking (top-left), a newly developed method enables to quantify the surface area of an electrode by monitoring the capacitance of the electrochemical double layer (see Chapter 3.1). For this approach, the capacitance of an electrode in blocking conditions is extracted from the imaginary impedance at a frequency of 180 mHz using electrochemical impedance spectroscopy. The originally introduced cell configuration, requiring a pre-lithiated LTO counter electrode, a μ-RE, and a potentiostat with impedance capability, was modified to allow the use of a conventional coin (half-)cell setup without μ-RE at a battery cycler (see Chapter 3.3). The impact of the electrode composition on the determination of the capacitance and the limitations of the method are discussed critically (see Chapter 4.2). Furthermore, by comparing the polycrystalline and the single-crystalline particle morphology (bottom), the effect of the morphology on the degradation phenomena of nickel-rich NCMs ($LiMO_2$) was elucidated. For the PC NCM, both extended cycling as well as a high SOC result in the cracking of the secondary agglomerates, while the SC particles remained intact (see Chapter 3.2). At high SOC, lattice oxygen is released from the NCM surface, being more pronounced for the PC NCM due to the exposure of inner surfaces (see Chapter 4.1). Upon extended cycling to a high upper cutoff potential and at elevated temperatures, particle cracking and the formation of a resistive oxygen-depleted surface layer (MO_{2-x}) induce electronic resistances within the secondary agglomerates, resulting in a diminished rate capability of the PC NCM in contrast to the SC NCM (see Chapter 4.3). Finally, through the determination of the structural stability limit of LCO, LNO, and NCMs dependent on their composition (top-right), both by electrochemical cycling experiments as well as through the onset of oxygen evolution in OEMS, the window for stable operation is found to reach higher SOCs for nickel-rich NCMs, providing more capacity without oxygen release and resistance build-up (see Chapter 5).

191

of nickel-rich NCMs, and thus the energy density and the cycle life of future LIBs. The findings of this work imply that a combination of two approaches, i.e., the targeted design of a single-crystalline particle morphology in combination with a surface doping or a radial gradient of the nickel content can overcome the current stability limit of conventional polycrystalline NCMs with a homogeneous composition. These customized µm-sized single-crystalline NCM particles may, e.g., feature a core with a nickel content of >85 mol% and an NCM111 surface layer. For an upper cutoff potential of 4.3 V_{Li}, which is still below the onset potential of the electrochemical electrolyte oxidation, the NCM111 surface would be delithiated to a degree of delithiation of 63 %SOC, which is still below the onset of oxygen release, while the nickel-rich core would deliver a capacity of 229 mAh/g for NCM851005 or 254 mAh/g for LNO. For an NCM111 surface layer of 10 wt%, the cathode active material can provide an overall specific capacity of 223 to 246 mAh/g, surpassing the typical capacity of nickel-rich NCMs by 2 to 12 %. If it was possible to synthesize such a customized NCM, ideally for a reasonable price, and if it could be repeatedly (de)lithiated without crack formation, the nickel-core would remain protected and the available capacity and, therefore, the energy density of LIBs could be enhanced significantly.

6.2 Potential Future Applications

The developed impedance-based method, enabling the determination of the surface area of an electrode in situ, provides a convenient and powerful analytical tool to quantify particle cracking. The use of this technique would facilitate quality management in CAM production by precisely measuring the surface area of synthesized CAMs. Furthermore, in electrode production, the extent of particle cracking upon electrode calendering can be monitored, which may be detrimental, e.g., for NCMs with a sensitive nickel-rich core, either synthesized with a radial gradient of the nickel content or for coated, surface-doped, or gas-treated CAMs. In symmetric cells, the determination of the pristine surface area using the single-point low-frequency impedance determination at 180 mHz takes only minutes, which enables the large-scale application with a high throughput as compared to the known alternative employing gas physisorption measurements on the order of hours. Furthermore, the method enables the tracking of the effect of synthesis conditions and particle morphology on particle cracking upon operation in situ, using simple half-cells without µ-RE, which are already used as a standard characterization tool.

Moreover, the results of this thesis indicate that the release of lattice oxygen is the main contributor to the degradation of layered lithium transition metal oxide CAMs and their loss of capacity at high SOC. Therefore, future work should focus on the optimization of the structural stability of the surface-near regions of nickel-rich NCMs by surface coatings and surface dopings. Even though the determination of the onset of oxygen release was tracked by intricate gas evolution measurements, the findings of this work enable to extract the stability of a CAM from simple charge/discharge cycling experiments with increasing upper cutoff potential. As this technique can be performed in simple half-cells, requiring only one (or two) cells per CAM, it provides a powerful screening tool for the research and development of CAMs. In particular, the benefits of surface dopings and surface coatings of polycrystalline NCMs can be verified, as they expose (possibly undoped/-coated) surfaces upon operation, while the single-crystalline NCMs may serve as model materials to evaluate the effectiveness of the used elements or compounds for surface dopings and/or coatings with regard to the structural stability of NCM CAMs.

Bibliography

[1]   Ritchie, H., Roser, M. & Rosado, P. *CO$_2$ and Greenhouse Gas Emissions* https://ourworldindata.org/co2-and-other-greenhouse-gas-emissions. [online; accessed 28 July 2022]. 2020.

[2]   Lindsey, R. & Dlugokencky, E. *Climate Change: Atmospheric Carbon Dioxide* https://www.climate.gov/news-features/understanding-climate/climate-change-atmospheric-carbon-dioxide. [online; accessed 28 July 2022]. 2022.

[3]   Liu, Z., Deng, Z., Davis, S. J., Giron, C. & Ciais, P. Monitoring global carbon emissions in 2021. *Nature Reviews Earth & Environment* **3,** 217 (2022).

[4]   Jackson, R. B., Friedlingstein, P., Le Quéré, C., Abernethy, S., Andrew, R. M., Canadell, J. G., Ciais, P., Davis, S. J., Deng, Z., Liu, Z., Korsbakken, J. I. & Peters, G. P. Global fossil carbon emissions rebound near pre-COVID-19 levels. *Environmental Research Letters* **17,** 031001 (2022).

[5]   Lacis, A., Hansen, J., Lee, P., Mitchell, T. & Lebedeff, S. Greenhouse Effect of Trace Gases, 1970-1980. *Geophysical Research Letters* **8,** 1035 (1981).

[6]   National Oceanic and Atmospheric Administration. *Global Climate Dashboard* https://www.climate.gov/climatedashboard. [online; accessed 28 July 2022]. 2022.

[7]   United Nations Framework Convention on Climate Change. *The Paris Agreement* https://unfccc.int/process-and-meetings/the-paris-agreement/the-paris-agreement. [online; accessed 29 July 2022]. 2015.

[8]   Tong, D., Farnham, D. J., Duan, L., Zhang, Q., Lewis, N. S., Caldeira, K. & Davis, S. J. Geophysical constraints on the reliability of solar and wind power worldwide. *Nature Communications* **12,** 6146 (2021).

[9]   Crabtree, G. W., Dresselhaus, M. S. & Buchanan, M. V. The hydrogen economy. *Physics Today* **57,** 39 (2004).

[10] Brandon, N. P. & Kurban, Z. Clean energy and the hydrogen economy. *Philosophical Transactions of the Royal Society A* **375,** 20160400 (2017).

[11] International Energy Agency. *Global Hydrogen Review 2021* https://www.iea.org/reports/global-hydrogen-review-2021. [online; accessed 19 December 2022]. 2021.

[12] Grey, C. P. & Hall, D. S. Prospects for lithium-ion batteries and beyond—a 2030 vision. *Nature Communications* **11,** 6279 (2020).

[13] Pellow, M. A., Emmott, C. J. M., Barnhart, C. J. & Benson, S. M. Hydrogen or batteries for grid storage? A net energy analysis. *Energy & Environmental Science* **8,** 1938 (2015).

[14] Pillot, C. *The Rechargeable Battery Market and Main Trends 2018-2030* https://www.bpifrance.fr/content/download/76854/831358/file/02-Presentation Avicenne-ChristophePillot-28Mai2019.pdf. [online; accessed 31 August 2022]. 2019.

[15] Ziegler, M. S. & Trancik, J. E. Re-examining rates of lithium-ion battery technology improvement and cost decline. *Energy & Environmental Science* **14,** 1635 (2021).

[16] Fleischmann, J., Herring, D., Liebach, F. & Linder, M. *Unlocking growth in battery cell manufacturing for electric vehicles* https://www.mckinsey.com/business-functions/operations/our-insights/unlocking-growth-in-battery-cell-manufacturing-for-electric-vehicles. [online; accessed 29 July 2022]. 2021.

[17] Liu, C., Chau, K. T., Wu, D. & Gao, S. Opportunities and challenges of vehicle-to-home, vehicle-to-vehicle, and vehicle-to-grid technologies. *Proceedings of the IEEE* **101,** 2409 (2013).

[18] Statistisches Bundesamt. *Gross electricity production in Germany* https://www.destatis.de/EN/Themes/Economic-Sectors-Enterprises/Energy/Production/Tables/gross-electricity-production.html. [online; accessed 14 September 2022]. 2022.

[19] Zeit Online. *Energiemonitor* https://www.zeit.de/wirtschaft/energiemonitor-deutschland-gaspreis-spritpreis-energieversorgung. [online; accessed 14 September 2022]. 2022.

[20] Woodward, M., Walton, B., Hamilton, J., Alberts, G., Fullerton-Smith, S., Day, E. & Ringrow, J. *Electric vehicles - Setting a course for 2030* https://www2.deloitte.com/us/en/insights/focus/future-of-mobility/electric-vehicle-trends-2030.html. [online; accessed 30 August 2022]. 2020.

[21] Li, W., Erickson, E. M. & Manthiram, A. High-nickel layered oxide cathodes for lithium-based automotive batteries. *Nature Energy* **5,** 26 (2020).

[22] Kraftfahrt-Bundesamt. *Bestand an Kraftfahrzeugen nach Umwelt-Merkmalen* https://www.kba.de/DE/Statistik/Fahrzeuge/Bestand/Umwelt/umwelt_node.html. [online; accessed 11 September 2022]. 2022.

[23] Zubi, G., Dufo-López, R., Carvalho, M. & Pasaoglu, G. The lithium-ion battery: State of the art and future perspectives. *Renewable and Sustainable Energy Reviews* **89,** 292 (2018).

[24] Ender, M. *Mikrostrukturelle Charakterisierung, Modellentwicklung und Simulation poröser Elektroden für Lithiumionenzellen* PhD thesis (Karlsruhe Institute of Technology, 2014).

[25] Xu, K. Electrolytes and Interphases in Li-Ion Batteries and Beyond. *Chemical Reviews* **114,** 11503 (2014).

[26] Landesfeind, J. & Gasteiger, H. A. Temperature and concentration dependence of the ionic transport properties of lithium-ion battery electrolytes. *Journal of the Electrochemical Society* **166,** A3079 (2019).

[27] Heider, U., Oesten, R. & Jungnitz, M. Challenge in manufacturing electrolyte solutions for lithium and lithium ion batteries quality control and minimizing contamination level. *Journal of Power Sources* **81-82,** 119 (1999).

[28] Myung, S.-T., Hitoshi, Y. & Sun, Y.-K. Electrochemical behavior and passivation of current collectors in lithium-ion batteries. *Journal of Materials Chemistry* **21,** 9891 (2011).

[29] Yang, H., Zhuang, G. V. & Ross, P. N. Thermal stability of $LiPF_6$ salt and Li-ion battery electrolytes containing $LiPF_6$. *Journal of Power Sources* **161,** 573 (2006).

[30] Solchenbach, S., Metzger, M., Egawa, M., Beyer, H. & Gasteiger, H. A. Quantification of PF_5 and POF_3 from Side Reactions of $LiPF_6$ in Li-Ion Batteries. *Journal of The Electrochemical Society* **165,** A3022 (2018).

[31] Jung, R., Metzger, M., Maglia, F., Stinner, C. & Gasteiger, H. A. Chemical versus electrochemical electrolyte oxidation on NMC111, NMC622, NMC811, LNMO, and conductive carbon. *The Journal of Physical Chemistry Letters* **8,** 48205 (2017).

[32] Metzger, M., Walke, P., Solchenbach, S., Salitra, G., Aurbach, D. & Gasteiger, H. A. Evaluating the High-Voltage Stability of Conductive Carbon and Ethylene Carbonate with Various Lithium Salts. *Journal of The Electrochemical Society* **167,** 160522 (2020).

[33] Zhang, B., Metzger, M., Solchenbach, S., Payne, M., Meini, S., Gasteiger, H. A., Garsuch, A. & Lucht, B. L. Role of 1,3-propane sultone and vinylene carbonate in solid electrolyte interface formation and gas generation. *The Journal of Physical Chemistry C* **119,** 11337 (2015).

[34] Peled, E. The Electrochemical Behavior of Alkali and Alkaline Earth Metals in Nonaqueous Battery Systems—The Solid Electrolyte Interphase Model. *Journal of The Electrochemical Society* **126,** 2047 (1979).

[35] Winter, M., Novak, P. & Monnier, A. Graphites for Lithium-Ion Cells: The Correlation of the First-Cycle Charge Loss with the Brunauer-Emmett-Teller Surface Area. *Journal of The Electrochemical Society* **145,** 428 (1998).

[36] Asenbauer, J., Eisenmann, T., Kuenzel, M., Kazzazi, A., Chen, Z. & Bresser, D. The success story of graphite as a lithium-ion anode material – fundamentals, remaining challenges, and recent developments including silicon (oxide) composites. *Sustainable Energy & Fuels* **4,** 5387 (2020).

[37] Peled, E. & Menkin, S. SEI: Past, Present and Future. *Journal of The Electrochemical Society* **164,** A1703 (2017).

[38] Jung, R., Metzger, M., Haering, D., Solchenbach, S., Marino, C., Tsiouvaras, N., Stinner, C. & Gasteiger, H. A. Consumption of Fluoroethylene Carbonate (FEC) on Si-C Composite Electrodes for Li-Ion Batteries. *Journal of The Electrochemical Society* **163,** A1705 (2016).

[39] Pritzl, D., Solchenbach, S., Wetjen, M. & Gasteiger, H. A. Analysis of Vinylene Carbonate (VC) as Additive in Graphite/$LiNi_{0.5}Mn_{1.5}O_4$ Cells. *Journal of The Electrochemical Society* **164,** A2625 (2017).

[40] Markevich, E., Salitra, G. & Aurbach, D. Fluoroethylene Carbonate as an Important Component for the Formation of an Effective Solid Electrolyte Interphase on Anodes and Cathodes for Advanced Li-Ion Batteries. *ACS Energy Letters* **2,** 1337 (2017).

[41] Ma, L., Ellis, L., Glazier, S. L., Ma, X. & Dahn, J. R. Combinations of $LiPO_2F_2$ and Other Electrolyte Additives in $Li[Ni_{0.5}Mn_{0.3}Co_{0.2}]O_2$/Graphite Pouch Cells. *Journal of The Electrochemical Society* **165,** A1718 (2018).

[42] Wetjen, M. *Studies on the Differentiation and Quantification of Degradation Phenomena in Silicon-Graphite Anodes for Lithium-Ion Batteries* PhD thesis (Technical University of Munich, 2018).

[43] Harlow, J. E., Ma, X., Li, J., Logan, E., Liu, Y., Zhang, N., Ma, L., Glazier, S. L., Cormier, M. M. E., Genovese, M., Buteau, S., Cameron, A., Stark, J. E. & Dahn, J. R. A Wide Range of Testing Results on an Excellent Lithium-Ion Cell Chemistry to be used as Benchmarks for New Battery Technologies. *Journal of The Electrochemical Society* **166,** A3031 (2019).

[44] Whittingham, M. S. The Role of Ternary Phases in Cathode Reactions. *Journal of The Electrochemical Society* **123,** 315 (1976).

[45] Whittingham, M. S. Electrical Energy Storage and Intercalation Chemistry. *Science* **192,** 1126 (1976).

[46] Markevich, E., Salitra, G., Chesneau, F., Schmidt, M. & Aurbach, D. Very Stable Lithium Metal Stripping-Plating at a High Rate and High Areal Capacity in Fluoroethylene Carbonate-Based Organic Electrolyte Solution. *ACS Energy Letters* **2,** 1321 (2017).

[47] Xue, W., Huang, M., Li, Y., Zhu, Y. G., Gao, R., Xiao, X., Zhang, W., Li, S., Xu, G., Yu, Y., Li, P., Lopez, J., Yu, D., Dong, Y., Fan, W., Shi, Z., Xiong, R., Sun, C.-J., Hwang, I., Lee, W.-K., Shao-Horn, Y., Johnson, J. A. & Li, J. Ultra-high-voltage Ni-rich layered cathodes in practical Li metal batteries enabled by a sulfonamide-based electrolyte. *Nature Energy* **6,** 495 (2021).

[48] Hobold, G. M., Lopez, J., Guo, R., Minafra, N., Banerjee, A., Meng, Y. S., Shao-Horn, Y. & Gallant, B. M. Moving beyond 99.9% Coulombic efficiency for lithium anodes in liquid electrolytes. *Nature Energy* **6,** 951 (2021).

[49] Weber, R., Genovese, M., Louli, A. J., Hames, S., Martin, C., Hill, I. G. & Dahn, J. R. Long cycle life and dendrite-free lithium morphology in anode-free lithium pouch cells enabled by a dual-salt liquid electrolyte. *Nature Energy* **4,** 683 (2019).

[50] Louli, A. J., Eldesoky, A., Weber, R., Genovese, M., Coon, M., DeGooyer, J., Deng, Z., White, R. T., Lee, J., Rodgers, T., Petibon, R., Hy, S., Cheng, S. J. H. & Dahn, J. R. Diagnosing and correcting anode-free cell failure via electrolyte and morphological analysis. *Nature Energy* **5,** 693 (2020).

[51] Eldesoky, A., Louli, A. J., Benson, A. & Dahn, J. R. Cycling Performance of NMC811 Anode-Free Pouch Cells with 65 Different Electrolyte Formulations. *Journal of The Electrochemical Society* **168,** 120508 (2021).

[52] Wandt, J., Jakes, P., Granwehr, J., Eichel, R.-A. & Gasteiger, H. A. Quantitative and time-resolved detection of lithium plating on graphite anodes in lithium ion batteries. *Materials Today* **21,** 231 (2018).

[53] Janakiraman, U., Garrick, T. R. & Fortier, M. E. Lithium Plating Detection Methods in Li-Ion Batteries. *Journal of The Electrochemical Society* **167,** 160552 (2020).

[54] Berg, C., Morasch, R., Graf, M. & Gasteiger, H. A. Comparison of Silicon and Graphite Anodes: Temperature-Dependence of Impedance Characteristics and Rate Performance. *Journal of The Electrochemical Society* **170,** 030534 (2023).

[55] Obrovac, M. N. & Chevrier, V. L. Alloy Negative Electrodes for Li-Ion Batteries. *Chemical Reviews* **114,** 11444 (2014).

[56] Wetjen, M., Solchenbach, S., Pritzl, D., Hou, J., Tileli, V. & Gasteiger, H. A. Morphological Changes of Silicon Nanoparticles and the Influence of Cutoff Potentials in Silicon-Graphite Electrodes. *Journal of The Electrochemical Society* **165,** A1503 (2018).

[57] Jantke, D., Bernhard, R., Hanelt, E., Buhrmester, T., Pfeiffer, J. & Haufe, S. Silicon-dominant anodes based on microscale silicon particles under partial lithiation with high capacity and cycle stability. *Journal of the Electrochemical Society* **166,** A3881 (2019).

[58] Graf, M., Berg, C., Bernhard, R., Haufe, S., Pfeiffer, J. & Gasteiger, H. A. Effect and Progress of the Amorphization Process for Microscale Silicon Particles under Partial Lithiation as Active Material in Lithium-Ion Batteries. *Journal of The Electrochemical Society* **169,** 020536 (2022).

[59] Schiele, A., Breitung, B., Mazilkin, A., Schweidler, S., Janek, J., Gumbel, S., Fleischmann, S., Burakowska-Meise, E., Sommer, H. & Brezesinski, T. Silicon Nanoparticles with a Polymer-Derived Carbon Shell for Improved Lithium-Ion Batteries: Investigation into Volume Expansion, Gas Evolution, and Particle Fracture. *ACS Omega* **3,** 16706 (2018).

[60] Dou, F., Shi, L., Chen, G. & Zhang, D. Silicon/Carbon Composite Anode Materials for Lithium-Ion Batteries. *Electrochemical Energy Reviews* **2,** 149 (2019).

[61] Manthiram, A. An Outlook on Lithium Ion Battery Technology. *ACS Central Science* **3,** 1063 (2017).

[62] Nitta, N., Wu, F., Lee, J. T. & Yushin, G. Li-ion battery materials: Present and future. *Materials Today* **18,** 252 (2015).

[63] He, Y.-B., Li, B., Liu, M., Zhang, C., Lv, W., Yang, C., Li, J., Du, H., Zhang, B., Yang, Q.-H., Kim, J.-K. & Kang, F. Gassing in $Li_4Ti_5O_{12}$-based batteries and its remedy. *Scientific Reports* **2,** 913 (2012).

[64] Bernhard, R., Meini, S. & Gasteiger, H. A. On-Line Electrochemical Mass Spectrometry Investigations on the Gassing Behavior of $Li_4Ti_5O_{12}$ Electrodes and Its Origins. *Journal of The Electrochemical Society* **161,** A497 (2014).

[65] Thackeray, M. M., F., D. W. I., Bruce, P. G. & Goodenough, J. B. Lithium Insertion into Manganese Spinels. *Materials Research Bulletin* **18,** 461 (1983).

[66] Gao, Y., Myrtle, K., Zhang, M., Reimers, J. N. & Dahn, J. R. Valence band of $LiNi_xMn_{2-x}O_4$ and its effects on the voltage profiles of $LiNi_xMn_{2-x}O_4$/Li electrochemical cells. *Physical Review B* **54,** 16670 (1996).

[67] Aurbach, D., Markovsky, B., Talyossef, Y., Salitra, G., Kim, H.-J. & Choi, S. Studies of cycling behavior, ageing, and interfacial reactions of $LiNi_{0.5}Mn_{1.5}O_4$ and carbon electrodes for lithium-ion 5-V cells. *Journal of Power Sources* **162,** 780 (2006).

[68] Leitner, K. W., Wolf, H., Garsuch, A., Chesneau, F. & Schulz-Dobrick, M. Electroactive separator for high voltage graphite/$LiNi_{0.5}Mn_{1.5}O_4$ lithium ion batteries. *Journal of Power Sources* **244,** 548 (2013).

[69] Pritzl, D. *Electrochemical Impedance Spectroscopy (EIS) and Surface Analysis of High-Energy Cathodes for Lithium-Ion Batteries* PhD thesis (Technical University of Munich, 2019).

[70] Padhi, A. K., Nanjundaswamy, K. S. & Goodenough, J. B. Phospho-olivines as Positive-Electrode Materials for Rechargeable Lithium Batteries. *Journal of The Electrochemical Society* **144,** 1188 (1997).

[71] Padhi, A. K., Nanjundaswamy, K. S., Masquelier, C., Okada, S. & Goodenough, J. B. Effect of Structure on the Fe^{3+}/Fe^{2+} Redox Couple in Iron Phosphates. *Journal of The Electrochemical Society* **144,** 1609 (1997).

[72] Wang, D., Wu, X., Wang, Z. & Chen, L. Cracking causing cyclic instability of $LiFePO_4$ cathode material. *Journal of Power Sources* **140,** 125 (2005).

[73] Chen, G., Song, X. & Richardson, T. J. Electron Microscopy Study of the $LiFePO_4$ to $FePO_4$ Phase Transition. *Electrochemical and Solid-State Letters* **9,** A295 (2006).

[74] Gabrisch, H., Wilcox, J. & Doeff, M. M. TEM Study of Fracturing in Spherical and Plate-like LiFePO$_4$ Particles. *Electrochemical and Solid-State Letters* **11,** A25 (2008).

[75] Xiao, J., Xu, W., Choi, D. & Zhang, J.-G. Synthesis and Characterization of Lithium Manganese Phosphate by a Precipitation Method. *Journal of The Electrochemical Society* **157,** A142 (2010).

[76] Lyle, E., Vaeli, R., Dutta, A. & Metzger, M. Melt Synthesis of Lithium Manganese Iron Phosphate: Part I. Composition, Physical Properties, Structural Analysis, and Charge/Discharge Cycling. *Journal of The Electrochemical Society* **169,** 060526 (2022).

[77] Lyle, E., Vaeli, R., Cormier, M. & Metzger, M. Melt Synthesis of Lithium Manganese Iron Phosphate: Part II. Particle Size, Electrochemical Performance, and Solid-State Lithium Diffusion. *Journal of The Electrochemical Society* **169,** 060527 (2022).

[78] Mizushima, K., Jones, P. C., Wiseman, P. J. & Goodenough, J. B. Li$_x$CoO$_2$ ($0 < x \leq 1$): A new cathode material for batteries of high energy density. *Materials Research Bulletin* **15,** 783 (1980).

[79] Lyu, Y., Wu, X., Wang, K., Feng, Z., Cheng, T., Liu, Y., Wang, M., Chen, R., Xu, L., Zhou, J., Lu, Y. & Guo, B. An Overview on the Advances of LiCoO$_2$ Cathodes for Lithium-Ion Batteries. *Advanced Energy Materials* **11,** 2000982 (2021).

[80] Lee, S. & Manthiram, A. Can Cobalt Be Eliminated from Lithium-Ion Batteries? *ACS Energy Letters* **7,** 3058 (2022).

[81] Schmuch, R., Wagner, R., Hörpel, G., Placke, T. & Winter, M. Performance and cost of materials for lithium-based rechargeable automotive batteries. *Nature Energy* **3,** 267 (2018).

[82] Lu, Z., MacNeil, D. D. & Dahn, J. R. Layered Li[Ni$_x$Co$_{1-2x}$Mn$_x$]O$_2$ cathode materials for lithium-ion batteries. *Electrochemical and Solid-State Letters* **4,** A200 (2001).

[83] MacNeil, D. D., Lu, Z. & Dahn, J. R. Structure and Electrochemistry of Li[Ni$_x$Co$_{1-2x}$Mn$_x$]O$_2$ ($0 \leq x \leq 1/2$). *Journal of The Electrochemical Society* **149,** A1332 (2002).

[84] Sun, Y.-K., Lee, D.-J., Lee, Y. J., Chen, Z. & Myung, S.-T. Cobalt-free nickel rich layered oxide cathodes for lithium-ion batteries. *ACS Applied Materials & Interfaces* **5,** 11434 (2013).

[85] Kim, U.-H., Jun, D.-W., Park, K.-J., Zhang, Q., Kaghazchi, P., Aurbach, D., Major, D. T., Goobes, G., Dixit, M., Leifer, N., Wang, C. M., Yan, P., Ahn, D., Kim, K.-H., Yoon, C. S. & Sun, Y.-K. Pushing the limit of layered transition metal oxide cathodes for high-energy density rechargeable Li ion batteries. *Energy & Environmental Science* **11,** 1271 (2018).

[86] Yoon, C. S., Ryu, H.-H., Park, G.-T., Kim, J.-H., Kim, K.-H. & Sun, Y.-K. Extracting maximum capacity from Ni-rich Li[Ni$_{0.95}$Co$_{0.025}$Mn$_{0.025}$]O$_2$ cathodes for high-energy-density lithium-ion batteries. *Journal of Materials Chemistry A* **6,** 4126 (2018).

[87] Li, J. & Manthiram, A. A Comprehensive Analysis of the Interphasial and Structural Evolution over Long-Term Cycling of Ultrahigh-Nickel Cathodes in Lithium-Ion Batteries. *Advanced Energy Materials* **9,** 1902731 (2019).

[88] Li, H., Zhang, N., Li, J. & Dahn, J. R. Updating the Structure and Electrochemistry of Li$_x$NiO$_2$ for $0 \leq x \leq 1$. *Journal of The Electrochemical Society* **165,** A2985 (2018).

[89] Bianchini, M., Roca-Ayats, M., Hartmann, P., Brezesinski, T. & Janek, J. There and Back Again—The Journey of LiNiO$_2$ as a Cathode Active Material. *Angewandte Chemie - International Edition* **58,** 10434 (2019).

[90] De Biasi, L., Schiele, A., Roca-Ayats, M., Garcia, G., Brezesinski, T., Hartmann, P. & Janek, J. Phase Transformation Behavior and Stability of LiNiO$_2$ Cathode Material for Li-Ion Batteries Obtained from In Situ Gas Analysis and Operando X-Ray Diffraction. *ChemSusChem* **12,** 2240 (2019).

[91] Kurzhals, P., Riewald, F., Bianchini, M., Sommer, H., Gasteiger, H. A. & Janek, J. The LiNiO$_2$ Cathode Active Material: A Comprehensive Study of Calcination Conditions and their Correlation with Physicochemical Properties. Part I. Structural Chemistry. *Journal of The Electrochemical Society* **168,** 110518 (2021).

[92] Riewald, F., Kurzhals, P., Bianchini, M., Sommer, H., Janek, J. & Gasteiger, H. A. The LiNiO$_2$ Cathode Active Material: A Comprehensive Study of Calcination Conditions and their Correlation with Physicochemical Properties Part II. Morphology. *Journal of The Electrochemical Society* **169,** 020529 (2022).

[93] Dahn, J. R., von Sacken, U. & Michal, C. A. Structure and electrochemistry of Li$_{1\pm y}$NiO$_2$ and a new Li$_2$NiO$_2$ phase with the Ni(OH)$_2$ structure. *Solid State Ionics* **44,** 87 (1990).

[94] Dahn, J. R., von Sacken, U., Juzkow, M. W. & Al-Janaby, H. Rechargeable LiNiO$_2$/Carbon Cells. *Journal of The Electrochemical Society* **138,** 2207 (1991).

[95] Ohzuku, T., Ueda, A. & Nagayama, M. Electrochemistry and Structural Chemistry of LiNiO$_2$ (R$\bar{3}$m) for 4 Volt Secondary Lithium Cells. *Journal of The Electrochemical Society* **140,** 1862 (1993).

[96] Noh, H.-J., Youn, S., Yoon, C. S. & Sun, Y.-K. Comparison of the structural and electrochemical properties of layered Li[Ni$_x$Co$_y$Mn$_z$]O$_2$ ($x = 1/3$, 0.5, 0.6, 0.7, 0.8 and 0.85) cathode material for lithium-ion batteries. *Journal of Power Sources* **233,** 121 (2013).

[97] Choi, J. & Manthiram, A. Structural and electrochemical characterization of the layered $LiNi_{0.5-y}Mn_{0.5-y}Co_{2y}O_2$ ($0 \leq 2y \leq 1$) cathodes. *Solid State Ionics* **176,** 2251 (2005).

[98] De Biasi, L., Kondrakov, A. O., Geßwein, H., Brezesinski, T., Hartmann, P. & Janek, J. Between Scylla and Charybdis: Balancing Among Structural Stability and Energy Density of Layered NCM Cathode Materials for Advanced Lithium-Ion Batteries. *The Journal of Physical Chemistry C* **121,** 26163 (2017).

[99] Jung, R., Morasch, R., Karayaylali, P., Phillips, K., Maglia, F., Stinner, C., Shao-Horn, Y. & Gasteiger, H. A. Effect of Ambient Storage on the Degradation of Ni-Rich Positive Electrode Materials (NMC811) for Li-Ion Batteries. *Journal of The Electrochemical Society* **165,** A132 (2018).

[100] Sicklinger, J., Metzger, M., Beyer, H., Pritzl, D. & Gasteiger, H. A. Ambient Storage Derived Surface Contamination of NCM811 and NCM111: Performance Implications and Mitigation Strategies. *Journal of The Electrochemical Society* **166,** A2322 (2019).

[101] Yoon, W.-S., Balasubramanian, M., Chung, K. Y., Yang, X.-Q., McBreen, J., Grey, C. P. & Fischer, D. A. Investigation of the charge compensation mechanism on the electrochemically Li-ion deintercalated $Li_{1-x}Co_{1/3}Ni_{1/3}Mn_{1/3}O_2$ electrode system by combination of soft and hard X-ray absorption spectroscopy. *Journal of the American Chemical Society* **127,** 17479 (2005).

[102] Shin, H. J., Kim, M., Kim, N., Jung, C., Chung, J. G., Kim, K. H. & Jeon, W. S. Local oxidation states of Ni, Co, and Mn atoms within pristine and charged $Li_xNi_{0.88}Co_{0.08}Mn_{0.04}O_2$ primary particles. *Journal of Physics and Chemistry of Solids* **148,** 109732 (2021).

[103] Lu, Z., Macneil, D. D. & Dahn, J. R. Layered Cathode Materials $Li[Ni_xLi_{(1/3-2x/3)}Mn_{(2/3-x/3)}]O_2$ for Lithium-Ion Batteries. *Electrochemical and Solid-State Letters* **4,** A191 (2001).

[104] Lu, Z., Beaulieu, L. Y., Donaberger, R. A., Thomas, C. L. & Dahn, J. R. Synthesis, Structure, and Electrochemical Behavior of $Li[Ni_xLi_{1/3-2x/3}Mn_{2/3-x/3}O2$. *Journal of The Electrochemical Society* **149,** A778 (2002).

[105] Thackeray, M. M., Kang, S.-H., Johnson, C. S., Vaughey, J. T., Benedek, R. & Hackney, S. A. Li_2MnO_3-stabilized $LiMO_2$ (M = Mn, Ni, Co) electrodes for lithium-ion batteries. *Journal of Materials Chemistry* **17,** 3112 (2007).

[106] Erickson, E. M., Schipper, F., Penki, T. R., Shin, J.-Y., Erk, C., Chesneau, F.-F., Markovsky, B. & Aurbach, D. Recent Advances and Remaining Challenges for Lithium Ion Battery Cathodes II. Lithium-Rich, $xLi_2MnO_3 \bullet (1\text{-}x)LiNi_aCo_bMn_cO_2$. *Journal of The Electrochemical Society* **164,** A6341 (2017).

[107] Teufl, T., Strehle, B., Müller, P., Gasteiger, H. A. & Mendez, M. A. Oxygen Release and Surface Degradation of Li- and Mn-Rich Layered Oxides in Variation of the Li_2MnO_3 Content. *Journal of The Electrochemical Society* **165,** A2718 (2018).

[108] Armstrong, R. A., Holzapfel, M., Novák, P., Kang, S.-H., Thackeray, M. M. & Bruce, P. G. Demonstrating Oxygen Loss and Associated Structural Reorganization in the Lithium Battery Cathode $Li[Ni_{0.2}Li_{0.2}Mn_{0.6}]O_2$. *Journal of the American Chemical Society* **128,** 8694 (2006).

[109] Strehle, B., Kleiner, K., Jung, R., Chesneau, F., Mendez, M., Gasteiger, H. A. & Piana, M. The Role of Oxygen Release from Li- and Mn-Rich Layered Oxides during the First Cycles Investigated by On-Line Electrochemical Mass Spectrometry. *Journal of The Electrochemical Society* **164,** A400 (2017).

[110] Croy, J. R., Kim, D., Balasubramanian, M., Gallagher, K., Kang, S.-H. & Thackeray, M. M. Countering the Voltage Decay in High Capacity $xLi_2MnO_3 \bullet (1-x)LiMO_2$ Electrodes (M=Mn, Ni, Co) for Li^+-Ion Batteries. *Journal of The Electrochemical Society* **159,** A781 (2012).

[111] Keil, P., Schuster, S. F., Wilhelm, J., Travi, J., Hauser, A., Karl, R. C. & Jossen, A. Calendar Aging of Lithium-Ion Batteries I. Impact of the Graphite Anode on Capacity Fade. *Journal of The Electrochemical Society* **163,** A1872 (2016).

[112] Birkl, C. R., Roberts, M. R., McTurk, E., Bruce, P. G. & Howey, D. A. Degradation diagnostics for lithium ion cells. *Journal of Power Sources* **341,** 373 (2017).

[113] Hartmann, L., Pritzl, D., Beyer, H. & Gasteiger, H. A. Evidence for Li^+/H^+ Exchange during Ambient Storage of Ni-Rich Cathode Active Materials. *Journal of The Electrochemical Society* **168,** 070507 (2021).

[114] Renfrew, S. E. & McCloskey, B. D. Residual Lithium Carbonate Predominantly Accounts for First Cycle CO_2 and CO Outgassing of Li-Stoichiometric and Li-Rich Layered Transition-Metal Oxides. *Journal of the American Chemical Society* **139,** 17853 (2017).

[115] Freiberg, A. T. S., Sicklinger, J., Solchenbach, S. & Gasteiger, H. A. Li_2CO_3 decomposition in Li-ion batteries induced by the electrochemical oxidation of the electrolyte and of electrolyte impurities. *Electrochimica Acta* **346,** 136271 (2020).

[116] Pritzl, D., Teufl, T., Freiberg, A. T. S., Strehle, B., Sicklinger, J., Sommer, H., Hartmann, P. & Gasteiger, H. A. Washing of nickel-rich cathode materials for lithium-ion batteries: Towards a mechanistic understanding. *Journal of the Electrochemical Society* **166,** A4056 (2019).

[117] Toma, T., Maezono, R. & Hongo, K. Electrochemical Properties and Crystal Structure of Li^+/H^+ Cation-Exchanged $LiNiO_2$. *ACS Applied Energy Materials* **3,** 4078 (2020).

[118] Zhou, Y., Hu, Z., Huang, Y., Wu, Y. & Hong, Z. Effect of solution wash on the electrochemical performance of $LiNi_{0.8}Co_{0.1}Mn_{0.1}O_2$ cathode materials. *Journal of Alloys and Compounds* **888,** 161584 (2021).

[119] Jung, R., Metzger, M., Maglia, F., Stinner, C. & Gasteiger, H. A. Oxygen Release and Its Effect on the Cycling Stability of $LiNi_xMn_yCo_zO_2$ (NMC) Cathode Materials for Li-Ion Batteries. *Journal of The Electrochemical Society* **164,** A1361 (2017).

[120] Wandt, J., Freiberg, A. T. S., Ogrodnik, A. & Gasteiger, H. A. Singlet oxygen evolution from layered transition metal oxide cathode materials and its implications for lithium-ion batteries. *Materials Today* **21,** 825 (2018).

[121] Freiberg, A. T. S., Roos, M. K., Wandt, J., De Vivie-Riedle, R. & Gasteiger, H. A. Singlet Oxygen Reactivity with Carbonate Solvents Used for Li-Ion Battery Electrolytes. *The Journal of Physical Chemistry A* **122,** 8828 (2018).

[122] Friedrich, F., Strehle, B., Freiberg, A. T. S., Kleiner, K., Day, S. J., Erk, C., Piana, M. & Gasteiger, H. A. Capacity Fading Mechanisms of NCM-811 Cathodes in Lithium-Ion Batteries Studied by X-ray Diffraction and Other Diagnostics. *Journal of The Electrochemical Society* **166,** A3760 (2019).

[123] Streich, D., Erk, C., Guéguen, A., Müller, P., Chesneau, F.-F. & Berg, E. J. Operando Monitoring of Early Ni-mediated Surface Reconstruction in Layered Lithiated Ni-Co-Mn Oxides. *The Journal of Physical Chemistry C* **121,** 13481 (2017).

[124] Li, N., Sallis, S., Papp, J. K., Wei, J., McCloskey, B. D., Yang, W. & Tong, W. Unraveling the Cationic and Anionic Redox Reactions in a Conventional Layered Oxide Cathode. *ACS Energy Letters* **4,** 2836 (2019).

[125] Choi, J. & Manthiram, A. Role of Chemical and Structural Stabilities on the Electrochemical Properties of Layered $LiNi_{1/3}Mn_{1/3}Co_{1/3}O_2$ Cathodes. *Journal of The Electrochemical Society* **152,** A1714 (2005).

[126] Wandt, J., Freiberg, A., Thomas, R., Gorlin, Y., Siebel, A., Jung, R., Gasteiger, H. A. & Tromp, M. Transition metal dissolution and deposition in Li-ion batteries investigated by operando X-ray absorption spectroscopy. *Journal of Materials Chemistry A* **4,** 18300 (2016).

[127] Jung, R., Linsenmann, F., Thomas, R., Wandt, J., Solchenbach, S., Maglia, F., Stinner, C., Tromp, M. & Gasteiger, H. A. Nickel, Manganese, and Cobalt Dissolution from Ni-Rich NMC and Their Effects on NMC622-Graphite Cells. *Journal of The Electrochemical Society* **166,** A378 (2019).

[128] Wachs, S. J., Behling, C., Ranninger, J., Möller, J., Mayrhofer, K. J. J. & Berkes, B. B. Online Monitoring of Transition-Metal Dissolution from a High-Ni-Content Cathode Material. *ACS Applied Materials & Interfaces* **13,** 33075 (2021).

[129] Ruff, Z., Xu, C. & Grey, C. P. Transition Metal Dissolution and Degradation in NMC811-Graphite Electrochemical Cells. *Journal of The Electrochemical Society* **168,** 060518 (2021).

[130] Thompson, L. M., Stone, W., Eldesoky, A., Smith, N. K., McFarlane, C. R. M., Kim, J. S., Johnson, M. B., Petibon, R. & Dahn, J. R. Quantifying Changes to the Electrolyte and Negative Electrode in Aged NMC532/Graphite Lithium-Ion Cells. *Journal of The Electrochemical Society* **165,** A2732 (2018).

[131] Thompson, L. M., Harlow, J. E., Eldesoky, A., Bauer, M. K. G., Cheng, J. H., Stone, W. S., Taskovic, T., McFarlane, C. R. M. & Dahn, J. R. Study of Electrolyte and Electrode Composition Changes vs Time in Aged Li-Ion Cells. *Journal of The Electrochemical Society* **168,** 020532 (2021).

[132] Solchenbach, S., Hong, G., Freiberg, A. T. S., Jung, R. & Gasteiger, H. A. Electrolyte and SEI Decomposition Reactions of Transition Metal Ions Investigated by On-Line Electrochemical Mass Spectrometry. *Journal of The Electrochemical Society* **165,** A3304 (2018).

[133] Delacourt, C., Kwong, A., Liu, X., Qiao, R., Yang, W. L., Lu, P., Harris, S. J. & Srinivasan, V. Effect of Manganese Contamination on the Solid-Electrolyte-Interphase Properties in Li-Ion Batteries. *Journal of The Electrochemical Society* **160,** A1099 (2013).

[134] Gilbert, J. A., Shkrob, I. A. & Abraham, D. P. Transition Metal Dissolution, Ion Migration, Electrocatalytic Reduction and Capacity Loss in Lithium-Ion Full Cells. *Journal of The Electrochemical Society* **164,** A389 (2017).

[135] Reimers, J. N. & Dahn, J. R. Electrochemical and In Situ X-Ray Diffraction Studies of Lithium Intercalation in Li_xCoO_2. *Journal of The Electrochemical Society* **139,** 2091 (1992).

[136] Amatucci, G. G., Tarascon, J. M. & Klein, L. C. CoO_2, The End Member of the Li_xCoO_2 Solid Solution. *Journal of The Electrochemical Society* **143,** 1114 (1996).

[137] Li, H., Liu, A., Zhang, N., Wang, Y., Yin, S., Wu, H. & Dahn, J. R. An Unavoidable Challenge for Ni-Rich Positive Electrode Materials for Lithium-Ion Batteries. *Chemistry of Materials* **31,** 7574 (2019).

[138] Kondrakov, A. O., Schmidt, A., Xu, J., Geßwein, H., Mönig, R., Hartmann, P., Sommer, H., Brezesinski, T. & Janek, J. Anisotropic Lattice Strain and Mechanical Degradation of High- and Low-Nickel NCM Cathode Materials for Li-Ion Batteries. *The Journal of Physical Chemistry C* **121,** 3286 (2017).

[139] Li, W., Asl, H. Y., Xie, Q. & Manthiram, A. Collapse of $LiNi_{1-x-y}Co_xMn_yO_2$ Lattice at Deep Charge Irrespective of Nickel Content in Lithium-Ion Batteries. *Journal of the American Chemical Society* **141,** 5097 (2019).

[140] Watanabe, S., Kinoshita, M., Hosokawa, T., Morigaki, K. & Nakura, K. Capacity fade of $LiAl_yNi_{1-x-y}Co_xO_2$ cathode for lithium-ion batteries during accelerated calendar and cycle life tests (surface analysis of $LiAl_yNi_{1-x-y}Co_xO_2$ cathode after cycle tests in restricted depth of discharge ranges). *Journal of Power Sources* **258,** 210 (2014).

[141] Ryu, H.-H., Namkoong, B., Kim, J.-H., Belharouak, I., Yoon, C. S. & Sun, Y.-K. Capacity Fading Mechanisms in Ni-Rich Single-Crystal NCM Cathodes. *ACS Energy Letters* **6,** 2726 (2021).

[142] Tian, F., Ben, L., Yu, H., Ji, H., Zhao, W., Iiu, Z., Monteiro, R., Ribas, R. M., Zhu, Y. & Huang, X. Understanding high-temperature cycling-induced crack evolution and associated atomic-scale structure in a Ni-rich $LiNi_{0.8}Co_{0.1}Mn_{0.1}O_2$ layered cathode material. *Nano Energy* **98,** 107222 (2022).

[143] Kim, J.-H., Kim, S. J., Yuk, T., Kim, J., Yoon, C. S. & Sun, Y.-K. Variation of Electronic Conductivity within Secondary Particles Revealing a Capacity-Fading Mechanism of Layered Ni-Rich Cathode. *ACS Energy Letters* **3,** 3002 (2018).

[144] Conforto, G., Ruess, R., Schröder, D., Trevisanello, E., Fantin, R., Richter, F. H. & Janek, J. Quantification of the Impact of Chemo-Mechanical Degradation on the Performance and Cycling Stability of NCM-Based Cathodes in Solid-State Li-Ion Batteries. *Journal of The Electrochemical Society* **168,** 070546 (2021).

[145] Ruess, R., Schweidler, S., Hemmelmann, H., Conforto, G., Bielefeld, A., Weber, D. A., Sann, J., Elm, M. T. & Janek, J. Influence of NCM Particle Cracking on Kinetics of Lithium-Ion Batteries with Liquid or Solid Electrolyte. *Journal of The Electrochemical Society* **167,** 100532 (2020).

[146] Delmas, C., Pérès, J. P., Rougier, A., Demourgues, A., Weill, F., Chadwick, A., Broussely, M., Perton, F., Biensan, P. & Willmann, P. On the behavior of the Li_xNiO_2 system: An electrochemical and structural overview. *Journal of Power Sources* **68,** 120 (1997).

[147] Li, W., Liu, X., Celio, H., Smith, P., Dolocan, A., Chi, M. & Manthiram, A. Mn versus Al in Layered Oxide Cathodes in Lithium-Ion Batteries: A Comprehensive Evaluation on Long-Term Cyclability. *Advanced Energy Materials* **8,** 1703154 (2018).

[148] Strehle, B., Friedrich, F. & Gasteiger, H. A. A Comparative Study of Structural Changes during Long-Term Cycling of NCM-811 at Ambient and Elevated Temperatures. *Journal of The Electrochemical Society* **168,** 050512 (2021).

[149] Rossen, E., Jones, C. D. W. & Dahn, J. R. Structure and electrochemistry of $Li_xMn_yNi_{1-y}O_2$. *Solid State Ionics* **57,** 311 (1992).

[150] Zhecheva, E. & Stoyanova, R. Stabilization of the layered crystal structure of $LiNiO_2$ by Co-substitution. *Solid State Ionics* **66,** 143 (1993).

[151] Zhang, N., Li, J., Li, H., Liu, A., Huang, Q., Ma, L., Li, Y. & Dahn, J. R. Structural, Electrochemical, and Thermal Properties of Nickel-Rich LiNi$_x$Mn$_y$Co$_z$O$_2$ Materials. *Chemistry of Materials* **30,** 8852 (2018).

[152] Jung, R., Strobl, P., Maglia, F., Stinner, C. & Gasteiger, H. A. Temperature Dependence of Oxygen Release from LiNi$_{0.6}$Mn$_{0.2}$Co$_{0.2}$O$_2$ (NMC622) Cathode Materials for Li-Ion Batteries. *Journal of The Electrochemical Society* **165,** A2869 (2018).

[153] Kasnatscheew, J., Röser, S., Börner, M. & Winter, M. Do Increased Ni Contents in LiNi$_x$Mn$_y$Co$_z$O$_2$ (NMC) Electrodes Decrease Structural and Thermal Stability of Li Ion Batteries? A Thorough Look by Consideration of the Li$^+$ Extraction Ratio. *ACS Applied Energy Materials* **2,** 7733 (2019).

[154] Ryu, H.-H., Park, G.-T., Yoon, C. S. & Sun, Y.-K. Suppressing detrimental phase transitions via tungsten doping of LiNiO$_2$ cathode for next-generation lithium-ion batteries. *Journal of Materials Chemistry A* **7,** 18580 (2019).

[155] Jindal, P. & Bhattacharya, J. Understanding the Thermal Runaway Behavior of Li-Ion Batteries through Experimental Techniques. *Journal of The Electrochemical Society* **166,** A2165 (2019).

[156] Wang, Z., Yang, H., Li, Y., Wang, G. & Wang, J. Thermal runaway and fire behaviors of large-scale lithium ion batteries with different heating methods. *Journal of Hazardous Materials* **379,** 120730 (2019).

[157] Bak, S.-M., Hu, E., Zhou, Y., Yu, X., Senanayake, S. D., Cho, S.-J., Kim, K.-B., Chung, K. Y., Yang, X.-Q. & Nam, K.-W. Structural changes and thermal stability of charged LiNi$_x$Mn$_y$Co$_z$O$_2$ cathode materials studied by combined in situ time-resolved XRD and mass spectroscopy. *ACS Applied Materials & Interfaces* **6,** 22594 (2014).

[158] Xia, J., Glazier, S. L., Petibon, R. & Dahn, J. R. Improving Linear Alkyl Carbonate Electrolytes with Electrolyte Additives. *Journal of The Electrochemical Society* **164,** A1239 (2017).

[159] Weber, D., Tripković, Đ., Kretschmer, K., Bianchini, M. & Brezesinski, T. Surface Modification Strategies for Improving the Cycling Performance of Ni-Rich Cathode Materials. *European Journal of Inorganic Chemistry* **2020,** 3117 (2020).

[160] Kim, J.-H., Ryu, H.-H., Kim, S. J., Yoon, C. S. & Sun, Y.-K. Degradation Mechanism of Highly Ni-Rich Li[Ni$_x$Co$_y$Mn$_{1-x-y}$]O$_2$ Cathodes with $x > 0.9$. *ACS Applied Materials & Interfaces* **11,** 30936 (2019).

[161] Langdon, J. & Manthiram, A. A perspective on single-crystal layered oxide cathodes for lithium-ion batteries. *Energy Storage Materials* **37,** 143 (2021).

[162] Sun, Y.-K., Myung, S.-T., Park, B.-C. & Yashiro, H. Improvement of the Electrochemical Properties of Li[Ni$_{0.5}$Mn$_{0.5}$]O$_2$ by AlF$_3$ Coating. *Journal of The Electrochemical Society* **155,** A705 (2008).

[163] Zheng, J. M., Zhang, Z. R., Wu, X. B., Dong, Z. X., Zhu, Z. & Yang, Y. The Effects of AlF_3 Coating on the Performance of $Li[Li_{0.2}Mn_{0.54}Ni_{0.13}Co_{0.13}]O_2$ Positive Electrode Material for Lithium-Ion Battery. *Journal of The Electrochemical Society* **155,** A775 (2008).

[164] Tesfamhret, Y., Younesi, R. & Berg, E. J. Influence of Al_2O_3 Coatings on HF Induced Transition Metal Dissolution from Lithium-Ion Cathodes. *Journal of The Electrochemical Society* **169,** 010530 (2022).

[165] Bao, W., Qian, G., Zhao, L., Yu, Y., Su, L., Cai, X., Zhao, H., Zuo, Y., Zhang, Y., Li, H., Peng, Z., Li, L. & Xie, J. Simultaneous Enhancement of Interfacial Stability and Kinetics of Single-Crystal $LiNi_{0.6}Mn_{0.2}Co_{0.2}O_2$ through Optimized Surface Coating and Doping. *Nano Letters* **20,** 8832 (2020).

[166] Sun, Y.-K., Myung, S.-T., Park, B.-C. & Amine, K. Synthesis of Spherical Nano- to Microscale Core-Shell Particles $Li[(Ni_{0.8}Co_{0.1}Mn_{0.1})_{1-x}(Ni_{0.5}Mn_{0.5})_x]O_2$ and their Applications to Lithium Batteries. *Chemistry of Materials,* 5159 (2006).

[167] Sun, Y.-K., Myung, S.-T., Park, B.-C., Prakash, J., Belharouak, I. & Amine, K. High-energy cathode material for long-life and safe lithium batteries. *Nature Materials* **8,** 320 (2009).

[168] Liao, J.-Y. & Manthiram, A. Surface-modified concentration-gradient Ni-rich layered oxide cathodes for high-energy lithium-ion batteries. *Journal of Power Sources* **282,** 429 (2015).

[169] Yoon, C. S., Park, K.-J., Kim, U.-H., Kang, K. H., Ryu, H.-H. & Sun, Y.-K. High-Energy Ni-Rich $Li[Ni_xCo_yMn_{1-x-y}]O_2$ Cathodes via Compositional Partitioning for Next-Generation Electric Vehicles. *Chemistry of Materials* **29,** 10436 (2017).

[170] Liu, T., Yu, L., Lu, J., Zhou, T., Huang, X., Cai, Z., Dai, A., Gim, J., Ren, Y., Xiao, X., Holt, M. V., Chu, Y. S., Arslan, I., Wen, J. & Amine, K. Rational design of mechanically robust Ni-rich cathode materials via concentration gradient strategy. *Nature Communications* **12,** 6024 (2021).

[171] Park, K.-J., Jung, H.-G., Kuo, L.-Y., Kaghazchi, P., Yoon, C. S. & Sun, Y.-K. Improved Cycling Stability of $Li[Ni_{0.90}Co_{0.05}Mn_{0.05}]O_2$ Through Microstructure Modification by Boron Doping for Li-Ion Batteries. *Advanced Energy Materials* **8,** 1801202 (2018).

[172] Kim, Y. S., Kim, J. H., Sun, Y.-K. & Yoon, C. S. Evolution of a Radially Aligned Microstructure in Boron-Doped $Li[Ni_{0.95}Co_{0.04}Al_{0.01}]O_2$ Cathode Particles. *ACS Applied Materials & Interfaces* **14,** 17500 (2022).

[173] Kim, H., Lee, S., Cho, H., Kim, J., Lee, J., Park, S., Joo, S. H., Kim, S. H., Cho, Y.-G., Song, H.-K., Kwak, S. K. & Cho, J. Enhancing Interfacial Bonding between Anisotropically Oriented Grains Using a Glue-Nanofiller for Advanced Li-Ion Battery Cathode. *Advanced Materials* **28,** 4705 (2016).

[174] Yan, P., Zheng, J., Liu, J., Wang, B., Cheng, X., Zhang, Y., Sun, X., Wang, C. & Zhang, J.-G. Tailoring grain boundary structures and chemistry of Ni-rich layered cathodes for enhanced cycle stability of lithium-ion batteries. *Nature Energy* **3,** 600 (2018).

[175] Rathore, D., Geng, C., Zaker, N., Hamam, I., Liu, Y., Xiao, P., Botton, G. A., Dahn, J. R. & Yang, C. Tungsten Infused Grain Boundaries Enabling Universal Performance Enhancement of Co-Free Ni-Rich Cathode Materials. *Journal of The Electrochemical Society* **168,** 120514 (2021).

[176] Han, X., Meng, Q., Sun, T. & Sun, J. Preparation and electrochemical characterization of single-crystalline spherical $LiNi_{1/3}Co_{1/3}Mn_{1/3}O_2$ powders cathode material for Li-ion batteries. *Journal of Power Sources* **195,** 3047 (2010).

[177] Kim, Y. Lithium Nickel Cobalt Manganese Oxide Synthesized Using Alkali Chloride Flux: Morphology and Performance As a Cathode Material for Lithium Ion Batteries. *ACS Applied Materials & Interfaces* **4,** 2329 (2012).

[178] Li, J., Cameron, A. R., Li, H., Glazier, S., Xiong, D., Chatzidakis, M., Allen, J., Botton, G. A. & Dahn, J. R. Comparison of Single Crystal and Polycrystalline $LiNi_{0.5}Mn_{0.3}Co_{0.2}O_2$ Positive Electrode Materials for High Voltage Li-Ion Cells. *Journal of The Electrochemical Society* **164,** A1534 (2017).

[179] Liu, G., Li, M., Wu, N., Cui, L., Huang, X., Liu, X., Zhao, Y., Chen, H., Yuan, W. & Bai, Y. Single-Crystalline Particles: An Effective Way to Ameliorate the Intragranular Cracking, Thermal Stability, and Capacity Fading of the $LiNi_{0.6}Co_{0.2}Mn_{0.2}O_2$ Electrodes. *Journal of The Electrochemical Society* **165,** A3040 (2018).

[180] Fan, X., Hu, G., Zhang, B., Ou, X., Zhang, J., Zhao, W., Jia, H., Zou, L., Li, P. & Yang, Y. Crack-free single-crystalline Ni-rich layered NCM cathode enable superior cycling performance of lithium-ion batteries. *Nano Energy* **70,** 104450 (2020).

[181] He, W., Li, X., Chen, J., Peng, F., Zhang, R., Liu, Y. & Xiao, Z. Effects of ionothermal and hydrothermal methods on structure and electrochemical performance of $LiNi_{1/3}Co_{1/3}Mn_{1/3}O_2$ cathode materials. *Materials Chemistry and Physics* **155,** 9 (2015).

[182] Zhang, Y., Du, K., Cao, Y., Lu, Y., Peng, Z., Fan, J., Li, L., Xue, Z., Su, H. & Hu, G. Hydrothermal preparing agglomerate $LiNi_{0.8}Co_{0.1}Mn_{0.1}O_2$ cathode material with submicron primary particle for alleviating microcracks. *Journal of Power Sources* **477,** 228701 (2020).

[183] Zheng, L., Bennett, J. C. & Obrovac, M. N. All-Dry Synthesis of Single Crystal NMC Cathode Materials for Li-Ion Batteries. *Journal of The Electrochemical Society* **167,** 130536 (2020).

[184]   Duan, J., Wu, C., Cao, Y., Huang, D., Du, K., Peng, Z. & Hu, G. Enhanced compacting density and cycling performance of Ni-riched electrode via building mono dispersed micron scaled morphology. *Journal of Alloys and Compounds* **695,** 91 (2017).

[185]   Schreiner, D., Zünd, T., Günter, F. J., Kraft, L., Stumper, B., Linsenmann, F., Schüßler, M., Wilhelm, R., Jossen, A., Reinhart, G. & Gasteiger, H. A. Comparative Evaluation of LMR-NCM and NCA Cathode Active Materials in Multilayer Lithium-Ion Pouch Cells: Part I. Production, Electrode Characterization, and Formation. *Journal of The Electrochemical Society* **168,** 030507 (2021).

[186]   Thommes, M., Kaneko, K., Neimark, A. V., Olivier, J. P., Rodriguez-Reinoso, F., Rouquerol, J. & Sing, K. S. W. Physisorption of gases, with special reference to the evaluation of surface area and pore size distribution (IUPAC Technical Report). *Pure and Applied Chemistry* **87,** 1051 (2015).

[187]   Brunauer, S., Emmett, P. H. & Teller, E. Adsorption of Gases in Multimolecular Layers. *Journal of the American Chemical Society* **60,** 309 (1938).

[188]   Beebe, R. A., Beckwith, J. B. & Honig, J. M. The Determination of Small Surface Areas by Krypton Adsorption at Low Temperatures. *Journal of the American Chemical Society* **67,** 1554 (1945).

[189]   Smith, A. J., Burns, J. C., Xiong, D. & Dahn, J. R. Interpreting High Precision Coulometry Results on Li-ion Cells. *Journal of The Electrochemical Society* **158,** A1136 (2011).

[190]   Langdon, J. & Manthiram, A. Crossover Effects in Batteries with High-Nickel Cathodes and Lithium-Metal Anodes. *Advanced Functional Materials* **31,** 2010267 (2021).

[191]   Wetjen, M., Pritzl, D., Jung, R., Solchenbach, S., Ghadimi, R. & Gasteiger, H. A. Differentiating the Degradation Phenomena in Silicon-Graphite Electrodes for Lithium-Ion Batteries. *Journal of The Electrochemical Society* **164,** A2840 (2017).

[192]   Wetjen, M., Trunk, M., Werner, L., Gernhäuser, R., Märkisch, B., Révay, Z., Gilles, R. & Gasteiger, H. A. Quantifying the Distribution of Electrolyte Decomposition Products in Silicon-Graphite Electrodes by Neutron Depth Profiling. *Journal of The Electrochemical Society* **165,** A2340 (2018).

[193]   Dose, W. M., Piernas-Muñoz, M. J., Maroni, V. A., Trask, S. E., Bloom, I. & Johnson, C. S. Capacity fade in high energy silicon-graphite electrodes for lithium-ion batteries. *Chemical Communications* **54,** 3586 (2018).

[194]   Metzger, M. *Studies on Fundamental Materials Degradation Mechanisms in Lithium-ion Batteries via On-line Electrochemical Mass Spectrometry* PhD thesis (Technical University of Munich, 2017).

[195] Dreyer, S. L., Kondrakov, A., Janek, J. & Brezesinski, T. In situ analysis of gas evolution in liquid and solid-electrolyte-based batteries with current and next-generation cathode materials. *Journal of Materials Research* **37,** 3146 (2022).

[196] Papp, J. K., Li, N., Kaufman, L. A., Naylor, A. J., Younesi, R., Tong, W. & McCloskey, B. D. A comparison of high voltage outgassing of $LiCoO_2$, $LiNiO_2$, and Li_2MnO_3 layered Li-ion cathode materials. *Electrochimica Acta* **368,** 137505 (2021).

[197] Imhof, R. & Novák, P. Oxidative Electrolyte Solvent Degradation in Lithium-Ion Batteries. An In Situ Differential Electrochemical Mass Spectrometry Investigation. *Journal of The Electrochemical Society* **146,** 1702 (1999).

[198] Schwenke, K. U., Solchenbach, S., Demeaux, J., Lucht, B. L. & Gasteiger, H. A. The Impact of CO_2 Evolved from VC and FEC during Formation of Graphite Anodes in Lithium-Ion Batteries. *Journal of The Electrochemical Society* **166,** A2035 (2019).

[199] Guéguen, A., Bolli, C., Mendez, M. A. & Berg, E. J. Elucidating the Reactivity of Tris(trimethylsilyl)phosphite and Tris(trimethylsilyl)phosphate Additives in Carbonate Electrolytes – A Comparative Online Electrochemical Mass Spectrometry Study. *ACS Applied Energy Materials* **3,** 290 (2020).

[200] Bernhard, R., Metzger, M. & Gasteiger, H. A. Gas Evolution at Graphite Anodes Depending on Electrolyte Water Content and SEI Quality Studied by On-Line Electrochemical Mass Spectrometry. *Journal of The Electrochemical Society* **162,** A1984 (2015).

[201] Metzger, M., Marino, C., Sicklinger, J., Haering, D. & Gasteiger, H. A. Anodic Oxidation of Conductive Carbon and Ethylene Carbonate in High-Voltage Li-Ion Batteries Quantified by On-Line Electrochemical Mass Spectrometry. *Journal of The Electrochemical Society* **162,** A1123 (2015).

[202] Metzger, M., Strehle, B., Solchenbach, S. & Gasteiger, H. A. Origin of H_2 Evolution in LIBs: H_2O Reduction vs. Electrolyte Oxidation. *Journal of The Electrochemical Society* **163,** A798 (2016).

[203] Guéguen, A., Streich, D., He, M., Mendez, M., Chesneau, F. F., Novák, P. & Berg, E. J. Decomposition of $LiPF_6$ in High Energy Lithium-Ion Batteries Studied with Online Electrochemical Mass Spectrometry. *Journal of The Electrochemical Society* **163,** A1095 (2016).

[204] Tsiouvaras, N., Meini, S., Buchberger, I. & Gasteiger, H. A. A Novel On-Line Mass Spectrometer Design for the Study of Multiple Charging Cycles of a Li-O_2 Battery. *Journal of The Electrochemical Society* **160,** A471 (2013).

[205] Oswald, S., Riewald, F. & Gasteiger, H. A. Novel Method for Monitoring the Electrochemical Capacitance by In Situ Impedance Spectroscopy as Indicator for Particle Cracking of Nickel-Rich NCMs: Part III. Development of a Simplified Measurement Setup. *Journal of The Electrochemical Society* **169,** 040552 (2022).

[206] Ogihara, N., Kawauchi, S., Okuda, C., Itou, Y., Takeuchi, Y. & Ukyo, Y. Theoretical and experimental analysis of porous electrodes for lithium-ion batteries by electrochemical impedance spectroscopy using a symmetric cell. *Journal of the Electrochemical Society* **159,** A1034 (2012).

[207] Ogihara, N., Itou, Y., Sasaki, T. & Takeuchi, Y. Impedance spectroscopy characterization of porous electrodes under different electrode thickness using a symmetric cell for high-performance lithium-ion batteries. *The Journal of Physical Chemistry C* **119,** 4612 (2015).

[208] Solchenbach, S., Pritzl, D., Kong, E. J. Y., Landesfeind, J. & Gasteiger, H. A. A Gold Micro-Reference Electrode for Impedance and Potential Measurements in Lithium Ion Batteries. *Journal of The Electrochemical Society* **163,** A2265 (2016).

[209] Ma, X., Harlow, J. E., Li, J., Ma, L., Hall, D. S., Buteau, S., Genovese, M., Cormier, M. & Dahn, J. R. Hindering Rollover Failure of Li[Ni$_{0.5}$Mn$_{0.3}$Co$_{0.2}$]O$_2$/ Graphite Pouch Cells during Long-Term Cycling. *Journal of The Electrochemical Society* **166,** A711 (2019).

[210] Linsenmann, F., Pritzl, D. & Gasteiger, H. A. A reference electrode for in situ impedance measurements in sodium-ion batteries. *Journal of the Electrochemical Society* **166,** A3668 (2019).

[211] Aiken, C. P., Harlow, J. E., Tingley, R., Hynes, T., Logan, E. R., Glazier, S. L., Keefe, A. S. & Dahn, J. R. Accelerated Failure in Li[Ni$_{0.5}$Mn$_{0.3}$Co$_{0.2}$]O$_2$/ Graphite Pouch Cells Due to Low LiPF$_6$ Concentration and Extended Time at High Voltage. *Journal of The Electrochemical Society* **167,** 130541 (2020).

[212] Liu, Y., Ma, L. & Dahn, J. R. Designing Positive/Positive and Negative/Negative Symmetric Cells with Electrodes Operating in the Same Potential Ranges as Electrodes in a Full Li-Ion Cell. *Journal of The Electrochemical Society* **168,** 080537 (2021).

[213] Brug, G. J., van den Eeden, A. L. G., Sluyters-Rehbach, M. & Sluyters, J. H. The analysis of electrode impedances complicated by the presence of a constant phase element. *Journal of Electroanalytical Chemistry* **176,** 275 (1984).

[214] Hirschorn, B., Orazem, M. E., Tribollet, B., Vivier, V., Frateur, I. & Musiani, M. Determination of effective capacitance and film thickness from constant-phase-element parameters. *Electrochimica Acta* **55,** 6218 (2010).

[215] Orazem, M. E., Frateur, I., Tribollet, B., Vivier, V., Marcelin, S., Pébère, N., Bunge, A. L., White, E. A., Riemer, D. P. & Musiani, M. Dielectric Properties of Materials Showing Constant-Phase-Element (CPE) Impedance Response. *Journal of The Electrochemical Society* **160,** C215 (2013).

[216] Hauck, B., Weiss, M. & Ivers-Tiffée, E. Physically Based Voltage Prediction for Lithium-Ion Batteries Using Transmission Line Models. *ECS Meeting Abstracts* **MA2021-02,** 416 (2021).

[217] De Levie, R. On Porous Electrodes in Electrolyte Solutions–IV. *Electrochimica Acta* **9,** 1231 (1964).

[218] Landesfeind, J., Hattendorff, J., Ehrl, A., Wall, W. A. & Gasteiger, H. A. Tortuosity Determination of Battery Electrodes and Separators by Impedance Spectroscopy. *Journal of The Electrochemical Society* **163,** A1373 (2016).

[219] Landesfeind, J., Pritzl, D. & Gasteiger, H. A. An analysis protocol for three-electrode Li-ion battery impedance spectra: Part I. Analysis of a high-voltage positive electrode. *Journal of the Electrochemical Society* **164,** A1773 (2017).

[220] Drvarič Talian, S., Bobnar, J., Sinigoj, A. R., Humar, I. & Gaberscek, M. Transmission Line Model for Description of the Impedance Response of Li Electrodes with Dendritic Growth. *The Journal of Physical Chemistry C* **123,** 27997 (2019).

[221] Moškon, J., Žuntar, J., Drvarič Talian, S., Dominko, R. & Gaberšček, M. A Powerful Transmission Line Model for Analysis of Impedance of Insertion Battery Cells: A Case Study on the NMC-Li System. *Journal of The Electrochemical Society* **167,** 140539 (2020).

[222] Moškon, J. & Gaberšček, M. Transmission line models for evaluation of impedance response of insertion battery electrodes and cells. *Journal of Power Sources Advances* **7,** 100047 (2021).

[223] Solchenbach, S., Huang, X., Pritzl, D., Landesfeind, J. & Gasteiger, H. A. Monitoring SEI Formation on Graphite Electrodes in Lithium-Ion Cells by Impedance Spectroscopy. *Journal of The Electrochemical Society* **168,** 110503 (2021).

[224] Oswald, S., Pritzl, D., Wetjen, M. & Gasteiger, H. A. Novel Method for Monitoring the Electrochemical Capacitance by In Situ Impedance Spectroscopy as Indicator for Particle Cracking of Nickel-Rich NCMs: Part I. Theory and Validation. *Journal of The Electrochemical Society* **167,** 100511 (2020).

[225] Amin, R. & Chiang, Y.-M. Characterization of Electronic and Ionic Transport in $Li_{1-x}Ni_{0.33}Mn_{0.33}Co_{0.33}O_2$ (NMC_{333}) and $Li_{1-x}Ni_{0.50}Mn_{0.20}Co_{0.30}O_2$ (NMC_{523}) as a Function of Li Content. *Journal of The Electrochemical Society* **163,** A1512 (2016).

[226] Morasch, R., Keilhofer, J., Gasteiger, H. A. & Suthar, B. Understanding Porous Electrode Impedance and the Implications for the Impedance Analysis of Li-Ion Battery Electrodes. *Journal of The Electrochemical Society* **168,** 080519 (2021).

[227] De Levie, R. The influence of surface roughness of solid electrodes on electrochemical measurements. *Electrochimica Acta* **10,** 113 (1965).

[228] Rammelt, U. & Reinhard, G. On the applicability of a constant phase element (CPE) to the estimation of roughness of solid metal electrodes. *Electrochimica Acta* **35,** 1045 (1990).

[229] Barbieri, O., Hahn, M., Herzog, A. & Kötz, R. Capacitance limits of high surface area activated carbons for double layer capacitors. *Carbon* **43,** 1303 (2005).

[230] Chmiola, J., Yushin, G., Gogotsi, Y., Portet, C., Simon, P. & Taberna, P. L. Anomalous increase in carbon at pore sizes less than 1 nanometer. *Science* **313,** 1760 (2006).

[231] Ji, H., Zhao, X., Qiao, Z., Jung, J., Zhu, Y., Lu, Y., Zhang, L. L., MacDonald, A. H. & Ruoff, R. S. Capacitance of carbon-based electrical double-layer capacitors. *Nature Communications* **5,** 3317 (2014).

[232] Ramaley, L. & Enke, C. G. The Double Layer Capacitance of Silver in Perchlorate Solution. *Journal of The Electrochemical Society* **112,** 947 (1965).

[233] Liu, K.-C. & Anderson, M. A. Porous nickel oxide/nickel films for electrochemical capacitors. *Journal of The Electrochemical Society* **143,** 124 (1996).

[234] Pajkossy, T. & Kolb, D. M. Double layer capacitance of Pt(111) single crystal electrodes. *Electrochimica Acta* **46,** 3063 (2001).

[235] Germain, P. S., Pell, W. G. & Conway, B. E. Evaluation and origins of the difference between double-layer capacitance behaviour at Au-metal and oxidized Au surfaces. *Electrochimica Acta* **49,** 1775 (2004).

[236] Pajkossy, T. & Kolb, D. M. Double layer capacitance of the platinum group metals in the double layer region. *Electrochemistry Communications* **9,** 1171 (2007).

[237] Coats, A. W. & Redfern, J. P. Thermogravimetric Analysis. *Analyst* **88,** 906 (1963).

[238] Saadatkhah, N., Carillo Garcia, A., Ackermann, S., Leclerc, P., Latifi, M., Samih, S., Patience, G. S. & Chaouki, J. Experimental methods in chemical engineering: Thermogravimetric analysis—TGA. *The Canadian Journal of Chemical Engineering* **98,** 34 (2020).

[239] Faenza, N. V., Bruce, L., Lebens-Higgins, Z. W., Plitz, I., Pereira, N., Piper, L. F. J. & Amatucci, G. G. Growth of Ambient Induced Surface Impurity Species on Layered Positive Electrode Materials and Impact on Electrochemical Performance. *Journal of The Electrochemical Society* **164,** A3727 (2017).

[240] Chen, Z., Wang, J., Huang, J., Fu, T., Sun, G., Lai, S., Zhou, R., Li, K. & Zhao, J. The high-temperature and high-humidity storage behaviors and electrochemical degradation mechanism of $LiNi_{0.6}Co_{0.2}Mn_{0.2}O_2$ cathode material for lithium ion batteries. *Journal of Power Sources* **363,** 168 (2017).

[241] Besli, M. M., Shukla, A. K., Wei, C., Metzger, M., Alvarado, J., Boell, J., Nordlund, D., Schneider, G., Hellstrom, S., Johnston, C., Christensen, J., Doeff, M. M., Liu, Y. & Kuppan, S. Thermally-driven mesopore formation and oxygen release in delithiated NCA cathode particles. *Journal of Materials Chemistry A* **7,** 12593 (2019).

[242] Schweiger, H.-G., Obeidi, O., Komesker, O., Raschke, A., Schiemann, M., Zehner, C., Gehnen, M., Keller, M. & Birke, P. Comparison of several methods for determining the internal resistance of lithium ion cells. *Sensors* **10,** 5604 (2010).

[243] Schilcher, C., Meyer, C. & Kwade, A. Structural and Electrochemical Properties of Calendered Lithium Manganese Oxide Cathodes. *Energy Technology* **4,** 1604 (2016).

[244] Sangrós Giménez, C., Finke, B., Schilde, C., Froböse, L. & Kwade, A. Numerical simulation of the behavior of lithium-ion battery electrodes during the calendaring process via the discrete element method. *Powder Technology* **349,** 1–11 (2019).

[245] Schweidler, S., de Biasi, L., Garcia, G., Mazilkin, A., Hartmann, P., Brezesinski, T. & Janek, J. Investigation into Mechanical Degradation and Fatigue of High-Ni NCM Cathode Material: A Long-Term Cycling Study of Full Cells. *ACS Applied Energy Materials* **2,** 7375 (2019).

[246] Sun, H.-H. & Manthiram, A. Impact of microcrack generation and surface degradation on a nickel-rich layered $Li[Ni_{0.9}Co_{0.05}Mn_{0.05}]O_2$ cathode for lithium-ion batteries. *Chemistry of Materials* **29,** 8486 (2017).

[247] Landesfeind, J. *Determination of Physical and Electrochemical Parameters for Lithium-Ion Batteries and Advanced Electrochemical Impedance Analysis* PhD thesis (Technical University of Munich, 2018).

[248] Märker, K., Reeves, P. J., Xu, C., Griffith, K. J. & Grey, C. P. Evolution of Structure and Lithium Dynamics in $LiNi_{0.8}Mn_{0.1}Co_{0.1}O_2$ (NMC811) Cathodes during Electrochemical Cycling. *Chemistry of Materials* **31,** 2545 (2019).

[249] Ge, M., Wi, S., Liu, X., Bai, J., Ehrlich, S., Lu, D., Lee, W.-K., Chen, Z. & Wang, F. Kinetic Limitations in Single-Crystal High-Nickel Cathodes. *Angewandte Chemie - International Edition* **60,** 17350 (2021).

[250] Kang, S. D. & Chueh, W. C. Galvanostatic Intermittent Titration Technique Reinvented: Part I. A Critical Review. *Journal of The Electrochemical Society* **168,** 120504 (2021).

[251] Sim, R., Lee, S., Li, W. & Manthiram, A. Influence of Calendering on the Electrochemical Performance of Li[Ni$_{0.9}$Mn$_{0.05}$Al$_{0.05}$]O$_2$ Cathodes in Lithium-Ion Cells. *ACS Applied Materials & Interfaces* **13,** 42898 (2021).

[252] Oswald, S., Pritzl, D., Wetjen, M. & Gasteiger, H. A. Novel Method for Monitoring the Electrochemical Capacitance by In Situ Impedance Spectroscopy as Indicator for Particle Cracking of Nickel-Rich NCMs: Part II. Effect of Oxygen Release Dependent on Particle Morphology. *Journal of The Electrochemical Society* **168,** 120501 (2021).

[253] Pang, P., Tan, X., Wang, Z., Cai, Z., Nan, J., Xing, Z. & Li, H. Crack-free single-crystal LiNi$_{0.83}$Co$_{0.10}$Mn$_{0.07}$O$_2$ as cycling/thermal stable cathode materials for high-voltage lithium-ion batteries. *Electrochimica Acta* **365,** 137380 (2021).

[254] Zhang, H., Omenya, F., Yan, P., Luo, L., Whittingham, M. S., Wang, C. & Zhou, G. Rock-Salt Growth-Induced (003) Cracking in a Layered Positive Electrode for Li-Ion Batteries. *ACS Energy Letters* **2,** 2607 (2017).

[255] Yan, P., Zheng, J., Chen, T., Luo, L., Jiang, Y., Wang, K., Sui, M., Zhang, J.-G., Zhang, S. & Wang, C. Coupling of electrochemically triggered thermal and mechanical effects to aggravate failure in a layered cathode. *Nature Communications* **9,** 2437 (2018).

[256] Teichert, P., Jahnke, H. & Figgemeier, E. Degradation Mechanism of Monocrystalline Ni-Rich Li[Ni$_x$Mn$_y$Co$_z$]O$_2$ (NMC) Active Material in Lithium Ion Batteries. *Journal of The Electrochemical Society* **168,** 090532 (2021).

[257] Qian, G., Zhang, Y., Li, L., Zhang, R., Xu, J., Cheng, Z., Xie, S., Wang, H., Rao, Q., He, Y., Shen, Y., Chen, L., Tang, M. & Ma, Z.-F. Single-crystal nickel-rich layered-oxide battery cathode materials: synthesis, electrochemistry, and intra-granular fracture. *Energy Storage Materials* **27,** 140 (2020).

[258] Zheng, J., Yan, P., Estevez, L., Wang, C. & Zhang, J. G. Effect of calcination temperature on the electrochemical properties of nickel-rich LiNi$_{0.76}$Mn$_{0.14}$Co$_{0.10}$O$_2$ cathodes for lithium-ion batteries. *Nano Energy* **49,** 538 (2018).

[259] Park, G.-T., Park, N.-Y., Noh, T.-C., Namkoong, B., Ryu, H.-H., Shin, J.-Y., Beierling, T., Yoon, C. S. & Sun, Y.-K. High-performance Ni-rich Li[Ni$_{0.9-x}$Co$_{0.1}$Al$_x$]O$_2$ cathodes via multi-stage microstructural tailoring from hydroxide precursor to the lithiated oxide. *Energy & Environmental Science* **14,** 5084 (2021).

[260] Geng, C., Rathore, D., Heino, D., Zhang, N., Hamam, I., Zaker, N., Botton, G. A., Omessi, R., Phattharasupakun, N., Bond, T., Yang, C. & Dahn, J. R. Mechanism of Action of the Tungsten Dopant in LiNiO$_2$ Positive Electrode Materials. *Advanced Energy Materials,* 2103067 (2021).

[261] Li, J., Li, H., Stone, W., Weber, R., Hy, S. & Dahn, J. R. Synthesis of Single Crystal LiNi$_{0.5}$Mn$_{0.3}$Co$_{0.2}$O$_2$ for Lithium Ion Batteries. *Journal of The Electrochemical Society* **164,** 3529 (2017).

[262] Fantin, R., Trevisanello, E., Ruess, R., Pokle, A., Conforto, G., Richter, F. H., Volz, K. & Janek, J. Synthesis and Postprocessing of Single-Crystalline $LiNi_{0.8}Co_{0.15}Al_{0.05}O_2$ for Solid-State Lithium-Ion Batteries with High Capacity and Long Cycling Stability. *Chemistry of Materials* **33,** 2624 (2021).

[263] Shishino, K., Yamada, T., Fujisawa, K., Motoi, M., Hatakeyama, T. & Teshima, K. Growth of Polyhedral $LiNi_{0.5}Co_{0.2}Mn_{0.3}O_2$ Crystals in a Molten Li_3BO_3 Flux and Their Role in Electrode Density and Dispersion Design. *ACS Applied Energy Materials* **5,** 2747 (2022).

[264] Logan, E. R., Hebecker, H., Ma, X., Quinn, J., Yang, H. J., Kumakura, S., Paulsen, J. & Dahn, J. R. A Comparison of the Performance of Different Morphologies of $LiNi_{0.8}Mn_{0.1}Co_{0.1}O_2$ Using Isothermal Microcalorimetry, Ultra-High Precision Coulometry, and Long-Term Cycling. *Journal of The Electrochemical Society* **167,** 060530 (2020).

[265] Oswald, S., Bock, M. & Gasteiger, H. A. Elucidating the Implications of Morphology on Fundamental Characteristics of Nickel-Rich NCMs: Cracking, Gassing, Rate Capability, and Thermal Stability of Poly- and Single-Crystalline NCM622. *Journal of The Electrochemical Society* **169,** 050501 (2022).

[266] Trevisanello, E., Ruess, R., Conforto, G., Richter, F. H. & Janek, J. Polycrystalline and Single Crystalline NCM Cathode Materials—Quantifying Particle Cracking, Active Surface Area, and Lithium Diffusion. *Advanced Energy Materials,* 2003400 (2021).

[267] Pritzl, D., Bumberger, A. E., Wetjen, M., Landesfeind, J., Solchenbach, S. & Gasteiger, H. A. Identifying Contact Resistances in High-Voltage Cathodes by Impedance Spectroscopy. *Journal of The Electrochemical Society* **166,** A582 (2019).

[268] Hewston, T. A. & Chamberland, B. L. A Survey of First-Row Ternary Oxides $LiMO_2$, (M = Sc-Cu). *Journal of Physics and Chemistry of Solids* **48,** 97 (1987).

[269] Molenda, J., Wilk, P. & Marzec, J. Structural, Electrical and Electrochemical Properties of $LiNiO_2$. *Solid State Ionics* **146,** 73 (2002).

[270] Rao, K. V. & Smakula, A. Dielectric properties of cobalt oxide, nickel oxide, and their mixed crystals. *Journal of Applied Physics* **36,** 2031 (1965).

[271] Aiken, J. G. & Jordan, A. G. Electrical Transport Properties of Single Crystal Nickel Oxide. *Journal of Physics and Chemistry of Solids* **29,** 2153 (1968).

[272] Li, F., Kong, L., Sun, Y., Jin, Y. & Hou, P. Micron-sized monocrystalline $LiNi_{1/3}Co_{1/3}Mn_{1/3}O_2$ as high-volumetric-energy-density cathode for lithium-ion batteries. *Journal of Materials Chemistry A* **6,** 12344 (2018).

[273] Li, J., Li, H., Stone, W., Glazier, S. & Dahn, J. R. Development of Electrolytes for Single Crystal NMC532/Artificial Graphite Cells with Long Lifetime. *Journal of The Electrochemical Society* **165,** A626 (2018).

[274] Oswald, S. & Gasteiger, H. A. The Structural Stability Limit of Layered Lithium Transition Metal Oxides Due to Oxygen Release at High State of Charge and Its Dependence on the Nickel Content. *Journal of The Electrochemical Society* **170,** 030506 (2023).

[275] Kasnatscheew, J., Evertz, M., Kloepsch, R., Streipert, B., Wagner, R., Cekic Laskovic, I. & Winter, M. Learning from Electrochemical Data: Simple Evaluation and Classification of $LiMO_2$-type-based Positive Electrodes for Li-Ion Batteries. *Energy Technology* **5,** 1670 (2017).

[276] Kondrakov, A. O., Geßwein, H., Galdina, K., de Biasi, L., Meded, V., Filatova, E. O., Schumacher, G., Wenzel, W., Hartmann, P., Brezesinski, T. & Janek, J. Charge-transfer-induced lattice collapse in Ni-rich NCM cathode materials during delithiation. *The Journal of Physical Chemistry C* **121,** 24381 (2017).

List of Figures

Acknowledgment

The success of this project is owed to the many who contributed – without you, this work would not have been possible. I am grateful to all of you!

Most importantly, without doubt, I want to express my deepest gratitude to

<center>**Prof. Hubert A. Gasteiger**</center>

for his exceptional guidance and the invaluable support over the past years in your group. I am infinitely thankful to you – not only for sharing your knowledge about (electro)chemistry but especially for your genuine passion for science, your way of critical thinking, and your inspirational nature, all nourishing the growth and the productive atmosphere of the entire group. Thank you for this unique opportunity – it was a great pleasure!

Special thanks go to **Veronika Pichler**: your endless patience and your exceptional organizational skills shield the group members from the pitfalls of intransparent bureaucratic jungles and let us focus on our scientific work. Thank you for all your efforts!

I am incredibly grateful to **Morten Wetjen** and **Daniel Pritzl**, who introduced me to the electrochemistry of batteries and guided me during the project of master's thesis. Thank you for all your support – both scientifically and personally!

I am happy to have had the chance to work with **Louis Hartmann**, **Moritz Bock**, and **Rebecca Wilhelm**. Thank you for your commitment to your research projects during your master's theses – you were a great support and I learned a lot from you!

In addition to our professional cooperation, I am thankful to **Tanja Zünd**, **Maximilian Graf**, **Christian Sedlmeier**, and **Leon Katzenmeier** for their company during our mountaineering adventures – thank you for the many amazing experiences!

Even though not having any overlap in our scientific work, I want to thank **Björn Stühmeier** for the great company on our safari in South Africa and during our sailing trips on windy days at Lake Starnberg.

Thank you, **Moritz Bock**, **Jonas Dickmanns**, **Simon Helmer**, **Anna-Lena Klenk**, **Bernadine Rinkel**, **Benita Schmidt**, and **Rebecca Wilhelm**, for proofreading (parts of) this written thesis.

I want to thank my parents **Ulrike** and **Jens Oswald** for the their life-long trust and support that you have given me.

Lastly, I would like to thank my partner **Anna-Lena Klenk** for supporting me in her selfless and unconditional way at any time – I am incredibly thankful that you are part of my life!

Scientific Contributions

Peer-Reviewed Articles

Stefan Oswald*, and Hubert A. Gasteiger, "The Structural Stability Limit of Layered Lithium Transition Metal Oxides Due to Oxygen Release at High State of Charge and Its Dependence on the Nickel Content", *J. Electrochem. Soc.*, **170**, 030506 (2023), DOI: 10.1149/1945-7111/acbf80.

Stefan Oswald*, Moritz Bock, and Hubert A. Gasteiger, "Elucidating the Implications of Morphology on Fundamental Characteristics of Nickel-Rich NCMs: Cracking, Gassing, Rate Capability, and Thermal Stability of Poly- and Single-Crystalline NCM622", *J. Electrochem. Soc.*, **169**, 050501 (2022), DOI: 10.1149/1945-7111/ac5f7f.

Stefan Oswald$^{=,}$*, Felix Riewald$^{=}$, and Hubert A. Gasteiger, "Novel Method for Monitoring the Electrochemical Capacitance by In Situ Impedance Spectroscopy as Indicator for Particle Cracking of Nickel-Rich NCMs: Part III. Development of a Simplified Measurement Setup", *J. Electrochem. Soc.*, **169**, 040552 (2022), DOI: 10.1149/1945-7111/ac67b3.

Stefan Oswald*, Daniel Pritzl, Morten Wetjen, and Hubert A. Gasteiger, "Novel Method for Monitoring the Electrochemical Capacitance by In Situ Impedance Spectroscopy as Indicator for Particle Cracking of Nickel-Rich NCMs: Part II. Effect of Oxygen Release Dependent on Particle Morphology", *J. Electrochem. Soc.*, **168**, 120501 (2021), DOI: 10.1149/1945-7111/ac3905.

Stefan Oswald*, Daniel Pritzl, Morten Wetjen, and Hubert A. Gasteiger, "Novel Method for Monitoring the Electrochemical Capacitance by In Situ Impedance Spectroscopy as Indicator for Particle Cracking of Nickel-Rich NCMs: Part I. Theory and Validation", *J. Electrochem. Soc.*, **167**, 100511 (2020), DOI: 10.1149/1945-7111/ab9187.

Articles in Preparation

Stefan Oswald$^{=,*}$, Moritz Bock$^=$, and Hubert A. Gasteiger, "Elucidating the Implications of Particle Morphology on the Capacity Retention and the Impedance Build-Up of Nickel-Rich NCMs in Full-Cells: Poly- vs. Single-Crystalline NCM851005", *manuscript in preparation.*

Rebecca Wilhelm$^{=,*}$, **Stefan Oswald**$^=$ and Hubert A. Gasteiger, "A Comprehensive Study on the Effect of Washing on Nickel-Rich NCMs: Part II. Impact of the Protonation on the Electrochemical Performance", *manuscript in preparation.*

Stefan Oswald$^{=,*}$, Rebecca Wilhelm$^=$, and Hubert A. Gasteiger, "A Comprehensive Study on the Effect of Washing on Nickel-Rich NCMs: Part I. Methodology for the Quantification of the Proton Content and the Li$^+$/H$^+$-Exchange Kinetics", *manuscript in preparation.*

Stefan Oswald$^=$, Louis Hartmann$^{=,*}$, Daniel Pritzl, Cheuck Hin Ching, Maximilian Graf, and Hubert A. Gasteiger, "Washing of Nickel-Rich Cathode Materials for Lithium-Ion Batteries: Mechanistic Insights and Influence of Washing Parameters on Cycling Performance of NCM851005", *manuscript in preparation.*

Oral Presentations

Stefan Oswald and Hubert A. Gasteiger, "Determining the Structural Stability of (Nickel-Rich) NCMs in Dependence of Composition and State of Charge", Batteries Gordon Research Seminar (2022), Ventura, USA.

Stefan Oswald, Felix Riewald, and Hubert A. Gasteiger, "Monitoring the Electrochemical Capacitance by In Situ Impedance Spectroscopy as Indicator for Particle Cracking of (Nickel-Rich) Cathode Active Materials: Development of a Simplified Measurement Setup", 241st Meeting of the Electrochemical Society (2022), Vancouver, Canada, DOI: 10.1149/MA2022-012368mtgabs.

Stefan Oswald, Moritz Bock, and Hubert A. Gasteiger, "Elucidating the Effect of the Morphology of Ni-Rich Cathode Active Materials on Their Long-Term Cycling Performance: Poly- Vs. Single Crystalline NCM851005", 240th Meeting of the Electrochemical Society (2021), online meeting, DOI: 10.1149/MA2021-023368mtgabs.

Stefan Oswald, Moritz Bock, and Hubert A. Gasteiger, "Study on the Effect of Crystal Size on the Performance of Ni-Rich Cathode Active Materials: Poly- vs. Single

Crystalline NCM622", Pacific Rim Meeting of the Electrochemical Society (2020), online meeting, DOI: 10.1149/MA2020-021144mtgabs.

Stefan Oswald, Daniel Pritzl, Morten Wetjen, and Hubert A. Gasteiger, "Effect of Oxygen Release on the Morphology of Nickel-Rich CAMs Monitored by In Situ Impedance Spectroscopy", Electrochemistry Undercover 2020 meeting of the Gesellschaft Deutscher Chemiker (2020), online meeting.

Stefan Oswald, Daniel Pritzl, Morten Wetjen, and Hubert A. Gasteiger, "Monitoring the Electrochemical Capacitance by In Situ Impedance Spectroscopy as Indicator for Particle Degradation of Ni-Rich Cathode Active Materials", 70th Annual Meeting of the International Society of Electrochemistry, Durban, South Africa.

Poster Presentations

Stefan Oswald[=], Rebecca Wilhelm[=], László Szentmiklósi, Boglárka Maróti, Ildikó Harsányi, and Hubert A. Gasteiger, "Effect of Washing on Nickel-Rich NCMs: Part I. Methodology for the Quantification of the Proton Content and the Li^+/H^+-Exchange Kinetics", International Battery Association Conference (2022), Bled, Slovenia.

Stefan Oswald and Hubert A. Gasteiger, "Determining the Structural Stability of (Nickel-Rich) NCMs in Dependence of Composition and State of Charge", Batteries Gordon Research Conference (2022), Ventura, USA.

Stefan Oswald and Hubert A. Gasteiger, "Quantification of NCM and LFP Particle Breaking During Charge-Discharge Cycling Using Impedance Spectroscopy", Electrochemistry der Gesellschaft Deutscher Chemiker (2018), Ulm, Germany.

* Corresponding author.

= These authors contributed equally to this work.